UNIVERSITÉ DE RENNES 1

Universität Bremen

PHD THESIS

UNIVERSITE DE RENNES 1 AND UNIVERSITY BREMEN

ECOLE DOCTORALE N° 596   UNIVERSITY BREMEN
Matière, Molécules, Matériaux   *Fachbereich 02*
Specialization : « *Molecular Chemistry* »

by
« Jonas HOFFMANN »

« Synthesis and Characterization of Main Group Elements in Organic Structures »

Research Units :
Université Rennes 1
UFR Sciences et Propriété de la Matière
Institut des Sciences Chimiques de
Rennes (UMR 6226-CNRS)

Universität Bremen
Fachbereich 02
Institut für Organische und
Analytische Chemie

Referees prior defense :

Olivier SIRI   Directeur de Recherche CNRS, Université Aix-Marseille
Christian MÜLLER   Professor, Freie Universität Berlin

This thesis was defended on 02.03.2021 at the University of Bremen

Jury Composition:

President :	Jens BECKMANN	Professor, Universität Bremen
Examiner :	Olivier SIRI	Directeur de Recherche CNRS, Université Aix-Marseille
	Christian MÜLLER	Professor, Freie Universität Berlin
Supervisor :	Muriel HISSLER	Professor, Université de Rennes 1
Supervisor :	Anne STAUBITZ	Professor, Universität Bremen
Student :	Björn Grabbet	Student, Universität Bremen

Title : Synthesis and Characterization of Main Group Elements in Organic Structures

Key words : Organometallic Chemistry, Main Group Chemistry, PAH

Abstract : This thesis focused on the effect of main group elements in optical active materials (dyes) and pursued two major projects which are 1) influence of late group 14 elements on π-conjugated systems and functional materials 2) embedding of triel/pnictogene (group 13/15 elements) units in organic structures for superior optoelectronic properties. Initially, various trimethyl(tetrel)-substituted azobenzenes were prepared and used as a synthetic precursor for larger azobenzene-based structures. Furthermore, the effect of the respective tetrel towards the optical properties and switching behaviour was investigated. The second subject was to compare the optoelectronic properties of five-membered tin-containing heterocycles (stannoles) with their thiophene analogs and to further evaluate their electrochemical stability for electropolymerization processes. Then, the implementation of boron/nitrogen or boron/ phosphorus units in polycyclic aromatic hydrocarbons (PAHs) was studied. The BN-substitution of electron-accepting coronene diimides led to fascinating optical properties that were studied in solution, solid-state and additional in organic electronic devices (OLED/OFET). A combination with a strong electron-donating group located at the boron atom resulted in the formation of donor-acceptor-donor triads with narrower HOMO-LUMO gaps and bathochromic shifted absorption. Moreover, these systems held unique solvent-dependent luminescence and redox properties. Apart from well-established BN-chemistry, also BP-substituted PAHs were theoretically investigated and concepts towards their synthesis were developed. For this, a variety of *bis*(biphenyl)phosphines were synthesized and reacted with electrophilic boron species.

Titre : Synthèse et caractérisation des éléments du groupe principal dans les structures organiques

Mots clés : Chimie organométallique, Chimie du groupe principal, HAP

Résumé : Cette thèse s'est concentrée sur l'effet des principaux éléments du bloc p dans les matériaux à propriétés optiques (colorants) et s'est articulée autour de deux projets majeurs qui sont 1) l'influence de l'insertion des éléments lourds du groupe 14 dans les systèmes π-conjugués et les matériaux fonctionnels sur les propriétes optoélectroniques 2) l'incorporation d'unités triel/pnictogène (éléments du groupe 13/15) dans des structures organiques pour des nouveles propriétés optoélectroniques. Initialement, divers azobenzènes substitués par un tétrel de triméthyle ont été préparés et utilisés comme précurseurs synthétiques. En outre, l'effet du tétrel sur les propriétés optiques et le comportement de commutation a été étudié. Le deuxième sujet était de comparer les propriétés optoélectroniques d'hétérocycles à cinq chaînons contenant de l'étain (stannoles) avec leurs analogues de thiophène et d'évaluer davantage leur stabilité électrochimique pour les procédés d'électropolymérisation. Ensuite, l'incorporation d'unitees bore/azote ou bore/ phosphore dans les hydrocarbures aromatiques polycycliques (HAP) a été étudiée. La substitution BN des coronènes diimides acceptant les électrons a conduit à des propriétés optiques qui ont été étudiées en solution, à l'état solide ainsi que dans des dispositifs électroniques (OLED/OFET). L'insertion d'un groupe donneur d'électrons fort situé sur de l'atome de bore a entraîné la formation de triades donneur-accepteur-donneur avec des orbitales HO/BV plus proches et une absorption décalée vers le rouge. De plus, ces systèmes possédaient des propriétés uniques de luminescence et d'oxydoréduction dépendant du solvant. Outre la chimie bien établie des dérivé BN, les HAP substitués par la fonction BP ont également été étudiés de manière théorique et des concepts pour leur synthèse ont été développés. Pour cela, une variété de *bis*(biaryl)phosphines ont été synthétisées et mises en réaction avec des espèces de bore électrophiles.

Titre : Synthese und Charakterisierung von Hauptgruppenelementen in organischen Strukturen

Schlüsselwörter : Organometallchemie, Hauptpgruppenchemie, PAKs

Kurzzusammenfassung : Diese Arbeit behandelt den Effekt von Hauptgruppenelemente auf optische aktive Materialien (Farbstoffe) in zwei Hauptprojekten: 1) Der Einfluss von Elementen der Gruppe-14 auf π-konjugierte Systeme und Funktionsmaterialien. 2) Die Einbettung von Triel/Pncitogen-Einheiten in organische Strukturen zur Modifikation von optoelektronische Eigenschaften. Eingangs wurden Trimethyl(tetrel)-substituierte Azobenzole hergestellt, welche als synthetische Vorstufe für weitere funktionale Azofarbstoffe dienen können. In dem zweiten Projekt wurden fünfgliedrige konjugierte Heterozyklen, welche Zinn beinhalten (Stannole), herstellt und ihre physikalischen Eigenschaften mit ihren Thiophenanaloga verglichen. Weiterhin wurde die elektrochemische Stabilität der Stannole untersucht, um ihren Einsatz in Elektropolymerisationsreaktionen zu evaluieren. Anschließend wurde die Implementierung von Bor/Stickstoff oder Bor/Phosphor-Gruppen in polyzyklischen aromatischen Kohlenwasserstoffen (PAKs) erforscht. Die BN-Substitution von elektronarmen Coronendiimiden führte zu neuartigen optischen Eigenschaften, welche in Lösung, im Feststoff und in organischer Elektronik (OLED/OFET) untersucht wurden. Elektronenschiebende Substituenten an dem Boratom resultierten in der Bildung von Donor-Akzeptor-Donor-Einheiten mit schmaller HOMO-LUMO Lücke und rotverschobener Absorption. Weiterhin zeigten diese Systeme einzigartige, lösungsmittelabhängige Emission und interessante Redoxeigenschaften. Neben der bereits gut untersuchten BN-Chemie wurden weiterhin BP-substituierte PAHs theoretisch untersucht und Konzepte für deren Synthesen entwickelt. Hierfür wurde ein Auswahl von *bis*(Biaryl)phosphinen hergestellt und mit elektrophilen Borspezies umgesetzt.

„Lehre tut viel, aber Aufmunterung tut alles."

-   **Johann Wolfgang von Goethe**

Versicherung an Eides Statt

Ich, _____

.

versiche an Eides Statt durch meine Unterschrift, dass ich die vorstehende Arbeit selbständig und ohne fremde Hilfe angefertigt und alle Stellen, die ich wörtlich dem Sinne nach aus Veröffentlichungen entnommen habe, als solche kenntlich gemacht habe, mich auch keiner anderen als der angegebenen Literatur oder sonstiger Hilfsmittel bedient habe.

Ich versichere an Eides Statt, dass ich die vorgenannten Angaben nach bestem Wissen und Gewissen gemacht habe und dass die Angaben der Wahrheit entsprechen und ich nichts verschwiegen habe.

Die Strafbarkeit einer falschen eidesstattlichen Versicherung ist mir bekannt, namentlich die Strafandrohung gemäß § 156 StGB bis zu drei Jahren Freiheitsstrafe oder Geldstrafe bei vorsätzlicher Begehung der Tat bzw. gemäß § 161 Abs. 1 StGB bis zu einem Jahr Freiheitsstrafe oder Geldstrafe bei fahrlässiger Begehung.

_____
Ort, Datum Unterschrift

Universität Bremen

Ort, Datum: _____

AFFIDAVIT

I, _____

.

hereby affirm in lieu of oath that the present dissertation is my own work and that I have duly referenced all passages cited from publications, either literally or in content, and that I have not used any literature or aides other than those referenced. I hereby affirm that to the best of my knowledge and belief, all the information I have supplied is true and that I have not failed to disclose any relevant facts. I am aware that making false statements in lieu of oath is an offense that, in the event of intention, pursuant to § 156 StGB may be punished by fine or up to three years' imprisonment and, if committed by negligence, pursuant to § 161 Abs. 1 StGB by fine or up to one year's imprisonment.

_____
Lieu, Date Signature

Acknowledgements

I would like to express my gratitude to all those who gave me the possibility to complete this degree.

First and foremost, I offer my sincerest gratitude to Anne Staubitz, my Bachelor/Master/PhD director, who welcomed me in her group already in Kiel. Initially, this thesis started in Kiel till I mentioned the wish to move. Then, you organized the cooperation with Prof. Muriel Hissler in Rennes. I am still incredibly grateful for this support. Our ways merged in Bremen again and I guess that I speak for both of us that Bremen itself was a demanding situation. Over the years a quite remarkable scientific infrastructure was built in Bremen and this is also due to your afford. Thank you further for the support with several scholarships, reference letters and during the preparation of this thesis. And foremostly to give me the freedom to perform the research I wanted to investigate besides, we 'stretched' the borders of any grant.

I greatly appreciate Prof. Muriel Hissler for being my second supervisor. Since I started in Rennes, I was amazed by the facility, the quality of research, the internationality, and the professionality of the institute. It was something special to have scientific meetings and talks with you, as I was amazed by your scope and depth of knowledge. Furthermore, thanks for the cooperation you organized to manufacture the devices. I always enjoyed the numerous non-scientific talks in our office. They were always entertaining and hilarious. I guess the thin wall and our loud chatting baited you often in the office. I will not forget the time we spent repairing the electrochemical setup and leaving after 4 h without any finished experiment to come back the next day finishing the full workload in 1 h.

I also want to thank Prof. Dr. Christian Müller and Dr. Olivier Siri, for taking the time to examine my work.

Special thanks to Emmanuel Jacques (IETR Rennes) and Bernard Geffroy (LPICM Palaiseau) for the collaboration in the field of organic electronics.

Thanks to the member of the Kiel group, especially Matti and Jan-Ole, Nils and Katrin for a lot of fun and good company. Special thanks to Miriam, who was always present and had some helpful advice for the switching experiments. Further, Thorsten and Fynn are to be thanked for giving me access to computational services. The NMR department, Holger, Gitta, Marion and Frank for measurements of a lot of compounds, especially as the NMR of Bremen was just a big magnet with an old computer.

Thanks to all current and former members of the Staubitz lab for continuous support and the nice work atmosphere. Big thanks to the BN-lab members Phil and Yannik for constant cooperation and scientific exchange. Especially to Yannik who intensively checked a lot of this thesis prior. Also, thanks to Anne H. for proofreading. Thanks to the whole Nachtsheim group for unbureaucratic cooperation in numerous cases over the years. Thanks to Julia for supporting me with thermal analysis, scanning electron microscope measurements and an unlimited supply of coffee. Thanks to our mass spec department (Thomas and Dorit), who did an excellent job in measuring always sensitive, flammable, and toxic compounds with the highest resolution possible. Also, thanks to the NMR department operated by Mr. Stelten and Mr. Willker for setting up every possible hetero core. Big thanks to Dominik for endless evenings of working and discussing science, people and politics. I will never forget the trip to the US with endless car rides, speedy hiking tours and chemistry rock stars (Baran/Yu). Thanks to Enno, Marian and Daniel for the X-Ray analysis and the whole Beckmann group for good company. Special thanks go to Daniel for supporting during the BP-project and constant scientific

General Summary

This thesis describes the synthesis, characterization and photophysical properties of novel π-conjugated systems embedding the p-block elements: boron, nitrogen, phosphorus, silicon, germanium and tin.

Preface A: Influence of heavy group 14 elements on π-conjugated systems and functional materials

Heavier organotetrels exhibit a dual functionality if embedded in heterocycles or organic functional materials. When incorporated into π-conjugated systems, they allow the stabilization of the LUMO level and lead to a red-shift of the absorption and the emission. On the other hand, exocyclic bonded organotetrels serve as leaving groups in cross-coupling or tetrel/metal exchange reactions.

Chapter I: Investigation of the optical properties of tin-containing heterocycles and studies on their electrochemical stability

The implementation of tin in a five-membered heterocycle, referred to as stannole, has a drastic influence on the electronic properties. The LUMO level is stabilized due to the σ^*-π^* conjugation of the exocyclic σ^*-bond orbitals with the butadiene's π^*-orbital, but the HOMO is much less unaffected (compared to the C analog). Therefore, stannoles feature a lower HOMO-LUMO gap than their thiophene analogs and exhibit a red-shifted absorption/emission. This was proven for *bis*-thienyl flanked stannole monomer and dimer which are the equivalent for terthiophene and sexithiophene (Fig. 1).
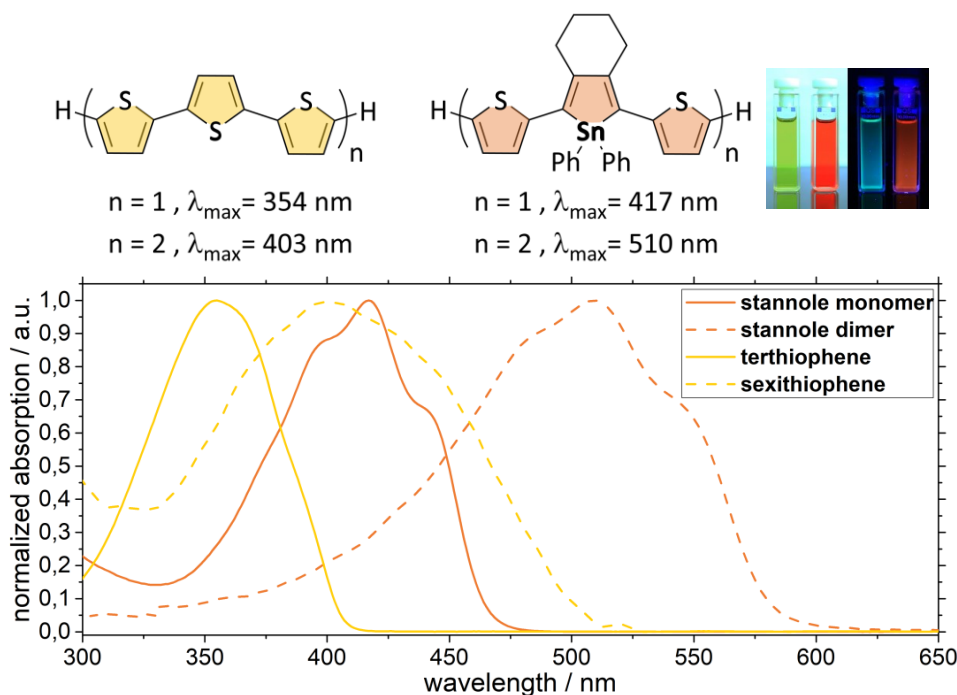
Fig. 1: Overview of thienyl-substituted stannoles, their oligothiophene analogs and their respective absorption spectra in DCM. Moreover, an image of the stannole monomer and dimer under ambient and UV light is depicted.

The stannole derivatives showed bathochromic shifts (Δ = 63/74 nm), broader bands and a relatively low optical energy gap (E_g = 2.66/2.13 eV) compared with the pure thienyl derivatives. In contrast to the oligothiophenes, the stannole dimer (n = 2) exhibited photoinstability. Despite the fact that the tin atom strongly effected the optical properties, the electrochemical behavior of the stannole monomer and dimer were similar to their thiophene analogs: The stannole dimer showed a fully reversible oxidation wave which was not observed for the stannole monomer. On account of the thiophene/stannole analogy, electropolymerization of thienyl-substituted monomeric stannole (n = 1)

was probed and an initial formation of electrodeposited films was observed. Over the course of the study, the electrochemical stability of the monomer and dimer was estimated by spectroelectrochemical methods and decomposition under oxidative conditions was found.

Overall, π-conjugated cyclic systems benefit from a substantial bathochromic shift upon implementation of a tin-atom but might suffer from the resulting instability towards light and oxidative conditions. However, for a further application in the field of organic electronics, the stannole-based materials require additional stereoelectronic stabilization at the tin atom to prevent decomposition effects. Then, the stannoles' broad absorption, high ε and low HOMO-LUMO gap should facilitate an application in organic solar cells (OSCs) or organic field-effect transistors (OFETs).

Chapter II: Influence of group 14 elements-based substituents on the photochromic π-system such as azobenzenes

The substitution of functional molecules along with heavier (organo)tetrels is highly promising as they could serve as synthetic precursors for metal-lithium exchange or transition-metal catalyzed cross-coupling reactions. This concept was realized for *ortho*-stannylated azobenzenes (Scheme 1).
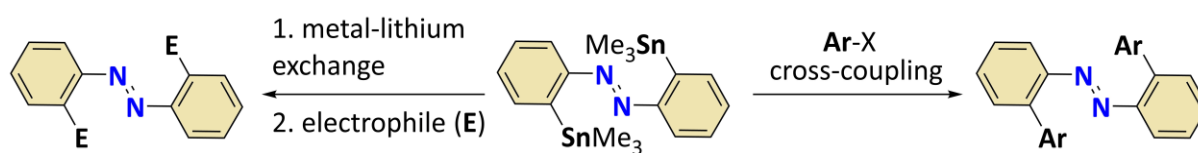
Scheme 1: 2,2'-*bis*(Trimethylstannyl)azobenzene as starting material for cross-coupling or metal-lithium exchange reactions.

The trimethyltin group was introduced *via* a cross-coupling route of hexamethylditin and an *ortho*-halogenated azobenzene. This was followed by a study of the tin-lithium-(copper)-exchange reaction sequences and quenching with various electrophiles. Using the 'soft' cuprate as a precursor higher yields could be obtained for 'soft' nucleophiles, e.g. methyl iodide or trimethylsilyl iodide. Furthermore, the *bis*(*ortho*-methythio)azobenzene could be obtained and its crystal structure was investigated for close atom interaction by Hirshfeld surface analysis. Overall, four *ortho*-trimethyltetrel substituted azobenzenes (C, Si, Ge, Sn) could be synthesized and the influence of the tetrel group towards the structural, thermal and photophysical properties of the azobenzene was investigated (Fig. 2).
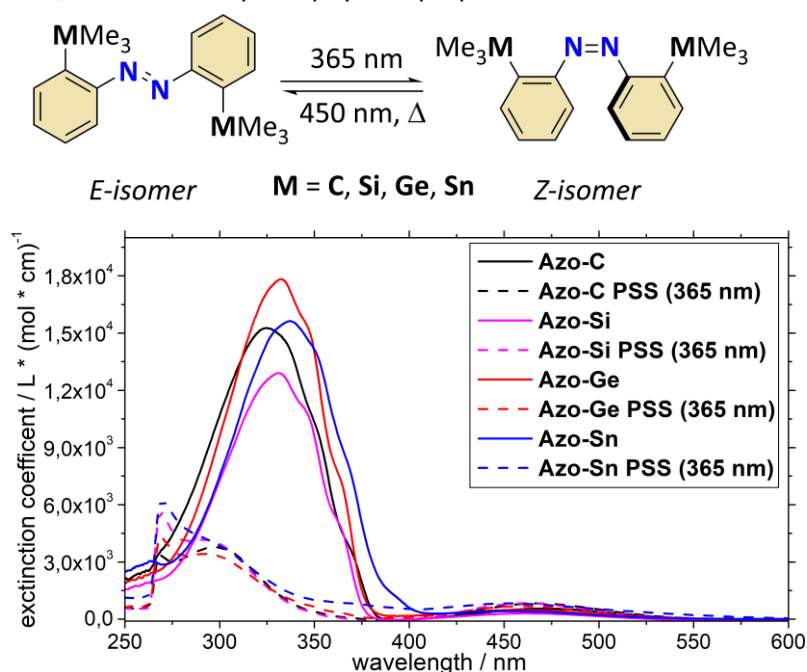

Fig. 2: Absorption spectra of tetrel-substituted azobenzenes before and after irradiation (365 nm).

These tetrel-substituted azobenzenes might be utilized for Si, Ge, and Sn-based cross-coupling reactions with aryl halides. Initial reactions under Stille cross-coupling conditions showed positive results for this transformation although the yield was yet optimizable. Besides opting for element-specific cross-coupling conditions, the potential of *ortho*-dinucleophilic azobenzenes as suitable precursors for *ortho*-bridged azobenzenes (diazocines) should be studied in the future.

Preface B: Embedding of triel/pnictogene units in organic structures for superior optoelectronic properties: Fundamentals, synthesis, photophysical and material analysis

The isoelectronic substitution of a CC unit in a cyclic π-system by a BN unit or BP unit effectively influences the geometry, polarization, aromaticity and foremost the HOMO-LUMO gap of the ring system. A resulting narrowing of the HOMO-LUMO gap is highly favored for materials with applications in organic electronics (OSC, OFET, OLED). The main differences between BN- and BP units in carbon scaffolds are geometrical and electronic factors: Whereas the nitrogen atom in BN-systems is found in trigonal planar geometries, phosphorus commonly prefers a pyramidal geometry in BP units. This P-pyramidalization is controllable by stereoelectronic substituents at the phosphorus.

Chapter III: Synthesis, optoelectronic properties, and application in organic devices (OLED/OFET) of novel boron/nitrogen-containing coronene diimides

The variety of reported BN-substituted polycyclic aromatic hydrocarbons (PAHs) concentrated on electron-rich and electron-neutral PAHs. The combination of BN units with electron-accepting PAHs was not achieved so far. One of the most investigated electron-accepting non-fullerene PAHs are rylene diimides, e.g. naphthalene diimide (**NDI**), perylene diimide (**PDI**) and coronene diimide (**CDI**). The longitudinal π-extension of the rylenes, e. g. from **NDI** to **PDI**, leads to a bathochromically shifted absorption/emission whereas the lateral π-extension, e.g. from **PDI** to **CDI**, results in inferior optical properties. In this project, it was investigated how the lateral π-extension with two BN units on **PDI**s, giving **BNCDI**s, influenced their optoelectronic properties. Therefore, the lateral core-extension of amino-substituted perylene diimides towards **BNCDI**s *via* electrophilic borylation was developed (Scheme 2).
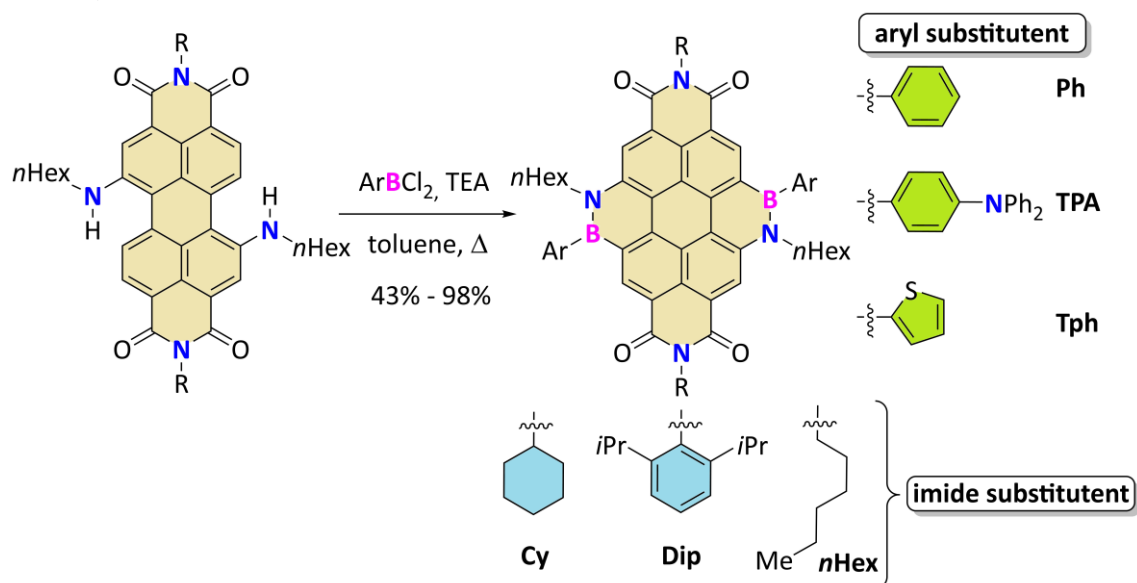
Scheme 2: Tandem electrophilic borylation with various aryldichloro boranes and 1,7-di(*n*-hexylamino)-substituted **PDI**s holding diverse substituent at the imide position led to the formation of seven novel **BNCDI**s.

In total, seven novel **BNCDI**s with varying aryl and imide substituents were synthesized in good to excellent yields. A judious choice of the imide and the aryl-substituents should influence the structure-property relation of these novel BN-PAHs in the solid-state and in solution.

In general, the **BNCDI**s exhibited beneficial optoelectronic properties compared with the parent all-carbon **CDI**s: Strong bathochromic shifts and higher molar extinction coefficients were obtained, supported by favorable fluorescence properties, e.g. small Stokes shifts and high quantum yields up to unity (Fig. 3).
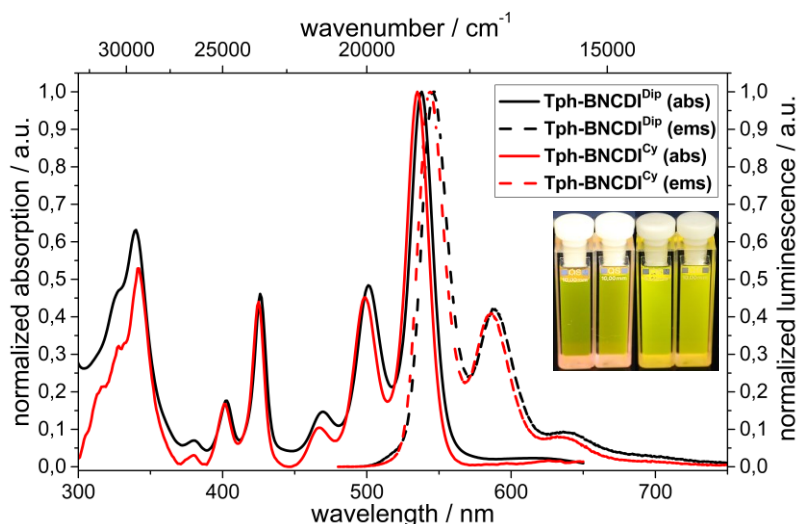
Fig. 3: Absorption and emission spectra of compounds **Tph-BNCDI^{Cy}** and **Tph-BNCDI^{Dip}**. Furthermore, a photograph of both substances with ambient light (left) and at irradiation of 365 nm (right) is displayed.

The absorption spectra disclosed that the electronic structure of **BNCDI**s was more relatable to the characteristics of **PDI**s than **CDI**s. In fact, the **BNCDI**s' frontier orbitals held mostly longitudinal (**PDI**-like) and fewer vertical (**CDI**-like) orientation and which explained this observation. The effect of the imide-substituents on the optoelectronic properties was marginal in solution but differed substantially in the solid. For the solid-state studies of the **BNCDI**s, two thienyl-substituted **BNCDI**s were chosen which only differ in the imide position (2,6-di*iso*propylphenyl vs. cyclohexyl) (Fig. 4).
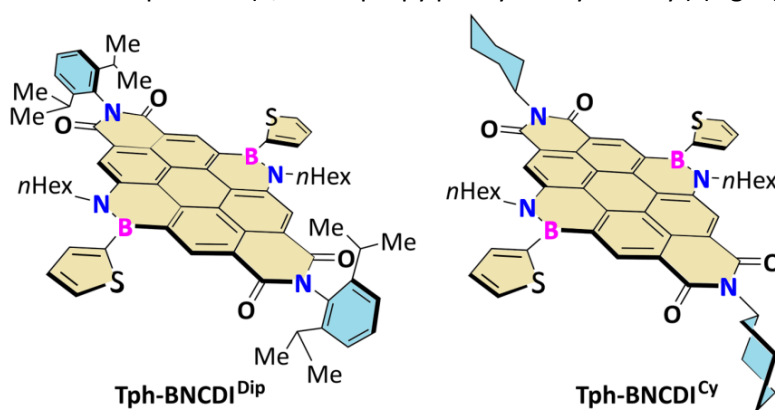
Fig. 4: Molecular structures of **Tph-BNCDI^{Cy}** and **Tph-BNCDI^{Dip}**.

The cyclohexyl- and 2,6-di*iso*propylphenyl-substituted **Tph-BNCDI**s showed divergent aggregation effects as determined by low-temperature luminescence spectroscopy. Furthermore, PMMA blends of both **Tph-BNCDI**s indicated strong aggregation-caused quenching (ACQ) processes upon increasing their concentration. In both experiments, it was shown that the cyclohexyl motif was less effective in preventing aggregation than the 2,6-di*iso*propylphenyl imide substituent.

However, the stronger aggregating **Tph-BNCDI^{Cy}** was implemented in an OFET device yielding low performance (on-/off-current ratio I_{on}/I_{off} = 36, field-effect mobilities (μ_{FE}) of approx. 10^{-8} cm^2 V^{-1} s^{-1}, threshold voltage $V_{th} \approx 20$ V) but indicated sufficient charge transportation. Due to their optimal optoelectronic properties, high thermal stability and charge transportation, both **Tph-BNCDI** derivatives were implemented in OLED devices. As neat **BNCDI**s suffered from adverse ACQ effects, they were co-evaporated with luminescent matrices (**DPVBi** or **CBP**) as emitters. The resulting electroluminescence spectrum varied depending on the matrix used and depending on the imide substituents on the **BNCDI** (Fig. 5).
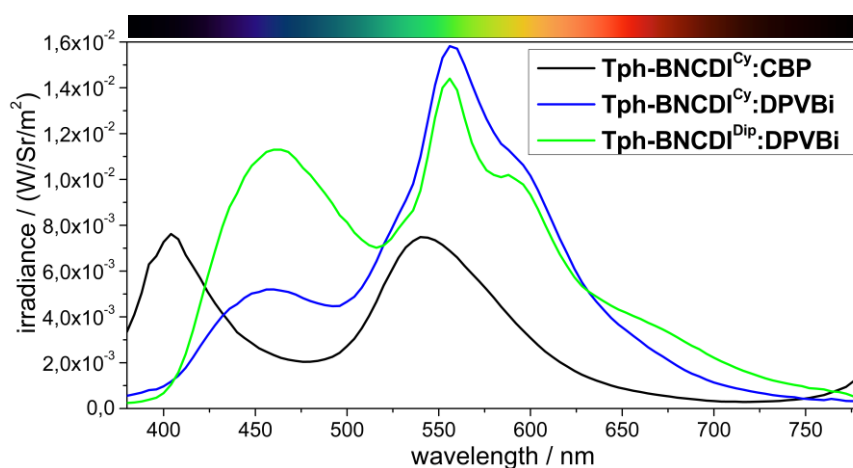
Fig. 5: Electroluminescence spectra of the brightest OLED devices including **Tph-BNCDI**s with different imide substituents or differing host matrices.

In combination with the blue-emitting matrices, in some cases white color emitting OLED (WOLED) devices with external quantum efficiency (EQE) up to 1.5% were achieved. Furthermore, low turn-on voltages (3.7 V) and luminance up to 1001 cd/m^2 were obtained. During this study it was found that upon increased **BNCDI** doping rates, the performance of the OLED devices decreased significantly. This was assigned to ACQ processes which were observed beforehand in the PMMA blend and low-temperature luminescence experiments.

After the influence of the imide substituent on the solid-state luminescence and the performance in OLED devices was studied, the effect of the aryl groups at the boron atom was investigated: For the first time in BN-chemistry, the boron atom of an electron-accepting BN-PAH was connected to a strong electron-donating substituent, here triphenylamine, leading to the formation of a D-A-D triad (Fig. 6).
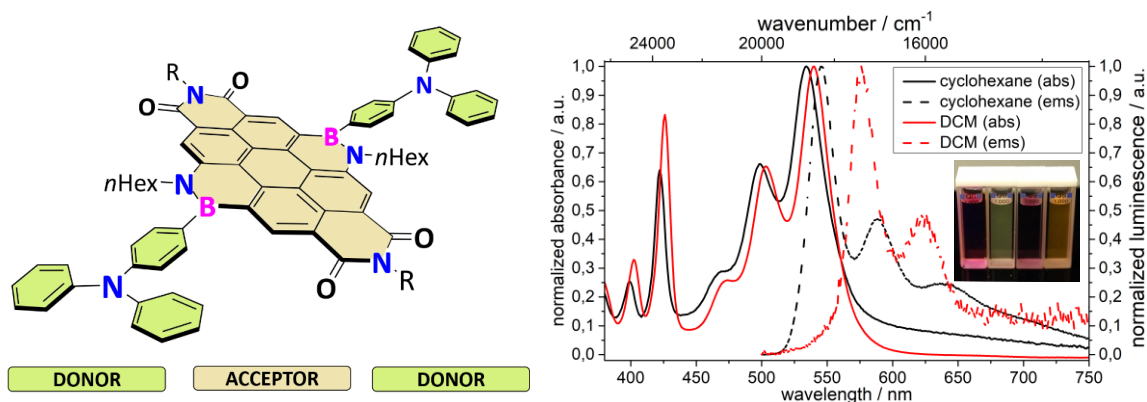
Fig. 6: Absorption and emission spectra of **TPA-BNCDI^{Cy}** in DCM and cyclohexane. The photograph shows **TPA-BNCDI^{Cy}** in DCM (left)/cyclohexane(right) and **TPA-BNCDI^{Dip}** in DCM (left)/cyclohexane(right) under irradiation with UV-lamp at 365 nm.

Surprisingly, the combination of strong electron-donating triphenylamine with electron-withdrawing **BNCDI** led to barely luminescent solutions in DCM solutions with a larger Stokes shift. However, it was found that solutions of **TPA-BNCDI**s in nonpolar solvents exhibited high fluorescence quantum yields

along with small Stokes shifts. Since such behavior was not present for phenyl/thienyl-substituted **BNCDI**s, the effect was clearly assignable to stereoelectronic effects of the triphenylamine-substituent at the boron atom. To estimate the unique electronic nature of **TPA-BNCDI**s, they were probed by cyclic voltammetric experiments and compared with a thienyl-substituted **BNCDI** (Fig. 7).
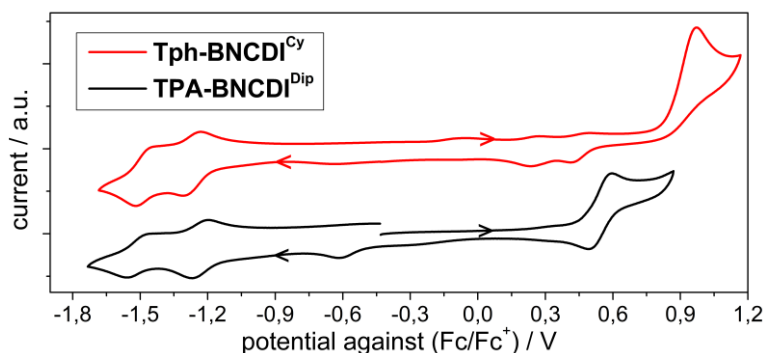
Fig. 7: Cyclic voltammogram of **TPA-BNCDI^{Dip}** and **Tph-BNCDI^{Cy}** (10^{-3} M) in DCM with nBu$_4$NPF$_6$ (0.2 M) as conducting salt.

The triphenylamine-substituted **BNCDI**s exhibited a fully reversible and lower oxidation potential than observed for the **Ph/Tph-BNCDI**s. Thus, it was concluded that the HOMO level of **TPA-BNCDI**s was more destabilized due to the electron-donating effect of the triphenylamine moieties. This could explain the strong solvent-dependency of the luminescence since a proposed intramolecular photoinduced electron transfer occurred in polar solvents. Moreover, the fully reversible redox character of the **TPA-BNCDI**s was observable by spectroelectrochemical experiments, proving the stability of the novel BN-based D-A-D triad.

Moreover, the effect of the triphenylamine motif onwards the response of the **BNCDI**s on Lewis bases and Lewis acids was investigated, giving rise to red-shifted species that show highly structured absorption bands occurring in the NIR region of the electromagnetic spectrum (Fig. 8).
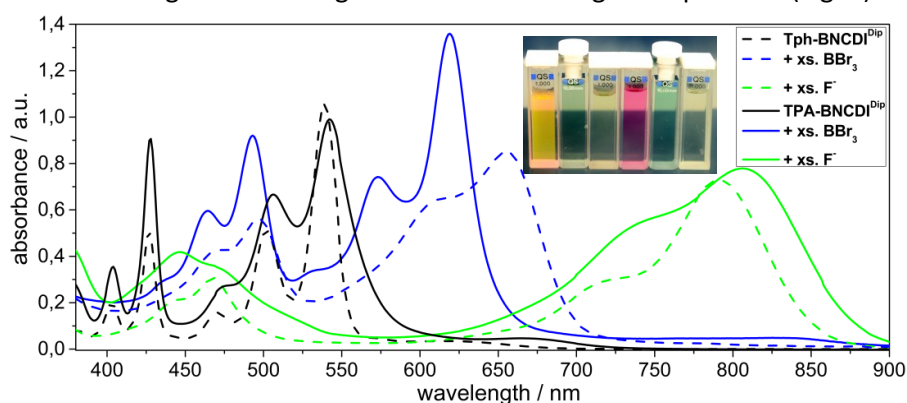
Fig. 8: Absorption spectra of **TPA-BNCDI^{Dip}/Tph-BNCDI^{Dip}** and their interaction with BBr$_3$ and TBAF. The photographic image is showing solutions of **Tph-BNCDI^{Dip}** in DCM, with BBr$_3$ and with TBAF (from left to right) as well as **TPA-BNCDI^{Dip}** in DCM, with BBr$_3$ and with TBAF.

Titration of **BNCDI**s with a fluoride source or boron tribromide revealed that the formation of the Lewis adducts occurred in a two-step process. Therefore, both BN units individually interacted as Lewis base/acid. Exceptionally, the fluoride **BNCDI** adduct was still emissive and showed a broad emission signal in the NIR region (700-1000 nm) which could be useful for detection purposes. Moreover, all **BNCDI**s exhibited interaction with weak-coordinating solvents, e.g. THF, acetonitrile or triethylamine, as indicated by bathochromic shifted absorption maxima. An ancillary effect of the triphenylamine-substituent towards the Lewis acidity/basicity or coordination by solvents was not found. It was concluded that conformational changes of the BN unit upon coordination had drastic effects on the

planarity of the coronene diimide core and therefore resulted in bathochromic shifted absorption/emission.

Chapter IV: Novel concepts to synthesize unique boron/phosphorus-embedded PAHs

Although numerous BN-substituted cyclic or polycyclic systems have been reported throughout the last decade, there were few reports about BP-substituted π-systems and a detailed investigation of their optoelectronic properties. BP-substituted π-conjugated polycyclic aromatic hydrocarbons hold great potential in organic electronics as a stabilization of the LUMO level should lead to a smaller HOMO-LUMO gap in comparison to CC/BN-PAHs. Furthermore, the potential of BP-substituted compounds for additional chemical modifications (oxidation, complexation) at the phosphorus atom, which can be utilized to fine-tune the optoelectronic properties, remains undisclosed so far due to its inaccessibility.

To investigate the effect of a BP-substitution, in this project the dibenzochrysene (**DBC**) and tetrathienonapthalene (**TTN**) motif were chosen as a carbon scaffold. Since the CC- and BN-substituted **DBC/TTN**s were already successfully synthesized, a direct comparison to the BP-substituted structures should be possible. Initially, the BP-substituted **DBC/TTN** were compared with their CC/BN congeners by computational methods, highlighting the geometric and electronic effects of the phosphorus in the BP units. Due to the spacious phosphorus and its pyramidal geometry, the corresponding **BP-DBC/TTN** exhibited a more twisted geometry or out-of-plane orientation of the BP unit compared with the corresponding CC/BN structures (Fig. 9).
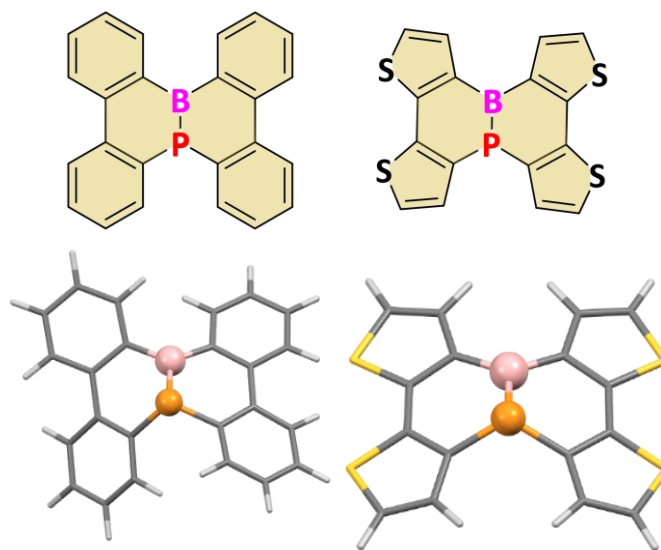
Fig. 9: BP-substituted dibenzo[g,p]chrysene (**BP-DBC**) and tetrathienonaphthalene (**BP-TTN**) and their optimized geometries (B3LYP-6-31G*).

The sum of angles at the phosphorus atoms (Σ = 309.88°/332.63°) indicated its pyramidalization and therefore less interaction of the phosphorus with the neighboring boron or carbon atoms was suspected. Moreover, the bonding of the novel BP-structures was analyzed by natural bond occupation (NBO) analysis. In the **BP-TTN** derivative, a B=P bond was present whereas the **BP-DBC** derivative held a single bond character combined with a Lewis pairs description. Since the lone pair at the phosphorus atom was weakly interacting with the boron atom, it might be accessible for further post-functionalization of the **BP-DBC** to modify the HOMO/LUMO levels. Apart from geometrical effects, the BP-structures modified the electronic structures of the **DBC** and **TTN** motifs: A stabilized LUMO level and bathochromic shifted absorption compared with the respective CC/BN-congeners were

found. Furthermore, the nucleus independent chemical shift (NICS) calculations revealed that the central ring held a decreased aromaticity compared with their CC/BN-congeners. All these theoretical insights were highly promising for an application in organic electronics.

In general, methods to access BP-substituted PAHs are barely reported and yet suffer from synthetical applicability. In analogy to BN-chemistry, novel synthetic methods to prepare BP-substituted PAHs by dual ring annulation reactions of a *bay*-positioned phosphine should be investigated (Scheme 3).
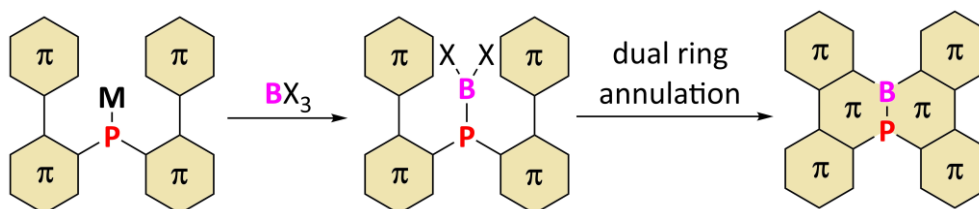
Scheme 3: Synthesis towards BP-annulated π-systems *via* borylation of *bis*(diaryl)phosphide and followed by tandem ring annulation reactions.

It was anticipated that the dual ring annulation reaction might be the most challenging part in this procedure since the P-B bond is not stable.

To perform these reactions, initially the precursor for the **BP-DBC** motif, the *bis*(biphenyl)phosphine was synthesized starting from a biphenyl Grignard and a phosphorous species (Scheme 4).
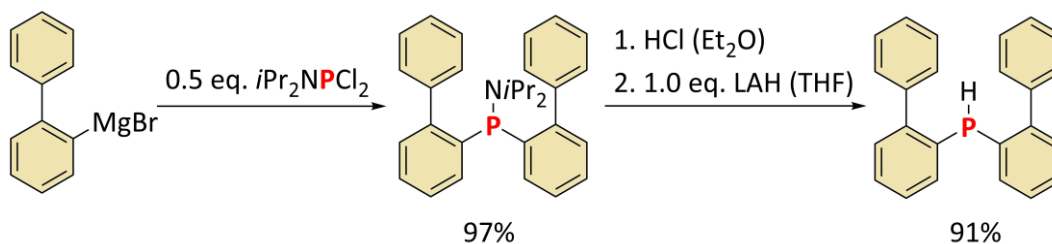
Scheme 4: Synthesis of the *bis*(biphenyl)phosphine succeed in high yields.

The aminodiarylphosphine and the key structure *bis*(biaryl)phosphine could be isolated in high yields after initial optimization. For these precursors and the borane-protected phosphine, crystal structures were obtained and showed sterically shielding of the phosphorus atom by the two biphenyl ligands which decreased oxidation reactions (Fig. 10).
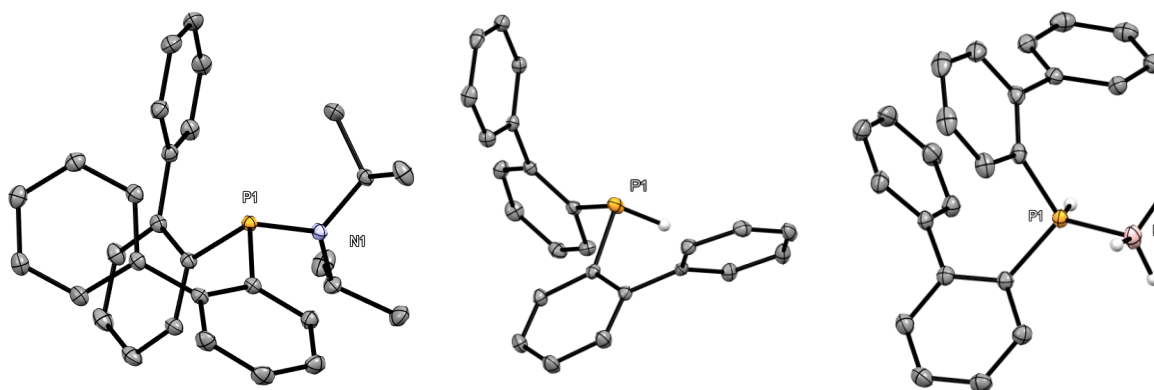
Fig. 10: Crystal structures of aminophosphine, the phosphine and the borane-protected phosphine.

The phosphine could be further transformed to the *bis*(biphenyl)phosphide and two (trimethyltetrel)phosphines to perform reactions with electrophilic boron species (Scheme 5).
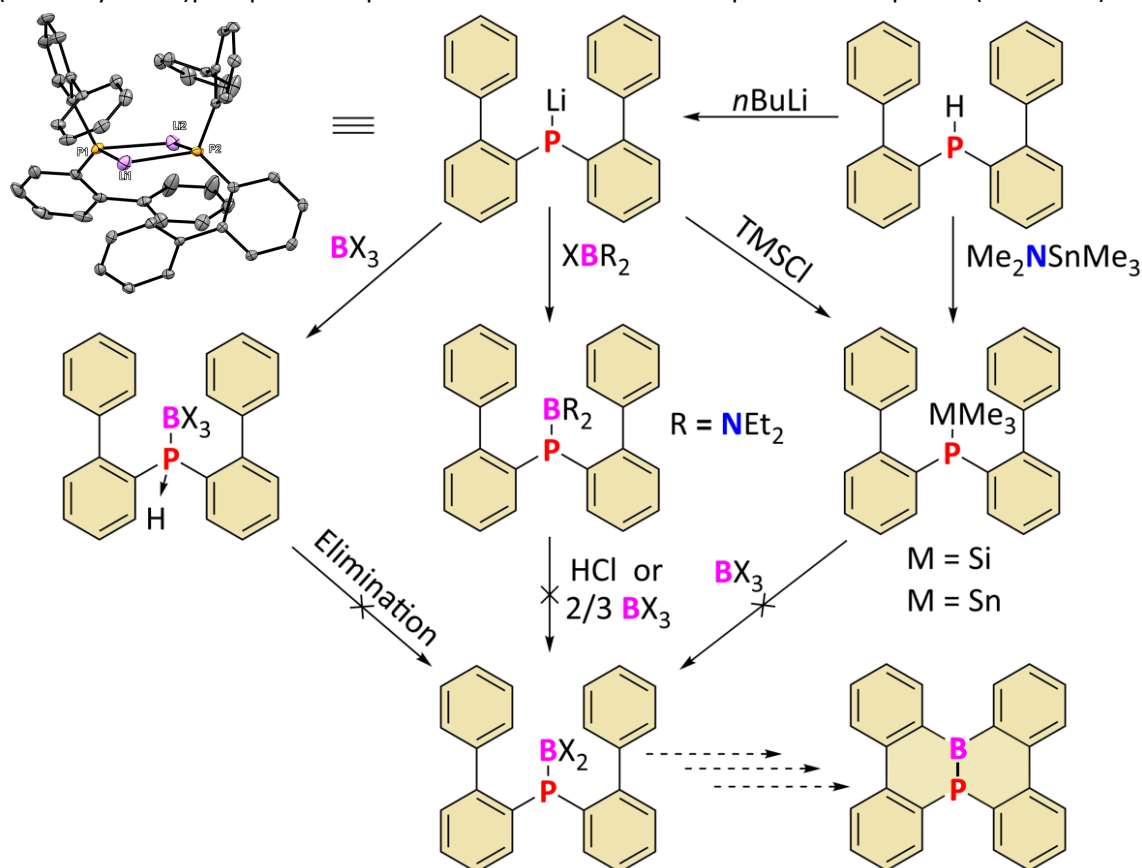
Scheme 5: Reaction sequence to obtain the BP-substituted PAHs.

The reaction of the phosphide or the trimethyltetrelphosphines with various boron electrophiles was unsuccessful and the formation of phosphine borane adducts was mostly observed. Initial attempts to form the Ar_2PBX_2 species by the elimination of a HX species from the phosphine borane failed. Tetrel(Si/Sn)-boron exchange reactions also led to the formation of the phosphine borane adducts.

However, the reaction of the nucleophilic phosphine derivatives with various electrophilic boranes revealed that the Lewis acidity of the boranes had a major effect on the reaction itself: Only the milder Lewis acid $(Et_2N)_2BCl$ could be reacted with the phosphide giving the respective BP-motif.

It was concluded that less Lewis acidic boranes support the stability of the phosphino boranes. Unfortunately, this contradicts with the required Lewis acidity to access the **BP-DBC** via ring annulation reaction (Scheme 6).
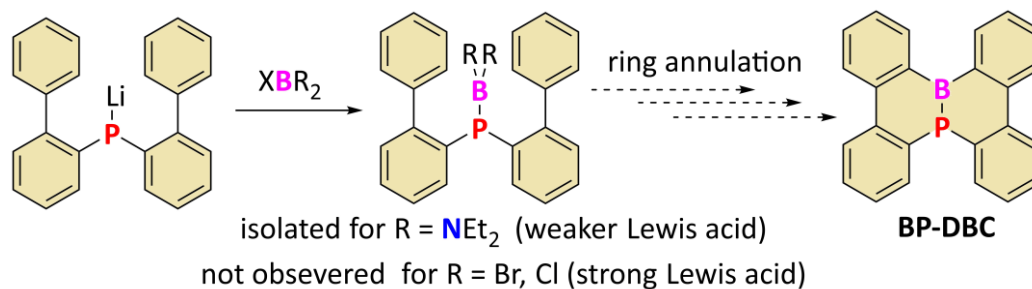
Scheme 6: The influence of the Lewis acidity on the stability of the BP-species opposes the required Lewis acidity for the ring annulation reaction towards the **BP-DBC**.

Although initial attempts to exchange the substituents at the boron atom failed, this could be a possible way to access a suitable precursor for the ring annulation reaction.

List of Contents

Scientific Output

R. Jurgeleit, B. Grimm-Lebsanft, B. M. Flöser, M. Teubner, S. Buchenau, L. Senft, J. Hoffmann, M. Naumova, C. Näther, I. Ivanovíc-Burmazovíc, M. Rübhausen, F. Tuczek, '*Catalytic Oxygenation of Hydrocarbons by Mono-µ-oxo Dicopper(II) Species Resulting from O-O Cleavage of Tetranuclear Cu(I)/Cu(II) Peroxo Complexes*', *Nat. Chem.* **2020**, *submitted*.

J. Hoffmann, M. Hissler, A. Staubitz, '*Perylene derivatives, their synthesis and their use in organic devices*', Patent, **2020**, DE102020205182.

J. Hoffmann, T. J. Kuczmera, E. Lork, A. Staubitz, '*Synthesis and Crystal Structure of (E)-1,2-bis[2-(methylsulfanyl)phenyl]diazene*', *Acta Cryst.* **2019**, *E75*, 1808-1811.

J. Hoffmann, T. J. Kuczmera, E. Lork, A. Staubitz, '*Synthesis, Structure, Thermal Behavior and cis/trans Isomerization of 2,2'-(EMe$_3$)$_2$ (E = C, Si, Ge, Sn) Substituted Azobenzenes*', *Molecules* **2019**, *24(2)*, 303.

S. Urrego-Riveros, M. Bremer, J. Hoffmann, A. Heitmann, T. Reynaldo, J. Buhl, P. J. Gates, F. D. Sönnichsen, M. Hissler, M. Gerken, A. Staubitz, '*Conjugated Oligomers with Alternating Heterocycles from a Single Monomer: Synthesis and Demonstration of Electroluminescence*', *Org. Chem. Front.* **2019**, *6*, 3636-3643.

S. Urrego-Riveros, I.-M. Ramirez y Medina, J. Hoffmann, A. Heitmann, A. Staubitz, ,*Syntheses and Properties of Tin Containing Conjugated Heterocycles*, *Chem. Eur. J.* **2018**, *24*, 5680-5696.

I.-M. Ramirez y Medina, M. Rohdenburg, F. Mostaghimi, J. Hoffmann, S. Grabowsky,V. Dorcet, M. Hissler, J. Beckmann, P. Swiderek, A. Staubitz, '*Tuning the Optoelectronic Properties of Stannoles by the Judicious Choice of the Organic Substituents,*' *Inorg. Chem.* **2018**, *57* (20), 12562-12575.

B. Thiedemann, P. J. Gliese, J. Hoffmann, P. G. Lawrence, F. D. Sönnichsen, A. Staubitz, *High molecular weight poly(N-methyl-B-vinylazaborine) - a semi-inorganic B-N polystyrene analogue*', *Chem. Comm.* **2017**, *53*, 7258.

Book Chapter

J. Hoffmann, P. J. Gliese, A. Staubitz, (eds. E. Hey-Hawkins and M. Hissler), *Smart Inorganic Polymers, book chapter: Group 13 - Group 15 Element Bonds Replacing Carbon-Carbon Bonds in Main Group Polyolefin Analogs*, **2019**, Wiley VCH, Weinheim.

Supervised Thesis

T. K. Kuczmera, bachelor thesis: *Preparation of ortho-substituted azobenzenes*, **2018**, University Bremen.

Presentations

'Extending the Bay-Area: Synthesis, Characterization and Application (OLED, OFET) of novel Azaborine-substituted Coronene diimides' - ACS national fall meeting **2019**, San Diego (oral presentation).

‚New Functional and Highly Stable Azaborine-Annulated Perylene Diimides' - Frühjahrssympossium **2018**, Konstanz (poster presentation).

'Studies on stannoles and their polymers concerning their application for organic electronics' - Russian-French workshop on hyper- and hypocoordinated compounds of the group 14 elements **2017**, Moscow (oral presentation).

‚New boron-nitrogen substituted perylene(*bis*)diimides' - International Conference On Phosphorus, Boron and Silicon - PBSi **2017**, Paris (poster presentation).

‚New Boron-Nitrogen Substituted Perylene(*bis*)diimides as Building Block for Polymers' - Frühjahrssympossium **2017**, Mainz (poster presentation).

Funding and Scholarships

Abbreviations

ACQ	Aggregation-caused quenching
AIE	Aggregation-induced emission
APCI	Atmospheric pressure chemical ionization
BHJSC	Bulk heterojunction solar cell
BiPh	Biphenyl
BiTph	Bithienyl
CBP	4,4'-*bis*(*N*-Carbazolyl)-1,1'-biphenyl
CDI	Coronene diimide
CIE	Commission Internationale d'Eclairage
COD	Cyclooctadiene
COSY	Correlation spectroscopy
*m*CPBA	*meta*-Chloroperoxybenzoic acid
CuPc	Copper phthalocyanine
CV	Cyclic voltammetry
Cy	Cyclohexyl
CyPen	Cyclopentyl
DBE	1,2-Dibromoethane
DBU	1,8-Diazabicyclo[5.4.0]undec-7-ene
o-DCB	*ortho*-Dichlorobenzene
DCM	Dichloromethane
DFT	Density functional theory
Dip	2,6-di*iso*propylphenyl
DPV	4,4'-*bis*(2,2-Diphenylvinyl)-1,1'-biphenyl
DSC	Differential scanning calorimetry
EI	Electron ionization
eq.	Equivalents
EQE	External quantum efficiency
FWHM	Full width at half maximum
HMBC	heteronuclear multiple bond correlation
HOMO	Highest occupied molecular orbital
HRMS	High resolution mass spectrometry
HSQY	Heteronuclear single quantum coherence
IQE	Internal quantum efficiency
ITO	Indium tin oxide

LAH	Lithium aluminum hydride
LUMO	Lowest unoccupied molecular orbital
NBS	*N*-Bromosuccinimide
NDI	Naphthalene diimide
NICS	Nucleus independent chemical shift
NIR	Near-infrared
NMP	*N*-Methylpyrrolidine
NMR	Nuclear magnetic resonance
NOESY	Nuclear overhauser enhancement and exchange spectroscopy
NPB	*N,N'*-Di(1-naphthyl)-*N,N'*-diphenyl-(1,1'-biphenyl)-4,4'-diamine
OFET	Organic field-effect transistor
OLED	Organic light-emitting diode
OSC	Organic solar cell
PAH	Polycyclic aromatic hydrocarbon
P3HT	Poly(3-hexylthiophen-2,5-diyl)
PCE	Power conversion efficiency
PDI	Perylene diimide
PMMA	Poly(methyl methacrylate)
PTCDA	Perylene tetracarboxylic dianhydride
TADF	Thermally activated delayed fluorescence
TD-DFT	Time-dependent density functional theory
TGA	Thermogravimetric analysis
THF	Tetrahydrofuran
TIPS	Tri(*iso*propyl)silyl
TMP	2,2,6,6-Tetramethylpiperidine
TMS	Trimethylsilyl
TPA	Triphenylamine
TPBi	2,2',2''-(1,3,5-Benzinetriyl)-*tris*(1-phenyl-1-H-benzimidazole)
Tph	Thiophene
WBI	Wiberg bond index

General Introduction: Main group chemistry in functional materials, photophysical fundamentals, OLED and OFET

Main group chemistry and especially p-block elements consolidated the basis of chemistry for the past two centuries. Studies of these elements gave rise to a wide variety of molecules with distinctive reactivity as well as unique structural and physical properties. Whereas the early stages of main group research were about understanding the fundamentals of the element-specific chemistry, in the past two decades progress was made on modification of π-conjugated organic scaffolds by p-block elements. This modification has emerged as an effective method for the development of novel materials.[1-4] This innovative field is based on the fact that main group elements bring notable features such as diverse coordination sphere, hypo/hypervalency, structural characteristics and foremost electronic effects. These would be not accessible solely with carbon-based π-conjugated materials. By a precise choice of main group elements, photophysical, electronic and solid-state properties of π-conjugated molecules or polymers became tunable. In particular, the utilization of main group elements in small molecules and polymeric structures was intensively researched. These studies included the utilization of elements such as boron,[5-8] nitrogen,[9] silicon,[10] phosphorus,[11, 12] sulfur[13, 14] as well as heavier atoms[11, 15] which resulted in novel functional π-conjugated materials (Fig. 1).

Fig. 1: Detail of the periodic table of elements: the p-block. The key-elements covered in this thesis are highlighted.

Recent examples of materials comprising a functional main group element were applied for small molecule activation with frustrated-Lewis pairs (FLP),[16] biological imaging,[17] as functional polymers,[18] and foremost in organic electronics.[4] Main group substituted materials had tremendously boosted the research in the field of organic light-emitting diodes (OLEDs), organic field-effect transistors (OFETs), organic solar cells (OSCs) and thus became an essential element in the design of molecular electronics. Especially in material science, main group elements were essential for accessing highly-defined novel polymeric materials with a designable HOMO-LUMO gap structure.[19]

In addition to being used to develop materials with structurally embedded main group elements, they have also been used in cross-coupling reactions catalyzed by transition metals. The use of boron,[20, 21] silicon[22, 23] or tin[24, 25] as leaving groups revolutionized modern organic chemistry itself.

Since main group elements influence the optoelectronic properties of chromatic structures and their potential application in functional materials, basic concepts of π-conjugated systems and their photophysics and organic devices (OLED/OFET) are explained in the following.

Organic π-Conjugated Systems

Since the exploration of conductivity in doped polyacetylene polymers by MacDiarmid, Heeger and Shirakawa in 1977,[26] which was recognized with a Nobel prize in 2000,[27-29] organic π-conjugated structures gained interest for application in the electronics sector due to their light-weight, mechanical flexibility, processability and low-cost efficiency.[30] So-called organic electronics were found since then in organic light-emitting diodes (OLEDs), organic field-effect transistors (OFETs) or organic solar cells (OSCs).

Organic semiconductors and π-extended systems can be simplified as a system of connected diene units forming extended π-orbitals and facilitating delocalization of electrons and semiconducting properties. In general, a combination of two sp^2 hybridized carbon atoms, as in ethylene, results in the formation of σ- and π-bond orbitals as a linear combination of two sp^2 orbitals and two p$_z$ orbitals. As a consequence, σ and π-orbitals split up into bonding and antibonding orbitals thereby the π-orbital represents the highest occupied molecular orbital (HOMO) and the π*-orbital the lowest unoccupied molecular orbital (LUMO) (Fig. 2, left).
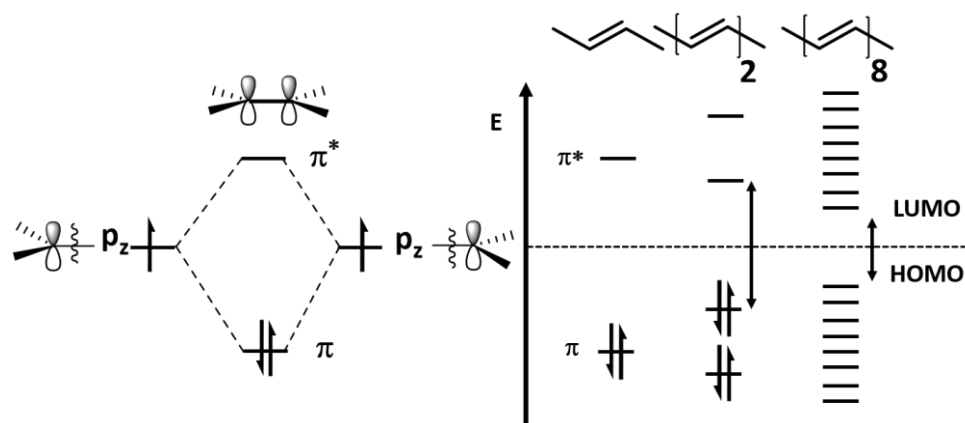
Fig. 2: Molecular orbital scheme of an π-bond in ethylene (left) and reduction of the HOMO-LUMO gap upon elongation of diene units (right).

Upon elongation of the π-conjugation as in a butadiene scaffold, each bonding and antibonding orbital is split into two more orbitals. In total the HOMO-LUMO gap is reduced upon lateral π-extension (Fig. 2, right). The combination with functional groups or heteroatoms on the diene's scaffold influences optical absorption/emission as well as redox properties. Such modification became a common concept in the band gap engineering processes. Especially the implementation of heteroelements in π-conjugated systems, as in thiophene, pyrrole, furan and siloles, became a common concept to tune the bandgap of organic semiconductors.

Fundamental Photophysics of Extended π-Conjugated Systems

Extended π-conjugated systems and chromophores often hold luminescence properties. The fundamental processes upon absorption of light in organic molecules are commonly described in a Perrin-Jablonski scheme (Scheme 1).
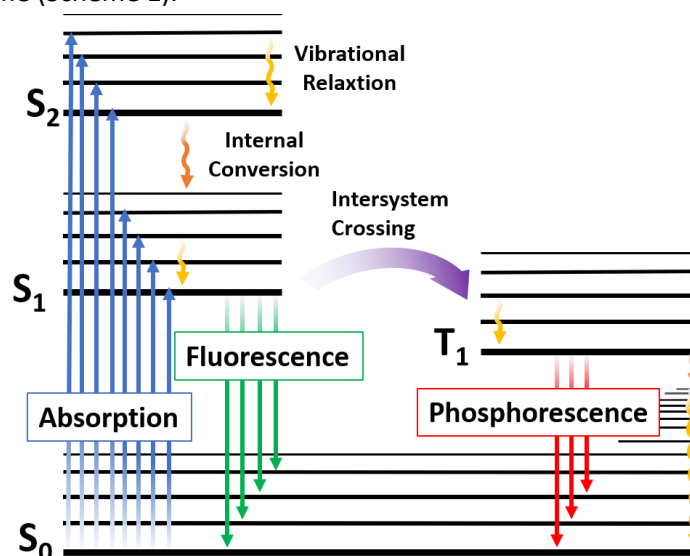
Scheme 1: Jablonski diagram for common transition events in organic luminophores.

The ground state, first excited state and second excited state are notated as S_0, S_1 and S_2 whereas the triplet state is referred to as T_1. Upon absorption of a photon, luminophores are excited into any vibrational state of S_1, S_2 or even in a higher singlet state. In the respective state, the excited molecule can occupy different vibrational levels which are stated to as $v = 0, 1, 2$ etc. Transitions from the lowest vibrational states in S_0 to the lowest vibrational state in the S_1 are denoted as 0-0 transitions. Since the absorption process occurs instantly (10^{-15} s), the molecules do not undergo any rearrangement. The absorption of the luminophore is based on the overlap of the vibrational wave function in the ground and excited state which results in a specific intensity distribution of the absorption spectrum. This concept is known as Franck-Condon-principle. Once the molecule was excited, it might undergo instant emission (fluorescence) from S_1 or S_n to vibrationally excited levels in S_0. The emission always occurs from the lowest vibrational level (Kasha's rule).[31] This process is considered as a fast (10^{-10}-10^{-7}s) and follows the Franck-Condon principle as well. If the emission occurs into a vibrationally excited state, a red-shift of the emitted wavelength is observed which is the so-called Stokes shift. Since the internal distances in the vibrational levels of the ground state and the excited state normally do not differ, vibrational states of absorption and emission are similar and often mirror-inverted. Excited molecules in the S_1 state might undergo a spin conversion to the respective T_1 state, referred to as intersystem crossing. The T_1 state is generally more energetic stabilized, therefore is the emission from T_1 to S_0 (phosphorescence, 10^{-10}-10 s) commonly bathochromic shifted compared with the fluorescence emission. Since the T_1 to S_0 transition is spin-forbidden, the rate constant for such a process is comparably lower than fluorescence. Besides radiative processes, molecules can undergo a non-radiative pathway to lose energy *via* relaxation processes, e.g. vibration or interaction with solvent molecules. A photophysical parameter to determine the efficiency of the overall luminescence process is the luminescence quantum yield (Φ_{lum}), representing the ratio of absorbed to emitted photons. On the one hand, a high quantum yield represents the fact that the ground and excited state feature the same location and the molecule is not undergoing geometrical changes in the excited state.[32] On the other hand, high luminescence quantum yields are proof of efficient energy conversion.

Organic Light-Emitting Diodes

In principle, electroluminescent materials convert electric energy into photon emission by recombination of holes and electrons forming excitons. Interest in organic-based electroluminescent materials technology rose due to their mechanical flexibility and low-cost approach in comparison to inorganic electroluminescent materials.[30] In particular, organic light-emitting diodes (OLEDs) became a conventional display technology in consumer electronics with superior performance compared with liquid crystal displays (LCD). In general, OLEDs are processed as multilayer structures of organic and inorganic compounds where each layer has a distinguished task regarding the functionality of the OLED. The most common architecture is based on an electron transporting level (ETL), an emissive layer (EML) and a hole transporting layer (HTL) which are sandwiched between two electrodes (Fig. 3, left).
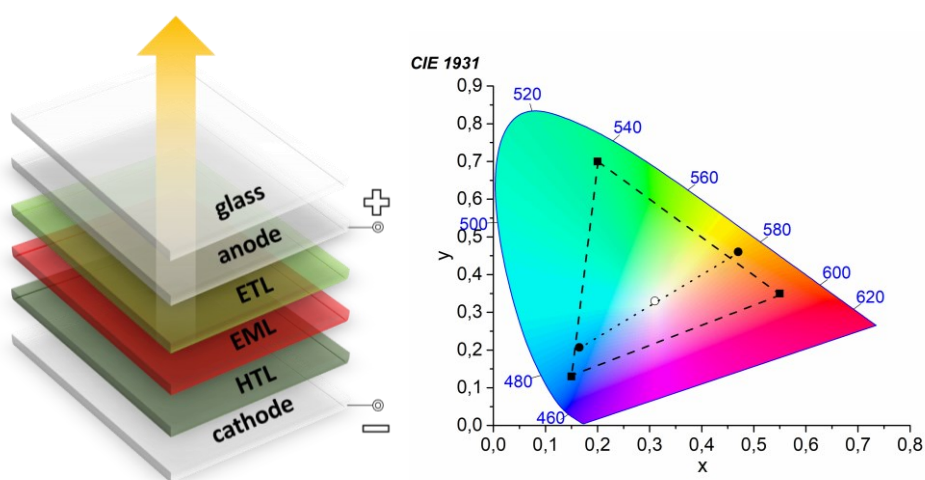
Fig. 3: Stacked setup of a layer OLED (left). A CIE diagram, according to CIE 1931, displaying the mixture of two (circles) or three (rectangle) emitting chromophores leading to the formation of white light (0.33, 0.33) (right).

Upon an applied voltage, injected charges in both ETL and HTL migrate to the EML to form singlet and triplet excitons which decay to the ground level within the release of radiation. During this process, the HOMO of the HTL is oxidized as the holes are injected whereas the LUMO of the ETL is reduced to transport electrons to the ETL. Hereby the energy gap between the HOMO and LUMO level of the emitting layer is decisive for the energy of the wavelength which is emitted. With respect to the emitter well-defined light is produced in this process. Of particular interest is the generation of white light with these devices which requires a well-blended mixture of red, blue and green light. White light emission is achieved either by the layering of three independent emitters with different colors (red, blue, green) in a single device or by focusing the emission of three OLEDs within one spot. Another method to achieve white organic light-emitting diodes (WOLEDs) is to combine several luminescent materials in the emitting layer of the devices. For this purpose, two or three complementary emitters are blend in a dopant/host configuration to achieve neat white light emission. To follow this concept, chromaticity is determined using the Commission Internationale d'Eclairage (CIE) chromaticity diagram (Fig. 3, right). Each emitted color can be expressed by the respective chromaticity coordinates x and y within the CIE chromaticity diagram. Pure white light with the chromaticity coordinates x = 0.33 and y = 0.33 is in the center of this diagram. A precise adjustment of the emitting colors in a binary or trinary arrangement of emitting molecules might lead to the color of choice. To obtain the desired white light, either turquoise and orange or blueish, orange and greenish colored lights are mixed. It should not be neglected that for WOLEDs also parameter like colour rendering index and color temperature are essential.[33]

In addition to the use of chromaticity as an important technical feature of an OLED, further parameters such as brightness (luminance in cd/m^2), efficiency (external quantum efficiency (EQE) in percentage), turn-on voltage (V_{on}) and long-term stability are essential characteristics. As a reference value for the efficiency of OLEDs, the EQE was set as the most important value. It is defined as the ratio of the produced photons to the electrons injected into the system. Theoretically, the efficiency of an organic emitting device is limited to fundamentals as spin-statistics and therefore internal quantum efficiency (IQE) (Fig. 4).
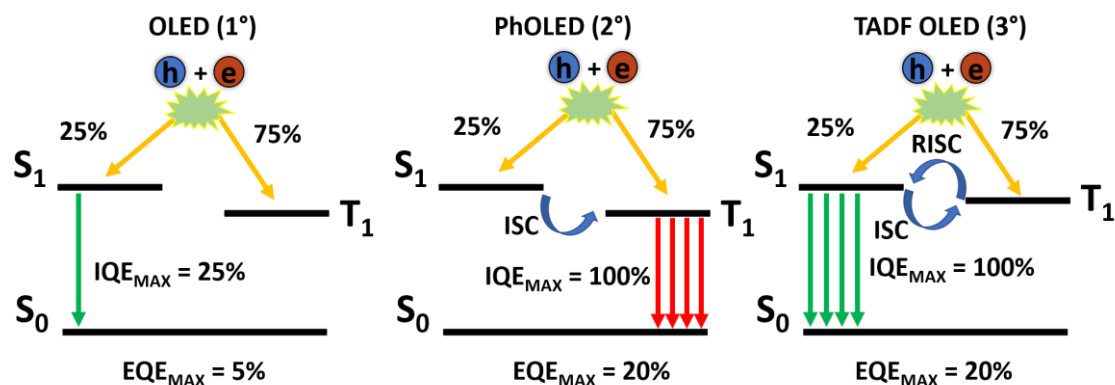
Fig. 4: Spin statistics and emission properties of an OLED device based on a fluorophore (left), phosphorescent material (middle) and TADF material (right).

The IQE in fluorescent materials is limited to 25% due to the emission of singlet excitons, since only spin-constant singlet-singlet emissions are allowed. In combination with an out-coupling efficiency of 20%, the experimentally achievable EQE of fluorescent organic light emitters are thus limited to 5%. Therefore, low-energy triplet emitters are more favorable, since the probability of accessing a triplet state is 75%. A specific molecular design also allows single excitons to emit from the triplet state after previous intersystem crossing (ISC) events and thus theoretically increase the IQE to 100%. Since purely organic triplet emitters are rare, the utilization of transition metals became prominent as they undergo metal-to-ligand charge transfer (MLCT) processes along with spin-orbit coupling. These are also referred as second-generation OLEDs. Common triplet emitters are functionalized with iridium(III) complexes, e.g. tris(2-phenylpyrdine)iridium(III) (Ir(ppy)$_3$). In OLEDs, they are utilized as highly efficient triplet emitters generating blue, red and green light.[34] The experimentally achievable EQE in this case is up to 20%. Due to the abundance of transition metals, the need for organic triplet emitters gained enormous interest. In the last decade, novel materials have been developed utilizing the triplet state of organic structures to generate thermally activated delayed fluorescence (TADF).[35] Due to the small energy difference between singlet and triplet state ($\Delta E_{ST} < 0.1$ eV) triplet excitations may undergo reverse intersystem cross (RISC) and emit a singlet exciton with thus a delayed fluorescence. Due to the access to triplet excitons, the IQE in TADF materials is 100% while the EQE in organic devices is about 20%. Furthermore, optimization of the triplet state led to a novel generation of OLEDs, which has been developed recently: The combination of TADF host materials and fluorescent emitters led to hyperfluorescence OLEDs. Another approach is the utilization of the triplet-triplet fusion (TTF) process to produce so-called TTF OLEDs.[36, 37]

Organic Field-Effect Transistor

A field-effect transistor (FET) is an electronic device that controls electrical current based on the phenomenon that charges on a nearby object can attract charges within a semiconductor channel (field-effect). It is essentially based on charge transport between a source and a gain electrode which are separated by a semiconductor and isolated from the gate electron by a dielectric material. The semiconductor acts as a channel for charge transport between the source and the drain. At the interface of the semiconductor and the dielectric layer, a charge is generated and therefore a changed bias at the gate electrode is detectable. If the semiconductor consists of semiconducting organic material it is referred as an organic field-effect transistor (OFET).[38, 39] Conjugated small organic molecules or polymers of p- or n-type are commonly utilized where the latter is strongly underrepresented.[40] Several architectures are possible in an OFET device: top-contact bottom-gate, top-contact top-gate, bottom-contact top-gate and bottom-contact bottom-gate type. When a positive or negative potential is applied to the gate electrode (V_g), electrons (n-type) and holes (p-type) accumulate at the interface of the organic semiconductor and dielectric layer (Fig. 5).
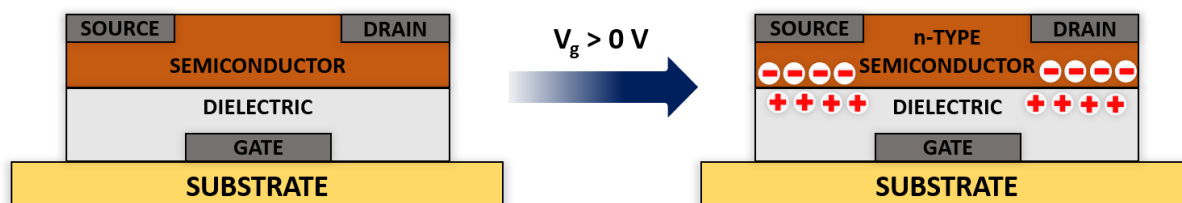
Fig. 5: As an example, the functionality of a bottom-contact bottom-gate OFET setup is shown.

This results in a measurable electric current with a defined voltage between the source and the drain electrode. The most important technical parameters for OFETs are defined by the mobility of electrons (μ_e) and holes (μ_h), as well as the ratio of electrical currents (I_{on}/I_{off}) of the gate voltage in an ON and OFF mode. Moreover, the threshold voltage (V_{th}), which is the minimum gate-to-source voltage that is required to create conduction between the source and drain, is a characteristic parameter. Although aiming for superior device performance, the fundamental nature of organic semiconducting materials (n-type or p-type) can be described in an OFET setup. For applications, an intense π-π-stacking behavior of the utilized small molecule or polymer is highly favorable as it enhances the intermolecular charge transfer.[41] This contrasts with their application in organic electroluminescent devices.

References

1. J. E. Anthony, *Chem. Rev.*, **2006**, *106*, 5028-5048.
2. J. E. Anthony, *Nat. Mater.*, **2014**, *13*, 773-775.
3. H. Usta, A. Facchetti, T. J. Marks, *Acc. Chem. Res.*, **2011**, *44*, 501-510.
4. T. Baumgartner, F. Jäkle, *Main Group Strategies towards Functional Hybrid Materials*, John Wiley & Sons Ltd, Hoboken, Chichester, 1st edn., **2018**.
5. C. D. Entwistle, T. B. Marder, *Chem. Mater.*, **2004**, *16*, 4574-4585.
6. D. Li, H. Zhang, Y. Wang, *Chem. Soc. Rev.*, **2013**, *42*, 8416-8433.
7. S. Yamaguchi, A. Wakamiya, *Pure Appl. Chem.*, **2006**, *78*, 1413-1424.
8. F. Jäkle, *Chem. Rev.*, **2010**, *110*, 3985-4022.
9. D. Chen, S.-J. Su, Y. Cao, *J. Mater. Chem. C*, **2014**, *2*, 9565-9578.
10. S. A. Ponomarenko, S. Kirchmeyer, *Conjugated Organosilicon Materials for Organic Electronics and Photonics*, in *Silicon Polymers*, ed. A. M. Muzafarov, Springer, Berlin, Heidelberg, **2011**, 33-110.
11. M. Hissler, P. W. Dyer, R. Réau, *Coord. Chem. Rev.*, **2003**, *244*, 1-44.
12. T. Baumgartner, R. Reau, *Chem. Rev.*, **2006**, *106*, 4681-4727.

13. T. P. Kaloni, P. K. Giesbrecht, G. Schreckenbach, M. S. Freund, *Chem. Mater.*, **2017**, *29*, 10248-10283.
14. W. Jiang, Y. Li, Z. Wang, *Chem. Soc. Rev.*, **2013**, *42*, 6113-6127.
15. S. M. Parke, M. P. Boone, E. Rivard, *Chem. Commun.*, **2016**, *52*, 9485-9505.
16. G. C. Welch, R. R. San Juan, J. D. Masuda, D. W. Stephan, *Science*, **2006**, *314*, 1124-1126.
17. J. C. Berrones-Reyes, C. C. Vidyasagar, B. M. Muñoz Flores, V. M. Jiménez-Pérez, *J. Lumin.*, **2018**, *195*, 290-313.
18. E. Hey-Hawkins, M. Hissler, *Smart Inorganic Polymers*, Wiley VCH, Weinheim, **2019**.
19. L. Zani, A. Dessì, D. Franchi, M. Calamante, G. Reginato, A. Mordini, *Coord. Chem. Rev.*, **2019**, *392*, 177-236.
20. N. Miyaura, K. Yamada, A. Suzuki, *Tetrahedron Lett.*, **1979**, *20*, 3437-3440.
21. N. Miyaura, A. Suzuki, *Chem. Rev.*, **1995**, *95*, 2457-2483.
22. Y. Hatanaka, T. Hiyama, *J. Org. Chem.*, **1988**, *53*, 918-920.
23. S. E. Denmark, C. S. Regens, *Acc. Chem. Res.*, **2008**, *41*, 1486-1499.
24. J. W. L. A. F. Renaldo, J. K. Stille, *Organic Syntheses*, **1989**, *67*, 86.
25. J. K. Stille, *Angew. Chem. Int. Ed. Engl.*, **1986**, *25*, 508-524.
26. H. Shirakawa, E. J. Louis, A. G. MacDiarmid, C. K. Chiang, A. J. Heeger, *J. Chem. Soc., Chem. Commun.*, **1977**, 578.
27. A. J. Heeger, *Angew. Chem. Int. Ed.*, **2001**, *40*, 2591-2611.
28. A. G. MacDiarmid, *Angew. Chem. Int. Ed.*, **2001**, *40*, 2581-2590.
29. H. Shirakawa, *Angew. Chem. Int. Ed.*, **2001**, *40*, 2574-2580.
30. R. Hamze, P. I. Djurovich, M. E. Thompson, **2016**, *2*, 195-241.
31. M. Kasha, *Discuss. Faraday Soc.*, **1950**, *9*, 14.
32. J. R. Lakowicz, *Principles of Fluorescence Spectroscopy*, Springer US, Boston, 3rd edn., **2006**.
33. K. Houser, M. Mossman, K. Smet, L. Whitehead, *Leukos*, **2015**, *12*, 7-26.
34. E. Longhi, L. De Cola, *Iridium(III) Complexes for OLED Application*, in *Iridium(III) in Optoelectronic and Photonics Applications*, ed. E. Zysman-Colman, John Wiley & Sons Ltd, Hoboken, Chichester, **2017**, 205-274.
35. H. Nakanotani, T. Higuchi, T. Furukawa, K. Masui, K. Morimoto, M. Numata, H. Tanaka, Y. Sagara, T. Yasuda, C. Adachi, *Nat. Commun.*, **2014**, *5*, 4016.
36. J.-H. Lee, C.-H. Chen, P.-H. Lee, H.-Y. Lin, M.-k. Leung, T.-L. Chiu, C.-F. Lin, *J. Mater. Chem. C*, **2019**, *7*, 5874-5888.
37. J. Adachi, H. Kakizoe, P. K. D. Tsang, A. Endo, *SID Symposium Digest of Technical Papers*, **2019**, *50*, 95-98.
38. W.-Y. Lee, J. Mei, Z. Bao, *OFETs: Basic Concepts and Material Designs*, in *The WSPC Reference on Organic Electronics: Organic Semiconductors*, eds. J.-L. Bredas and S. R. Marder, **2016**, vol. 2, 19-83.
39. H. Klauk, *Organic Electronics: Materials, Manufacturing and Applications*, Wiley VCH, Weinheim, **2006**.
40. M. Stolar, T. Baumgartner, *Phys. Chem. Chem. Phys.*, **2013**, *15*, 9007-9024.
41. C. R. Newman, C. D. Frisbie, D. A. da Silva Filho, J.-L. Brédas, P. C. Ewbank, K. R. Mann, *Chem. Mater.*, **2004**, *16*, 4436-4451.

Preface for Chapters 1 and 2: Influence of Group 14 Elements on Chromatic π-Conjugated Systems and Functional Materials

Besides being located in the same main group, chemical elements from group 14 (carbon, silicon, germanium, tin and lead) are utterly diverse. While carbon is classified as a non-metal element, silicon and germanium are metalloids, while tin and lead are defined as metals. Such strong inner group trends correlate with the fact that group 14 elements (tetrels) feature differing charge/radii ratios and are chemically more related to their diagonal neighbors in the periodic table.[1] Due to differing electron negativities of carbon (χ = 2.50), silicon (χ = 1.70), germanium (χ = 2.00), tin (χ = 1.96) and lead (χ = 1.60),[2] tetrel-hydrogen species, with the electronegativity of hydrogen (χ = 2.20), might occur with inverted polarity: While hydrocarbons feature partly positively charged hydrogen atoms, heavier tetrels reveal more negatively charged hydrogen atoms (hydrides), which are commonly used as reduction agents, e.g. triethylsilane.

In general, the substitution of carbon by heavier tetrels in π-conjugated systems was intensively studied in the last three decades. With respect to the already established silicon research in the field of functional materials, e.g. silicon-based electronics, organosilicons are already well developed. Contrariwise, the use of the other group 14 heavy elements, especially germanium and tin, in organic materials was less pronounced until now. Especially the incorporation of lead in organic structures is less studied due to the generally low dissociation enthalpy of Pb-C bonds and the ability to undergo homolytic cleavage of tetracoordinate organolead compounds.[3] However, since silicon, germanium and tin hold different physical properties (electronegativity, polarizability, covalent radii) as well as chemical properties (redox behavior, bond dissociation energies and hyper-/hypovalency) compared with carbon, their integration into π-system to tune physical and chemical material properties developed intensively.

The implementation of heavier tetrels in π-conjugated systems has become a useful tool to tune the electronic and optical properties but also to access reactivity towards transition metal-catalyzed cross-coupling reactions.

After the implementation of silicon in a five-membered heterocyclic π-conjugated systems and successful usage as electron-transporting material in an OLED in 1996,[4] studies of germanium and tin heteroles followed thereafter. It was found that group 14 heteroles (siloles, germoles, stannoles) exhibited a high electron affinity due to σ*-π* conjugation effects (*vide infra*). Apart from this electronic feature, the implementation of organotetrels into organic materials represents a versatile method to tune the solubility, flexibility and processability in organic devices due to the length/flexibility of the Si/Ge/Sn-C bond. In the following, the influence of organotetrels on the optical properties and functionality of chromatic π-conjugated systems will be discussed for compounds with an *exo-* or *endo*cyclic substitution pattern (Fig. 6).

σ*-π* conjugation   leaving group

endo-cyclic   *exo*-cyclic

M = Si, Ge, Sn
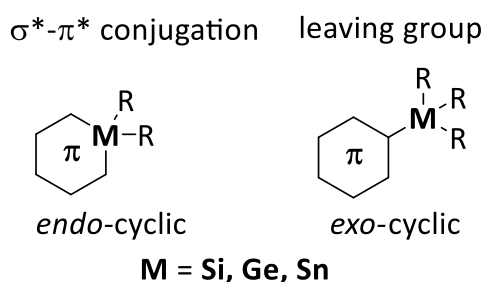
Fig. 6: Embedment of heavier organoterels in π-conjugated systems in *exo-* or *endo*-cyclic position.

As organotetrel substituents influence the HOMO-LUMO gap when embedded into π-conjugated systems, the focus will be on optoelectronic functional materials and their physicochemical properties. For exocyclically catenated tetrel moieties, their effects in tetrel/metal exchange reactions and as leaving groups in cross-coupling reactions will be highlighted. The latter method became more prominent. Due to the nucleophilic character of the carbon in combination with a heavier tetrel (Si, Ge, Sn), transition metal-catalyzed cross-coupling reactions for each organotetrel were reported, e.g. Hiyama-Denmark (Si)[5, 6], germanium-based[7, 8] or Stille cross-coupling (tin)[9, 10].

References

1. N. Wiberg, A. F. Holleman, E. Wiberg, G. Fischer, *Lehrbuch der Anorganischen Chemie*, in *Kapitel XV. Die Kohlenstoffgruppe („Tetrele")*, De Gruyter, Berlin, Boston, 102 edn., **2007**, 861.

2. N. Wiberg, A. F. Holleman, E. Wiberg, G. Fischer, *Lehrbuch der Anorganischen Chemie*, in *Kapitel VI. Der Molekülbau*, De Gruyter, Berlin, Boston, 102 edn., **2007**, 146.

3. T. Kano, S. Saito, *Lead in Organic Synthesis*, in *Main Group Metals in Organic Synthesis*, eds. H. Yamamoto and K. Oshima, Wiley-VCH, Weinheim, **2004**, 721-751.

4. K. Tamao, M. Uchida, T. Izumizawa, K. Furukawa, S. Yamaguchi, *J. Am. Chem. Soc.*, **1996**, *118*, 11974-11975.

5. Y. Hatanaka, T. Hiyama, *J. Org. Chem.*, **1988**, *53*, 918-920.

6. S. E. Denmark, C. S. Regens, *Acc. Chem. Res.*, **2008**, *41*, 1486-1499.

7. T. Nakamura, H. Kinoshita, H. Shinokubo, K. Oshima, *Org. Lett.*, **2002**, *4*, 3165-3167.

8. J. W. Faller, R. G. Kultyshev, *Organometallics*, **2002**, *21*, 5911-5918.

9. C. Cordovilla, C. Bartolomé, J. M. Martínez-Ilarduya, P. Espinet, *ACS Catalysis*, **2015**, *5*, 3040-3053.

10. J. K. Stille, *Angew. Chem. Int. Ed. Engl.*, **1986**, *25*, 508-524.

Chapter 1: Influence of Group 14 Elements in *Endo*cyclic π-Conjugated Systems Using the Example of Stannoles

1.1 General Introduction

Initial theoretical investigations by Yamaguchi and Tamao[1] generated considerable interest in substituting the sp³-hybridized atom in a cyclopentadienyl scaffold with heavier organotetrels. As predicted by calculations, silole, the silicon-substituted cyclopentadiene congener, exhibited a more stabilized LUMO than cyclopentadiene itself. Due to an overlap of the π* orbital of the butadiene fragment and the σ* orbital of the exocyclic Si-C fragments (σ*-π* conjugation) the stabilization of the LUMO is realized (Fig. 7).[1-3]
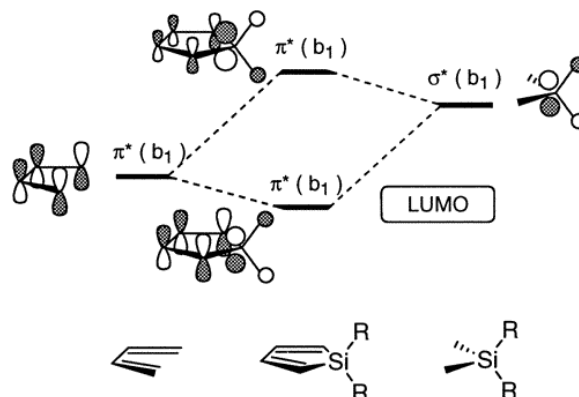
Fig. 7: The interactions of the π*-orbital of butadiene with the σ*-orbitals of the silicon atom stabilizes the LUMO in siloles. Adapted with permission.[4]

But not only silicon was investigated in this field: Germanium has a similar covalent radius (1.20 Å) compared to silicon (1.11 Å) due to d-block contraction[5] but holds an electronegativity (χ = 2.02) which is much closer to carbon (χ = 2.50) than silicon (χ = 1.74). In fact, this small difference has a substantial impact on the chemical stability of siloles/germoles as carbon-substituted germanium is much more stable to bases and nucleophiles than the corresponding siloles. Hence, polymerization procedures using Suzuki-conditions are exclusively applicable to germoles, as siloles would undergo decomposition.[6] However, to compare the photophysics of these cyclopentadienyl analogs, a series of silicon, germanium and tin-substituted 2,5-dithienylmetalloles were synthesized.[4] It was found that a substantial bathochromic shift in the UV/Vis absorption spectra is observed when the cyclopentadiene scaffold (**1**, λ_{abs} = 368 nm) was substituted by heavier group 14 elements forming siloles (**2/3**, λ_{abs} = 418/409 nm), germoles (**4**, λ_{abs} = 428 nm) and stannoles (**5**, λ_{abs} = 430 nm) (Fig. 8).

X = **C** (R = Ph), **1**, $\lambda_{abs/ems}$ = 368/461 nm

X = **Si** (R = Ph), **2**, $\lambda_{abs/ems}$ = 418/515 nm

X = **Si** (R = CyPen), **3**, $\lambda_{abs/ems}$ = 409/492 nm

X = **Ge** (R = CyPen), **4**, $\lambda_{abs/ems}$ = 428/479 nm

X = **Sn** (R = CyPen), **5**, $\lambda_{abs/ems}$ = 430/479 nm
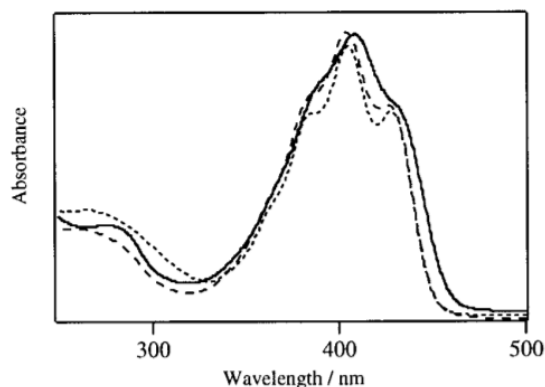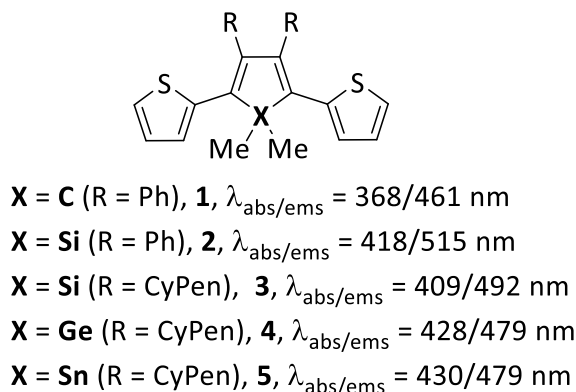
Fig. 8: (Left) Optical properties of chemical structures including different 2,5-dithienylmetalloles. (Right) Absorption spectra of 2,5-dithienylsilole (**3**, solid line), 2,5-dithienylgermole (**4**, dashed line), 2,5-dithienylstannole (**5**, dotted line). Adapted with permission.[4]

In general, the σ*-stabilization effect was calculated to be greater for tin than for germanium and silicon. Contrary to this effect, the ionic radii of tetrels increase with the period and therefore the σ*-π* orbital overlap is decreased. Therefore, both compensate each other and larger bathochromic shifts following the periodic trend within the tetrels were not observed. The reported dithienyl-substituted metalloles were only slightly emissive in solution ($\Phi_{lum} < 9\%$), while the originating cyclopentadienyl scaffold was almost non-emissive ($\Phi_{lum} < 1\%$). However, the silole derivatives are also efficient emitters, especially in the solid-state.

Based on the investigations by Ben Zhong Trang on the aggregation-induced emission (AIE) phenomenon of propeller-like 1-methyl-1,2,3,4,5-pentaphenylsilole (**6**), a new branch of research originated.[7-9] It was found that the silole (**7**) was only barely emissive in ethanol but became highly emissive by the addition of water (Fig. 9).

twisted (non-emissive)   *coplanar* (emissive)
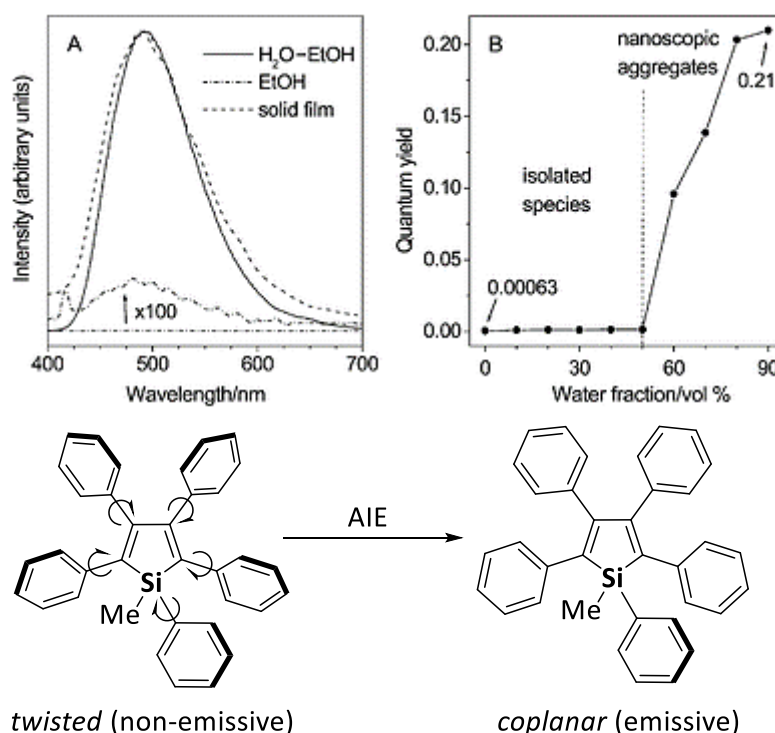
Fig. 9: Emission spectra of 1-methyl-1,2,3,4,5-pentaphenylsilole (**6**) in solid film (dashed line), ethanol (dotted line) and water/ethanol mixture (solid line) B) Luminescence quantum yield depending on the water fraction in an ethanol/water mixture of **6**. Adapted with permission.[7]

The silole's phenyl groups strongly induce a non-radiative decay of the excited state in solution, while in the aggregated state, a rotary restriction is present, and the non-radiative decay is unfavored. The aggregated state was 330 times more emissive than the silole in solution.[7] Comparing all group 14 metalloles, siloles and germoles showed intense AIE behavior while stannoles were not affected by this phenomenon.[10] Most recently, luminescent stannoles with good luminescence in the solid-state ($\Phi_{lum} = 11.1\%$) and film ($\Phi_{lum} = 24.4\%$) along with AIE characteristics were reported.[11] Initial results prevailed that AIE luminophores in general are promising candidates for organic electronics and luminescent devices.[12]

Notwithstanding, due to substantial stabilization of the LUMO and AIE behavior, group 14 element metalloles gained interest as electron-transporting and emitting material for optoelectronic applications. From all group 14 element metalloles, silole-based derivatives have been heavily studied and used in different devices.[13, 14] For example, silole-based derivatives were used as active material in organic electronic devices, e.g. thin-film transistors (TFT) and photovoltaic devices, in both their

monomeric or polymeric form.[13, 15-17] As a matter of fact, the 2,5-diarylsilole's electron mobility exceeded that of the commonly used tris(8-hydroxyquinoline) aluminum (Alq$_3$) as electron-transporting material in an OLED. Furthermore, the device held lower turn-on voltage (V$_{on}$) and a good luminance of 1620 cd/m^2 with 3 times longer driving time than Alq$_3$.[18] Germoles-based materials were intensively studied as active material in bulk heterojunction solar cells (BHJSCs)[19] and showed high power conversion efficiencies up to 7.2%[20]. Moreover, germoles derivatives were utilized in light-emitting devices which were characterized by a low V$_{on}$ (2.8 V), high luminance (29700 cd/m^2), and good external quantum efficiency (EQE = 3.4%). The respective silole derivative exhibited similar performance: V$_{on}$ (2.9 V), high luminance (26100 cd/m^2), and good external quantum efficiency (EQE = 5.2%).[21] For stannoles, such a broad variety of applications has not been reported so far and still needs to be evaluated.

1.1.1 Heavier Tetrels in Polycyclic Aromatic Hydrocarbons

Group 14 metalloles were embedded in larger π-conjugated systems, e.g. heterofluorenes, and the effects of the heteroatom (silicon, germanium and tin) in respect of their optoelectronic properties was evaluated (Fig. 10).[22]

M = **Si** (R= Me): **7**, $\lambda_{abs/ems}$ = 307/337 nm   **11**, $\lambda_{abs/ems}$ = 367/402 nm

M = **Si** (R = Ph): **8**, $\lambda_{abs/ems}$ = 315/365 nm   **12**, $\lambda_{abs/ems}$ = 358/414 nm

M = **Ge** (R = Ph): **9**, $\lambda_{abs/ems}$ = 308/331 nm   **13**, $\lambda_{abs/ems}$ = 368/411 nm

M = **Sn** (R = Ph): **10**, $\lambda_{abs/ems}$ = 309 nm/none **14**, $\lambda_{abs/ems}$ = 363/410 nm
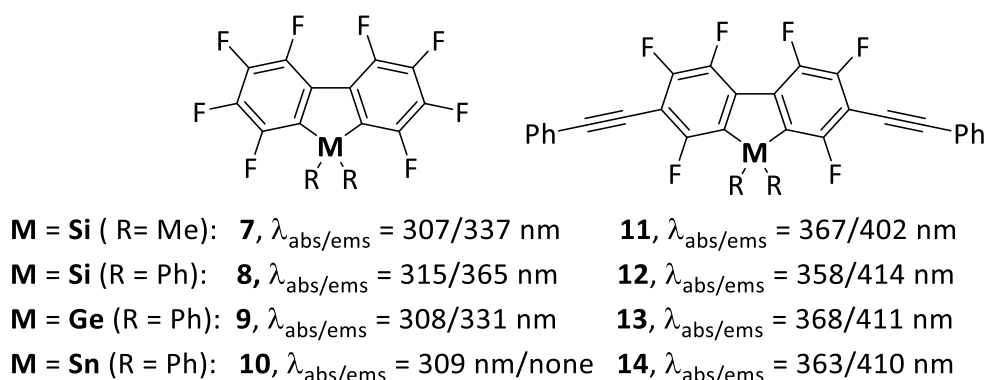
Fig. 10: Overview of tetrel-substituted octafluoroheterofluorenes and their absorption/emission properties.[22]

Octafluoroheterofluorenes exhibited absorption bands in the UV region (307 - 315 nm) and the nature of the tetrel had mostly no effect on the absorption properties. In the contrary, the emission properties were strongly affected. While low to moderate luminescence quantum yields for siloles (Φ_{lum} = 0.20 for **7** and Φ_{lum} = 0.26 for **8**) were observed, the respective germoles and stannoles were barely (Φ_{lum} = 0.03 for **9**) or not emissive (**10**) in solution. Upon disubstitution with phenylacetylene in 2,7-positions, bathochromically shifted absorption and emission properties as well as impressively increased quantum yields (Φ_{lum} = 1.00 for **11**, **12**, **13** and Φ_{lum} = 0.65 for **14**) resulted. This effect could be assigned to an additional stabilization of the LUMO level upon laterally extended π-conjugation. In tin-substituted chromophores, an increased intersystem crossing and a non-radiative decay are present, which results in weak luminescent properties due to vibrational relaxation.[22] Besides these examples of highly luminescent tetracoordinated tin-substituted materials, pentacoordinate tin and lead structures exhibited advantageous phosphorescence emission as the triplet states were accessible due to the strong spin-orbital coupling.[23] This should be considered when evaluating organotin and organolead structures as potential phosphorescent rather than fluorescent chromophores.

The substitution of larger polycyclic aromatic hydrocarbons (PAHs) with silicon, germanium or tin was performed on triphenylenes, to which the tetrels were connected externally to obtain derivatives of heterosumanenes (Fig. 11).
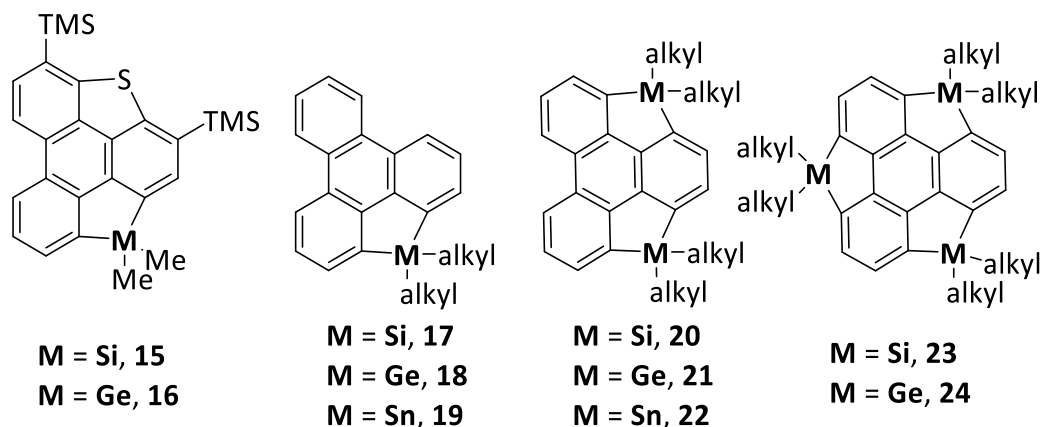
Fig. 11: Overview of tetrel-substituted triphenylenes and sumanenes.

Though substitution with trimethylsilyl groups in *ortho*-positions of the triphenylenothiophene resulted in a bathochromic shift of the absorption and emission maxima, the introduction of bridging group 14 elements into the π-backbone (**15-16**) had no further impact.[24, 25] Inspired by this work, neat triphenylene was *exo*-bridged with alkylsilicon, alkylgermanium or alkyltin moieties once, twice or even thrice. All species exhibited absorption from 240-300 nm and emission from 330-430 nm.[26, 27] The first bridging organotetrel unit (**17-19**) showed the highest influence on the optical properties, whereas a second (**20-22**) and third (**23-24**) substitution resulted only in marginally red-shifted absorption and emission maxima.[27] Potential usage of organotetrel substituted sumanenes could be as nanographene derivatives in organic electronics in respect to the stabilized LUMO level.

1.1.2 Late Group 14 Elements in Functional Dyes

Next to organic electronic applications, the implementation of tetrels in dye structures for bioimaging, particularly for stimulated emission depletion (STED) microscopy, represents a field of application of main group chemistry. As fluorescein and rhodamines, common fluorophores, are based on the xanthene motif, efforts were made to substitute the central oxygen atom with organotetrels. For instance, silicon-substituted rhodamines and fluorescein were reported[28] and became commercially available STED dyes. The introduction of an organotetrel into the xanthene scaffold led to a bathochromic shift of the absorption and emission wavelength owing to a stabilization of the LUMO due to σ*-π*-conjugation of the tetrels' σ* orbital with the xanthenes' π* orbital. Aside from silicon, a variety of tetrels was implemented to substitute the oxygen atom of the pyronine scaffold to investigate the influence of the tetrels on the optoelectronic properties of the dye (Fig. 12, left).[29]

X = O, **25**, $\lambda_{abs/ems}$ = 547/562 nm   X = C (R = Me), **29**, $\lambda_{abs/ems}$ = 418/511 nm

X = Si, **26**, $\lambda_{abs/ems}$ = 634/648 nm   X = C (R = Ph), **30**, $\lambda_{abs/ems}$ = 431/552 nm

X = Ge, **27**, $\lambda_{abs/ems}$ = 621/634 nm   X = Si (R = Me), **31**, $\lambda_{abs/ems}$ = 446/544 nm

X = Sn, **28**, $\lambda_{abs/ems}$ = 614/628 nm   X = Si (R = Ph), **32**, $\lambda_{abs/ems}$ = 459/558 nm
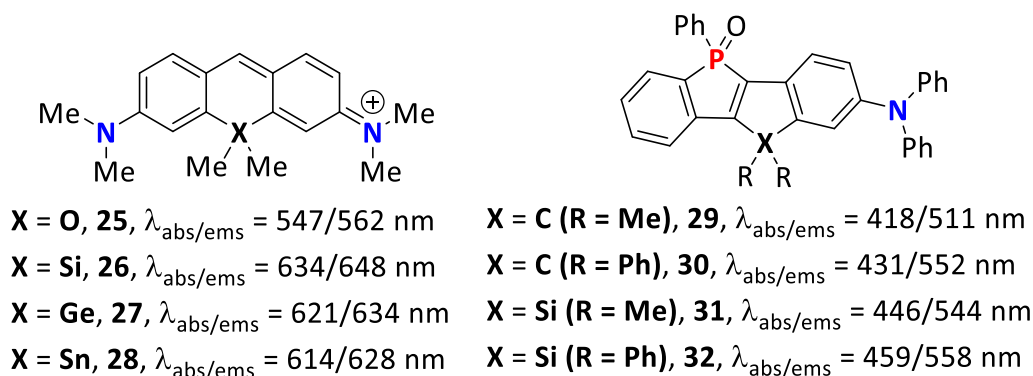
Fig. 12: Overview of common tetrel-embedded dyes for bioimaging and their photophysical properties.[29, 30]

In sum, the substitution of the oxygen-atom in a pyronine scaffold by silicon, germanium and tin led to a bathochromic shift of the absorption and emission maxima. The silicon atom had the strongest effect on the optical properties of the chromophoric system compared to germanium and tin atoms. This observation might be related to the large atom radius of the tetrel and the decreased orbital interaction upon increasing the size of the tetrel. Staining of tubulin with a silicon-based rhodamine derivative led to a high spatial resolution (29 ± 11 nm) in a STED microscopy image.[31] Due to the combination of high photostability and bathochromic shifted absorption/emission, silicon-substituted rhodamine derivatives were used in live STED where the dye is exposed to high-intensity laser light multiple times.[32]

In analogy to the cyclopentadiene/metallole relation (Fig. 8), the substitution of an sp³-hybridized carbon atom by a silicon atom in an annulated phosphole-based PAH had a beneficial impact on the optical properties (Fig. 12, right). The absorption and emission maxima were shifted bathochromically by approx. 30 nm. As the dye should be used as the STED probe, the photostability of the dye has a high priority. It was shown that the silicon-substituted derivative was more photostable than the carbon analog. Furthermore, it was found that phenyl groups at the silicon atom provide sterically shielding and, therefore, the photodegradation was less pronounced than with methyl groups.[30] Compared to common STED dyes, these phosphole-based materials withstand photobleaching which allowed multicolor STED application.[33]

1.1.3 Group 14 Dibenzoheteroles in Annulative π-Extension Reactions

The benefits of group 14 element heteroles are not limited to σ*-π* conjugation and the respective stabilization of the LUMO level for optical active materials. Since organo-silicon,[34, 35] -germanium[36-38] and -tin[39, 40] derivatives are well known as leaving groups in cross-coupling reactions, group 14 element heteroles could also be utilized in palladium-catalyzed ring-opening annulative reactions. This idea originated from reactions of dibenzozirconoles with dihalobenzenes which allowed metallafluorenes ring-opening annulative π-extension (APEX) reactions.[41] Such reaction types are highly desirable since they lead to the synthesis of fused PAHs from relatively simple aromatic compounds in a one-pot reaction.[42] A similar reaction type was investigated for sila- and stannafluorenes in particular. For instance, silafluorenes (**25**) were converted in an APEX reaction with phenanthrene (**26**) to give the dibenzo[g,p]chrysene (**DBC**) derivative **tBu₂DBC** (Scheme 2).[43]
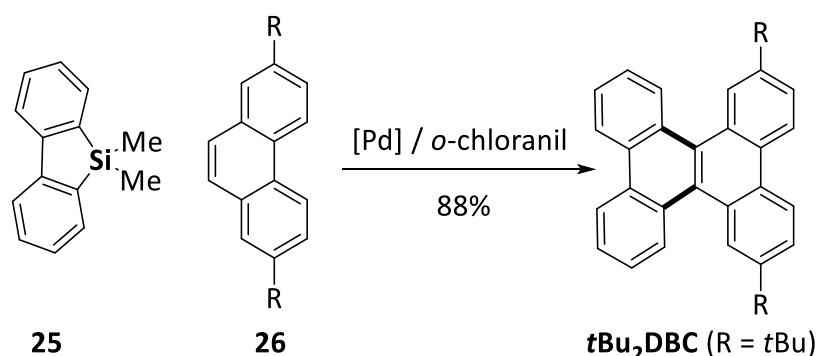
Scheme 2: Synthesis of **tBu₂DBC** using silafluorene (**25**) as precursor in a palladium catalyzed cross-coupling reaction.[44] Formed bonds are highlighted bold.

The scope of this method could be extended to a variety of symmetric or unsymmetric-substituted **DBC** derivatives. If germafluorene (**27**) and stannafluorene (**28**) were utilized as starting material, the yields decreased drastically (21%/0%). Moreover, stannafluorenes were successively subjected to

palladium-catalyzed cross-coupling reaction to form diverse polycyclic aromatic hydrocarbons without the aid of any oxidant. The stannafluorene was reacted with 1,2-dihaloarenes or 1,1-dibromoalkenes in a Stille type reaction. This method could be further employed for the synthesis of several terphenylenes (**29**), diphenanthrothiophenes (**30**) or further heteroterphenylenes (Scheme 3).[45]
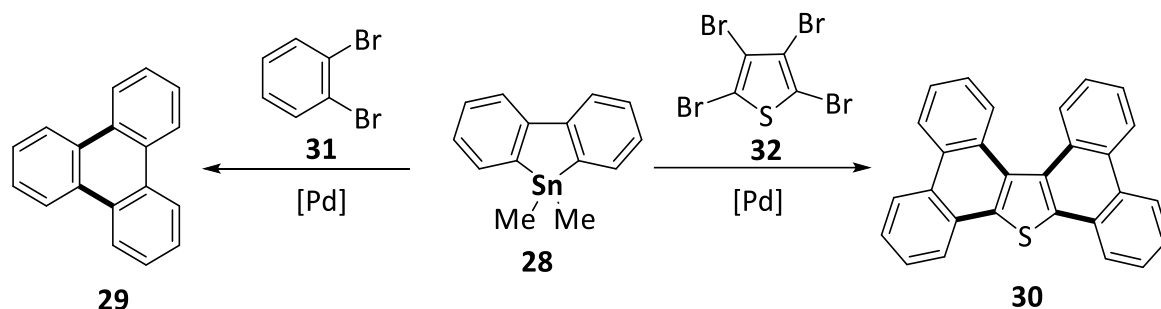
Scheme 3: Synthesis of different PAHs using dibenzostannole (**28**) as precursor in palladium catalyzed cross-coupling reactions.[45] Formed bonds are highlighted bold.

The chemical behavior of these unique group 14 element dibenzoheteroles highlighted the fact, that these heterocycles tend to undergo ring-opening reactions upon oxidative or cross-coupling conditions. This should be respected since an application in the field of organic electronics might be related to a strong redox process in devices.

1.2   Potential of Monomeric and Polymeric Stannoles in Optoelectronic Devices

As the endocyclic implementation of organotetrels in π-conjugated systems were revised briefly, the key aspect in this subsection concerns the five-membered tin-substituted heterocycles: Stannoles (Fig. 13).
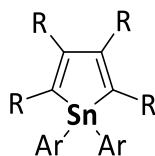
Fig. 13: Typical structure of a stannole bearing aryl groups at the tin atom, stabilizing the heterole.

Compared with siloles and germoles, stannoles have not been used for the development of active material in the field of optoelectronic devices. Initial investigation on the substitutional effect showed that the aryl-substituents at the tin atom had less influence on the optoelectronic properties compared with the substituent in the 2,5-position (Fig. 14).[46]

λ_{abs} = 418 nm (Ar = Ph, **33**) λ_{abs} = 440 nm (Ar = Ph, **36**)

λ_{abs} = 414 nm (Ar = pPhOMe, **34**) λ_{abs} = 440 nm (Ar = pPhOMe, **37**)

λ_{abs} = 427 nm (Ar = C_6F_5, **35**) λ_{abs} = 448 nm (Ar = C_6F_5, **38**)
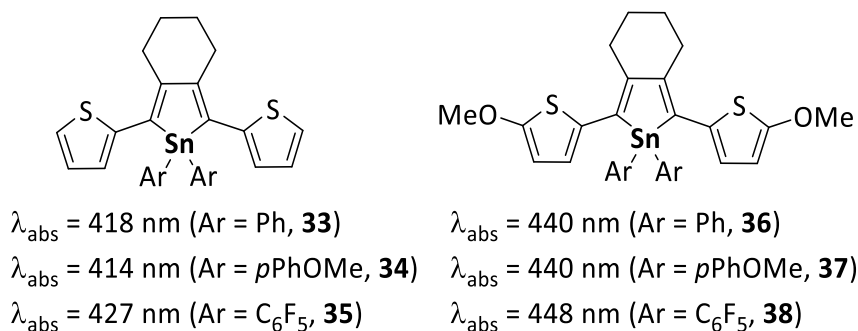
Fig. 14: Influence of the substituents at the tin and on the stannole ring towards the absorption maxima.[46]

The absorption maxima of stannole-based derivatives were bathochromic shifted upon substitution with electron-donating 2-methoxythienyl substituents in 2- and 5-position due to stabilization of the HOMO level. A further red-shift was observed upon the introduction of electron-withdrawing pentafluorobenzene motifs at the tin atom. In this case, both the HOMO and LUMO level were stabilized. Especially the LUMO level is affected by the σ*-π* conjugational effects and the nature of the exocyclic bond substituent *vide supra*.

In general, the modification of the π-backbone of the stannoles is a promising method to fine-tune the HOMO-LUMO gap, more than changing the substituents on the tin atom.[46] Another way to reduce the HOMO-LUMO gap in stannole-based materials is the lateral π-extension as in semiconducting polymers. So far two examples were presented (Fig. 15).
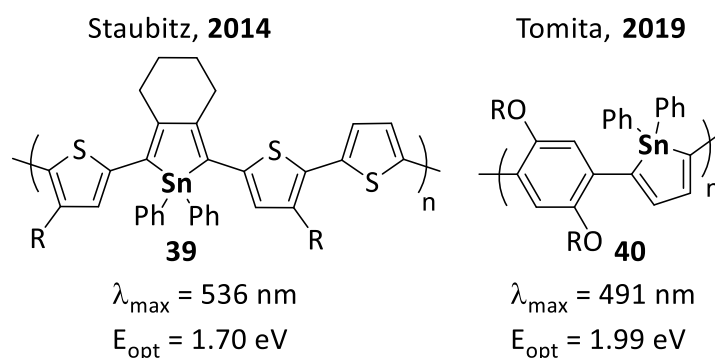
Fig. 15: Polymeric stannoles presented by Staubitz and coworkers[47] and Tomita and coworkers[48].

Extending the π-conjugated system by the copolymerization of thienyl-substituted stannoles led to a material with broad low-energy absorption (λ_{max} = 536 nm) in solution and a small optical band gap (E_{opt} = 1.70 eV) in a thin film.[47] Recently, another stannole-based polymer was prepared by the transmetalation of a polymerized (dialkoxyphenyl)-titanacyclopentadiene with organotin halides. The resulting polymeric material exhibited a broad UV/Vis absorption (λ_{max} = 491 nm) in solution and the polymer had a low optical band gap in the film (E_{opt} = 1.99 eV).[48]

For both structures, it was shown that by the implementation of a tin-atom instead of a sulfur-atom (as in thiophene) a substantial bathochromic shift resulted and the optical band gap of the material narrowed. Although accessing conjugated thiophene-based polymers by catalytic cross-coupling reactions or oxidative reactions,[49, 50] electropolymerizations of redox-active monomers became a powerful method to directly deposit the *in situ* formed polymers on transparent electrodes for electroluminescent devices.[51] Especially thienyl, pyrrole and aniline motifs are readily polymerizable under oxidative conditions (Scheme 4).[52, 53]
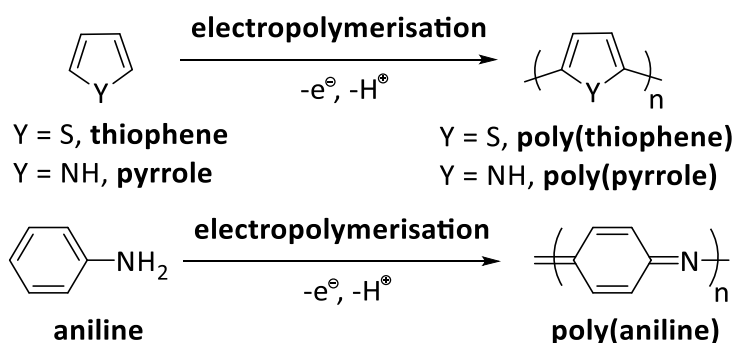
Scheme 4: Electropolymerization of thiophene, pyrrole and aniline. The product of the oxidative polymerization of aniline, poly(aniline) is found in various forms, e.g. leucoemaraldine, protoemeraldine, emeraldine and nigraniline, which are not all depicted here.[52, 53]

This concept proved also transferable to thienyl-substituted heteroles, e.g. phospholes[54, 55] and selenophenes,[56] where the thienyl moieties were oxidatively coupled, but the oxidation-sensitive heterole remained unaffected (Scheme 5).[55]

Y = S, **EDOT**
Y = Se, **EDOS**

Y = S, **PEDOT**
Y = Se, **PEDOS**

R^1 = H, R^2 = H, **41**
R^1 = CyPen, R^2 = EDO, **42**

R^1 = H, R^2 = H, **43**
R^1 = CyPen, R^2 = EDO, **44**
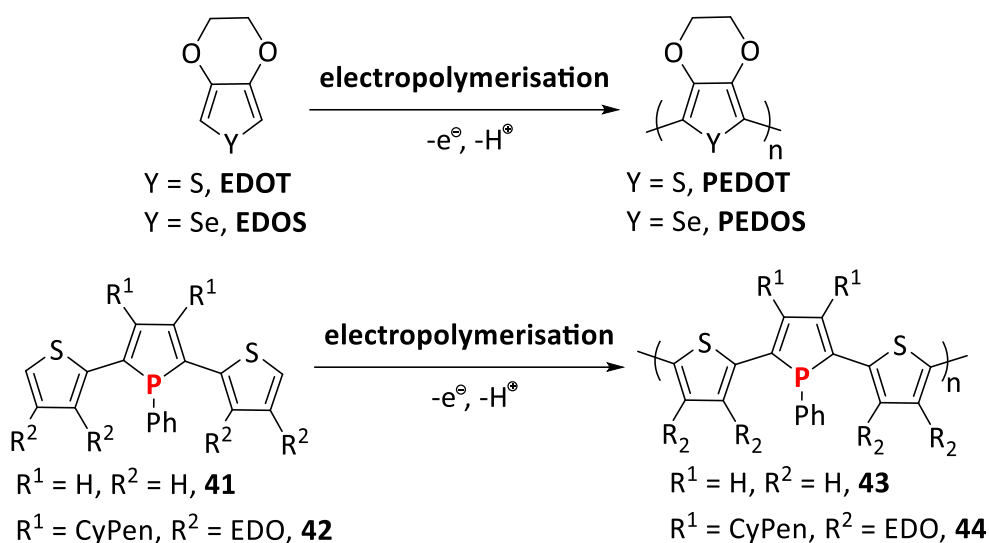
Scheme 5: Electropolymerization of **EDOS/EDOT**[56] and of thienyl-substituted phosphole **41/42**.[54, 55]

Transferring this methodology to stannole-based materials would require the intrinsic stability of the tin-heterocycle. In contrast to phosphorus(III)-based heteroles, stannoles are in fact air-stable. Moreover, the reported stannoles were surprisingly stable under cross-coupling conditions (depending on the substitution on Sn),[47] although conditions can be found in which they undergo cross-coupling.[57]

1.3   Objectives

As the implementation of stannoles into organic electronic devices has not been reported yet and the presented studies are focused on fundamental and synthetic aspects of stannoles,[58] investigations of stannole-based oligomeric and polymeric materials and their application in organic electronics were of fundamental interest.

For this purpose, the thienyl-substituted stannole should be investigated as model compounds and furthermore its dimeric and polymeric forms should be compared to its respective thiophene analogs to highlight the beneficial optoelectronic effect of the tin-atom (Fig. 16).

monomer (St1)   dimer (St2)   polymer (PSt)

terthiophene   sexithiophene   poly(thiophene)
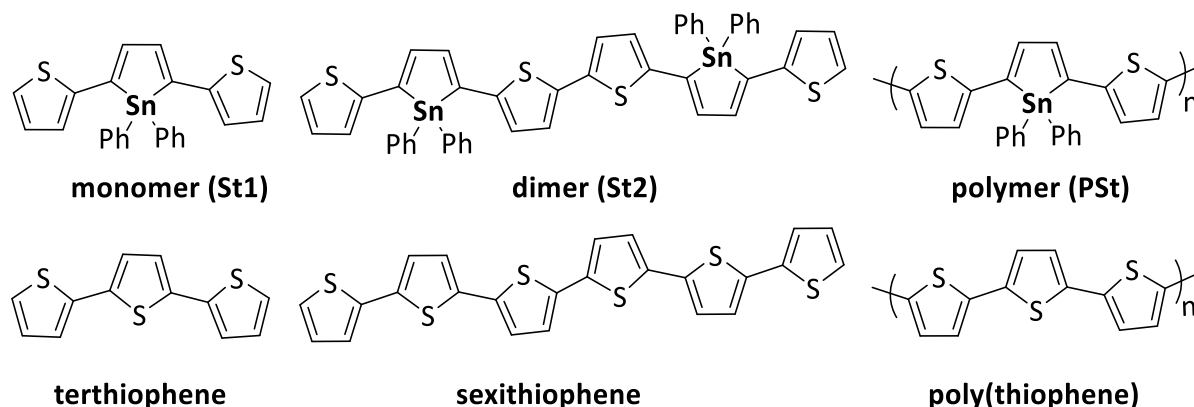
Fig. 16: Stannole monomer **St1**, dimer **St2** and polymer **PSt** and their sulfur analogs **terthiophene**, **sexithiophene** and **poly(thiophene)**.

Especially key parameters like the optical and electronic properties of the stannoles should be recorded and compared to the respective oligothiophenes. In advance, it is expected that the stannole materials hold a stabilized LUMO compared to their thiophene analogs which should result in a lower HOMO-LUMO gap and moreover, a bathochromically shifted absorption/emission.

In comparison to robust thiophene oligomers, a crucial aspect for the application of stannoles in devices is their thermal, photo- and electrochemical stability which should be further evaluated. Apart from the fact that stannole monomer and dimer should be accessible by common synthetic methods, the synthesis of stannole polymers has been very challenging and was only realized by copolymerization[47] or transmetalation of a titanocene-polymer[48] yet. As a key problem of the copolymerization with dielectrophilic thienyl-substituted stannoles and dinucleophilic thiophene, the solubility of the resulting stannole polymer was identified.[47] To take advantage of the low solubility, direct deposition of the polymeric material on electrodes electropolymerization should be investigated in this chapter. In general, the process of electropolymerization is characterized by its facile and scalable formation of thin films on conductive electrodes. Moreover, if the polymeric films are deposited on transparent electrodes, they can be directly utilized for electrochromic devices.[51] From a synthetic point of view, the functionalization of any thienyl-substituted structure with halides or leaving groups becomes obsolete, thus saves complex synthetic procedures. Furthermore, compared to the stannole-including copolymer, the necessity of a thienyl-based comonomer is not given since the stannole is already decorated with two polymerizable thienyl substituents (Scheme 6).
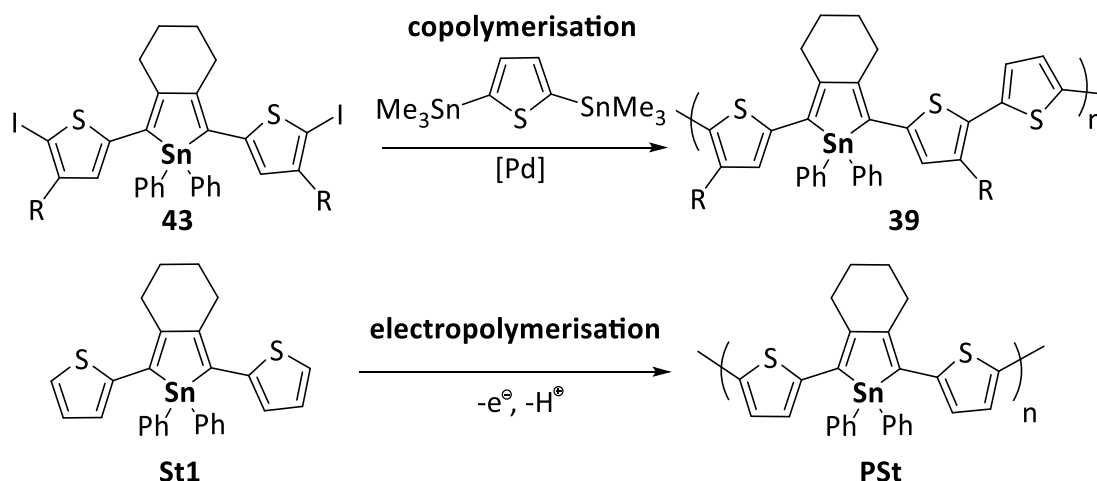
Scheme 6: Polymer **39** presented by Staubitz and coworkers[47] which was obtained through copolymerization (top). Proposed formation of polymeric stannoles by electropolymerization upon oxidation (bottom).

The resulting polymer of the electropolymerization should hold a thiophene to stannole ration of 2:1 which is lower compared with the copolymers with 3:1. Therefore, the photophysical influence of the stannole ring in the respective polymer should be reinforced. Since the endocyclic bonded tin atom withstood ring-opening under cross-coupling conditions during the (co)polymerization process,[47] the stability of stannoles in an oxidative electropolymerization should be investigated as well. Comparable studies of the electropolymerization of *bis*-thienylphospholes already showed that the heterole was not affected by the oxidation process during the electropolymerization.[55] Therefore, it might be feasible that only the thienyl-groups are involved in the polymerization process and the stannoles rings will not be attacked.

1.4 Result and Discussion

Scientific Contribution

In this cooperation project, the thienyl-substituted diynes (**44/52**) were synthesized by me. The reactions towards the stannoles (**St1/St2**) with the Rosenthal's reagent were conducted by Isabel-Maria Ramirez-y-Medina from the Staubitz group (Bremen). The reaction towards **St1** with the Negishi reagent was performed by me. Apart from the standard characterization of the stannoles, all photophysical, thermal, electrochemical analysis of the stannoles was performed by me.

1.4.1 Synthesis

To perform the full photophysical characterization and electrochemical experiments, initially thienyl-substituted stannole **St1** and its dimer **St2** were prepared (Fig. 17).
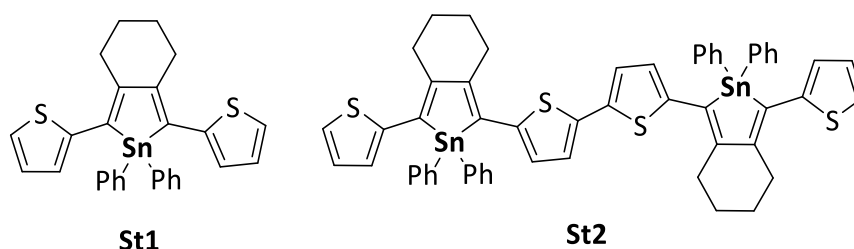
Fig. 17: Stannole monomer **St1** and its dimer **St2**.

To access the thienyl-substituted stannoles, reductive metalation of thienyl-substituted diynes with zirconocene species[59, 60] has been investigated is followed by transmetalation with diphenyltin dichloride. Therefore, the thienyl-substituted diyne **44** was synthesized by Sonogashira reaction[46] from iodothiophene (**45**) and octa-1,7-diyne (**46**) in 65% yield (Scheme 7).
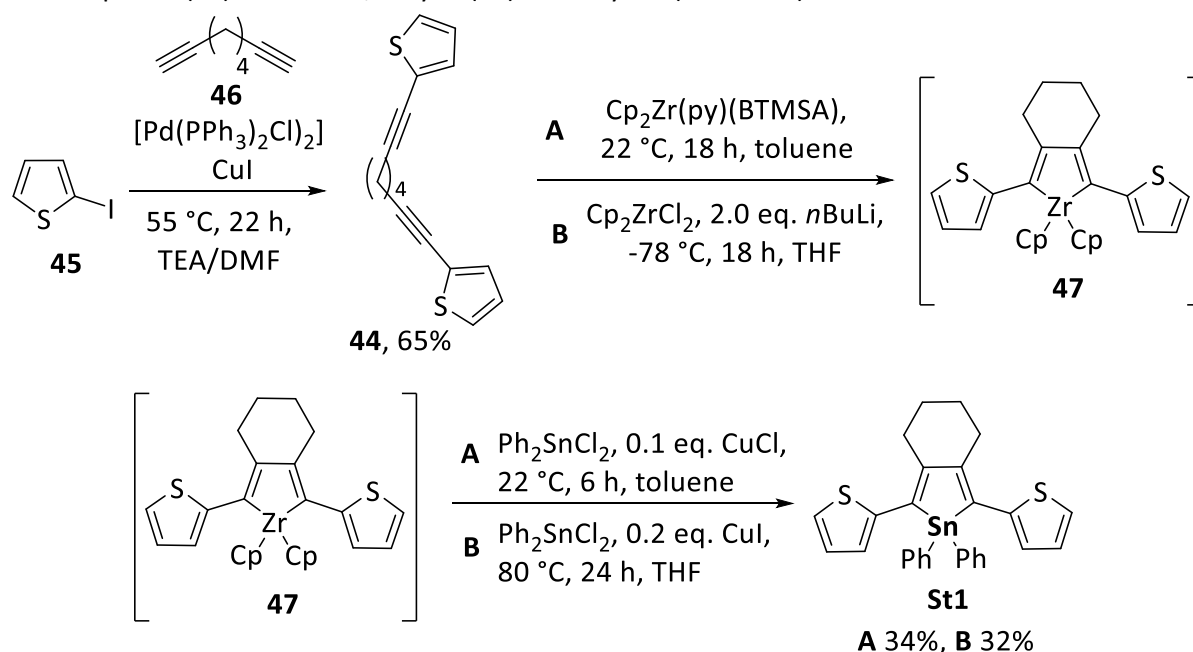
Scheme 7: Synthesis towards the stannole monomer **St1** with either Rosenthal's reagent (route A) or Negishi reagent (route B).

The synthesis of the *bis*(thienyl)-substituted stannole **St1** was conducted using two different reagents: The Rosenthal's zirconocene[59, 60] and the Negishi reagent[61] were used. A detailed study comparing both reagents had been previously reported.[59] The Negishi reagent was prepared *in situ* at low temperature

and mixed with the diyne **44**. The resulting zirconocene **47** was transmetalated with copper(I) iodide and diphenyltin dichloride in Fagan-Nugent reaction[62, 63] at elevated temperatures to give the stannole **St1** in a yield of 32%. Another synthetic pathway was previously reported by our group:[46] The dyine was brought to reaction with Rosenthal's zirconocene (**48**) to give intermediate **47**, which was not isolated but directly transmetalated with diphenyltin dichloride and copper(I) chloride to give the stannole derivative **St1** in 34% yield.

To access the corresponding dimeric stannole derivative **St2**, a synthetic strategy similar to Tilley and co-workers[64] and reported similarly by Réau and coworkes[65] was used. Sonogashira coupling of 2-bromothiophene (**49**) and octa-1,7-diyne (**46**) furnished 2-(octa-1,7-diyne)thiophene (**50**). In another Sonogashira reaction of 5,5'-dibromo-2,2'-bithiophene (**51**) with two equivalents of, the precursor **52** was obtained in a good yield of 71% (Scheme 8).
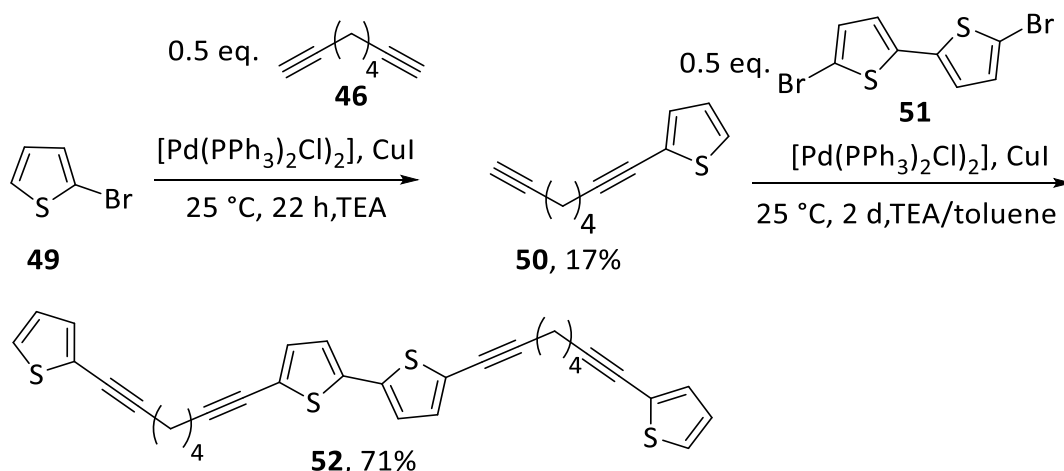
Scheme 8: Synthesis towards the 5,5'-*bis*(8-(thiophen-2-yl)octa-1,7-diyn-1-yl)-2,2'-bithiophene (**52**).

The procedure to access the stannole dimer **St2** was similar as described above. Due to the formation of two intermediate zirconoles, this time only the high potent Rosenthal's reagent (**48**) was used. Therefore, the alkyne **52** was subjected to a reductive intramolecular ring closure with Rosenthal's reagent (**48**) to provide a zirconacyclopentadiene **53** intermediate *in situ* (Scheme 9).
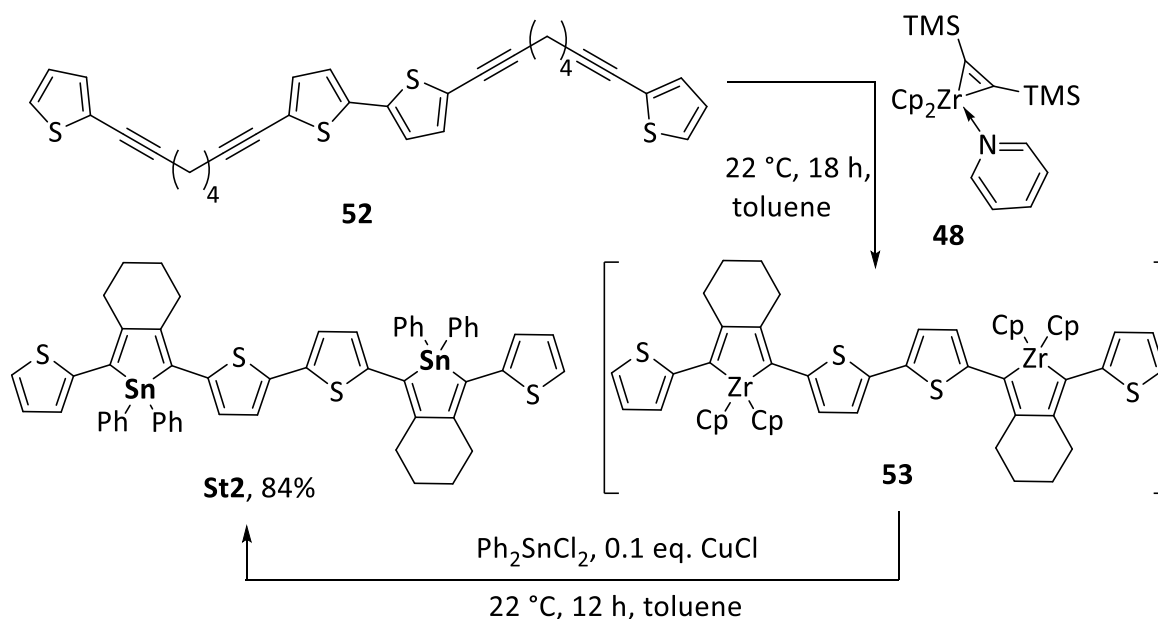
Scheme 9: Synthesis of stannole **St2** starting from the respective dynes **52**, reaction with Rosenthal's reagent (**48**) and transmetalation towards the respective stannole.

A subsequent transmetalation reaction with diphenyltin dichloride and copper chloride as additive furnished the desired stannole **St2** in a high yield of 84%. Although stannole **St1** was well soluble in aromatic or halogenated solvents, stannole **St2** exhibited a poor solubility in common organic solvents (toluene, chloroform, DCM). Their chemical identity was proven by ^{1}H, ^{13}C{^{1}H}, ^{119}Sn{^{1}H} NMR spectroscopy, HRMS and FTIR spectroscopy. The chemical shift of **St2** in the ^{119}Sn{^{1}H} NMR spectrum was found at δ = -81.0 ppm. This chemical displacement is similar to that of compound **St1** (δ = -82.4 ppm) indicating a similar chemical environment. Surprisingly, the stannole derivative **St2** showed rapid decomposition after exposition towards ambient light, which was not observed for stannole **St1**. The decomposition of **St2** after 120 min exposure to sunlight was analyzed by ^{119}Sn{^{1}H} NMR analysis and no signal was detectable (Fig. 18).
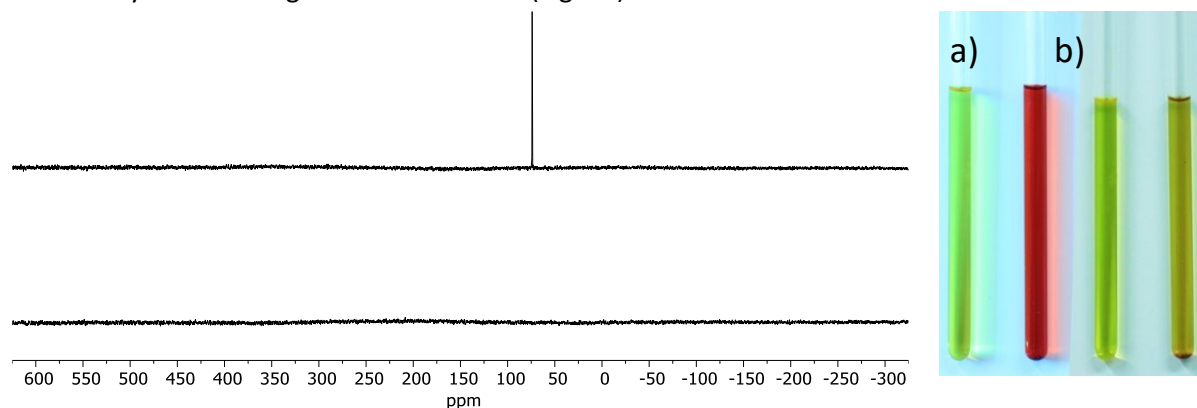
Fig. 18: ^{119}Sn{^{1}H} NMR (223 MHz) spectra before (top) and after (bottom) exposition of **St2** towards light for 2 h in CDCl$_3$. Furthermore, solutions of **St1** (left) and **St2** (right) in CDCl$_3$ as prepared (a) and after 180 min (b) upon exposition to ambient light.

The respective ^{1}H NMR spectra of **St2** showed unassignable signals in the aromatic region and a shift of the signals for the cyclohexyl protons to a higher field (Fig. 19).
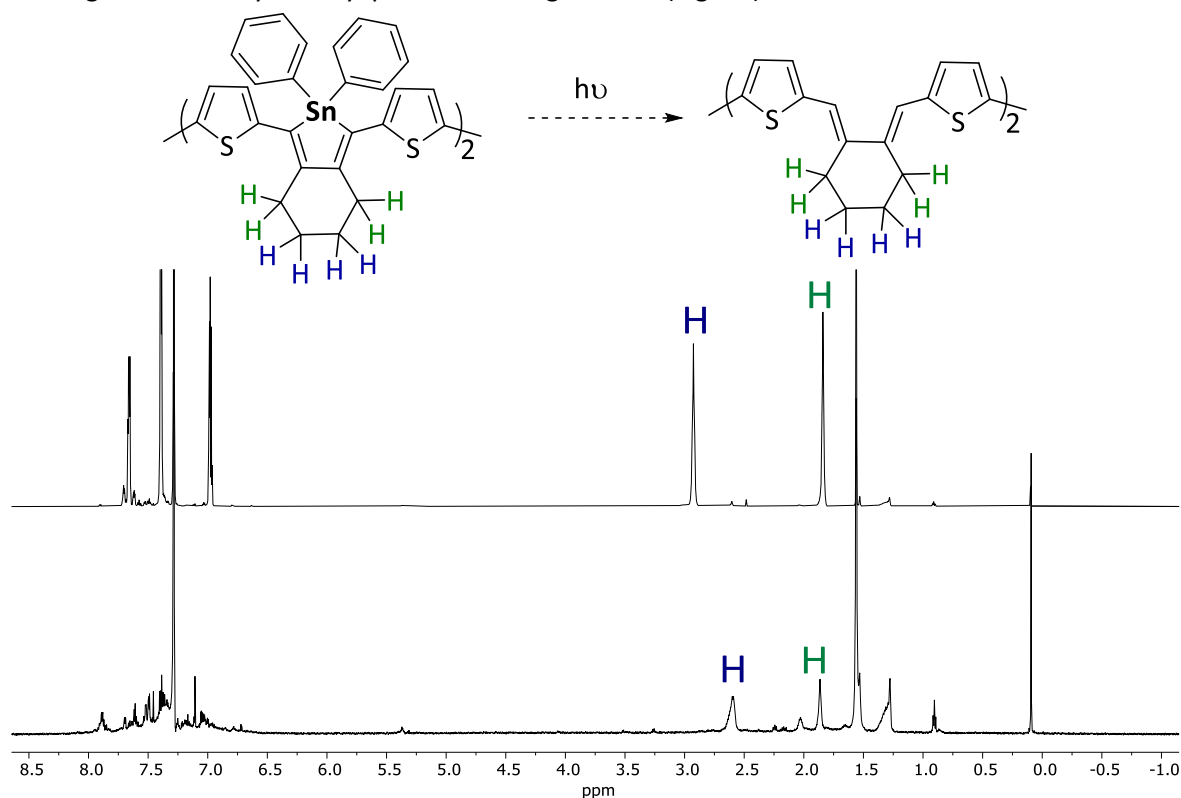
Fig. 19: ^{1}H NMR (600 MHz) spectra before (top) and after (bottom) exposition of **St2** towards the light for 2 h in CDCl$_3$. The signals at approx. δ = 3.0 and 1.9 ppm are dedicated to the CH$_2$ protons of the cyclohexyl ring.

The latter observation might indicate that the tin-atom was released from the cyclopentadiene ring and therefore it is suspected that a ring-opened structure was formed, as observed for acidolysis of similar zirconocene structures.[59]

The thermal stability of stannoles **St1** and **St2**, and their thienyl analogs was investigated by thermogravimetric analysis (TGA) and revealed that both stannoles were thermally stable and decomposed (5% mass loss) over 200 °C (Fig. 20).
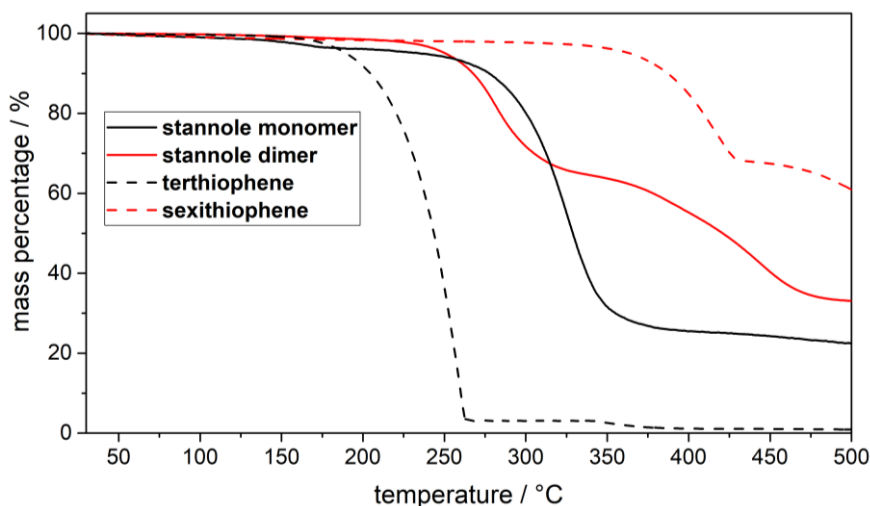
Fig. 20: Thermogravimetric analysis of both stannoles compared to their thienyl analogs with a heating rate of 10 °C/ min under a nitrogen flow of 20 mL/min in an open aluminum crucible (40 μL).

Compound **St1** underwent a continuous loss of mass, whereas **St2** exhibited a two-step mass loss. Both stannoles were not as thermally stable as their thienyl-analogs.

1.4.2 Photophysical Characterization

To estimate the effect of a lateral extension of the conjugated system (both extended π-conjugation and σ*π*-conjugation) in stannoles, comparative UV/Vis absorption studies were conducted for stannole derivative **St1** and its dimer **St2** (Fig. 21, Tab. 1).
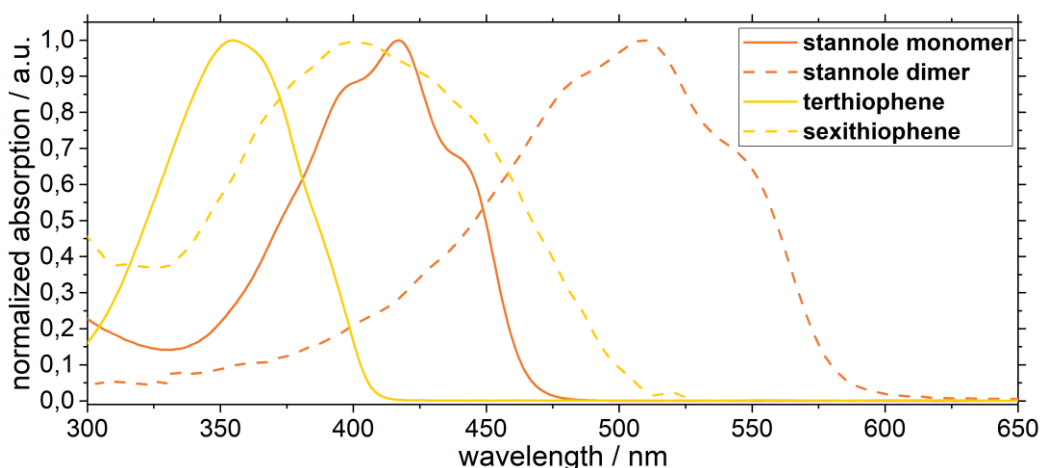
Fig. 21: Absorption spectra of **St1**, **St2**, **terthiophene** and **sexithiophene** in DCM.

Stannole **St2** exhibited a bathochromically shifted absorption (λ_{max} = 510 nm) in comparison to the absorption of **St1** (λ_{max} = 417 nm, Δ(**St2**-**St1**) = 93 nm, Fig. 21, left) along with a significantly broadened absorption indicated by the peaks full width at half maximum (FWMH(**St2**) = 113 nm, FWMH(**St1**) = 75 nm). The absorption maxima of stannole **St2** were found in the range of stannole-containing polymers (λ_{max}(**39**) = 536 nm,[47] λ_{max}(**40**) = 491 nm[48]).

In contrast to their thienyl analogs **ter**- and **sexithiophene**, the thienyl-substituted stannoles exhibited red-shifted and broader absorption signals as indicated by $\lambda_{abs, max}$ and the FWMH values (Tab. 1).

Tab. 1: Overview of absorption and emission properties of stannole derivatives **St1**, **St2** and their thienyl analogs.

	$\lambda_{abs,max}$[a] / nm	FWMH / nm	lg(ε)	E_{opt}[b] / eV	$\lambda_{em, max}$[a] / nm	FWHM / nm	Δv_{Stokes} / cm^{-1}	Φ_{lum}
St1	417	75	4.32	2.66	512	114	4450	0.013[c]
St2	510	113	4.71	2.13	620	189	3479	0.026[d]
terthiophene	354[e]	62[f]	4.34[e]	3.04[f]	407[e]	58[f]	3679[f]	0.066[e]
sexithiophene	436[e]	85[f]	4.68[e]	2.46[f]	502[e]	86[f]	3016[f]	0.41[e]

[a] Measured in DCM solutions (approx. 10^{-5}-10^{-6} M.) [b] Calculated from the offset wavelength derived from the lowest energy absorption band. [66, 67] [c] Measured against quinine sulfate in 0.1 M H_2SO_4 in water. [d] Measured against fluorescein in 0.1 M NaOH in water. [e] Measured in dioxane literature.[68] [f] Based on data derived from literature.[68]

A reasonably linear relationship was observed between the λ_{onset} of the thienyl-substituted stannoles and thiophene oligomers versus the inverse of the chain length (Fig. 22).
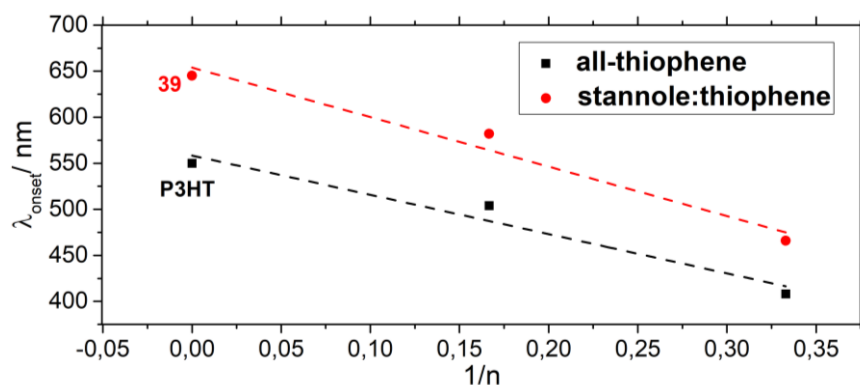
Fig. 22: Plot of λ_{onset} of oligothiophenes and thienyl-substituted stannoles against 1/n. As polymers **P3HT**[69] and the stannole copolymer **39**[47] were chosen.

It became evident that the π-extension of the stannoles followed the same trend as it was observed for the increase of the λ_{onset} for oligothiophenes. As aforementioned, a substantial bathochromic shift of the thiophene-substituted stannoles compared with the oligothiophenes was found.

As the luminescence properties of stannoles are largely unknown yet,[4] the photoluminescence of stannole **St1** and **St2** was investigated (Fig. 23, Tab. 1).
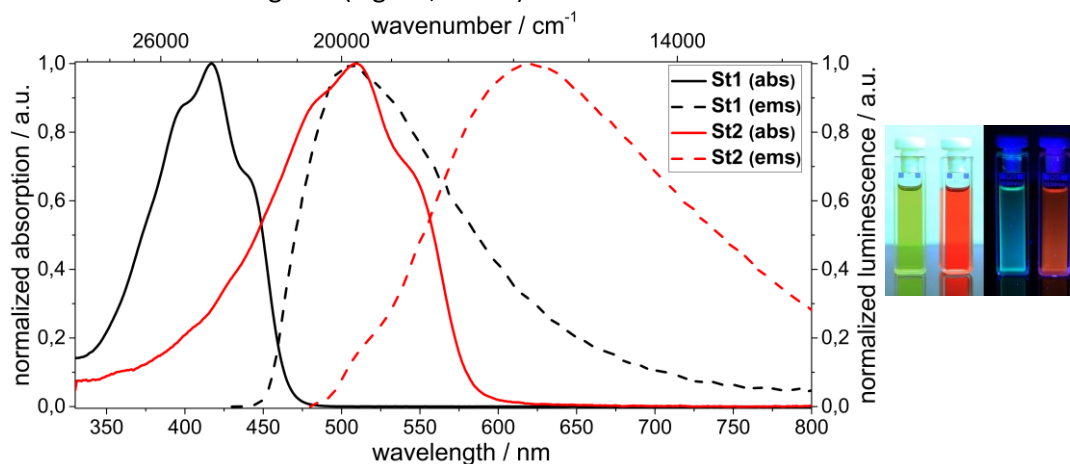
Fig. 23: Absorption (solid line) and luminescence spectra (dashed line) of stannoles **St1** (black) and **St2** (red) obtained in DCM. Furthermore, photographs of solutions of **St1** and **St2** in DCM under ambient light and irradiated at 365 nm.

The luminescence spectrum of stannole **St1** showed one band (λ_{max} = 512 nm) with a large Stokes shift ($\Delta\nu_{Stokes}$ = 4450 cm^{-1}) indicating strong conformational changes between the ground state of the stannole **St1** and its excited state. Stannole **St2** emitted in the lower-energy region (λ_{max} = 620 nm) with a broader band (FWMH(**St2**) = 189 nm) compared with stannole **St1** (FWMH(**St1**) = 114 nm) and with a smaller Stokes shift ($\Delta\nu_{Stokes}$ = 3479 cm^{-1}). In general, stannole **St1** and **St2** were only slightly emissive in DCM solutions (Φ_{lum} = 0.013 for **St1**, Φ_{lum} = 0.026 for **St2**), which may be due to the heavy atom effect of tin.[4] To obtain more fine- structured luminescence spectra, **St1** and **St2** were subjected to low-temperature (77 K) luminescence spectroscopy in glassy state (Fig. 24).
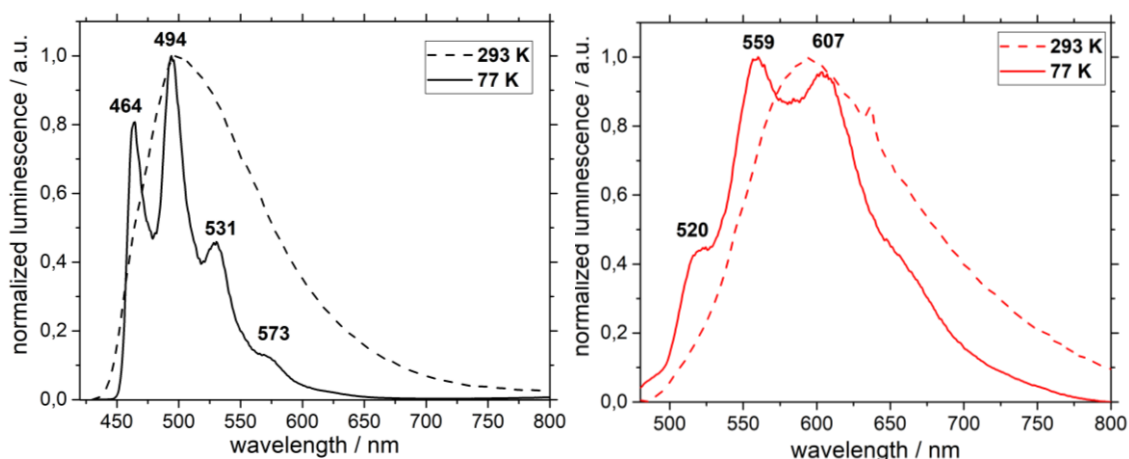
Fig. 24: Luminescence spectra of **St1** (left) and **St2** (right) at 293 K (dashed line) and 77 K (solid line) measured in 2-methyltetrahydrofuran (10^{-5} M).

At lower temperatures, the contributions of the vibrational modes are reduced and fine-structural vibronic bands become visible. The emission spectrum of stannole **St1** was slightly hypsochromically shifted and exhibited three intense signals (464 nm, 494 nm, 531 nm) and a weak signal at 573 nm. The low-temperature luminescence signal of **St2** was less structured, but still exhibited three distinguishable signals (520 nm, 559 nm, 607 nm). Compared with the room temperature and low-temperature luminescence spectra of terthiophene and sexithiophene a bathochromic shift (**St1** vs. **terthiophene**: Δ = 63 nm, **St2** vs. **sexithiophene** Δ = 74 nm), broader emission, but also larger Stokes shift's and decreased luminescence quantum yields were observed for the stannoles **St1** and **St2** (Tab. 1).[68] The latter observation can be assigned to the heavy atom effect of the tin allowing a more non-emissive pathway for luminescence relaxation.[4]

1.4.3 Electrochemistry

Since absorption spectroscopy already indicated that the HOMO-LUMO gap was significantly narrowed from stannole **St1** to its dimer **St2**, we investigated the electrochemical properties of both *via* cyclic voltammetry (Fig. 25, Tab. 2).
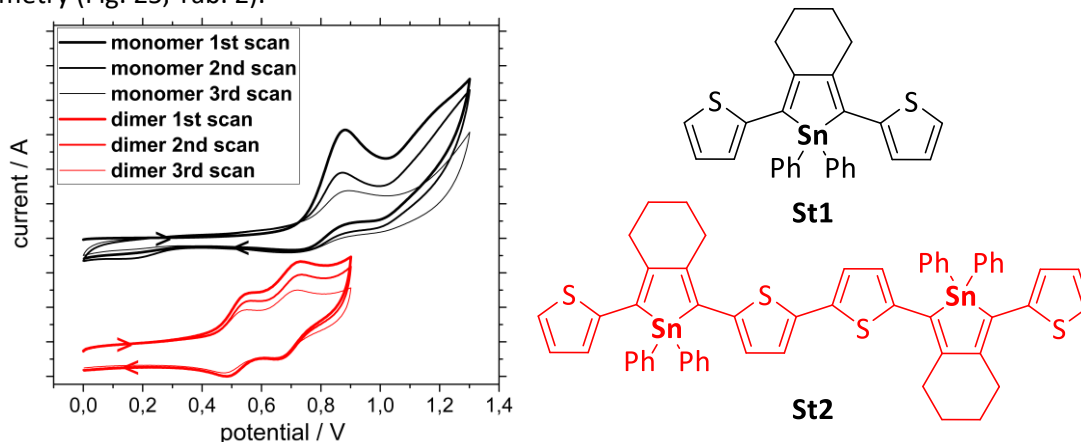
Fig. 25: Cyclic voltammogram of stannole **St1** (black) and **St2** (red) in DCM with *n*Bu$_4$NPF$_6$ (0.2 M) as conducting salt using platinum working electrodes at 200 mV/s sweep rate. The voltammogram was referenced against a calomel electrode.

Tab. 2: Overview of electrochemical data and of **St1** and **St2** and their respective thiophene analogs.

	$E_{Ox1}(_{1/2})$ / V	$E_{Ox2}(_{1/2})$ / V	Δ / V
St1	+0.89	-	-
St2	+0.51	+0.70	0.19
terthiophene	+1.05[70]	-	-
sexithiophene	+0.84[70]	+1.05	0.21

The cyclic voltammogram of **St1** exhibited a non-reversible oxidation process,[46] whereas dimer **St2** had two oxidation waves at lower potential ($E_{Ox1}(_{1/2})$ = 0.51 V, $E_{Ox2}(_{1/2})$ = 0.70 V, Δ = 0.19 V) which were totally reversible. Evidently, **St1** reacted during the CV measurement. This could be an indication for electropolymerization.

The appearance of a two-electron process in **St2** indicated the occurrence of a dicationic **St2**$^{2+}$ species. Strikingly, the electrochemical behavior of *bis*-thienyl-substituted stannoles **St1** and **St2** was similar to their all-thienyl analogs **ter**- and **sexithiophene**: The electrochemical oxidation of terthiophene showed one oxidation wave ($E_{Ox1}(_{1/2})$ = 1.05 V), whereas sexithiophene exhibited two reversible oxidation signals ($E_{Ox1}(_{1/2})$ = 0.84 V, $E_{Ox2}(_{1/2})$ = 1.05 V, Δ = 0.21 V).[70] Therefore, the conclusion could be drawn that the implementation of stannole heterocycles in thienyl-systems does not drastically affect the overall electrochemical behavior. From the electrochemical analysis, the resulting HOMO and LUMO levels of **St1** and **St2** were estimated and revealed that the extension of the conjugated system from **St1** (E_{HOMO} = -5.12 eV, E_{LUMO} = -2.46 eV) to the dimer **St2** increased the HOMO (E_{HOMO} = -4.85 eV) but stabilized the LUMO (E_{LUMO} = -2.72 eV) level (Tab. 3).

Tab. 3: Overview of the HOMO/LUMO levels of **St1** and **St2**.

	$E_{Ox,onset}$ / V	E_{HOMO} / eV	E_{opt}[a] / eV	E_{LUMO}[b] / eV
St1	0.72	-5.12[a]	2.66	-2.46
St2	0.45	-4.85[a]	2.13	-2.72

[a] Calculated from the offset wavelength derived from the lowest energy absorption band. [66, 67] [b] Calculated according to E_{HOMO} = - (+ E_{onset}(Ox) + 4.40) eV[67] and E_{LUMO} = E_{HOMO} + $E_{bg,opt}$.[66]

1.4.4   Electropolymerization

After redox characterization of the stannole monomer and the dimer, a stannole polymer was prepared *via* cyclic electrochemical oxidation starting from stannole **St1** (Scheme 10).
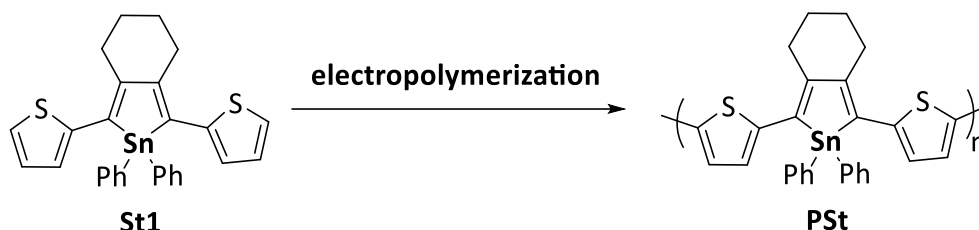
Scheme 10: Electropolymerization of *bis*-thienyl stannole **St1** to access polymer **PSt**.

The formation of polymers from thienyl-substituted stannoles **St1** was conducted by multi-scan electrochemical oxidation in DCM on a platinum disk electrode with a sweep rate of 200 mV/s. However, in dichloromethane, the deposition of a film was not observed. To facilitate the electrodeposition on the electrode (platinum), a nonpolar solvent (*n*-pentane) was added, resulting in the occurrence of a reddish film on the electrodes after several cycles of electrochemical oxidation (Fig. 26, left).
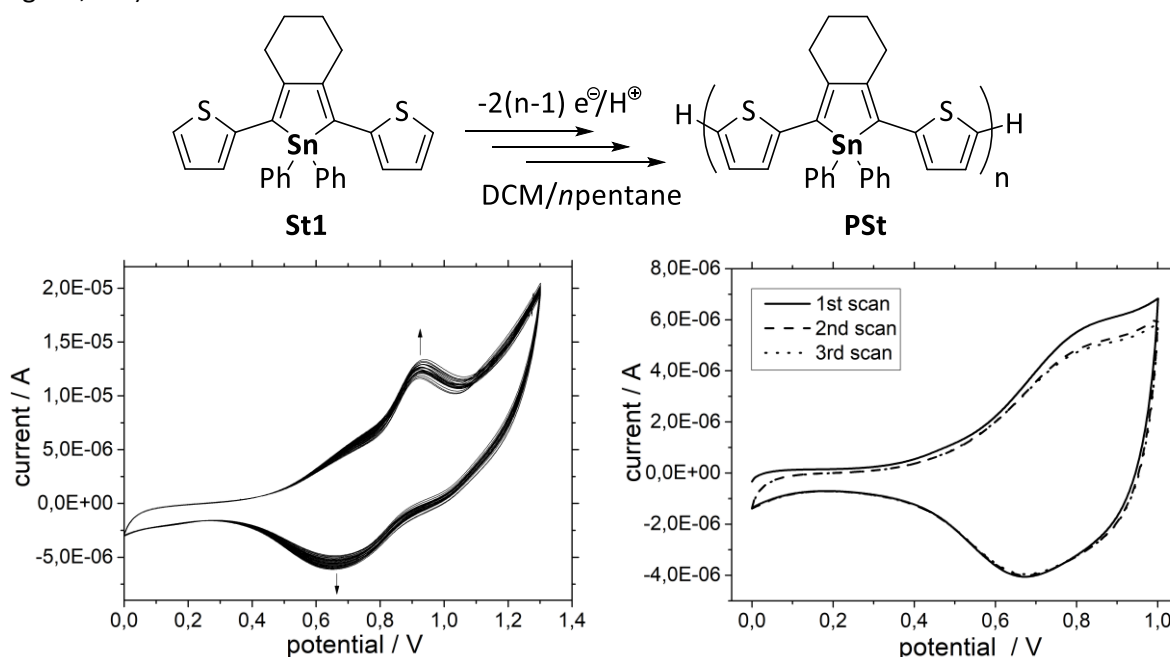
Fig. 26: Multi-scan voltammogram of **St1** (left) in DCM/*n*-pentane (1/1) (2×10^{-3} M) with *n*Bu$_4$NPF$_6$ (0.2 M) as conducting salt and a sweep rate of 200 mV/s on a platinum electrode. After washing the electrode with DCM, a voltammogram (right) in a monomer-free DCM/*n*-pentane (1/1) solution with *n*Bu$_4$NPF$_6$ (0.2 M) was conducted. Both were referenced against a calomel electrode.

Electropolymerization was accomplished by repeating cycling between 0.0 V and +1.3 V. The oxidation currents increased with the number of cycles, indicating the formation of electroactive films on the surface of the Pt working electrode. After 50 cycles, a reddish film on the electrode was formed at the electrode being insoluble in organic solvents and held a specific electrochemical response. The modified electrodes were rinsed with DCM and studied by CV's in monomer-free DCM solutions containing 0.2 M Bu$_4$NPF$_6$ at a scan rate of 200 mV/s (Fig. 26, right). The film exhibited n- and p-doping processes. However, it could not be verified that the organotin moiety was still present in the formed polymer. The transfer of this procedure to electrodes that are suitable for scanning-electron

microscope surface analysis, e.g. platinum sheet, remained unsuccessful or revealed the absence of any tin in the deposited film. The release of tin might indicate further decomposition processes. When a chemical oxidant, (iron(III) chloride) was used instead, there was also no distinct product.

It was expected that stannoles exhibit lower stability towards oxidation procedures compared to their thienyl analogs, *vide supra*, therefore the electropolymerization and the electrochemical stability of the stannoles were studied in detail. The proposed electropolymerization mechanism[71] suggests that the stannole's radical cation **St1$^{+\cdot}$**, dimer dication **St2^{2+}** and dimer **St2** require intrinsic stability and further resistance against acidic conditions as the formation of protons during the process occurs (Scheme 11).
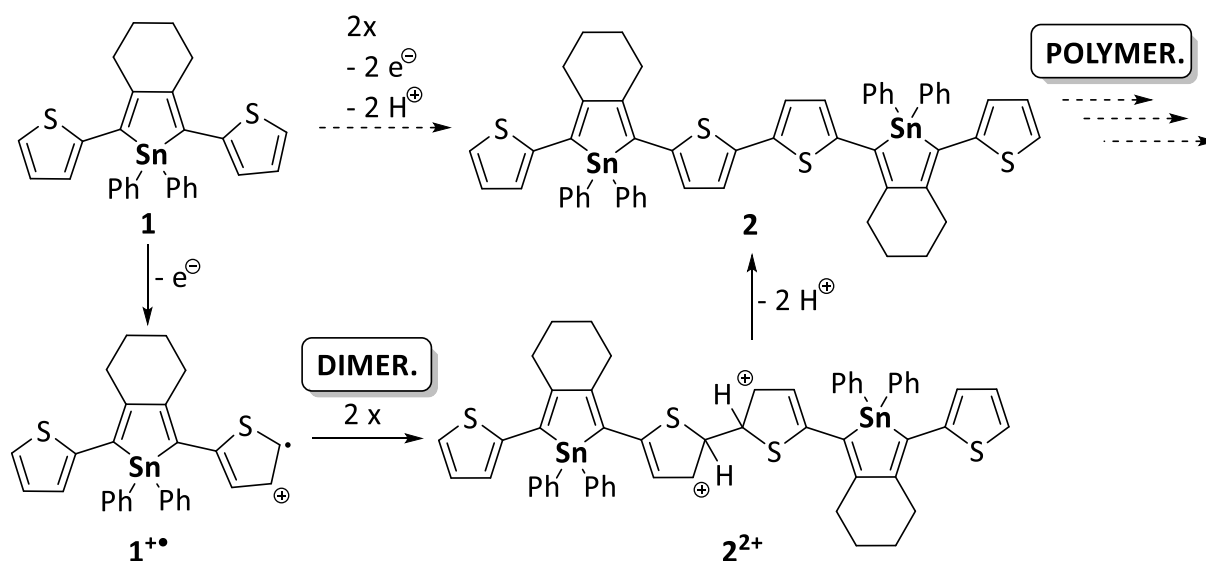
Scheme 11: Proposed mechanism of an oxidative polymerization of thienyl-substituted **St1**.

To obtain insights into these electroactive species, the stability of all electroactive species should be investigated under electrochemical oxidation conditions.

1.4.5 Spectroelectrochemical Investigation

A versatile method to investigate these processes is the combination of absorption spectroscopy and *in situ* oxidation. For **terthiophene** and **sexithiophene** the formation of the radical cations were formed by oxidation with iron(III) chloride and in case of the **sexithiophene**, the dication **sexithiophene^{2+}** was formed by oxidation with iodine (Fig. 27).[70]
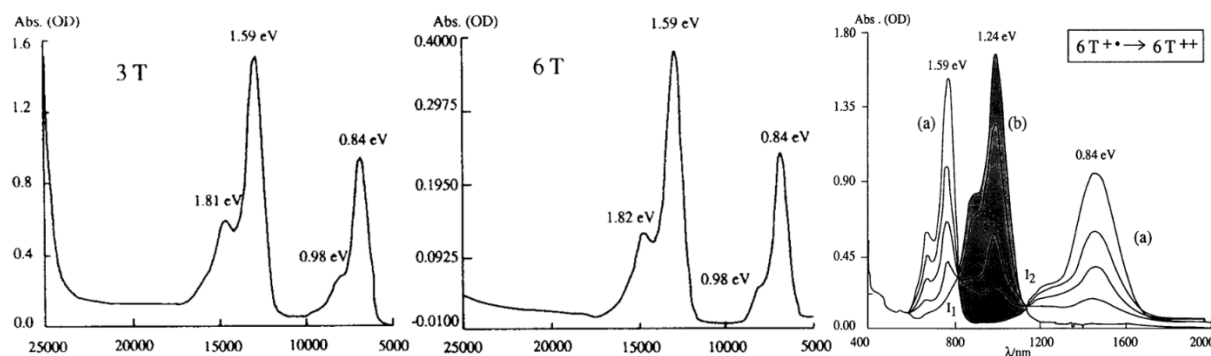
Fig. 27: Absorption spectra of **terthiophene$^{+\cdot}$** (λ_{abs} = 685/780 and 1270/1480 nm) (left) and the **sexithiophene$^{+\cdot}$** (λ_{abs} = 681/780 and 1270/1480 nm)(middle). Absorption spectrum of the formation of **sexithiophene$^{+\cdot}$** radical cation (λ_{abs} = 780 and 1480 nm), and of the **sexithiophene^{2+}** (λ_{abs} = 1000 nm) (right). Adapted with permission.[70]

Interestingly, the absorption spectra of radical cations **terthiophene**[+·] and **sexithiophene**[+·] had the same absorption behavior. Interestingly, the **terthiophene** could not be oxidized to its dicationic form as is readily underwent polymerization.[70]

Due to the presented thiophene/stannole analogy, these experiments were as well performed with the stannole derivatives. Therefore, the oxidization experiments were conducted in a UV/Vis-NIR spectroelectrochemical setup which allows to oxidize the respective stannole species and observe their absorption *in situ*. As cell, an Omni Cell Spec with a Pt grid as the working electrode, a Pt wire as the counter electrode and SCE reference electrode were used. It needs to be pointing out that the described spectroelectrochemical experiments are quasi-static since the diffusion in the cell is limited and the electrode potential is changed incrementally. Therefore, the experiments are not fully analogous to the processes which occur in multi-scan experiments, but they are a good approximation. First, stannole **St1** was subjected to spectrochemical analysis and the non-reversible oxidation process, as it was determined by cyclic voltammetry, was investigated (Fig. 28).
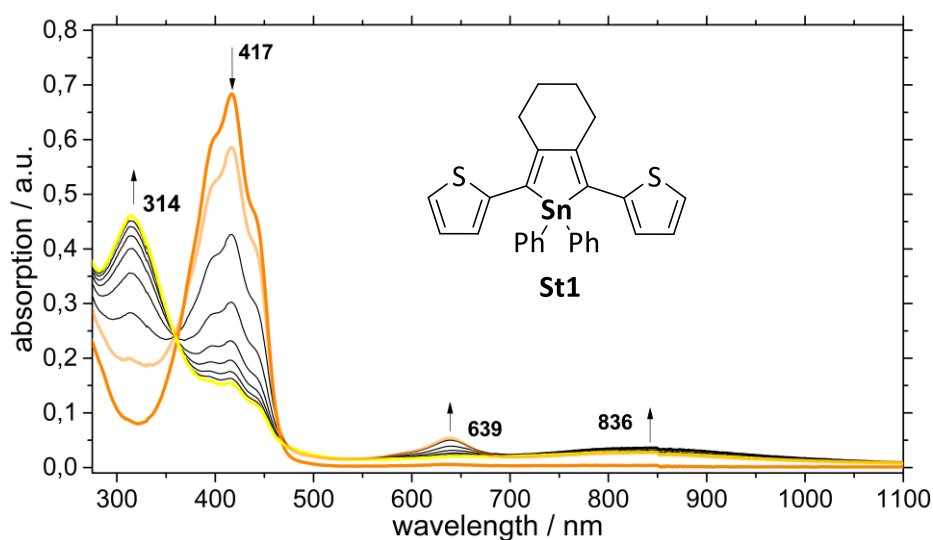
Fig. 28: Stacked absorption spectra of stannole **St1** in DCM with nBu$_4$NPF$_6$ (0.2 M) as conducting salt upon oxidation starting from 0.80 V and recording a spectrum every 2 min. The process was not reversible.

The absorption spectra were unaffected until a voltage of 0.8 V was applied and novel species (639 nm, 700-1000 nm) occurred and disappeared again. The arising bands could be due to either the doping of electropolymerized oligomers or the absorption of intermediate doped **St1**[+·] or **St2**[2+] species. In analogy to its thiophene analog **terthiophene**, the formation of the **St1**[+·] should result in two well-structured absorption bands (λ_{abs} = 780 nm, 1480 nm)[70] which was barely observed. Upon further oxidation, the peak (417 nm) for **St1** decreased. However, a novel peak (314 nm) occurred, which was assigned to the decomposition of the stannole, based on the spectrum of a previously observed ring-opened butadiene form (λ_{max} = 334 nm), in which tin was absent.[59, 72]

Since the novel signals of **St1** (639 nm, 700 -1000 nm) could be related to the formation of (doped) oligomers, their radical cations, or di-cations, spectroelectrochemical investigations were performed for comparison on its oligomer **St2** as well (Fig. 29), to elucidate which of these species are present.
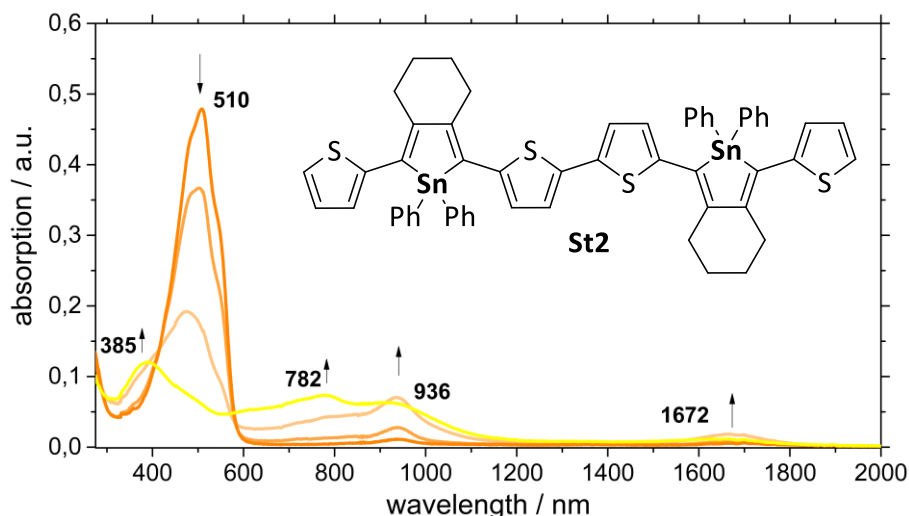
Fig. 29: Stacked absorption spectra of stannole **St2** in DCM with nBu$_4$NPF$_6$ (0.2 M) as conducting salt upon oxidation. Since decomposition occurred immediately even at 0.0 V, the spectra were recorded starting immediately from 1.3 V.

Although stannole **St1** was relatively inert to oxidation in the spectrochemical setup, **St2** underwent electrochemical oxidation even at low potential. A fast decline of the **St2** absorption band (510 nm) was observed; however, new absorption bands in the NIR region (936 nm, 1672 nm) appeared. None of them were in accordance with the species we observed in the oxidation of **St1** (Fig. 29). The simultaneously rising of the signals at 936 nm and 1672 nm bands indicated the formation of a **St2**$^{+\cdot}$ species. Also, in this case, the analogy of **St2** and **sexithiophene** exists: Chemical oxidation of sexithiophene, resulted in the formation of absorption bands at 780 nm and 1480 nm, which were both assigned to the **sexithiophene**$^{+\cdot}$ intermediate (Fig. 27).[70] As this is relatively close to the bands observed for the oxidation of **St2**, a formation of **St2**$^{+\cdot}$ can be assumed.

To disprove that electropolymerization took place in the spectroelectrochemical setup, a 2,5-di(2-methoxythienyl)stannole[46] (**StOMe**), which is chemically unable to undergo oxidative oligomerization, because the reactive sites are blocked by methoxy groups, was subjected to similar experiments (Fig. 30).
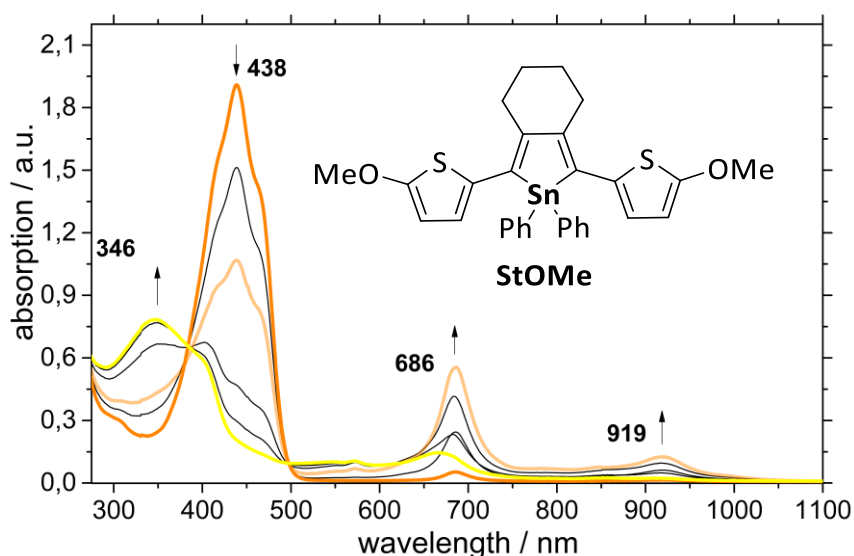
Fig. 30: Stacked absorption spectra of **StOMe** in DCM with nBu$_4$NPF$_6$ (0.2 M) as conducting salt upon oxidation. Since decomposition immediately occurred even at 0.0 V the spectra were recorded starting from 0.6 V.

Upon oxidation, the formation of novel species (686 nm, 919 nm), presumably **StOMe**[+·] species, was detected while at the same time the absorption signal of the stannole (438 nm) itself decreased rapidly. In comparison to stannole **St1**, the same set of absorption signals was found with the only difference that all signals were red-shifted due to the methoxy-substituents.[46] Again, the appearance of a signal at 346 nm indicated the decomposition of the stannole by oxidation and the existence of a ring-opened form.

In all cases, the formation of the radical cationic species was observed which indicated that an electropolymerization is generally possible but suffers from the decomposition of the thienyl-substituted stannole. Since electropolymerization is a rapid process, which is driven by kinetics, it provides milder conditions than in spectroelectrochemical setups. Although, all stannole derivatives exhibited instability against oxidation or light and therefore a formation of electropolymers is highly unlikely. Still, increasing the stability of the stannoles or the rate of oxidative coupling of two monomers could form stannole polymers by electropolymerization.

1.5 Summary and Outlook

Thienyl-based stannole monomers and dimers were synthesized, and their physical properties were compared with their respective thiophene oligomers. As the electrochemical analysis revealed, the electronic states differed significantly as well as the absorption and emission properties. It was shown that thienyl-substituted stannoles show similar trends in their optoelectronic properties compared to their all thienyl-analogs but exhibit a lower HOMO-LUMO gap, which is impressively displayed by their absorption/emission maxima (Fig. 31).
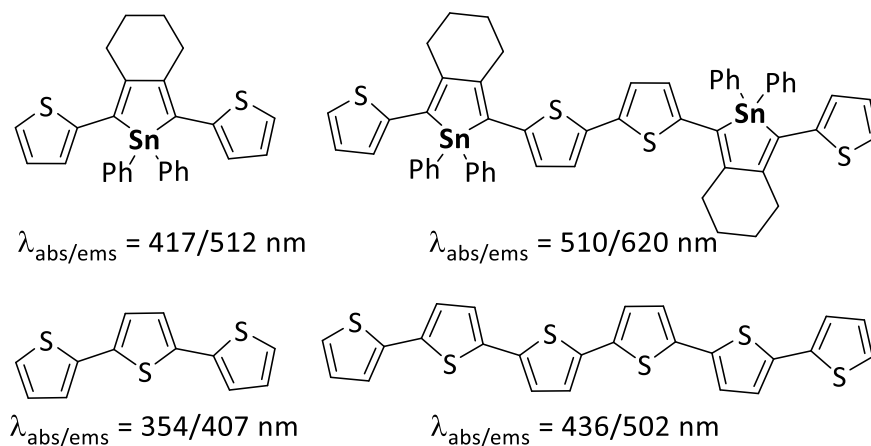
Fig. 31: Photophysical properties of thiophene-flanked stannoles and the respective thiophene oligomers.

In contrast to **sexithiophene**, the stannole dimer **St2** underwent rapid photodegradation which was clearly related to the narrowed HOMO-LUMO gap since such behavior was not observed for the stannole monomer. Therefore, it might be concluded that low-band gap materials based on stannoles could drastically suffer from photo-induced decomposition processes.

Further attempts were made to subject the thienyl-substituted stannoles to electropolymerization and the deposition of an electroactive polymer film was observed. However, supporting spectroelectrochemical investigations showed that stannoles were not stable under the applied spectroelectrochemical conditions. Supposedly, the lacking stability of the stannole radical cation was the limiting factor for the electropolymerization (Scheme 12).
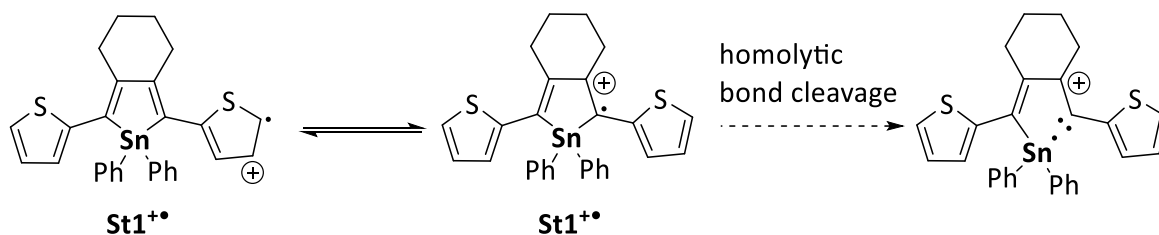
Scheme 12: Proposed decomposition of stannole radical cation.

To seek stable stannole derivatives, which do not undergo decomposition, but are capable of electropolymerization, the HOMO/LUMO levels require more adjustments. To stabilize the Sn-C bond, the radical cation should be more located at the thienyl moiety than at the stannole.

For such an effect, the implementation of electron-rich thiophenes, such as in ethylenedioxythiophene, could be advantageous (Scheme 13).
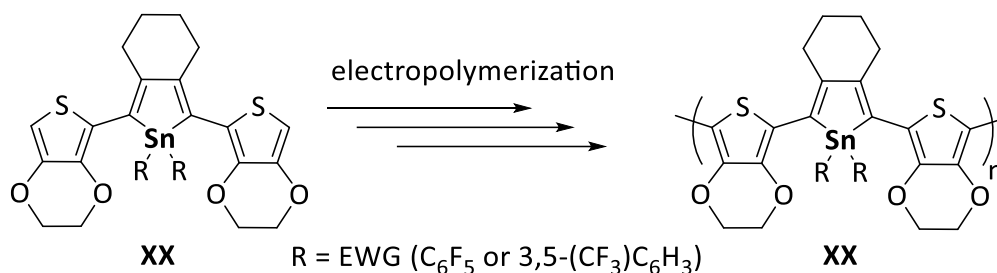
Scheme 13: Ethylenedioxythiophene-flanked stannoles should exhibit improved stability towards electropolymerization.

To compensate for the stabilization of the HOMO level due to the ethylendioxythiophenes, electron-withdrawing groups (EWG) might be catenated to the tin atom to destabilize both HOMO and LUMO level. Consequently, the overall HOMO-LUMO gap should be constant and the risk of photodegradation processes should be reduced due to narrowed HOMO-LUMO gaps.

When aiming at applications of stannoles in organic electronic derives, it needs to be stated that stannoles are barely fluorescent and exhibited photostability in solution. Therefore, an application in organic field-effect transistors (OFETs) or organic solar cells (OSC) might be more reasonable than an implementation as electroluminescent materials in OLEDs. For instance, the corresponding oligothiophene sexithiophene was successfully applied in OFET devices with resulting high hole mobility (4×10^{-4} cm^{2}V^{-1} s^{-1}).[73] Though, the conductivity and charge carrier mobility of stannoles in such devices would be highly interesting due to the narrowed HOMO-LUMO gaps.

Integration of one stannole unit in polymeric thiophene-based materials, e.g. in poly(3-hexylthiophene) (P3HT), or oligothiophene-based materials, e.g. dicyanovinylthiophenes, seem promising g due to the stabilized LUMO level of the stannole (Fig. 32).
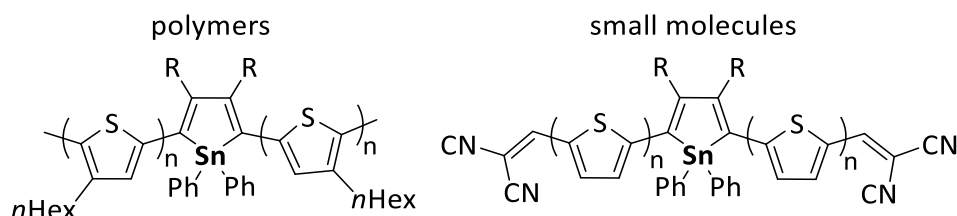
Fig. 32: Potential stannole incorporated polymers and small molecules for organic electronics.

For both examples, the combination of electron-rich thiophenes with the accepting stannoles or dicyanovinyl groups should decrease the overall HOMO-LUMO gap due to the alternating combination of donor and acceptor groups. The application of such molecules in the field of organic solar cells might be feasible.

1.6   References

1.   S. Yamaguchi, K. Tamao, *Bull. Chem. Soc. Jpn.*, **1996**, *69*, 2327-2334.
2.   V. N. Khabashesku, V. Balaji, S. E. Boganov, O. M. Nefedov, J. Michl, *J. Am. Chem. Soc.*, **1994**, *116*, 320-329.
3.   S. Yamaguchi, K. Tamao, *J. Chem. Soc., Dalton Trans.*, **1998**, 3693-3702.
4.   S. Yamaguchi, Y. Itami, K. Tamao, *Organometallics*, **1998**, *17*, 4910-4916.
5.   B. Cordero, V. Gomez, A. E. Platero-Prats, M. Reves, J. Echeverria, E. Cremades, F. Barragan, S. Alvarez, *Dalton Trans.*, **2008**, 2832-2838.
6.   Z. Fei, J. S. Kim, J. Smith, E. B. Domingo, T. D. Anthopoulos, N. Stingelin, S. E. Watkins, J.-S. Kim, M. Heeney, *J. Mater. Chem.*, **2011**, *21*, 16257.

7.   J. Luo, Z. Xie, J. W. Lam, L. Cheng, H. Chen, C. Qiu, H. S. Kwok, X. Zhan, Y. Liu, D. Zhu, B. Z. Tang, *Chem. Commun.*, **2001**, 1740-1741.

8.   Z. Zhao, B. He, B. Z. Tang, *Chem. Sci.*, **2015**, *6*, 5347-5365.

9.   A. Qin, B. Z. Tang, *Aggregation-Induced Emission: Fundamentals and Applications*, John Wiley & Sons Ltd, Hoboken, Chichester, **2013**.

10. H. J. Tracy, J. L. Mullin, W. T. Klooster, J. A. Martin, J. Haug, S. Wallace, I. Rudloe, K. Watts, *Inorg. Chem.*, **2005**, *44*, 2003-2011.

11. Y. M. I. M. Ramirez, M. Rohdenburg, E. Lork, A. Staubitz, *Chem. Commun.*, **2020**, *56*, 9775-9778.

12. M. Yu, R. Huang, J. Guo, Z. Zhao, B. Z. Tang, *PhotoniX*, **2020**, *1*, 11.

13. Y. Cai, A. Qin, B. Z. Tang, *J. Mater. Chem. C*, **2017**, *5*, 7375-7389.

14. M. Shimizu, *Silole-Based Materials in Optoelectronics and Sensing*, in *Main Group Strategies towards Functional Hybrid Materials*, eds. T. Baumgartner and F. Jäkle, John Wiley & Sons Ltd., Hoboken, Chichester, **2018**, 163-195.

15. H. Usta, G. Lu, A. Facchetti, T. J. Marks, *J. Am. Chem. Soc.*, **2006**, *128*, 9034-9035.

16. J. Ohshita, *Macromol. Chem. Phys.*, **2009**, *210*, 1360-1370.

17. G. Lu, H. Usta, C. Risko, L. Wang, A. Facchetti, M. A. Ratner, T. J. Marks, *J. Am. Chem. Soc.*, **2008**, *130*, 7670-7685.

18. M. Uchida, T. Izumizawa, T. Nakano, S. Yamaguchi, K. Tamao, K. Furukawa, *Chem. Mater.*, **2001**, *13*, 2680-2683.

19. S. M. Parke, M. P. Boone, E. Rivard, *Chem. Commun.*, **2016**, *52*, 9485-9505.

20. H. Zhong, Z. Li, F. Deledalle, E. C. Fregoso, M. Shahid, Z. Fei, C. B. Nielsen, N. Yaacobi-Gross, S. Rossbauer, T. D. Anthopoulos, J. R. Durrant, M. Heeney, *J. Am. Chem. Soc.*, **2013**, *135*, 2040-2043.

21. R. Kondo, T. Yasuda, Y. S. Yang, J. Y. Kim, C. Adachi, *J. Mater. Chem.*, **2012**, *22*, 16810.

22. K. Geramita, J. McBee, T. D. Tilley, *J. Org. Chem.*, **2009**, *74*, 820-829.

23. W.-L. Jia, Q.-D. Liu, R. Wang, S. Wang, *Organometallics*, **2003**, *22*, 4070-4078.

24. M. Saito, T. Tanikawa, T. Tajima, J. D. Guo, S. Nagase, *Tetrahedron Lett.*, **2010**, *51*, 672-675.

25. M. Saito, T. Tanikawa, T. Tajima, J. D. Guo, S. Nagase, *J. Organomet. Chem.*, **2010**, *695*, 1035-1041.

26. D. Zhou, Y. Gao, B. Liu, Q. Tan, B. Xu, *Org. Lett.*, **2017**, *19*, 4628-4631.

27. T. Tanikawa, M. Saito, J. D. Guo, S. Nagase, M. Minoura, *Eur. J. Org. Chem.*, **2012**, *2012*, 7135-7142.

28. J. B. Grimm, T. A. Brown, A. N. Tkachuk, L. D. Lavis, *ACS Cent. Sci.*, **2017**, *3*, 975-985.

29. Y. Koide, Y. Urano, K. Hanaoka, T. Terai, T. Nagano, *ACS Chem. Biol.*, **2011**, *6*, 600-608.

30. R. A. Adler, C. Wang, A. Fukazawa, S. Yamaguchi, *Inorg. Chem.*, **2017**, *56*, 8718-8725.

31. G. Lukinavicius, G. Y. Mitronova, S. Schnorrenberg, A. N. Butkevich, H. Barthel, V. N. Belov, S. W. Hell, *Chem. Sci.*, **2018**, *9*, 3324-3334.

32. G. Lukinavicius, L. Reymond, E. D'Este, A. Masharina, F. Gottfert, H. Ta, A. Guther, M. Fournier, S. Rizzo, H. Waldmann, C. Blaukopf, C. Sommer, D. W. Gerlich, H. D. Arndt, S. W. Hell, K. Johnsson, *Nat. Methods*, **2014**, *11*, 731-733.

33. C. Wang, M. Taki, Y. Sato, A. Fukazawa, T. Higashiyama, S. Yamaguchi, *J. Am. Chem. Soc.*, **2017**, *139*, 10374-10381.

34. S. E. Denmark, C. S. Regens, *Acc. Chem. Res.*, **2008**, *41*, 1486-1499.

35. Y. Hatanaka, T. Hiyama, *J. Org. Chem.*, **1988**, *53*, 918-920.

36. M. Kosugi, T. Tanji, Y. Tanaka, A. Yoshida, K. Fugami, M. Kameyama, T. Migita, *J. Organomet. Chem.*, **1996**, *508*, 255-257.

37. J. W. Faller, R. G. Kultyshev, *Organometallics*, **2002**, *21*, 5911-5918.

38. T. Nakamura, H. Kinoshita, H. Shinokubo, K. Oshima, *Org. Lett.*, **2002**, *4*, 3165-3167.

39. J. W. L. A. F. Renaldo, J. K. Stille, *Organic Syntheses*, **1989**, *67*, 86.

40. J. K. Stille, *Angew. Chem. Int. Ed. Engl.*, **1986**, *25*, 508-524.

41. C. L. Hilton, C. R. Jamison, B. T. King, *J. Am. Chem. Soc.*, **2006**, *128*, 14824.

42. W. Matsuoka, H. Ito, K. Itami, *Angew. Chem. Int. Ed.*, **2017**, *56*, 12224-12228.

43. K. Ozaki, K. Kawasumi, M. Shibata, H. Ito, K. Itami, *Nat. Commun.*, **2015**, *6*, 6251.

44. K. Itami, Y. Yano, H. Ito, Y. Segawa, *Synlett.*, **2016**, *27*, 2081-2084.

45. I. Nagao, M. Shimizu, T. Hiyama, *Angew. Chem. Int. Ed.*, **2009**, *48*, 7573-7576.

46. Y. M. I. M. Ramirez, M. Rohdenburg, F. Mostaghimi, S. Grabowsky, P. Swiderek, J. Beckmann, J. Hoffmann, V. Dorcet, M. Hissler, A. Staubitz, *Inorg Chem*, **2018**, *57*, 12562-12575.

47. J. Linshoeft, E. J. Baum, A. Hussain, P. J. Gates, C. Nather, A. Staubitz, *Angew. Chem. Int. Ed.*, **2014**, *53*, 12916-12920.

48. Y. Matsumura, M. Sugihara, S. E. Tan, T. Sato, K. Hayashi, H. Nishiyama, W. M. Zhou, S. Inagi, I. Tomita, *Macromol. Rapid Commun.*, **2019**, *40*, e1800929.

49. Y. J. Cheng, S. H. Yang, C. S. Hsu, *Chem. Rev.*, **2009**, *109*, 5868-5923.

50. I. Osaka, R. D. McCullough, *Regioregular and Regiosymmetric Polythiophenes*, in *Conjugated Polymer Synthesis*, ed. Y. Chujo, Wiley VCH, Weinheim, **2010**.

51. S. Cosnier, A. Karyakin, *Electropolymerization: Concepts, Materials and Applications*, Wiley-VCH, Weinheim, 1st edn., **2010**.

52. M. D. Imisides, R. John, P. J. Riley, G. G. Wallace, *Electroanalysis*, **1991**, *3*, 879-889.

53. W. J. Feast, J. Tsibouklis, K. L. Pouwer, L. Groenendaal, E. W. Meijer, *Polymer*, **1996**, *37*, 5017-5047.

54. C. Hay, C. Fischmeister, M. Hissler, L. Toupet, R. Réau, *Angew. Chem. Int. Ed.*, **2000**, *39*, 1812-1815.

55. V. Lemau de Talance, M. Hissler, L. Z. Zhang, T. Karpati, L. Nyulaszi, D. Caras-Quintero, P. Bauerle, R. Reau, *Chem. Commun.*, **2008**, 2200-2202.

56. P. Yadav, S. Singhal, A. Patra, *Synth. Met.*, **2020**, *260*, 116264.

57. I. Nagao, M. Shimizu, T. Hiyama, *Angew. Chem.*, **2009**, *121*, 7709-7712.

58. S. Urrego-Riveros, Y. M. I. M. Ramirez, J. Hoffmann, A. Heitmann, A. Staubitz, *Chemistry*, **2018**, *24*, 5680-5696.

59. S. Urrego-Riveros, Y. M. I. M. Ramirez, D. Duvinage, E. Lork, F. D. Sonnichsen, A. Staubitz, *Chemistry*, **2019**, *25*, 13318-13328.

60. J. Linshoeft, *Synlett.*, **2014**, *25*, 2671-2672.

61. E. Negishi, S. J. Holmes, J. M. Tour, J. A. Miller, F. E. Cederbaum, D. R. Swanson, T. Takahashi, *J. Am. Chem. Soc.*, **1989**, *111*, 3336-3346.

62. P. J. Fagan, W. A. Nugent, *J. Am. Chem. Soc.*, **1988**, *110*, 2310-2312.

63. P. J. Fagan, W. A. Nugent, J. C. Calabrese, *J. Am. Chem. Soc.*, **1994**, *116*, 1880-1889.

64. M. C. Suh, B. Jiang, T. D. Tilley, *Angew. Chem. Int. Ed.*, **2000**, *39*, 2870-2873.

65. C. Hay, M. Hissler, C. Fischmeister, J. Rault-Berthelot, L. Toupet, L. Nyulászi, R. Réau, *Chem. Eur. J.*, **2001**, *7*, 4222-4236.

66. P. I. Djurovich, E. I. Mayo, S. R. Forrest, M. E. Thompson, *Org. Electron.*, **2009**, *10*, 515-520.

67. J. L. Bredas, R. Silbey, D. S. Boudreaux, R. R. Chance, *J. Am. Chem. Soc.*, **1983**, *105*, 6555-6559.

68. R. S. Becker, J. Seixas de Melo, A. L. Maçanita, F. Elisei, *J. Phys. Chem.*, **1996**, *100*, 18683-18695.

69. Z. Fei, P. Boufflet, S. Wood, J. Wade, J. Moriarty, E. Gann, E. L. Ratcliff, C. R. McNeill, H. Sirringhaus, J. S. Kim, M. Heeney, *J. Am. Chem. Soc.*, **2015**, *137*, 6866-6879.

70. D. Fichou, G. Horowitz, B. Xu, F. Garnier, *Synth. Met.*, **1990**, *39*, 243-259.

71. Philippe Blanchard, A. Cravino, E. Levillain, *Electrochemistry of Oligothiophenes and Polythiophenes*, in *Handbook of Thiophene-Based Materials: Applications in Organic Electronics and Photonics*, eds. I. F. Perepichka and D. F. Perepichka, John Wiley & Sons, Ltd, Chichester, **2009**.

72. G. He, W. Torres Delgado, D. J. Schatz, C. Merten, A. Mohammadpour, L. Mayr, M. J. Ferguson, R. McDonald, A. Brown, K. Shankar, E. Rivard, *Angew. Chem. Int. Ed.*, **2014**, *53*, 4587-4591.

73. F. Dinelli, M. Murgia, P. Levy, M. Cavallini, F. Biscarini, D. M. de Leeuw, *Phys. Rev. Lett.*, **2004**, *92*, 116802.

1.7   Experimental Part

All NMR spectra were carried out at 23 °C. ^{1}H NMR (600 MHz) and ^{13}C{^{1}H} NMR (150 MHz) spectra were recorded on a Bruker Avance Neo spectrometer equipped with a TXI probe head or a Bruker DRX 500 (^{1}H NMR (500 MHz) and ^{13}C{^{1}H} NMR (126 MHz)). ^{119}Sn{^{1}H} NMR (223 MHz) spectra were recorded on a Bruker Avance Neo spectrometer equipped with a BBO probe head or a Bruker DRX 500 (186 MHz). The ^{119}Sn{^{1}H} NMR spectra were referenced externally against tetramethylsilane in CDCl$_3$. Where possible, NMR signals were assigned using ^{1}H COSY, ^{1}H/^{1}H NOESY, ^{1}H/^{13}C{^{1}H} HSQC and ^{1}H/^{13}C{^{1}H} HMBC experiments. As NMR solvent CDCl$_3$ (Deutero, 99.9%, stored over alumina) was used. IR spectra were recorded on a Nicolet Thermo iS10 scientific spectrometer with a diamond ATR unit. Electron impact (EI) mass experiments were measured using the direct inlet or indirect inlet methods, with a source temperature of 200 °C on a MAT95 XL double-focusing mass spectrometer from Finnigan MAT. The ionization energy of the electron impact ionization was 70 eV. Atmospheric pressure chemical ionization (APCI) experiments were performed on a Bruker Impact II from Bruker Daltonics. The electrochemical studies were carried out under argon using an Eco Chemie Autolab PGSTAT 30 potentiostat for cyclic voltammetry. The following three-electrode configuration was used: the working electrode was a platinum disk, the reference electrode was a saturated calomel electrode and the counter-electrode a platinum wire. All potentials were internally referenced to the ferrocene/ ferrocenium couple. For the measurements, concentrations of 10^{-3} M of the electroactive species were used in a 0.2 M solution of tetrabutylammonium hexafluorophosphate (Sigma Aldrich, >99%) in degassed DCM. The scanning rate was 200 mV/s. For thermal analysis, a Mettler Toledo a DSC/TGA 3+ was used. Melting points were measured on a Büchi M-5600 Melting Point apparatus. UV/Vis spectra were recorded on a Perkin Elmer Lambda 14 spectrometer at 20 °C using a quartz cuvette with a length of 1 cm. The UV-Vis emission spectra measurements were recorded on a FL 920 Edinburgh Instrument and corrected for the response of the photomultiplier. Quantum yields were calculated relative to quinine sulfate (Φ_{lum} = 0.54 in 0.1 M H$_2$SO$_4$) and fluorescein (Φ_{lum} = 0.91 in 0.1 M NaOH). The low-temperature measurements were performed with a combination of a Dewar and EPR tubes in 2-methyltetrahydrofuran as a solvent. Spectroelectrochemical experiments were performed in DCM with nBu$_4$NPF$_6$ as conductive salt (0.2 M). As UV/NIR spectrometer a Jasco V-770 was used. As cell, an Omni Cell Spec with a Pt grid as the working electrode, a Pt wire as the counter electrode and SCE reference electrode were used. Furthermore, a Princeton applied Research Model 362 Scanning Potentiostat was used to apply the voltage given. Column chromatography was carried out by using the column machine PuriFlash 4250 from Interchim. Silica gel columns of the type PF (PuriFlash) -50 (μm grain size) SiHP (Silica gel High Performance) PF-50SiHP-JPF0120, and PF-50SiHP-JP-F0220 were used. The sample was applied using a dry load method using Celite®.

The reference for the spectroelectrochemical investigation, compound StannoleOMe (**StOMe**) and the Rosenthal reagent (**48**) was previously synthesized according to literature.[1, 2]

1.7.1 Synthesis of 1,8-*bis*(Thiophen-2-yl)octa-1,7-diyne (**44**)
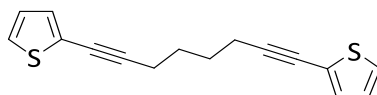
The synthetic procedure was adapted from the literature.[3] In a glovebox, a mixture of 2-iodothiophene (**45**, 5.00 g, 23.8 mmol), [Pd(PPh$_3$)$_4$] (555 mg, 480 µmol) and copper(I)iodide (91.4 mg, 480 µmol) in triethylamine (8.0 mL) and DMF (14 mL) was stirred at 20 °C. After the addition of 1,7-octadiyne (**46**, 600 mg, 5.65 mmol), the red-brown suspension was stirred at 55 °C for 20 h. The reaction was quenched with a sat. aq. ammonium chloride solution (1 x 30 mL). The aqueous layer was extracted with diethyl ether (3 x 30 mL) and the combined organic layers were washed with H$_2$O (1 x 100 mL). The phases were separated and dried over magnesium sulfate. After filtration, the volatiles were removed *in vacuo*. The residue was purified by column chromatography (silica gel, 1/20 DCM/*n*-hexane, R$_f$ = 0.18) to give the product as a yellow waxy solid (**44**, 2.15 g, 7.95 mmol, 65%). **^{1}H NMR** (600 MHz, CDCl$_3$): δ = 7.17 (dd, ^3J = 5.2 Hz, ^4J = 1.0 Hz, 2H, Tph-*H*-5), 7.12 (dd, ^3J = 3.6 Hz, ^4J = 1.0 Hz, 2H, Tph-*H*-3), 6.94 (dd, ^3J = 5.2 Hz, 3.6 Hz, 2H, Tph-*H*-4), 2.54 - 2.43 (m, 4H, C≡C-C*H*$_2$), 1.82 - 1.72 (m, 4H, C≡C-(CH$_2$)-C*H*$_2$) ppm. **^{13}C{^{1}H} NMR** (150 MHz, CDCl$_3$): δ = 131.17 (Tph-*C*-3), 126.91 (Tph-*C*-5), 126.10 (Tph-*C*-4), 124.19 (Tph-*C*-2), 93.95 (C≡*C*-CH$_2$), 74.22 (*C*≡C-CH$_2$), 27.85 (C≡C-*C*H$_2$), 19.43 (C≡C-(CH$_2$)-*C*H$_2$) ppm. **HRMS** (EI, 70 eV, MAT95, direct): *m/z* calcd. for C$_{16}$H$_{14}$S$_2$ [M-H]$^+$ 270.05314 found 270.05306. **IR** (ATR): υ = 3107 (w), 2939 (w), 2860 (w), 1516 (w), 1449 (w), 1427 (m), 1355 (w), 1294 (w), 1275 (w), 1237 (w), 1222 (w), 1185 (m), 1141 (w), 1083 (w), 1043 (w), 1015 (w), 897 (w), 846 (m), 829 (s), 741 (w), 691 (s), 662 (m) cm^{-1}. **Mp**.: 44 °C

1.7.2 Synthesis of the Stannole Monomer (**St1**)
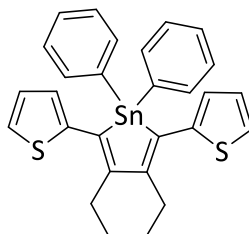
Method A: In a Schlenk flask, ZrCp$_2$Cl$_2$ (540 mg, 1.85 mmol) and 1,8-*bis*(thiophen-2-yl)octa-1,7-diyne (**44**, 500 mg, 1.85 mmol) were dissolved in THF (50 mL). To this *n*BuLi (1.48 mL, 3.70 mmol, 2.5 M in *n*-hexane) was added at -78 °C. After the mixture was slowly warmed to 25 °C and then stirred for 14 h. To this a suspension of copper(I)iodide (70 mg, 0.37 mmol) and diphenyltin dichloride (636 mg, 1.85 mmol) in THF (15 mL) was added. The reaction mixture was stirred at 80 °C for 24 h and after filtration all volatiles were removed *in vacuo*. The residue was filtered over basic alumina and the product was obtained after recrystallization from *n*-heptane/DCM (3:1) as orange crystals (321 mg, 0.60 mmol, 32%). Method B: The synthetic procedure was adapted from the lit.[3]: In a glovebox, 1,8-*bis*(thiophen-2-yl)octa-1,7-diyne (**44**, 800 mg, 2.96 mmol) and Rosenthal´s zirconocene (**48**, 1.39 g, 2.96 mmol) were dissolved in toluene (8 mL). The dark red solution was stirred at 22 °C for 18 h under a N$_2$ atmosphere. Diphenyltin dichloride (1.02 g, 2.96 mmol) and copper(I)chloride (30 mg, 30 µmol) in toluene (2 mL) were added to the solution. The reaction mixture was stirred at 22 °C for further 6 h. The reaction was quenched with water (1 x 100 mL) and extracted with DCM (3 x 100 mL). The combined organic layers were dried over magnesium sulfate, filtered and concentrated *in vacuo*. The crude product was purified by column chromatography (silica gel 15 µm grain size, *n*-hexane, R$_f$ = 0.36) to give the product as a yellow solid (**St1**, 540 mg, 1.01 mmol, 34%). **^{1}H NMR** (500 MHz, CDCl$_3$): δ = 7.63

(dd, $^3J_{SnH}$ = 22.3, 17.2 Hz, ^3J = 6.4 Hz, ^4J = 3.0 Hz, 4H, Ph-H-2,6), 7.41 - 7.32 (m, 6H, Ph-H-4, Ph-H-3,5), 7.27 - 7.25 (m, 2H, Tph-H-5), 6.99 - 6.91 (m, 4H, Tph-H-3,4), 2.94 - 2.86 (m, 4H, CH_2), 1.85 - 1.78 (m, 4H, CH$_2$-CH_2) ppm. **^{13}C{^{1}H} NMR** (126 MHz, CDCl$_3$): δ = 149.75 ($^2J_{SnC}$ = 38.6 Hz, stannole-C-3), 145.94 ($^2J_{SnC}$ = 35.8 Hz, Tph-C-2), 138.27 ($^1J_{SnC}$ = 248.4 Hz, Ph-C-1), 137.41 ($^2J_{SnC}$ = 22.3 Hz, Ph-C-2,6), 130.18 (stannole-C-2), 129.54 ($^4J_{SnC}$ = 6.5 Hz, Ph-C-4), 129.36 ($^3J_{SnC}$ = 11.7 Hz, Tph-C-3), 129.03 ($^3J_{SnC}$ = 27.6 Hz, Ph-C-3,5), 127.11 (Tph-C-5), 125.94 (Tph-C-4), 31.96 (CH$_2$), 23.41 ((CH$_2$)-CH$_2$) ppm. **^{119}Sn{^{1}H} NMR** (187 MHz, CDCl$_3$): δ = -82.4 (s) ppm. **HRMS** (EI, 70 eV, MAT95, direct): m/z calcd. for C$_{28}$H$_{24}$S$_2$^{116}Sn [M]$^+$ 540.03314 found 540.03303. **IR** (ATR): υ = 3060 (w), 2935 (w), 2359 (w), 1633 (w), 1515 (w), 1493 (w), 1478 (m), 1428 (m), 1411 (w), 1381 (w), 1348 (w), 1329 (w), 1283 (w), 1250 (w), 1211 (m), 1189 (w), 1134 (w), 1074 (m), 1059 (m), 1020 (w), 996 (w), 966 (w), 924 (w), 848 (m), 801 (m), 781 (w), 723 (m), 686 (s) cm^{-1}. **Mp**.: 156 °C.

1.7.3 Synthesis of 2-(Octa-1,7-diyn-1-yl)thiophene (**50**)
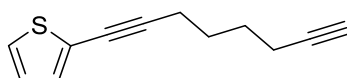
The synthetic procedure was adapted from the literature.[4] In a glovebox [Pd(PPh$_3$)$_2$Cl$_2$] (373 mg, 530 µmol) and copper(I)iodide (100 mg, 530 µmol) were added to a solution of 2-bromothiophene (**49**, 4.33 g, 26.5 mmol) and octa-1,7-diyne (**46**, 2.81 g, 26.5 mmol) in triethylamine (80 mL). The reaction mixture was stirred for 14 h at 25 °C. Afterwards all volatiles were removed in vacuo, and the residue was extracted with diethyl ether (3 x 100 mL). Then, the solvent was removed, the dark oil was filtered, and the crude oil was used for Kugelrohr distillation (100-120°°C, 1.5 x 10^{-1} mbar) to afford a yellowish oil (**50**, 823 mg, 4.40 mmol, 17%). **^{1}H NMR** (601 MHz, CDCl$_3$): δ = 7.17 (dd, ^3J = 5.2 Hz, ^4J = 1.1 Hz, 1H, Tph-H-3), 7.12 (dd, ^3J = 3.6 Hz, ^4J = 1.1 Hz, 1H, Tph-H-5), 6.93 (dd, ^3J = 5.2, 3.6 Hz, 1H, Tph-H-4), 2.46 (t, ^3J = 6.7 Hz, 2H, Tph-C≡C-CH_2), 2.26 (td, ^3J = 6.8 Hz, ^4J = 2.7 Hz, 2H, CH_2-C≡CH), 1.96 (t, ^4J = 2.7 Hz, 1H, C≡CH), 1.77 - 1.66 (m, 4H, Tph-C≡C-CH$_2$-(CH_2)$_2$) ppm. **^{13}C{^{1}H} NMR** (151 MHz, CDCl$_3$): δ = 131.11 (Tph-C-3), 126.87 (Tph-C-5), 126.07 (Tph-C-4), 124.14 (Tph-C-2), 93.87 (Tph-C≡C-CH$_2$), 84.20 (C≡CH), 74.16 (Tph-C≡C-CH$_2$), 68.70 (C≡CH), 27.68/27.61 (C≡C-CH$_2$), 19.33 (Tph-C≡C-CH$_2$-CH$_2$), 18.11 (CH$_2$-CH$_2$-C≡CH) ppm. **HRMS** (EI, 70 eV, MAT95, direct): m/z calcd. for C$_{12}$H$_{11}$S [M-H]$^+$ 187.0576 found 187.05796; calcd. for C$_{12}$H$_{12}$S [M]$^+$ 188.06597, found 188.06513. **IR** (ATR): υ = 3293 (w), 3105 (w), 2942 (w), 2861 (w), 2223 (w), 2115 (w), 1518 (w), 1427 (m), 1326 (w), 1238 (w), 1189 (w), 1080 (w), 1043 (w), 843 (m), 829 (m), 696 (s) cm^{-1}.

1.7.4 Synthesis of 5,5'-*bis*(8-(Thiophen-2-yl)octa-1,7-diyn-1-yl)-2,2'-bithiophene (**52**)
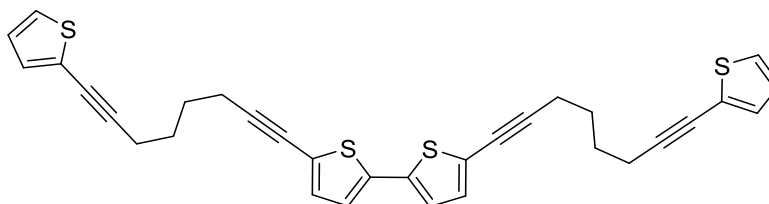
The synthetic procedure was adapted from the literature.[4] In a glovebox, [Pd(PPh$_3$)$_2$Cl$_2$] (52 mg, 74 µmol) and copper(I)iodide (35 mg, 67 µmol) were added to a solution of 5,5'-dibromo-2,2'-bithiophene (**51**, 602 mg, 1.86 mmol) and 2-(octa-1,7-diyn-1-yl)thiophene (**50**, 700 mg, 3.72 mmol) in triethylamine (30 mL) and toluene (30 mL) at 25 °C. This heterogeneous yellow mixture was stirred for 2 d at 25 °C. Subsequently, all volatiles were removed in vacuo, and the residue was extracted with diethyl ether (3 x 100 mL) and all volatiles were removed again. After purification by column chromatography on silica gel (column machine, 120 g, cyclohexane/diethyl ether, 99:1), the product

was isolated as yellowish solid (**52**, 715 mg, 1.32 mmol, 71%). **^{1}H NMR** (601 MHz, CDCl$_3$): δ = 7.18 (dd, ^{3}J = 5.2 Hz, ^{4}J = 1.2 Hz, 2H, Tph-*H*-3), 7.14 (dd, ^{3}J = 3.6 Hz, ^{4}J = 1.1 Hz, 2H, Tph-*H*-5), 7.01 (d, ^{3}J = 3.8 Hz, 2H, BiTph-*H*-4), 6.97 (d, ^{3}J = 3.8 Hz, 2H, BiTph-*H*-3), 6.94 (dd, ^{3}J = 5.2, 3.6 Hz, 2H, Tph-*H*-4), 2.50 (m$_c$, 8H, C≡C-C*H*$_2$), 1.70 (m$_c$, 8H, C≡C-CH$_2$-C*H*$_2$) ppm. **^{13}C{^{1}H} NMR** (151 MHz, CDCl$_3$): δ = 137.08 (BiTph-*C*-5), 132.01 (BiTph-*C*-3), 131.14 (Tph-*C*-3), 126.88 (Tph-*C*-4), 126.09 (Tph-*C*-5), 124.12 (Tph-*C*-2), 123.56 (BiTph-*C*-4), 123.24 (BiTph-*C*-2), 95.43 (Tph-C≡*C*), 93.89 (BiTph-C≡*C*), 74.23/74.14 (Tph-*C*≡C), 27.81/27.76 (C≡C-*C*H$_2$), 19.50/19.38 (C≡C-CH$_2$-*C*H$_2$) ppm. **HRMS** (EI, 70 eV, MAT95, direct): *m/z* calculated for C$_{32}$H$_{26}$S$_4$ [M-H]$^{+\cdot}$ 538.09119 found 538.09200. **IR** (ATR): υ = 3073 (w), 2936 (w), 2898 (w), 2861 (w), 2839 (w), 2220 (w), 1510 (w), 1423 (w), 1184 (w), 1044 (w), 865 (m), 845 (m), 829 (m), 694 (s) cm^{-1}. **Mp**.: 91.5 °C.

1.7.5 Synthesis of the Stannole Dimer (**St2**)
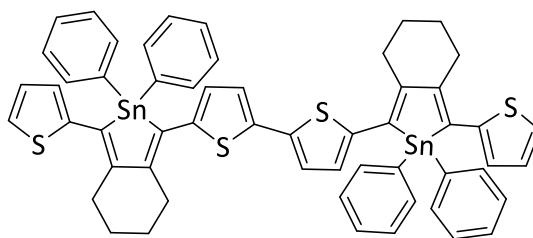
In a glovebox, 5,5'-*bis*(8-(thiophen-2-yl)octa-1,7-diyn-1-yl)-2,2'-bithiophene (**52**, 200 mg, 371 µmol) and Rosenthal´s zirconocene (**48**, 349 mg, 742 µmol) were dissolved in toluene (8 mL) and the dark red solution was stirred for 18 h at 22 °C under a nitrogen atmosphere. Subsequently, diphenyltin dichloride (255 mg, 742 µmol), copper(I)chloride (7.3 mg, 74 µmol) and toluene (2 mL) were added to the solution in a glovebox. The reaction mixture was stirred at 22 °C for further 12 h. The mixture was quenched under ambient atmosphere with methanol (100 mL) and the precipitate was collected by centrifugation. In the dark, the precipitate was washed by Soxhlet extraction with methanol and *n*-hexane. The precipitate in the Soxhlet filter was identified as pure product, which was extracted with DCM. After removal of the solvent, the product was obtained as a red powder (**St2**, 338 mg, 311 µmol, 84%). The product was sensitive to light.

^{1}H NMR (600 MHz, CDCl$_3$): δ = 7.68-7.59 (m, $^{3}J_{SnH}$ = 24.1, 21.4 Hz, 8H, Ph-*H*-2,6), 7.41 - 7.34 (m, 12H, Ph-*H*-3,4,5), 7.27 - 7.25 (m, 2H, Tph-*H*-5), 7.03 - 6.99 (m, 2H, Tph-*H*-3), 6.99 - 6.93 (m, 4H, BiTph-*H*-3,4), 6.86 - 6.83 (m, 2H, Tph-*H*-4), 2.94 - 2.87 (m, 8H, C*H*$_2$-CH$_2$), 1.85 - 1.82 (m, 8H, CH$_2$-C*H*$_2$) ppm. **^{13}C{^{1}H} NMR** (151 MHz, CDCl$_3$): δ = 149.90 (stannole-*C*-4), 149.53 (stannole-*C*-3), 145.93 (Tph-*C*-2), 144.59 (BiTph-*C*-5), 138.18 ($^{1}J_{SnC}$ = 248.4 Hz, Ph-*C*-1), 138.2 (BiTph-*C*-2), 137.4 ($^{2}J_{SnC}$ = 22.3 Hz, Ph-*C*-2,6), 131.0 (Tph-*C*-4), 130.6 (stannole-*C*-5), 130.5 (stannole-*C*-2), 129.6 ($^{4}J_{SnC}$ = 6.5 Hz, Ph-*C*-4), 129.4 (BiTph-*C*-3), 129.1 ($^{3}J_{SnC}$ = 27.6 Hz, Ph-*C*-3,5), 127.2 (BiTph-*C*-4), 126.0 (Tph-*C*-5), 123.2 (Tph-*C*-3), 32.10 (*C*H$_2$-CH$_2$), 32.00 (*C*H$_2$-CH$_2$), 23.38 (CH$_2$-*C*H$_2$) ppm. **^{119}Sn{^{1}H} NMR** (224 MHz, CDCl$_3$): δ = -81.0 (s) ppm. **HRMS** (APCI): *m/z* calcd. for C$_{56}$H$_{45}$S$_4$Sn$_2$ [M+H]$^{+}$ 1087.06117, found 1087.05980. **IR** (ATR): υ = 3073 (w), 2930 (w), 2899 (w), 1488 (w), 1479 (w), 1428 (w), 1250 (w), 1072 (w), 996 (w), 782 (m), 724 (m), 694 (s) cm^{-1}.

1.7.6 References for the Experimental Part

1. J. Linshoeft, E. J. Baum, A. Hussain, P. J. Gates, C. Nather, A. Staubitz, *Angew. Chem. Int. Ed.*, **2014**, *53*, 12916-12920.
2. S. Urrego-Riveros, Y. M. I. M. Ramirez, D. Duvinage, E. Lork, F. D. Sonnichsen, A. Staubitz, *Chemistry*, **2019**, *25*, 13318-13328.
3. Y. M. I. M. Ramirez, M. Rohdenburg, F. Mostaghimi, S. Grabowsky, P. Swiderek, J. Beckmann, J. Hoffmann, V. Dorcet, M. Hissler, A. Staubitz, *Inorg Chem*, **2018**, *57*, 12562-12575.
4. C. Hay, M. Hissler, C. Fischmeister, J. Rault-Berthelot, L. Toupet, L. Nyulászi, R. Réau, *Chem. Eur. J.*, **2001**, *7*, 4222-4236.

Chapter 2: Influence of The Group 14 Elements-Based Substituents on Photochromic π-Systems Such as Azobenzenes

Originally utilized as a motif for dyes and pigments,[1] azobenzene chromophores gained significance as molecular switches.[2] Azobenzenes benefit from conformational changes upon external stimuli along with their high photostability but also from facile synthesis and relatively small photo fatigue.[3] Upon irradiation with ultraviolet light (λ = 365 nm), azobenzenes can undergo isomerization to form the meta-stable *cis*-isomer which is convertible to the *trans*-isomer by applying light of a higher wavelength or by thermal relaxation. Both light-induced isomerization processes occur in the range of picoseconds,[4] whereas the thermal relaxation occurs in less than a second up to months depending on the substitution pattern.[5] Moreover, both isomers feature different geometries and dipole moments. While the planar *trans*-azobenzene has no dipole moment, *cis*-azobenzene exhibits a twisted geometry and has a substantial dipole moment (μ = 3.0 D).[6] In general, two mechanisms for the isomerization of azobenzenes were described: An inversion mechanism of one C-N bond or a rotational mechanism around the azo group (Scheme 14).[7]
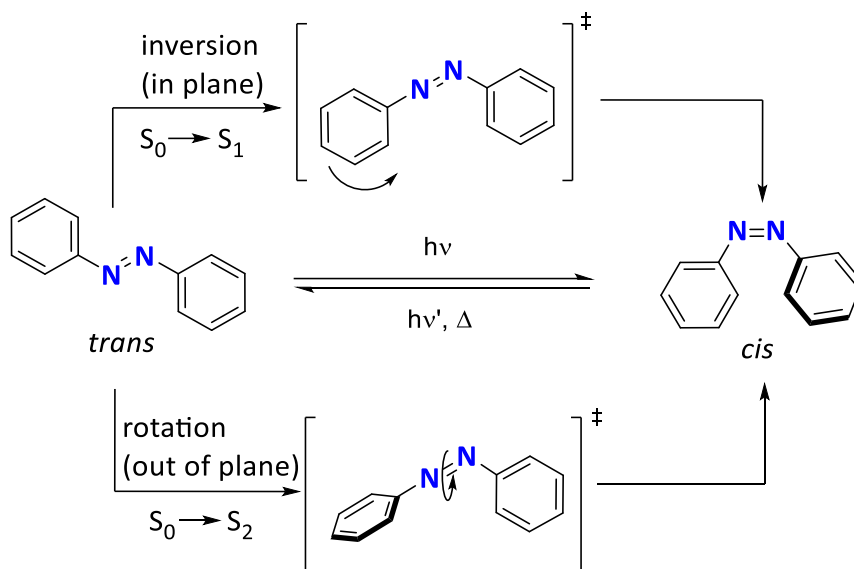
Scheme 14: Proposed mechanism for the *trans*/*cis*-isomerization of azobenzene.[7]

The substitution pattern of an azobenzene has a direct influence on the photochromic properties like absorption behavior, *cis*/*trans* ratio and half-life time of the thermal relaxation. Mostly the photophysical properties of azobenzenes are tuned by asymmetric substitution of both phenyl rings with auxochrome groups, e.g. in methyl orange and red azobenzenes-based dyes. In some cases, the implementation of main group elements in *ortho*-position became a concept to modulate the photophysical properties of azobenzenes. Moreover, this substitution pattern facilitates the coordination of main group elements by the azo group and therefore became a subject of current research. This topic originated from the interaction of various *ortho*-metalated azobenzenes based on palladium,[8] nickel and platinum,[9] which had been introduced by C-H activation methods. In the last decade, even more, such cyclometalated azobenzene-based systems were reported and remained a useful tool for azobenzene post-functionalization.[10]

2.1.1   *Ortho*-Substituted Azobenzenes Bearing Main Group Elements

Focusing more on the photophysical properties, *ortho*-substitution with boron moieties hindered the photoswitchability of the azobenzene motif but turned azobenzenes (**54-55**) into a strong luminophore which resulted from boron-nitrogen interactions of the azo group (Fig. 33).[11-13]

54, λ_{abs} = 386 nm,   **55**, λ_{abs} ($\pi\pi^*$/$n\pi^*$)= 521/552 nm

λ_{ems} = 503 nm, Φ_{lum} = 0.20 λ_{ems} = 572 nm, Φ_{lum} = 0.32
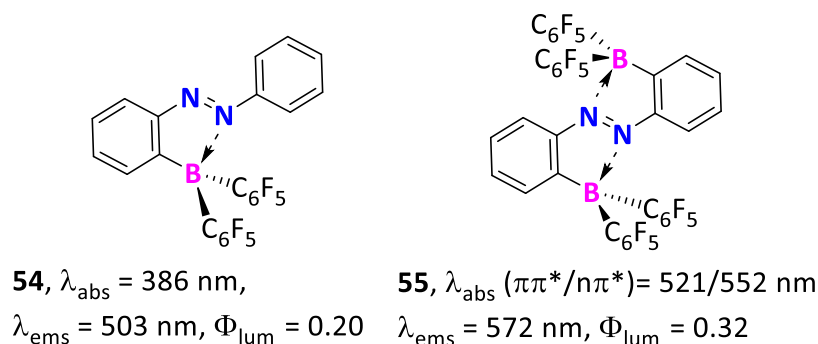
Fig. 33: Luminophores based on organoboron-substituted azobenzenes **54** and **55**.[11-13]

Further examples of *ortho*-substituted azobenzenes were synthesized by Kano and coworkers[11-19] bearing organophosphorus, -silicon, -germanium and -tin moieties on mono- or disubstituted azobenzenes. As seen for the examples of monotetrel-substituted azobenzenes (**56-58**), the influence of the substituent towards the absorption properties was mostly insignificant but still, a slight red-shift was observable (λ_{abs} ($\pi\pi^*$, $n\pi^*$) = (325-327 nm, 446-450 nm), compared to unsubstituted azobenzene (λ_{abs} ($\pi\pi^*$, πn^*) = (318 nm, 441 nm) (Fig. 34).[17, 20]

X = SiMe$_3$, **56**, λ_{abs} ($\pi\pi^*$/$n\pi^*$)= 325/450 nm   **X = H**, **59**, λ_{abs} ($\pi\pi^*$/$n\pi^*$)= 330/444 nm

X = GeMe$_3$, **57**, λ_{abs} ($\pi\pi^*$/$n\pi^*$)= 325/446 nm   **X = SiMe$_3$**, **60**, λ_{abs} ($\pi\pi^*$/$n\pi^*$)= 343/457 nm

X = Sn(nBu)$_3$, **58**, λ_{abs} ($\pi\pi^*$/$n\pi^*$)= 327/446 nm   **X = SiF$_3$**, **61**, λ_{abs} ($\pi\pi^*$/$n\pi^*$)= 378 nm/n.n.
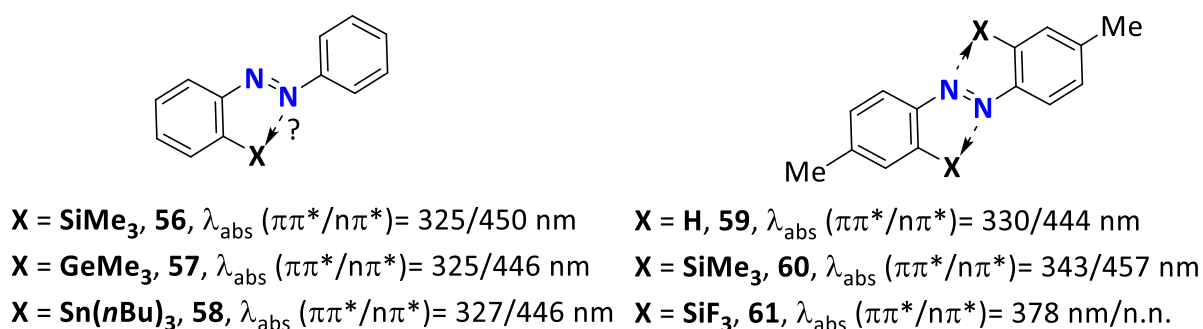
Fig. 34: Overview of *ortho*-substituted azobenzenes bearing a main group element.[17, 20] The reference for di*ortho*-substituted azobenzenes was dimethylazobenzene[21].

The bathochromic shift of the tetrel-substituted azobenzenes might be due to the inductive effect of the electron-accepting organotetrel groups or σ^*-π^* conjugation effects. Expected coordination of a nitrogen atom towards the tetrels was not observed by hetero NMR analysis or X-ray analysis.

Attaching two trimethylsilyl groups in *ortho*-position of 4,4'-dimethylazobenzene resulted in a bathochromic shift of the azobenzene's photophysical properties (**60**, λ_{abs} ($\pi\pi^*$, $n\pi^*$) = (343 nm, 457 nm) compared to 4,4'-dimethylazobenzene (**59**, λ_{abs} ($\pi\pi^*$, $n\pi^*$) = (330 nm, 444 nm) (Fig. 34). Upon introducing fluorosilyl moieties in *ortho*-position, the nitrogen atoms occupied an empty orbital of the fluorine atom and stabilized the silicon atom in its five-coordinate state. Absorption spectra of azobenzene **61** revealed an additional red-shift of the absorption maximum. This effect was attributed to weak nitrogen-silicon interaction due to the overlap of σ^*- and π^*-orbitals.[17] Moreover, these azobenzenes were switchable upon irradiation by cleaving the hypercoordination of silicon from its five-membered state to a four-coordinated state as observed by ^{29}Si NMR experiments.[14] Also, the

trifluorosilyl-substituted azobenzene **61** exhibited weak fluorescence which is exclusive for commonly non-fluorescent azobenzenes.[17]

Although describing the introduction of organotetrels (organosilicon, -germanium, -tin) in *ortho*-positions, the aforementioned reports did not cover the scope of any further reactions with the organotetrel-substituted azobenzenes. Commonly, organotetrels are great precursors for transition metal-catalyzed cross-coupling reactions, e.g. Stille reaction, or tetrel-metal exchange reactions, e.g. tin-lithium exchange. Special interest in stannylated azobenzenes was risen by the Staubitz group as the tin derivatives could act in both reaction types. The stannylated azobenzenes were accessed by using hexamethylditin and a palladium catalyst giving the trimethylstannyl-substituted azobenzenes (Scheme 15).[22, 23]

$(Me_3Sn)_2, [Pd(PPh_3)_4] \ (2 \ mol\%)$

THF, 150 °C (μw), 10 min

95% for *para,* 88% for *meta,*
53% for *ortho*
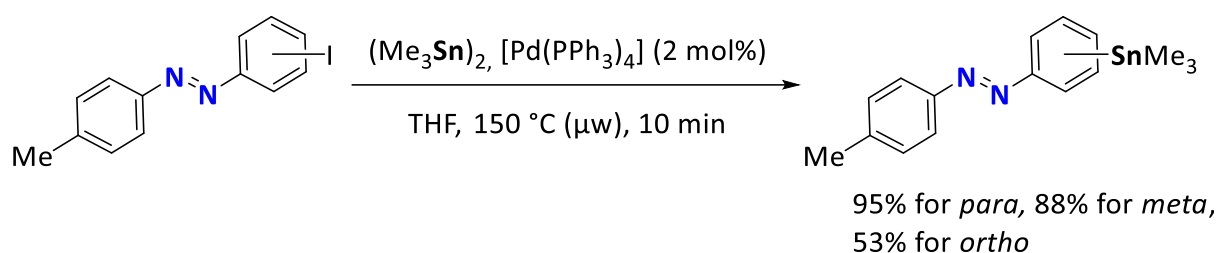
Scheme 15: Stannylation of halogenated azobenzene using a palladium catalyst at elevated temperature.[22, 23]

This complex method was originally chosen since lithium-halide exchange reactions could lead to the reduction of the azo unit due to its electrophilicity and redox activity. As a result, often low yields for such a reaction type or the formation of substituted hydrazines were reported.[24, 25] Whereas the stannylation in the *para*- and *meta*-substitution azobenzene occurred in high yields, the substitution in *ortho*-position led to low yields. Therefore, an interaction of the neighboring azo group resulting in lower yields was suspected.

However, the tetrel-metal exchange was investigated in *ortho/meta/para*-stannylated azobenzenes by addition of an organolithium species and quenching with an electrophile (E) (Scheme 16).[23]

E = MeI, TMSCl, Me₂CO, DMF...

1. 1.0 eq. MeLi,
2. 1.1 eq. **E**

THF, -78 °C

via

$\delta ^{119}Sn = -300 \ ppm$
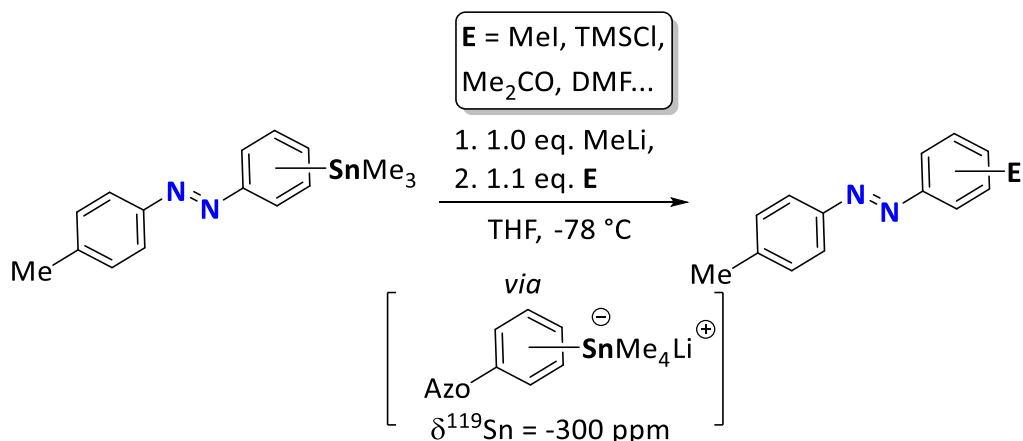
Scheme 16: Reaction of stannylated azobenzenes with methyl lithium and quenching with electrophiles.[23]

Using a selective tin-lithium exchange reaction in here, prevented the attack on the azo unit. However, the initial tin-lithium exchange occurred after the formation of an intermediate tin-lithium ate complex which was proven by ^{119}Sn VT-NMR ($\delta ^{119}Sn = -300 \ ppm$) experiments. The lithiated azobenzene was then quenched with different electrophiles like methyl iodide and trimethylsilyl chloride, but also aldehydes, amides, cyanates and thiocyanates. This protocol was applied to *ortho*-, *meta*- and *para*-

stannylated azobenzenes and resulted in the finding that the *ortho*-substituted azobenzenes were obtained in lower yields than their *meta*- and *para*-substituted azobenzenes.[23]

As this method presented an efficient way to obtain also dinucleophilic azobenzenes, it was utilized in a project that dealt with the formation of disilylated azobenzenes[26] and further azobenzenes-siloxane polymers, to which I contributed.[27] These works will not be further discussed in this thesis.

Apart from being used for tin-lithium exchange reactions, stannylated aromatics are valuable for the formation of large π-conjugated systems *via* palladium-catalyzed cross-coupling reactions. Therefore, stannylated azobenzenes could be subjected to Stille cross-coupling reaction conditions to obtain *para*-substituted aryl-azobenzenes (Scheme 17).[22]
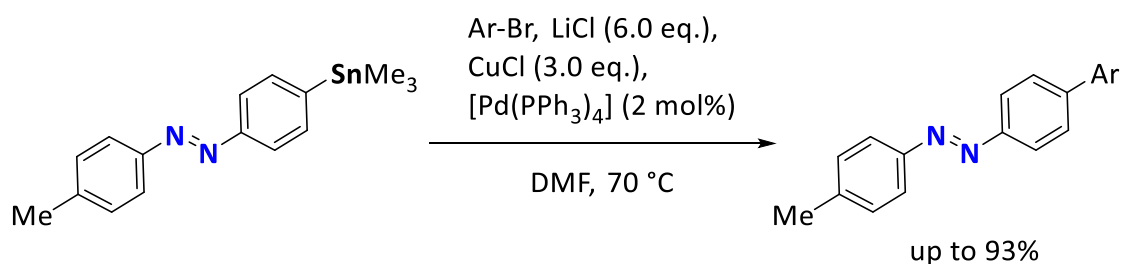
Scheme 17: Stille cross-coupling of stannylated azobenzenes.[22]

This methodology was applicable to both electron-withdrawing and electron-rich electrophiles in high yields of 70% to 93%. Furthermore, this protocol tolerated aryl halides bearing functional groups (aldehydes, ester, cyano) giving rise to precursors for larger azobenzene-based functional materials.[22]

2.2 Objectives

Since reported results showed that the functionalization of *ortho*-substituted azobenzenes differed significantly from its *meta* and *para*-isomers, the aim of this chapter was to investigate methods to synthesize *ortho*-substituted *bis*(trimethyltetrel)azobenzenes and to compare their structural, photophysical and thermal properties. Apart from the fact that these materials could possess novel optical properties and absorption/switching behavior, they could be useful for further post-functionalization as metal-lithium exchange and cross-coupling reactions (Scheme 18).
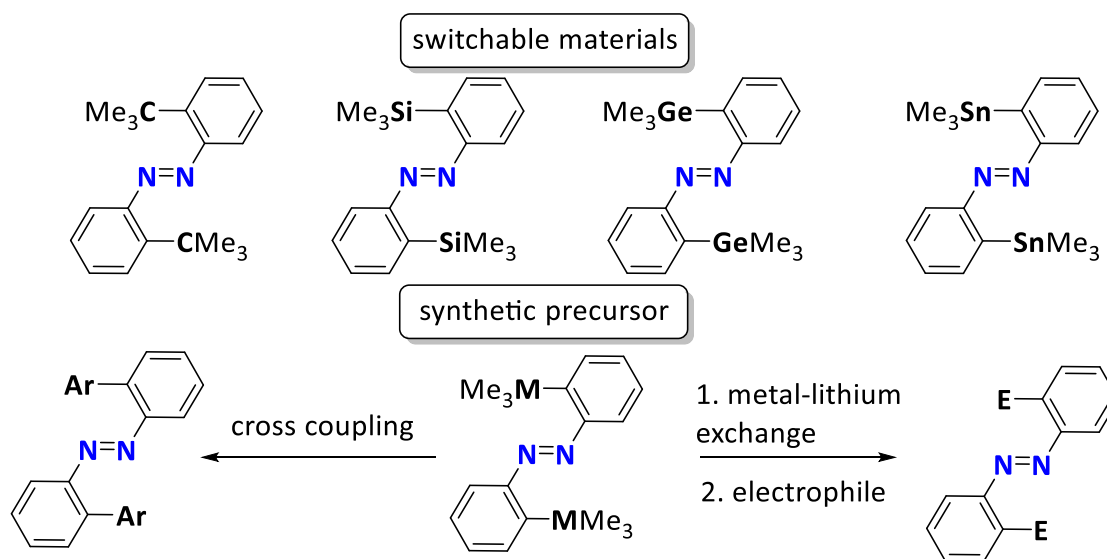
Scheme 18: Targeted metalated azobenzenes.

2.3 Synthetical Approach

In general, the synthesis of symmetric azobenzenes was already investigated intensively and is represented by various practicable and applied methods.[28] Reports also showed that metalated azobenzene could also be obtained by aniline oxidation or Mills reaction but the reported yields were unsatisfactory.[20] To obtain *ortho*-metalated azobenzenes, a synthetic pathway including an oxidative or reductive coupling of an *ortho*-haloaniline **63** or nitrobenzene **64** followed by a transition metal-mediated cross-coupling of azobenzene **65** is postulated (Scheme 19).
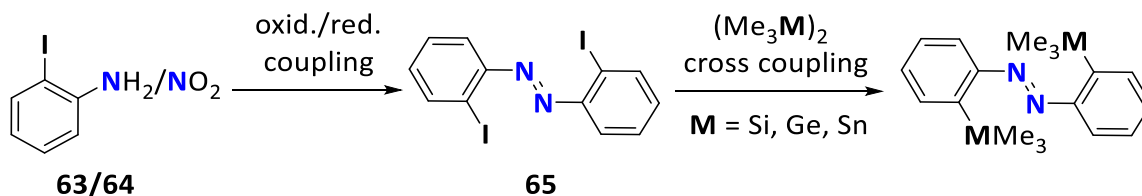
Scheme 19: Synthesis towards *ortho*-metalated azobenzenes.

Utilization of various hexamethylditetrels would be a facile way to access metalated azobenzenes *via* cross-coupling reactions. The synthesis of silylated-, germanylated- and stannylated azobenzenes could be useful for further transition metal-catalyzed cross-coupling reaction with aryl halides. Although the tin-lithium exchange is a well-investigated method for *meta* and *para*-stannylated azobenzenes, the metalation of an *ortho*-stannylated azobenzene (**66**) might suffer from additional coordination of the azo-unit. To further expand the scope of nucleophiles also a transmetalation towards copper should be performed (Scheme 20).
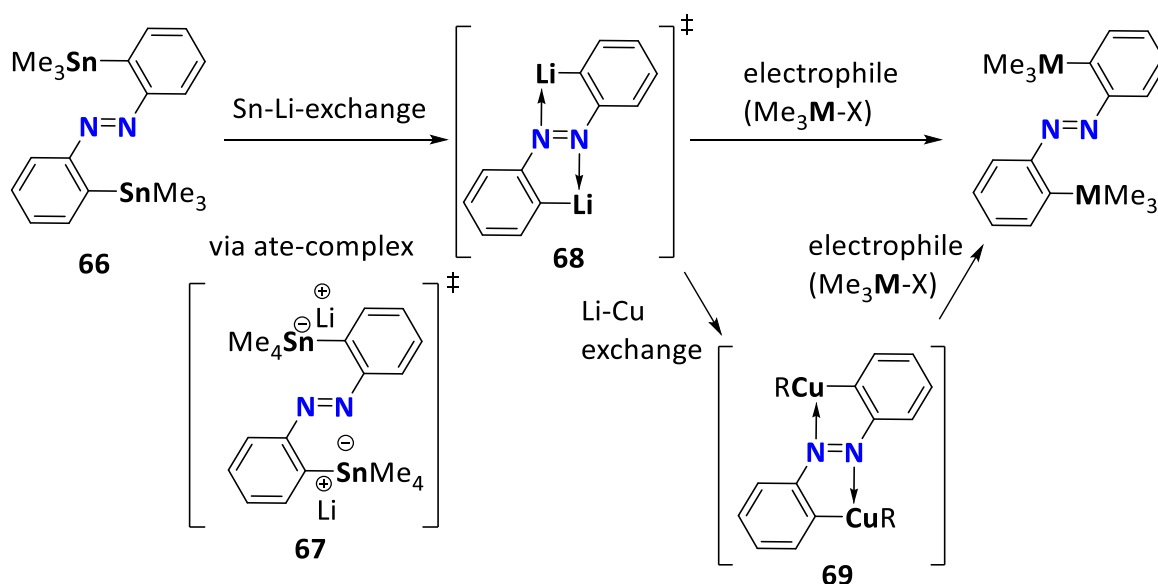
Scheme 20: Concept for a dual tin-lithium exchange and possible lithium-copper transmetalation to obtain *ortho*-substituted azobenzenes. The presented lithium and copper species can present solvents or other ligands in their coordination sphere.

The tin-lithium exchange, *via* a suspected ate-complex **67** should be followed by either direct quenching with a variety of electrophiles or by a transmetalation *via* a nucleophilic copper species **69** and an electrophilic substitution. The latter methodology might be advantageous for electrophiles that are chemically softer, as it was discovered for organocopper species in general.[29] In all cases, the role of the azo unit as additional coordination partners in close proximity to the respective metal species should be considered and significantly differs from already presented examples of *meta*/*para*-metalated azobenzenes.[23]

Another great advantage of using stannylated azobenzenes as precursors is the ability to act as a nucleophile in transition metal-catalyzed cross-coupling reaction which should be studied as well. To investigate the cross-coupling ability of *ortho*-trimethyltetrel substituted azobenzenes, the tin derivative was chosen as the most promising cross-coupling partner for Stille cross-coupling reaction (Scheme 21).
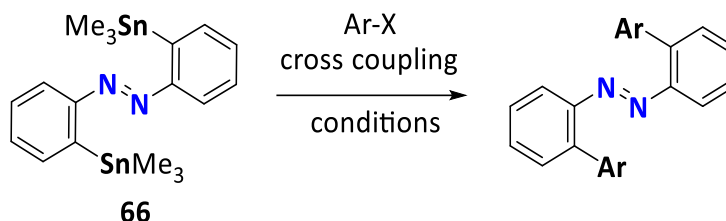
Scheme 21: Utilization of stannylated azobenzene **66** as a precursor for 2,2'-diaryl substituted azobenzenes.

Initial results for this methodology for *para/meta*-substituted azobenzenes might be transferable for the *ortho*-substituted azobenzenes. The success of this methodology might be an alternative to common C-H activation methods for *ortho*-arylated azobenzenes.

2.4   Results and Discussion

The methodology for stannylation of *ortho*-iodinated azobenzenes as well as tin-lithium and tin-lithium-copper exchange reactions were optimized and overall, four tetrel-substituted azobenzenes (C, Si, Ge, Sn) were synthesized. Apart from that, the influence of different trimethyltetrels in both *ortho*-positions of the azobenzene on the structural, thermal and photophysical properties of these molecules was studied (Scheme 22).
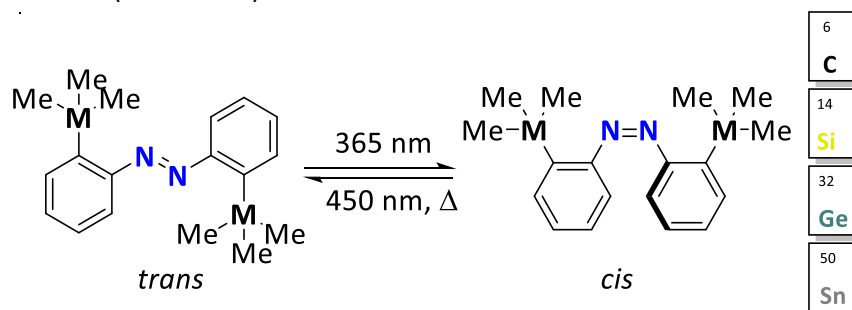
Scheme 22: Photoisomerization of trimethyltetrel-substituted *ortho*-azobenzenes.

The results were published (*Molecules* **2019**, *24(2)*, 303) and are attached below.

Transmetalation reactions

The precursor 2,2'-*bis*(trimethylstannyl)azobenzene (**66**) was used for tin-lithium exchange or tin-lithium-copper exchange generating trimethyltetrel-substituted azobenzenes. Further investigations with other organic electrophiles were also conducted (Scheme 23)
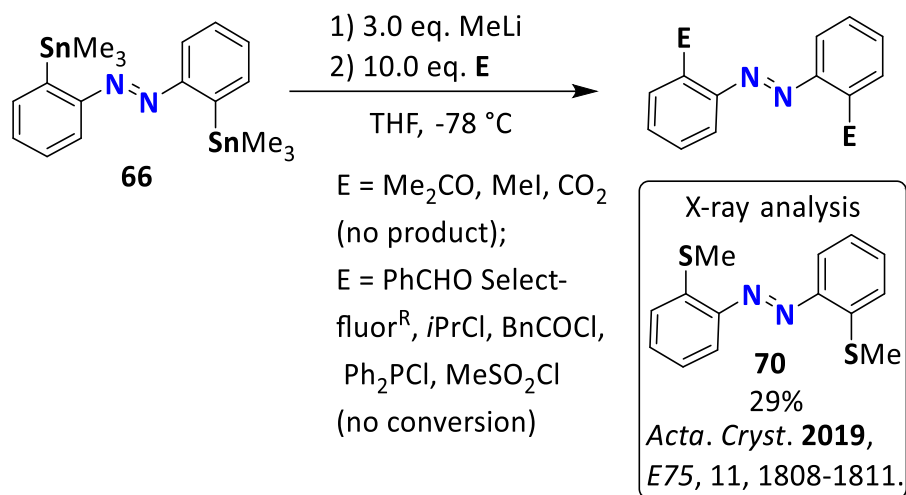
Scheme 23: Reaction of various electrophiles with stannylated **66** azobenzene after tin-lithium exchange reaction.

From the broad scope of electrophiles, conversion was only observed for dimethyl disulfide, carbon dioxide, acetone and methyl iodide whereas the other reactants showed no interaction with the lithiated azobenzenes at all. This observation contrasted with the reactivity of *meta*- and *para*-lithiated azobenzenes, which reacted successfully with various electrophiles.[23] Overall, only the isolation of the 2,2'-*bis*(methylsulfanyl)azobenzene **70** succeeded, giving an isolated yield of 29%. For this compound, a detailed X-ray analysis was conducted to investigate if there was any weak interaction between the methylsulfanyl moiety and the azo group. The results were published in research communication and the original article is attached below (*Acta Cryst.* **2019**, *E75*, 1808-1811).

Cross-coupling reactions

The 2,2'-*bis*(trimethylstannyl)azobenzene was also used as a reactant for transmetallation reactions and a brief study about its reactivity in Stille cross-coupling reactions was conducted. Initial results with *para*-substituted monostannylated azobenzenes were already reported.[22] Therefore, we used the same reaction conditions to draw a direct comparison of the behavior of the *ortho*-substituted distannylated azobenzenes (Scheme 24).
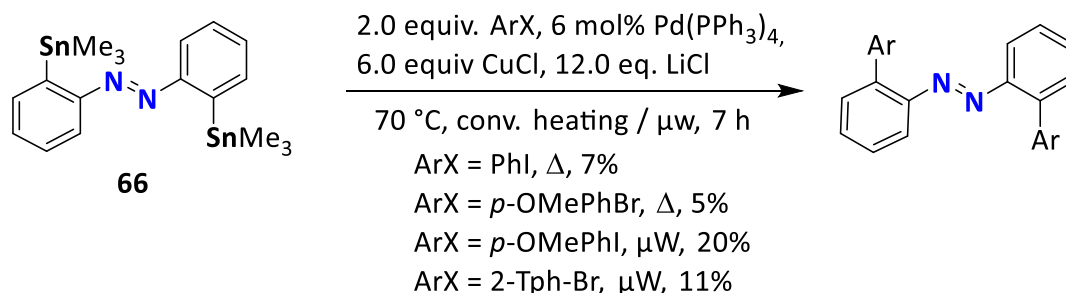
Scheme 24: Cross-coupling reaction of *bis*-stannylated azobenzenes **66** with various aryl halides. Results were presented in the bachelor thesis of my student Thomas. J. Kuczmera.

Even though identical reaction conditions as reported for *para-* and *meta-*stannylated azobenzenes[22] were utilized, the yields were unsatisfactory in most cases. It was concluded that the *ortho-*position is either electronically unfavored or sterically hindered compared with similar cross-coupling reactions in *meta/para-*position. By variation of catalyst load, additive or solvent, the yield might be improved, however this was not further investigated in the course of this thesis.

2.4.1.1 Publication: Synthesis, Structure, Thermal Behavior and cis/trans Isomerization of 2,2'-(EMe₃)₂ (E= C, Si, Ge, Sn) Substituted Azobenzenes

Full paper

Abstract

The synthesis of a series of 2,2'-*bis*(trimethyltetrel) azobenzenes is reported, evaluating the different synthetic approaches that different group 14 element substituents individually require. The synthetic access to the carbon substituted congener is very different from the heavier tetrels, in that the key step is the formation of the N=N bond in azobenzene, rather than the azobenzene-C bond. Sn could be introduced with a cross-coupling route, whereas the Si and Ge congeners were prepared by a stannylation-lithiation-electrophilic quenching sequence. Iodo-lithium exchange was also a possible route to obtain the dilithiated species, which can be attributed to the chelating effect of the nitrogen atoms. However, the organo-lead species could not be obtained *via* these routes. The resulting structures were fully characterized (NMR, FTIR, HRMS and XRD). Furthermore, their thermal properties (TGA and DSC) and their photoswitching behavior in solution (UV-VIS & NMR experiments) were investigated and compared for the different tetrels (C, Si, Ge, Sn).

Scheme 25: Photoisomerization of trimethyl tetrel-substituted *ortho*-azobenzenes.

Scientific Contribution

The experiments and the analysis were performed by me and partly by Thomas J. Kuczmera, who did his fully supervised Bachelor thesis with me.[30] The X-ray analysis and refinement was conducted by Enno Lork. The manuscript was written by me and Anne Staubitz.

Supporting Information

Further reactions, NMR spectra, switching experiments and thermal analysis are available free of charge online.

Reproduction note

The journal is an open source journal. Therefore, no special permission is required to reuse all or part of the article published by the publisher, including figures and tables.

molecules

MDPI

Article

Synthesis, Structure, Thermal Behavior and *cis/trans* Isomerization of 2,2'-(EMe$_3$)$_2$ (E = C, Si, Ge, Sn) Substituted Azobenzenes

Jonas Hoffmann [1,2,3,4], **Thomas Josef Kuczmera** [1], **Enno Lork** [5] ⓘ **and Anne Staubitz** [1,2,3,*] ⓘ

[1]   Institute for Analytical and Organic Chemistry, University of Bremen, Leobener Straße 7,
      D-28359 Bremen, Germany; jonas.hoffmann@uni-bremen.de (J.H.); kuczmera@uni-bremen.de (T.J.K.)
[2]   MAPEX Center for Materials and Processes, University of Bremen, Bibliothekstraße 1,
      D-28359 Bremen, Germany
[3]   Otto-Diels-Institute for Organic Chemistry, University of Kiel, Otto-Hahn-Platz 4, D-24098 Kiel, Germany
[4]   Université Rennes, CNRS, ISCR-UMR 6226, 263 Av. du Général Leclerc, F-35042 Rennes, France
[5]   Institute for Inorganic Chemistry and Crystallography, University of Bremen, Leobener Straße 7,
      28359 D-Bremen, Germany; enno.lork@uni-bremen.de
*   Correspondence: staubitz@uni-bremen.de; Tel.: +49-421-218-63210

check for
updates

Abstract: The synthesis of a series of 2,2'-bis(trimethyltetrel) azobenzenes is reported, evaluating the different synthetic approaches that different group 14 element substituents individually require. The synthetic access to the carbon substituted congener is very different from the heavier tetrels, in that the key step is the formation of the N=N bond in azobenzene, rather than the azobenzene-C bond. Sn could be introduced with a cross-coupling route, whereas the Si and Ge congeners were prepared by a stannylation-lithiation-electrophilic quenching sequence. Iodo-lithium exchange was also a possible route to obtain the dilithiated species, which can be attributed to the chelating effect of the nitrogen atoms. However, the organo-lead species could not be obtained via these routes. The resulting structures were fully characterized (NMR, FTIR, HRMS and XRD). Furthermore, their thermal properties (TGA and DSC) and their photoswitching behavior in solution (UV-VIS & NMR experiments) were investigated and compared for the different tetrels (C, Si, Ge, Sn).

1. Introduction

In main group chemistry, trends within a group play an important role for the understanding of how particular properties of a molecule can be tuned. By selecting a congener, in which an atom is replaced by another element from the same group, the geometric shape of the molecules can be changed. For instance, in organic compounds, carbon atoms can be replaced by heavier tetrels (Si, Ge, Sn and Pb) to give semi-inorganic hydrocarbons [1]. However, size is not the only change; optophysical properties can also be influenced substantially. For example, it has been shown that for cyclopentadiene analogs, in which the sp^3 substituted C atom is replaced by a heavier group 14 element, the HOMO-LUMO gap (HOMO = highest occupied molecular orbital; LUMO = lowest unoccupied molecular orbital) is reduced due to σ*-π* conjugation [2–6]. Due to our interest in both main group chemistry and photoswitchable molecules, we systematically investigated the influence that could be exerted by tetrels in the *ortho*-position of azobenzenes, as well as the structural influences this substitution might trigger: Azobenzenes are thermally and photochemically stable molecular switches that can undergo a reversible *trans–cis* isomerization under illumination. The properties of

azobenzenes, such as absorption maxima and switching behavior, can be tuned by their substitution pattern [7–11]. *Ortho*-substituted azobenzenes distinguish themselves from most molecular switches by their significantly longer thermal relaxation times of the *cis*-isomer back to their *trans*-isomers [12,13]. This property makes *ortho*-substituted azobenzenes suitable for several applications where long half-life times of the thermal relaxation are required, giving rise to new materials and dyes, e.g., external stimuli responsive polymers [14,15].

In general, *ortho*-azobenzenes can be accessed either by using C–H activation methods with late transition metals like nickel, palladium, platinum or ruthenium [16,17], by deprotonation with metal bases [18,19], or by direct halogen-lithium exchange [19,20]. The latter has been shown to proceed with high efficiency in the synthesis of several *ortho*-substituted organometallic azobenzenes (Scheme 1) [21].

$$E = Si, R = Me, 80\%$$
$$E = Ge, R = Me, 98\%$$
$$E = Sn, R = n\text{-Bu}, 65\%$$
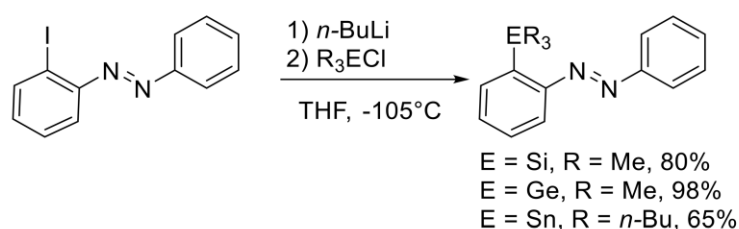
Scheme 1. Functionalization of monosubstituted azobenzenes with organotetrels [21].

This methodology is superior to the classical azocoupling approach and could be used with a high variety of electrophiles. It should also be mentioned that in this study, the *ortho*-bis(silyl) azobenzene (compound **6** in our study) was synthesized by oxidation of the respective amine. This product was used for mono-desilylation to give the monosilylated azobenzene displayed above [21]. Other metalation methods were used to introduce pentacoordinated silyl atoms in azobenzene motifs [20,22]. It was also found that substitution with heavier group 14 elements, which convey a positive inductive effect on the aromatic ring, resulted in a slight bathochromic shift of the absorption maxima compared to unsubstituted azobenzene.

Since we developed a method for the lithiation of azobenzenes by halogen-lithium exchange reactions for *para*- and *meta*-substituted azobenzenes [23,24], we were interested to transfer this methodology towards disubstituted *ortho*-azobenzenes. This process involved the synthesis of tin-substituted azobenzenes through a Kelly-Stille cross-coupling reaction, followed by a low temperature tin-lithium exchange. Functionalization could be achieved by quenching the lithiated species with a variety of electrophiles at low temperatures. Initial results showed that the structure-reactivity relationship of the *meta*-, *para*- and *ortho*-azobenzenes in the Kelly-Stille cross-coupling reaction led to significant differences in yields (*para*: 93%, *meta*: 88% and *ortho*: 43%). An advantage of a functionalization methodology that involves stannylated groups in the reagents is the good shelf-life and the potential use of these reagents as nucleophilic components in Stille type cross-coupling reactions. This was already reported for *para*-azobenzenes and gives access to substitutions with aromatic or vinylic groups [25].

In this work, we were interested in the detail of the structure/property relationship of different tetrel-substituted azobenzenes. In contrast to previous studies, the carbon congener is included and both *ortho*-positions of the azobenzene are substituted.

2. Results

The investigation started with the synthesis of *ortho*-substituted azobenzenes, in which the substituent was always EMe$_3$ with E = C, Si, Ge and Sn (E = Pb proved inaccessible). Therefore, we prepared a 2,2′-substituted difunctional azobenzene through the oxidation of 2-iodoaniline (**1**) with manganese dioxide to give 2,2′-diiodoazobenzene (**2**) in a yield of 82% (Scheme 2) [26].
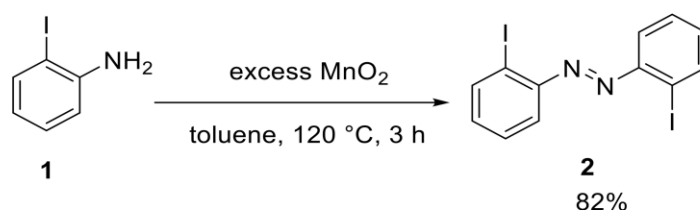
Scheme 2. Oxidative azocoupling to give the difunctional azobenzene **2**, which can be used as the electrophilic component in cross-coupling reactions.

It needs to be pointed out that azobenzenes with di-*ortho*-substituents are more difficult to prepare than those with the same substituents in *meta*- and *para*-position. Oxidizing reagents, like copper(I) bromide/air [25], copper(II)/silver(I)/tetra-*n*-butylammonium bromide [27] or diacetoxyiodobenzene [28], were explored in the synthesis, but in all cases no conversion was observed.

Following the iodo-lithium exchange, which was already reported [20], 2,2'-diiodo-azobenzene (**2**) was treated with *n*-butyllithium at a low temperature (−105 or −78°C) and quenched with a trimethylsilyl chloride electrophile (Scheme 3). The reactions proceeded very cleanly, which in our experience is different to *meta*- and *para*-iodinated azobenzenes, where the electrophilic N=N group can be attacked by the nucleophilic *n*-butyllithium. This suggests a significant stabilization of the *ortho*-lithiated species by an N→Li coordination.
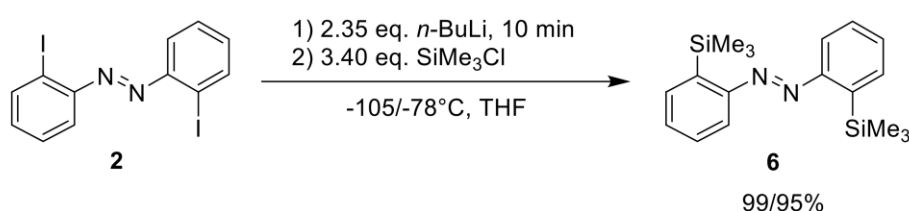
Scheme 3. Direct metalation of azobenzene **2** to give the trimethylsilyl-substituted azobenzene **6**. (Experimental details can be found in the SI).

Although this is a very effective route to synthesize these *ortho*-substituted azobenzenes, we were interested in obtaining the tetrel-substituted compounds under cross-coupling conditions. Therefore, the next step to generate the EMe$_3$ *ortho*-substituted azobenzenes was a palladium catalyzed cross-coupling procedure with Me$_3$E-EMe$_3$ reagents. Since this reaction has been already reported for *meta*- and *para*-substituted azobenzenes for E = Sn, we adapted to the reaction conditions also for other tetrels, for which this type of reagent was available (Si, Ge and Sn) (Scheme 4, Table 1).
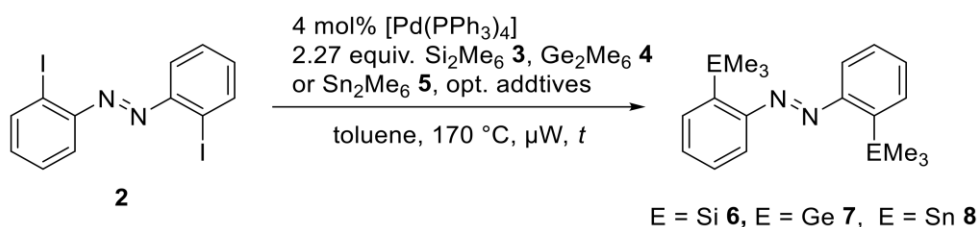
Scheme 4. Different hexamethyl dimetals were used in a Stille-Kelly type cross-coupling protocol.

Table 1. Overview of used substrates and reagents for the synthesis of dimetalated azobenzenes.

Entry	M	Additive	Time/h	Yield
1	Si	-	1/8	0%, no conversion [a]
2	Si	2.00 equiv. Cs_2CO_3	1	0%, no conversion [a]
3	Ge	-	1/8	0%, no conversion [b]
4	Ge	2.00 equiv. Cs_2CO_3	1	0%, no conversion [b]
5	Sn	-	1	60% isolated product [c]
6	Pb	-	1	not performed [d]

[a] For a similar procedure, see References [29,30]. [b] For a similar procedure, see Reference [31]. [c] For a similar procedure used for azobenzenes, see References [24,25]. [d] This toxic substance decomposes at higher temperatures [32].

We initially assumed that the metal-metal bond dissociation energy (BDE) might have a substantial impact on the reactivity towards the oxidative addition of the catalyst. The bond dissociation energies for hexamethyl dielement species have been reported: BDE (Me_3C-CMe_3) = 76.0 kcal/mol [33], BDE (Me_3Si-$SiMe_3$) = 69.1 kcal/mol [34] and 79.7 kcal/mol [35], BDE (Me_3Ge-$GeMe_3$) = 69.1 kcal/mol [34], BDE (Me_3Sn-$SnMe_3$) = 61.6 kcal/mol and BDE (Me_3Pb-$PbMe_3$) = 54.6 kcal/mol [34]. Since the BDE of the tin dimer is relatively lower than the other hexamethyl dielement compounds, we assumed that a more labile tin-tin bond would react more easily, but it was surprising that neither the Me_3Si-$SiMe_3$ (**3**) reagent, nor the Me_3Ge-$GeMe_3$ (**4**) reagent provided any conversion. Steric reasons may be a potential issue: The C–Sn bond is longer and thus may lead to less congestion in the *ortho*-positions. Thus, the Stille-Kelly type cross-coupling reaction with the hexamethylditin (**5**) was optimized towards the reaction temperature, reaction time and catalyst load (Scheme 5, Table 2): We envisaged that with this reagent in hand, alternative routes to the other *ortho*-substituted azobenzenes may be also accessible via tin-lithium exchange and electrophilic quenching processes (see below).
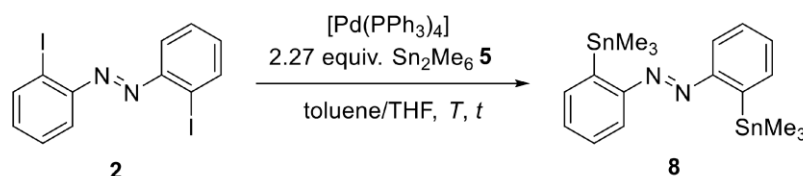
Scheme 5. Stille-Kelly type coupling of azobenzene **8**.

Table 2. Overview of the Stille-Kelly reaction optimization for the di-stannylated azobenzene **8**.

Entry	Cat. Load	Temp.	Time/h	Yield
1	4 mol%	130 °C, conv. Heating	8	17%
2	4 mol%	130 °C, conv. Heating	16	19%
3	6 mol%	170 °C, µW	1	31%
4	4 mol%	170 °C, µW	1	27%
5	2 mol%	170 °C, µW	1	49%
6	3 mol%	170 °C, µW	1	60%
7	3 mol% [a]	170 °C, µW	1	7%
8	11 mol%	170 °C, µW	1	14%
9	11 mol% [b]	170 °C, µW	1	96%

[a] Copper(I) chloride (6.0 equiv.) and lithium chloride (12.0 equiv.) were added. [b] 6.70 equiv. Sn_2Me_6 was used.

It was found that increasing the reaction temperature from 130 °C to 170 °C, along with changing from conventional to microwave assisted heating (entries 2 and 4), led to an increase in yield and a decrease in reaction time. Furthermore, the catalyst to hexamethyldistannane (**5**) ratio had a crucial impact on the success of the reaction. Increasing only the catalyst load led to a decrease in the yield (60% to 14%, entries 6 and 8). Additives like copper (I) halides [36] and lithium chloride [37] also lowered the yield of the product (entry 7). Interestingly, a high catalyst load in combination with a high amount of hexymethyldistannane (**5**) resulted in nearly quantitative yield. Combined with

51

the fact that the reaction vessels always contained an insoluble black precipitate after the reaction, we assumed that the autocatalytic agglomeration of the palladium catalyst that can occur more easily with higher catalyst loadings may be the cause of this observation [38]. With an excess of hexamethyldistannane (**5**), agglomeration was not observed (see the high difference in yield for entries 6, 8 and 9), presumably because the desired reaction was accelerated compared to the agglomeration process. Since hexamethyldistannane (**5**) is an expensive and toxic compound, a high excess and high amount of organotin waste is not desirable. Therefore, we performed further reactions with only 2.27 equivalents of this organotin compound, accepting the somewhat lower yield. We also tested whether the stannylated product **8** might react with the iodinated starting material **2** in a standard Stille reaction, but this was not the case, which excludes this reaction as a cause for the lower yields from entries 7 to 8 (see SI).

To access the other *ortho*-substituted azobenzenes for EMe$_3$ (E = C, Si, Ge), we followed a transmetalation procedure which was already reported for di-stannylated *meta*- and *para*-azobenzenes [23]. Initially, the metalation temperature and time were optimized, with trimethylsilyl chloride (**9**) being used as an electrophile (Scheme 6, Table 3).
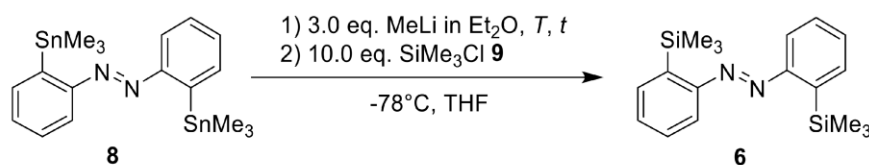
Scheme 6. Trimethylsilyl chloride **9** was used as a test electrophile to obtain optimized reaction parameters.

Table 3. Optimization of the tin-lithium exchange and the reaction with **9**.

Entry	T	Lithiation Time	Yield [a]
1	−78 °C	60 min	87%
2	−60 °C	60 min	55%
3	−40 °C	60 min	49%
4	−20 °C	60 min	20%
5	0 °C	60 min	5%
6	−78 °C	1 min	69%
7	−78 °C	3 min	64%
8	−78 °C	9 min	71%
9	−78 °C	30 min	74%
10	−78 °C	90 min	79%

[a] Yields were determined by using 1,3,5-tri*iso*-propylbenzene as an internal reference for ^{1}H NMR analysis.

It was found that increasing the temperature for the lithiation reaction led to a decrease in product and an emergence of unassignable signals in the ^{1}H NMR spectra. However, the metalation time played only a minor role in the formation of the product (Entries 6–10). The best conditions were found to when the lithiation temperature was −78 °C and a metalation time of 90 min was used. To expand the variety of electrophiles to less hard organometals, we made use of a transmetalation from the hard, reactive lithium towards the softer and less reactive cuprate, which was initially reported by Knochel [39]. This methodology has so far not been applied to azobenzene chemistry (Scheme 7).
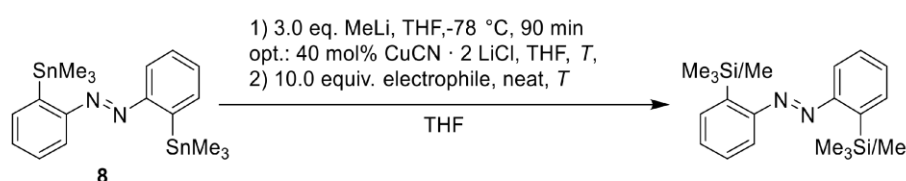
Scheme 7. In addition to the tin-lithium exchange, we investigated the subsequent transmetalation to organocuprates and further quenching with electrophiles.

We tested this reaction sequence with several electrophiles and different metalation temperatures (Table 4).

Table 4. To widen the scope of the transmetalation to softer electrophiles, an organocuprate was introduced by using CuCN · 2 LiCl as softer organometallic reagent. The transmetalation temperature varied from −78 °C to −40 °C.

Entry	E	Metal	Metalation T.	Yield [a]
1	Me$_3$SiCl	[Li]	−78 °C	87%
2	Me$_3$SiCl	[Li]	−40 °C	73%
3	Me$_3$SiCl	[Cu]	−78 °C	90%
4	Me$_3$SiCl	[Cu]	−40 °C	7%
5	Me$_3$SiI	[Li]	−78 °C	50% [b]
6	Me$_3$SiI	[Cu]	−78 °C	17% [b]
7	Me$_3$SiI	[Cu]	−40 °C	30% [b]
8	MeI	[Cu]	−78 °C	5%
9	MeI	[Cu]	−40 °C	56%
10	MeI	[Li]	−78°C	0%

[a] Yields were determined by using 1,3,5-tri*iso*-propylbenzene as an internal reference for ^{1}H NMR analysis. [b] As a side reaction, THF might have undergone a ring-opening ether cleavage to form 4-iodo-butyloxytrimethylsilane [40].

The yield decreased if the temperature for the lithiated species was changed from −78 °C to −40 °C (Entries 1 and 2), which may be an indication of a reductive attack by the organolithium reagent on the azo group [18]. The transmetalation to copper at −78 °C provided largely the same yields (Entry 3), although at −40 °C, using the cuprate gave a very low yield of 7% (Entry 4). For Me$_3$SiI, a decrease in yield after the transmetalation to copper was observed (Entries 5–7), which was unexpected as this electrophile is softer. With methyl iodide as an electrophile, we could observe an increase in the yield by increasing the transmetalation temperature from −78°C to −40 °C (Entries 8 and 9). In that case, using the cuprate was essential for the reaction, because the lithiated species did not react with the electrophiles (Entry 10).

With both methods in hand, we incorporated new trimethyltetrel halides. In dependence of the nature of the respective electrophile, we were interested in the reactivity towards the hard organolithium or the soft organocuprate (Scheme 8, Table 5).
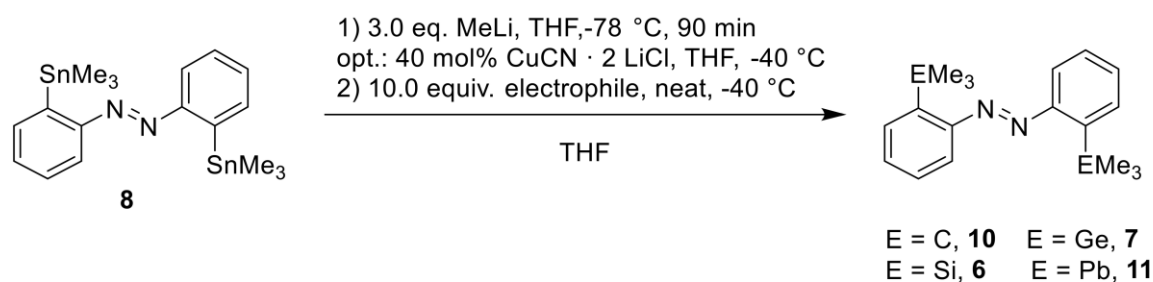
Scheme 8. Metalation to obtain di-metalated azobenzenes **10**, **11** and **6**, **7**.

Table 5. Transmetalation of di-stannylated azobenzene **8** with methyl lithium or further metalation to the cuprate and the reactions of these organometallic reagents with electrophilic trimethyltetrel species.

Entry	E	Metal	Yield
1	Me$_3$CCl	[Li] or [Cu]	both 0%
2	Me$_3$SiCl	[Li] or [Cu]	87%/90%
3	Me$_3$GeCl	[Li] or [Cu]	60%/0% [a]
4	Me$_3$PbBr	[Li] or [Cu]	both 0%

[a] The reaction resulted in a complex mixture of products in which **7** could not be isolated.

Besides the above mentioned trimethylsilyl chloride (**9**), the reaction of trimethylgermanyl chloride (**12**) to give the digermanylated azobenzene (**7**) could be performed in a good yield of 60% (Entry 3). With *tert*-butyl chloride (**13**) and trimethyllead bromide (**14**), neither reaction was successful, irrespective of whether the lithium or copper species (Entries 1 and 4) were used, but for different reasons: The nucleophilic substitution of *tert*-butyl chloride (**13**) would be highly disfavored for an S_N2 reaction due to its steric hindrance, and also because a S_N1 reaction is unlikely under these nonpolar reaction conditions. The reaction with trimethyllead bromide (**14**) was unsuccessful with both the lithium or copper nucleophile. It is possible that the trimethyllead bromide did react, but that the lead(IV)-substituted azobenzene was then too reactive to be isolated; recent examples of this are given in Reference [41]. This hypothesis is supported by the fact that after the reactions, a shiny insoluble black precipitate could be observed, which are probably decomposition products from lead.

Since we were interested in comparing the influence of different trimethyltetrel substituents in *ortho*-position of the azobenzenes, we obtained the carbon-derivative via oxidation of the respective aniline (Scheme 9).
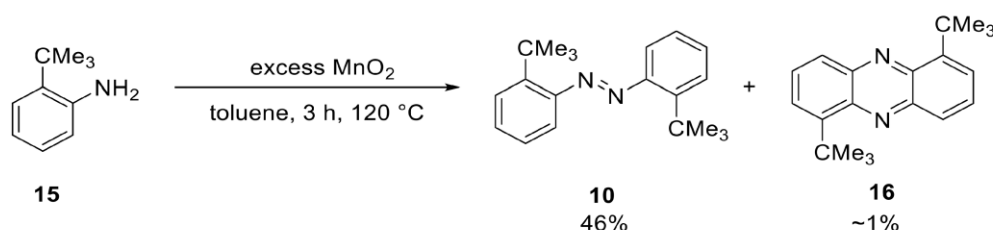
Scheme 9. Oxidative azocoupling of aniline **15** with manganese dioxide as an oxidant. The product **10** and by-product **16** could be separated by column chromatography.

The product **10** was isolated in a moderate yield of 46%, but surprisingly, we could also isolate a side product, which was characterized by NMR, HRMS, FTIR and XRD and was found to be a phenazine derivative (Scheme 9 and Figure 1).
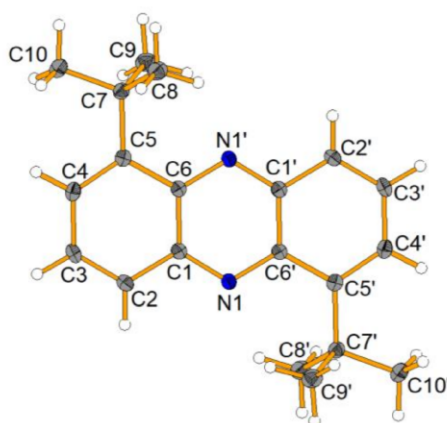
Figure 1. Molecular structure of the isolated phenazine **16**, showing 50% probability ellipsoids.

It is not clear at present how this side product formed, but the literature suggests that elevated temperature and oxidative conditions favor the formation of the very thermodynamically stable phenazines [27].

With the series of *ortho*-tetrel substituted azobenzenes in hand, we were interested in the comparison of their structures and the effect of the group 14 elements on the physical properties of the azobenzenes.
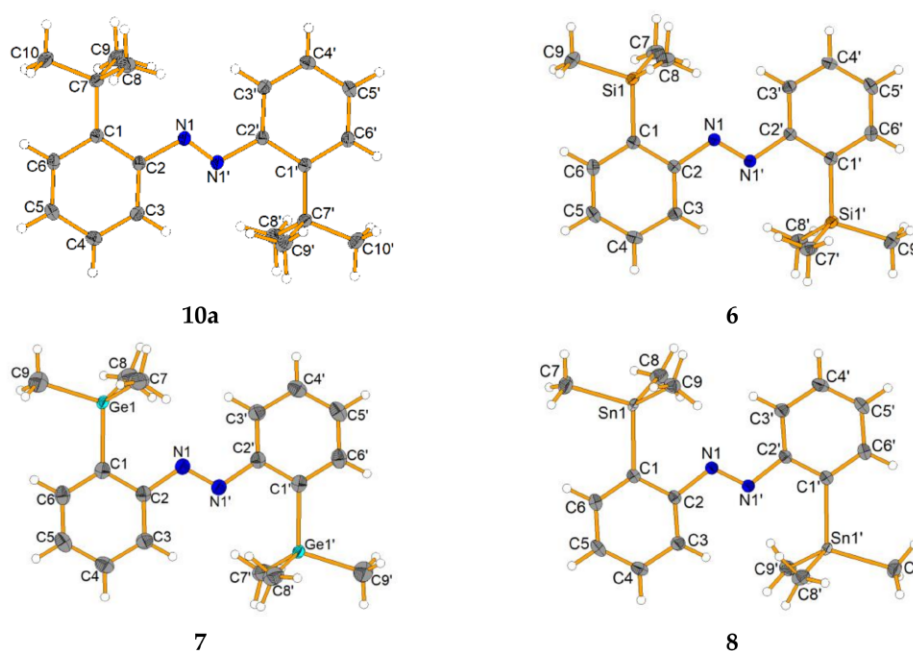
Figure 2. Molecular structures of molecules **10a**, **6**, **7** and **8**, showing a 50% probability of ellipsoids. **10** crystalizes with two molecules in the asymmetric unit, only one is shown (**10a**). The Sn-atom of **8** is disordered over two positions with occupancies of 90% and 10%, respectively. For reasons of clarity only the major component is shown.

The crystal structures of all molecules were determined (Figure 2). Since the interaction of tetrels in the *ortho*-position of azobenzenes has been reported for electron deficient fluorinated silyl groups [42,43], we were interested in how the structural parameters of our crystals would compare with the mono-substituted compounds described by Kano. A special interest was the N=N and carbon-tetrel bond, as well as the possible interaction of the group 14 element with the azo group, which is here indicated by the distance and the torsion from the phenyl ring and the azo group (Table 6).

Table 6. Overview of the important crystallographic parameters of compounds **10**, **6**, **7** and **8**.

	10a [1]	10b [1]	6	7	8
Crystal system	Triclinic		Monoclinic		
Space group	P-1		P2$_1$/c		
N-N bond length (Å)	1.2556(17)	1.2509(18)	1.258(2)	1.256(3)	1.2511(19)
C1-tetrel bond length (Å)	1.5348(14)	1.5374(14)	1.8856(14)	2.0234(18)	2.144(1) [2]
N1-tetrel distance (Å)	2.9402(16)	2.909118	3.0151(11)	3.0441(14)	3.047(1) [2]
Torsion angle C1-C2-N1-N1′ (°)	−163.3(1)	−164.8(1)	175.0(1)	177.1(2)	−177.3(1)
CCSD No.	1880127		1880130	1880129	1880128

[1] The asymmetric unit consists of two crystallographic independent molecules. [2] Distances to main component are given.

The *ortho*-substitution had only a marginal effect on the length of the azo group (from 1.2509(18) Å to 1.258(2) Å). However, as expected, the distance of the carbon-tetrel bond increased from the lighter to the heavier elements (1.5348(14) Å (For E = C) to 2.144(1) Å (for E = Sn)). The nitrogen-tetrel distance did not indicate any interaction of the azo group with the respective tetrels (2.9091(18) Å for Si to 3.0471 Å for Sn). This can be compared with azobenzenes with SiMe$_2$F (2.585(3) Å) and SiF$_3$ (2.371(4) Å) [41]: These much-shortened distances indicated that the lone pair of the nitrogen atom was able to coordinate to the Lewis acidic silicon center, which was not observed in our case. Furthermore, the ^{29}Si NMR shift of this compound was to be found at ^{29}Si{^{1}H} NMR: δ = −4.04 ppm, which is a typical shift for

tetracoordinated silicon species. This is well aligned with Kano's work [41], who reported a ^{29}Si{^{1}H} NMR-shift of −3.8 ppm for a trimethylsilyl substituted azobenzene, as compared to −16.8 ppm if one of the Me groups was replaced by F, or even −57.8 ppm for a SiF$_3$ group in this position. Furthermore, the crystal structure differs in the fact that in the case of a nitrogen-tetrel interaction, a four-membered ring would result, whereas the structures from Kano showed interaction with the second nitrogen atom of the azo group, resulting in a five membered ring; for this to happen, the aromatic rings would need to rotate by approximately 180°, which was not observed. Upon substitution with higher congeners than carbon or silicon, the germanium and tin substituted azobenzene exhibited a carbon-tetrel bond length of 2.0234(18) Å and 2.144(1) Å, which can be considered as an ordinary organotetrel bond length. However, the torsion angles for the CMe$_3$ substituted azobenzene were surprisingly far from planar (by ca. 15–17°), which was in contrast to Kano's work on Si and also our results on the SiMe$_3$ substituted compounds, which show almost no distortion. We assumed that the sterical hindrance of the *tert*-butyl group, in comparison with the short C(Ph)–C(CMe$_3$) bond, forced the system to undergo distortion. Due to more flexible and longer C–Si, C–Ge and C–Sn bonds, we observed less planar distortion (3–6°).

Since azobenzenes can undergo *trans/cis* isomerization, we studied the effect of the different group 14 elements on the general absorption properties, the *cis/trans* equilibrium in the dark and the photostationary state (PSS) at 365 nm and 450 nm through UV and NMR spectroscopy (Scheme 10).

trans　　　　　　　E = C **10**, Si **6**, Ge **7**, Sn **8**　　　*cis*
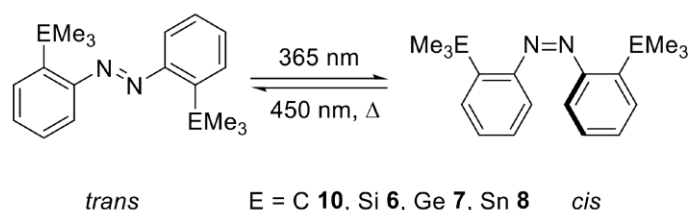
Scheme 10. Light/thermally induced isomerization of synthesized azobenzenes **10** and **6**–**8**.

In general, the UV spectra of the azobenzenes exhibit a strong ππ* absorption around 330 nm and a weak absorption for the nπ* band of the *cis*-isomer around 475 nm (Figure 3a,b). Upon irradiation of the azobenzenes with UV light (365 nm), we observed a significant decrease in the absorbance of these molecules (Figure 3a), which can be assumed to switch to the respective *cis*-isomer. Blue light (450 nm) shifts the photostationary state (PSS) to the *trans*-isomers (Figure 3b).
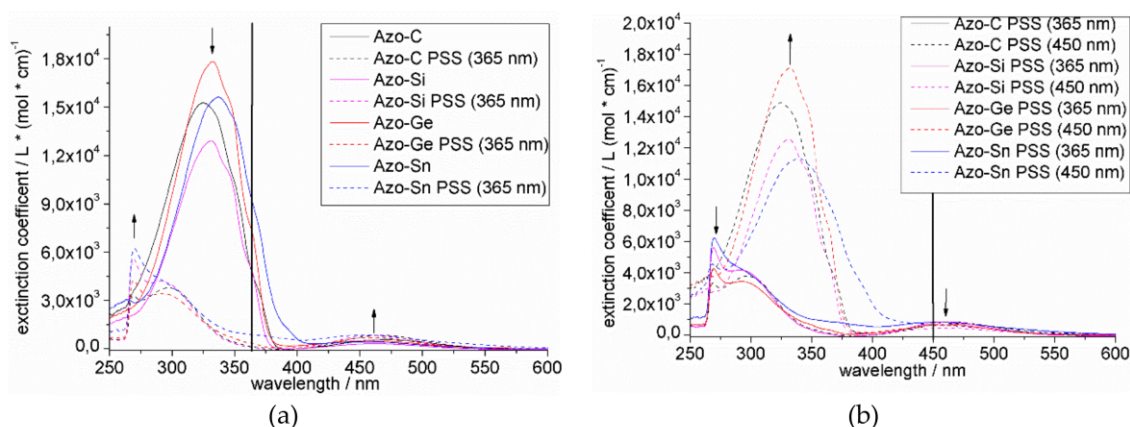
Figure 3. (**a**) Absorption spectra of azobenzenes **6**, **7**, **8** and **10** before and after irradiation with 365 nm light for 3 min. (**b**) Absorption spectra of azobenzenes **6**, **7**, **8** and **10** after irradiation with 365 nm light for 3 min, followed by irradiation with 450 nm light for 3 min. In each case, the black vertical lines indicate the irradiation wavelengths.

In all cases, the switching was totally reversible but the tin-substituted azobenzene **8** showed a decrease and broadening of the ππ* band (Figure 3b), which was not expected, and may indicate a photochemical decomposition process.

To obtain the ratio of the *cis/trans*-isomer in the PSS, we combined irradiation experiments with ^{1}H NMR analysis. The result of this experiment for molecule **6** is shown below (Figure 4).
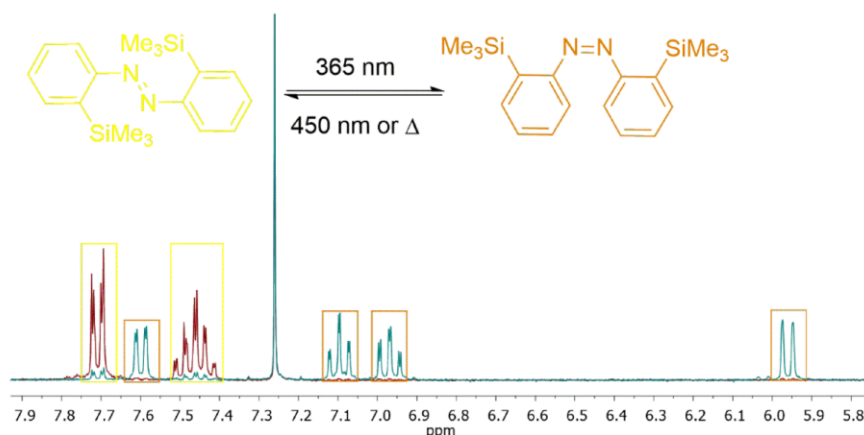
Figure 4. ^{1}H NMR (300 MHz) spectra of compound **6** before (red) and after (blue) irradiation with 365 nm light (15 min) in CDCl$_3$.

To compare the general trends upon substitution with different tetrels on the azobenzenes, we compared the collected isomerization information (Table 7).

Table 7. Collected data of the absorption spectra and switching experiments.

Compound	ππ* Band ε (L mol^{-1} cm^{-1})	PSS (as Synthesized) NMR *cis:trans*	PSS (365 nm) *cis:trans*	$\tau_{1/2}$ NMR (h)	$\tau_{1/2}$ UV (h)
10 (C)	15272 (325 nm)	1:99	80:20	55.61	17.07
6 (Si)	12907 (331 nm)	1:99	83:17	62.17	20.45
7 (Ge)	17818 (333 nm)	1:99	91:9	65.84	16.75
8 (Sn)	15632 (338 nm)	1:99	73:27 [a]	11.46 [a]	17.38 [a]

[a] Compound **8** presumably underwent decomposition upon irradiation.

Upon substitution of these compounds with heavier group 14 elements, we observed a slight bathochromic shift of the ππ* band (325 nm to 338 nm). This could be explained by the effect of the decreasing torsion angle due to the bulky trimethyltetrel groups, allowing extended π-conjugation (Table 8). However, the effect of the heavier tetrels on the extinction coefficient of the azobenzene system is rather small.

All systems contained only a small amount of the *cis*-isomer 'as synthesized'. Upon irradiation with 365 nm light, the maximum amount of the *cis*-isomer was found to range from 80% to 91% from E = C to E = Ge, respectively. Therefore, the PSS is substantially influenced by the tetrel. For E = Sn, however, the ratio appeared much lower, but this could also be attributed to photodecomposition. Irradiation with 450 nm light did not result in a complete switching to the *trans*-isomer, which can be observed by the existence of the nπ*-band in the UV-VIS spectra. Unfortunately, irradiation with 365 nm and 450 nm light caused the tin-substituted azobenzene **8** to experience some decomposition, which was detected by UV and ^{1}H NMR spectroscopy. This may be caused by a small C–Sn bond-dissociation energy. We further observed the thermal relaxation of the *cis*-azobenzenes that had been obtained after irradiation with 365 nm light with UV-VIS and NMR spectroscopy. The half-life times (τ) in the NMR experiments were determined to be between 55.61 h to 65.84 h, in which an increasing half-life time with heavier tetrels trend could be observed. The UV experiments for compounds **6**, **7** and **10** revealed

half-life times of 17.07 h to 20.45 h. In this case, no correlation between the tetrel substitution and the half-life time could be found (for all data see the SI). There is a substantial discrepancy between the half-life times measured by the two techniques. It needs to be pointed out in this context that the concentrations in the NMR were higher by approximately 2 orders of magnitude. Although half-life times should not be concentration dependent in general, they can be different if agglomerations and the stacking of molecules occur, which is likely to be the case for the compounds under investigation.

These systems were also analyzed by dynamic scanning calorimetry (DSC). To ensure thermal stability in the temperature range of investigation of these compounds, thermogravimetric analysis (TGA) was conducted (see SI). The compounds showed mass loss at 208 °C (C, **10**), 188 °C (Si, **6**), 196 °C (Ge, **7**) and 248 °C (Sn, **8**). However, when a TGA experiment on molecule **10** was interrupted at mass loss and the residue was analyzed by NMR spectroscopy, no decomposition was observed. Therefore, we assumed that the azobenzene evaporated at the higher temperature, accounting for the observed loss of mass.

In general, these compounds showed endothermic melting signals at onset temperatures of 87 °C (E = C), 69 °C (E = Si **6**), 83 °C (E = Ge) and 102 °C (E = Sn **8**), and exothermic crystallization peaks of 16 °C (E = C **10**), 50 (E = Si), (48 °C (E = Ge) and 56 °C (E = Sn **8**) (Figure 5, Table 8)). In general, the melting temperature increased within the main group of compounds **6–8**, but compound **10** proved to be an exception. Although the temperature ramps were slow (0.5 K/min), the melting peaks were not completely sharp, additionally, the crystallization peaks showed multiple crystallization events due to spontaneous seeding (for all data see the SI).
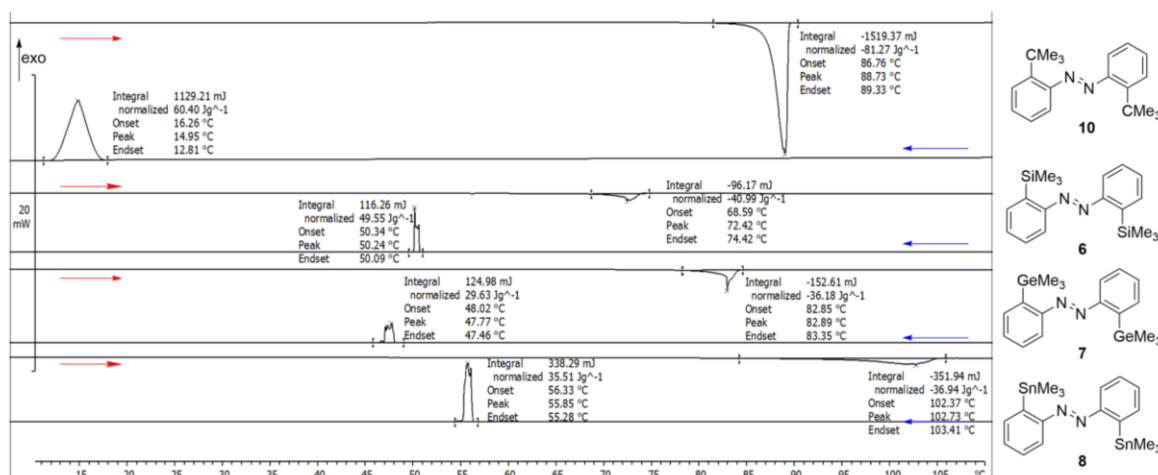
Figure 5. Stacked dynamic scanning calorimetry (DSC) spectra of all target compounds. The DSC experiments were performed with crystals with a heating rate of 0.5 K/min and a flow of nitrogen gas of 20 mL/min. As an example, compound **10** was analyzed after three cycles by ^{1}H- and ^{13}C{^{1}H} NMR spectroscopy and showed no degree of decomposition.

Table 8. Results of the thermoanalytic experiments.

	10	6	7	8
T_{fusion} (Onset) (°C)	86.76	68.59	82.85	102.37
H_{fusion} (KJ/mol)	23.93	13.37	15.13	15.05
$T_{solidif.}$ (Onset) (°C)	16.26	50.34	48.02	56.33
$H_{solidif.}$ (KJ/mol)	−17.78	−16.16	−12.39	−18.03

We observed that with faster DSC measuring modes (10 K/min) there was a high degree of amorphousness in the structures (see SI). With slower DSC methods (0.5 K/min), the difference between the fusion and solidification measured with the slower DSC method enthalpies are still existent and may be related to a non-crystallizing part of the molecules. The fusion enthalpy of compound **10**

was 23.93 KJ/mol, which is rather high in comparison of the other azobenzenes (**6**: 13.37 KJ/mol, **7**: 15.13 KJ/mol, **8**: 15.05 KJ/mol).

3. Discussion

We have described the synthesis, characterization (XRD, NMR, HRMS FTIR), switching and thermal behavior for four azobenzenes in detail. The synthesis for azobenzene **8** was conducted via Stille-Kelly cross-coupling with optimized reaction conditions and a high yield. Attempts to synthesize azobenzenes **6** and **7** using the respective Me_6M_2 (M = Si, Ge) compound and the same method did not succeed. However, the synthesis for azobenzenes **6** and **7** was performed through tin-lithium exchange with further reaction with the respective trimethyltetrel halides. For *ortho*-halogenated azobenzenes, *ortho*-lithiated species can also be obtained by a simple halogen-metal exchange. The lithium atom *ortho*-position is particularly stabilized by coordination with the *N* atoms of the azogroup, which facilitates the reaction. Also, the first tin-lithium-copper transmetalation on *ortho*-azobenzenes has been tested to enhance the reactivity of the nucleophile towards softer electrophiles. Since the reaction with *tert*-butyl chloride (**13**) (whether via the tin-lithium or tin-lithium-copper transmetalation procedure) was not successful, we decided to obtain azobenzene **10** via the oxidation of the corresponding aniline. Furthermore, as a byproduct, a phenazine **16** could be isolated and completely characterized. Due to the nucleophilic character of the three *ortho*-metalated azobenzenes (Si, Ge, Sn), these molecules could be prospective molecules for cross-coupling reactions, see for example silicon [43,44], germanium [45–47] or tin [48,49].

4. Materials and Methods

4.1. General Information

For inert reactions, a nitrogen filled glovebox from Pure Lab[HE] and standard Schlenk techniques were used. Except for the preparation of the 2,2′-diiodoazobenzene (**2**) and 2,2′-di(*tert*-butyl)azobenzene (**10**), all reactions were carried out under inert conditions.

All glassware for the inert reactions was dried in an oven at 200 °C for several hours prior to use. Additionally, before starting the reaction, the glassware was heated under vacuum (about 5×10^{-2} mbar) and flushed at least three times with argon. The NMR tubes were dried at 110 °C for several hours.

Microwave irradiated reactions were carried out using an Emrys[TM] Optimizer instrument (Biotage, Uppsala, Sweden), in which the temperature was measured with an external IR detector. MeLi was titrated prior to usage with menthol, using 2,2′-bipyridine as an indicator [50].

For chromatographic purification, silica gel 60 (MERCK, Darmstadt, Germany, 0.015–0.40 mm) was used. If stated, Celite® 503 (Carl Roth GmbH & Co. KG, Karlsruhe, Germany) was used as a filtration aid. Thin layer chromatography was performed by using thin layer chromatography (TLC) Silicagel 60 F254 from MERCK. A UV lamp (λ = 254 nm) was used for detection.

NMR spectra were recorded at 300 K on a Bruker AvanceNeo 500 (Bruker, Rheinstetten, Germany) (500 MHz (^{1}H), 125 MHz (^{13}C{^{1}H}), 187 MHz (^{119}Sn{^{1}H}), 100 MHz (^{29}Si {^{1}H})). Where possible, NMR signals were assigned using ^{1}H COSY, ^{1}H/^{13}C HSQC and ^{1}H/^{13}C HMBC experiments. ^{1}H and ^{13}C {^{1}H} NMR spectra (125 MHz) were referenced against the residual solvent signal, $CDCl_3$ (^{1}H: δ = 7.26 ppm, ^{13}C: δ = 77.16 ppm). ^{119}Sn{^{1}H} and ^{29}Si{^{1}H} NMR spectra (187 and 100 MHz) were measured based on the external reference of the ^{1}H-NMR signal of tetramethylsilane.

Reaction controls by ^{1}H-NMR and some ^{13}C{^{1}H} spectra were performed on a Bruker Avance WB 360 instrument (Bruker, Rheinstetten, Germany) (^{1}H: 360 MHz, ^{13}C{^{1}H}: 91 MHz). The switching experiments were performed on a Bruker ARX300 (Bruker, Rheinstetten, Germany) (300 MHz (^{1}H)) or Bruker AvanceNeo 500 (Burker, Rheinstetten, Germany) (500 MHz (^{1}H)).

Thermal analyses were performed on a standalone Mettler Toledo DSC 3+ STAR (Mettler-Toledo, Columbus, OH, USA) or a Mettler Toledo TGA/DSC 3+ System (Mettler-Toledo, Columbus, OH, USA), where 40 µL and 100 µL aluminum crucibles were used. For TGA experiments, no lids were used,

whereas in DSC experiments pierced lids were used. Thermo analytical data was analyzed with the STARe software (Version 14.01, Mettler-Toledo, Columbus, OH, USA) by Mettler Toledo.

Infrared spectra were recorded on a NICOLET i510 FT-IR spectrometer from Thermo Fisher SCIENTIFIC (Thermo Fisher SCIENTIFIC, Waltham, MA, USA) with a diamond window in an area ranging from 500–4000 cm^{-1} with a resolution of 4 cm^{-1}. All samples were measured 16 times against a background scan. Melting points were measured by DSC or using a BÜCHI Melting Point M-560 instrument (BÜCHI, Essen, Germany).

Electron impact (EI) mass experiments were measured using the direct inlet or indirect inlet methods, with a source temperature of 200 °C on a MAT95 XL double-focusing mass spectrometer from Finnigan MAT (Thermo Fisher SCIENTIFIC, Waltham, MA, USA). The ionization energy of the electron impact ionization was 70 eV. Atmospheric pressure chemical ionization (APCI) experiments were performed on a Bruker Impact II from Bruker Daltonics (Bruker Daltonics, Bremen, Germany).

For the UV switching experiments, a 365 nm (Ocean Optics USB 4000, Sahlmann Photochemical Solutions, Bad Segeberg, Germany, full width at half maximum (FWHM) 10 nm, 1.0 W) and a 443 nm LED lamp (Ocean Optics USB 4000, Sahlmann Photochemical Solutions, Bad Segeberg, Germany, FWHM 19 nm, 0.9 W) were used, while ensuring a constant distance towards the cuvettes of 1 cm. The NMR switching experiments were performed with a circular aligned lamp consisting of four high power UV-LEDs (365 nm) 300 mW in power each, produced by "Sahlmann Photochemichal Solutions". For switching experiments, quartz cuvettes from Hellma Analytics (Hellma Analytics, Muehlheim an der Ruhr, Germany) (10 mm) or Quartz NMR tubes from Deutero (Deutero GmbH, Kastellaun, Germany) were used.

UV-VIS spectra were recorded at a resolution of 0.1 nm on a UV-2700 spectrometer from Shimadzu (Shimadzu, Kyoto, Japan) with a double monochromator. In all cases, cyclohexane was used as a solvent.

X-ray measurements were carried out at 100 K on a Bruker Venture D8 diffractometer (Bruker, Karlsruhe, Germany) with Mo-Kα (0.7107 Å) radiation. All structures were solved by intrinsic phasing and refined based on F2 by use of the SHELX program package, as implemented in OLex 1.2 [51]. All non-hydrogen atoms were refined using anisotropic displacement parameters. Hydrogen atoms attached to carbon atoms were included in geometrically calculated positions using a riding model. All crystals were obtained by slow evaporation of an acetonitrile/dichloromethane mixture at 25 °C.

4.2. Syntheses

4.2.1. 2,2′-Diiodoazobenzene (**2**)

Adapted with changes from Takahashi et al. [26]. A solution of 2-iodoaniline (**1**) (2.00 g, 9.13 mmol) and MnO_2 (20.0 g, 230 mmol) in toluene (200 mL) was stirred for 3 h at 120 °C. After the reaction, the mixture was cooled to 25 °C, filtered through Celite®, washed with toluene (200 mL) and the solvent was removed under reduced pressure. The red solid that was obtained was dissolved in DCM (5 mL) and purified by filtration through a short plug of silica (eluent: *n*-pentane). After evaporation of the solvent, the dark orange solid was dried (4.6×10^{-2} mbar, 25 °C, 4 h) to give a red compound (1.63 g, 3.76 mmol, 82%).

^{1}H NMR (500 MHz, $CDCl_3$) δ = 8.04 (dd, ^3J = 7.9 Hz, ^4J = 1.3 Hz, 2H, H-3), 7.77 (dd, ^3J = 7.9 Hz, ^4J = 1.6 Hz, 2H, H-6), 7.46 (ddd, ^3J = 7.9, 7.3 Hz, ^4J = 1.3 Hz, 2H, H-5), 7.20 (ddd, ^3J = 7.9, 7.3 Hz, ^4J = 1.6 Hz, 2H, H-4) ppm. ^{13}C{^{1}H} NMR (126 MHz, $CDCl_3$) δ = 150.87 (C-1), 139.94 (C-3), 132.80 (C-4), 129.06 (C-5), 118.26 (C-6), 103.22 (C-2) ppm. IR (ATR): ν = 3055 (w), 2921 (w), 2851 (w), 1924 (w), 1838 (w), 1806 (w), 1699 (w), 1561 (m), 1455 (m), 1013 (s), 953 (m), 760 (s), 714 (s) cm^{-1}. HRMS (EI, MAT 95 XL): *m/z* calcd. $C_{12}H_8N_2I_2^+$ 433.87715 found 433.87701. R$_f$ (*n*-pentane): 0.51. Mp (Büchi): 146 °C

4.2.2. 2,2′-Bis(trimethylstannyl)azobenzene (**8**)

Adapted with changes from Strüben et al. [25] In a glovebox, a microwave vial was charged with 2,2′-diiodoazobenzene (**2**) (200 mg, 0.46 mmol), hexamethylditin (**5**) (422 mg, 1.03 mmol),

tetrakis(triphenyl)phosphinopalladium(0) (15.7 mg, 13.0 µmol), THF (0.5 mL) and toluene (4.0 mL). The reaction mixture was heated for 1 h at 170 °C using microwave irradiation. The solution was cooled to 25 °C, filtered, rinsed with toluene (10.0 mL) and all volatiles were removed under reduced pressure. Then, the compound was dissolved in DCM (2 mL) and filtered through a short plug of silica (eluent: *n*-pentane). After the solvent was removed, an orange solid (142 mg, 0.28 mmol, 61%) was received. ^{1}H NMR (500 MHz, CDCl$_3$) δ = 7.78 (dd, ^3J = 7.8 Hz, ^4J = 1.4 Hz, 2H, H-6), 7.74 (dd, ^3J = 7.1 Hz, ^4J = 1.4 Hz, 2H, H-3), 7.47 (td, ^3J = 7.1 Hz, ^4J = 1.4 Hz, 2H, H-5), 7.43 (td, ^3J = 7.1 Hz, ^4J = 1.4 Hz, 2H, H-4), 0.32 (s, 18H, CH$_3$) ppm. ^{13}C{^{1}H} NMR (126 MHz, CDCl$_3$) δ = 157.12 (C-1), 146.53 (C-2), 136.65 (C-3), 130.33 (C-4), 129.52 (C-2), 117.73 (C-6), −7.33 (C-7) ppm. ^{119}Sn{^{1}H} NMR (187 MHz, CDCl$_3$) −34.36 ppm. IR (ATR): ν = 3050 (w), 2974 (w), 2909 (w), 2609 (w), 2354 (w), 1965 (w), 1932 (w), 1902 (w), 1853 (w), 1820 (w), 1432 (w), 1294 (w), 1188 (m), 1110 (m), 754 (s), 706 (s) cm^{-1}. HRMS (APCI): *m/z* calcd. [C$_{18}$H$_{26}$N$_2$Sn$_2$ + H]$^+$ 509.02140 found 509.02126. R$_f$: (*n*-pentane): 0.84. Mp (DSC; Onset): 102.37 °C

4.2.3. 2,2′-Bis(trimethylsilyl)azobenzene (6)

In an inert tube 2,2′-bis(trimethylstannyl)azobenzene (**4**) (80.0 mg, 0.16 mmol) was dissolved under Schlenk conditions in THF (5.00 mL) and cooled to −78 °C. MeLi (1.88 M in THF, 0.25 mL, 0.47 mmol) was added within 5 min and after 1 h at this temperature, trimethylsilyl chloride (**9**) (200 µL, 171 mg, 1.57 mmol) was added to the black reaction mixture in one portion. The reaction mixture was warmed to 25 °C over 14 h and the solvent was removed under reduced pressure. The brown solid, dissolved in DCM (3.00 mL), was purified by a short plug of silica (eluent: *n*-pentane). The first orange fraction was filtered through a PTFE filter (0.45 µm). From the filtrate, the solvent was removed to obtain an orange solid (43 mg, 0.132 mmol, 82%). ^{1}H NMR (500 MHz, CDCl$_3$): δ = 7.72 (dd, ^3J = 7.7 Hz, ^4J = 1.3 Hz, 4H, H-3 and H-6), 7.48 (ddd, ^3J = 7.7, 7.2 Hz, ^4J = 1.3 Hz, 2H, H-5), 7.44 (ddd, ^3J = 7.7, 7.2 Hz, ^4J = 1.3 Hz, 2H, H-4), 0.40 (s, 18H, CH$_3$) ppm. ^{13}C{^{1}H} NMR (125 MHz, CDCl$_3$): δ = 157.27 (C-1), 142.95 (C-2), 134.97 (C-3), 130.14/130.11 (C-4 and C-5), 114.68 (C-6), 0.70 (C-7) ppm. ^{29}Si{^{1}H} NMR (100 MHz, CDCl$_3$): δ = 4.04 ppm. IR (ATR): ν = 3059 (w), 2946 (w), 2987 (w), 2853 (w), 1968 (w), 1937 (w), 1859 (w), 1737 (w), 1581 (w), 1561 (w), 1465 (w), 1424 (w); 1296 (w), 1241 (m), 1119 (m), 1075 (w), 831 (s), 778 (s), 747 (m), 720 (s), 676 (m) cm^{-1}. HRMS(EI): *m/z* calcd. C$_{18}$H$_{26}$N$_2$Si$_2$$^+$ 326.16290 found 326.16245. R$_f$ (*n*-pentane): 0.63. Mp (DSC; Onset): 68.59 °C

4.2.4. 2,2′-Bis(trimethylgermanyl)azobenzene (7)

A schlenk tube was filled with 2,2′-bis(trimethylstannyl)azobenzene (**4**) (80.0 mg, 0.16 mmol) in THF (5.00 mL) and cooled to −78 °C. Then, MeLi (1.88 M in THF, 0.25 mL, 0.47 mmol) was added within 5 min and after 1 h at this temperature, trimethylgermanium chloride (**14**) (200 µL, 171 mg, 1.57 mmol) was added to the dark reaction mixture in one portion. The reaction mixture was warmed to 25 °C over 14 h and the solvent was removed under reduced pressure. The brown solid, dissolved in DCM (3.00 mL), was purified by column chromatography (silica, *n*-pentane). From the filtrate, the solvent was removed to obtain an orange solid (31 mg, 0.09 mmol, 60%). ^{1}H NMR (500 MHz, CDCl$_3$): δ = 7.78–7.64 (m, 4H, H-3 and H-6), 7.49–7.39 (m, 4H, H4 and H5), 0.49 (s, 18H, CH$_3$) ppm. ^{13}C{^{1}H} NMR (125 MHz, CDCl$_3$): δ = 156.59 (C-1), 146.12 (C-2), 134.21 (C-3), 130.11 (C-4), 129.52 (C-2), 114.98 (C-6), 0.32 (C-7) ppm. IR (ATR): ν = 3057 (w), 2962 (w), 2905 (w), 1563 (w), 1463 (w), 1432 (w), 1407 (w), 1295 (w), 1234 (m), 1114 (m), 1064 (w), 953 (w), 818 (m), 777 (s), 751 (m), 719 (m), 658 (m) cm^{-1}. HRMS (APCI): *m/z* calcd. [C$_{18}$H$_{26}$N$_2$Ge$_2$ + H]$^+$ 417.06085 found 417.06072. R$_f$ (*n*-pentane): 0.78. Mp (DSC; Onset): 82.85 °C

4.2.5. 2,2′-Di(*tert*-butyl)azobenzene (10)

Adapted with changes from Takahashi et al. [26] 2-*tert*-butylaniline (**15**) (5.00 g, 33.5 mmol) was dissolved in toluene (800 mL) and MnO$_2$ (50.0 g, 575 mmol) was added portionwise. The reaction mixture was heated to 120 °C. After 3 h at 120 °C, the orange reaction mixture was filtered with the help

of Celite$^®$. The solvent was evaporated, the organic phase was washed with aq. HCl (2 M, 300 mL), and then the organic phase was dried over MgSO$_4$. After removal of the solvent, the product was dried in a vacuum (4 mbar, 110 °C, 5h) and could be isolated without further purification (2.26 g, 7.68 mmol, 46%, purity > 95%). For even higher purity, the compound was subjected to column chromatography (silica, *n*-pentane). The first isolated band was the mentioned yellow byproduct (62 mg, 0.22 mmol, 1.31%). The second band was the orange product (620 mg, 2.11 mmol, 13%). ^{1}H NMR (500 MHz, CDCl$_3$) δ = 7.54–7.50 (m, 4H, H-3 and H-6), 7.40 (td, ^3J = 7.6 Hz, ^4J = 1.4 Hz 2H, H-5), 7.32 (mc, 2H, H-4), 1.56 (s, 18 H, CH$_3$).^{13}C{^{1}H} NMR (126 MHz, CDCl$_3$): δ = 151.93 (*C*-1), 148.60 (*C*-2), 130.37 (*C*-5), 126.80 (*C*-4), 126.76 (*C*-3), 117.05 (*C*-6), 36.33 (*C*(CH$_3$)$_3$), 32.16 (CH$_3$) ppm. IR (ATR): ν = 2948 (w), 2918 (w), 2904 (w), 2859 (w), 1478 (m), 1465 (w), 1435 (w), 1388 (w), 1354 (w), 1289 (w), 1277 (w), 1250 (w), 1196 (w), 1160 (w), 1086 (w), 1050 (w), 947 (w), 926 (w), 769 (s), 750 (s) cm^{-1}. HRMS (EI): *m/z* calcd. C$_{20}$H$_{26}$N$_2{}^+$ 294.20905 found 294.20851. R$_f$ (*n*-pentane): 0.76. Mp (DSC; Onset): 86.76 °C

4.2.6. Isolated By-Product: 1,6-Di-(*tert*-butyl)phenanzine (**16**)

^{1}H NMR (500 MHz, CDCl$_3$) δ = 8.11 (m$_c$, 2H, H-4,9), 7.70 (m$_c$, 4H, H-3,8 and H-2,7), 1.76 (s, 18H, CH$_3$) ppm. ^{13}C{^{1}H} NMR (126 MHz, CDCl$_3$) δ = 148.46 (*C*-1,6), 142.19 (*C*-4a,10a or *C*-5a,10), 141.89 (*C*-4a, 10a or *C*-5a,10a), 129.48 (*C*-3,8), 129.01 (*C*-4,9), 126.05 (*C*-2,7), 36.97 (*C*(CH$_3$)$_3$), 31.22 (CH$_3$) ppm. IR (ATR): ν = 2997 (w), 2949 (w), 2902 (w), 2864 (w), 1616 (w), 1532 (w), 1481 (w), 1471 (w), 1383 (w), 1353 (w), 1343 (w), 1271 (w), 1126 (w), 997 (m), 932 (w), 857 (w), 813 (m), 748 (s) cm^{-1}. HRMS (EI): *m/z* calcd. C$_{20}$H$_{24}$N$_2{}^+$ 292.19340 found 292.19284, calcd. [M-CH$_3$]$^+$ 277.16993 found 277.16993, calcd. [M-C$_3$H$_6$]$^+$ 250.14645 found 250.14621, calcd. [M-C$_4$H$_9$]$^+$ 235.12297 found 235.12263. R$_f$ (*n*-pentane): 0.81. Mp (DSC; Onset): 193.89 °C

5. Conclusions

Four 2,2'-bis(trimethylelement)azobenzenes have been synthesized with E = C, Si, Ge and Sn. The synthetic route that has to be selected is highly dependent on the element: With carbon, substitution reactions with a nucleophilic azobenzene and a carbon electrophile were unsuccessful because of the small size of the carbon atom and its low reactivity. With Si and Ge however, a dilithiated azobenzene or the corresponding cuprate could be used as a precursor, illustrating the higher electrophilic character. However, this species can only easily be produced from a stannylated precursor, which can be prepared through a Stille-Kelly cross-coupling reaction. While the latter procedure proceeds very well for tin, a similar reaction was not possible for the corresponding hexamethyldigermanium and hexamethyldisilane. The lead azobenzene could not be isolated at all, which we ascribe to the instability of Pb(IV) compared to Pb(II).

Appendix A

X-Ray Crystallography

There are only a few crystal structures reported for di-*ortho*-substituted azobenzenes: A structure with methyl groups in *ortho*-position [52], with fluorodimethylsilyl groups [43] and boron derivatives [42] have been reported. Compared with the N=N bond in pure *trans*-azobenzene (1.249(4) Å) [52], the azo groups in our compounds have very similar N=N bond lengths (**10**: 1.251(2), **6**: 1.257(3), **7**: 1.256(3), **8**: 1.251(2) Å. The Crystal data and structure refinement for azobenzenes **10**, **6**–**8** are given (Table A1); therefore, these substituents have hardly any influence on the character of the azo group.

Table A1. Crystal data and structure refinement for azobenzenes **10**, **6**–**8**.

	10	6	7	8
Chemical formula	$C_{20}H_{26}N_2$	$C_{18}H_{26}N_2Si_2$	$C_{18}H_{26}N_2Ge_2$	$C_{18}H_{26}N_2Sn_2$
Formula weight (g mol^{-1})	294.43	326.59	415.59	507.79
Crystal system	Triclinic	Monoclinic	Monoclinic	Monoclinic
Space group	P-1	P2$_1$/c	P2$_1$/c	P2$_1$/c
a (Å)	8.6142(2)	10.8005(3)	10.8027(5)	10.7087(3)
b (Å)	9.7497(2)	6.9267(2)	7.0849(3)	7.1755(2)
c (Å)	11.5720(3)	13.1555(3)	13.0359(6)	13.1481(4)
α (°)	70.3510(10)	90	90	90
β (°)	71.0950(10)	91.0610(10)	91.1550(10)	91.1950(10)
γ (°)	77.6290(10)	90	90	90
V (Å^3)	859.85(4)	984.02(5)	997.51(8)	1010.08(5)
Z	2	2	2	2
Dcalc (g cm^{-3})	1.137	1.102	1.384	1.670
μ (mm^{-1})	0.066	0.179	3.012	2.472
F (000)	320.0	352.0	424.0	496.0
Crystal size (mm^3)	$0.27 \times 0.24 \times 0.14$	$0.25 \times 0.10 \times 0.10$	$0.32 \times 0.25 \times 0.19$	$0.20 \times 0.10 \times 0.10$
2Theta range for data collection (°)	4.468 to 62.148	6.194 to 56.992	7.524 to 61.08	6.198 to 59.982
Reflections. collected	51512	32222	9934	64977
Independent Reflections	5512	2500	3018	2937
Final R indexes [I >= 2simga(I)]	$R_1 = 0.0471$, $wR_2 = 0.1086$	$R_1 = 0.0356$, $wR_2 = 0.0785$	$R_1 = 0.0247$, $wR_2 = 0.0675$	$R_1 = 0.0127$, $wR_2 = 0.0287$
Final R indexes [all data]	$R_1 = 0.0755$, $wR_2 = 0.1240$	$R_1 = 0.0560$, $wR_2 = 0.0889$	$R_1 = 0.0278$, $wR_2 = 0.0699$	$R_1 = 0.0156$, $wR_2 = 0.0299$
GooF (F^2)	1.015	1.045	1.065	1.081
Largest diff. peak/hole (e Å^{-3})	0.39/−0.23	0.29/−0.28	0.76/−0.42	0.48/−0.50
CCSD No.	1880127	1880130	1880129	1880128

So far, only one of the crystal structures of 2,6-dimethoxy substituted phenazines was reported [53]. In the following, the structural parameters for our obtained phenazine are given (Figure A1, Table A2).
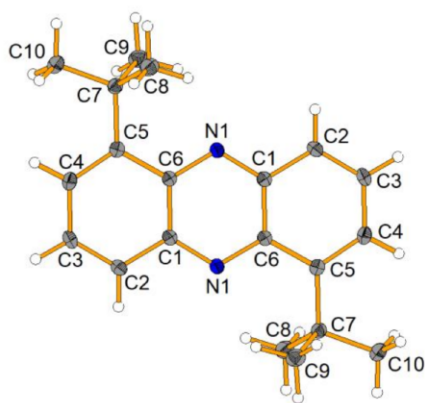
Figure A1. Molecular structure of phenazine **16**, showing a 50% probability of ellipsoids.

Table A2. Crystal data and structure refinement for phenazine **16**.

	16
Chemical formula	$C_{20}H_{24}N_2$
Formula weight (g mol^{-1})	292.41
Temperature (K)	100
Crystal system	Monoclinic
Space group	P2$_1$/c
a (Å)	12.4209(4)
b (Å)	6.2653(2)
c (Å)	12.3389(4)
α (°)	90
β (°)	119.2690(10)
γ (°)	90
V (Å^3)	837.63(5)
Z	2
D$_{calc}$ (g cm^{-3})	1.159
μ (mm^{-1})	0.068
F (000)	316.0
Crystal size (mm^3)	$0.25 \times 0.17 \times 0.15$
2Theta range for data collection (°)	6.604 to 56.996
Reflections. collected	20978
Independent Reflections	2132
Final R indexes [I >= 2simga(I)]	$R_1 = 0.0417$, $wR_2 = 0.0948$
Final R indexes [all data]	$R1 = 0.0632$, $wR_2 = 0.1082$
GooF (F^2)	1.024
Largest diff. peak/hole (e Å^{-3})	0.33/−0.19
CCSD No.	1880126

CCDC 1880126-1880130 (**16**, **10**, **8**, **7**, **6**) contain the supplementary crystallographic data for this paper. The data can be obtained free of charge from The Cambridge Crystallographic Data Centre via www.ccdc.cam.ac.uk/structures.

References

1. Rivard, E. Group 14 inorganic hydrocarbon analogues. *Chem. Soc. Rev.* **2016**, *45*, 989–1003. [CrossRef] [PubMed]

2. Yamaguchi, S.; Tamao, K. Theoretical Study of the Electronic Structure of 2,2′-Bisilole in Comparison with 1,1′-Bi-1,3-cyclopentadiene: σ*-π* Conjugation and a Low-Lying LUMO as the Origin of the Unusual Optical Properties of 3,3′,4,4′-Tetraphenyl-2,2′-bisilole. *Bull. Chem. Soc. Jpn.* **1996**, *69*, 2327–2334. [CrossRef]

3. Yamaguchi, S.; Itami, Y.; Tamao, K. Group 14 metalloles with thienyl groups on 2,5-positions: Effects of group 14 elements on their π-electronic structures. *Organometallics* **1998**, *17*, 4910–4916. [CrossRef]

4. Linshoeft, J.; Baum, E.J.; Hussain, A.; Gates, P.J.; Näther, C.; Staubitz, A. Highly tin-selective stille coupling: synthesis of a polymer containing a stannole in the main chain. *Angew. Chem. Int. Ed.* **2014**, *53*, 12916–12920. [CrossRef] [PubMed]

5. Urrego-Riveros, S.; Ramirez y Medina, I.-M.; Hoffmann, J.; Heitmann, A.; Staubitz, A. Syntheses and properties of tin-containing conjugated heterocycles. *Chem. Eur. J.* **2017**, *24*, 5680–5696. [CrossRef]

6. Ramirez y Medina, I.-M.; Rohdenburg, M.; Mostaghimi, F.; Grabowsky, S.; Swiderek, P.; Beckmann, J.; Hoffmann, J.; Dorcet, V.; Hissler, M.; Staubitz, A. Tuning the optoelectronic properties of stannoles by the judicious choice of the organic substituents. *Inorg. Chem.* **2018**, *57*, 12562–12575. [CrossRef] [PubMed]

7. Bandara, H.M.D.; Burdette, S.C. Photoisomerization in different classes of azobenzene. *Chem. Soc. Rev.* **2012**, *41*, 1809–1825. [CrossRef]

8. Beharry, A.A.; Woolley, G.A. Azobenzene photoswitches for biomolecules. *Chem. Soc. Rev.* **2011**, *40*, 4422–4437. [CrossRef]

9. Dong, M.; Babalhavaeji, A.; Samanta, S.; Beharry, A.A.; Woolley, G.A. Red-shifting azobenzene photoswitches for in vivo use. *Acc. Chem. Res.* **2015**, *48*, 2662–2670. [CrossRef] [PubMed]

10. Mahimwalla, Z.; Yager, K.G.; Mamiya, J.-I.; Shishido, A.; Priimagi, A.; Barrett, C.J. Azobenzene photomechanics: Prospects and potential applications. *Polym. Bull.* **2012**, *69*, 967–1006. [CrossRef]

11. Merino, E.; Ribagorda, M. Control over molecular motion using the cis-trans photoisomerization of the azo group. *Beilstein J. Org. Chem.* **2012**, *8*, 1071–1090. [CrossRef]

12. Ahmed, Z.; Siiskonen, A.; Virkki, M.; Priimagi, A. Controlling azobenzene photoswitching through combined ortho-fluorination and -amination. *Chem. Commun.* **2017**, *53*, 12520–12523. [CrossRef]

13. Bléger, D.; Schwarz, J.; Brouwer, A.M.; Hecht, S. o-Fluoroazobenzenes as readily synthesized photoswitches offering nearly quantitative two-way isomerization with visible light. *J. Am. Chem. Soc.* **2012**, *134*, 20597–20600. [CrossRef]

14. Yu, Y.; Nakano, M.; Ikeda, T. Directed bending of a polymer film by light. *Nature* **2003**, *425*, 145. [CrossRef]

15. Kizilkan, E.; Strueben, J.; Jin, X.; Schaber, C.F.; Adelung, R.; Staubitz, A.; Gorb, S.N. Influence of the porosity on the photoresponse of a liquid crystal elastomer. *Roy. Soc. Open Sci.* **2016**, 3. [CrossRef]

16. Nguyen, T.H.L.; Gigant, N.; Joseph, D. Advances in direct metal-catalyzed functionalization of azobenzenes. *ACS Catal.* **2018**, *8*, 1546–1579. [CrossRef]

17. Kakiuchi, F.; Matsumoto, M.; Tsuchiya, K.; Igi, K.; Hayamizu, T.; Chatani, N.; Murai, S. The ruthenium-catalyzed silylation of aromatic C–H bonds with triethylsilane. *J. Organomet. Chem.* **2003**, *686*, 134–144. [CrossRef]

18. Nguyen, T.T.T.; Boussonnière, A.; Banaszak, E.; Castanet, A.-S.; Nguyen, K.P.P.; Mortier, J. Chemoselective deprotonative lithiation of azobenzenes: Reactions and mechanisms. *J. Org. Chem.* **2014**, *79*, 2775–2780. [CrossRef]

19. Li, J.; Cong, W.; Gao, Z.; Zhang, J.; Yang, H.; Jiang, G. Rh(III)-catalyzed regioselective mono- and di-iodination of azobenzenes using alkyl iodide. *Org. Biomol. Chem.* **2018**, *16*, 3479–3486. [CrossRef]

20. Yamamura, M.; Kano, N.; Kawashima, T.; Matsumoto, T.; Harada, J.; Ogawa, K. Crucial role of N···Si interactions in the solid-state coloration of disilylazobenzenes. *J. Org. Chem.* **2008**, *73*, 8244–8249. [CrossRef]

21. Kano, N.; Komatsu, F.; Kawashima, T. Synthesis and structure of azobenzenes bearing silyl, germyl, and stannyl groups at 2-position. *Chem. Lett.* **2001**, *30*, 338–339. [CrossRef]

22. Kano, N.; Komatsu, F.; Yamamura, M.; Kawashima, T. Reversible photoswitching of the coordination numbers of silicon in organosilicon compounds bearing a 2-(phenylazo)phenyl group. *J. Am. Chem. Soc.* **2006**, *128*, 7097–7109. [CrossRef]

23. Strueben, J.; Hoffmann, J.; Naether, C.; Staubitz, A. Crystal structures of 3,3'-bis(hydroxydimethylsilanyl) azobenzene and 4,4'-bis(hydroxydimethylsilane)azobenzene. *Acta Cryst. E* **2016**, *72*, 1590–1594. [CrossRef]

24. Strueben, J.; Lipfert, M.; Springer, J.-O.; Gould, C.A.; Gates, P.J.; Sönnichsen, F.D.; Staubitz, A. High-yield lithiation of azobenzenes by tin-lithium exchange. *Chem. Eur. J.* **2015**, *21*, 11165–11173. [CrossRef]

25. Strueben, J.; Gates, P.J.; Staubitz, A. Tin-functionalized azobenzenes as nucleophiles in stille cross-coupling reactions. *J. Org. Chem.* **2014**, *79*, 1719–1728. [CrossRef]

26. Takahashi, H.; Ishioka, T.; Koiso, Y.; Sodeoka, M.; Hashimoto, Y. Anti-androgenic activity of substituted azo- and azoxy-benzene derivatives. *Bio. Pharm. Bull.* **2000**, *23*, 1387–1390. [CrossRef]

27. Seth, K.; Roy, S.R.; Kumar, A.; Chakraborti, A.K. The palladium and copper contrast: A twist to products of different chemotypes and altered mechanistic pathways. *Catal. Sci. Tech.* **2016**, *6*, 2892–2896. [CrossRef]

28. Monir, K.; Ghosh, M.; Mishra, S.; Majee, A.; Hajra, A. Phenyliodine(III) diacetate (PIDA) mediated synthesis of aromatic azo compounds through oxidative dehydrogenative coupling of anilines: Scope and mechanism. *Eur. J. Org. Chem.* **2013**, *2014*, 1096–1102. [CrossRef]

29. Gooßen, L.J.; Ferwanah, A.-R.S. A mild and efficient protocol for the catalytic silylation of aryl bromides. *Synlett* **2000**, *2000*, 1801–1803. [CrossRef]

30. McNeill, E.; Barder, T.E.; Buchwald, S.L. Palladium-catalyzed silylation of aryl chlorides with hexamethyldisilane. *Org. Lett.* **2007**, *9*, 3785–3788. [CrossRef]

31. Komami, N.; Matsuoka, K.; Yoshino, T.; Matsunaga, S. Palladium-catalyzed germylation of aryl bromides and aryl triflates using hexamethyldigermane. *Synthesis* **2018**, *50*, 2067–2075. [CrossRef]

32. Arnold, D.P.; Wells, P.R. Hexamethyldilead: I. Preparation, thermal decomposition and methanolysis. *J. Organomet. Chem.* **1976**, *111*, 269–283. [CrossRef]

33. Zavitsas, A.A. The relation between bond lengths and dissociation energies of carbon–carbon bonds. *J. Phys. Chem.* **2003**, *107*, 897–989. [CrossRef]

34. Lappert, M.F.; Pedley, J.B.; Simpson, J.; Spalding, T.R. Bonding studies of compounds of boron and the group IV element: VI. Mas spectrometric studies on compounds Me_4M and $Me_3M–M'Me_3$ (M and M' = C, Si, Ge, Sn, and Pb): Thermochemical data. *J. Organomet. Chem.* **1971**, *29*, 195–208. [CrossRef]

35. Dávalos, J.Z.; Baer, T. Thermochemistry and dissociative photoionization of $Si(CH_3)_4$, $BrSi(CH_3)_3$, $ISi(CH_3)_3$, and $Si_2(CH_3)_6$ studied by threshold photoelectron–photoion coincidence spectroscopy. *J. Phys. Chem. A* **2006**, *110*, 8572–8579. [CrossRef]

36. Farina, V.; Kapadia, S.; Krishnan, B.; Wang, C.; Liebeskind, L.S. On the nature of the "copper effect" in the stille cross-coupling. *J. Org. Chem.* **1994**, *59*, 5905–5911. [CrossRef]

37. Casado, A.L.; Espinet, P.; Gallego, A.M. Mechanism of the stille reaction. 2. Couplings of aryl triflates with vinyltributyltin. Observation of intermediates. A more comprehensive scheme. *J. Am. Chem. Soc.* **2000**, *122*, 11771–11782. [CrossRef]

38. Aggarwal, V.K.; Staubitz, A.C.; Owen, M. Optimization of the mizoroki−heck reaction using design of experiment (DoE). *Org. Process. Res. Dev.* **2006**, *10*, 64–69. [CrossRef]

39. Knochel, P.; Yeh, M.C.P.; Berk, S.C.; Talbert, J. Synthesis and reactivity toward acyl chlorides and enones of the new highly functionalized copper reagents RCu(CN)ZnI. *J. Org. Chem.* **1988**, *53*, 2390–2392. [CrossRef]

40. Krueerke, U. Halogen-austausch an chlorsilanen und die tetrahydrofuran-spaltung durch brom- und jodsilane. *Chem. Ber.* **1962**, *95*, 174–182. [CrossRef]

41. Olaru, M.; Kather, R.; Hupf, E.; Lork, E.; Mebs, S.; Beckmann, J. A monoaryllead trichloride that resists reductive elimination. *Angew. Chem. Int. Ed.* **2018**, *57*, 5917–5920. [CrossRef]

42. Yoshino, J.; Kano, N.; Kawashima, T. Fluorescent azobenzenes and aromatic aldimines featuring an N–B interaction. *Dalton Trans.* **2013**, *42*, 15826–15834. [CrossRef]

43. Kano, N.; Yamamura, M.; Kawashima, T. 2,2'-Disilylazobenzenes featuring double intramolecular nitrogen⋯silicon coordination: A photoisomerizable fluorophore. *Dalton Trans.* **2015**, *44*, 16256–16265. [CrossRef]

44. Denmark, S.E.; Regens, C.S. Palladium-catalyzed cross-coupling reactions of organosilanols and their salts: practical alternatives to boron- and tin-based methods. *Acc. Chem. Res.* **2008**, *41*, 1486–1499. [CrossRef]

45. Hatanaka, Y.; Hiyama, T. Cross-coupling of organosilanes with organic halides mediated by a palladium catalyst and tris(diethylamino)sulfonium difluorotrimethylsilicate. *J. Org. Chem.* **1988**, *53*, 918–920. [CrossRef]

46. Kosugi, M.; Tanji, T.; Tanaka, Y.; Yoshida, A.; Fugami, K.; Kameyama, M.; Migita, T. Palladium-catalyzed reaction of 1-aza-5-germa-5-organobicyclo[3.3.3]undecane with aryl bromide. *J. Organomet. Chem.* **1996**, *508*, 255–257. [CrossRef]

47. Faller, J.W.; Kultyshev, R.G. Palladium-catalyzed cross-coupling reactions of allyl, phenyl, alkenyl, and alkynyl germatranes with aryl iodides. *Organometallics* **2002**, *21*, 5911–5918. [CrossRef]

48. Nakamura, T.; Kinoshita, H.; Shinokubo, H.; Oshima, K. Biaryl synthesis from two different aryl halides with tri(2-furyl)germane. *Org. Lett.* **2002**, *4*, 3165–3167. [CrossRef]

49. Cordovilla, C.; Bartolomé, C.; Martínez-Ilarduya, J.M.; Espinet, P. The stille reaction, 38 years later. *ACS Catal.* **2015**, *5*, 3040–3053. [CrossRef]

50. Tanaka, R.; Kawahara, T.; Shinto, Y.; Nakayama, Y.; Shiono, T. An alternative method for the preparation of trialkylaluminum-depleted modified methylaluminoxane (dMMAO). *Macromolecules* **2017**, *50*, 5989–5993. [CrossRef]

51. Dolomanov, O.V.; Bourhis, L.J.; Gildea, R.J.; Howard, J.A.K.; Puschmann, H. OLEX2: A complete structure solution, refinement and analysis program. *J. Appl. Crystallogr.* **2009**, *42*, 339–341. [CrossRef]

52. Harada, J.; Ogawa, K.; Tomoda, S. Molecular Motion and Conformational Interconversion of Azobenzenes in Crystals as Studied by X-ray Diffraction. *Acta Cryst. Sec. B* **1997**, *53*, 662–672. [CrossRef]

53. Nawata, Y.; Iwasaki, H.; Saito, Y. The Crystal Structure of Bis(pyridine-2-carboxamido)nickel(II) Dihydrate. *Bull. Chem. Soc. Jpn.* **1967**, *40*, 515–521. [CrossRef]

Sample Availability: Samples of the compounds **6**, **7**, **8** and **10** are available from the authors.

2.4.1.2 Publication: Synthesis and crystal structure of (*E*)-1,2-*bis*[2-(methylsulfanyl)-phenyl]diazene

Research communication

Abstract

The title compound, $C_{14}H_{14}N_2S_2$, was obtained by transmetallation of 2,2'-*bis*-(trimethylstannyl)azo-benzene with methyl lithium, and subsequent quenching with dimethyl disulfide. The asymmetric unit comprises two half-molecules, the other halves being completed by inversion symmetry at the midpoint of the azo group. The two molecules showed only slight differences with respect to N=N, S—N and aromatic C=C bonds or angles. Hirshfeld surface analysis revealed that except for one weak H···S interaction, intermolecular interactions were dominated by van der Waals forces only.
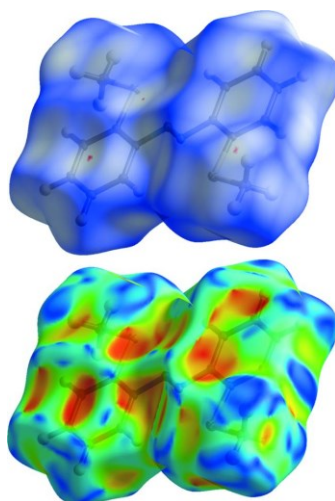
Fig. 35: Hirshfeld surface plot of one structure of the 2,2'-di(methylsulfanyl)azobenzene (**70**).

Scientific Contribution

The synthesis of the compound was done by Thomas J. Kuczmera, who did his fully supervised Bachelor thesis with me.[30] The characterization and analysis were performed by me. The X-ray analysis and refinement was conducted by Enno Lork. The manuscript was written by me and Anne Staubitz.

Supporting Information

Further details on the refinement, data collection and atomic coordinates are available free of charge online.

Reproduction note

The journal is an open source journal. Therefore, no special permission is required to reuse all or part of article published by the publisher, including figures and tables.

research communications

Synthesis and crystal structure of (*E*)-1,2-bis[2-(methylsulfanyl)phenyl]diazene

Jonas Hoffmann,[a,b] Thomas J. Kuczmera,[a,b] Enno Lork[c] and Anne Staubitz[a,b]*

[a]Institute for Organic and Analytic Chemistry, University Bremen, Leobener Strasse 7, 28359 Bremen, Germany, [b]MAPEX, Center for Materials and Processes, University of Bremen, Bibliothekstr. 1, 28359 Bremen, Germany, and [c]Institute for Inorganic Chemistry and Crystallography, University of Bremen, Leobener Strasse 7, 28359 Bremen, Germany. *Correspondence e-mail: staubitz@uni-bremen.de

The title compound, $C_{14}H_{14}N_2S_2$, was obtained by transmetallation of 2,2′-bis(trimethylstannyl)azobenzene with methyl lithium, and subsequent quenching with dimethyl disulfide. The asymmetric unit comprises two half-molecules, the other halves being completed by inversion symmetry at the midpoint of the azo group. The two molecules show only slight differences with respect to N=N, S—N and aromatic C=C bonds or angles. Hirshfeld surface analysis reveals that except for one weak H···S interaction, intermolecular interactions are dominated by van der Waals forces only.

1. Chemical context

The molecular switch azobenzene can undergo isomerization from its thermodynamically stable *trans* form to the meta-stable *cis* form using external stimuli such as light, temperature or pressure. Azobenzenes are common motifs in dyes because of their high thermal and photochemical stability (Yesodha *et al.*, 2004; Lagrasta *et al.*, 1997). We recently presented methods to substitute azobenzenes in the *ortho*, *meta* and *para*-positions with trimethyltin as a novel functionalization method, giving rise to a dual tin–lithium exchange (Strüben *et al.*, 2014, 2015; Hoffmann *et al.*, 2019). In particular, we described the effect on the di*ortho*-substitution on azobenzenes with trimethyl-tetrels and the resulting effects on the switching properties (Hoffmann *et al.*, 2019). In this context, we present here a novel di*ortho*-substituted azobenzene, $(C_7H_7NS)_2$, (I), bearing two methylsulfide groups.
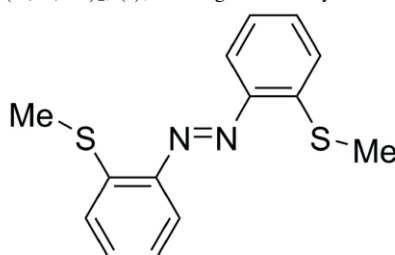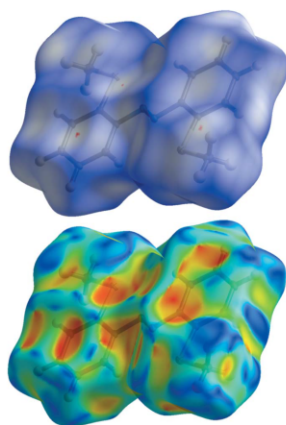
2. Structural commentary

The asymmetric unit of the title compound consists of two half-molecules (**Ia** and **Ib**), the other halves being completed by application of inversion symmetry. The midpoints of the N=N bonds are located on inversion centres, resulting in a

68

research communications
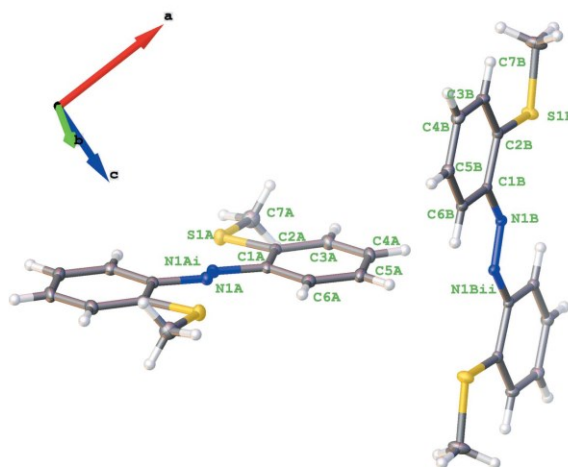
Figure 1
Molecular structures (**Ia** left, **Ib** right) of the title compound with labelling and displacement ellipsoids drawn at the 50% probability level. [Symmetry codes: (i) x, $1 - y$, $-z$; (ii) $1 - x$, $1 - y$, $1 - z$.]

Figure 3
Crystal packing in a view along the b axis. To distinguish the different molecules, all sulfur atoms within the unit cell are labelled.

trans-configuration for the central N=N bonds (Fig. 1). As indicated by the C6A—C1A—N1A—N1A^i and C6B—C1B—N1B—N1B^{ii} [symmetry codes: (i) $-x$, $1 - y$, $-z$; (ii) $1 - x$, $1 - y$, $1 - z$] torsion angles of 13.2 (2) and −5.3 (2)°, respectively, in both molecules the phenyl rings are twisted slightly with respect to the azo unit. A weak distortion is also found for the N1—C1—C2—S1 torsion angles of −3.06 (16)° for **Ia** and −2.06 (15)° for **Ib**. The N=N bond lengths differ marginally [1.255 (2) Å for **Ia**, 1.264 (2) Å for **Ib**], as do comparable C—C bonds. For example, the C1—C2 bond in **Ia** is at 1.408 (2) Å slightly shorter than **Ib** [1.415 (2) Å]. In comparison, this bond is longer than all other C—C distances in the ring because of repulsion of the nitrogen and the sulfur atoms attached to C1 and C2, respectively. In both molecules, the S···N distances [2.8625 (13) Å for **Ia**, 2.8761 (11) Å for **Ib**] are too long to be considered as attractive interactions. Fig. 2 represents an overlay plot of the two molecules, showing there are only slight conformational differences.

3. Supramolecular features and Hirshfeld surface analysis

The packing of **Ia** and **Ib** in the crystal is shown in Fig. 3. Despite the presence of phenyl rings and a parallel arrange-

ment of the molecules, only weak offset π–π interactions are observed; the shortest centroid-to-centroid distance is $Cg2\cdots Cg2(1 - x, 1 - y, -z) = 3.7525$ (8) Å with a slippage of 1.422 Å. To further investigate the intermolecular interactions, Hirshfeld surfaces (Hirshfeld, 1977) and fingerprint plots were generated for both molecules using *CrystalExplorer17.5*

Figure 2
Overlay presentation of molecules **Ia** and **Ib**.
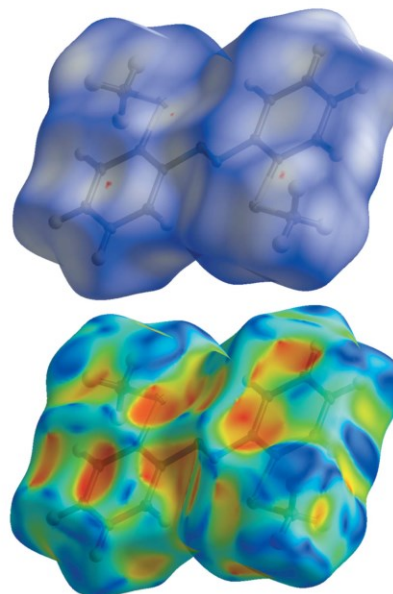
Figure 4
Hirshfeld surface of **Ia** mapped with d_{norm} (top) and shape index (bottom), displaying no significant intermolecular interactions.

research communications
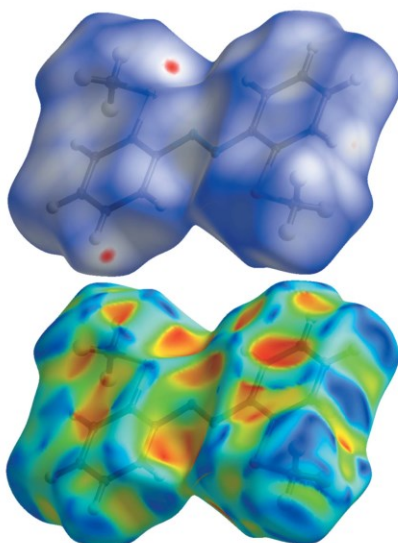
Figure 5
Hirshfeld surface of **Ib** mapped with d_{norm} (top) and shape index (bottom) with indication of an S⋯H interaction.

(McKinnon *et al.*, 2004). Hirshfeld surface analysis depicts intermolecular interactions by different colors, representing short or long contacts and further the relative strength of the interaction. The generated Hirshfeld surfaces mapped over d_{norm} and the shape index are shown in Fig. 4 for **Ia** and in Fig. 5 for **Ib**. Whereas in **Ia** a significant intermolecular interaction is not apparent, characteristic red spots near S1*B* and H5*B* indicate weak S⋯H interactions in **Ib**. The respective supramolecular arrangement is shown in Fig. 6. The sulfur atom S1*B* interacts with a phenyl proton (H4*B*) of another molecule of **Ib** (S⋯H distance = 2.811 Å). The two-dimensional fingerprint plots for molecule **Ib** for quantification of the contributions of each type of non-covalent interaction to the Hirshfeld surface (McKinnon *et al.*, 2007) are given in Fig. 7. The packing is dominated by H⋯H contacts, representing van der Waals interactions (44.5% contribution to the surface), followed by C⋯H and S⋯H interactions, which contribute with 24.0% and 18.1%, respectively. The contri-
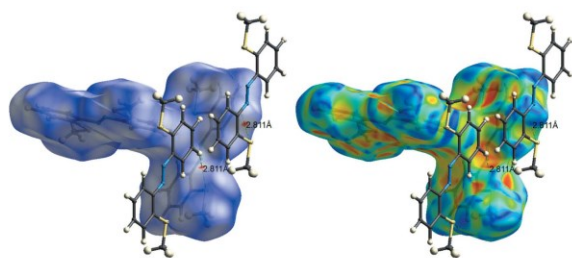
Figure 6
Hirshfeld surface of **Ib** mapped with d_{norm} (left) and shape index (right), together with the interaction of a neighbouring molecule.
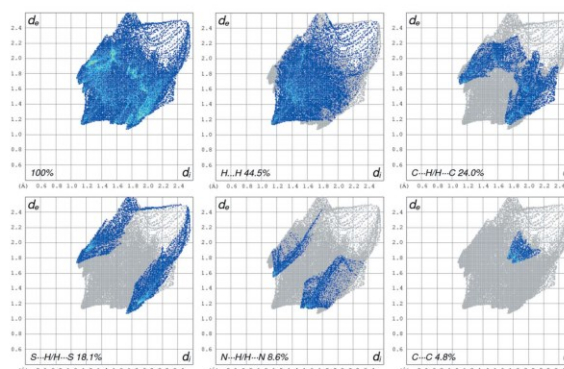
Figure 7
Two-dimensional fingerprint plots for **Ib**, delineated into H⋯H, C⋯H, S⋯H, N⋯H, C⋯C interactions.

butions of the N⋯H (8.6%) and C⋯C (4.8%) interactions are less significant.

4. Database survey

A search of the Cambridge Structural Database (CSD version 5.4.0; update August 2019; Groom *et al.*, 2016) revealed no azobenzene-based structures that contain methyl thioethers. However, some general *ortho*-substituted azobenzenes have been deposited (Yamamura *et al.*, 2008; Kano *et al.*, 2001; Hoffmann *et al.*, 2019). Additionally, some di*ortho*-substituted thioazoxybenzenes were reported previously (Szczygelska-Tao *et al.*, 1999; Kertmen *et al.*, 2013). For the structure of an azobenzene compound with an inversion centre at the N═N bond, see: Bohle *et al.* (2007).

5. Synthesis and crystallization

The synthesis of 2,2′-*bis*(trimethylstannyl)azobenzene was recently described (Hoffmann *et al.*, 2019). For further details of a similar transmetallation of a stannylated azobenzene, see: Strüben *et al.* (2015). Dimethyl disulfide (99%) was purchased from Acros Organics and was used without further purification. Methyl lithium (1.88 *M* in diethyl ether, titrated against 2,2′-bipyridine) was purchased from Acros Organics. THF was purchased from VWR and was dried and degassed with a solvent purification system by Inert Technology.

2,2′-*bis*(Methylthio)azobenzene

In an inert reaction tube, 2,2′-*bis*(trimethylstannyl)azo-stannyl)azobenzene (200 mg, 0.39 mmol) was dissolved under Schlenk conditions in THF (12.5 ml) and cooled to 195 K. Then MeLi (1.88 *M* in diethyl ether, 0.63 ml, 1.18 mmol) was added within 5 min and after 1.5 h at this temperature, dimethyl disulfide (0.35 ml, 3.94 mmol) was added in one ration. The reaction mixture was warmed to 298 K over 14 h and the solvent was removed under reduced pressure. The obtained orange solid was purified in a silica column (Merck, 0.015–0.40 mm) with a gradient of eluents from *n*-pentane to

70

research communications

Table 1
Experimental details.

Crystal data	
Chemical formula	$C_{14}H_{14}N_2S_2$
M_r	274.39
Crystal system, space group	Monoclinic, $P2_1/c$
Temperature (K)	100
a, b, c (Å)	13.0656 (5), 12.1787 (4), 8.3471 (3)
β (°)	96.154 (1)
V (Å^3)	1320.55 (8)
Z	4
Radiation type	Mo $K\alpha$
μ (mm^{-1})	0.39
Crystal size (mm)	$0.21 \times 0.18 \times 0.17$
Data collection	
Diffractometer	Bruker D8 Venture CMOS
Absorption correction	Multi-scan (*SADABS*; Krause *et al.*, 2015)
T_{min}, T_{max}	0.580, 0.746
No. of measured, independent and observed [$I > 2\sigma(I)$] reflections	21000, 3292, 2842
R_{int}	0.065
$(\sin \theta/\lambda)_{max}$ (Å^{-1})	0.668
Refinement	
$R[F^2 > 2\sigma(F^2)], wR(F^2), S$	0.034, 0.089, 1.04
No. of reflections	3292
No. of parameters	165
H-atom treatment	H-atom parameters constrained
$\Delta\rho_{max}, \Delta\rho_{min}$ (e Å^{-3})	0.44, −0.38

Computer programs: *APEX3* and *SAINT* (Bruker, 2016), *SHELXT* (Sheldrick, 2015a), *SHELXL* (Sheldrick, 2015b) and *OLEX2* (Dolomanov *et al.*, 2009).

dichloromethane giving dark-orange crystals (31 mg, 0.11 mmol; yield 29%). Single crystals suitable for X-ray analysis were obtained by slow evaporation from a saturated *n*-heptane solution.

^{1}H NMR (500 MHz, CDCl$_3$): δ = 7.76 (*dd*, ^3J = 8.1 Hz, ^4J = 1.4 Hz, 2H, *H*6), 7.40 (*td*, ^3J = 8.0, 7.3 Hz, ^4J = 1.4 Hz, 2H, *H*4), 7.32 (*dd*, ^3J = 8.0 Hz, ^4J = 1.1 Hz, 2H, *H*3), 7.20 (*td*, ^3J = 8.1, 7.3Hz, ^4J = 1.1 Hz, 2H, *H*5), 2.53 (*s*, 6H, *H*7) ppm.

^{13}C{^{1}H} NMR (125 MHz, CDCl$_3$): δ = 149.08 (*C*1), 141.00 (*C*2), 131.56 (*C*4), 124.81 (*C*3), 124.75 (*C*5), 118.02 (*C*6), 15.02 (*C*7) ppm.

HRMS (EI, 70 eV, MAT95, direct): *m/z*: calculated for C$_{14}$H$_{14}$N$_2$S$_2^+$ 274.05929 found 274.05944.

MS (EI): *m/z* 273.9 (5%) [*M*]$^+$, 258.9 (100%) [*M* − CH$_3$]$^+$, 243.9 (5%) [*M* − C$_2$H$_6$]$^+$, 107.9 (13%) [*M* − C$_8$H$_{10}$N$_2$S]$^+$.

IR (ATR): ν = 3059 (*w*), 2986 (*w*), 2961 (*w*), 2918 (*w*), 2852 (*w*), 1575 (*m*), 1561 (*w*), 1457 (*m*), 1433 (*s*), 1298 (*w*), 1249 (*w*), 1217 (*m*), 1162 (*m*), 1065 (*s*), 1035 (*m*), 951 (*m*), 863 (*w*), 803 (*w*), 761 (*s*), 726 (*s*), 674 (*s*) cm^{-1}.

M.p.: 429 K

R_f: (*n*-pentane: dichloromethane 3:1): 0.55.

6. Refinement

Crystal data, data collection and structure refinement details are summarized in Table 1. All H atoms were positioned geometrically and refined using a riding model: C—H = 0.95–0.98 Å with U_{iso}(H) = 1.5U_{eq} (C-methyl) and 1.2U_{eq}(C)(C-phenyl).

References

Bohle, D. S., Dorans, K. S. & Fotie, J. (2007). *Acta Cryst.* E**63**, o889–o890.
Bruker (2016). *APEX3* and *SAINT*. Bruker AXS Inc. Madison, Wisconsin, USA.
Dolomanov, O. V., Bourhis, L. J., Gildea, R. J., Howard, J. A. K. & Puschmann, H. (2009). *J. Appl. Cryst.* **42**, 339–341.
Groom, C. R., Bruno, I. J., Lightfoot, M. P. & Ward, S. C. (2016). *Acta Cryst.* B**72**, 171–179.
Hirshfeld, F. L. (1977). *Theor. Chim. Acta*, **44**, 129–138.
Hoffmann, J., Kuczmera, T. J., Lork, E. & Staubitz, A. (2019). *Molecules*, **24**, 303.
Kano, N., Komatsu, F. & Kawashima, T. (2001). *Chem. Lett.* **30**, 338–339.
Kertmen, A., Szczygelska-Tao, J. & Chojnacki, J. (2013). *Tetrahedron*, **69**, 10662–10668.
Krause, L., Herbst-Irmer, R., Sheldrick, G. M. & Stalke, D. (2015). *J. Appl. Cryst.* **48**, 3–10.
Lagrasta, C., Bellobono, I. R. & Bonardi, M. (1997). *J. Photochem. Photobiol. Chem.* **110**, 201–205.
McKinnon, J. J., Jayatilaka, D. & Spackmann, M. A. (2007). *Chem. Commun.* pp. 3814–3816.
McKinnon, J. J., Spackman, M. A. & Mitchell, A. S. (2004). *Acta Cryst.* B**60**, 627–668.
Sheldrick, G. M. (2015a). *Acta Cryst.* A**71**, 3–8.
Sheldrick, G. M. (2015b). *Acta Cryst.* C**71**, 3–8.
Strüben, J., Gates, P. J. & Staubitz, A. (2014). *J. Org. Chem.* **79**, 1719–1728.
Strüben, J., Lipfert, M., Springer, J.-O., Gould, C. A., Gates, P. J., Sönnichsen, F. D. & Staubitz, A. (2015). *Chem. Eur. J.* **21**, 11165–11173.
Szczygelska-Tao, J., Biernat, J. F., Kravtsov, V. C. & Simonov, Y. A. (1999). *Tetrahedron*, **55**, 8433–8442.
Yamamura, M., Kano, N., Kawashima, T., Matsumoto, T., Harada, J. & Ogawa, K. (2008). *J. Org. Chem.* **73**, 8244–8249.
Yesodha, S. K., Sadashiva Pillai, C. K. & Tsutsumi, N. (2004). *Prog. Polym. Sci.* **29**, 45–74.

2.5 Summary and Outlook

Overall, the 2,2'-*bis*(trimethylstannyl)azobenzene was evaluated as a potential synthetic precursor for the synthesis of di*ortho*-substituted azobenzenes using tin-lithium-(copper) exchange and cross-coupling reactions (Scheme 26).
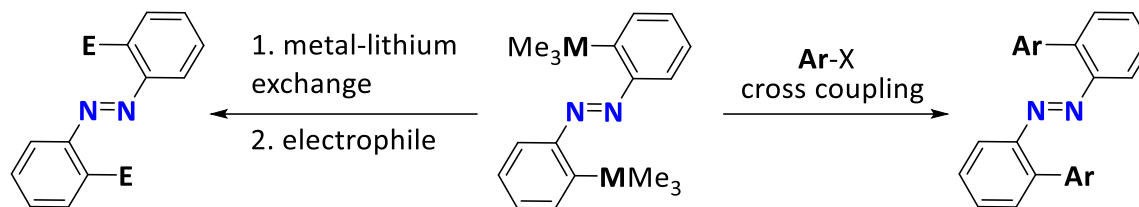
Scheme 26: 2,2'-*bis*(Trimethylstannyl)azobenzene as starting material for cross-coupling or metal-lithium-exchange reactions.

The transmetalation in *ortho*-position was optimized and a variety of products could be isolated. The reactivity was not comparable to previously reported *meta/para*-stannylated azobenzenes. Furthermore, a whole series of *ortho*-substituted *bis*(trimethyltetrel)azobenzenes was investigated regarding their structural, thermal and photophysical properties, focusing on the effect of the tetrels (C, Si, Ge, Sn). Whilst the stannylated azobenzene exhibited the highest bathochromically shifted absorption, it was photolabile. Cross-coupling reactions of *bis*-stannylated *ortho*-azobenzene showed conversion to the desired products in moderate yields. At this stage, further optimization is required to access *ortho*-substituted aryl-azobenzenes.

As we succeeded in preparing a dinucleophilic *ortho*-substituted azobenzene, also ethylene-bridged azobenzene, also known as diazocines, should be synthetically accessible (Scheme 27).
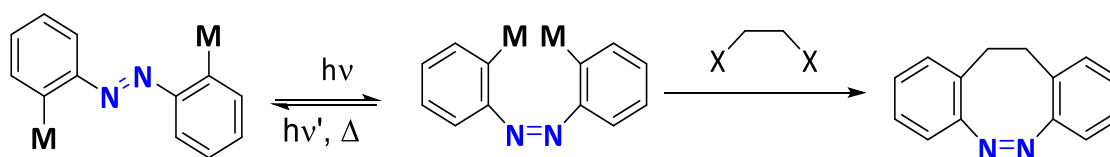
Scheme 27: *Ortho*-metalated azobenzenes may represent a useful precursor for bridged azobenzenes.

These novel photoswitches gained interest due to their higher photoconversion and their inverted switching ability in reference to azobenzenes: the *cis*-isomer is more thermodynamically stable than the *trans*-isomer (Scheme 28).[31, 32]
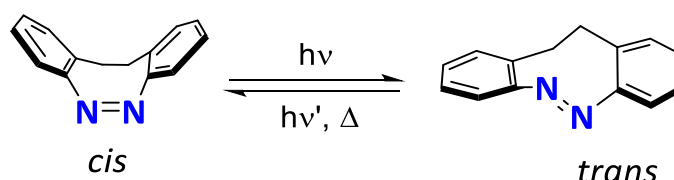
Scheme 28: Structure a bridged azobenzene, referred to as diazocine, with its two isomers.[31, 32]

Initial results for heterodiazocines bearing nitrogen, oxygen or sulfur in bridge positions showed superior photophysical properties like bathochromically shifted absorbance and high switching efficiencies compared with azobenzenes.[33, 34]

2.6   References

1.   R. M. Christie, *Azo dyes and pigments*, in *Colour Chemistry*, The Royal Society of Chemistry, 2nd edn., **2015**, 72-97.
2.   A. A. Beharry, G. A. Woolley, *Chem. Soc. Rev.*, **2011**, *40*, 4422-4437.
3.   H. M. Bandara, S. C. Burdette, *Chem. Soc. Rev.*, **2012**, *41*, 1809-1825.
4.   T. Nägele, R. Hoche, W. Zinth, J. Wachtveitl, *Chem. Phys. Lett.*, **1997**, *272*, 489-495.
5.   J. Calbo, C. E. Weston, A. J. White, H. S. Rzepa, J. Contreras-Garcia, M. J. Fuchter, *J. Am. Chem. Soc.*, **2017**, *139*, 1261-1274.
6.   G. S. Hartley, R. J. W. Le Fèvre, *J. Chem. Soc.*, **1939**, 531-535.
7.   E. M. Tan, S. Amirjalayer, S. Smolarek, A. Vdovin, F. Zerbetto, W. J. Buma, *Nat. Commun.*, **2015**, *6*, 5860.
8.   A. C. Cope, R. W. Siekman, *J. Am. Chem. Soc.*, **1965**, *87*, 3272-3273.
9.   J. P. Kleiman, M. Dubeck, *J. Am. Chem. Soc.*, **1963**, *85*, 1544-1545.
10.   T. H. L. Nguyen, N. Gigant, D. Joseph, *ACS Catalysis*, **2018**, *8*, 1546-1579.
11.   J. Yoshino, N. Kano, T. Kawashima, *Chem. Commun.*, **2007**, 559-561.
12.   J. Yoshino, A. Furuta, T. Kambe, H. Itoi, N. Kano, T. Kawashima, Y. Ito, M. Asashima, *Chemistry*, **2010**, *16*, 5026-5035.
13.   J. Yoshino, N. Kano, T. Kawashima, *Dalton Trans.*, **2013**, *42*, 15826-15834.
14.   M. Yamamura, N. Kano, T. Kawashima, T. Matsumoto, J. Harada, K. Ogawa, *J. Org. Chem.*, **2008**, *73*, 8244-8249.
15.   A. Yamamoto, E. Ohta, N. Kishigami, N. Tsukahara, Y. Tomiyori, H. Sato, Y. Matsui, Y. Kano, K. Mizuno, H. Ikeda, *Tetrahedron Lett.*, **2013**, *54*, 4049-4053.
16.   H. Nakanotani, T. Higuchi, T. Furukawa, K. Masui, K. Morimoto, M. Numata, H. Tanaka, Y. Sagara, T. Yasuda, C. Adachi, *Nat. Commun.*, **2014**, *5*, 4016.
17.   N. Kano, M. Yamamura, T. Kawashima, *Dalton Trans.*, **2015**, *44*, 16256-16265.
18.   M. Yamamura, N. Kano, T. Kawashima, *J. Am. Chem. Soc.*, **2005**, *127*, 11954-11955.
19.   N. Kano, M. Yamamura, X. Meng, T. Yasuzuka, T. Kawashima, *Dalton Trans.*, **2012**, *41*, 11491-11496.
20.   N. Kano, F. Komatsu, T. Kawashima, *Chem. Lett.*, **2001**, *30*, 338-339.
21.   S. Yamamoto, N. Nishimura, S. Hasegawa, *Bull. Chem. Soc. Jpn.*, **1971**, *44*, 2018-2025.
22.   J. Strueben, P. J. Gates, A. Staubitz, *J. Org. Chem.*, **2014**, *79*, 1719-1728.
23.   J. Strueben, M. Lipfert, J. O. Springer, C. A. Gould, P. J. Gates, F. D. Sonnichsen, A. Staubitz, *Chemistry*, **2015**, *21*, 11165-11173.
24.   A. R. Katritzky, J. Wu, S. V. Verin, *Synthesis*, **1995**, *1995*, 651-653.
25.   T. T. Nguyen, A. Boussonniere, E. Banaszak, A. S. Castanet, K. P. Nguyen, J. Mortier, *J. Org. Chem.*, **2014**, *79*, 2775-2780.
26.   J. Struben, J. Hoffmann, D. Presa-Soto, C. Nather, A. Staubitz, *Acta Cryst. E*, **2016**, *72*, 1590-1594.
27.   M. Dowds, D. Bank, J. Strueben, D. P. Soto, F. D. Sönnichsen, F. Renth, F. Temps, A. Staubitz, *J. Mater. Chem. C*, **2020**, *8*, 1835-1845.
28.   E. Merino, *Chem. Soc. Rev.*, **2011**, *40*, 3835-3853.
29.   P. Knochel, B. Betzemeier, *Transmetalation Reactions Producing Organocopper Reagents*, in *Modern Organocopper Chemistry*, ed. N. Krause, Wiley-VCH, Weinheim, **2002**, 45-78.
30.   T. J. Kuczmerea, *Bachlor Thesis: Preparation of ortho-substituted Azobenzenes*, University Bremen, **2018**.
31.   R. Siewertsen, H. Neumann, B. Buchheim-Stehn, R. Herges, C. Nather, F. Renth, F. Temps, *J. Am. Chem. Soc.*, **2009**, *131*, 15594-15595.
32.   R. Siewertsen, J. B. Schonborn, B. Hartke, F. Renth, F. Temps, *Phys. Chem. Chem. Phys.*, **2011**, *13*, 1054-1063.
33.   P. Lentes, E. Stadler, F. Rohricht, A. Brahms, J. Grobner, F. D. Sonnichsen, G. Gescheidt, R. Herges, *J. Am. Chem. Soc.*, **2019**, *141*, 13592-13600.

34.   M. Hammerich, C. Schutt, C. Stahler, P. Lentes, F. Rohricht, R. Hoppner, R. Herges, *J. Am. Chem. Soc.*, **2016**, *138*, 13111-13114.

Preface for Chapters 3 and 4: BN and BP units as Substitutes for C=C Units

Introduction

Ethylene represents the smallest possible unsaturated alkene consisting of two carbon and four hydrogen atoms. By the substitution of one carbon atom by a boron atom and the other carbon atom by a nitrogen or phosphorus atom, the same number of valence electrons are shared between the two atoms. This gives rise to its BN or BP analogs named aminoborane (H_2N-BH_2) and phosphinoborane (H_2P-BH_2). Although they are formally isoelectronic, the energetically accessible structures of these molecules can be geometrically quite different (Scheme 29).

ethylene
planar

ethylene
rotated

aminoborane
planar

aminoborane
rotated/pyramidal

phosphinoborane
planar

'borylphosphine'
bend/pyramdial

'borylphosphine'
rotated/pyramidal
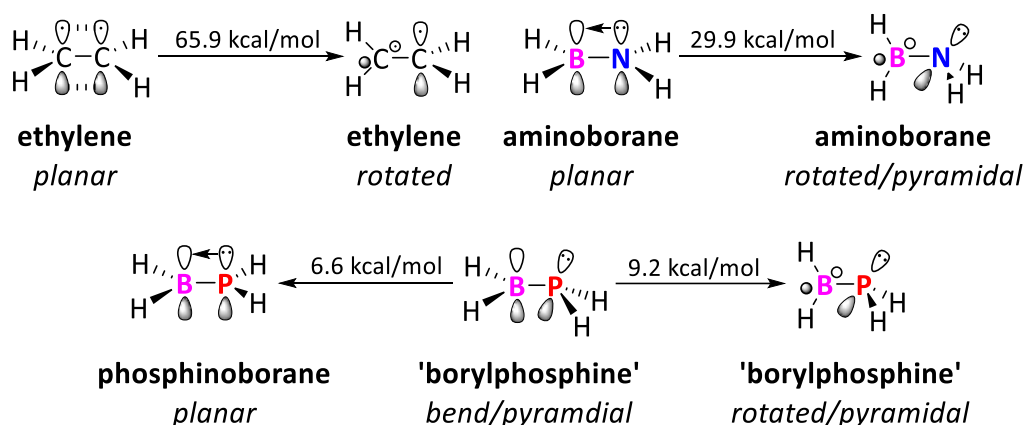
Scheme 29: Structure of ethylene, its BN-analog aminoborane and the BP-analog phosphinoborane with adiabatic rotational barriers. The twisted ethylene, which represents a diradical, was derived from experimental values.[1] Since the values for aminoborane and phosphinoborane/borylphosphine are not experimentally reported, calculated values (*ab initio* with CCSD(T)/CBS)[2] were used.

The carbon-carbon bond in ethylene is based on the overlap of two sp^2 hybrid orbitals forming a σ-bond and interaction of two p_z orbitals giving the π-bond in a planar configuration. The rotation of the C-C bond in ethylene by 90° is highly unfavored as the π-bonding is strongly reduced and diradicals would be formed.[3] As opposed to ethylene, aminoborane has a significantly lower rotation barrier (to convert from its planar thermodynamically favored form to its rotated form. The planarity of the aminoborane was confirmed by microwave spectroscopy in the gas phase.[4] In its rotated form, the bond order of the B-N bond is effectively lower than for the planar one due to insufficiently overlapping p-orbitals. The experimental rotational barrier for interconversion of one form to another is not reported to date but was calculated by *ab-initio* methods to be 29.9 kcal/mol.[2] Similar values (17-27 kcal/mol) were experimentally determined for substituted aminoboranes.[5] Although ethylene and aminoborane are considered as isoelectronic, the B-N bond in unsubstituted aminoborane was found to be highly polarized with an overall dipole moment of $\mu = 1.84$ D[4] whereas ethylene has none. The dipole moment of aminoborane is a result of the highly polarized BN σ-bond and is to some extent compensated by nitrogen's lone pair donation into the boron's vacant p_z orbital in the π-bond.[6] Due to its polarity and reactivity, monomeric aminoborane undergoes head-to-tail oligomerization to form four-, and six-membered cycles but also linear oligomeric and polymeric structures[7] and was only observed below -155 °C.[8] This is a remarkable difference between aminoborane and ethylene that can be isolated.

Phosphinoborane diverges significantly from the structure of ethylene/aminoborane: Its most stable form is pyramidal at the phosphorus atom and converts to its planar or rotated form by a relatively low rise in energy (Scheme 29). Due to the greater covalent radius of phosphorus (1.07(3) Å) compared to nitrogen (0.706(13) Å),[9] there are longer bond lengths and less overlap efficiency of the lone pair with the boron's vacant p_z-orbital. The calculated σ and π-bond energies for H_2BPH_2 (77.6 kcal/mol and 9.2 kcal/mol) are significantly lower compared to H_2BNH_2 (109.8 kcal/mol and 29.9 kcal/mol).[2] Owing to this lack of stabilization, more geometrical forms, compared to ethylene or aminoborane, with low rotational barriers are found. Due to their importance, a planar form is referred to as phosphinoborane whereas a form that is pyramidal at the phosphorus atom is referred to as borylphosphine motifs (Scheme 29). The latter structure is represented by a bent configuration (borylphosphine) at the phosphorus atom, whereas the hydrogen atoms on the boron atom are in plane with the B-P bond. As a result of the P-pyramidalization, the BP π-interaction is only weak, which increases the Lewis basicity of the phosphorus atom and the Lewis acidity of the boron atom (relative to the related aminoborane). The strongest BP π-interaction is present in the planar structure, which mimics the ethylene and aminoborane structures the best. Due to the increased B-P π-interaction in the phosphinoborane form, the calculated B-P bond border of 2.01 is higher than in borylphosphine with a bond order of 1.35.[10, 11] The dipole moment of unsubstituted phosphinoborane remains unknown as unsubstituted phosphinoborane cannot be isolated, presumably because it readily oligomerizes and hydrolyses. However, dipole moments for borylphosphine (μ = 0.82 D) and phosphinoborane (μ = 1.21 D) were calculated by theoretical methods.[11] Thus, they are slightly reduced compared to aminoborane's dipole moment (μ = 1.84 D)[4].

The isoelectronic substitution of the carbon atoms in ethylene with combinations of group 13 and 15 elements show the variety of structural and energetic changes based on σ- and π-interactions and geometrical factors. Especially the presence of phosphinoborane/borylphosphine structures contradicts a concept of CC/BN/BP-isosterism in ethylene analogs. However, a judicious choice of non-hydrogen substituents at the heteroatoms may stabilize specific structures by steric or electronic effects; thus, structural motifs that are transition states in phosphinoborane can become stable conformers with appropriate substituents. These influences will be discussed in the next chapters.

Comparison of Boron-Nitrogen and Boron-Phosphorus Bonds in Intermolecular Systems

Much work on the potential of poly(aminoboranes) and poly(phosphinoboranes), bearing mostly one aryl or alkyl group at the pnictogen, has been carried out in the last decades.[12, 13] Investigations on more stable perarylated monomeric aminoboranes or phosphinoboranes were already conducted in the middle of the last century. Fundamental comparative studies of aryl-substituted tricoordinated boron/nitrogen and boron/phosphorus units were performed in 1961 by Coates and Livingstone.[14] In this study, it was observed that in the infrared absorption spectrum of diphenylphosphino diphenylborane (**71**), the B-P vibration band appeared at a larger wavenumber (υ = 1445 cm^{-1}) than the B-N vibration in the corresponding diphenylamino diphenylborane (**72**, υ = 1375 cm^{-1}). However, substitution with a heavier phosphorus atom should lead to the contrary effect and therefore, it was assumed that the double bond in the phosphinoborane was stronger than for aminoborane.

These initial investigations led to the comparative study of the polarity of amino- and phosphinoboranes as well. Despite the large electronegativity differences of boron (χ = 2.01) and nitrogen (χ = 3.07), only a small dipole moment for aryl-substituted aminoboranes (**72**, μ = 1.0 D) was found.

This observation was explained by opposing electronic effects (Fig. 36).[14]
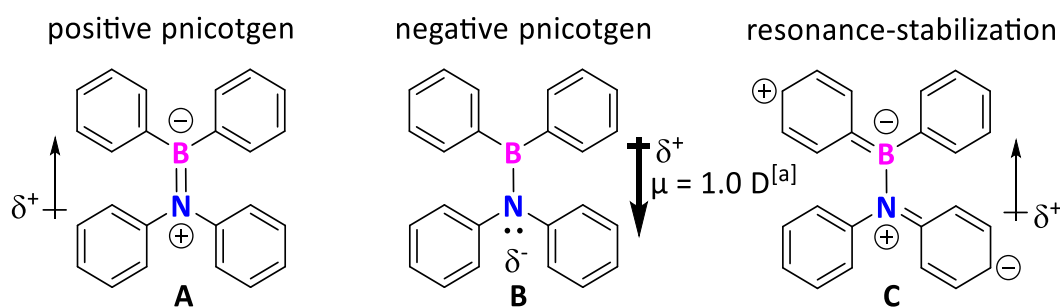
Fig. 36: Diphenylamino diphenylborane (**72**) and three structures which display an explanation for the overall dipole moment situation. The dipole moment depicted in bold represents the experimentally determined dipole vector. The chart is in accordance to the literature.[14] [a] Measured in benzene.

The polarization of the σ-bond in the aminoborane is compensated to some extent by the donation of the nitrogen's lone pair to the vacant p_z-orbital of the boron resulting in a formally negative charge at the boron and a positive charge at the nitrogen (**A**). In another resonance form, the π-electrons are mainly located at the nitrogen atom giving it a partial negative charge (**B**). This form is stabilized by the electron-accepting ability of the phenyl rings. The compensation of both these effects accounts for the low dipole moment in arylated aminoboranes. Any compensation of the more negative nitrogen atom by resonance stabilization (**C**) was excluded since the π-electrons are highly located at the BN unit's π-bond. Therefore, mostly resonance structures **A** and **B** are responsible for the low dipole moment whereas **B** explains the experimentally observed dipole moment the best. Interestingly, in H_2NBH_2[4] and Me_2NBPh_2[14] the dipole moment is located from N→B, which can be attributed to form **A**. Therefore, the direction and magnitude of the dipole moment are highly dependent on the substituents.

Although the electronegativities of both boron and phosphorus are almost equal (χ = 2.01/2.06), a greater dipole moment for aryl-substituted phosphinoborane (μ = 2.2 D) compared to aryl-substituted aminoboranes (μ = 0.8 D) was observed. According to comparative studies of substituents at the phosphinoborane, it was found that the negative charge is accumulated at the phosphorus atom, although it is the more electropositive element, best described in (**E**) (Fig. 37).
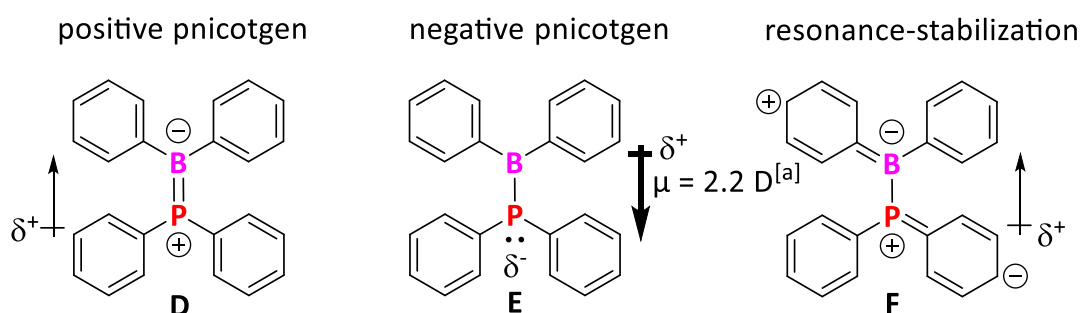
Fig. 37: Representation of diphenylphosphino diphenylborane (**71**) in three bonding situations with a different formal approximation to explain the greater dipole moment compared to its BN-congener. The dipole moment depicted in bold represents the experimentally determined dipole moment. The representation is based on literature descriptions.[a] Experimental dipole moment for a similar compound ($Ph_2BP(m$Tol$)_2$), since diphenylphosphino diphenylborane is insoluble.[14]

Due to the lack of the σ-bond polarization in phosphinoboranes, the π-interaction with the phenyl substituents (**F**) is the dominant effect compared to a donation of the phosphorus lone pair towards boron (**D**). The experimental finding of monomeric diphenylphosphino diphenylborane was assigned

to the fact that the aryl groups at the phosphorus atom actively support the formation of a π-bond towards the thereby saturated boron atom (**F**). This further explained the compound's stability against hydrolysis compared to the arylated aminoboranes. Overall, Coates and Livingstone considered the phosphorus atom to be a weak π-donor towards the boron atom due to an insufficient overlap of the 3p orbitals of the phosphorus atom and the vacant 2p orbital of the boron atom. Later, Pestana and Power[15] suggested that the weak π-interaction resulted from the favored pyramidalization of the phosphorus atom in a planar structure as it was observed for unsubstituted phosphinoborane (Scheme 29).

To understand the overall BN/BP-relations in cyclic π-conjugated systems, it is worthwhile to discuss the general interaction of only nitrogen or phosphorus with aryl substituents: Three-valent nitrogen-containing organic π-conjugates are commonly found in a planar configuration whereas three-valent organophosphorus π-systems are rather found in their pyramidal than their planar form due to energic advantages. The reason for this effect is the nature of the respective lone pair: The nitrogen's lone pair is a strong π-donor, the phosphorus lone pair exhibits weak π-donor but high σ-character if embedded in a carbon scaffold.[16] Hence the (sp³-hybridized) phosphorus form is found predominately tetrahedral as embedded in organic structures. Due to its pyramidal shape and high inversion barrier (ΔG = 30-35 kcal/mol), it cannot integrate into a planar carbon scaffold, without disturbing the planarity of the system. In general, planar (sp²-hybridized) phosphorus compounds are rarely reported but should have comparable π-donation abilities compared to a sp²-hybridized nitrogen atom.[17] Due to this fact, stabilization of the sp²-hybridized phosphorus atoms or molecular modifications to access lower inversion barriers are still investigated intensively.[16] Fundamentally different geometries of each phosphorus or nitrogen, as embedded in carbon scaffolds, influence the organic structure's electronic property directly.

This tenet applies as well for the combination of both pnictogens with a boron atom to give aminoborane or phosphinoborane/borylphosphine-like structures. In fact, a direct BP-analog of a planar aryl-substituted aminoborane is only possible if the π-bond overlap is maximized and the planar phosphinoborane form occurs. Upon decreased π-bond overlap a borylphosphoshine analog results. To characterize the bonding situation in aryl-substituted BP-compounds, commonly the B-P bond length and the sum of angles at the phosphorus are considered. The classification of perarylated phosphinoboranes (planar) and borylphosphines (pyramidal) was intensively reviewed by Bailey and Pringle (Fig. 38).[18]
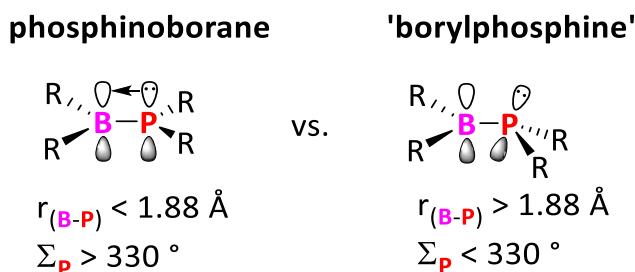
Fig. 38: Definition of perarylated borylphosphine and phosphinoborane by structural factors determined by X-ray analysis according to Bailey and Pringle.[18]

According to their definition, a B-P bond length shorter than 1.88 Å and a sum of angles at the phosphorus atom greater than $\Sigma_P > 330°$ is defined as phosphinoborane bonding situation. In cases of longer bond lengths and a smaller sum of angles, the BP-compound is classified as borylphosphine.

The formation of either phosphinoborane or borylphosphines is to some extent predictable based on electronic effects. The B-P bond orbital overlap is maximized when the boron atom bears electron-withdrawing groups and the phosphorus atom is attached to electron-donating groups. The planarized B-P bond results in a phosphinoborane motif. As an example, this electronic stabilization of dimesitylphosphine *bis*(pentafluorophenyl)borane, which holds a phosphinoborane bonding mode, was reported by Stephan.[19] Due to the Lewis pair character of the B-P bond in borylphosphines and the pyramidal geometry of the BP unit, intermolecular head-to-tail connections are more likely in this bonding mode. This was observed for the *bis*(pentafluorophenyl)phosphino diphenylborane which formed dimeric structures which were published by Stephan and coworkers.[20] Besides electronic stabilization, sterically demanding substituents also stabilize a planar phosphinoborane conformer. An example of a sterically stabilized phosphinoborane is the dimesitylphosphine dimesitylborane which had a trigonal planar phosphorus (Σ_P = 360°).[15]

In general, it is expected that arylated aminoborane derivatives will be found exclusively as planar form, while BP-compounds may be found as both planar (phosphinoborane) or pyramidal (borylphosphine) structure depending on stereoelectronic effects.

Incorporation of BN/BP units in Carbocycles

The incorporation of main group elements of the groups 13 or 15 results in drastic effects onto the optoelectronic properties of π-conjugated systems.[21] When graphene is doped with phosphorus or nitrogen, this leads to p-type materials, whereas boron doping results in n-type graphene.[22] In small organic molecules, the incorporation of the electron-deficient group 13 elements is recognized for stabilizing the LUMO level in π-conjugated systems. Group 15 elements, on the other hand, increase the HOMO level due to their additional electron density originating from their lone pair. To display the effect of boron, nitrogen or phosphorus on the location of the HOMO/LUMO levels 9-heterofluorene has been investigated theoretically (Fig. 39).[23]
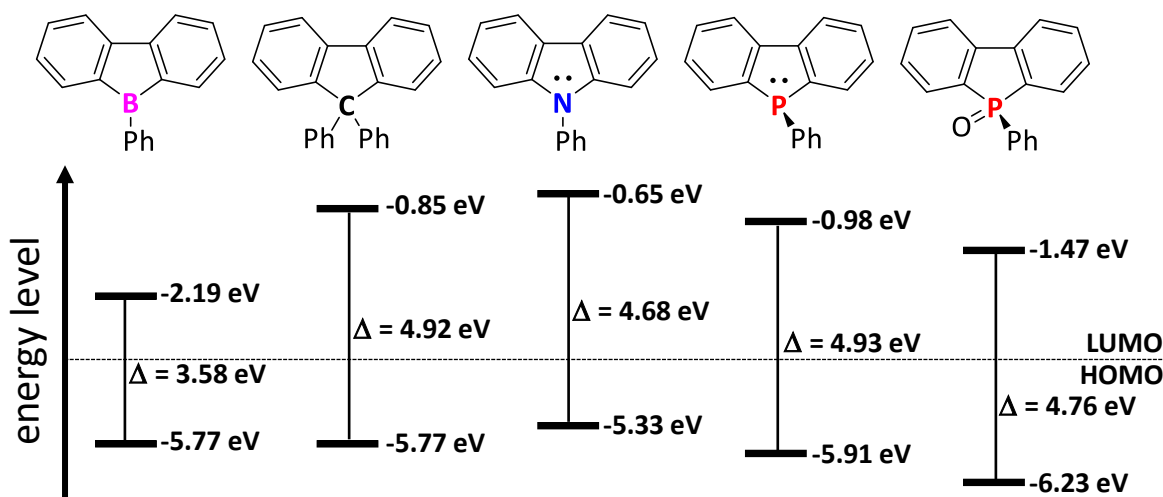
Fig. 39: HOMO and LUMO levels of phenyl-9-heterofluorenes and 9,9'-diphenylfluorene calculated with B3LYP/6-31G(d) level of theory.[23]

The implementation of the boron atom in a fluorene scaffold leads to a strongly stabilized LUMO level in comparison to the 9,9-diphenylfluorene due to the interaction of the empty p_z orbital of the boron atom with the π-conjugated system and the desymmetrization of the molecular frontier orbitals.[24] Notably, 9-borafluorene is isolobal to a fluorenyl cation and only has 12 π-electrons. Overall, the HOMO level is not affected by this substitution with a boron atom.

Implementation of a nitrogen atom in the fluorene scaffold (carbazole) slightly stabilizes the LUMO level and raises the HOMO level leading to a smaller HOMO-LUMO gap (4.92 eV vs. 4.68 eV). Other carbazoles, e.g. 4,4'-*bis*(*N*-carbazolyl)-1,1-biphenyl (**CBP**), exhibit high triplet state energies which make them excellent host materials in optoelectronic devices.[25]

A phosphorus atom in a heterofluorene, referred to as dibenzophosphole, stabilizes the LUMO and HOMO at the same time while the overall energy gap is similar to the fluorene motif (4.92 eV vs. 4.93 eV). A unique advantage of using phosphorus in conjugated π-conjugated systems is the possibility of chemical modification on the phosphorus atom.[26-28] Here oxygenation allows stabilizing both the HOMO/LUMO level while the energy gap is reduced compared to fluorene (4.92 eV vs. 4.76 eV). Moreover, other oxidation states of the phosphorus atom in benzophospholes with unique HOMO/LUMO levels are accessible and therefore modified dibenzophospholes are widely used in optoelectronics.[29] In general it is expected that heterofluorenes with low-lying LUMO levels, e.g. dibenzophospholes and borafluorenes, supposedly are good electron-transporting and injecting materials while heterofluorenes with high-lying HOMO and high triplet state energy, e.g. carbazoles, are excellent hole transporting material.

The heterofluorenes impressively display the effect of a single heteroelement in a π-conjugated structure on the HOMO-LUMO gap. An extension of this concept is the combinations of two heteroelements in carbocyclic systems: Elements from group 13 and 15 in one heterocycle could on the one hand stabilize the LUMO level (group 13 element) and higher the HOMO level as well (group 15 element). This combination might cause a lower HOMO-LUMO gap and a therefore bathochromic shift.

The integration of group 13/15 elements combinations in a six-membered π-conjugated carbocycle maintains the overall amount of six delocalized π-electrons which is highly favorable. Especially the boron/nitrogen and boron/phosphorus heterocycles 1,2-azaborine and 1,2-phosphaborine gained interest due to their geometrical and optoelectronic properties. Since a direct comparative study of benzene, 1,2-azaborine and 1,2-phosphaborine has not been reported yet, the HOMO/LUMO levels were calculated in this thesis by DFT methods to clarify the effect of substitution with the respective combination of hetero elements (Fig. 40).
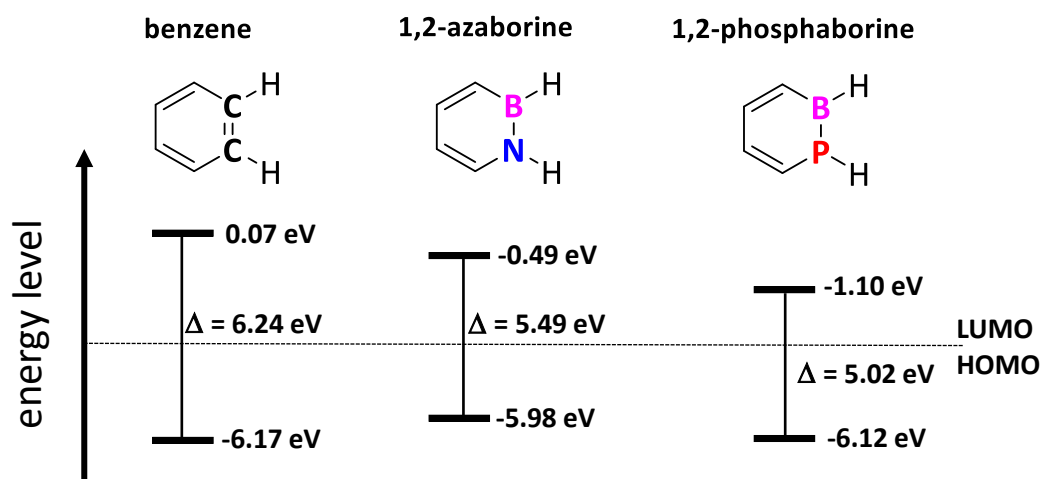
Fig. 40: Calculated HOMO/LUMO levels of benzene, its BN-analog 1,2-azaborine and BP-analog 1,2-phosphaborine with B3LYP/6-31G(d,p) level of theory.

The isoelectronic and isosteric substitution with a BN unit in benzene results in a stabilization of both HOMO and LUMO levels due to the electron-accepting and donating nature of boron and nitrogen atoms. Thus, the energy gap is reduced from 6.24 eV in benzene to 5.49 eV in 1,2-azaborine.

Substitution of the nitrogen atom by phosphorus lowers both the LUMO and HOMO level while the total HOMO-LUMO gap is reduced to 5.02 eV.

As seen by this comparison, 1,2-azaborines and 1,2-phosphaborines exhibit differing HOMO/LUMO levels. This should influence their physical properties, e.g. stability, electronic and optical properties, and chemical behavior. As 1,2-azaborines and 1,2-phosphaborine hold different levels of exploration both congeners will be revised separately.

1,2-Azaborines

The most stable and best-studied structure among the structural isomers of azaborine is represented by the 1,2-azaborine[30] and gained more focus than 1,3- and 1,4-azaborine structures (Fig. 41).

1,2-azaborine   1,3-azaborine   1,4-azaborine
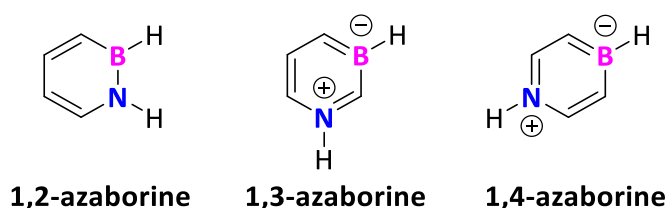
Fig. 41: The three azaborine isomers: 1,2-dihydro-1,2-azaborine, 1,3-dihydro-1,3-azaborine and 1,4-dihydro-1,4-azaborine.

The aromaticity of 1,2-azaborines and its isomers has been well investigated, indicating a certain degree of aromaticity for all of them, with the 1,3-isomer being the most aromatic.[30-32] However, reports on the Diels-Alder reaction of 1,2-azaborines show a certain diene character. Thus, experimentally the aromaticity lies between furan and thiophene.[33, 34]

The interest in 1,2-azaborine chemistry has grown due to their application in pharmaceuticals,[35-38] potential hydrogen storage materials,[39-41] organic synthesis,[42] materials science[43-45] and most notably in organic electronic (*vide infra*). These developments were achieved since the synthetic pioneering work of Piers,[46] Liu[46, 47] and Ashe[48] in the past two decades revived BN-chemistry as they made 1,2-azaborines accessible by efficient reactions under mild conditions. The first substituted 1,2-azaborine, BN-phenanthrene, was isolated by Dewar in 1959, whereas the unsubstituted 1,2-dihydro-1,2-azaborine had not been isolated until 2008 when Liu and coworkers[49] described its synthesis *via* an olefin metathesis reaction. Its X-ray analysis revealed a planar ring structure with a B-N bond length of 1.446(2) Å and a sum of angles at both nitrogen and boron of $\Sigma = 360°$. Since then, the physical properties of these structures have been deeply investigated. The general effect of substituting a carbon scaffold with a BN unit was impressively displayed by the absorption spectra of benzene and 1,2-dihydro-1,2-azaborine (Fig. 42).[47]
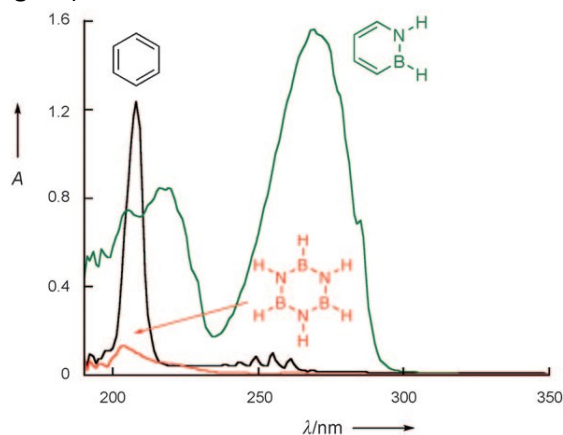
Fig. 42: UV/Vis absorption spectra of benzene, borazine and 1,2-dihydro-1,2-azaborine. Adapted with permission from.[47]

The direct comparison of the B-band in benzene (λ_{max} = 255 nm, ε = 977 L mol^{-1} cm^{-1}) with the most intense absorption band of 1,2-azaborine (λ_{max} = 269 nm, ε = 15632 L mol^{-1} cm^{-1}) showed a small bathochromic shift. However, the increased intensity and broadness of the azaborines' absorption signal displays the effect of an isosteric BN-substitution.[47] On the one hand the higher intensity of the absorption band might be due to the absence of transitions that are symmetry forbidden in benzene. On the other hand, it can be explained by the stabilization of both HOMO and LUMO levels, see Fig. 40, and a greater dipole moment compared to benzene. In fact, high dipole moments in the ground state (μ = 2.15 D) and in the first excited state (μ = 3.11 D), as determined by a combination of photoemission spectroscopy (PES) and computational chemistry, were found for 1,2-dihydro-1,2-azaborine. The high dipole moments are a plausible explanation for the broadening of the absorption signal and the increased extinction coefficient ε.[50] The general electronic structure of 1,2-azaborines was elucidated by a microwave spectrum of 1,2-dihydro-1,2-azaborine and its ^{10}B and ^{2}H isotopologues in combination with MP2 calculation. This suggested the following description of the polarization to explain the present dipole moment (Fig. 43).[51]
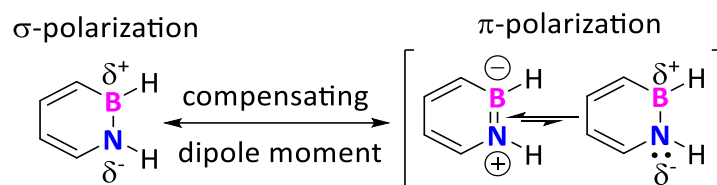
Fig. 43: Compensation effects leading to a low overall dipole moment of 1,2-dihydro-1,2-azaborine. The π-bond is equally located at the boron and nitrogen atom.[51]

Due to these compensating effects of σ- and π-polarization, the overall polarization (2.15 D)[50] is smaller than expected for a polarized BN unit but similar to aminoborane (1.84 D)[4] and Ph$_2$NBPh$_2$ (1.0 D)[14]. The π-polarization is based on the fact that the nitrogen's lone pair adds electron density to the boron and therefore a formal negative charge results. This explanation was in accordance with the interpretation delivered by Coates and Livingstone for the dipole moment in diphenylamino diphenylborane (Fig. 36).[14] 1,2-Azaborines are still under fundamental investigation and a most recent example represent the vitality of this field: Vapor deposition on Au(111) and Cu(111) surfaces revealed that azaborine itself forms dimeric structures due to its dipolar nature.[52] These observations should be taken into consideration when azaborine motifs are embedded in organic devices and might form supramolecular structures.

1,2-Phosphaborines

While the phosphorus-boron equivalent of borazine (B$_3$N$_3$H$_6$), phosphaborazine (B$_3$P$_3$H$_6$), was already published in 1962 by English,[53] the BP-equivalent of 1,2-azaborine, 1,2-phophaborine, remains elusive. So far the unsubstituted 1,2-dihydro-1,2-phosphaborine was exclusively described by computational studies as a thermodynamically stable six π-electron system.[54] Only two derivatives have been synthesized yet, the hexa-aryl-substituted 1,2-phosphaborines.

They were accessed by 1,1-insertion of a phenylphosphinidene into a pentaarylborole by photolysis which remained the only synthetic pathway for 1,2-phosphinboranes so far (Scheme 30).[55]
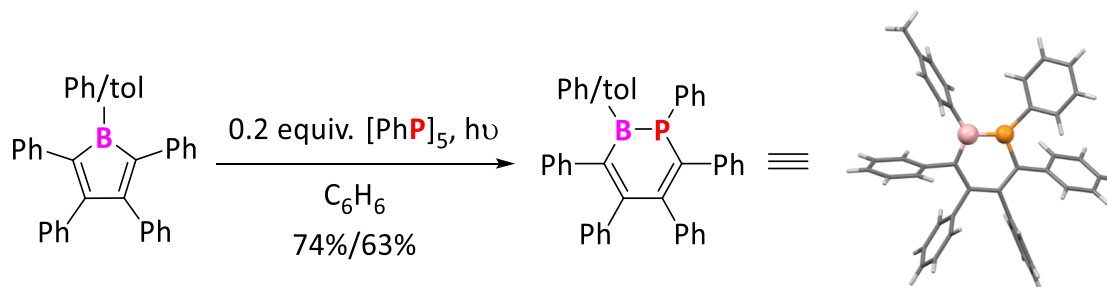
Scheme 30: Using penta-aryl borole and phenylphosphine pentamer to obtain substituted 1,2-phosphinoboranes *via* 1,1-insertion reaction. The crystal structure of the tolyl derivative is displayed to the right.[55]

The isolated 1,2-phosphaborine showed an ^{11}B NMR resonance at δ = 38.4 ppm and a ^{31}P NMR resonance at δ = -77.6 ppm, indicating both tricoordinated boron and phosphorus atoms. The planar structure of the substituted 1,2-phosphaborine was confirmed by X-ray diffraction experiments and gave insights into the bonding situation. The B-P bond length was determined (1.799(4) Å) which is a common value for BP double bonds. However, the sum of all angles was 359° for boron and 357° for phosphorus which shows that in this system both atoms exhibit an almost trigonal planar geometry. Therefore, by the criteria suggested by Bailey and Pringle[18] this system displayed a classic phosphinoborane structure with a BP double bond (Fig. 38). In comparison to the acyclic phosphinoborane structures, in which a stereoelectronic stabilization generates planar BP units, this heterocyclic approach intrinsically resulted in the formation of a planar BP unit. Therefore, the geometric confinement by placing it in a ring structure, combined with π-delocalization in a heterocycle might be a further feature to stabilize a phosphinoborane mode. The 1,2-phosphaboranes were subjected to electrochemical and photophysical characterization to determine the effect of the BP unit on the butadiene scaffold. The absorption of both phosphaborine derivatives showed the lowest energy absorption in the UV-region (λ_{max} = 366 nm (ε = 6200 M^{-1} cm^{-1}) / 367 nm (ε = 6400 M^{-1} cm^{-1})),[55] which were bathochromically shifted in comparison to the hexaphenyl-1,2-azaborine (λ_{max} = 315 nm (ε = 17500 M^{-1} cm^{-1}))[56]. The most intense absorption signals, which were responsible for the respective luminescence, were observed in the UV region as well (λ_{max} = 260 nm (ε = 29000 L mol^{-1} cm^{-1}). The emission spectrum of these molecules consisted of three bands (λ_{max} = 369, 370 nm) and large Stokes shifts (Δv_{Stokes} = 91700 cm^{-1} and 90900 cm^{-1}). Nucleus-independent chemical shift (NICS) calculations suggested a moderate aromaticity (NICS(0) = -6.00 ppm, NICS(1) = -17.65 ppm) for the substituted 1,2-phosphaborine in comparison to its 1,2-azaborine (NICS(0) = -5.15 ppm, NICS(1) = -20.15 ppm) or benzene (NICS(0) = -8.18 ppm, NICS(1) = -29.68 ppm) analogs.[55]

This example shows that the substitution of benzene with either a BN- or BP unit led to modifications of their optoelectronic properties while the geometrical properties remained similar. In both cases, the absorption/emission properties were modulated upon substitution with heteroatoms combined from groups 13 and 15. To use the presented optoelectronic effect of a BN/BP-substitution, and to stabilize the BN or BP-bonds on the other hand, the embedding of BN/BP-heterocycles in polycyclic aromatic hydrocarbons became a well-established concept. In the following BN- and BP-substituted PAHs will be considered separately.

References

1. W. v. E. Doering, W. R. Roth, F. Bauer, R. Breuckmann, T. Ebbrecht, M. Herbold, R. Schmidt, H.-W. Lennartz, D. Lenoir, R. Boese, *Chem. Ber.*, **1989**, *122*, 1263-1275.
2. D. J. Grant, D. A. Dixon, *J. Phys. Chem. A*, **2006**, *110*, 12955-12962.
3. J. I. C. Wu, P. v. R. Schleyer, *Pure Appl. Chem.*, **2013**, *85*, 921-940.
4. M. Sugie, H. Takeo, C. Matsumura, *Chem. Phys. Lett.*, **1979**, *64*, 573-575.
5. R. M. Minyaev, D. J. Wales, T. R. Walsh, *J. Phys. Chem. A*, **1997**, *101*, 1384-1392.
6. P. G. Campbell, A. J. Marwitz, S. Y. Liu, *Angew. Chem. Int. Ed.*, **2012**, *51*, 6074-6092.
7. I. Haiduc, D. B. Sowerby, *The chemistry of inorganic homo- and heterocycles.* , Acad. Press, New York, **1987**, vol. 1: XXIV, 1–416.
8. H. A. McGee, C. T. Kwon, *Inorg. Chem.*, **1970**, *9*, 2458-2461.
9. B. Cordero, V. Gomez, A. E. Platero-Prats, M. Reves, J. Echeverria, E. Cremades, F. Barragan, S. Alvarez, *Dalton Trans.*, **2008**, 2832-2838.
10. R. T. Paine, H. Noeth, *Chem. Rev.*, **1995**, *95*, 343-379.
11. T. L. Allen, A. C. Scheiner, H. F. Schaefer, *Inorg. Chem.*, **1990**, *29*, 1930-1936.
12. A. Staubitz, A. P. M. Robertson, M. E. Sloan, I. Manners, *Chem. Rev.*, **2010**, *110*, 4023-4078.
13. J. Hoffmann, P. J. Gliese, A. Staubitz, *Group 13–Group 15 Element Bonds Replacing Carbon–Carbon Bonds in Main Group Polyolefin Analogs*, in *Smart Inorganic Polymers*, eds. Evamarie Hey-Hawkins and M. Hissler, Wiley-VCH, Weinheim, **2019**, 17-39.
14. G. E. Coates, J. G. Livingstone, *J. Chem. Soc.*, **1961**, 1000.
15. D. C. Pestana, P. P. Power, *J. Am. Chem. Soc.*, **1991**, *113*, 8426-8437.
16. K. Fujimoto, A. Osuka, *Chem. Sci.*, **2017**, *8*, 8231-8239.
17. J. Kapp, C. Schade, A. M. El-Nahasa, P. von Ragué Schleyer, *Angew. Chem. Int. Ed.*, **1996**, *35*, 2236-2238.
18. J. A. Bailey, P. G. Pringle, *Coord. Chem. Rev.*, **2015**, *297-298*, 77-90.
19. J. H. W. LaFortune, Z. W. Qu, K. L. Bamford, A. Trofimova, S. A. Westcott, D. W. Stephan, *Chemistry*, **2019**, *25*, 12063-12067.
20. S. J. Geier, T. M. Gilbert, D. W. Stephan, *Inorg. Chem.*, **2011**, *50*, 336-344.
21. M. Stepien, E. Gonka, M. Zyla, N. Sprutta, *Chem. Rev.*, **2017**, *117*, 3479-3716.
22. X. Wang, G. Sun, P. Routh, D. H. Kim, W. Huang, P. Chen, *Chem. Soc. Rev.*, **2014**, *43*, 7067-7098.
23. R. F. Chen, C. Zheng, Q. L. Fan, W. Huang, *J. Comput. Chem.*, **2007**, *28*, 2091-2101.
24. H. Braunschweig, I. Krummenacher, J. Wahler, *Chapter One - Free Boroles: The Effect of Antiaromaticity on Their Physical Properties and Chemical Reactivity*, in *Adv. Organomet. Chem.*, eds. A. F. Hill and M. J. Fink, Academic Press, Cambridge, **2013**, vol. 61, ch. Free Boroles: The Effect of Antiaromaticity on Their Physical Properties and Chemical Reactivity, 1-53.
25. M. A. Baldo, S. R. Forrest, *Phys. Rev. B: Condens. Matter*, **2000**, *62*, 10958-10966.
26. F. Riobé, R. Szűcs, C. Lescop, R. Réau, L. Nyulászi, P.-A. Bouit, M. Hissler, *Organometallics*, **2017**, *36*, 2502-2511.
27. P. A. Bouit, A. Escande, R. Szucs, D. Szieberth, C. Lescop, L. Nyulaszi, M. Hissler, R. Reau, *J. Am. Chem. Soc.*, **2012**, *134*, 6524-6527.
28. R. Szucs, P. A. Bouit, L. Nyulaszi, M. Hissler, *ChemPhysChem*, **2017**, *18*, 2618-2630.
29. P. Hibner-Kulicka, J. A. Joule, J. Skalik, P. Bałczewski, *RSC Advances*, **2017**, *7*, 9194-9236.
30. M. Baranac-Stojanovic, *Chemistry*, **2014**, *20*, 16558-16565.
31. R. Carion, V. Liégeois, B. Champagne, D. Bonifazi, S. Pelloni, P. Lazzeretti, *J. Phys. Chem. Lett.*, **2010**, *1*, 1563-1568.
32. S. Dey, D. Manogaran, S. Manogaran, H. F. Schaefer, 3rd, *J. Phys. Chem. A*, **2018**, *122*, 6953-6960.
33. R. J. Burford, B. Li, M. Vasiliu, D. A. Dixon, S. Y. Liu, *Angew. Chem. Int. Ed.*, **2015**, *54*, 7823-7827.
34. Y. Garcia-Rodeja, I. Fernandez, *J. Org. Chem.*, **2016**, *81*, 6554-6562.
35. Y. Liu, S. Y. Liu, *Org. Biomol. Chem.*, **2019**, *17*, 7002-7006.
36. H. Lee, M. Fischer, B. K. Shoichet, S. Y. Liu, *J. Am. Chem. Soc.*, **2016**, *138*, 12021-12024.
37. P. Zhao, D. O. Nettleton, R. G. Karki, F. J. Zecri, S. Y. Liu, *ChemMedChem*, **2017**, *12*, 358-361.

38. D. H. Knack, J. L. Marshall, G. P. Harlow, A. Dudzik, M. Szaleniec, S. Y. Liu, J. Heider, *Angew. Chem. Int. Ed.*, **2013**, *52*, 2599-2601.

39. Z. X. Giustra, L.-Y. Chou, C.-K. Tsung, S.-Y. Liu, *Organometallics*, **2016**, *35*, 2425-2428.

40. P. G. Campbell, E. R. Abbey, D. Neiner, D. J. Grant, D. A. Dixon, S. Y. Liu, *J. Am. Chem. Soc.*, **2010**, *132*, 18048-18050.

41. P. G. Campbell, L. N. Zakharov, D. J. Grant, D. A. Dixon, S. Y. Liu, *J. Am. Chem. Soc.*, **2010**, *132*, 3289-3291.

42. Z. X. Giustra, X. Yang, M. Chen, H. F. Bettinger, S. Y. Liu, *Angew. Chem. Int. Ed.,* **2019**, *58*, 18918-18922.

43. H. Lin, C. R. McConnell, B. Jilus, S.-Y. Liu, F. Jäkle, *Macromolecules*, **2019**, *52*, 4500-4509.

44. B. Thiedemann, P. J. Gliese, J. Hoffmann, P. G. Lawrence, F. D. Sonnichsen, A. Staubitz, *Chem. Commun.*, **2017**, *53*, 7258-7261.

45. W. M. Wan, A. W. Baggett, F. Cheng, H. Lin, A. N. Lamm, S. Y. Liu, F. Jakle, *Chem. Commun.*, **2016**, *52*, 13616-13619.

46. M. J. D. Bosdet, W. E. Piers, *Can. J. Chem.*, **2009**, *87*, 8-29.

47. A. J. Marwitz, M. H. Matus, L. N. Zakharov, D. A. Dixon, S. Y. Liu, *Angew. Chem. Int. Ed.*, **2009**, *48*, 973-977.

48. A. J. Ashe, *Organometallics*, **2009**, *28*, 4236-4248.

49. A. J. V. Marwitz, M. H. Matus, L. N. Zakharov, D. A. Dixon, S.-Y. Liu, *Angew. Chem.*, **2009**, *121*, 991-995.

50. A. Chrostowska, S. Xu, A. N. Lamm, A. Maziere, C. D. Weber, A. Dargelos, P. Baylere, A. Graciaa, S. Y. Liu, *J. Am. Chem. Soc.*, **2012**, *134*, 10279-10285.

51. A. M. Daly, C. Tanjaroon, A. J. Marwitz, S. Y. Liu, S. G. Kukolich, *J. Am. Chem. Soc.*, **2010**, *132*, 5501-5506.

52. C. J. Murphy, A. W. Baggett, D. P. Miller, S. Simpson, M. D. Marcinkowski, M. F. G. Mattera, A. Pronschinske, A. Therrien, M. L. Liriano, E. Zurek, S.-Y. Liu, E. C. H. Sykes, *J. Phys. Chem. C*, **2015**, *119*, 14624-14631.

53. E. W. David, *Organo-phosphorus-boron compound and method of making same,* US-3035095A, **1962**.

54. M.-D. Su, *Mol. Phys.*, **2015**, *113*, 1590-1599.

55. J. H. Barnard, P. A. Brown, K. L. Shuford, C. D. Martin, *Angew. Chem. Int. Ed.*, **2015**, *54*, 12083-12086.

56. H. Braunschweig, C. Horl, L. Mailander, K. Radacki, J. Wahler, *Chemistry*, **2014**, *20*, 9858-9861.

Chapter 3: BN-Substituted Coronene Diimides

3.1 Introduction to BN-Substituted Polycyclic Aromatic Hydrocarbons

Polycyclic aromatic hydrocarbons (PAHs) show outstanding electronic and optoelectronic properties and have applications in organic electronics.[1-6] Due to the tunability of the HOMO-LUMO gap, beneficial conductivity, thermal stability and low-cost raw materials, PAHs are ideal materials for organic solar cells (OSC), organic field-effect transistors (OFET), and organic light-emitting devices (OLED).[7-9] BN-substituted polycyclic aromatic hydrocarbons (BN-PAHs) combine the intrinsically high photostability and thermal stability of PAHs with the electronic properties of BN units. This leads to unique materials with significantly changed absorption, emission and redox properties compared to full carbon PAHs in solution and in the solid-state. In addition, due to the inherent dipole moment of the BN units, it is expected that the orientation in the solid (packing) and the respective charge mobility of the BN-PAH will improve. This could directly affect the performance of materials in organic electronic devices, especially in organic field-effect transistors (OFETs).

There are numerous examples of novel synthetic routes towards BN-substituted PAHs[10-13] and tetracoordinate BN-substituted compounds.[11, 12, 14, 15] But the robust electrophilic annulation reaction, which was initially reported by Dewar[16] in 1958, became most prominent for BN-substituted PAHs because of its synthetic ease (Scheme 31).
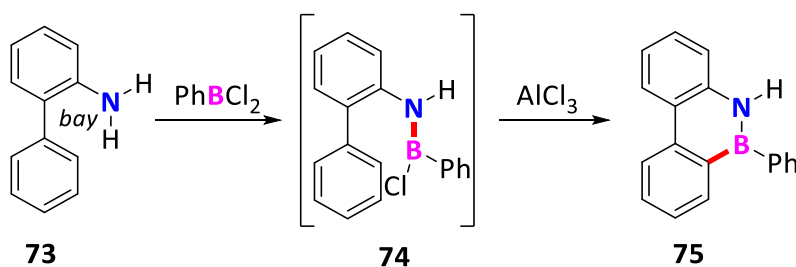
Scheme 31: Synthesis towards a BN-phenanthrene represented by Dewar and coworkers [16]. The novel bond is highlighted in red.

Commonly a *bay*-positioned amine, here 2-aminobiphenyl (**73**), reacts with an electrophilic boron species to form an intermediate arylamino chloroarylborane (**74**). A subsequent Friedel-crafts-type electrophilic borylation yields the BN-PAH, here BN-phenanthrene (**75**). In comparison to a variety of other BN-syntheses, this method became widely used due to the accessibility of the precursors and due to facile synthesis.

Compared to the only weakly fluorescent phenanthrene (**76**, $\Phi_{lum} = 0.09$), the BN-phenanthrene **75** was highly emissive ($\Phi_{lum} = 0.61$) and exhibited a bathochromic shift of the absorption (λ_{abs}(**75**) = 326 nm vs. λ_{abs}(**76**) = 293 nm) (Fig. 44).[17]

76	**75**	**77**
λ_{abs} = 293 nm	λ_{abs} = 326 nm	λ_{abs} = 446 nm
λ_{ems} = 347 nm	λ_{ems} = 341 nm	λ_{ems} = 450 nm
Φ_{lum} = 0.09	Φ_{lum} = 0.61	Φ_{lum} = 0.58
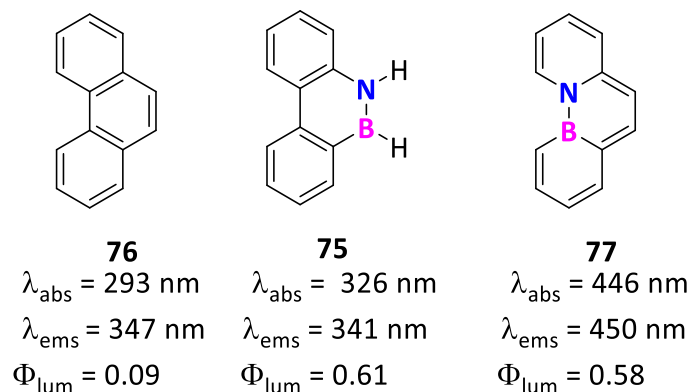
Fig. 44: Structures of phenanthrene (**76**), BN-phenanthrene (**75**) and internalized BN-phenanthrene **77**.[17]

Furthermore, integration of an internalized BN unit in BN-phenanthrene **77** led to an even more drastic effect on the optical properties (λ_{abs} = 446 nm, λ_{ems} = 450 nm, Φ_{lum} = 0.58). This highlights the tuning of the HOMO-LUMO gap by BN-substitution depending on its position in the PAH.[17]

Compared to the rather small BN-phenanthrene **75**, many π-extended BN-substituted PAHs were reported in the last decade. The focus here will be on functional boron/nitrogen-substituted materials with an application in organic electronic devices (OFET, OLED, OSC).[18, 19] Remarkable work by Nakamura, Pei and other researchers was done by merging fundamental main group chemistry with the appliance by utilizing BN-substituted PAHs (Fig. 45).
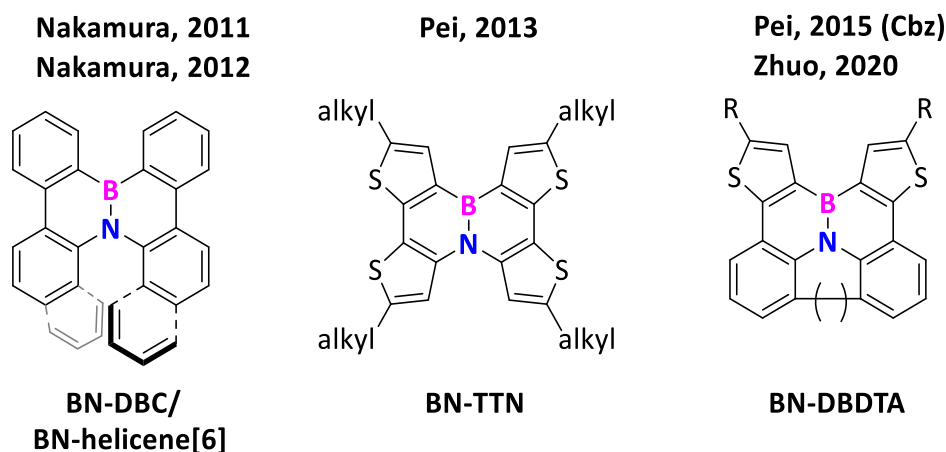
Fig. 45: Molecular structures of **BN-BDC** reported by Nakamura,[20, 21] **BN-TTC** reported by Pei[22] (left) and coronene derivative **BN-DBDTA** independently reported by Pei[23] and Zhuo[24].

As the first example employing a tandem borylation reaction, the BN-substituted dibenzochrysene (**BN-DBC**) and its condensed dimer (**BN-DBC₂**) were synthesized by Nakamura and coworkers in 2011. The deprotonation of a *bay*-positioned amine, *bis*(biphenyl)amine (**78**), with *n*BuLi and reaction with boron trichloride at low temperature gave the intermediate *bis*(biphenyl)amino dichloroborane (**80**) *in situ* (Scheme 32).[20, 21]
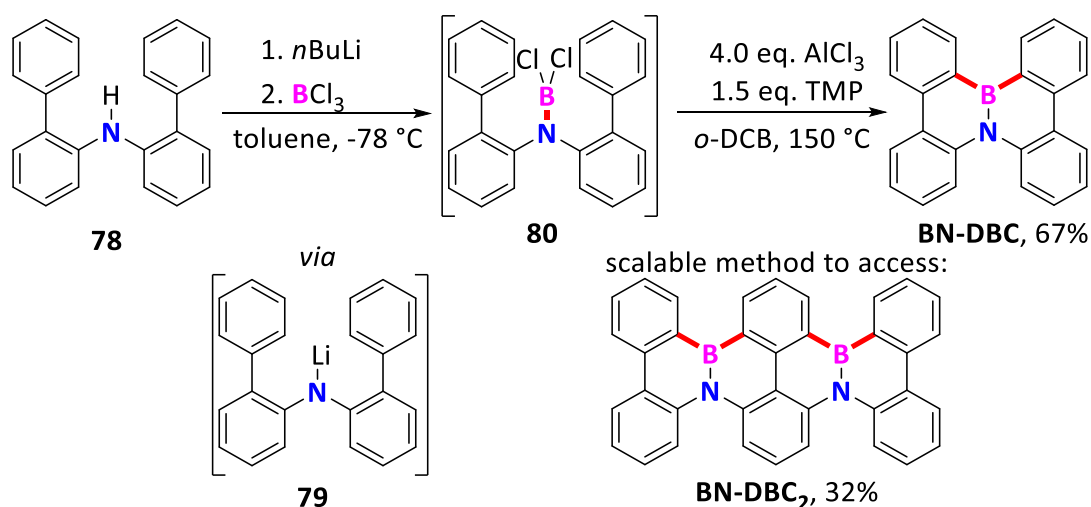
Scheme 32: Synthesis of **BN-DBC** *via* lithiation of *bis*(biphenyl)amine (**78**), reaction with boron trichloride, and final tandem ring-annulation reaction. This methodology was slightly adapted to access the dimer **BN-DBC₂**.[20, 21] The formed bonds here are highlighted in red.

The final ring annulation reaction was conducted with a mixture of a Lewis acid ($AlCl_3$) and an organic nitrogen-base (TMP) to give the **BN-DBC** as a product. This procedure could be applied to access its dimer **BN-DBC$_2$** by simply scaling the amounts of reagents, proving the robustness of this method. Single-crystal X-Ray diffraction analysis revealed a B-N bond length of 1.426(3) Å, which is shorter than in 1,2-azaborine (1.446(2) Å)[25] and diphenylamino diphenylborane (1.441(2) Å, **72**)[26]. The effect of the BN-substitution was analyzed by subjecting this structure and its carbon-analog, dibenzochrysene (**DBC**), to time-resolved microwave conductivity (TRMC) measurements. The **BN-DBC** exhibited intrinsic hole mobility of $\mu_h = 0.07$ cm^2 V^{-1} s^{-1}, which was found to be tenfold higher than that of its carbon analog. This effect was assigned to the strong intermolecular electronic coupling of neighboring **BN-DBC**s, which differed from its chrysene analog as estimated from the X-ray structure. The electrochemical analysis showed that upon BN-substitution, the HOMO-LUMO gap remained similar while LUMO and HOMO of **BN-DBC** were both stabilized.[20] Further photophysical analyses were presented later[27] and revealed that BN-substitution of dibenzochrysene led to a blue shift of the absorption maximum (λ_{max}(**BN-DBC**) = 340 nm, λ_{max}(**DBC**) = 351 nm) and no change of the fluorescence maximum (λ_{max}(**BN-DBC**) = 410 nm, λ_{max}(**DBC**) = 409 nm). Compared to **DBC**, a higher triplet emission energy due to localization of the singly occupied molecular orbitals (SOMO) at the nitrogen and boron atoms was found.[27] Since the observed triplet energy gap ($\Delta(T_1\text{-}S_0)$ = 2.84 eV) was close to typical values for the blue-emitting matrix, 4,4'-*bis*(N-carbazolyl)-1,1'-biphenyl (**CBP**), the **BN-DBC** was used as a host in a phosphorescent organic light-emitting diode (PhOLED) with Ir(ppy)$_3$ as a green emitter. In combination with Ir(ppy)$_3$ (10%), the resulting devices exhibited superior performance characterized by their lower driving voltage, longer lifetime and EQEs of up to 19.5% compared to the same devices using **CBP** only. The all-carbon **DBC**, which had lower triplet energy, did not give a usable OLED device (EQE = 0.008%) at all, which underlines the necessity of a BN unit in these chrysene derivatives for optimal triplet-level modeling.[27] As initial X-ray analysis of **BN-DBC** showed the presence of both the *P*- and *M*-enantiomers,[20] the design was improved by implementing naphthalene units at the nitrogen atom to give rise to the first helical **BN-helicene[6]**.[21] Investigation of hole and electron mobility by TOF methods of (*P*)-**BN-helicene[6]** and the racemate showed that the enantiopure material had similar hole mobility ($\mu_h = 4.6 \times 10^{-4}$ cm^2 V^{-1} s^{-1}) but no detectable electron transport capacity. This hole mobility was not observed for the respective racemate. It was concluded that the orientation in the homochiral film had a drastic influence on the charge mobility. A conformational instability of the BN-helicenes was not observed.[21]

Using a similar synthetic procedure, Pei and coworkers[22] synthesized BN-substituted tetrathienylnaphthalenes (**BN-TTN**) (Scheme 33).
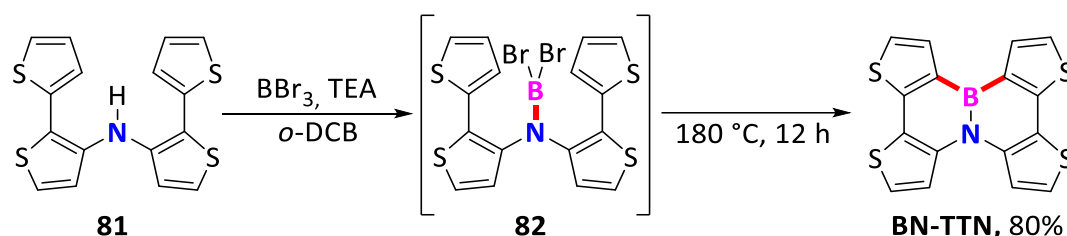
Scheme 33: Synthesis of **BN-TTN** *via* borylation of *bis*(bithienyl)amine (**81**) followed by tandem electrophilic borylation.[22] The formed bonds here are highlighted red.

Due to the electron-rich thienyl substituents, the formation of the BN-heterocycles could be achieved without initial deprotonation with *n*BuLi and additional Lewis acid. Instead, it was sufficient to use boron tribromide and triethylamine. X-ray diffraction analysis revealed a B-N bond length of

1.4774(6) Å, which is slightly longer than the B-N bond length in **BN-DBC**. The twist of the central naphthalene unit was smaller (16.60°) than for **BN-DBC** (38.87°). For improved processability, the **BN-TTN** was substituted with *n*-propyl and *n*-hexyl chains at the thiophene's 5-position. The supramolecular packing differed for both derivatives. The *n*-propyl-substituted derivative **BN-TTN** exhibited a helical packing with a close π-π stacking distance (3.44 Å) and a near dipole intermolecular distance (6.763 Å) of the BN units. The *n*-hexyl-substituted derivative showed a layered packing motif, short CH-π distance (2.72 Å) and longer intermolecular dipole interaction (9.207 Å). Due to close π-stacking distances, low-lying HOMO/LUMO levels (E_{HOMO} = -5.38 eV, E_{LUMO} = -2.07 eV) and thermal stability (>350 °C), the potential of such compounds for organic devices were promising. Consequently, the performance of these structures was tested in OFET devices. The *n*-propyl **BN-TTN** exhibited a high hole mobility (μ_h = 0.12 cm^2 V^{-1} s^{-1}) while lower hole mobilities (μ_h = 0.03 cm^2 V^{-1} s^{-1}) for the *n*-hexyl-substituted **BN-TTN** were found.[22] In a more comprehensive study, alkyl chains on the **BN-TTN** were varied subsequently from methyl to hexyl chains whereas *n*-propyl **BN-TTN** represented the highest hole mobility.[28] The optoelectronic properties of **BN-TTN** could be compared with its all-carbon analog tetrathienylnaphthalene (**TTN**): The absorption maxima in solution were shifted hypsochromically for **BN-TTN**s (λ_{max} = 324 nm) compared to the all-carbon **TTN** (λ_{max} = 364 nm).[29] The electrochemical gap was smaller in the **BN-TTN** (ΔE = 3.31 eV)[22] than in the all-carbon **TTN** (ΔE = 4.01 eV)[29] since the **BN-TTN**s LUMO (E_{LUMO} = -1.43 eV) was more stabilized.

As the **BN-TTN** was found in a twisted conformation, and the C-B bonds were longer than the C-N bonds, the design was stiffened by substitution of two thienyl units with a carbazole or diphenylamino scaffold. The syntheses of the respective systems were conducted via electrophilic ring annulation reaction (Scheme 34).[23, 24]

83 (Cbz) (n = 1)
84 (n = 1 - 4)

BN-DBDTA (Cbz) (n = 1)
BN-DBDTN$_{1-4}$ (n = 1 - 4)
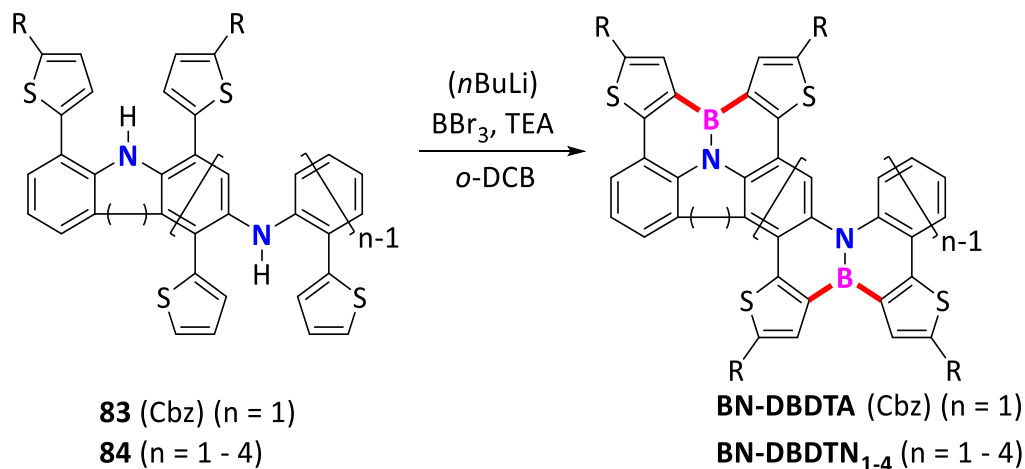
Scheme 34: Synthesis of dibenzodithienonapthylene derivatives *via* borylation of *bis*(biaryl)amine **83/84** followed by tandem (Pei[23]) or multiple electrophilic borylation (Zhuo[24]). New formed bonds here are highlighted red.

Due to the increased rigidity of the carbazole backbone, DFT calculations suggested total planarity of the resulting BN-substituted dibenzodithienoacenapthylene (**BN-DBDTA**). Postfunctionalization of this BN-compound could be performed by bromination *via* NBS, followed by Suzuki reaction with various heteroarenes. This improved the stability of the BN units against a variety of oxidative or basic reagents or even cross-coupling conditions as they were embedded in PAHs.[23] Aryl-substituted **BN-DBDTA** derivatives exhibited a broad variation in absorption (λ_{max} = 301-404 nm) and emission (λ_{max} = 425-567 nm, Φ_{lum} = 0.03-0.43).

In a more recent example, the BN-substituted dibenzodithienonapthylene (**BN-DBDTN₁**) was utilized for the synthesis of its dimers, trimers and tetramers. Analogous to the **BN-DBC**, the electrophilic borylation was performed on up to four *bay*-positioned diarylamines at the same time. The absorption and emission properties of the mono-, di-, tri- and tetramers were determined and a typical bathochromic shift of both the absorption maxima (λ_{max} = 357-420 nm) and emission maxima (λ_{max} = 388-433 nm) was observed upon increasing conjugation length. Surprisingly, these structures stabilized the BN unit in such a way that the sulfur atom in the thiophene could be selectively oxidized with *m*CPBA while the BN unit remained unaffected. The following optical measurements revealed a bathochromic shift in absorption and emission for the thiophene oxide and dioxide derivatives.[24]

Over the last decade, several examples of BN-PAHs were presented, bearing more than one BN unit in the periphery of the π-system. In two examples, referred to as heterosuperbenzenes, BN-substituted coronenes were synthesized *via* tandem internal or three peripheral ring annulation reactions (Fig. 46).

Pei, 2014
internal BN-units

Pei, 2015 and Zhang, 2015
peripheral BN-units

BN-DBTTC

TABC
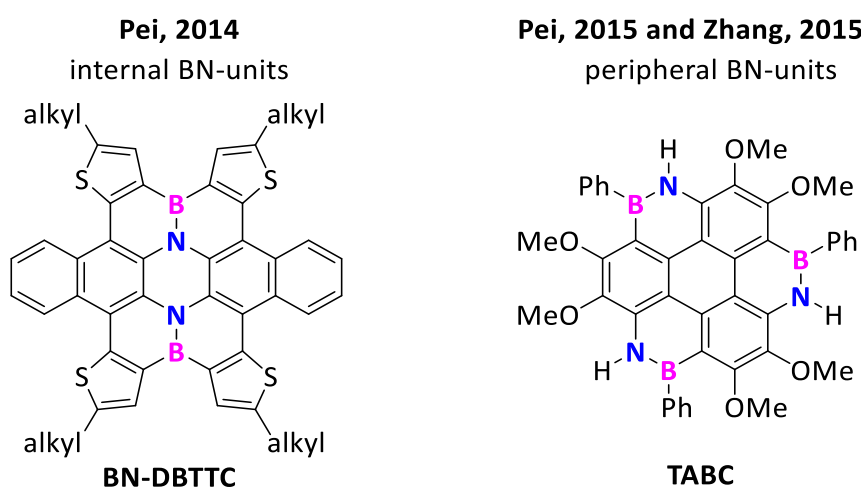
Fig. 46: Heterocoronenes reported by Pei[30] holding two internal BN units (left) and coronene derivatives with three peripheral BN units independently reported by Pei[31] and Zhang[32] (right).

Starting from azaacenes, Pei and coworkers[30] synthesized a BN-coronene with two internal BN units referred to as BN-dibenzotetrathienocoronene (**BN-DBTTC**). X-ray diffraction analysis revealed that these BN-nanographene structures exist in curved conformers. Due to the thermal stability (> 450 °C) of **BN-DBTTC** and their low HOMO level (E_{HOMO}(CV) = -5.07 eV), their performance was tested in an OFET setup. The resulting devices exhibited high hole mobility (μ_h = 0.23 cm² V⁻¹ s⁻¹), accompanied by a low threshold (-3.0 V) and a high on/off ratio (>10⁴). In combination with fullerene-materials and a semiconducting polymer (PTB7), this BN-compound was embedded most recently in an OSC device. A better power conversion efficiency (PCE = 4.75%) and an increased device lifetime were found in an OSC device compared to the solely fullerene/PTB7 version (PCE = 3.91%).[33]

Another example of a BN-substituted coronene was independently reported by Zhang and coworkers[32] and Pei and coworkers[31] in 2015. The tri(azaboro)coronene (**TABC**) was obtained by electrophilic borylation with dichlorophenyl borane of a triphenylene with three amino groups in *bay*-position. X-ray diffraction analysis disclosed the total planarity of the BN-coronene core with a C_3-symmetry and planar nitrogen/boron atoms ($\Sigma_{B/N}$ = 360°). The HOMO level was determined by cyclic voltammetry (CV) and PES measurements and gave values of E_{HOMO}(CV) = -5.40 eV[31]/5.29 eV[32] and E_{HOMO}(PES) = -5.65 eV[31]. Compared to the all-carbon coronene, the energy gap was increased by 0.30 eV since multiple BN units in a graphene-like structure can lead to larger HOMO-LUMO gaps.[31]

This was also observable by the hypsochromic shift of the absorption bands (λ_{abs} = 308, 322, 375 nm) compared to its all-carbon coronene derivative (λ_{abs} = 321, 345, 375 nm) and the reduced molar extinction coefficient ((ε_{max} = 25000[32] vs. 101900[34] M^{-1} cm^{-1}). The luminescence quantum yields (Φ_{lum} = 0.21[31]/0.42[32]) were superior compared to the value of its carbon analog (Φ_{lum} = 0.098[34]). In both reports, high thermal stabilities (>300 °C) were observed, but the compound decomposed in wet solvents *via* protodeborylation and B-Ph bond cleavage. The hydrolyzed structure was analyzed and exhibited a hypsochromically shifted absorption (λ_{max} = 303 nm) and stabilized HOMO (E_{HOMO}(CV) = -5.54 eV). Therefore, it was suggested that the aryl groups on the boron atom had an electron-donating effect on the optical properties and their cleavage could be a suitable method for band-gap tuning in semiconductors.[32]

Most of the examples represent BN-substituted electron-neutral and electron-rich π-systems, but the combination of BN-heterocycles with electron-deficient PAHs was less investigated. The combination of an azaborine unit and the strongly electron-accepting perylene diimide (**PDI**) scaffold to form a **Ph-BNPDI^{Cy}** *via* common BN-annulation was presented by Zhang and coworkers in 2014 (Scheme 35).[35]
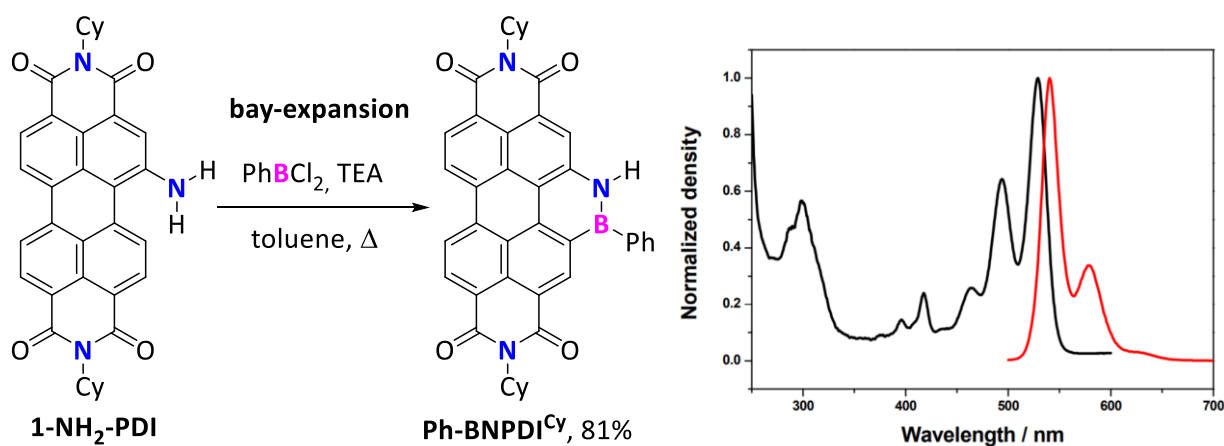
Scheme 35: Synthesis of **BN-PDI^{Cy}** from **1-NH$_2$-PDI** and the respective absorption/emission spectra. Adapted with permission.[35]

The absorption spectrum of **Ph-BNPDI^{Cy}** exhibited an intense maximum (λ_{max} = 529 nm) and a shoulder (λ_{max} = 494 nm). The effect of the BN-substitution was evident since the absorption maximum was red-shifted by 61 nm in comparison to the respective all carbon **benzo-PDI** (λ_{max} = 468 nm).[36] Due to the stabilization of the LUMO by 0.30 eV, compared to the **benzo-PDI**, it was suggested that the azaborine had electron-donating abilities in this case.

However, compared to a recently published **azabenzo-PDI** (λ_{max} = 475 nm),[37] where the BN unit of the **Ph-BNPDI^{Cy}** was preplaced by a CN-unit, also a red-shift of 54 nm is present. Interestingly, the only difference between **Ph-BNPDI^{Cy}** and **azabenzo-PDI** is the boron atom, whose effect on the absorption behavior is quite remarkable. A reason for this was not found in the distribution of the HOMO/LUMO levels, as they were the same in both structures. It was claimed that the BN unit's dipole moment of the **Ph-BNPDI^{Cy}** was the cause for the strong bathochromic shift.[35] The emission maximum was bathochromically shifted by the same value and the luminescence quantum yield (Φ_{lum} = 0.81) was slightly higher compared to the **benzo-PDI** (Φ_{lum} = 0.77) and lower than **azabenzo-PDI** (Φ_{lum} = 0.83).

However, the **Ph-BNPDI^{Cy}** showed superior thermal stability (> 400 °C) and therefore the structure was suitable for vapor deposition processing for the production of organic electronic devices. In combination with a blue-emitting matrix, 4,4'-*bis*(N-carbozyl)-1,1'-biphenyl (**CBP**), the **Ph-BNPDI^{Cy}** was

incorporated in a multilayer organic light-emitting diode (OLED). The highest external quantum efficiency (EQE) was obtained for a **Ph-BNPDI^Cy** dopant ratio of 1.0% with a value of EQE = 1.57%. The electroluminescence spectra of the devices were red-shifted and held a diminished luminance with increasing **Ph-BNPDI^Cy** dopant ratio (Fig. 47).
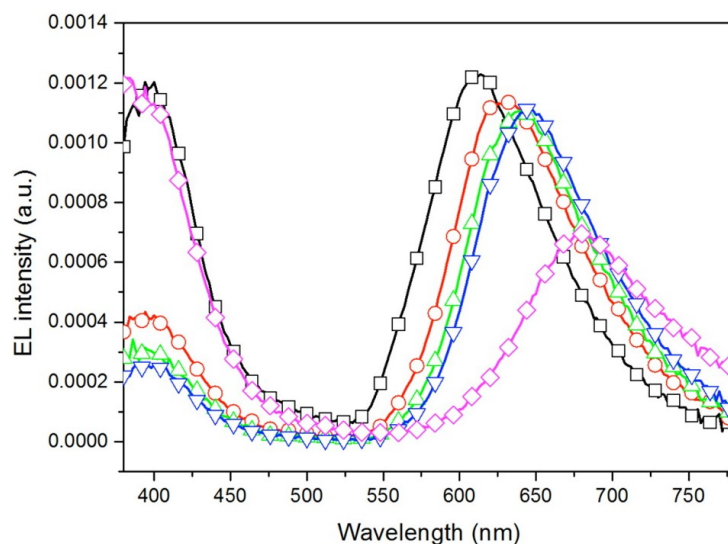
Fig. 47: Electroluminance spectra for OLEDs with **Ph-BNPDI^Cy** doping ratios of 1% (black), 5% (red), 10% (green), 15% (blue), and 100% (magenta). Adapted with permission.[35]

The use of the neat **Ph-BNPDI^Cy** as an emissive layer in the OLED resulted in a barely emissive device with diminished EQE (0.05%). This was assigned to aggregation-caused quenching (ACQ) processes.[35]

In summary, the integration of BN units in PAHs has several advantages. Due to the high reliability of electrophilic borylation reactions, bottom-up approaches to form large PAHs or graphene-like structures are easy to perform. Furthermore, it was shown that the BN motif is highly stabilized by the large carbon scaffold. In most cases a beneficial modification of the optical properties, e.g. increased luminescence quantum yield, bathochromic shift, was observed for a BN-substitution.

3.2 BN-substituted Coronene Diimides (BNCDIs)

3.2.1 Motivation and Model System

Considering the electronic structure of the most present BN-PAHs, they contain relatively electron neutral or even electron-rich rings.[13, 38-41] The combination of BN units with electron-accepting PAHs has been barely investigated until now. Among all PAH-based acceptor materials, rylene (naphthalene/perylene/coronene) diimide (**NDI**, **PDI**, **CDI**) dyes have been most intensively studied because of their excellent (photo)chemical and thermal stability, high absorption coefficients and fluorescence quantum yield.[42-44] As an example, the highest n-channel mobility (μ = 8.50 cm^2 V^{-1} s^{-1}) in an air-stable OFET is based on a naphthalene diimide copolymer.[45] The incorporation of single electron-rich heteroatoms (O,[46] S,[47-49] N[50, 51]) became a promising method for the modification of the optical and electronic properties of these acceptor materials. However, the implementation of BN units into these structures, such as in BN-substituted perylene diimide (**Ph-BNPDI^{Cy}**),[35] remained rare so far.

The objective of this project was to integrate two BN units in an electron-accepting coronene diimide (**CDI**) structure forming a *bis*-BN-substituted **CDI** (**BNCDI**). Furthermore, its photophysical properties were to be studied in comparison to its all-carbon congener coronene diimide, which was presented by Müllen and coworkers[52] in 2011 (Fig. 48).
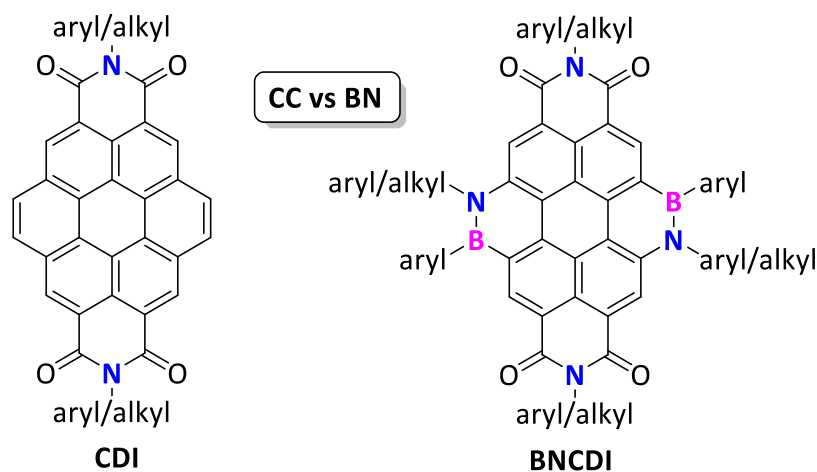
Fig. 48: Molecular structures of coronene diimide (**CDI**) and *bis*-BN-substituted coronene diimide (**BNCDI**). For synthetic purposes and stabilization reasons the BN units might be decorated with aryl substituent.

In addition to studies on the general effect of the BN-substitution, further investigations of the structure-property relationship in respect to the B/N-substituents should be conducted. In fact, the opportunity of tuning the energy gap for the absorption of light of BN-PAHs by adapting the substituents on boron and nitrogen has been unexploited so far. For synthetic reasons, the boron atom has been mostly decorated with electron neutral ligands (phenyl or mesityl). Moreover, the combination of electron-rich motifs at the B/N atom with the electron-accepting coronene diimide represents formally a donor-acceptor-donor (D-A-D) structure, which is commonly used motifs in all-carbon π-conjugated materials. Such types of BN-PAHs were virtually not investigated yet.

Besides the electronic tuning of the **BNCDI**, the modification of the solubility and solid-state properties should be investigated. As it can be expected that the imide groups are electronically decoupled from the **BNCDI** core, these groups can be varied to modify the stacking behavior without altering the optoelectronic properties. Since functionalization of rylene diimides by variation of the imide function was broadly studied prior, the obtained knowledge from **NDI** and **PDI** chemistry[53, 54] should be transferable to the parent **BNCDI**.

3.2.2   Preliminary Work

In my master thesis initial research on the synthesis of 1,7-isomeric pure **PDI**s, their substitution with *n*-hexylamine and the reaction with dichlorothienyl borane (**TphBCl₂**) was performed (Scheme 36).[55]

1,7-DB-PDI^Cy   **1,7-DHA-PDI^Cy**, 8%   **Tph-BNCDI^Cy**, 42%
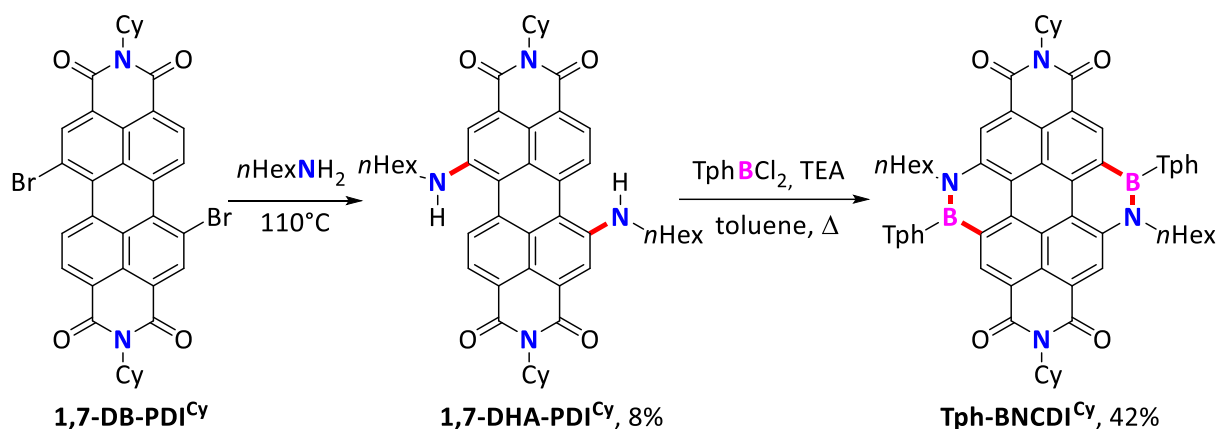
Scheme 36: First synthesis of a **BNCDI** was presented in my master thesis.[55] For the imide substituent the cyclohexyl motif was utilized to allow a comparative study with **Ph-BNPDI^Cy**. Novel formed bonds are highlighted in red.

For the synthesis of the isomeric pure **1,7-DB-PDI^Cy**, a method presented by Jager and coworkers[56] was utilized. The amination process, similar to Wasielewski and coworkers[57], towards **1,7-DHA-PDI^Cy** resulted in low yields and further equal amounts of the dehalogenation product (**1-HA-PDI^Cy**) were formed due to the high temperature in this process. The boron component, thienyldichloro borane (**TphBCl₂**), was synthesized from tetra(2-thienyl)stannane,[58] which was an inefficient process characterized by its low yield. With both precursors in hand, the thienyl-substituted **Tph-BNCDI^Cy** was synthesized, analyzed and initial absorption/luminescence spectra were recorded. The compound showed no luminescence in the solid-state as a result of strong aggregation. Additionally, the synthesis towards the phenyl-derivative **Ph-BNCDI^Cy** was conducted and a UV/Vis spectrum was recorded although the material was not analytically pure. Any further studies on the structure-property relationship were not conducted in the master thesis.[55]

3.3 Synthesis of BNCDIs

After the synthesis of **Tph-BNCDI**[Cy], the structure-property relationship in solid-state and solution of **BNCDI**s should be investigated by a judicious choice of substituents (Fig. 49).
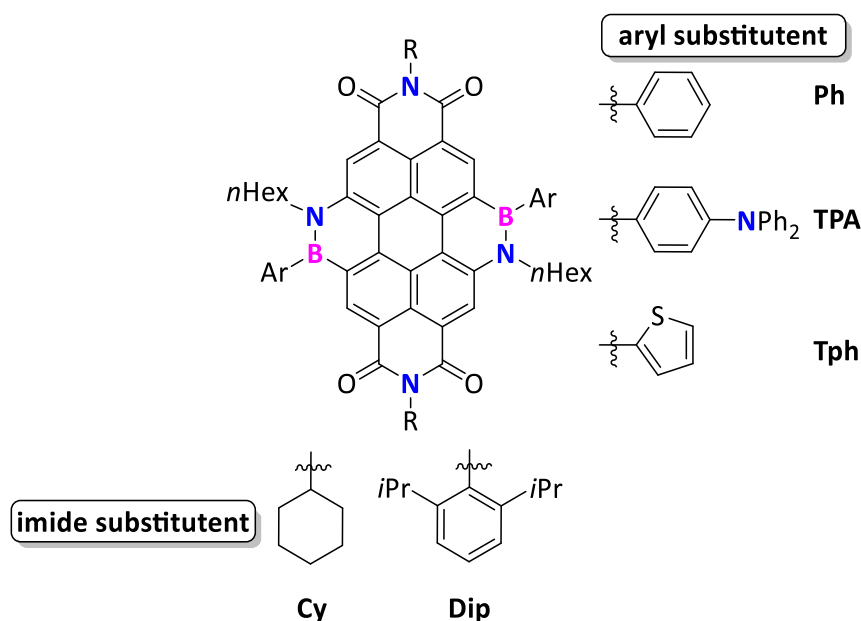
Fig. 49: To modulate the solid-state properties and the optoelectronic properties of the **BNCDI**s the imide and the boryl substituent should be substituted with differing groups.

Next to the presented cyclohexyl substituent at the imide position, further, a 2,6-di*iso*propylphenyl (Dip) group can be attached to the **BNCDI** to modulate the aggregation behavior without affecting the optoelectronic properties. Furthermore, the aryl group at the **BNCDI** can be varied from thienyl to phenyl and triphenylamine to benchmark the effect of the aryl group on the optoelectronic properties.

3.3.1 Synthesis of the Amino-Substituted Perylene Diimides

Since strong aggregation for cyclohexyl-substituted **BNCDI**s was observed, more spacious 2,6-di*iso*propylphenyl (Dip) groups were implemented at the imide position to reduce π-π stacking phenomena. It was expected that the resulting **BNCDI**^{Dip}, compared to the cyclohexyl-substituted derivatives, would have same the optoelectronic properties in solution but less aggregation in the solid-state. The synthetic procedure to access the **1,7-DB-PDI**^{Dip} precursor was described beforehand.[56] The most challenging part in synthesizing **BNCDI** derivatives was the amination of the brominated **PDI** precursors. Therefore, the amination of the 1,7-dibromoperylene diimides **1,7-DB-PDI**^{Cy} or **1,7-DB-PDI**^{Dip} was optimized by reduction of the applied temperature from 110 °C to 60 °C and extension of reaction time from eight hours to three days (Scheme 37).

1,7-DB-PDI (R = Cy, Dip)   **1-HA-7-Br-PDI (R = Cy, Dip)**   **1,7-DHA-PDI (R = Cy, Dip)**
                                              observed but not isolated   50% for both
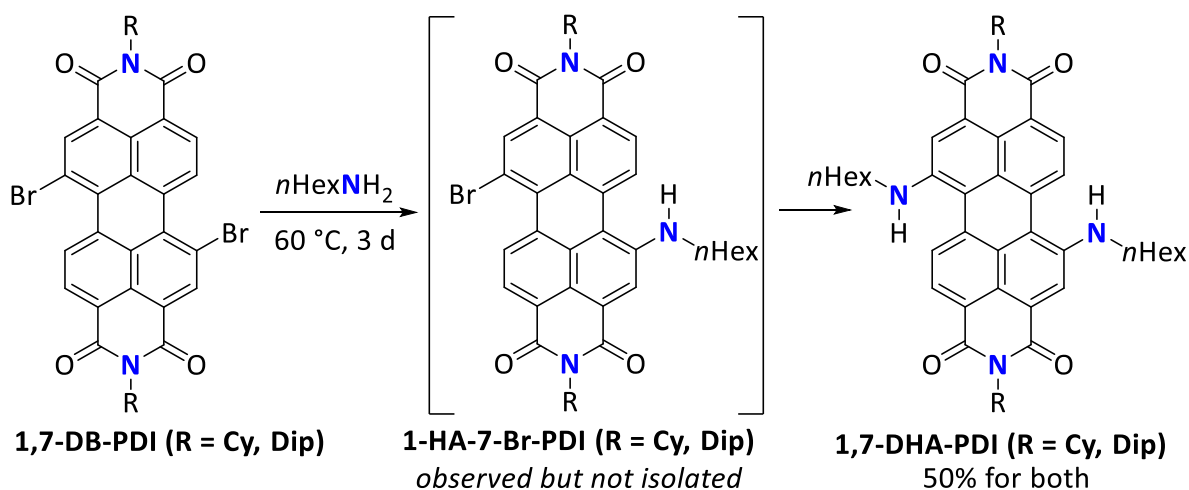
Scheme 37: The synthesis towards 1,7-substituted di(alkylamino) perylene diimides **1,7-DHA-PDI**^{Cy} or **1,7-DHA-PDI**^{Dip} starting from 1,7-dibromo-substituted **PDI**s (**1,7-DBr-PDI**^{Cy} or **1,7-DBr-PDI**^{Dip}). The synthetic details are found in the experimental part.

By this method, the dehalogenation of the mono-aminated intermediate **1-HA-7-Br-PDI**$^{Cy/Dip}$ could be suppressed, and the two observed products could be separated by chromatography. From the initial 8% isolated yield of the product,[55] now both derivatives could be isolated with a yield of 50% each. Unfortunately, it was not possible to upscale this reaction beyond the 2.0 mmol scale without diminishing the yield.

During the synthetic process also the product of a transamination could be isolated (Scheme 38).

1,7-DB-PDI^{Dip} **1,7-DHA-PDI**^{nHex}
                                                                              9%
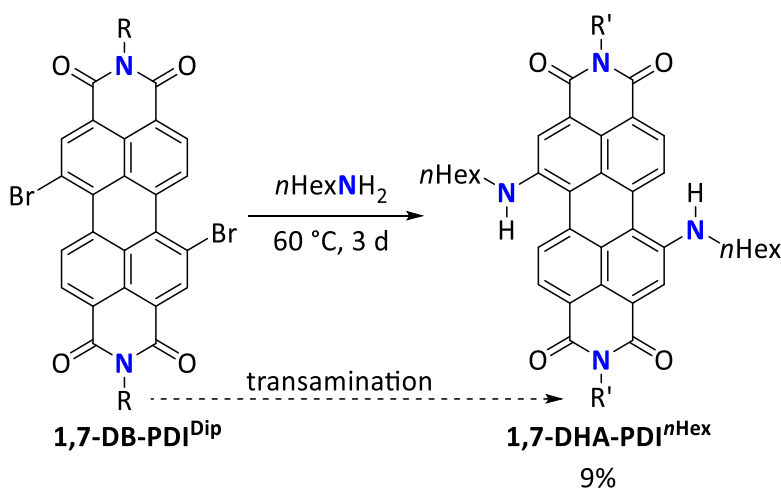
Scheme 38: As side-reaction the transamination of the imide substituent was observed during the amination process. Synthetic details are found in the experimental part.

The concept of using primary amine as reagent and solvent was transferable to *n*butylamine but not to cyclohexylamine or aniline. Though, in the case of *n*-butylamine, the product could not be separated from the monoaminated product. Therefore, the *n*-hexyl moiety was the only substituent that was attachable to the nitrogen atom. Further attempts for coupling of *n*-hexylamine in NMP with pyridine as a base, under Buchwald-Hartwig conditions[59] or copper-mediated cross coupling[60] remained unsuccessful. Therefore, the *n*-hexyl chain remained the only accessible nitrogen-substituent of the azaborine-unit in the **BNCDI** scaffold.

3.3.2   Synthesis of the Aryldichloroboranes

To vary the nature of the aryl substituent at the boron atom, the synthesis of aryldichloro boranes (ArBCl$_2$) was investigated as well. Aryldichloroboranes (ArBCl$_2$) are accessible by electrophilic arene borylation of silylated aromatic systems *via* silicon-boron exchange but so far only a small amount of ArBCl$_2$ species is reported.[61] Therefore, a variety of trimethylsilyl-substituted five-membered heterocycles were synthesized and reacted with boron trichloride at low temperatures (Scheme 39).

Y = **O**, X = H, **85**   **FurTMS**, 22%   **FurBCl$_2$**, no product

Y = **N**Me, X = H, **86**   **MePyrTMS**, 53%   **MePyrBCl$_2$**, no product

Y = **S**, X = Br , **49**   **TphTMS**, 78%   **TphBCl$_2$**, 72%
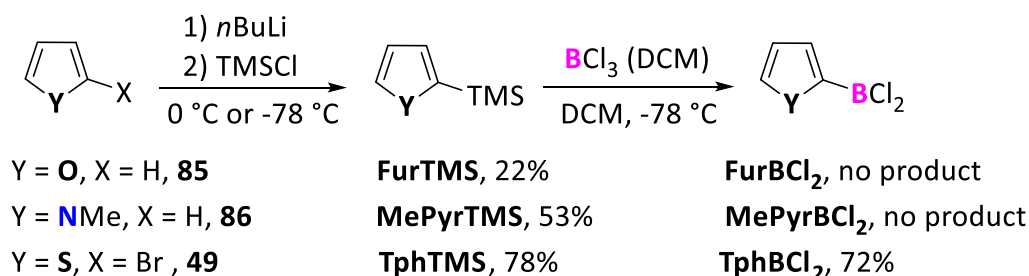
Scheme 39: Synthesis of five-membered heterocyclic boryl derivatives. Synthetic details are found in the experimental part.

For thiophene and *N*-methylpyrrole medium to high yields were obtained in the lithiation-silylation reactions. For furan, a lower yield resulted due to the high volatility of the product **FurTMS**. However, all silylated heterocycles were mixed at low temperatures with boron trichloride solution and the resulting material was distilled. The thienyl dichloroborane (**TphBCl$_2$**) was isolated in high yields whereas only decomposition for the furan (**FurBCl$_2$**) and *N*-methylpyrrole (**MePyrBCl$_2$**) derivatives was observed.

Moreover, reported *bis*-borylation of *bis*-silylated thiophene and bithiophene was investigated (Scheme 40).

X = Br, n = 1, **87**   n = 1, **89**, 99%

X = Br, n = 2, **51** ← CHCl$_3$/AcOH   n = 2, **90**, 92% (from **51**),

X = H, n = 2, **88** ── NBS, 52%   60% (from **88**)
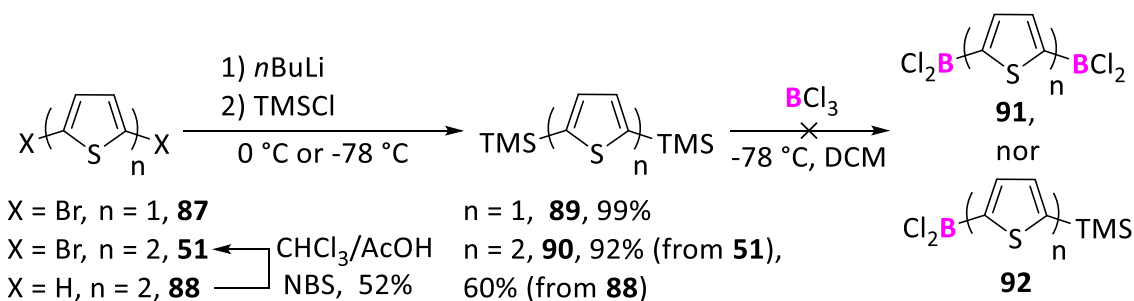
Scheme 40: *bis*-Borylation of thiophene and bithiophene. Detailed synthetic procedures are found in the experimental part.

The *bis*-silylation of thiophene was performed by lithiation of the halogenated precursor (**87**) followed by quenching with trimethylsilyl chloride. Similarly, the *bis*-silylation of bithiophene (**88**) was conducted by the reaction of *n*BuLi with bithiophene (**88**) or the dihalogenated bithiophene (**51**). The latter method resulted in higher yields. As observed by Braunschweig and coworkers,[62] the reaction of

an excess condensed boron trichloride (neat) with *bis*(2,5-trimethylsilyl)thiophene (**89**) should always form the monoborylated product **92**. Unfortunately, these results were not reproducible with boron trichloride solutions. The borylation of *bis*-silylated bithiophene **90**, according to a literature procedure,[62] did not form the desired product **91** nor the mono-borylated bithiophene **92**. Instead, only unidentifiable material was obtained. Therefore, the synthesis of functional mono- or dithiophenes was not further conducted.

Another synthesis of an aryldichloroborane was reported by Marder and coworkers[63] comprising the electron-rich triphenylamine motif. For its synthesis, a silylated triphenylamine was reacted with boron trichloride to form the aryldichloroborane (**TPABCl₂**) (Scheme 41).
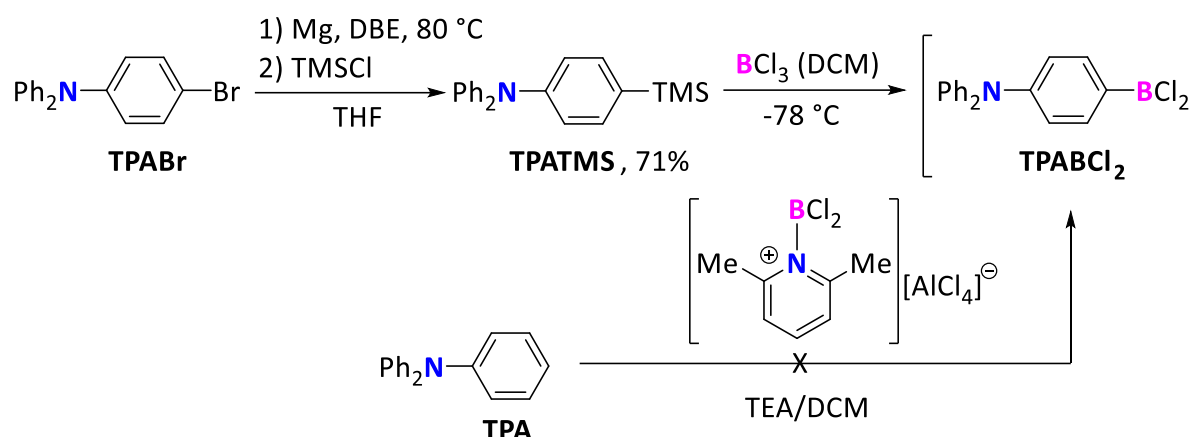
Scheme 41: Synthesis of borylated triphenylamine **TPABCl₂** from silylated triphenylamine **TPATMS**, which was previously synthesized from the halogenated triphenylamine derivative **TPABr**, or neat triphenylamine (**TPA**). Synthetic details are found in the experimental part.

As reported, the **TPABCl₂** could not be isolated and was therefore used *in situ* for further reactions. In addition to this procedure, another reported method[64] using unsubstituted triphenylamine (**TPA**) and [2,6-lutidineBCl₂][AlCl₄] was used. However, the **TPABCl₂** could not be accessed by this methodology.

3.3.3 Ring-Annulation Reactions Towards Various **BNCDIs**

Using a well-established electrophilic borylation reaction of *bay*-positioned arylamines,[65] in total seven novel BN-substituted coronene diimides (**BNCDIs**) were synthesized. The aryl groups (phenyl, 2-thienyl, 4-triphenylamine) at the boron atom were varied and different substituents (*n*-hexyl, cyclohexyl, 2,6-di*iso*propylphenyl) at the imide position were implemented (Scheme 42).
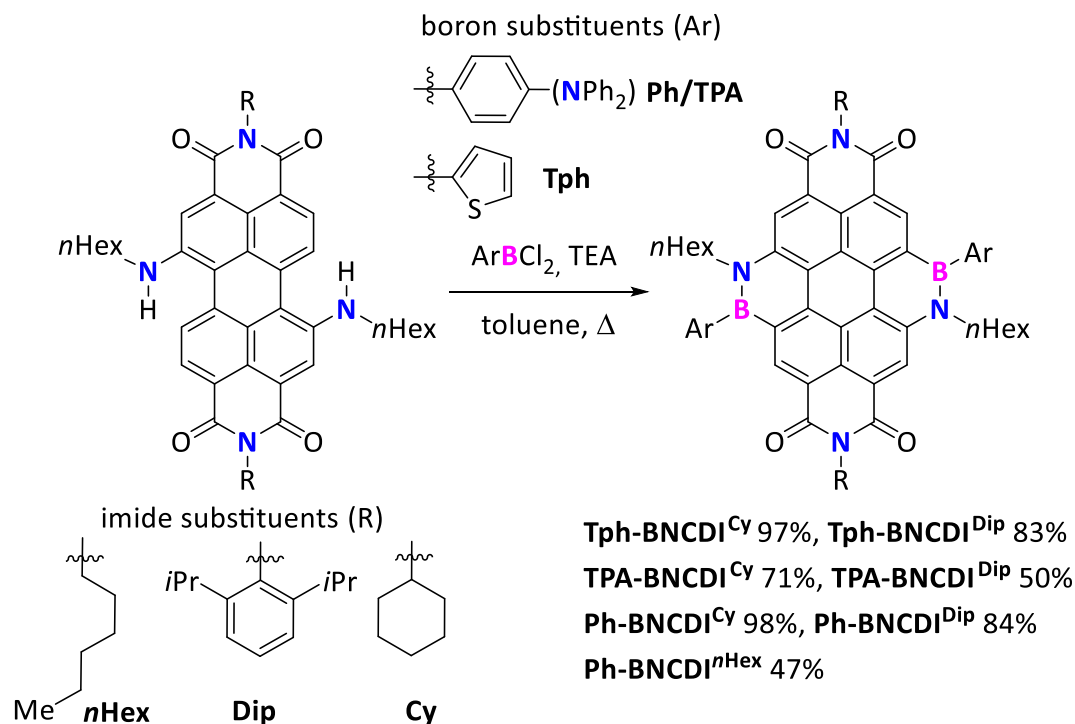
Scheme 42: Tandem electrophilic borylation with various aryldichloroboranes and 1,7-di(n-hexylamino)-substituted **PDI**s holding various substituents at the imide position led to the formation of seven novel **BNCDI**s. Synthetic details are found in the experimental part.

The dual ring annulation reactions using either 2-thienyl, phenyl- or triphenylamino dichloroborane proceeded in moderate to excellent yields. The obtained purple/red amorphous powders showed good solubility in halogenated solvents, toluene, and THF. Since the aromatic perylene protons gave rise to only two signals and the carbon atoms located at the imide position were only gave two signals, the ^{1}H and ^{13}C NMR spectra revealed that both **BNCDI**s were regioisomerically pure (Fig. 50).
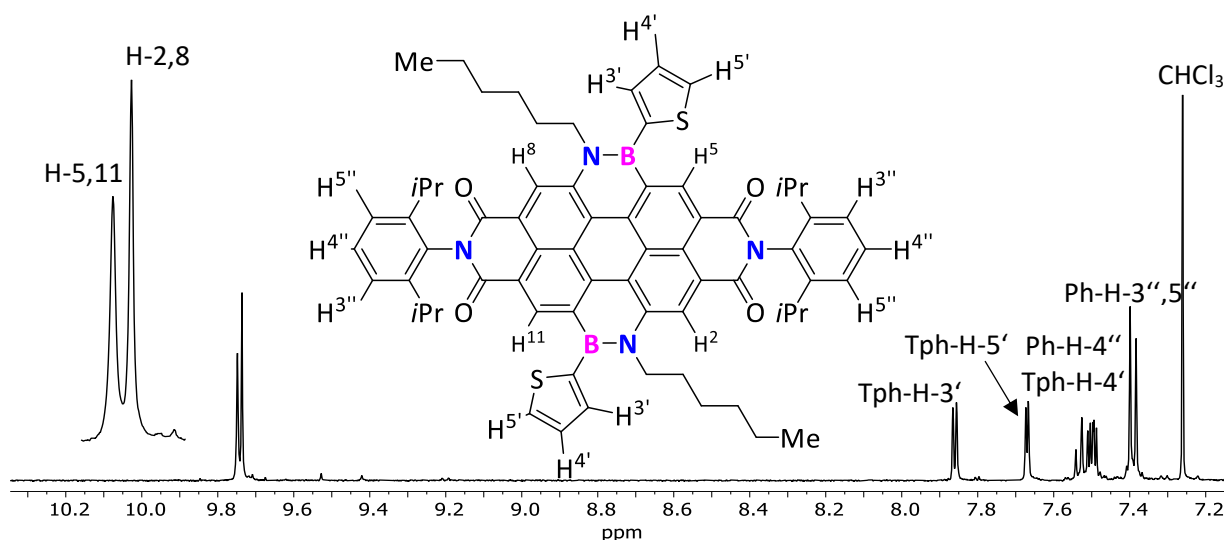
Fig. 50: ^{1}H NMR (500 MHz, CDCl$_3$) spectrum of **Tph-BNCDI^{Dip}** with a focus on the low-field region displaying all aromatic protons.

The H-5,11 and H-2,8 appeared at deshielded chemical shifts, which is typical for perylene/coronene diimides. Due to the C$_2$ symmetry of the molecule, only one set of aromatic rylene protons was found. The chemical structures of all **BNCDI**s were verified by ^{1}H, ^{11}B{^{1}H} and ^{13}C{^{1}H} NMR spectroscopy, FTIR analysis, and high-resolution mass spectrometry (HRMS). Furthermore, all proton and carbon atoms could be assigned by 2D NMR techniques.

Attempts to grow crystals of all **BNCDI** derivatives failed even though using different techniques because only micro-crystallites were formed.

3.4 Overview

With that panoply of **BNCDI**s in hand, an in depth study on their structure-property relationship followed with the focus on two key-aspects: Substitution of the imide or the aryl substituent.

Initial results will present the basic optoelectronic properties of the **BNCDI**s, with the example of thiophene-substituted **Tph-BNCDI**s. Furthermore, the influence of the imide substituents (cyclohexyl and di*iso*propylphenyl), towards the luminescence in solid-state and performance in organic devices will be shown.

In a second study, investigations on the effect of the electronic-donating nature of the aryl substituents towards the optoelectronic properties of the **BNCDI**s are presented. Moreover, general aspects as interaction with Lewis acids/bases and solvents will be discussed intensively.

3.5 Thienyl-Substituted BNCDIs with Varying Imide Substituents

3.5.1 Introduction to Rylene Diimides and Their Photophysical Properties

Rylene diimides are polycyclic aromatic chromophores based on fused naphthalene units which are linked in their *peri*-position and capped with two imide groups. These PAHs are widely used in the dye industry,[66] fluorescence labeling[67, 68] and foremost organic semiconducting devices[69]. In particular, perylene diimides (**PDI**s) and naphthalene diimides (**NDI**s) are the most prominent rylene diimides owing to their outstanding photochemical and thermal stability.[54] Moreover, perylene diimides serve as precursors for dibenzocoronene diimides (**dibenzo-CDI**s), dinapthocoronene diimides (**dinaptho-CDI**s) and coronene diimides (**CDI**) which can be considered as core-extended perylene diimides. So far **CDI**s gained interest mostly for synthetic reasons,[70, 71] but less for their photophysical properties. [52, 72-74] In contrast to a longitudinal π-extension in rylene diimides,[43] Müllen and coworkers[52] reported that a lateral π-extension of **PDI**s to **CDI**s and **dibenzo-CDI**s resulted in hypsochromic shifted absorption maxima compared to their **PDI** analogs (Fig. 51).[75]
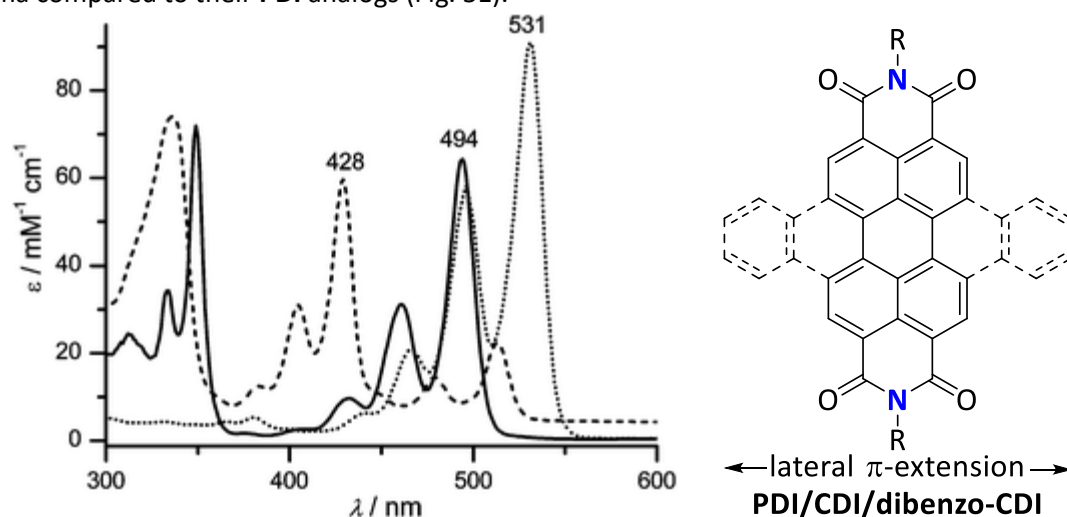
Fig. 51: Absorption spectra of **CDI** (dashed line), **dibenzo-CDI** (solid line) and **PDI** (dotted line). Adapted with permission.[75]

Evidently, the absorption spectrum of **CDI** exhibited a strongly decreased absorption intensity for the lowest energy transition (λ = 510 nm) compared to the **PDI**. This observation can be attributed to the different localization of the electron-density in the HOMO and LUMO level of the **CDI** compared to the **PDI**. The lateral π-extension of a perylene diimide with two CC units does not affect the LUMO level but influences the localization and size of the HOMO orbital coefficients of the **CDI**. In fact, the HOMO orbital of the coronene diimide is equivalent to the HOMO of pure coronene.[76] Due to the **PDI**-like LUMO and the coronene-like HOMO, which were orthogonally aligned, the observed absorption characteristics result.[75]

Notwithstanding, these major drawbacks of a lateral π-extension might be compensable by substitution with a BN unit. In fact, the **Ph-BNPDI^Cy** has a substantial bathochromic shift (61 nm) compared to the respective all-carbon **benzo-PDI**.[35, 36] This was explained by the authors with the present dipole moment of the introduced BN unit.[35] Another explanation could be that the lateral π-extension with a BN unit leaves the frontier orbitals unchanged and therefore a **PDI**-like absorption/emission is obtained.

It was further reported that the **Ph-BNPDI^Cy** suffered from aggregation-caused quenching (ACQ) effects since the neat **Ph-BNPDI^Cy** was barely emissive in an OLED device. Such aggregation is well investigated in PAHs[77] and especially rylene diimides as they have a strong tendency to undergo intermolecular π-

π stacking.[78] While these aggregates are desirable for charge transport,[79, 80] they result in adverse photophysical properties of the rylene diimides when aggregated. To prevent aggregation of rylene diimides, the functionalization of the *bay*-area,[78, 81, 82] the *ortho*-positions,[83, 84] or the imide positions[85-87] became common. The latter method holds the advantage that it leaves the rylene core unaffected as the imide substituent is electronically decoupled from the rylene core. Furthermore, the imide-substitution is synthetically more versatile than substitutions on the rylene core and enables the formation of a series of compounds with varying imide substituents. The fundamentals of designing judiciously chosen imide substituents were based on the fact that sterically demanding or branched substituents increased the solubility of the rylene diimides by prevention π-π stacking effects. Apart from bulky aryl groups, e.g. 2,6-di*iso*propylphenyl (Dip), branched alkyl groups, so-called alkyl swallow tails,[87] are well-established motifs to increase the solubility. Furthermore, the imide-substituents define the aggregation behavior of the rylene diimides as they tune π-π contacts, the formed agglomerates and film morphology.[53] Overall, it should be noticed that the imide substituents play a major role in tuning the structure-property relationship of rylene diimides in organic electronic devices.

In the following the effect of a BN-substitution of coronene diimide (**CDI**) to give the BN-analog **BNCDI** and the resulting optoelectronic properties were studied. Furthermore, two different imide substituents and their effect towards the solid-state properties of the **BNCDI**s was investigated. As example, structures of the thienyl-substituted **Tph**-**BNCDI**s either with cyclohexyl (Cy) and di*iso*propylphenyl (Dip) substituent were chosen (Fig. 52).
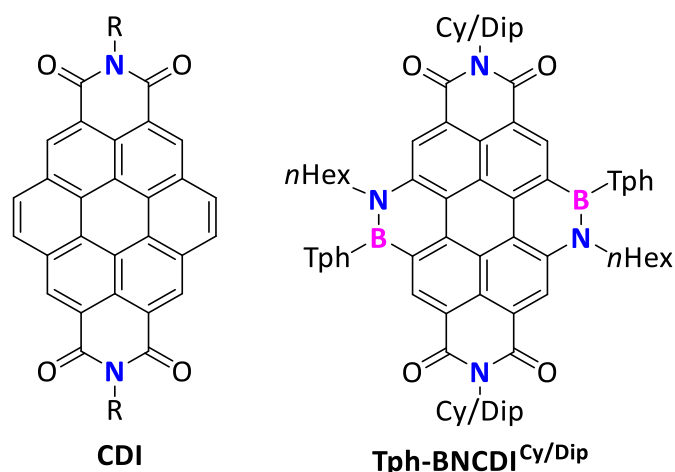
Fig. 52: Molecular structures of **CDI** and **Tph**-**BNCDI**s substituted with cyclohexyl or di*iso*propylphenyl at the imide positions.

As initially strong aggregation for the cyclohexyl-substituted **Tph**-**BNCDI**[Cy] was observed, the di*iso*propylphenyl-substituted **BNCDI**s are expected to aggregate less. This assumption is based on the fact that among a broad variety of alkyl or aryl-substituted **PDI**s, only the di*iso*propylphenyl-substituted **PDI** held no aggregation in high concentrated tetrachloromethane solutions. This was dedicated to the sterical shielding of the four *iso*propyl groups located at the orthogonal-oriented phenyl ring.[88]

3.5.2 Optical Properties of the Thienyl-Substituted **BNCDI**s in Solution

To evaluate the effect of the BN-substitution on the **CDI** scaffold, the optical properties of the **Tph-BNCDI**s were analyzed by UV/Vis absorption and fluorescence spectroscopy in DCM (Fig. 53, Tab. 4).
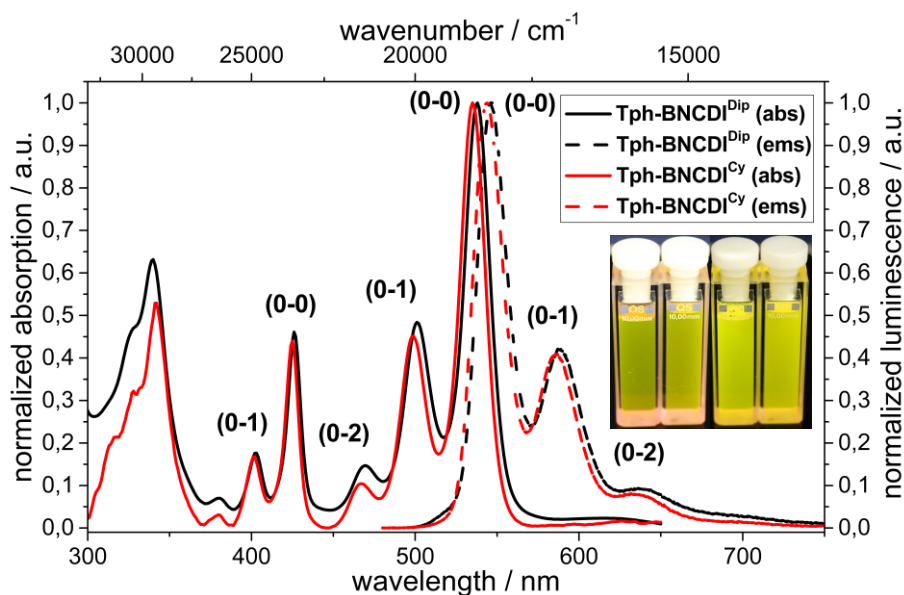
Fig. 53: Absorption and emission spectra of **Tph-BNCDI**[Cy] and **Tph-BNCDI**[Dip] and a photograph of both substances with ambient light (left) and under UV-light (365 nm) (right). The vibronic transitions are labeled for clarity.

Tab. 4: Overview of optoelectronic properties of both **BNCDI**s.

compound	λ_{abs}[a] / nm	$lg(\varepsilon)$[a]	E_{opt}[b] / eV	λ_{ems}[a] / nm	$\Delta\nu_{Stokes}$[a] /cm^{-1}	Φ_{lum}[c]
Tph-BNCDI[Cy]	535	4.74	2.24	544	310	0.95
Tph-BNCDI[Dip]	538	4.85	2.23	546	272	0.94

[a] Measured in DCM solutions (10^{-5}-10^{-6} M). [b] Calculated from the offset wavelength derived from the lowest energy absorption band.[89, 90] [c] Referenced externally against fluorescein in 0.1 M NaOH.

The absorption spectra of both **Tph-BNCDI**s were characterized by their intense maxima at 535/538 nm and a high extinction coefficient ($\varepsilon \approx$ 70794-74131 M^{-1} cm^{-1}). The absorption bands exhibited well-resolved typical vibrionic fine structure and held the strongest band ($S_0{\to}S_1$) at 535/538 nm with further transitions at 498/501 nm and 466/470 nm from the 0-0, 0-1 and 0-2 vibronic bands. The higher energetic transitions ($S_0{\to}S_2$) occurred at 425/426 nm and 401/401 nm for the respective 0-0 and 0-1 vibronic transitions.[91, 92] Moreover, a distinct absorption band is found between 300-350 nm. As expected, the effect of the imide substituents (Cy or Dip) on the optical properties was marginal in solution.[87]

Both **Tph-BNCDI**s exhibited strong luminescence (Φ_{lum} = 0.94/0.95) and small Stokes shifts ($\Delta\nu_{Stokes}$ = 310 cm^{-1} and 272 cm^{-1}) in DCM solution indicating a high rigidity in the ground and excited state. As expected for such a system, the bands were mirror images of the absorbance spectra including the vibronic fine structure with bands at 545/546 nm, 585/588 nm and 634/638 nm. This was attributed to the $S_1{\to}S_0$ transitions and the respective 0-0, 0-1 and 0-2 vibronic bands.[93]

In general, the absorption maxima of the here presented **BNCDI**s were red-shifted compared to their CC-analog **CDI^{Dip}** (λ_{abs} = 494 nm), [52] the **PDI^{Cy}** (λ_{abs} = 525 nm),[87] the CN-isoster **diaza-CDI** (λ_{abs} = 488 nm)[94] and previously reported BN-monosubstituted **Ph-BNPDI^{Cy}** (λ_{abs} = 529 nm)[35] (Fig. 54).

PDI^{Dip}	Ph-BNPDI^{Cy}	Tph-BNCDI$^{Cy/Dip}$	CDI^{Dip}	diaza-CDI^{Dip}
λ_{abs} = 525 nm	λ_{abs} = 529 nm	λ_{abs} = 535/538 nm	λ_{abs} = 494 nm	λ_{abs} = 488 nm
λ_{ems} = 540 nm	λ_{ems} = 540 nm	λ_{ems} = 544/546 nm	λ_{ems} = 498 nm	λ_{ems} = 502 nm
Φ_{lum} = 0.98	Φ_{lum} = 0.81	Φ_{lum} = 0.94/0.95	Φ_{lum} = 0.69	Φ_{lum} = 0.25
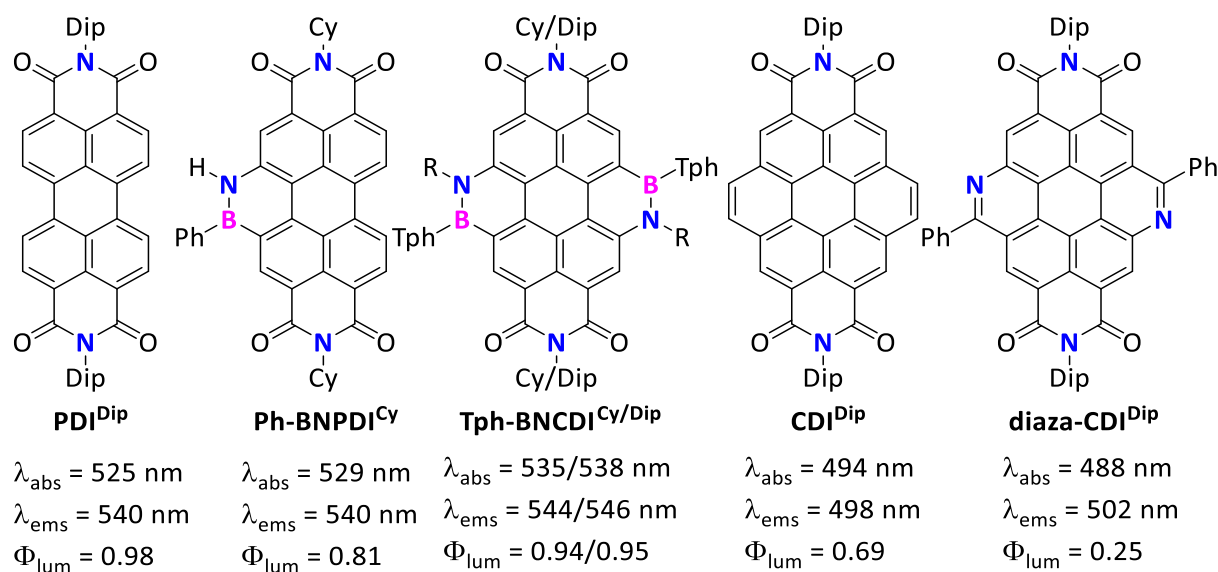
Fig. 54: Comparison of the photophysical properties of **PDI**,[52] **Ph-BNPDI^{Cy}**,[35] the here presented **BNCDI**, its all-carbon analog **CDI**[52] and the CN analog **diaza-CDI**[94].

Compared to all carbon **PDI^{Dip}** (Φ_{lum} = 0.98)[87] and **CDI^{Dip}** (Φ_{lum} = 0.69)[52] similar quantum yields were observed. Only, the CN-isoster **diaza-CDI** (Φ_{lum} = 0.25)[94] was less emissive.

Overall, the bathochromic shift of the absorption maxima λ_{max}(**BNCDI**) = 535/538 nm) of the **BNCDI**s compared to the all-carbon **CDI** (λ_{max}(**CDI**) = 494 nm)[52] was distinct. This effect was attributed to the decrease of the HOMO-LUMO gap due to the BN units, an increased dipole moment and foremost to the orientation of the frontier orbitals.

If one compares the characteristics of the absorption spectra of **Tph-BNCDI**s and **CDI**, systematic differences are found. In fact, the absorption spectra of both **BNCDI**s was more related to the absorption spectrum of a **PDI** than a **CDI** (Fig. 51). Therefore, it was concluded that upon adding two BN units to a perylene core and extending the π-conjugated system in a lateral fashion, the absorption properties of the perylene core were maintained. Interestingly, the absorption bands of **BNCDI**s at 350 nm and 425 nm are both absent in the absorption spectrum of **PDI^{Cy}** but are found in the absorption spectrum of the reported **CDI** unit (Fig. 51). [52, 76] Therefore, it could be concluded that the absorption of the **PDI**-like and the **CDI**-like system were both present in the **BNCDI**s. More details on this hypothesis will be discussed below.

3.5.3 Theoretical Calculations

To understand the optoelectronic properties of **BNCDIs** in comparison of their C=C congener **CDI**, theoretical calculations *via* density functional theory (DFT) were conducted. The ground state-geometry was optimized, and the respective frontier orbitals and energies were extracted to investigate the effect of the BN units to the coronene core (Fig. 55).

PDI-like

LUMO (Tph-BNCDI^{Cy}, E = -3.06 eV)

PDI-like

LUMO (Tph-CDI^{Cy}, E = -2.91 eV)

PDI-like

HOMO (Tph-BNCDI^{Cy}, E = -5.69 eV)

coronene-like

HOMO (Tph-CDI^{Cy}, E = -5.97 eV)

coronene-like

HOMO-4 (Tph-BNCDI^{Cy}, E = -6.55 eV)

PDI-like

HOMO-1(Tph-CDI^{Cy}, E = -6.14 eV)
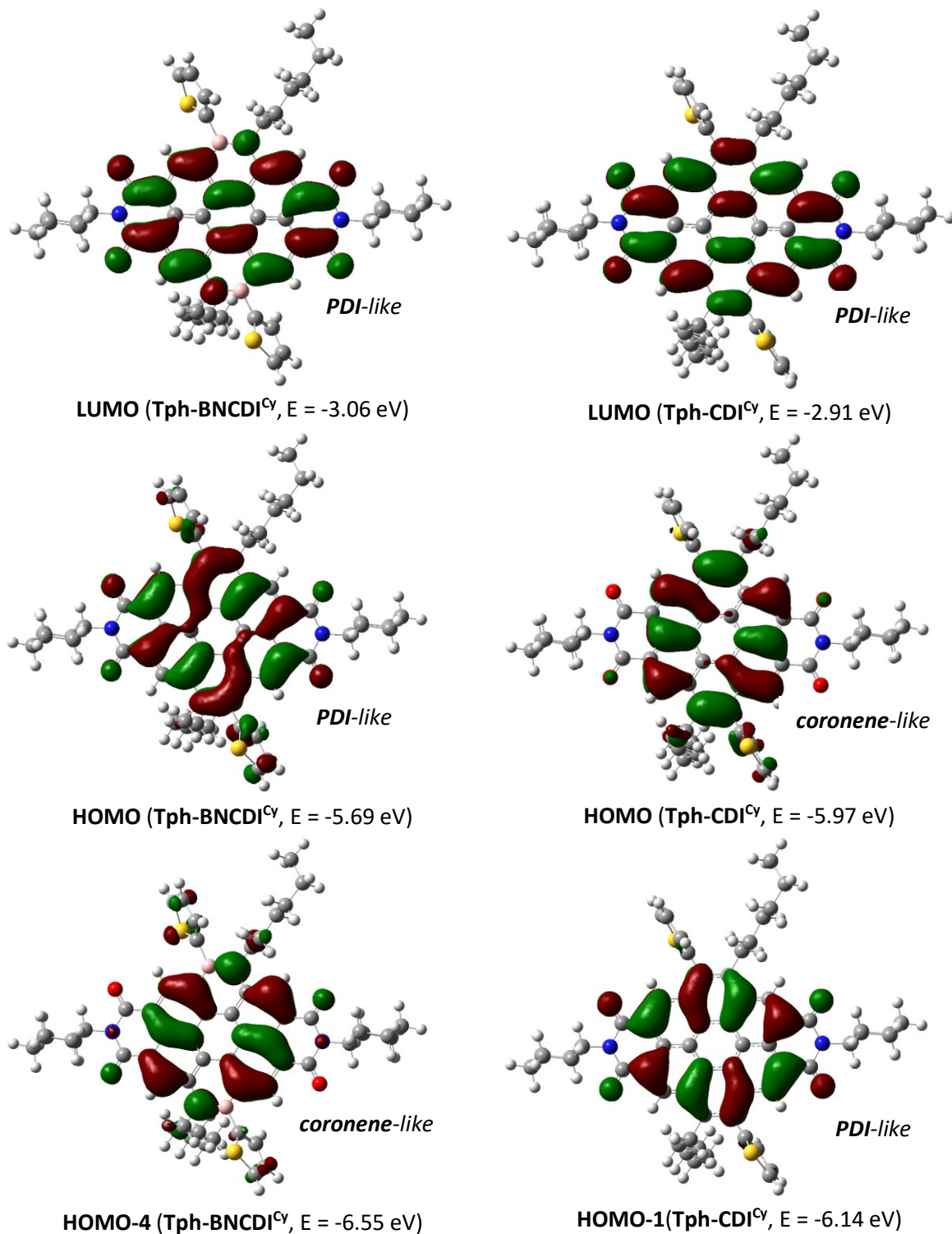
Fig. 55: Display of the frontier orbitals of **Tph-BNCDI^{Cy}** and **Tph**-**CDI^{Cy}** calculated with B3LYP 6-31G*.

The electronic effect of the BN-substitution of the coronene core was clearly visible by comparing the LUMO/HOMO energy levels of **Tph-BNCDI^{Cy}** and **Tph-CDI^{Cy}**. It became evident that an isoelectronic

substitution of two C=C-units by two BN units stabilized the LUMO level (-3.06 eV vs. -2.91 eV) and destabilized the HOMO level (-5.69 eV vs. -5.97 eV) resulting in a smaller HOMO-LUMO gap (2.63 eV vs. 3.06 eV).

The form of the LUMO in both structures was similar to the ones of common rylene diimides[76] and therefore barely affected by the BN-substitution. In contrast, the shape of the HOMO changed drastically: The all-carbon coronene core of **Tph-CDI^{Cy}** exhibited a coronene-like organization of the HOMO whereas the HOMO of the **Tph-BNCDI^{Cy}** was more related to the typical HOMO of **PDI**s[95] *vide supra*. Furthermore, it was found that the coronene-like HOMO of the **Tph-BNCDI^{Cy}** was found in the HOMO-4 whereas the **PDI**-like HOMO of the **Tph-CDI^{Cy}** is displayed in the HOMO-1. This was in agreement to the above-mentioned hypothesis to explain the absorption behavior of the **Tph-BNCDI^{Cy}**. Additionally, the present $S_0 \rightarrow S_2$ transition, which might occur from the HOMO-4 to the LUMO level, and was similar described for a more general CDI motif.[96] Moreover, in both cases, the imide substituents displayed a node located at the imide's nitrogen which underlined the fact that imide substituents are barely interacting with the electronical features of these systems being in perfect agreement with the observed optical properties.

Additionally, nuclear independent chemical shift (NICS)[97-99] calculations for both **BNCDI** and **CDI** were conducted. The NICS values were determined 1 Å above the center of the respective ring and in plane (0 Å). In general, the NICS(0) values correspond majorly to the σ-π contribution to aromaticity and NICS(1) corresponds to the π-π contribution to aromaticity of the respective system.[99] They revealed that the aromaticity of the annulated rings decreased for the BN-derivatives: The azaborine ring had a NICS(0) = -3.25 ppm and NICS(1) = -6.01 whereas the same ring in the **CDI** showed a NICS(0) = -8.68 ppm and NICS(1) = -11.09 ppm. The reduced aromaticity of the BN-structure is a result of the more localized π-electrons on the B-N bond. This trend was in good agreement with the observations for BN-substituted PAHs in general. A detailed NICS analysis of all rings for both **BNCDI** and **CDI** is given in the experimental part.

3.5.4 Electrochemical Characterization

To further estimated the influence of the BN unit on the **CDI** motif, the redox properties of **Tph-BNCDI^{Cy}** and **Tph-BNCDI^{Dip}** were investigated using cyclic voltammetry experiments. Both **BNCDI**s exhibited two fully reversible distinctive reductive waves which is typical for rylene diimide systems[100] as both imides are reduced (Fig. 56, Tab. 5).
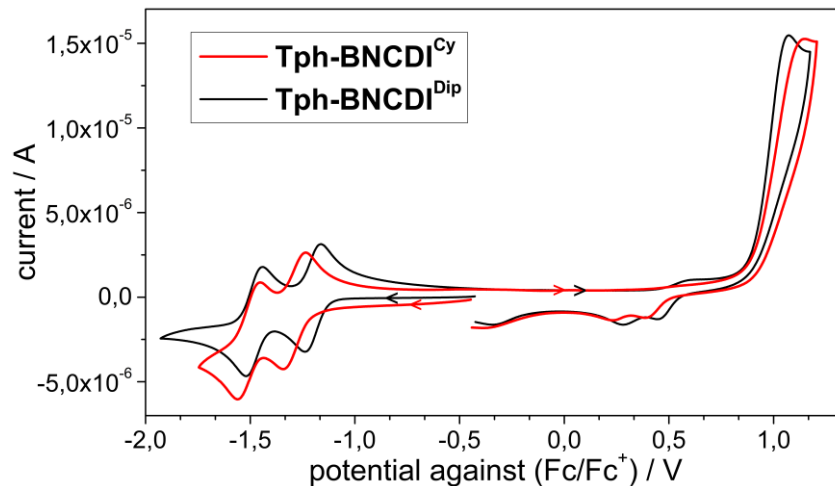
Fig. 56: Cyclic voltammogram of **Tph-BNCDI^{Cy}** (red) and **Tph-BNCDI^{Dip}** (black) in DCM with nBu$_4$NPF$_6$ (0.2 M) as conducting salt using platinum working electrodes at 200mV/s sweep rate.

Tab. 5: Overview of the redox properties and the energy level of the HOMO and LUMO levels of both **BNCDI**s.

Compound	E$_{ox, onset}$ /V	E$_{red, onset}$ /V	E$_{LUMO}$ / eV	E$_{HOMO}$ / eV	ΔE / eV	E$_{opt}$ / eV
BNCDI^{Cy}	0.74	-1.10	-3.69	-5.54	1.85	2.24
BNCDI^{Dip}	0.82	-1.05	-3.75	-5.62	1.87	2.23

All values were referenced against the ferrocene/ferrocenium redox couple. The HOMO/LUMO levels were derived from E$_{LUMO}$= -4.8 eV- E$_{red, onset}$ and E$_{HOMO}$= -4.8 eV - E$_{ox, onset}$.[90]

The onset potentials for the first reductive wave were E$_{red, onset}$ =-1.10/-1.05 V and therefore the energy level of the LUMO (E$_{LUMO}$ = -3.69/-3.75 eV) could be estimated. The electrochemical oxidation of both **Tph-BNCDI**s led to irreversible processes (E$_{ox, onset}$ = 0.74/0.82 V) giving rise to the respective HOMO levels (E$_{LUMO}$ = -5.54/-5.62 eV). Evidently, only a marginal effect of the imide substituents on the oxidation/reduction was found, since the HOMO-LUMO gap was constant (ΔE = 1.85/1.87 eV).

In comparison with the conventional **CDI**s, the LUMO level (E$_{LUMO}$ = -3.69 eV) was unchanged.[75] But since **CDI**s optical gap (E$_{opt}$ = 2.46 eV)[75] was larger than for the **BNCDI**s (E$_{opt}$ ≈ 2.23 eV), it can be concluded that the **BNCDI**s have a destabilized HOMO and therefore lower the HOMO-LUMO gap. This was in good agreement with the calculation presented above.

The same trend was observed for the CN-isoster of the **BNCDI**s, the **diaza-CDI**, were a similar LUMO level (E$_{LUMO}$ = -3.69 eV) and larger optical gap (E$_{opt}$ = 2.47 eV) were reported.[94] These electronic effects of the BN-substitution on the **CDI** were in great agreement with the above-mentioned theoretical investigations.

3.5.5 Luminescence of **Tph-BNCDI**s at Low Temperature

As described before, the influence of the imide group on the luminescence in solution was rather modest. In the following, the structure-property relationship of the **BNCDI**s in relation to their imide substitution in the solid-state was studied (Fig. 57).
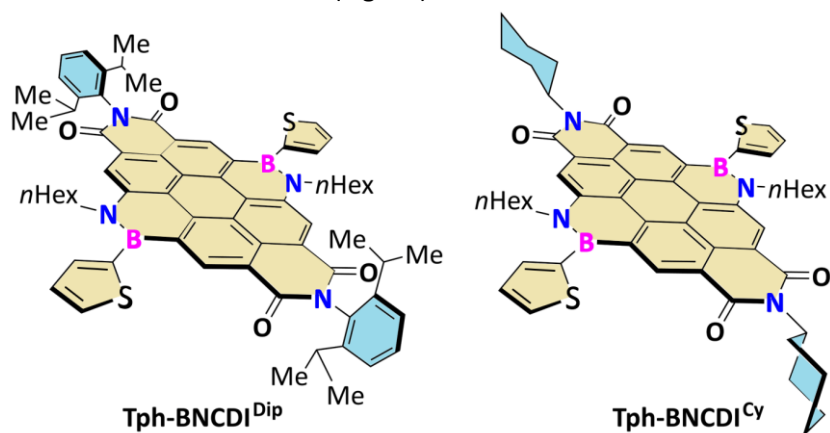
Fig. 57: Molecular structures **BNCDI**s substituted with cyclohexyl or di*iso*propylphenyl at the imide positions.

To investigate the temperature-dependent emission behavior of the novel **Tph-BNCDI**s, they were analyzed in *iso*pentane which forms a glassy state when frozen (113 K). The luminescence of both **BNCDI**s was completely quenched at 150 K, were *iso*pentane was still in the liquid state (Fig. 58).
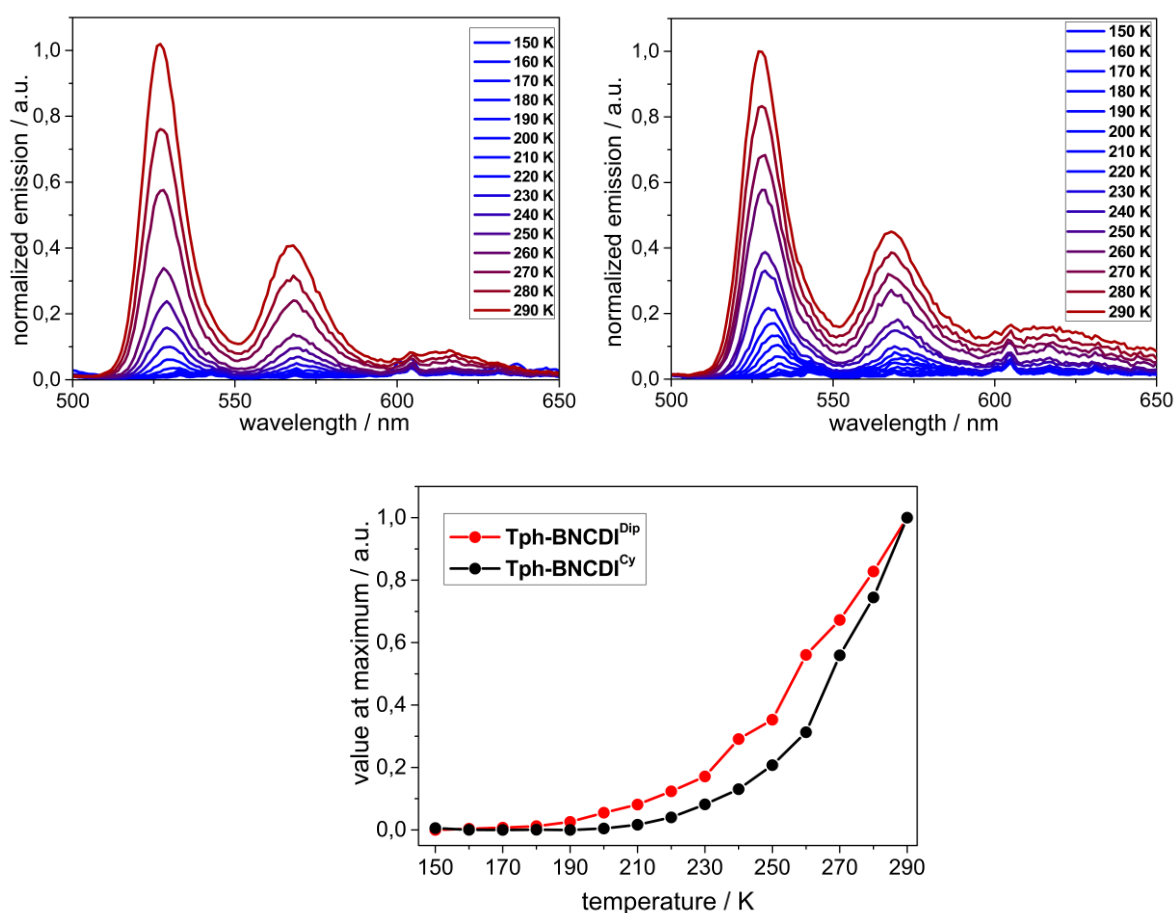
Fig. 58: Emission spectra of **Tph-BNCDI**^{Cy} (top, left) and **Tph-BNCDI**^{Cy} (top, right) in *iso*pentane (5.3 x 10^{-6} M) upon heating from 150 K to 290 K. Comparison luminescence maxima of **Tph-BNCDI**^{Cy} (black) and **Tph-BNCDI**^{Dip} (red).

Detailed temperature-resolved investigation showed that the luminescence properties are depending on the temperature and no appearance of other emission bands occurred. This behavior is

characteristic of an aggregation-caused quenching (ACQ)[101, 102] process due to the reduced solubility of the **BNCDI**s at lower temperatures and further aggregation events. Additional investigation showed that this quenching effect correlated with the nature of the imide group: The luminescence of **Tph-BNCDI**^{Cy} the more rapidly quenched than the **Tph-BNCDI**^{Dip} upon cooling down (Fig. 58, bottom). These results could be indicative of an aggregation behavior of the **Tph**-**BNCDI**s in organic devices.

Similar quenching effects were obtained for the **PDI**^{Cy} and **PDI**^{Dip} which highlighted the effect of the imide substituent on the aggregation in the solid-state. The details of synthesis, characterization and low-temperature luminescence experiments of both **PDI**s can be found in the experimental part.

3.5.6 Optical Properties of the **BNCDI**s in PMMA Matrix

Notwithstanding the initial observations on ACQ behavior and the fact that both **BNCDI** were not emissive in the solid-state, it was assumed to generate high luminescence solid-state materials by dispersing the **BNCDI**s in poly(methylmethacrylate) (PMMA) matrix. The blending experiments were performed with dopant ratios of 0.75%, 1.5%, 4.8%, 9.0% and 50% (Fig. 59).

Tph-BNCDI^{DIP} **(PMMA)**
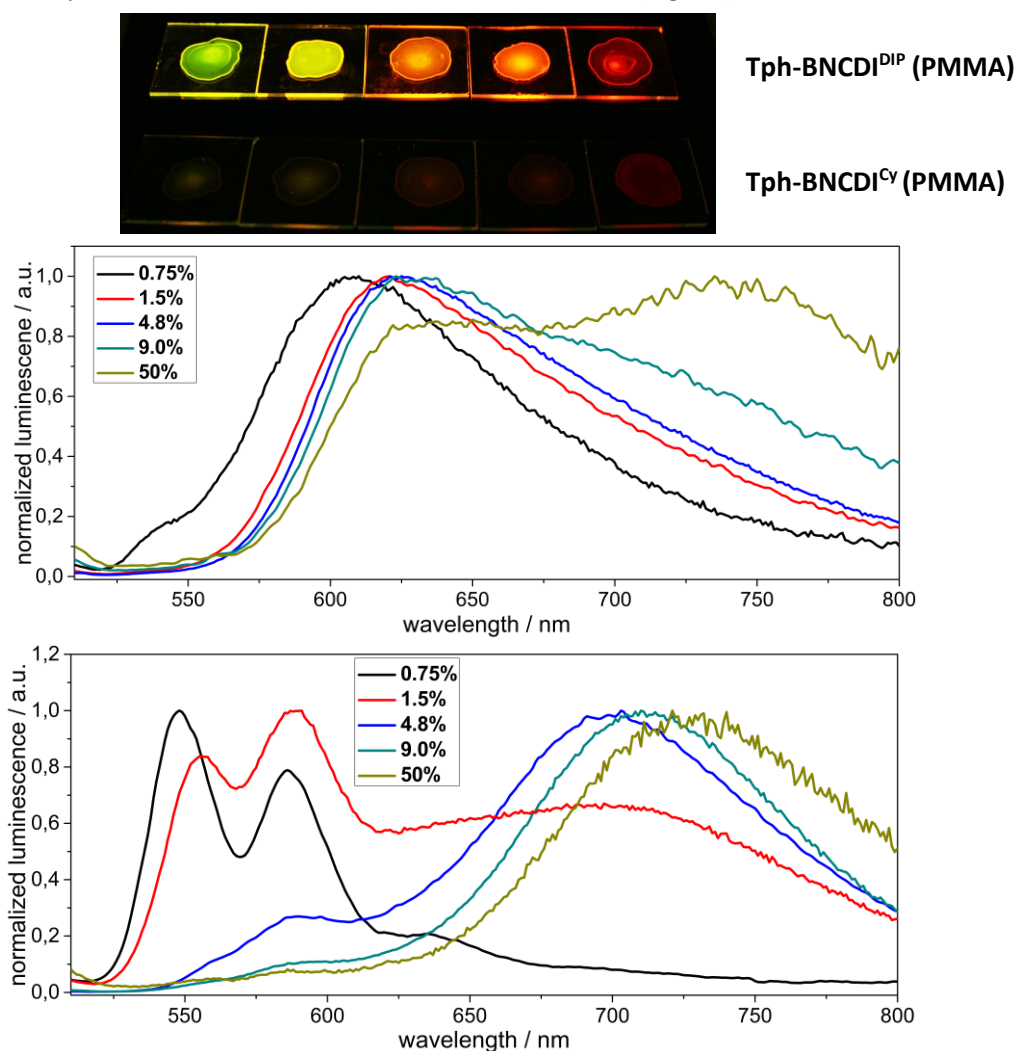
Tph-BNCDI^{Cy} **(PMMA)**

Fig. 59: Image of the PMMA films with different weight ratios (from left to right: 0.75%, 1.5%, 4.8%, 9.0% and 50%) of both **Tph-BNCDI**s under irridiation of UV light (365 nm)(top). Emission spectra of the PMMA blends of **Tph-BNCDI**^{Cy} (middle) and **Tph-BNCDI**^{Dip} (bottom) with different dopant ratios.

The emission properpties of **Tph-BNCDI**^{Cy} and **Tph-BNCDI**^{Dip} in wavelength and intensities of the emitted light were visible to the naked eye (Fig. 59, top). In fact, the luminescence of the **Tph-BNCDI**^{Dip} changed from yellow-greenish to a deep red while the luminescence of the **Tph-BNCDI**^{Cy} was barely

visible and underlined the aggregation-caused quenching in this **BNCDI** derivative. Compared to the optical properties observed in solution, a low amount of **Tph-BNDI**[Cy] (0.75%) in PMMA resulted in a red-shifted emission with a broad signal around 605 nm (Fig. 59, middle). This represented a shift of approximately 80 nm towards the signal observed in DCM solution (Fig. 53) and might arise from emission of aggregates.[103] Upon increasing the dopant rate, bathochromic shifts and broadening of the signals towards the NIR region were noticed. Using an equal amount of **Tph-BNCDI**[Cy] and PMMA a new band could be observed at 750 nm covering the whole emission spectra from 600 nm to 800 nm whilst the fluorescence was barely visible because of ACQ effects.

Repeating the experiment but changing the imide substituent from cyclohexyl to di*iso*propylphenyl moiety, drastic changes in the solid-state emission were observed. In the marginal dopant rate of 0.75% the emission spectrum of **Tph-BNCDI**[Dip] was only slightly red-shifted and exhibited the same characteristics as in solution (Fig. 53). Since the vibrionic transitions were clearly observable, it was assumed that only monomeric emission occurred. Doubling of the **Tph-BNCDI**[Dip] dopant rate (1.5%) resulted in a small bathochromic shift of the first emission band and an increase of the 0-1 transition. However, when such monomers begin to aggregate, the 0-1 transition commonly increases as it was for similar aggregated **PDI**s.[44, 104] Moreover, a new broad band arose (λ = 610-800 nm) with a maximum around 705 nm. With increasing the dopant rate an emission signal in the dark red region (690-730 nm) was visible which was, again, indicative for the emission of aggregates.[103]

Comparing the experimental results for **Tph-BNCDI**[Cy] and **Tph-BNCDI**[Dip] several conclusions were drawn. For the same dopant ratios (0.75% and 1.5%) monomeric emission for **Tph-BNCDI**[Dip] was detected but not for **Tph-BNCDI**[Cy]. This led to the conclusion that the di*iso*propylphenyl substituent of **Tph-BNCDI**[Dip] was more efficient to prevent aggregation than the cyclohexyl-substituent of **Tph-BNCDI**[Cy]. This observation was in good agreement with knowledge obtained from the **PDI** derivatives.[88]

The difference between the **Tph-BNCDI**[Cy] and **Tph-BNCDI**[Dip] in the PMMA films was also investigated by optical microscopy. In the **Tph-BNCDI**[Cy]/PMMA blend needle-like agglomerates[105] were observed whereas nano-spheres[106] in the **Tph-BNCDI**[Dip]/PMMA blend could be detected (see experimental part, Fig. 84).

From the luminescence experiments at low temperature and in PMMA blends, the conclusion could be drawn that the imide substituents had a strong influence on the aggregation in the solid-state resulting in tuning the luminescence properties. These preliminary experiments were good indicators for the performance of both **Tph-BNCDI**s in organic light-emitting diodes.

3.5.7 Thermal Properties of **Tph-BNCDI**s

The thermal properties of both **Tph-BNCDI** were studied and compared to their **PDI** derivatives to evaluate their stability towards thermal evaporation processes to manufacture OLEDs (Fig. 60).

structure	T_{95} / °C
Tph-BNCDI^{Cy}	396
PDI^{Cy}	403
Tph-BNCDI^{Dip}	391
PDI^{Dip}	449
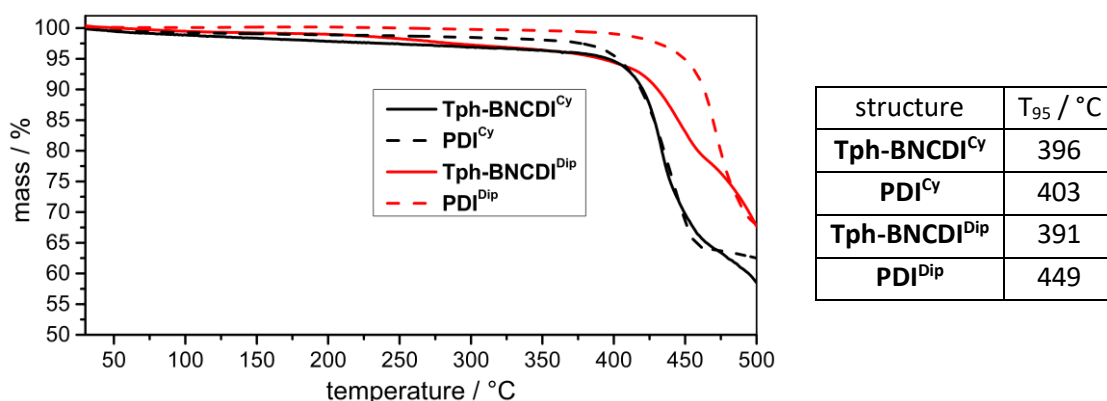
Fig. 60: Thermogravimetric analysis of **BNCDI**s and **PDI**s with 10 °C/min with 20 mL/min nitrogen gas flow. Furthermore, the temperature (T_{95}) is given at which 5% mass loss occurred.

Both **Tph-BNCDI**s decomposed at temperatures higher than 390 °C which was comparable to the decomposition temperatures of respective **PDI^{Dip}** and **PDI^{Cy}**. This analysis underlines the concept of stabilizing labile BN units in thermally stable PAH structures and suggested sufficient stability for thermal evaporation processes. Furthermore, in dynamic scanning calorimetry (DSC) experiments no melting or crystallization in the range of -80 °C to 300 °C could be observed for both **BNCDI**s. This supports the fact that both amorphous **BNCDI**s showed no crystallization or phase transition at this temperature range which is essential for sufficient performance in OLED devices.

3.5.8 Organic Electronic Devices with **Tph-BNCDI**s

To study the charge transport ability of **Tph-BNCDI**s, the **Tph-BNCDI^{Cy}**, which showed more intense aggregation behavior, was integrated in an bottom-gate bottom-contact n-type OFET device. The OFET was manufactured and analyzed by Emmanuel Jacques at IETR (Univ. Rennes 1, France). The transfer characteristics of the OFET were measured in linear and saturated regime (i.e. V_{DS} = 20 V and V_{DS} = 50 V) (Fig. 61).
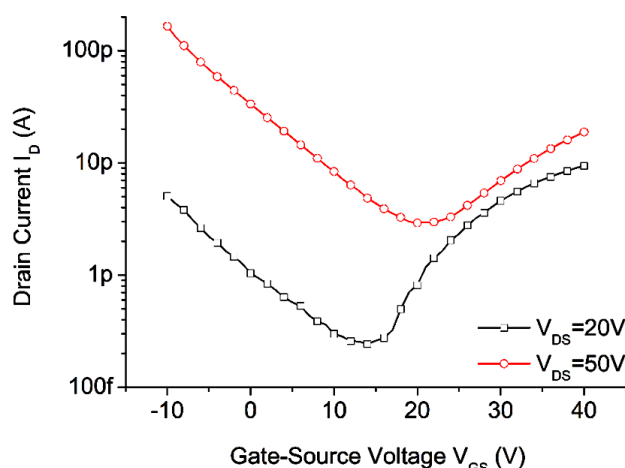
Fig. 61: Transfer characteristics in linear (20 V) and saturated (50 V) regime of the n-type OFET with **Tph-BNCDI^{Cy}** measured under ambient conditions.

The linear field-effect mobility was estimated to μ_{FE} = 1.02 x 10^{-8} cm^2 V^{-1} s^{-1} while in the saturated regime, field-effect mobility was μ_{FE} = 4.34 x 10^{-8} cm^2 V^{-1} s^{-1}. The classical electrical parameters of OFET were defined by its low conductivity (μ_e = 3.42 x 10^{-6} cm^2 V^{-1} s^{-1}), low on/off-current ratio (I_{on}/I_{off} = 36)

and high threshold voltage ($V_{th} \approx 21$ V). The OFET device was also annealed at 150 °C to induce reorganization of the semiconducting layer. At this temperature, the linear field-effect mobility was slightly increased to $\mu_{FE} = 2.68 \times 10^{-8}$ cm^2 V^{-1} s^{-1} and the threshold voltage was shifted ($V_{th} \approx 16$ V) due to a decreased defect density in the device. This preliminary result showed that the **BNCDI**s in general are capable of charge transportation in organic devices.

After evaluating the solid-state luminescence in PMMA matrix, promising optoelectronic, thermal and charge transportation properties, both **Tph-BNCDI**s were used as emitters in organic light emitting devices (OLEDs). The manufacturing of the devices was conducted by Bernard Geffroy at LPICM (Palaiseau, France). The general set-up for the multistack OLEDs was is displayed below (Fig. 62).
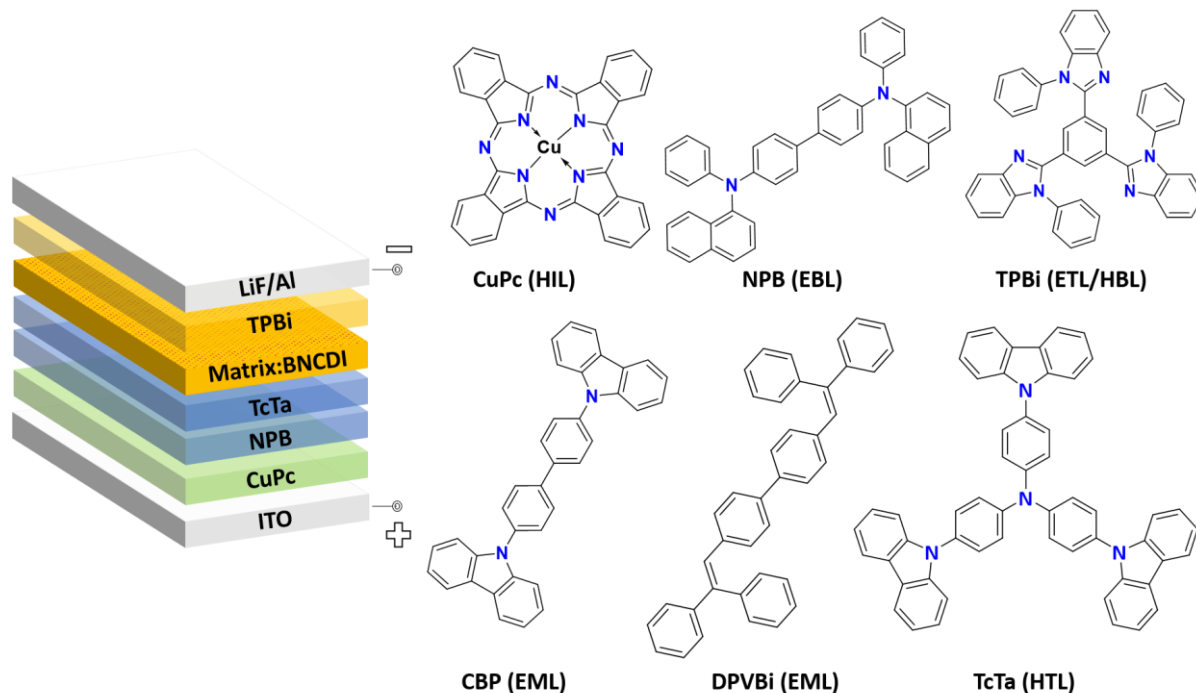
Fig. 62: Architecture of the utilized multi-stack OLED and molecular structure of the two utilized matrices.

Copper phthalocyanine (CuPc) represented the hole injection layer (HIL), *N,N'*-di(1-naphthyl)-*N,N'*-diphenyl-(1,1'-biphenyl)-4,4'-diamine (NPB) was the electron blocking layer (EBL), *tris*-(4-carbazoyl-9-yl-phenyl)-amine (TcTa) the hole transporting layer (HTL) and 2,2',2''-(1,3,5-benzinetriyl)-tris(1-phenyl-1-H-benzimidazole) (TPBi) was the electron transporting and hole blocking layer (ETL/HBL). The **Tph-BNCDI**s were co-sublimed with two different blue-matrices (**CBP** or **DPVBi**) defining the weight-ratio by adjusting the partial pressure of the respective substrates. The general set-up for the multistack OLEDs was ITO/CuPc (10 nm)/NPB (40 nm)/TcTa (10 nm)/EML (20 nm)/ TPBi (50 nm)/LiF (1.2 nm)/Al (100 nm).

Since no luminescence in the solid **Tph-BNCDI$^{Cy/Dip}$** was observed, all devices were realized with a matrix/dopant set-up with either 4,4'-*bis*(*N*-carbazolyl)-1,1'-biphenyl (**CBP**) or 4,4'-*bis*(2,2-diphenylvinyl)-1,1'-biphenyl (**DPVBi**) as host and the respective **BNCDI**s as dopant.

The first OLED devices (**A**-**B**) with doping ratios of 1.5% and 3% **Tph-BNCDI**^{Cy} were constructed with **CBP** as a matrix to a draw direct conclusion to the reported **Ph-BNPDI**^{Cy35} OLED. The observed electroluminescence spectra revealed two main emission bands at 400 nm, arising from the host, and a broader emission at 550 nm from the **Tph-BNCDI**^{Cy} (Fig. 63).
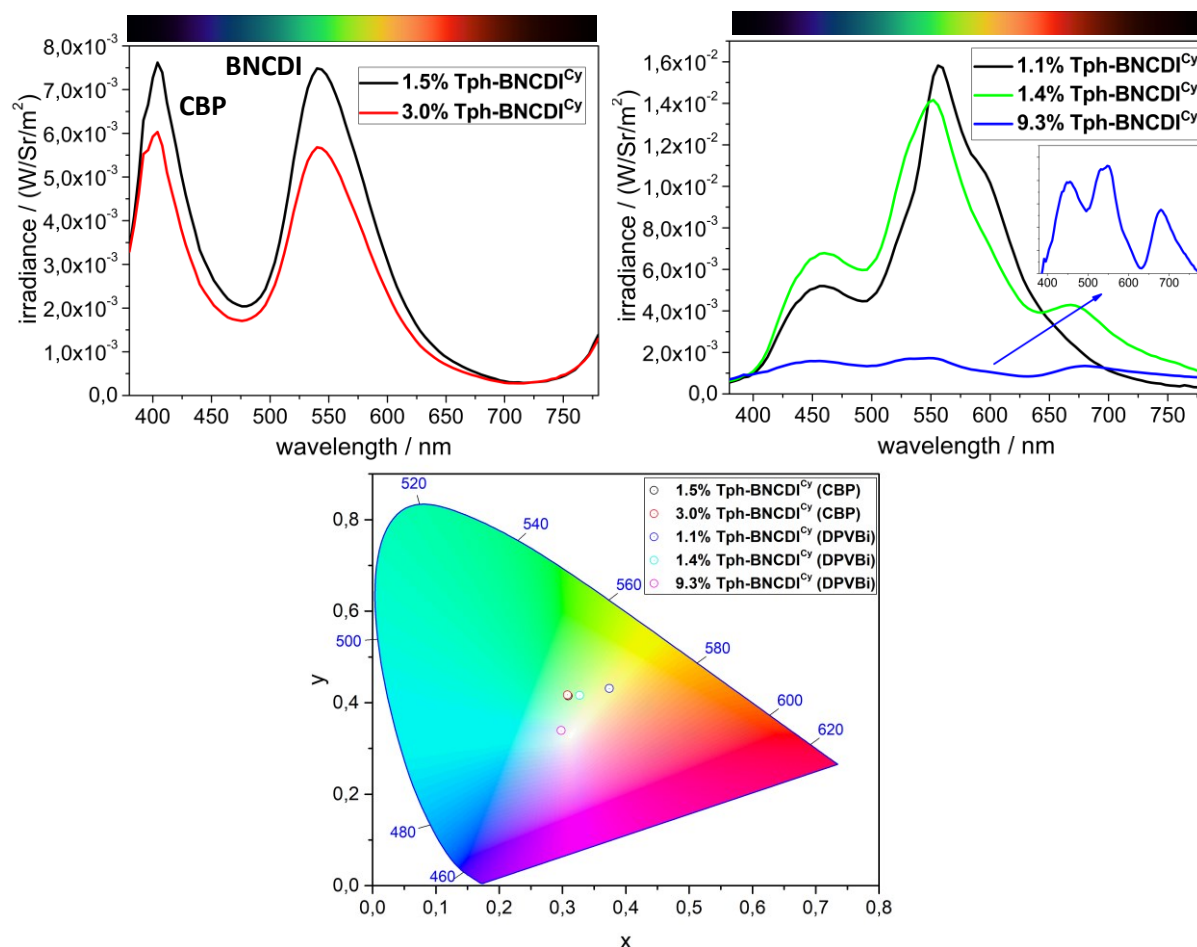
Fig. 63: Electroluminescence spectra of **Tph-BNCDI**^{Cy} with **CBP** as host system with dopant rates of 1.5% and 3% (top, left) and of **Tph-BNCDI**^{Dip} with **DPVBi** and dopant rates of 1.1%, 1.4% and 9.3% (top right). Furthermore, the respective CIE chromaticity diagram of all **Tph-BNCDI**^{Cy}-based devices is displayed (bottom).

The OLEDs gave yellow and green light as evidenced by the CIE coordinates (Fig. 63, bottom, Tab. 6).

Tab. 6: Electroluminescent performance of devices **A**-**E**.

composition	device	doping ratio (%)	EQE[a] (%)	cd/A[a]	lm/W[a]	luminance[b] (cd/m^2)	CIE values[b] x; y
CBP: **Tph-BNCDI**^{Cy}	**A**	1.5	0.7	1.5	0.5	442	0.309; 0.415
	B	3.0	0.6	1.3	0.4	371	0.308; 0.417
DPVBi: **Tph-BNCDI**^{Cy}	**C**	1.1	1.4	3.3	1.3	1001	0.374; 0.431
	D	1.4	1.4	2.7	1.1	842	0.327; 0.416
	E	9.3	0.3	0.4	0.1	117	0.298; 0.339

[a] Recorded at 10 mA/cm². [b] Recorded at 30 mA/cm².

The increase of the doping ratio (device A/B) did not modify the performance of the OLED. Furthermore, the luminance (442/317 cd/m²) and the EQE (0.7/0.6%) of both devices were at a low level compared to the reported **Ph-BNPDI**^{Cy} OLED, with the **CBP** as host (EQE values up to 1.5% and luminance (>1000 cd/m²)).[35]

Since these devices' performances were low, an another blue-emitter **DPVBi** was used as a matrix and with a dopant rate from 1.1% to 9.3% **Tph-BNCDI^{Cy}** (devices **C-E,** Fig. 63). The observed electroluminescence for device **C** showed two significant bands at 450 nm, from the host, and 540 nm, from **Tph-BNCDI^{Cy}**, resulting in a turquoise light (x = 0.252, y = 0.344). Device **C** exhibited an EQE of 1.4%, a brightness of 1001 cd m^{-2}, and a power efficiency of 1.3 Lm W^{-1}. The raise of the dopant rate to 9.3% (device **E**) decreased the overall performance of the device (Tab. 6). Presumably with higher dopant ratio of **Tph-BNCDI^{Cy}** ACQ processes are favored which was expected from the experiments in the PMMA blend and observed as well in the OLED consisting of **Ph-BNPDI^{Cy}**.[35].

Since the best matrix/dopant interaction was obtained with **DPVBi** in the previous devices, devices **F-J** with **Tph-BNCDI^{Dip}** were fabricated with the same matrix. Since the only difference between **Tph-BNCDI^{Cy}** and **Tph-BNCDI^{Dip}** was in their supramolecular arrangement and not their optoelectronic properties, a direct conclusion towards the effect of the imide substituent can be drawn. Device **F** exhibits two main emission bands located at 460 nm and with slightly higher intensity at 560 nm resulting from the matrix and the **Tph-BNCDI^{Dip}** (Fig. 64, Tab. 7).
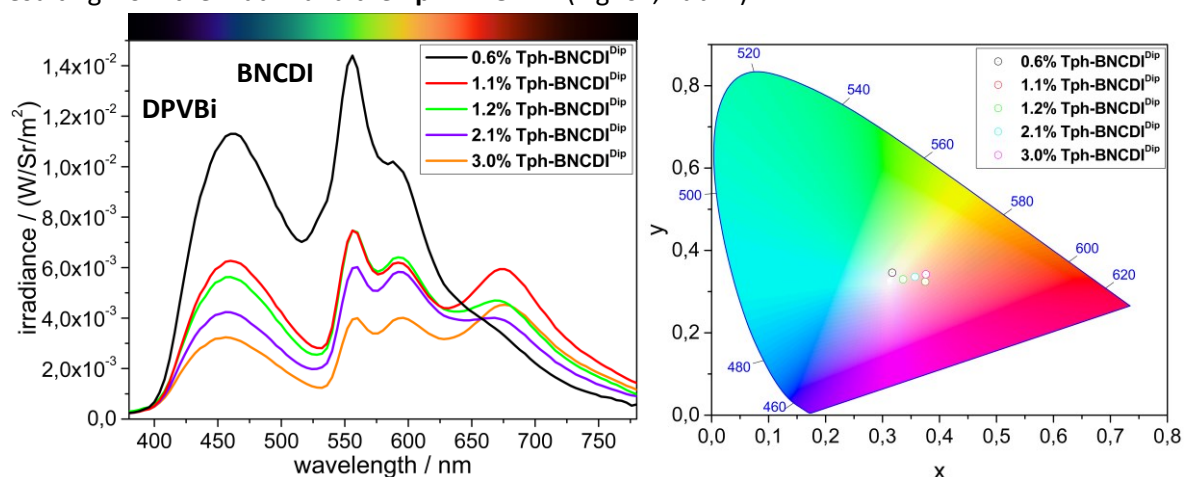
Fig. 64: Electroluminescence spectra of devices **F-J** with different dopant rate of **Tph-BNCDI^{Dip}** in **DPVBi** matrix (left) and the respective CIE chromaticity diagram (right).

Tab. 7: Electroluminescent performance of devices **F-J**.

composition	device	doping ratio (%)	EQE[a] (%)	cd/A[a]	lm/W[a]	luminance[b] (cd/m^2)	CIE values[b] x; y
	F	0.6	1.5	2.7	1.3	800	0.317; 0.346
DPVBi:	**G**	1.1	1.3	1.8	0.9	530	0.347; 0.336
Tph-	**H**	1.2	1.1	1.6	0.7	480	0.357; 0.336
BNCDI^{Dip}	**I**	2.1	0.9	1.3	0.6	380	0.376; 0.342
	J	3.0	0.8	1.0	0.5	275	0.375; 0.324

[a] Recorded at 10 mA/cm^2. [b] Recorded at 30 mA/cm^2.

The latter band showed a small shoulder which might be related to the vibronic structure of the **BNCDI** core. The CIE coordinates (device **F**: x = 0.317; y = 0.346) are close to white light (x = 0.330; y = 0.330). Device **F** exhibited an EQE of 1.5%, a brightness of 800 cd m^{-2}, and power efficiency of 1.3 Lm W^{-1}. Upon increasing the amount of **Tph-BNCDI^{Dip}** (devices **G-J**) the overall intensity decreased whereas a new band at 690 nm occurred. This might be related to aggregation processes. In fact, a similar band was observed in the blend of **Tph-BNCDI^{Dip}** with PMMA (Fig. 59). By increasing the dopant ratio, the performance of these devices decreased significantly. Interestingly, devices **G-J** showed light emission at the region of white light.

3.5.9 Conclusion on Thienyl-Substituted **BNCDI**s with Varying Imide Substituents

Initially, the optoelectronic properties of thienyl-substituted **BNCDI**s were investigated. A large bathochromic shift and a higher ε compared to the reported all-carbon coronene diimides were observed. The reason for this was the different appearance of the frontier orbitals and a smaller HOMO-LUMO gap. The imide substituents (cyclohexyl or di*iso*propylphenyl) had virtually no influence on the optoelectronic properties in solution but in the solid-state matrices (OLEDs and PMMA) and in low-temperature luminescence studies: It was found that the cyclohexyl moiety was less effective in preventing aggregation-caused quenching than the di*iso*propylphenyl substituent.

In PMMA blends the **Tph-BNCDI^{Cy}** held emission of aggregates even with weight ratios low as 0.75%. In comparison to this, the **Tph-BNCDI^{Dip}** exhibited solution-like emission at the same weight ratio. As both materials were deployed in host matrices in a multi-stack OLED setup the same trend was observed: The **Tph-BNCDI^{Cy}** displayed inferior aggregation-caused quenching properties compared to the **Tph-BNCDI^{Dip}.** Apart from being non-luminescent in aggregated state, by blending the **BNCDI**s with a blue-emitting matrix it was demonstrated that white light emission in a multi-layered OLED device could be achieved (Fig. 65).
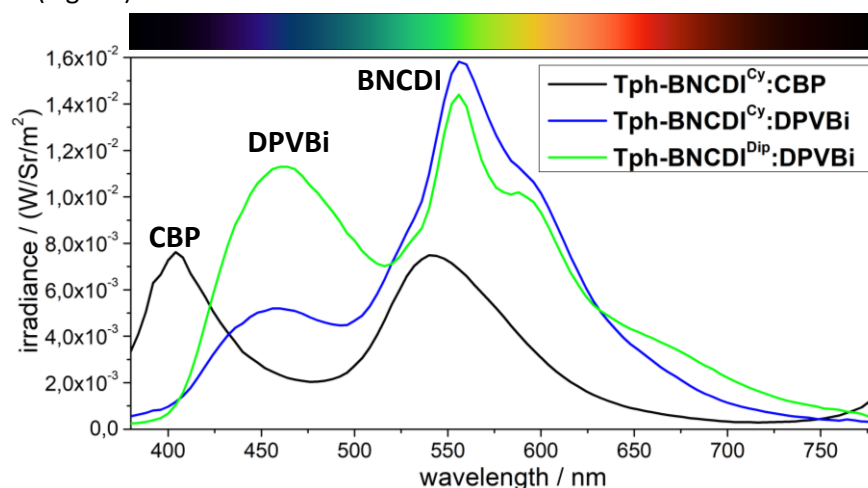
Fig. 65: Electroluminescence spectra of devices **A**, **C** and **F** with either **Tph-BNCDI^{Dip}** or **Tph-BNCDI^{Cy}** and the **DPVBi** or **CBP** matrix.

For both **BNCDI**s it was found that upon increasing the weight ratio of the **BNCDI**s a decreased OLED efficiency was observed. This could be due to ACQ processes. Overall, the OLED performance was sufficient with a maximum EQE of 1.5% and a luminance up to 1001 cd/m^2.

3.6 Variation of the Boryl Substituents in BNCDIs Leading to D-A-D Systems

As the general features of **Tph-BNCDI**s were introduced, the influence of the aryl-substituents at the boron atoms on their optoelectronic features was then examined. Mild and strong electron-donating groups at the boron atom should modulate the HOMO-LUMO gap to result in a bathochromically shifted absorption and emission. This would be favorable for light-harvesting or emitting devices.

In particular, the influence of the aryl's electron-donating strength towards the electron-accepting **CDI** forming a donor-acceptor-donor (D-A-D) triad was the focus of this study (Fig. 66).
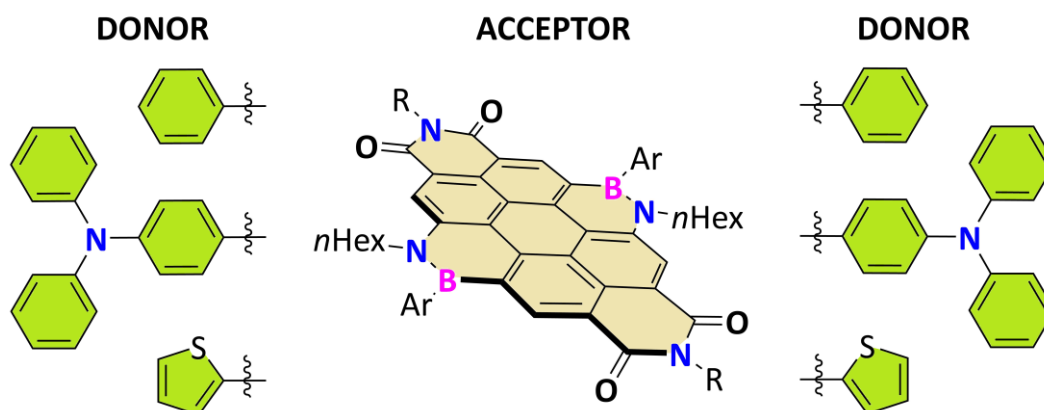
Fig. 66: A **BNCDI**, flanked with phenyl, thienyl or triphenylamine formally displays a D-A-D motif.

Moreover, the effect of the additional nitrogen lone pairs arising from the triphenylamine should be studied concerning the interaction of **BNCDI**s with Lewis bases and acids.

3.6.1 Introduction to D-A-D Structures

Considering carbon-based π-conjugated materials, donor (D) - acceptor(A) conjugates have been widely used for organic electronics,[107, 108] two-photon absorption[109] and non-linear optics.[110] Molecular designs representing push-pull **D-A** dyads and symmetric **D-A-D** triads are of special interest since they can serve as active material in ambipolar charge transfer semiconductors[111] and solar cells.[112, 113] Furthermore, **D-A** dyads and **D-A-D** triads often exhibit bathochromically shifted absorptions through intramolecular charge transfer (ICT) processes.[114]

For example, electron-accepting perylene diimides (**PDI**s), symmetrically flanked with electron-donating groups, exhibited substantially lower HOMO-LUMO gaps, due to the stabilization of the HOMO level caused by the donor unit (Fig. 67).[115]
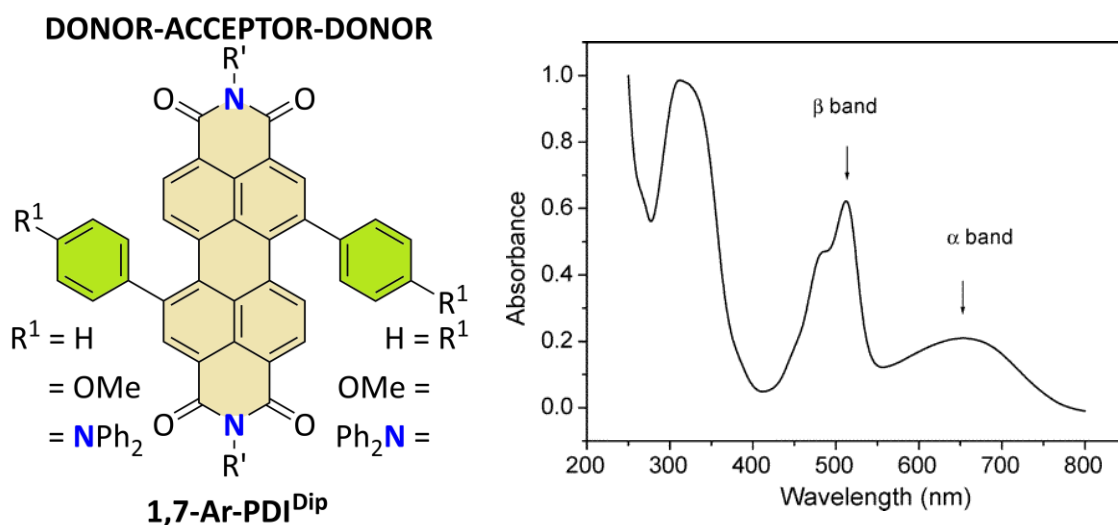
Fig. 67: Perylene diimides were substituted with various aryl groups to investigate their influence on the optoelectronical properties. The substitution with a triphenylamine motif resulted in the occurrence of a charge-transfer (CT) band (550-780 nm). Adapted with permission.[115]

In fact, a bathochromic shift of the absorption bands was observed following the trend of electron-donating ability, e.g. **1,7-Ph-PDI** (λ_{max} = 556 nm), **1,7-*p*-anisole-PDI** (λ_{max} = 573 nm) and **1,7-TPA-PDI** (λ_{max} = 512/653 nm). The absorption spectrum of the latter compound exhibited a dual band which was exclusively found for the strong electron-donating TPA group. The novel band was assigned to a charge-transfer (CT) transition from the triphenylamine to the **PDI**-core. Throughout this study, it was found that with increasing electron-donating strength of the aryl substituent, less defined vibronic bands and reduced luminescence quantum yields due to an increasing CT character were found. The TPA-substituted **PDI** was not emissive.[115] For the same **1,7-TPA-PDI** the absence of luminescence was dedicated to photoinduced electron transfer (PET) due to electron transfer from the TPA group to the **PDI** core after excitation.[116]

Based on this study, more **PDI**s with strong electron-donating amino groups were synthesized comprising TPA, carbazole (CBz), dimethylamine (NMe₂) and pyrrole (Pyr) groups in 1,7-position of the **PDI**.[59] Interestingly, all these structures showed broad CT-based absorption and emission bands in the NIR region of the electromagnetic spectrum. The low optical bandgap (E_{opt}(**1,7-TPA-PDI**) = 1.66 eV) and high HOMO levels (E_{HOMO}(**1,7-TPA-PDI**) = -5.73 eV) of these materials were ideal for application as p-type conductor in a p-n heterojunction solar cell and an OFET. The best performance of these **PDI** derivatives was found for the TPA-substituted **PDI** with a power conversion efficiency of η = 0.3% and hole mobility of μ_h = 8.5 x 10^{-7} cm^2 V^{-1} s^{-1}.

Aiming at the same 1,7-substitution pattern, **PDI**s also were combined with oxygen and sulfur-based electron-donating aryl groups, e.g. thienyls, thianthrenes and methoxyphenyls, to form D-A-D triads. Likewise, strong, red-shifted absorption and emission bands were observed. Apparently, both phenomena were based on charge-transfer processes. Due to the catenation of bithiophene a low optical band gap (E_{opt} = 1.59 eV) could be obtained within this D-A-D system. Moreover, an electron mobility of μ_e = 4.4 x 10^{-4} cm^2 V^{-1} s^{-1} was observable by TOF methods.[117]

However, the investigation of complex BN-PAH structures is still in its infancy, and thus, such molecular designs have not been realized for any BN-substituted PAHs yet. Synthetically, **D-A-D** triads may be generated in a symmetrical di-BN-substituted PAH by the introduction of electron-donating substituents (**D**) to the two BN units which are incorporated and located in the periphery of the acceptor (**A**) system. As depicted above, this concept was realized for the **BNCDI**s presented in this work. The electron-accepting **BNCDI** were combined with mildly, medium and strongly electron-donating groups attached to the boron atoms. The effect of such a resulting structure-property relation will be discussed below.

3.6.2   Optical Properties

To investigate the influence of the aryl groups of the properties on the **BNCDI**s, the photophysical properties of all seven **BNCDI**s were recorded using UV/Vis absorption and photoluminescence spectroscopy (Tab. 8).

All **BNCDI**s showed an absorption band with vibronic fine structures in the higher energy region (380-440 nm) and an absorption band with two vibronic shoulders in a lower energy region (450 -580 nm) The substitution of **BNCDI**s with strongly electron-donating triphenylamine (TPA) moieties led to an only marginal bathochromic shift from 536 nm (**Ph-BNCDI^{Cy}**) to 541 nm (**TPA-BNCDI^{Cy}**) and 540 nm (**TPA-BNCDI^{Dip}**) in absorption. (Fig. 68).
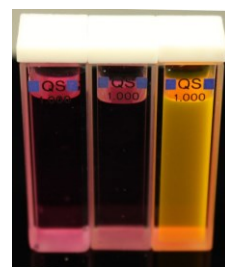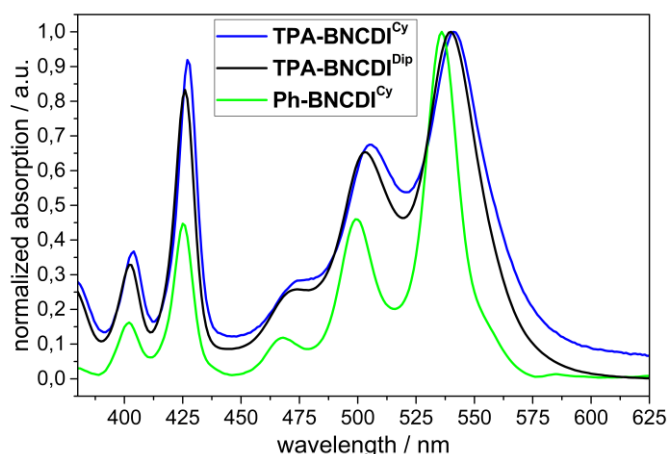
Fig. 68: Absorption spectra of **Ph-BNCDI^{Cy}**, **TPA-BNCDI^{Cy}** and **TPA-BNCDI^{Dip}** in DCM (10^{-5} M) and a photographic image of **TPA-BNCDI^{Cy}** and **TPA-BNCDI^{Dip}** and **Ph-BNCDI^{Cy}** in DCM solutions at an irradiation wavelength of 365 nm. The yellow-greenish luminescence is absent for **TPA-BNCDI^{Cy}** and **TPA-BNCDI^{Dip}** in DCM solution.

However, noteworthy line broadening for the $S_0{\rightarrow}S_1$ transitions (450-575 nm) and lower optical band gaps (E_{opt} = 2.19 eV for **TPA-BNCDI^{Cy}**, E_{opt} = 2.16 eV for **TPA-BNCDI^{Dip}**) compared to thienyl and phenyl-substituted **BNCDI**s (E_{opt} = 2.23-2.30 eV) were observed. A clear effect of the triphenylamine moiety on the intensity of the high energy transitions (380-440 nm, $S_0{\rightarrow}S_2$) in relation to the low energy transitions (450-580 nm) was concluded for both **TPA-BNCDI^{Cy}**/**TPA-BNCDI^{Dip}** compared to **Ph-BNCDI^{Cy}**.

The **TPA-BNCDI**s did not exhibit any broad CT-based emission as it was observed for the above given D-A-D examples *vide supra*.

Tab. 8: Overview of the optical and thermal properties of all **BNCDI**s in DCM solutions.

Compound	λ_{abs}[a] / nm	$lg(\varepsilon)$[a]	E_{opt}[b] /eV	λ_{ems}[a] / nm	$\Delta\nu_{Stokes}$[a] /cm^{-1}	Φ_{lum}[c]	T_{95}[d] / °C
Ph-BNCDI^{Cy}	536	4.80	2.30	544	285	0.95	390
Ph-BNCDI^{Dip}	539	4.91	2.23	543	137	0.88	411
Ph-BNCDI^{nHex}	536	4.75	2.25	546	342	0.91	404
TPA-BNCDI^{Cy}	540	4.68	2.19	581	1307	< 0.01	359
TPA-BNCDI^{Dip}	541	4.66	2.16	574	1158	< 0.01	363
Tph-BNCDI^{Cy}	535	4.74	2.24	544	310	0.95	396
Tph-BNCDI^{Dip}	538	4.85	2.23	546	272	0.94	391

[a] Measured in DCM solutions (10^{-5}-10^{-6} M). [b] Calculated from the offset wavelength derived from the lowest energy absorption band. [89, 90] [c] Referenced externally against fluorescein in 0.1 M NaOH. [d] TGA measurement: temperature at which 95% of the mass was still present at a heating rate of 10 K/min and nitrogen flow of 20 mL/min (see experimental part).

Analysis of the luminescence in DCM solutions showed that substitution with phenyl/thienyl groups in **Ph/Tph-BNCDI**s gave compounds emitting green light with high quantum yields (Φ_{lum} = 0.88 - 0.95) and small Stokes shifts ($\Delta\nu_{Stokes}$ = 137 - 342 cm^{-1}). Furthermore, TPA-substituted **BNCDIs** showed a barely visible luminescence in DCM (Tab. 9, also photographic image Fig. 68).

Although the luminescence of **TPA-BNCDI^{Cy}** and **TPA-BNCDI^{Dip}** in DCM solutions was much less intense, a well-defined emission band was found with maxima at 581 nm for **TPA-BNCDI^{Cy}** and 574 nm for **TPA-BNCDI^{Dip}** with comparable Stokes shifts (($\Delta\nu_{Stokes}$ = 1307 cm^{-1} (**TPA-BNCDI^{Cy}**) and 1158 cm^{-1} (**TPA-BNCDI^{Dip}**) and very low luminescence quantum yields (Φ_{lum} = <0.01 for both). However, for solutions in nonpolar solvents (*n*-pentane, *n*-hexane, cyclohexane) an intense luminescence was observed for **TPA-BNCDI^{Cy}**/**TPA-BNCDI^{Dip}**. To further investigate this phenomenon, the **TPA-BNCDI**s were subjected to UV/Vis absorption and photoluminescence spectroscopy in cyclohexane and DCM (Fig. 69).
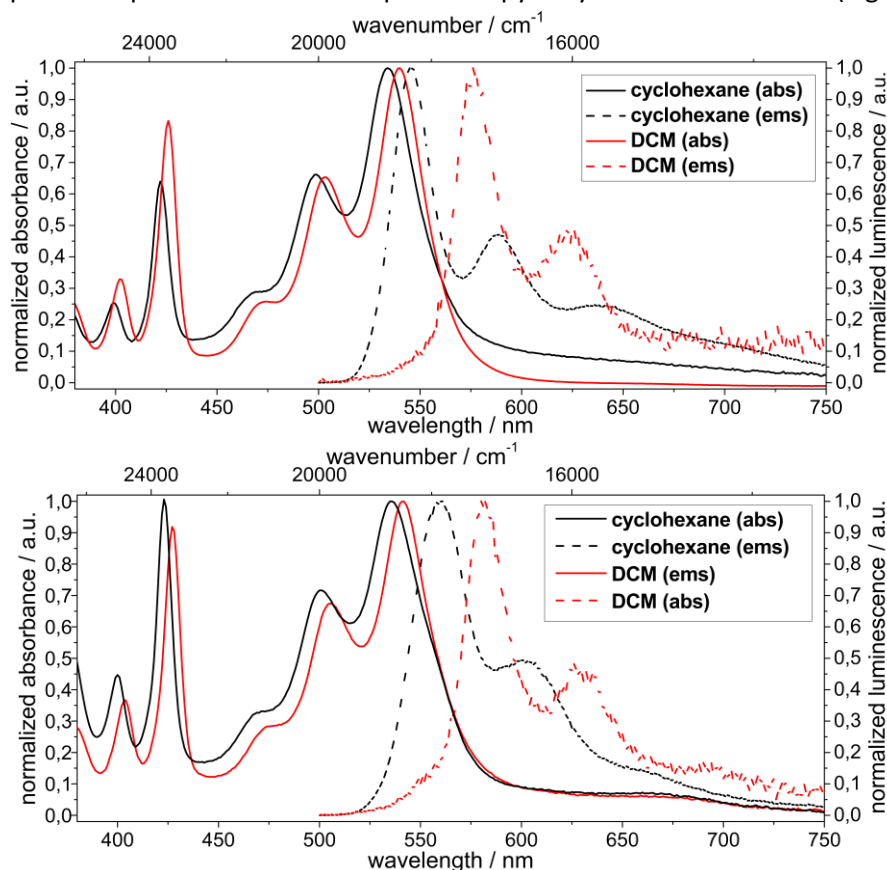
Fig. 69: Absorption and emission spectra of **TPA-BNCDI^{Cy}** (left) and **TPA-BNCDI^{Dip}** (right) in DCM (red) and cyclohexane (black). The concentrations were 10^{-6}-10^{-7} M.

For both the polar (DCM) and nonpolar (cyclohexane) solvents, the UV/Vis spectra of **TPA-BNCDI^{Cy}/TPA-BNCDI^{Dip}** appeared similar with a slight hypsochromic shift, and the vibronic transitions were clearly visible. However, since absorption and emission spectra were mirror images, it is assumed that the main transition occurs between the frontier orbitals of the **BNCDI** core without any direct influence of the TPA groups. Again, no broad CT-based emission or absorption band was observable for the **TPA-BNCDI**s.

In contrast to the low luminescence quantum yields in DCM ($\Phi_{lum} < 0.01$), in cyclohexane solutions, the **TPA**-**BNCDI**s exhibited a strong emission (at 545 nm for **TPA-BNCDI^{Cy}**, and at 560 nm for **TPA-BNCDI^{Dip}**) with high luminescence quantum yields ($\Phi_{lum} = 0.81/0.39$) and small Stokes shifts (($\Delta\nu_{Stokes} = 378$ cm^{-1}/835 cm^{-1}) (Tab. 9).

Tab. 9: Overview of the optical of all **BNCDI**s in DCM solutions. The photograph shows **TPA-BNCDI^{Cy}** in DCM (left)/cyclohexane(right) and **TPA-BNCDI^{Dip}** in DCM (left)/cyclohexane(right) under irradiation with UV-lamp (365 nm).

compound	solvent	λ_{abs}[a] / nm	lg(ε)[a]	E_{opt}[b]/eV	λ_{ems}[a] / nm	$\Delta\nu_{Stokes}$[a] /cm^{-1}	Φ_{lum}[c]
TPA-BNCDI^{Cy}	DCM	540	4.68	2.19	581	1307	<0.01
	cyclohexane	534	4.64	2.18	545	378	0.81
TPA-BNCDI^{Dip}	DCM	541	4.66	2.16	574	1158	<0.01
	cyclohexane	535	4.51	2.15	560	835	0.39

[a] Measured in solutions (10^{-5}-10^{-6} M). [b] Calculated from the offset wavelength derived from the lowest energy absorption band. [89, 90] [c] Referenced externally against fluorescein in 0.1 M NaOH.

As phenyl- and thienyl-substituted **BNCDI**s were highly emissive in both DCM and cyclohexane, this solvent-depending quenching effect was assigned exclusively to electronic and steric effects from the triphenylamine moiety in **TPA-BNCDI^{Cy}** and **TPA-BNCDI^{Dip}**. An explanation for this phenomenon will be given later in the text.

3.6.3 Electrochemical Characterization

A different tool for the investigation of the electronic effects of the substitution with either electron neutral or donating aryl substituents is cyclic voltammetry measurements. All measurements were performed in DCM with a three-electrode configuration: working electrode (platinum disk), reference electrode (calomel electrode) and counter-electrode (platinum wire). For all **BNCDI**s, two-electron fully reversible reduction waves were observed irrespective of the aryl substituent at the boron atom. The calculated LUMO levels, ranging from $E_{LUMO} = -3.75$ eV to $E_{LUMO} = -3.66$ eV, were slightly more stabilized compared to **CDI^{Dip}** ($E_{LUMO} = -3.62$ eV)[52] (Tab. 10). While the electrochemical oxidation of **Ph/Tph**-**BNCDI**s was found to be irreversible, both **TPA-BNCDI**s exhibited a reversible oxidation process (Fig. 70).
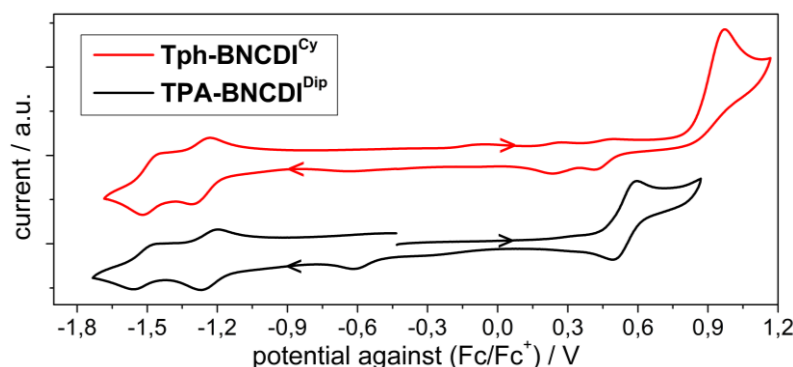
Fig. 70: Cyclic voltammogram of **TPA-BNCDI^{Dip}** and **Tph-BNCDI^{Cy}** (10^{-3} M) in DCM with nBu$_4$NPF$_6$ (0.2 M) as conducting salt.

Tab. 10: Overview of electrochemical properties of all **BNCDI**s performed in DCM with Bu_4NPF_6 (0.2 M), a scan rate of 200 mV/s and ferrocene/ferrocenium as reference.

	E_{ox} / V	E_{red1} / V	E_{red2} / V	$E_{ox, onset}$ / V	$E_{red, onset}$ / V	ΔE / eV	E_{LUMO}[a] / eV	E_{HOMO}[a] / eV
Ph-BNCDI^{Cy}	+0.93	-1.30	-1.50	0.77	-1.09	1.86	-3.71	-5.57
Ph-BNCDI^{Dip}	+1.00	-1.20	-1.49	0.83	-1.05	1.88	-3.75	-5.63
Ph-BNCDI^{nhex}	+0.95	-1.26	-1.48	0.72	-1.07	1.79	-3.73	-5.52
TPA-BNCDI^{Cy}	+0.54	-1.32	-1.63	0.36	-1.15	1.51	-3.66	-5.16[b]
TPA-BNCDI^{Dip}	+0.54	-1.19	-1.50	0.41	-1.09	1.50	-3.71	-5.21[b]
Tph-BNCDI^{Cy}	+0.93	-1.26	-1.48	0.74	-1.10	1.84	-3.69	-5.54
Tph-BNCDI^{Dip}	+0.99	-1.22	-1.49	0.82	-1.05	1.87	-3.75	-5.62

All values were corrected against the ferrocene/ferrocenium redox couple. [a] Derived from E_{LUMO}= -4.8 eV- E_{red} and E_{HOMO}= -4.8 eV- E_{ox}.[90] [b] Under the assumption that the TPA unit contributes to the HOMO.

Moreover, the oxidation potential was shifted to a lower value with triphenylamine groups attached at the boron atom. The difference between the oxidation values **Ph/Tph**-**BNCDI**s and **TPA-BNCDI**s was approx. 0.35 V. The respective HOMO for both **TPA-BNCDI**s was energetically destabilized E_{HOMO} = -5.16/5.21 eV. The total electric energy gap was reduced from $\Delta E \approx 1.85$ eV for **Ph/Tph-BNCDI**s to $\Delta E \approx 1.50$ eV for TPA-substituted **BNCDI**s. It is evident that this reduced oxidation potential originates from the TPA groups. These findings were not in agreement with the absence of a strong bathochromic shift in the absorption spectra. Therefore, it is suspected that the TPA-groups are electronically decoupled from the **BNCDI** core. However, triphenylamine moieties on **PDI**s[118] are known to be susceptible to undergo oxidative electropolymerization, but this behavior was not observed for **TPA-BNCDI**^{Cy} or **TPA-BNCDI**^{Dip}.

3.6.4   Spectroelectrochemical Characterization

To further conduct investigations on the electronic structure of the novel **BNCDI**s and especially the effect of the TPA-substitution, the absorption spectra of the oxidized/reduced **BNCDI**s were measured in DCM solutions. The electroactive species were generated in a spectroelectrochemical setup, which combines a potentiostat with a UV/NIR analysis. The discussed spectroelectrochemical experiments were quasi-static since the electrode potential was changed incrementally followed by the recording of absorption spectra. Upon oxidation/reduction, the resulting electroactive species of chromophoric structures might be found in the NIR. Since diffusion in the cell is limited a high local charge is transferred onto the analyte. Due to the ambipolarity of **TPA-BNCDI** and their fully reversible redox properties, the **(TPA-BNCDI)**$^{•+}$ and **(TPA-BNCDI)**$^{2+}$ species and their electrochemical stability was probed. At an applied voltage of 1.0 V, drastic changes in the absorption spectrum were observed.

The signal of the neutral **TPA-BNCDI^{Dip}** species at around 540 nm decreased, while a new band with maxima at 700 nm and 774 nm appeared (Fig. 71).
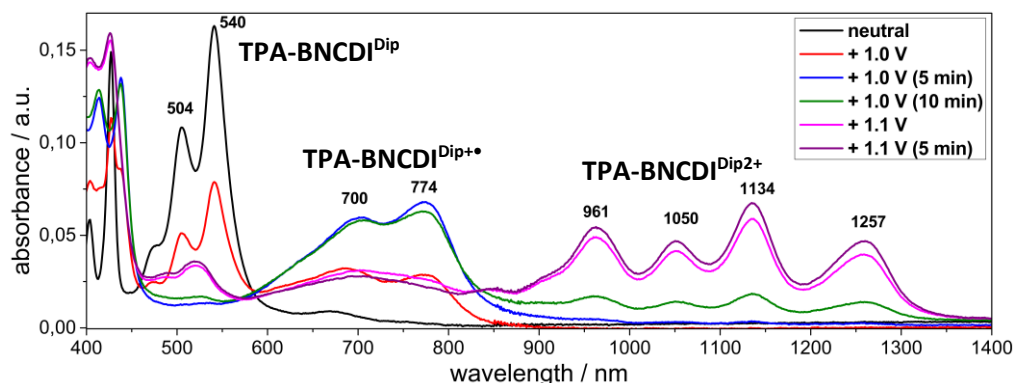
Fig. 71: Absorption spectra: Formation of **(TPA-BNCDI^{Dip})$^{+\bullet}$** and **(TPA-BNCDI^{Dip})$^{2+}$** upon oxidation in DCM with nBu$_4$NPF$_6$ (0.2 M).

In the case of applying a constant potential of 1.0 V for 5 min, the intensity of the new band increased and after 10 min, a stabilization of the formed species was observed. This was assigned as radical cationic **(TPA-BNCDI^{Dip})$^{+\bullet}$** species with the charge presumably located at the nitrogen atom of the triphenylamine motif. Furthermore, novel bands arose and stabilized with higher potential (1.1 V) at >900 nm that could not be clearly assigned. The occurrence of the absorption signals with that bathochromic shift indicated the presence of two spatially separated radical cations (Scheme 43).
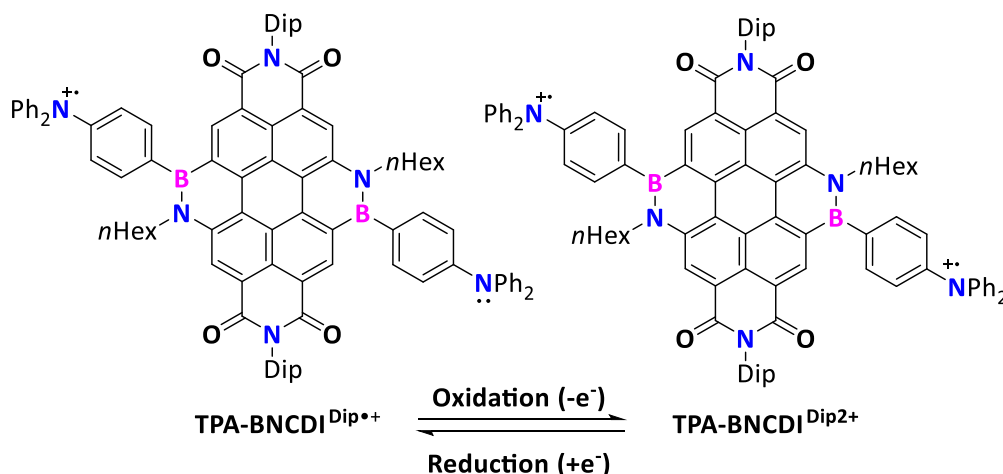
Scheme 43: Proposed localization of the **(TPA-BNCDI^{Dip})$^{+\bullet}$** and **(TPA-BNCDI^{Dip})$^{2+}$** radicals.

The effective localization of the charges remained unknown yet but is under current quantum chemical investigations.

To prove the reversibility of this process, as evaluated from cyclic voltammetry experiments, the oxidized **(TPA-BNCDIDip)$^{2+}$** was regenerated to the following **(TPA-BNCDI^{Dip})$^{+\bullet}$** and its neutral state (Fig. 72).
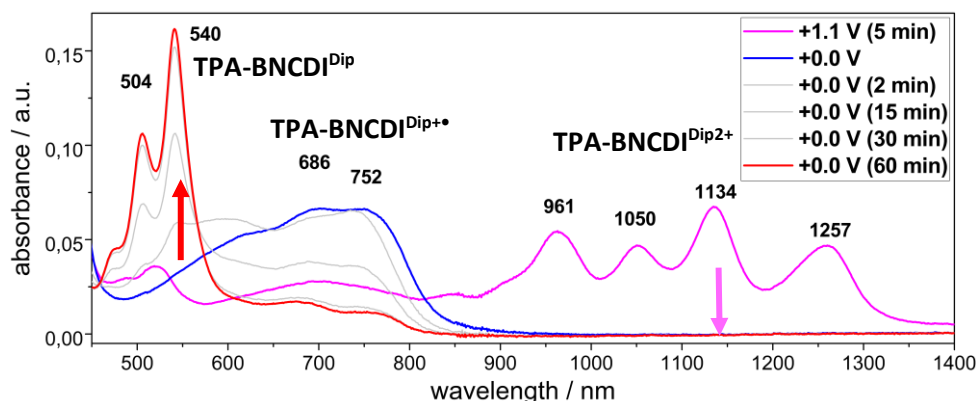
Fig. 72: Absorption spectra: Regeneration of the neutral **TPA-BNCDI^{Dip}** in DCM with nBu$_4$NPF$_6$ (0.2 M).

The process exhibited nearly quantitative reversibility, which demonstrates promising electrochemical stability of BN units in acceptor systems in combination with a redox-active group. Similar spectroelectrochemical experiments performed on triphenylamine-substituted **PDI**s showed that upon oxidation, also absorption bands in the NIR region occurred, which were reversible upon subsequent reduction.[118]

The spectroelectrochemical reduction of **TPA-BNCDI** and **Tph-BNCDI** was also characterized. As the resulting spectra differed only marginally, an ancillary effect of the TPA-substituent to the **BNCDI** scaffold in the reduction process was excluded. Both experiments can be found in the experimental part. This observation was in good agreement with the initial electrochemical studies and the quantum chemical calculations on the **Tph-BNCDI**s

3.6.5 Discussion on the Photophysical Properties of the **TPA-BNCDI**s

The most striking feature of these analyses were that the optoelectronic properties of the investigated molecules were highly dependent on the nature of the aryl-substituent at the boron atom. The contribution of the aryl group to the ground state was indicative for the electronic nature of the triphenylamine-substituents (Fig. 68). The slight bathochromic shift of the absorption signal and the increase of the absorption band dedicated to the S$_0$→S$_2$ transition were a result of the extended π-conjugation in the vertical axis of the **TPA-BNCDI**s. Though, the bathochromic shift of the absorption is less significant compared to the reduction of the HOMO level by approx. 0.35 V. This could indicate that the TPA groups were less involved in the absorption process. The observed loss of vibronic pattern for the **TPA-BNCDI**s compared to the **Ph/Tph-BNCDI**s might be assigned to the larger transition dipole moment or to a twist of the rylene core. The latter was previously described in 1,7-substituted **TPA-PDI**s.[115]

However, the excited state of the **Ph/Tph-BNCDI**s differed from the **TPA-BNCDI**s substantially: The molecules had a strong solvent dependent luminescence. This behavior was attributed solely to the sterical-electronic nature of the triphenylamine moiety. As such observations were not reported for similar BN-PAHs, the all-carbon PAHs with D-A-D structures were referred to. Combination of electron-accepting **PDI**s and two electron-donating triphenylamines, as in *bay*-substituted **TPA-PDI**s, [115, 119] suffered from luminescence quenching due to intramolecular charge transfer (ICT) processes *vide supra*. Due to the stereoelectronic influence of the triphenylamine motif, commonly D-A or D-A-D structures comprising triphenyl moieties are suspected to undergo (TICT)[114, 120-123] processes. However,

all these D-A-D triads had in common, that the absorption spectra had a π-π*- and an ICT-based transition. As this was not observed in the unperturbed absorption spectra of the **TPA-BNCDI**s (Fig. 68), those classical mechanisms are not considered as the foundation of the solvent dependency.

Intensive studies on perylene diimides with different electron donors located at one imide position have been performed. The utilized donor groups were: *p*-anisole, 4-phenylcarbazole, triphenylamine and (biphenyl)diphenylamine. All derivatives besides the triphenylamine-substituted **PDI** were strongly emissive in solution. For the triphenylamine-substituted **PDI**, an ultrafast fluorescence decay time (τ = 0.27 ns) and an increased non-radiative constant (k_{nr} = 36.8 x 10^8 s^{-1}) was found. This was assigned to a photoinduced electron transfer (PET) from the triphenylamine to the **PDI** core.[124]

Transferring this knowledge to the parent **TPA-BNCDI**, a solvent-depending photoinduced reductive electron transfer mechanism[125] is proposed (Scheme 44).
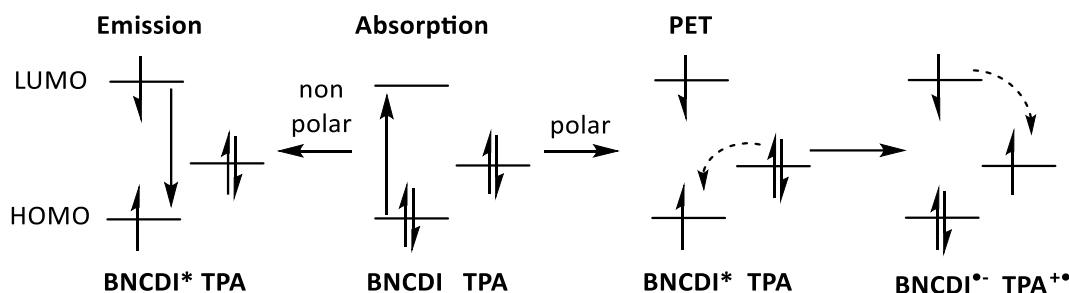
Scheme 44: Proposed fluorescence (non-polar solvent) and intramolecular PET (polar solvent) mechanism for **TPA**-**BNCDI**s.

In nonpolar solvents, **TPA-BNCDI**s held high luminescence quantum yields (Φ_{lum} > 0.38) indicating an efficient absorption/emission process. Upon photoexcitation in polar solvents, the TPA-group transfers an electron to the LUMO level of the excited **BNCDI***. As the consequence, a radical anion **BNCDI**$^{\bullet-}$ and radical cation a TPA$^{+\bullet}$ are generated. Later, the charge transfer complex decays to the ground state without emission of a photon. Since the **TPA-BNCDI**s were still slightly emissive in DCM solutions, it is assumed that a small portion of the excited molecules undergoes fluorescence with a bathochromic shift due to solvatochromism.

These considerations are supported by the results of the electrochemical analysis: In comparison with the phenyl- and thienyl-substituted **BNCDI**s, the oxidation potential of **TPA-BNCDI**s was lowered by approx. 0.35 V but the absorption spectra were not affected by this. Therefore, the TPA motif did not appear to interfere with the $S_0{\rightarrow}S_1$ absorption or $S_1{\rightarrow}S_0$ emission process but should have a destabilized HOMO level. This facilitates an electron transfer from the TPA group to the excited **BNCDI** core. Therefore, the luminescence quenching was not observed for **Tph/Ph-BNCDI**s.

To support the intramolecular PET theory, the energy change for a PET process was calculated by the Rehm-Weller equation [126] in its simplified version (Eq. 1).[125]

$$\Delta G_{PET} \;=\; E_{Ox,onset} - E_{red,onset} - E_{00} - \Delta G_{solv}^0 \;\; \text{(Eq. 1)}$$

Here, the E_{00} represents the intersection of absorption and emission, and ΔG_{solv}^0 is a correction term which includes the coulomb potential for the respective radical ion species in the given solvent. However, the contribution of this term is neglectably low in polar solvents (acetonitrile, DCM).[127-129] On the contrary this term is important for PET processes in nonpolar solvents, as the ions are less likely to be solvated.

However, using Eq. 1, the electrochemical onset values (Tab. 10) and E_{00} (2.18 eV), the difference between the first excited state and the charge separated state could be calculated. The ΔG of **TPA-**

BNCDI^{Cy} and for **TPA-BNCDI^{Dip}** was -0.68 eV or -15.7 kcal/mol. It is considered that values below $\Delta G < -0.50$ eV indicate an efficient PET process with increased luminescence quenching rate.[125]

This PET process would explain the absence of any CT-based absorption or emission band and the decreased luminescence in polar solvents. As this hypothesis is still under investigation and a dark-state quenching[130] cannot be excluded yet, quantum chemical calculations in cooperation with D. Jacquemin (Univ. Nantes) should shine light in this topic.

3.6.6   Lewis Behavior of **BNCDI**s

The stabilizing effect of the intramolecular Lewis acid-base interaction between the nitrogen and boron atom in **BNCDI**s was investigated by the addition of Lewis acids and bases. Since the BN units were embedded at the periphery of an intrinsically chromatic structure, the optical response of the **BNCDI**s should be analyzable. Most recent examples for these interactions are described for fluoride anions, as Lewis base, and boron tribromide, which coordinates to the nitrogen atom, as a Lewis acid.[131-133] Therefore, the interaction of the present **BNCDI**s with either fluoride or boron tribromide was probed. To analyze the influence of the triphenylamine substituent, a Lewis base itself, towards the Lewis behavior, **TPA-BNCDI^{Dip}** was compared to the **Tph-BNCDI^{Dip}** motif. Both structures were dissolved in DCM and an excess of BBr$_3$ or TBAF was added and UV/Vis spectra were recorded (Fig. 73).
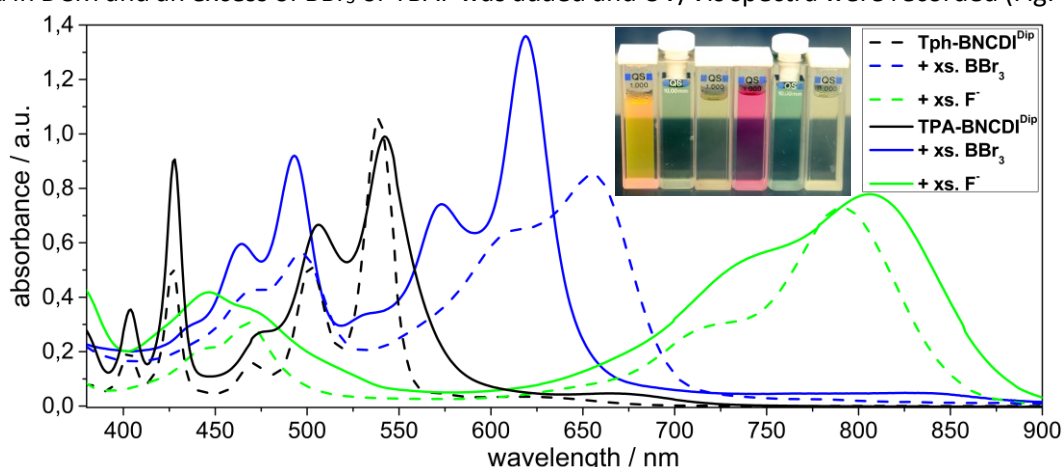
Fig. 73: Absorption spectra of **TPA-BNCDI^{Dip}**/**Tph-BNCDI^{Dip}** and their interaction with BBr$_3$ and TBAF. The photographic image shows solutions of **Tph-BNCDI^{Dip}** in DCM, with BBr$_3$ and with TBAF (from left to right) as well as **TPA-BNCDI^{Dip}** in DCM, with BBr$_3$ and with TBAF.

Upon addition of an excess of tetrabutylammonium fluoride (TBAF) to DCM solutions of **TPA-BNCDI^{Dip}** and **Tph-BNCDI^{Dip}**, the color of the solution changed from red to light green, coming along with a lack of any visible luminescence. In contrast, the interaction of **BNCDI**s with BBr$_3$ led to the formation of a bluish solution. Both interactions will be revised separately in the following section.

3.6.7   Interaction with Lewis Bases (F$^-$)

The absorption spectra of **BNCDI** with a fluoride source showed new absorption bands in the NIR region with peaks around 791/805 nm and a small shoulder at 709/730 nm. In the higher energy region of absorption (390 - 450 nm), two signals were detected which could be assigned to the $S_0 \rightarrow S_2$ transition including its vibronic fine structure. The substantial bathochromic shift of 252/262 nm compared to the neat **BNCDI**s points to large geometrical changes of **BNCDI** upon fluoride addition. The strong electron-donating nature of the triphenylamine substituent at the boron atom led to a smaller bathochromic shift than for the thienyl group. The absorption spectra of **Tph-BNCDI^{Dip}** interacting with

fluoride anions were similar to the absorption spectra of **Tph-BNCDI^{Dip}** radical anion and dianion species implying similar localization of the reduced species.

Due to the strong bathochromic shift of **TPA-BNCDI^{Dip}/Tph-BNCDI^{Dip}** in combination with a fluoride source, it was expected that the resulting adduct complexes undergo fluorescence quenching as reported previously for several highly polar Lewis acid/base adduct systems.[35] Contrary to these reported results, a strong emission band in the UV/Vis region (380-600 nm) and in the NIR region (700-950 nm) was observed (Fig. 74).
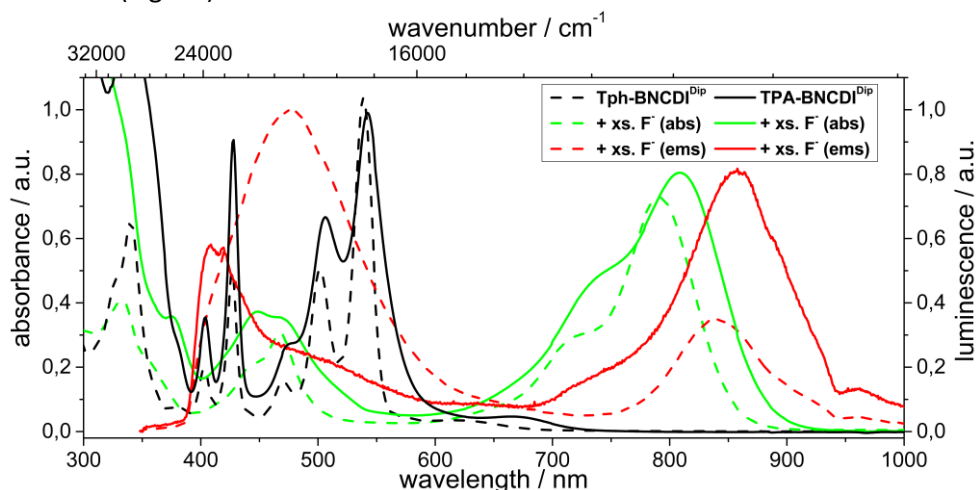
Fig. 74: Absorption and emission spectra (excited at 375 nm), of **Tph-BNCDI^{Dip}** and of **TPA-BNCDI^{Dip}** before and after addition of an excess TBAF in DCM.

Furthermore, marginal Stokes shifts (($\Delta\nu_{Stokes}$ = 737 cm^{-1} for **TPA-BNCDI^{Dip}**, $\Delta\nu_{Stokes}$ = 692 cm^{-1} for **Tph-BNCDI^{Dip}**) of the most bathochromically shifted absorption band and the respective emission band were observed. In both experiments the quantum yield could not be determined since it was below the validated level (Φ_{lum} = <0.10) of the setup.

Titration of the fluoride source with **Tph-BNCDI^{Dip}** and **TPA-BNCDI^{Dip}** revealed two-step processes (Fig. 75).
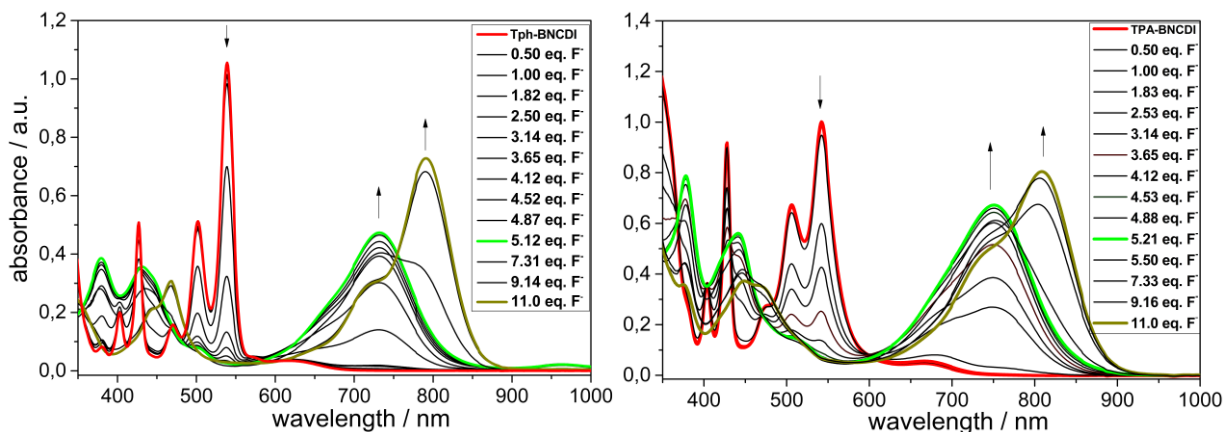
Fig. 75: Absorption spectra of **Tph-BNCDI^{Dip}** (left) and **TPA-BNCDI^{Dip}** (right) and their interaction with TBAF measured in DCM.

Upon addition of 0.5 equivalents of TBAF a decrease of the **BNCDI** bands was observed, which indicated that this experiment is highly sensitive towards its analyte and could be useful for sensing applications. Upon adding more fluoride anions, we noted new absorption bands (600-820 nm) which might arise from the interaction of one fluoride anion with the **BNCDI**s to form the monofluoride adduct. The limit of interaction was achieved if the system was treated with 11.0 equivalents of fluoride anions indicated by the evolution of another band (600-900 nm) with two peaks (710 nm and

810 nm). There was no auxiliary effect of the triphenylamine moiety seen in this experiment. However, the coordination of the fluoride was reversible by dilution of the solutions or mixture with protic solvents.

Attempts to determine the Lewis acidity with triethylphosphine oxide *via* Gutmann-Beckett method[134, 135] failed unfortunately as no interaction was observed.

3.6.8 Interaction with Lewis Acids (BBr₃)

The addition of BBr_3 to **TPA-BNCDI^Dip** and **Tph-BNCDI^Dip** led to the formation of a blue species with red-shifted absorption maxima ($\lambda_{max} = 619/656$ nm) and shoulder peaks (573/608 nm), displaying a vibronic fine structure (Fig. 76).
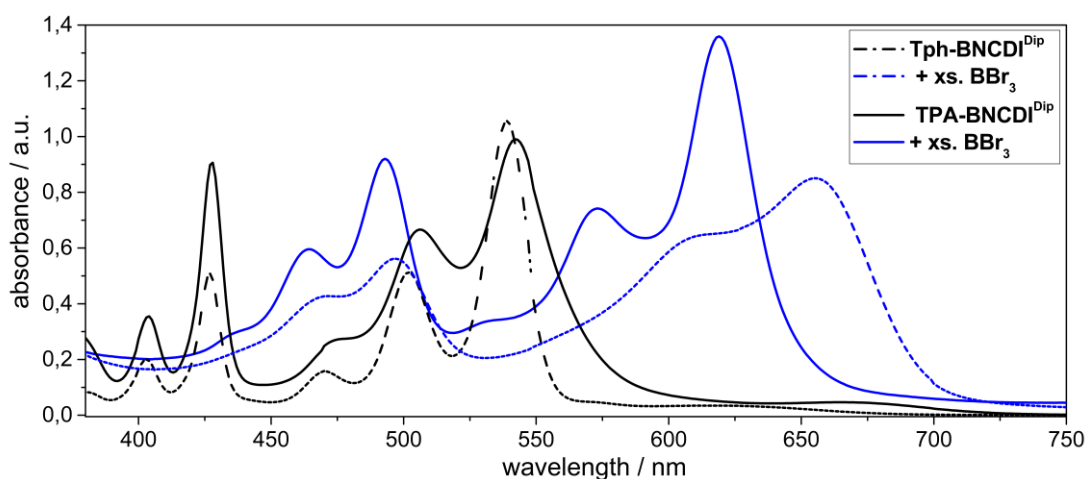
Fig. 76: Absorption spectra of **TPA-BNCDI^Dip/Tph-BNCDI^Dip** and their interaction with BBr_3.

In the higher energy absorbing region, two new signals (493/497 nm, 464/468 nm) were found with a similar vibronic appearance. Although the small absorption shifts of **TPA-BNCDI^Dip** compared to **Tph-BNCDI^Dip**, a strong influence of the triphenylamine moiety in this experiment could be excluded. In contrast to the fluoride adducts, the **BBr₃ BNCDI** adducts were not emissive.

When investigating the titration of BBr_3 with **TPA-BNCDI^Dip** and **Tph-BNCDI^Dip**, an additional Lewis activity of the nitrogen lone pair of the triphenylamine group was not found. But in analogy to the study with a Lewis base, a two-step process with clearly distinguished intermediates was found. Further detailed titrations with boron tribromide were conducted with **Tph-BNCDI^Dip** and **TPA-BNCDI^Dip** dissolved in DCM (Fig. 77).
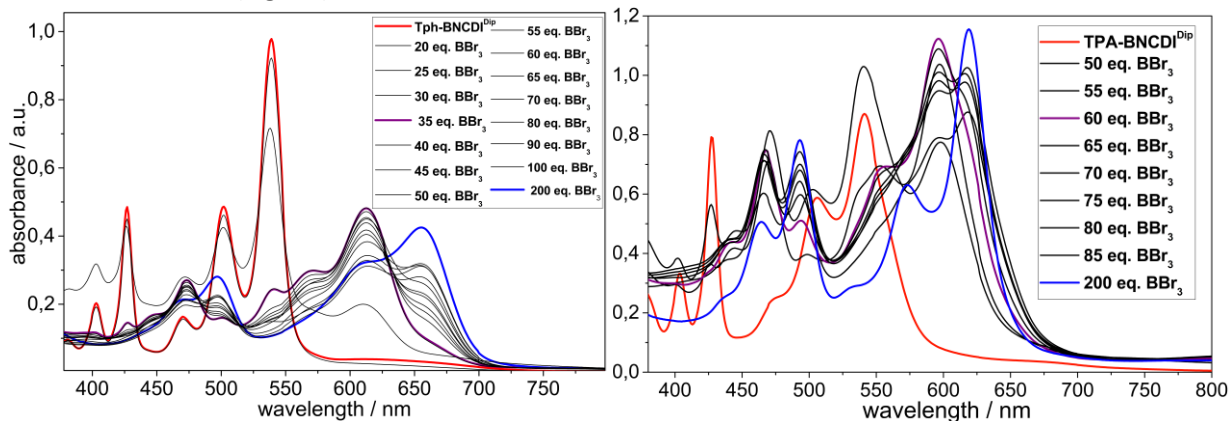
Fig. 77: Absorption spectra of **TPA-BNCDI^Dip** (left) and **Tph-BNCDI^Dip** (right) interaction with BBr_3. The titration was performed under nitrogen atmosphere, using anhydrous DCM.

The titration of **Tph-BNCDI**^{Dip} with BBr$_3$ gave similar results as for the **TPA-BNCDI**^{Dip}. Although the final species of the **TPA-BNCDI**^{Dip} was slightly hypsochromic shifted, there was no fundamental difference between the thienyl and triphenylamine derivative. Still, the intermediary signal for the **Tph-BNCDI**^{Dip} (620 nm) was formed with fewer equivalents compared to the formation of the **TPA-BNCDI**^{Dip} species (590 nm). In general, this process was completely reversible by dilution or the addition of a protic solvent, e.g. methanol.

3.6.9 Weak Interactions with Coordinating Solvents

Due to the fact that drastic changes in absorption spectra using a strong Lewis base or acid were observed, the interactions with non-coordinating and coordinating solvents were further investigated. Therefore, **TPA-BNCDI**^{Cy} and **Tph-BNCDI**^{Cy} were dissolved in various solvents whereat cyclohexane, DCM, THF, ethyl acetate, triethylamine and acetonitrile represent solvents that may form a high variety of possible interactions with the **BNCDI**s. For cyclohexane, DCM and THF, slight changes in the absorption spectra were observed that could be assigned to their polarity (Fig. 78).
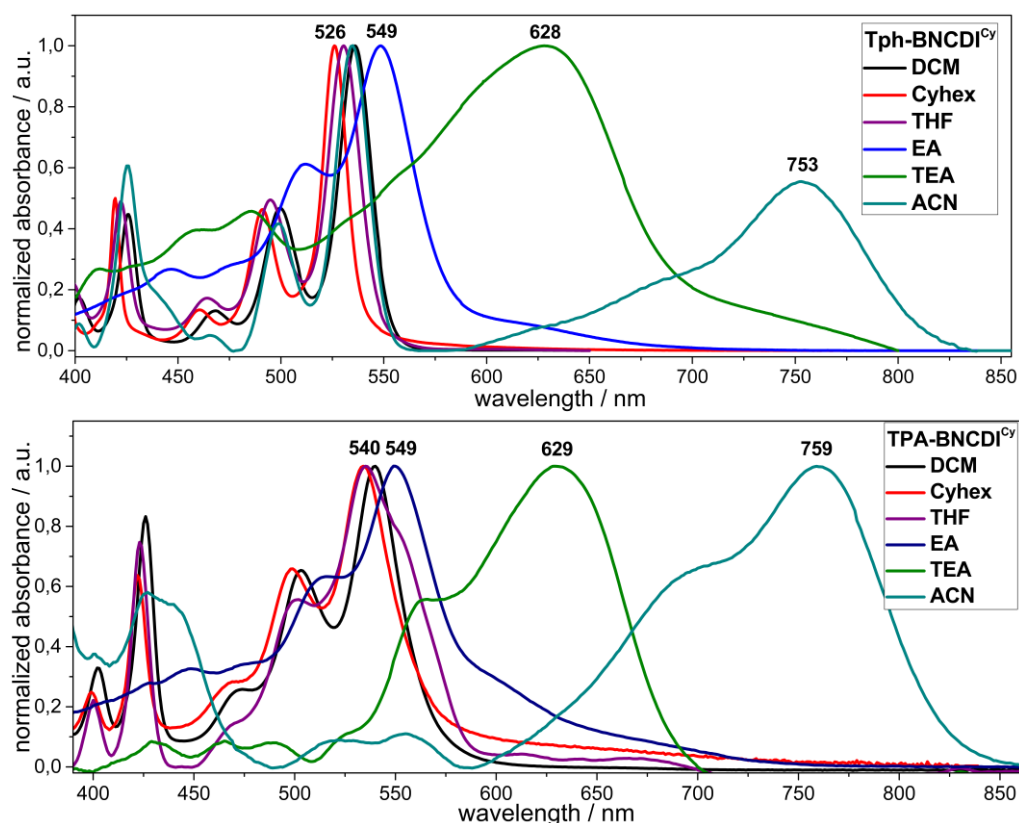
Fig. 78: Interaction of **Tph-BNCDI**^{Cy} (top) and **TPA-BNCDI**^{Cy} (bottom) with a variety of diffrently coordinating solvents.

However, strong interactions with coordinating solvents like acetonitrile, TEA or even the weaker coordinating ethyl acetate (EA) were observed. Since complexation was possible with weak or moderate Lewis bases, e.g. ethyl acetate, THF, tertiary amines or acetonitrile, we concluded that the BN unit showed a weak interaction of the empty boron orbital with the oxygen/nitrogen lone pair of the Lewis base. In most cases, the **BNCDI** species retained the characteristically structured vibronic absorption bands. The observed effect was not limited to TPA-substituted **TPA-BNCDI**^{Cy}, as the thienyl-substituted **Tph-BNCDI**^{Dip} exhibited the same behavior. Therefore, an additional effect of the triphenylamine's lone pair was excluded. These findings were especially interesting, since all carbon rylene diimides are only weakly solvatochromic.[136]

3.6.10 Discussion on the Lewis Behavior

To further estimate the influence of the TPA-group on the optoelectronic properties of the **BNCDI**s, the Lewis basicity/acidity of the **BNCDI**s were investigated. Interaction with fluoride anions and boron tribromide occurred in a consecutive two-step coordination of the Lewis species to the **BNCDI**s with drastic changes in absorption behavior. Due to geometrical changes of either the boron or nitrogen atom in the **BCDNI** scaffold, bathochromic shifts resulted (Scheme 45).

nitrogen = Lewis base   R = n-Hex   boron = Lewis acid
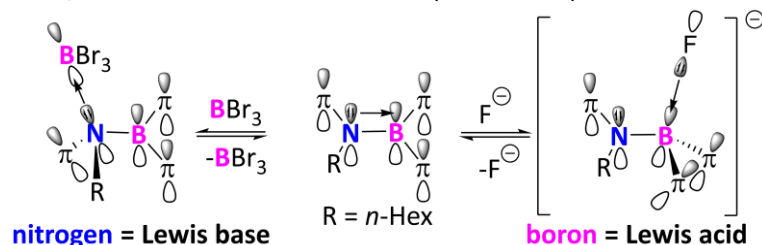
Scheme 45: Schematic formation of different Lewis adducts and the influence on the BN-scaffold. All complexes were reversible by adding a protic solvent or strong dilution.

This strong bathochromic shift was expected since fluoride anions react with the unoccupied p_z orbital of the boron atom and donate their two electrons to the boron atom leading to an anionic four-coordinate boron atom which dispenses the electron density towards the perylene core. The formal reduction of the **BNCDI** by addition of a fluoride source was further proved by the fact that the absorption spectra were congruent with the absorption bands which were obtained in the spectroelectrochemical reduction of these compounds. These experiments are displayed in the experimental part. Coordination of a Lewis acid (BBr_3) by the azaborines' nitrogen atom resulted also in a bathochromically shifted absorption. Also, here a two-step addition process was found *via* titration. Overall, it was found that the electronic influence of the triphenylamine was neglectable to the resulting species and further, no Lewis activity of the TPA moiety was found.

The **BNCDI**s also exhibited interactions with weaker coordinating solvents (THF, EA, TEA and ACN) resulting in drastic changes of the absorption spectra but retaining the characteristic vibronic bands. Here as well the TPA-groups contributed solely due to their electron-donating nature to the system. Overall depending on the donor strength of the aryl group differing photophysical properties resulted based on geometrical changes of the **BNCD**Is.

3.6.11 Conclusion on the Boryl Substituents in **BNCDI**s

In this sub-chapter, it was shown that the combination of electron-accepting **BNCDI** with electron-donating phenyl/thienyl/triphenylamine substituents at the boron atom led to the formal generation of a **D-A-D** triads. While substitution of the **BNCDI** scaffold with phenyl and thienyl substituents barely had any influence on the optoelectronic properties, the substitution with strong electron-donating triphenylamine groups resulted in broader absorption signals and a marginal bathochromic shift. Strikingly, the triphenylamine-substituted **BNCDI**s showed solvent-depending quenching processes since they were highly luminescent in nonpolar solvents but only barely emissive in more polar solvents. The electrochemical analysis showed that the **TPA-BNCDI**s had a lower oxidation potential. In contrast to the **Ph/Tph-BNCDI**s, the **TPA-BNCDI**s exhibited fully reversible redox characteristics. This was further demonstrated by the spectroelectrochemical investigation of radical species in reduction and oxidation processes where **TPA-BNCDI**s showed high reversibility of all redox processes. This supports the idea of an intramolecular photoinduced electron transfer quenching mechanism. However, the role of the BN-substitution in this process is still being evaluated.

BN-substitution has a high variety of novel features to a commonly used motif for organic electronics. Especially, interaction with Lewis base/acid and interactions with solvents are unique features for BN-substituted systems. Due to interaction that influenced the geometry directly, BN-species that partly absorb and emit in the NIR region were observed and could be useful for detection purposes.

3.7 Overall Conclusion and Perspective for BNCDIs

As BN-chemistry is already well established, existing synthetic concepts could be used to synthesize novel acceptor structures comprising a BN-motif. The key objective in this regard was to expand a π-system laterally by the introduction of BN units and to further investigate their influence on the photophysical properties in solution, solid-state and in organic electronic devices.

Overall, the syntheses of seven novel **BNCDI**s were developed and their optoelectronic properties were studied with a focus on the substitution with different imide groups and the effect of electron-donating groups at the boron atom (Scheme 46).
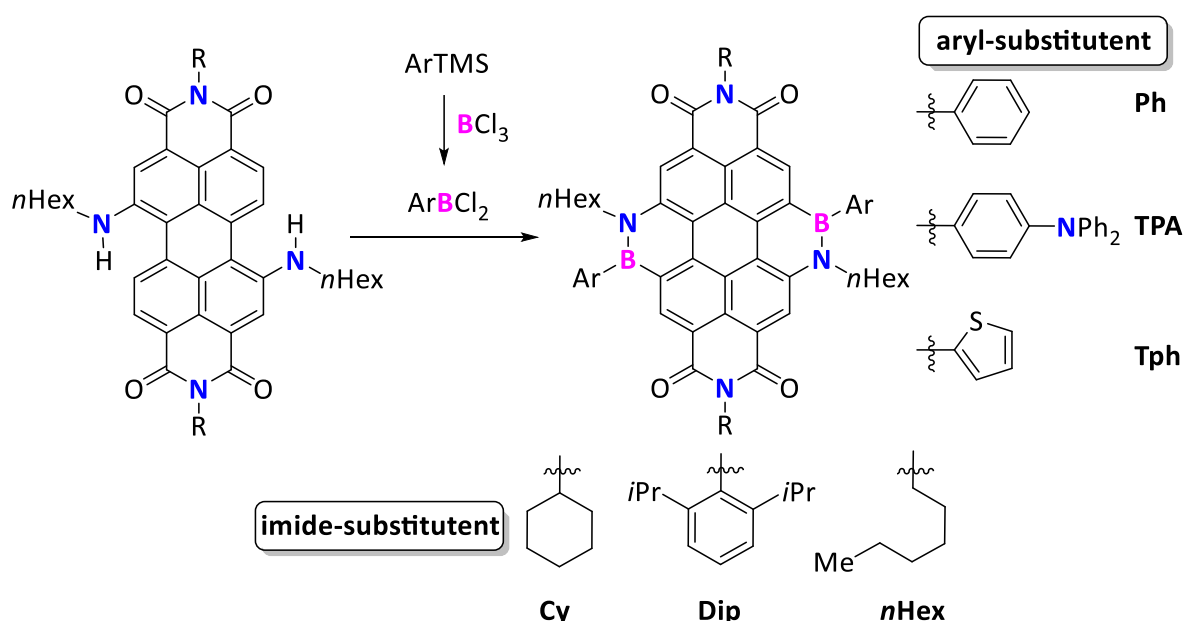
Scheme 46: Synthesis of various **BNCDI**s with varying imide or aryl substituent.

In comparison with the all-carbon **CDI**s, a substantial bathochromic shift in absorption and emission as well as an increase of overall chromaticity, e.g. higher absorption coefficient (ε), broader absorption bands and higher luminescence quantum yield, was found for all **BNCDI**s when investigated in solution. The bathochromic shift of the absorption was attributed to the smaller HOMO-LUMO gap and to the increased dipole moment caused by the BN units.

Interestingly, the absorption spectra of the **BNCDI**s were similar to the absorption of both **CDI**s and **PDI**s. This could be attributed to the occupied frontier orbitals of the **BNCDI**s which were *PDI-like* (longitudinal) in the HOMO and *coronene-like* (vertical) in the HOMO-4. Therefore, a bathochromically shifted absorption of BN-PAHs is not exclusively based on the stabilization of the HOMO/LUMO levels but also due to the interference of the BN unit with the localization of the frontier orbitals. Therefore, lateral π-expansion of PAHs and in particular rylene diimides using BN-chemistry could overcome photophysical disadvantages of all-carbon lateral π-expansion. As the overall absorbance of the **BNCDI**s is advantageous compared to those of **PDI**s and **CDI**s, **BNCDI**s are promising candidates for an application of organic solar cells or dye-sensitized solar cells.

When the imide substituent was varied from cyclohexyl (Cy) to di*iso*propylphenyl (Dip), the influence on the solid-state properties and on the performance in organic devices differed. By using simple low-temperature luminescence and light microscopic methods, a strong agglomeration of the cyclohexyl-substituted **Tph-BNCDI** compared to the di*iso*propylphenyl derivative was found.

To evaluate the general charge transportation characteristics of **BNCDI**s, an n-type OFET with this material was manufactured. **Tph-BNCDI^{Cy}** was integrated into a bottom-gate bottom-contact n-type OFET. The classical electrical parameters of OFET were below average: A low conductivity ($\mu_e = 3.42 \times 10^{-6}$ cm^{-2} V^{-1} s^{-1}), poor on/off-current ratio ($I_{on}/I_{off} = 36$), low field-effect mobilities ($\mu_{FE} = 1.02 \times 10^{-8}$ cm^2 V^{-1} s^{-1}) and high threshold voltage ($V_{th} \approx 21$ V) were observed. In the here presented OFET, the effect of both BN units on the stacking behavior of the **BNCDI**s or respective charge-transfer mechanisms could not be clarified. It is imaginable that the BN units have a head-to-tail orientation of the BN dipole moments in the solid-state that might differ from their all-carbon analogs. Therefore, further investigations of **BNCDI**s in OFET devices should concentrate more on the effect of the π-expanded **BNCDI** compared to the respective **PDI**s and **CDI**s.

When both **Tph-BNCDI**s were implemented in multi-stack OLEDs in combination with blue-emitting matrices, the Dip-substituted **BNCDI** emitted pure white light. This was proof of the concept that a mixture of blue-emitting matrix and greenish-emitting **BNCDI**s can form a WOLED. The OLEDs exhibited a low turn-on voltage along with the highest external quantum efficiency of 1.5%, which is a modest value for any fluorophore-based OLED.

In the future, the full potential of diimide-substituted BN-PAHs should be explored. The variability of the imide substituent without altering the general photophysical properties of the **BNCDI**s is the greatest advantage. To tune the solid-state properties of the **BNCDI**s, more spacious or branched substituents on the imide position might be integrated which defines their further application (Fig. 79).
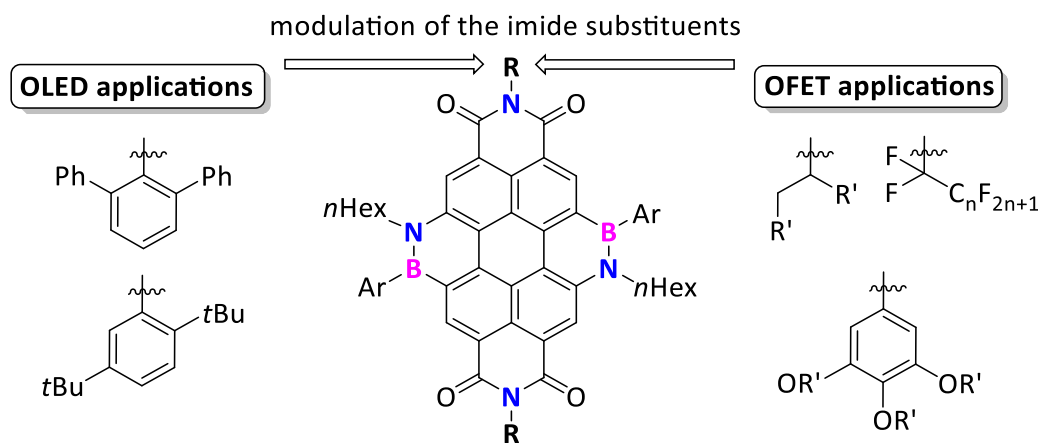
Fig. 79: Variation of the imide substituents in **BNCDI**s could define its purpose in organic electronics.

For example, terphenyl groups at the imide position might impede close π-π-contacts and therefore lead to a more monomeric emission of the **BNCDI**s in the solid-state. This would be preferable for the application of the **BNCDI**s in OLED devices. Since it was reported that spacious substituents at the imide position hinder the internal electron transport,[137] long branched alkyl chains located at the imide position should allow close π-π-contacts and alter the morphology of the **BNCDI**s in film. Those characteristics would be essential for a high charge transport property in n-type OFET devices. Not only long branched hydrocarbons are potential imide substituents for the application in OFET devices: It was shown that perfluoroalkyl chains at the imide position modulate the packing, increase the electron affinity, and shield the radical anions against environmental influences in n-type OFETs.[138] Therefore, the integration of such motifs in **BNCDI**s would be promising for high-performance OFET applications.

After investigation of the influence of the imide substituent on the performance of the **BNCDI**s in the solid-state, the impact of the aryl substituents at the boron atom followed. Such a study linking the optoelectronic properties with the substitutional effects at the boron atom in a BN-PAH remains elusive so far and might highlight novel features for upcoming BN-substituted systems. For the investigations, neutral and electron-donating heterocycles (phenyl, thienyl, triphenylamine) were connected to the boron atom.

In particular, the combination of the electron-accepting **BNCDI** with strong electron-donating triphenylamine at the boron atom led formally to a **D-A-D** triad, which is a common motif for molecules utilized in optoelectronic devices (Fig. 80).
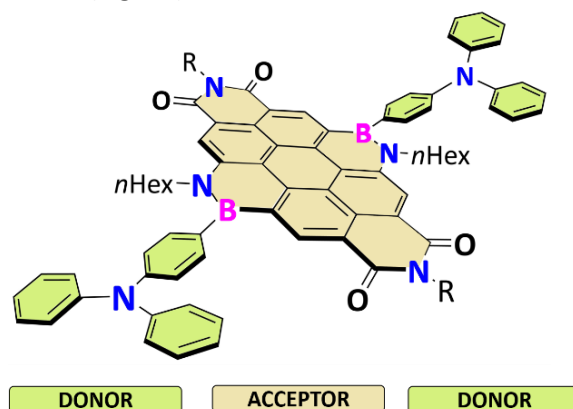
Fig. 80: Triphenylamine-substituted **BNCDI**s display **D-A-D** triads.

While the phenyl and thienyl-substituents barely had any influence on the optoelectronic properties of **BNCDI**s, the triphenylamine-substituted **BNCDI**s differed tremendously from them in terms of luminescence and electronic structure. The amphoteric TPA-substituted **BNCDI**s exhibited barely any luminescence in polar solvents but were highly luminescent in nonpolar solvents. Since this behavior occurred along with the lower oxidation potential of the **TPA-BNCDI**s, it is suspected that an intramolecular PET process in polar solvents was favored. The free energy change of the charge-transfer process was calculated as -15.7 kcal/mol, which is high enough to explain the low luminescence quantum yield of **TPA-BNCDI**s in polar solvents. A variation of the boryl-substituent with other electron-donating groups, e.g. anisole or carbazole, could help to understand this process in detail and might result in substantial bathochromic shifts. However, the general synthetic inaccessibility of ArBCl$_2$ species, which has been sought to expand, limits this approach. The role of the BN unit and a detailed quenching mechanism is still under theoretical investigation.

To further qualify the effect of strongly electron-donating TPA-groups at the boron atom, all **BNCDI**s were subjected to spectroelectrochemistry to investigate the absorption behavior of the radical species obtained after reduction or oxidation. Interestingly, the observed species exhibited well-defined absorbance in the NIR region (900-1300 nm) of the electromagnetic spectrum indicating the presence of a biradical species. Moreover, the **TPA-BNCDI** showed surprisingly high reversibility of all redox processes proving its amphoteric redox character. This was not reported for any larger BN-substituted PAHs before. Since the **TPA-BNCDI**s exhibited fully reversible redox processes and multi-charge storage, their implementation in ambipolar OFET devices[139] appears promising and should be investigated in the future. Since similar triphenyl-substituted **PDI**s were successfully utilized in two-photon absorption and non-linear optics,[140] **TPA-BNCDI**s could exhibit similar characteristics due to their D-A-D motif.

Furthermore, in this study, the **BNCDI**s and their interaction with Lewis bases/acids and solvents of different polarities were deeply investigated. While changes in absorption and emission for BN-systems after treating them with Lewis bases/acids were known beforehand, the attachment of two BN units to a chromophore led to absorption and emission of the **BNCDI**s in the near-infrared region of the electromagnetic spectrum. It is proposed that strong conformational changes of the BN units in the periphery of the **CDI** scaffold led to this observation. An additional effect of the TPA-substitution pattern and further Lewis base activity was not found.

Electron-donating groups at the boron atom had a low influence on the absorption maxima of the **BNCDI**s. Therefore, the enlargement of the π-system by lateral extension of the **BNCDI** scaffold could be an alternative to lower the HOMO-LUMO gap. This has already been studied for all-carbon coronene diimides (**CDI**s). A narrower optical gap, an energetically higher LUMO level and increased quantum yields were observed as **CDI** (E_{opt} = 2.46 eV, E_{LUMO} = -3.62 eV, Φ_{lum} = 0.69) were compared to **dibenzo-CDI** (E_{opt} = 2.42 eV, E_{LUMO} = -3.75 eV, Φ_{lum} = 0.80), **dinaphtho-CDI** (E_{opt} = 2.07 eV, E_{LUMO} = -3.84 eV, Φ_{lum} = 0.42).[52]

Therefore, it would be intriguing to obtain the according **di(benzo/naphtho)-BNCDI**s to compare them with the all-carbon **di(benzo/naphtho)-CDI**s (Fig. 81).

di(benzo/naphtho)-BNCDI   vs.   di(benzo/naphtho)-CDI
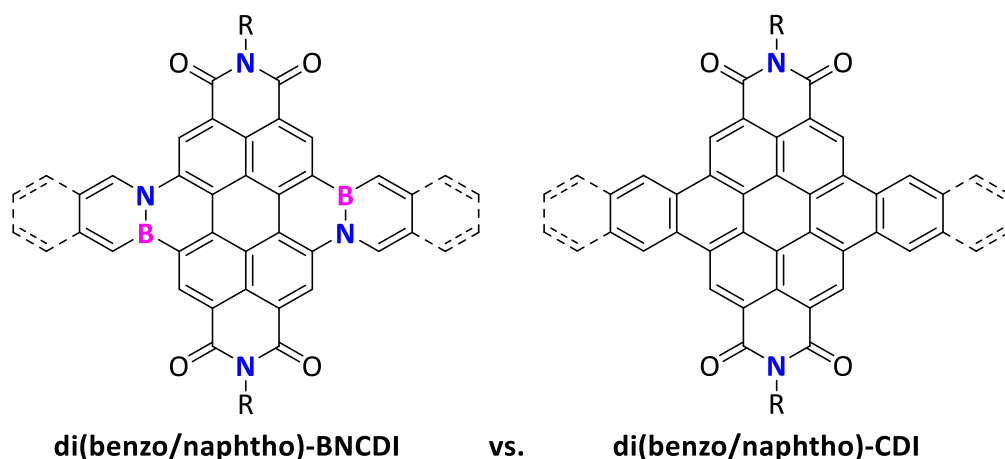
Fig. 81: Lateral π-extension of **BNCDI**s towards **di(benzo/dinaphtho)-BNCDI**s to compare them with already existing **dibenzo(dinaphtho)-CDI**.

Especially the formation of a **dinaphtho-BNCDI** could be interesting since its all-carbon derivative **dinaphto-CDI** exhibited a strong bathochromically shifted absorption (λ_{max} = 573 nm) compared to the smaller **CDI** (Δ = 79 nm) and **PDI** (Δ = 48 nm) derivatives.[52]

In general, these chromatic **BNCDI** derivatives might be promising dyes for OLED, OFET or organic photovoltaics, like dye-sensitized solar cells (DSSC) or organic solar cells (OSC), due to their photophysics and low-lying LUMO. For processing and morphologic reasons, bulk heterojunction (BHJ) organic solar cells could be a feasible way to access organic photovoltaics as well. Therefore, the synthesis of a polymeric **BNCDI** would be highly interesting.

A facile pathway to obtain such a polymer could be *via* copolymerization of a difunctionalized **BNCDI** with a difunctional electron-donating heterocycle (Scheme 47).
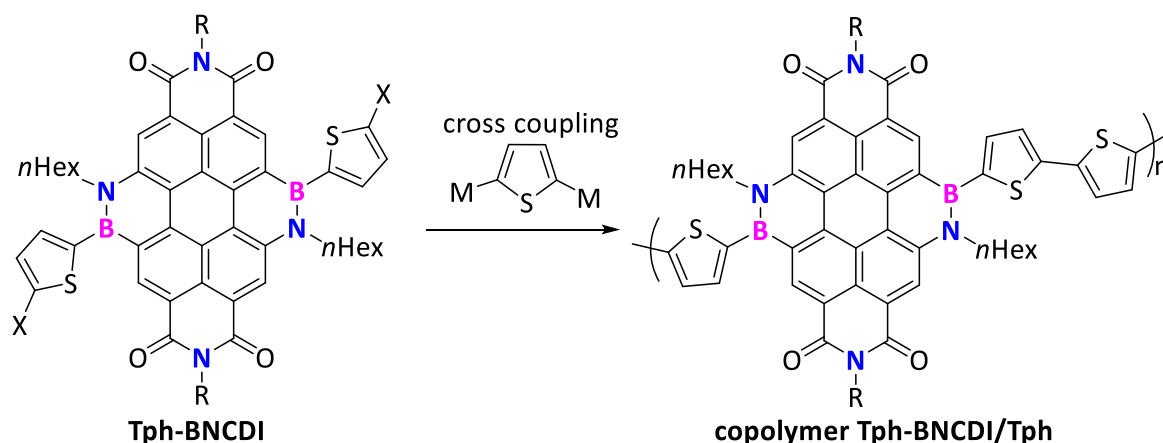
Scheme 47: Proposed synthesis of copolymer **Tph-BNCDI/Tph** *via* cross coupling of a functionalized **Tph-BNCDI** with a dinucleophilic thiophene.

The advantage of such a donor-acceptor design would be the utilization in a single layer setup in an OSC device as well as the prospected narrowed HOMO-LUMO gap due to the extension of the π-system.

Overall, the **BNCDI**s represent a substance class with a high potential for application in optoelectronic devices and sensors. Furthermore, the presented structures help to understand the effect of BN units implemented into common PAH structures. Especially the optical behavior of BN-substitutes under influence of oxidative or reductive conditions or in combination with Lewis acids or bases puts a different complexion on BN-substituted PAHs.

3.8 References

1.   J. E. Anthony, *Chem. Rev.*, **2006**, *106*, 5028-5048.
2.   M. Stepien, E. Gonka, M. Zyla, N. Sprutta, *Chem. Rev.*, **2017**, *117*, 3479-3716.
3.   J. Mei, Y. Diao, A. L. Appleton, L. Fang, Z. Bao, *J. Am. Chem. Soc.*, **2013**, *135*, 6724-6746.
4.   C. Aumaitre, J. F. Morin, *Chem. Rec.*, **2019**, *19*, 1142-1154.
5.   Z. Liu, Y. Wu, Q. Zhang, X. Gao, *J. Mater. Chem. A*, **2016**, *4*, 17604-17622.
6.   C. Wang, H. Dong, W. Hu, Y. Liu, D. Zhu, *Chem. Rev.*, **2012**, *112*, 2208-2267.
7.   J. Wu, W. Pisula, K. Mullen, *Chem. Rev.*, **2007**, *107*, 718-747.
8.   A. Narita, X. Y. Wang, X. Feng, K. Mullen, *Chem. Soc. Rev.*, **2015**, *44*, 6616-6643.
9.   L. Schmidt-Mende, A. Fechtenkotter, K. Mullen, E. Moons, R. H. Friend, J. D. MacKenzie, *Science*, **2001**, *293*, 1119-1122.
10.   T. Kaehler, M. Bolte, H. W. Lerner, M. Wagner, *Angew. Chem. Int. Ed.*, **2019**, *58*, 11379-11384.
11.   M. Vanga, R. A. Lalancette, F. Jakle, *Chemistry*, **2019**, *25*, 10133-10140.
12.   K. Liu, R. A. Lalancette, F. Jakle, *J. Am. Chem. Soc.*, **2017**, *139*, 18170-18173.
13.   Y. Appiarius, T. Stauch, E. Lork, P. Rusch, N. C. Bigall, A. Staubitz, *Org. Chem. Front.*, **2020**.
14.   M. M. Morgan, M. Nazari, T. Pickl, J. M. Rautiainen, H. M. Tuononen, W. E. Piers, G. C. Welch, B. S. Gelfand, *Chem. Commun.*, **2019**, *55*, 11095-11098.
15.   K. Liu, R. A. Lalancette, F. Jakle, *J. Am. Chem. Soc.*, **2019**, *141*, 7453-7462.
16.   M. J. S. Dewar, V. P. Kubba, R. Pettit, *J. Chem. Soc.*, **1958**, 3073-3076.
17.   M. J. Bosdet, C. A. Jaska, W. E. Piers, T. S. Sorensen, M. Parvez, *Org. Lett.*, **2007**, *9*, 1395-1398.
18.   J. Huang, Y. Li, *Front. Chem.*, **2018**, *6*, 341.
19.   J.-Y. Wang, J. Pei, *Chin. Chem. Lett.*, **2016**, *27*, 1139-1146.
20.   T. Hatakeyama, S. Hashimoto, S. Seki, M. Nakamura, *J. Am. Chem. Soc.*, **2011**, *133*, 18614-18617.

21. T. Hatakeyama, S. Hashimoto, T. Oba, M. Nakamura, *J. Am. Chem. Soc.*, **2012**, *134*, 19600-19603.

22. X. Y. Wang, H. R. Lin, T. Lei, D. C. Yang, F. D. Zhuang, J. Y. Wang, S. C. Yuan, J. Pei, *Angew. Chem. Int. Ed.*, **2013**, *52*, 3117-3120.

23. X. Y. Wang, D. C. Yang, F. D. Zhuang, J. J. Liu, J. Y. Wang, J. Pei, *Chemistry*, **2015**, *21*, 8867-8873.

24. Y. Chen, W. Chen, Y. Qiao, X. Lu, G. Zhou, *Angew. Chem.*, **2020**, *132*, 7188-7196.

25. E. R. Abbey, L. N. Zakharov, S. Y. Liu, *J. Am. Chem. Soc.*, **2008**, *130*, 7250-7252.

26. H. Sachdev, N. Zahn, V. Huch, *Z. Anorg. Allg. Chem.*, **2009**, *635*, 2112-2119.

27. S. Hashimoto, T. Ikuta, K. Shiren, S. Nakatsuka, J. Ni, M. Nakamura, T. Hatakeyama, *Chem. Mater.*, **2014**, *26*, 6265-6271.

28. X.-Y. Wang, F.-D. Zhuang, X. Zhou, D.-C. Yang, J.-Y. Wang, J. Pei, *J. Mater. Chem. C*, **2014**, *2*, 8152-8161.

29. A. Yamamoto, E. Ohta, N. Kishigami, N. Tsukahara, Y. Tomiyori, H. Sato, Y. Matsui, Y. Kano, K. Mizuno, H. Ikeda, *Tetrahedron Lett.*, **2013**, *54*, 4049-4053.

30. X. Y. Wang, F. D. Zhuang, R. B. Wang, X. C. Wang, X. Y. Cao, J. Y. Wang, J. Pei, *J. Am. Chem. Soc.*, **2014**, *136*, 3764-3767.

31. X. Y. Wang, F. D. Zhuang, X. C. Wang, X. Y. Cao, J. Y. Wang, J. Pei, *Chem. Commun.*, **2015**, *51*, 4368-4371.

32. G. Li, W. W. Xiong, P. Y. Gu, J. Cao, J. Zhu, R. Ganguly, Y. Li, A. C. Grimsdale, Q. Zhang, *Org. Lett.*, **2015**, *17*, 560-563.

33. Z. Zhong, X.-Y. Wang, F.-D. Zhuang, N. Ai, J. Wang, J.-Y. Wang, J. Pei, J. Peng, Y. Cao, *J. Mater. Chem. A*, **2016**, *4*, 15420-15425.

34. D. Wu, H. Zhang, J. Liang, H. Ge, C. Chi, J. Wu, S. H. Liu, J. Yin, *J. Org. Chem.*, **2012**, *77*, 11319-11324.

35. G. Li, Y. Zhao, J. Li, J. Cao, J. Zhu, X. W. Sun, Q. Zhang, *J. Org. Chem.*, **2015**, *80*, 196-203.

36. H. Langhals, S. Kirner, *Eur. J. Org. Chem.*, **2000**, 365-380.

37. A. Goujon, L. Rocard, T. Cauchy, P. Hudhomme, *J. Org. Chem.*, **2020**, *85*, 7218-7224.

38. T. Kaehler, M. Bolte, H.-W. Lerner, M. Wagner, *Angew. Chem.*, **2019**, *131*, 11501-11506.

39. P. B. Pati, E. Jin, Y. Kim, Y. Kim, J. Mun, S. J. Kim, S. J. Kang, W. Choe, G. Lee, H.-J. Shin, Y. S. Park, *Angew. Chem.*, **2020**.

40. S. Wang, D.-T. Yang, J. Lu, H. Shimogawa, S. Gong, X. Wang, S. K. Mellerup, A. Wakamiya, Y.-L. Chang, C. Yang, Z.-H. Lu, *Angew. Chem.*, **2015**, *127*, 15289-15293.

41. F. D. Zhuang, Z. H. Sun, Z. F. Yao, Q. R. Chen, Z. Huang, J. H. Yang, J. Y. Wang, J. Pei, *Angew. Chem.*, **2019**, *131*, 10818-10822.

42. L. Chen, C. Li, K. Müllen, *J. Mater. Chem. C*, **2014**, *2*, 1938-1956.

43. T. Weil, T. Vosch, J. Hofkens, K. Peneva, K. Müllen, *Angew. Chem.*, **2010**, *122*, 9252-9278.

44. F. Würthner, C. R. Saha-Möller, B. Fimmel, S. Ogi, P. Leowanawat, D. Schmidt, *Chem. Rev.*, **2015**, *116*, 962-1052.

45. Z. Zhao, Z. Yin, H. Chen, L. Zheng, C. Zhu, L. Zhang, S. Tan, H. Wang, Y. Guo, Q. Tang, Y. Liu, *Adv. Mater.*, **2017**, *29*.

46. P. Osswald, D. Leusser, D. Stalke, F. Wurthner, *Angew. Chem. Int. Ed. Engl.*, **2004**, *44*, 250-253.

47. G. Li, D. Li, X. Liu, H. Xu, J. Zhang, S. Wang, Z. Liu, B. Tang, *Chem. Commun.*, **2019**, *55*, 9661-9664.

48. D. Sun, D. Meng, Y. Cai, B. Fan, Y. Li, W. Jiang, L. Huo, Y. Sun, Z. Wang, *J. Am. Chem. Soc.*, **2015**, *137*, 11156-11162.

49. Y. Zhou, B. Xue, C. Wu, S. Chen, H. Liu, T. Jiu, Z. Li, Y. Zhao, *Chem. Commun.*, **2019**, *55*, 13570-13573.

50. A. D. Hendsbee, J.-P. Sun, W. K. Law, H. Yan, I. G. Hill, D. M. Spasyuk, G. C. Welch, *Chem. Mater.*, **2016**, *28*, 7098-7109.

51. F. You, X. Zhou, H. Huang, Y. Liu, S. Liu, J. Shao, B. Zhao, T. Qin, W. Huang, *New J. Chem.*, **2018**, *42*, 15079-15087.

52. C. L. Eversloh, C. Li, K. Mullen, *Org. Lett.*, **2011**, *13*, 4148-4150.

53. F. Wurthner, *Chem. Commun.*, **2004**, 1564-1579.

54. A. Nowak-Krol, K. Shoyama, M. Stolte, F. Wurthner, *Chem. Commun.*, **2018**, *54*, 13763-13772.
55. J. Hoffmann, *Master Thesis: Synthesis and Characterization of Novel Perylene Diimides and Their Derivatives*, University Kiel, **2016**.
56. S. Sengupta, R. K. Dubey, R. W. Hoek, S. P. van Eeden, D. D. Gunbas, F. C. Grozema, E. J. Sudholter, W. F. Jager, *J. Org. Chem.*, **2014**, *79*, 6655-6662.
57. M. J. Ahrens, M. J. Tauber, M. R. Wasielewski, *J. Org. Chem.*, **2006**, *71*, 2107-2114.
58. B. Wrackmeyer, H. Nöth, *Chem. Ber.*, **1976**, *109*, 1075-1088.
59. Y. Shibano, H. Imahori, C. Adachi, *J. Phys. Chem. C*, **2009**, *113*, 15454-15466.
60. A. Shafir, S. L. Buchwald, *J. Am. Chem. Soc.*, **2006**, *128*, 8742-8743.
61. J. R. Pratt, F. H. Pinkerton, S. F. Thames, *J. Organomet. Chem.*, **1972**, *38*, 29-36.
62. H. Braunschweig, A. Damme, J. O. Jimenez-Halla, C. Horl, I. Krummenacher, T. Kupfer, L. Mailander, K. Radacki, *J. Am. Chem. Soc.*, **2012**, *134*, 20169-20177.
63. Z. Zhang, R. M. Edkins, J. Nitsch, K. Fucke, A. Steffen, L. E. Longobardi, D. W. Stephan, C. Lambert, T. B. Marder, *Chem. Sci.*, **2015**, *6*, 308-321.
64. J. R. Lawson, V. Fasano, J. Cid, I. Vitorica-Yrezabal, M. J. Ingleson, *Dalton Trans.*, **2016**, *45*, 6060-6070.
65. S. A. Iqbal, J. Pahl, K. Yuan, M. J. Ingleson, *Chem. Soc. Rev.*, **2020**.
66. A. Herrmann, K. Müllen, *Chem. Lett.*, **2006**, *35*, 978-985.
67. C. Jung, B. K. Muller, D. C. Lamb, F. Nolde, K. Mullen, C. Brauchle, *J. Am. Chem. Soc.*, **2006**, *128*, 5283-5291.
68. T. Weil, T. Vosch, J. Hofkens, K. Peneva, K. Mullen, *Angew. Chem. Int. Ed.*, **2010**, *49*, 9068-9093.
69. X. Zhan, A. Facchetti, S. Barlow, T. J. Marks, M. A. Ratner, M. R. Wasielewski, S. R. Marder, *Adv. Mater.*, **2011**, *23*, 268-284.
70. Q. Yan, K. Cai, C. Zhang, D. Zhao, *Org. Lett.*, **2012**, *14*, 4654-4657.
71. W. Mao, J. Zhang, X. Li, C. Li, H. Tian, *Chem. Commun.*, **2017**, *53*, 5052-5055.
72. U. Rohr, C. Kohl, K. Müllen, A. van de Craats, J. Warman, *J. Mater. Chem.*, **2001**, *11*, 1789-1799.
73. F. Nolde, W. Pisula, S. Müller, C. Kohl, K. Müllen, *Chem. Mater.*, **2006**, *18*, 3715-3725.
74. C. Zhang, K. Shi, K. Cai, J. Xie, T. Lei, Q. Yan, J. Y. Wang, J. Pei, D. Zhao, *Chem. Commun.*, **2015**, *51*, 7144-7147.
75. Y. Avlasevich, C. Li, K. Müllen, *J. Mater. Chem.*, **2010**, *20*, 3814.
76. M. Adachi, Y. Nagao, *Chem. Mater.*, **2001**, *13*, 662-669.
77. Y. Huang, J. Xing, Q. Gong, L. C. Chen, G. Liu, C. Yao, Z. Wang, H. L. Zhang, Z. Chen, Q. Zhang, *Nat. Commun.*, **2019**, *10*, 169.
78. Q. Zhao, S. Zhang, Y. Liu, J. Mei, S. Chen, P. Lu, A. Qin, Y. Ma, J. Z. Sun, B. Z. Tang, *J. Mater. Chem.*, **2012**, *22*, 7387.
79. J. Ide, R. Mereau, L. Ducasse, F. Castet, Y. Olivier, N. Martinelli, J. Cornil, D. Beljonne, *J. Phys. Chem. B*, **2011**, *115*, 5593-5603.
80. Z. Chen, V. Stepanenko, V. Dehm, P. Prins, L. D. Siebbeles, J. Seibt, P. Marquetand, V. Engel, F. Wurthner, *Chemistry*, **2007**, *13*, 436-449.
81. F. Zhang, Y. Ma, Y. Chi, H. Yu, Y. Li, T. Jiang, X. Wei, J. Shi, *Sci. Rep.*, **2018**, *8*, 8208.
82. M. J. Lin, A. Jimenez, C. Burschka, F. Wurthner, *Chem. Commun.*, **2012**, *48*, 12050-12052.
83. S. Nakazono, S. Easwaramoorthi, D. Kim, H. Shinokubo, A. Osuka, *Org. Lett.*, **2009**, *11*, 5426-5429.
84. X. Li, H. Wang, J. A. Schneider, Z. Wei, W.-Y. Lai, W. Huang, F. Wudl, Y. Zheng, *J. Mater. Chem. C*, **2017**, *5*, 2781-2785.
85. B. Zhang, H. Soleimaninejad, D. J. Jones, J. M. White, K. P. Ghiggino, T. A. Smith, W. W. H. Wong, *Chem. Mater.*, **2017**, *29*, 8395-8403.
86. J. L. Banal, H. Soleimaninejad, F. M. Jradi, M. Liu, J. M. White, A. W. Blakers, M. W. Cooper, D. J. Jones, K. P. Ghiggino, S. R. Marder, T. A. Smith, W. W. H. Wong, *J. Phys. Chem. C*, **2016**, *120*, 12952-12958.
87. A. Rademacher, S. Märkle, H. Langhals, *Chem. Ber.*, **1982**, *115*, 2927-2934.
88. Z. Chen, B. Fimmel, F. Wurthner, *Org. Biomol. Chem.*, **2012**, *10*, 5845-5855.
89. P. I. Djurovich, E. I. Mayo, S. R. Forrest, M. E. Thompson, *Org. Electron.*, **2009**, *10*, 515-520.

90. J. L. Bredas, R. Silbey, D. S. Boudreaux, R. R. Chance, *J. Am. Chem. Soc.*, **1983**, *105*, 6555-6559.

91. J. Seibt, P. Marquetand, V. Engel, Z. Chen, V. Dehm, F. Würthner, *Chem. Phys.*, **2006**, *328*, 354-362.

92. H. Langhals, *Heterocycles*, **1995**, *40*, 477.

93. R. Gvishi, R. Reisfeld, Z. Burshtein, *Chem. Phys. Lett.*, **1993**, *213*, 338-344.

94. L. Hao, W. Jiang, Z. Wang, *Tetrahedron*, **2012**, *68*, 9234-9239.

95. F. Wurthner, C. R. Saha-Moller, B. Fimmel, S. Ogi, P. Leowanawat, D. Schmidt, *Chem. Rev.*, **2016**, *116*, 962-1052.

96. J. Calbo, A. Doncel-Giménez, J. Aragó, E. Ortí, *Theor. Chem. Acc.*, **2018**, *137*.

97. P. V. R. Schleyer, C. Maerker, A. Dransfeld, H. Jiao, N. J. R. van Eikema Hommes, *J. Am. Chem. Soc.*, **1996**, *118*, 6317-6318.

98. B. Goldfuss, P. v. R. Schleyer, *Organometallics*, **1997**, *16*, 1543-1552.

99. P. V. R. Schleyer, M. Manoharan, Z. X. Wang, B. Kiran, H. Jiao, R. Puchta, N. J. R. van Eikema Hommes, *Org. Lett.*, **2001**, *3*, 2465-2468.

100. S. K. Lee, Y. Zu, A. Herrmann, Y. Geerts, K. Müllen, A. J. Bard, *J. Am. Chem. Soc.*, **1999**, *121*, 3513-3520.

101. Y. Hong, J. W. Lam, B. Z. Tang, *Chem. Soc. Rev.*, **2011**, *40*, 5361-5388.

102. Y. Hong, J. W. Lam, B. Z. Tang, *Chem. Commun.*, **2009**, 4332-4353.

103. J. Sung, P. Kim, B. Fimmel, F. Wurthner, D. Kim, *Nat Commun*, **2015**, *6*, 8646.

104. Y.-S. Ma, C.-H. Wang, Y.-J. Zhao, Y. Yu, C.-X. Han, X.-J. Qiu, Z. Shi, *Supramol. Chem.*, **2007**, *19*, 141-149.

105. A. L. Briseno, S. C. Mannsfeld, C. Reese, J. M. Hancock, Y. Xiong, S. A. Jenekhe, Z. Bao, Y. Xia, *Nano Lett.*, **2007**, *7*, 2847-2853.

106. Y. Yu, Y. Li, Z. Qin, R. Jiang, H. Liu, Y. Li, *J. Colloid Interface Sci.*, **2013**, *399*, 13-18.

107. S. Horiuchi, T. Hasegawa, Y. Tokura, *J. Phys. Soc. Jpn.*, **2006**, *75*, 051016.

108. X. Wan, C. Li, M. Zhang, Y. Chen, *Chem. Soc. Rev.*, **2020**, *49*, 2828-2842.

109. J. Song, K. Zhao, H. Zhang, C.-K. Wang, *Mol. Phys.*, **2018**, *117*, 672-680.

110. R. Sen, S. P. Singh, P. Johari, *J. Phys. Chem. A*, **2018**, *122*, 492-504.

111. K. Zhou, H. Dong, H. L. Zhang, W. Hu, *Phys. Chem. Chem. Phys.*, **2014**, *16*, 22448-22457.

112. Y. Sun, G. C. Welch, W. L. Leong, C. J. Takacs, G. C. Bazan, A. J. Heeger, *Nat Mater*, **2011**, *11*, 44-48.

113. A. Leliege, P. Blanchard, T. Rousseau, J. Roncali, *Org. Lett.*, **2011**, *13*, 3098-3101.

114. R. Misra, S. P. Bhattacharyya, *Intramolecular Charge Transfer: Theory and Applications*, Wiley VCH, Weinheim, **2018**.

115. C. C. Chao, M. K. Leung, Y. O. Su, K. Y. Chiu, T. H. Lin, S. J. Shieh, S. C. Lin, *J. Org. Chem.*, **2005**, *70*, 4323-4331.

116. M. Kojima, A. Tamoto, N. Aratani, H. Yamada, *Chem. Commun.*, **2017**, *53*, 5698-5701.

117. S. Vajiravelu, L. Ramunas, G. Juozas Vidas, G. Valentas, J. Vygintas, S. Valiyaveettil, *J. Mater. Chem.*, **2009**, *19*, 4268.

118. S.-H. Hsiao, Y.-Z. Chen, *J. Electroanal. Chem.*, **2017**, *799*, 417-423.

119. A. Keerthi, S. Valiyaveettil, *J. Phys. Chem. B*, **2012**, *116*, 4603-4614.

120. Z. R. Grabowski, K. Rotkiewicz, W. Rettig, *Chem. Rev.*, **2003**, *103*, 3899-4032.

121. S. Sasaki, G. P. C. Drummen, G.-i. Konishi, *J. Mater. Chem. C*, **2016**, *4*, 2731-2743.

122. H. Li, J. Han, H. Zhao, X. Liu, Y. Luo, Y. Shi, C. Liu, M. Jin, D. Ding, *J Phys Chem Lett*, **2019**, *10*, 748-753.

123. R. Misra, S. P. Bhattacharyya, **2018**.

124. B. Xu, C. Wang, W. Ma, L. Liu, Z. Xie, Y. Ma, *The Journal of Physical Chemistry C*, **2017**, *121*, 5498-5502.

125. J. R. Lakowicz, *Principles of Fluorescence Spectroscopy*, Springer US, Boston, 3rd edn., **2006**.

126. D. Rehm, A. Weller, *Z. Phys. Chem.*, **1970**, *69*, 183-200.

127. M. R. Wasielewski, M. P. Niemczyk, *J. Am. Chem. Soc.*, **1984**, *106*, 5043-5045.

128. H. A. Staab, G. Voit, J. Weiser, M. Futscher, *Chem. Ber.*, **1992**, *125*, 2303-2310.

129. J. S. Lindsey, J. K. Delaney, D. C. Mauzerall, H. Linschitz, *J. Am. Chem. Soc.*, **1988**, *110*, 3610-3621.
130. D. Escudero, *Acc. Chem. Res.*, **2016**, *49*, 1816-1824.
131. Y. Chen, W. Chen, Y. Qiao, G. Zhou, *Chemistry*, **2019**, *25*, 9326-9338.
132. G. Li, Y. Zhao, J. Li, J. Cao, J. Zhu, X. W. Sun, Q. Zhang, *J. Org. Chem.*, **2015**, *80*, 196-203.
133. M. Lepeltier, O. Lukoyanova, A. Jacobson, S. Jeeva, D. F. Perepichka, *Chem. Commun.*, **2010**, *46*, 7007-7009.
134. M. A. Beckett, G. C. Strickland, J. R. Holland, K. Sukumar Varma, *Polymer*, **1996**, *37*, 4629-4631.
135. U. Mayer, V. Gutmann, W. Gerger, *Monatshefte für Chemie / Chemical Monthly*, **1975**, *106*, 1235-1257.
136. H. Langhals, *Description of properties of binary solvent mixtures*, in *Similarity models in organic chemistry, biochemistry and related fields*, eds. R. I. Zalewski, T. M. Krygowski and J. Shorter, Elsevier, Amsterdam u.a., **1991**, vol. 42, 283-342.
137. Y. Zheng, F. M. Jradi, T. C. Parker, S. Barlow, S. R. Marder, S. S. Saavedra, *ACS Appl. Mater. Interfaces*, **2016**, *8*, 34089-34097.
138. R. Schmidt, J. H. Oh, Y. S. Sun, M. Deppisch, A. M. Krause, K. Radacki, H. Braunschweig, M. Konemann, P. Erk, Z. Bao, F. Wurthner, *J. Am. Chem. Soc.*, **2009**, *131*, 6215-6228.
139. C. Rost, D. J. Gundlach, S. Karg, W. Rieß, *J. Appl. Phys.*, **2004**, *95*, 5782-5787.
140. L. Cao, L. Xu, D. Zhang, Y. Zhou, Y. Zheng, Q. Fu, X.-F. Jiang, F. Lu, *Chem. Phys. Lett.*, **2017**, *682*, 133-139.

3.9 Experimental

NMR-tubes and glassware were dried in an oven at 200 °C overnight before use. If not stated otherwise, all reaction vessels were heated to minimum of 200 °C under a vacuum (1.3 x 10^{-2} mbar to 6.2 x 10^{-2} mbar) and purged with nitrogen or argon at least three times before adding the reagents. Syringes were purged with nitrogen or argon three times prior use. Unless noted otherwise, a nitrogen filled glovebox from Inert, Innovative Technology, Inc. Company (< 0.1 ppm O_2 and < 0.1 ppm H_2O) was used for all reactions. All dry solvents were obtained from a solvent purification system (SPS, from Inert, Innovative Technology, Inc. Comp), degassed by three freeze-pump-thaw cycles and stored under a nitrogen atmosphere unless noted otherwise. In general, solvents were distilled prior to use except for HPLC grade solvents. For Kugelrohr distillation a Kugelrohr oven from Büchi was used.

All NMR spectroscopic measurements were carried out at 300 K. ^{1}H NMR spectra were recorded on a Bruker DRX 500 (500 MHz), a Bruker Avance 600 (600 MHz), a Bruker Avance Neo (600 MHz) with a TXI probe head or a Bruker Avance Neo (600 MHz) with BBO prop head. ^{13}C{^{1}H} NMR spectra were recorded on a DRX 500 (125 MHz), a Bruker Avance 600 (150 MHz), a Bruker Avance Neo (150 MHz) with a TXI probe head or a Bruker Avance Neo (150 MHz) with BBO probe head. ^{1}H and ^{13}C{^{1}H} NMR spectra were referenced against the residual solvent signals. ^{11}B{^{1}H} NMR spectra were recorded on a Bruker DRX 500 (180 MHz) spectrometer. The reference of the ^{11}B{^{1}H} NMR spectra was $BF_3 \cdot OEt_2$ in $CDCl_3$. The ^{11}B{^{1}H} NMR spectra of the **BNCDI**s were performed using a quartz tube and a blank spectrum of $CDCl_3$ was subtracted to ensure that weak/broad signals could be detected without interference of the glass peak from residual boron in the probe head. ^{29}Si{^{1}H} NMR spectra were recorded on a Bruker Avance Neo (119 MHz) spectrometer with BBO probe head. The reference for ^{29}Si{^{1}H} NMR spectra was tetramethylsilane in $CDCl_3$. Where possible, NMR signals were assigned using ^{1}H COSY, ^{1}H/^{1}H NOESY, ^{1}H/^{13}C{^{1}H} HSQC and ^{1}H/^{13}C{^{1}H} HMBC experiments. IR spectra were recorded on a Perkin Elmer Paragon 1000 FT-IR spectrometer with a A531-G Golden-Gate ATR-unit or a Nicolet Thermo iS10 scientific spectrometer with a diamond ATR unit. Melting points were measured with a BÜCHI Melting Point M-560 instrument. Electron impact (EI) mass spectrometric experiments were measured using the direct inlet or indirect inlet methods on a MAT95 XL double-focusing mass spectrometer from Finnigan or a JEOL JMS-100 GCV (AccuTOFGCV) mass spectrometer. The ionization energy of the electron impact ionization was 70 eV. Atmospheric pressure chemical ionization (APCI) and electron spray ionization (ESI) experiments were performed on a Bruker Impact II from Bruker Daltonics. UV/Vis spectra were recorded on a Perkin Elmer Lambda 14 or a Jasco V-770 spectrometer at 20 °C using a quartz cuvette with a length of 1 cm. The UV-Vis emission and excitation spectra measurements were recorded on a FL 920 Edinburgh Instrument and corrected for the response of the photomultiplier. Quantum yields were calculated relative to fluorescein (Φ_{lum} = 0.90 in 0.1 N NaOH). Excitation was performed at 460 nm. The NIR emission spectra were recorded on a C9920-03 Hamamatsu system equipped with a UV/Vis detector (350-950 nm) and a NIR detector (950-1700 nm) at the SCANMAT facility. Excitation was performed at 375 nm with a diode laser. Unless stated otherwise chromatographic purifications were performed with silica gel (Merck, grain size 15-40 µm). Thin layer chromatography (TLC) was performed by using TLC Silicagel 60 F254 from MERCK on alumina plates. For the detection of the spots, a UV lamp (λ = 254/366 nm) was used.

Prior analysis all **BNCDI**s were purified by semipreparative GPC: Compounds were solubilized in HPLC grade chloroform (stabilized with 1% ethanol). Prior to injection, the solution was filtered through a 0.45 µm PTFE filter. Purification was performed on a LC-9160 II NEXT system from the Japan Analytical

Industry Co., Ltd. (JAI) equipped with coupled UV-vis 4Ch NEXT through a set of two JAIGEL-2H columns at an elution rate of 10 mL/min (CHCl₃).

The syntheses and characterizations of the **PDI^Cy**, regioisomeric pure **1,7-DB-PTCDA** and **1,7-DB-PDI^Cy** were previously described in my master thesis.[1] For **TphBCl₂**, **1,7-DHA-PDI^Cy**, **Tph-BNCDI^Cy** and **Ph-BNCDI^Cy** the synthesis was presented in my master thesis, but the synthetic processes and analytics were partly changed or updated.

3.9.1 *N,N'*-(2,6-Di*iso*propylphenyl)-perylene-3,4,9,10-tetracaboxylic acid diimide (**PDI^Dip**)
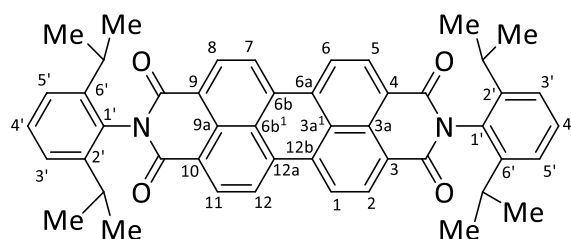
This synthetic procedure was combined from two methods[2, 3]: Under a nitrogen atmosphere a mixture of perylene-3,4,9,10-tetracarboxylic dianhydride (**PTCDA**, 1.00 g, 2.54 mmol), imidazole (30 g) and 2,6-di*iso*propylaniline (1.06 g, 6.00 mmol) was heated to 140 °C for 4 h. After cooling to 60 °C, ethanol (50 mL) was added to the reaction mixture. At 25 °C the reaction mixture was treated with aq. hydrochloric acid (2 M, 50 mL). The precipitate that formed was collected by vacuum filtration, washed with distilled water (300 mL), dried at 120 °C for 24 h, and purified by column chromatography (DCM, silica gel, R$_f$(DCM) = 0.68) to give the product (**PDI^Dip**, 704 mg, 0.99 mmol, 39%, Lit.[3]: 49%) as a red solid. **¹H NMR** (601 MHz, CDCl₃): δ = 8.80 (d, ^3J = 7.9 Hz, 4H, *H*-2,5,8,11), 8.75(d, ^3J = 7.9 Hz, 4H, *H*-1,6,7,12), 7.51 (t, ^3J = 7.8 Hz, 2H, Ph-*H*-4'), 7.36 (d, ^3J = 7.8 Hz, 2H, Ph-*H*-3',5'), 2.76 (sept., ^3J = 6.8 Hz, 4H,C*H*(CH₃)), 1.19 (d, ^3J = 6.8 Hz, 24H, CH(C*H*₃)) ppm. **¹³C{¹H} NMR** (151 MHz, CDCl₃): δ = 163.61 (*C*(O)N), 145.77 (Ph-*C*-2',6'), 135.22 (*C*-6a,6b,12a,12b), 132.25 (*C*-2,5,8,11), 130.64 (Ph-*C*-1'), 130.33 (*C*-3a,9a), 129.86 (Ph-*C*-4'), 127.00 (*C*-3a¹,6b¹), 124.28 (Ph-*C*-3',5'), 123.57 (*C*-3,4,9,10), 123.48 (*C*-1,6,7,12), 29.37 (*C*H(CH₃)₂), 24.17 (*C*H₃) ppm. **HRMS** (EI): *m/z* [M]⁺˙ Calcd. for C₄₈H₄₂N₂O₄ 710.31391; found 710.31455. **IR** (ATR): υ = 3031 (w), 2959 (m), 2925 (m), 1771 (m), 1703(s), 1664 (s), 1592 (s), 1577 (s), 1382 (m), 1345 (s), 1301 (w), 1337 (s), 1248 (m), 1178 (m), 834 (m), 815 (m), 741 (m), 689 (w) cm⁻¹. The analytical data were in agreement with reported values.[3]

3.9.2 1,7-Dibromo-*N,N'*-*bis*(Di*iso*propylphenyl)-perylene-3,4,9,10-tetracaboxylic acid diimide (**1,7-DB-PDI^Dip**)
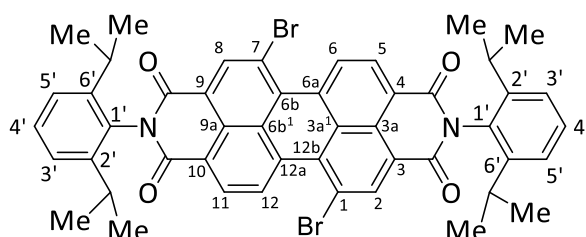
This synthetic procedure was adapted from lit.[4]: Under nitrogen atmosphere a mixture of 1,7-dibromoperylene-3,4,9,10-tetracaboxylic acid dianhydride (**1,7-DB-PTCDA**, 3.79 g, 6.89 mmol) and NMP (40 mL) was placed in an ultrasonic bath for 1 h. Then 2,6-di*iso*propylaniline (7.36 g, 41.5 mmol) and acetic acid (2.25 mL, 39.5 mmol) were added and the reaction was heated to 120 °C for 4 d. After cooling to 25 °C to the reaction mixture water (100 mL) was added. The precipitate was collected by

vacuum filtration and washed with water (600 mL) and methanol (150 mL) and cooled to -10 °C for 12 h. The solid was collected by filtration and washed with cold methanol (50 mL). The resulting powder was dried (2.0 x 10^{-2} mbar, 200 °C, 14 h) and was purified by column chromatography (eluent: DCM, R_f(DCM) = 0.75). The product was obtained as a dark red solid (**1,7-DB-PDI^{Dip}**, 3.80 g, 4.37 mmol, 63%, lit.[4]: 66%). **^{1}H NMR** (601 MHz, CDCl$_3$) δ = 9.57 (d, ^3J = 8.1 Hz, 2H, *H*-6,12), 9.02 (s, 2H, *H*-2,8), 8.81 (d, ^3J = 8.2 Hz, 2H, *H*-5,11), 7.52 (t, ^3J = 7.8 Hz, 2H, Ph-*H*-4'), 7.37 (d, ^3J = 7.8 Hz, 2H, Ph-*H*-3',5'), 2.74 (sept., ^3J = 6.7 Hz, 4H, C*H*), 1.19 (dd, ^3J = 6.7 Hz, ^4J = 1.8 Hz, 24H, C*H$_3$*) ppm. **^{13}C{^{1}H} NMR** (151 MHz, CDCl$_3$): δ = 163.15 ((*C*(O)N)-4,10), 162.65 ((*C*(O)N)-3,9), 145.75 (Ph-*C*-2',6'), 138.63 (*C*-2,8), 133.59 (*C*-6b,12b), 133.43 (*C*-6a,12a), 130.80 (*C*-5,11), 130.27 (Ph-*C*-1'), 130.05 (Ph-*C*-4'), 129.79 (*C*-3,9), 128.87 (*C*-6,12), 127.85 (*C*-3a,9a), 124.36 (Ph-*C*-3',5'), 123.35 (*C*-4,10), 123.02 (*C*-3a^1,6b^1), 121.22 (*C*-1,7), 29.45 (*C*H(CH$_3$)), 24.19 and 24.16 (*C*H$_3$) ppm. **HRMS** (EI): *m/z* [M]$^{+\cdot}$ Calcd. for C$_{48}$H$_{40}$N$_2$O$_4$^{79}Br$_2$ 866.13493; Found 866.13370. **IR** (ATR): υ = 2959 (m), 2925 (m), 1707 (s), 1668 (s), 1589 (s), 1383 (m), 1336 (s), 1248 (m), 1178 (m), 834 (m), 809 (m), 746 (m), 692 (w) cm^{-1}. The analytical data were in agreement with previously reported values.[4]

3.9.3 1,7-Di(*n*-hexylamino)-*N*,*N*'-di(cyclohexyl)perylene-3,4,9,10-tetracaboxylic acid diimide (**1,7-DHA-PDI^{Cy}**)
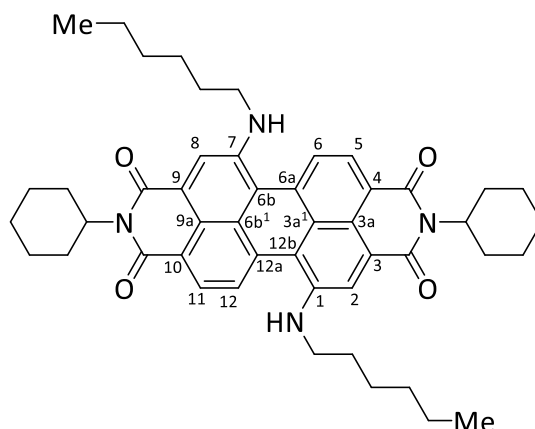
Under an argon atmosphere, 1,7-dibromo-*N*,*N*'-di(cyclohexyl)perylene-3,4,9,10-tetracarboxylic acid diimide (**1,7-DB-PDI^{Cy}**, 100 mg, 140 µmol) and *n*-hexylamine (10.0 mL, 76.0 mmol) were mixed. The mixture was stirred at 60 C for 3 d. Subsequently, the excess of *n*-hexylamine was removed at a rotary evaporator (80 °C, 10 mbar). The crude product was purified by column chromatography (silica, eluent: DCM, R_f(DCM) = 0.68) to yield the product as a green solid (**1,7-DHA-PDI^{Cy}**, 53 mg, 70.4 µmol, 50%). **^{1}H NMR** (600 MHz, CDCl$_3$): δ = 8.60 (d, ^3J = 8.1 Hz, 2H, *H*-6,12), 8.16 (d, ^3J = 8.1 Hz, 2H, *H*-5,11), 7.96 (s, 2H, *H*-2,8), 5.59 (t, ^3J = 4.6 Hz, 2H, N*H*), 5.01 (tt, ^3J = 12.1, 3.6 Hz, 2H, C*H*), 3.19 (q, ^3J = 6.8 Hz , 4H, NH-C*H$_2$*), 2.57 (qd, ^3J = 12.1, 3.0 Hz, 4H, CH-C*H$_{ax}$*), 1.93 (d, ^3J = 12.6 Hz, 4H, CH-CH$_2$-C*H$_{ax}$*), 1.83 - 1.71 (m, 6H, CH-C*H$_{eq}$* and CH-(CH$_2$)$_2$-C*H$_{ax}$*), 1.66 (quin., ^3J = 7.1 Hz, 4H, NH-(CH$_2$)-C*H$_2$*), 1.51 - 1.21 (m, 18H, CH-CH$_2$-C*H$_{eq}$*, CH-(CH$_2$)$_2$-C*H$_{eq}$* and NH-(CH$_2$)$_2$-(C*H$_2$*)$_3$), 0.93 (t, ^3J = 7.1 Hz, 6H, C*H$_3$*) ppm. **^{13}C{^{1}H} NMR** (150 MHz, CDCl$_3$): δ = 164.36 ((*C*(O)N)-3,9), 163.91 ((*C*(O)N)-4,10), 145.89 (*C*-1,7), 133.86 (*C*-6a,12a), 129.89 (*C*-4,10), 126.97 (*C*-5,11), 123.17 (*C*-3,9), 122.45 (*C*-3a,9a), 121.46 (*C*-6,12), 120.66 (*C*-3a^1,6b^1), 117.94 (*C*-2,8), 116.73 (*C*-6b,12b), 54.00 (*C*H), 44.75 (NH-*C*H$_2$), 31.64 (NH-CH$_2$-*C*H$_2$), 29.44 (CH-*C*H$_2$), 29.27 (NH-(CH$_2$)$_2$-*C*H$_2$), 27.09 (NH-(CH$_2$)$_3$-*C*H$_2$), 26.76 (CH-CH$_2$-*C*H$_2$), 25.68 (CH-(CH$_2$)$_2$-*C*H$_2$), 22.74 (NH-(CH$_2$)$_4$-*C*H$_2$), 14.15 (*C*H$_3$) ppm. **HRMS** (APCI): *m/z* [M+H]$^+$ Calcd. for C$_{48}$H$_{57}$N$_4$O$_4$ 753.43743; Found 753.43686. **IR** (ATR): υ = 3314 (w), 2924 (m), 2851 (m), 1687 (s), 1641 (s), 1584 (s), 1568 (s), 1512 (w), 1452 (w), 1421 (m), 1330 (s), 1280 (m), 1257 (m), 1190 (m), 1124 (w), 1102 (w), 984 (m), 895 (w), 866 (w), 805 (m), 750 (m), 653 (m), 643 (m) cm^{-1}.

3.9.4 1,7-Di(*n*-hexylamino)-*N*,*N'*-*bis*(2,6-di(*iso*proypyl)phenyl)perylene-3,4,9,10-tetracaboxylic acid diimide (**1,7-DHA-PDI$^{\text{Dip}}$**)
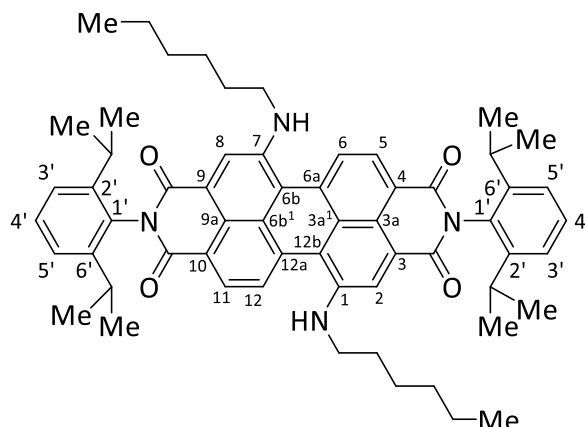
Under an argon atmosphere, 1,7-dibromo-*N*,*N'*-*bis*(di*iso*proypylphenyl)perylene-3,4,9,10-tetracarboxylic acid diimide (**1,7-DB-PDI$^{\text{Dip}}$**, 100 mg, 117 µmol) and *n*-hexylamine (10.0 mL, 76.0 mmol) were mixed. The mixture was stirred at 60 °C for 3 d. Subsequently, the excess of *n*-hexylamine was removed at a rotary evaporator (80 °C, 10 mbar). The crude product was purified by column chromatography (silica, eluent: DCM, R$_f$(DCM) = 0.74) to yield the product as a green solid (**1,7-DHA-PDI$^{\text{Dip}}$**, 54 mg, 59.3 µmol, 51%). The reaction was also performed on a 2.34 mmol scale where the product was isolated in lower yield (**1,7-DHA-PDI$^{\text{Dip}}$**, 204 mg, 0.22 mmol, 10%). As side-product (R$_f$(DCM) = 0.55) the product of transamination **1,7-DHA-PDI^{nhex}** was isolated as a green solid (187 mg, 0.20 mmol, 9%). **^{1}H NMR** (600 MHz, CDCl$_3$): δ = 8.91 (d, ^3J = 8.1 Hz, 2H, *H*-6,12), 8.46 (d, ^3J = 8.1 Hz, 2H, *H*-5,11), 8.30 (s, 2H, *H*-2,8), 7.49 (t, ^3J = 7.8 Hz, 2H, Ph-*H*-4'), 7.35 (d, ^3J = 7.8 Hz, 4H, Ph-*H*-3',5'), 5.81 (t, ^3J = 7.8 Hz, 2H, N*H*), 3.48 (q, ^3J = 7.1 Hz, 4H, NH-C*H*$_2$), 3.33-3.27 (m, 4H, NH-C*H*$_2$), 2.77 (sept., ^3J = 6.6 Hz, 4H, Ph-(C*H*)-(CH$_3$)$_2$), 1.79 (quin., ^3J = 7.1 Hz, 4H, NH-(CH$_2$)-C*H*$_2$), 1.43 - 1.32 (m, 8H, NH-(CH$_2$)$_2$-(C*H*$_2$)$_3$), 1.22 - 1.16 (m, 24H, Ph-(CH)-(C*H*$_3$)$_2$), 0.91 (t, ^3J = 7.0 Hz, 6H, C*H*$_3$) ppm. **^{13}C{^{1}H} NMR** (150 MHz, CDCl$_3$): δ = 163.84 ((*C*(O)N)-3,9), 163.75 ((*C*(O)N)-4,10), 146.19 (*C*-1,7), 145.67 (Ph-*C*-2',6'), 134.40 (*C*-6a,12a), 130.94 (Ph-*C*-1'), 130.54 (*C*-4,10), 129.51 (Ph-*C*-4'), 127.54 (*C*-5,11), 124.03 (Ph-*C*-3',5'), 123.24 (*C*-3,9), 123.00 (*C*-3a^1,6b^1), 121.78 (*C*-6,12), 120.42 (*C*-3a,9a), 118.85 (*C*-2,8), 117.21 (*C*-6b,12b), 44.90 (NH-C*H*$_2$), 31.46 (NH-CH$_2$-*C*H$_2$), 29.71 (NH-(CH$_2$)$_2$-*C*H$_2$), 29.51 (Ph-(*C*H)-(CH$_3$)$_2$), 26.90 (NH-(CH$_2$)$_3$-*C*H$_2$), 24.05 and 24.03 (Ph-(CH)-(*C*H$_3$)$_2$), 22.56 (NH-(CH$_2$)$_4$-*C*H$_2$), 14.00 (*C*H$_3$) ppm. **HRMS** (ESI): *m/z* [M+H]$^+$ Calcd. for C$_{60}$H$_{69}$N$_4$O$_4$ 909.53152; Found 909.53133. **IR** (ATR): υ = 3338 (w), 2956 (m), 2925 (m), 2855 (m), 1690 (s), 1653 (m), 1583 (m), 1568 (m), 1507 (m), 1456 (m), 1421 (m), 1338 (s), 1276 (s), 1197 (m), 1125 (m), 866 (m), 840 (m), 805 (m), 764 (m), 750 (s), 737 (m), 691 (m) cm^{-1}.

3.9.5 1,7-Di(*n*-hexylamino)-*N*,*N'*-di(*n*-hexyl)perylene-3,4,9,10-tetracaboxylic acid diimide (**1,7-DHA-PDI^{nhex}**)
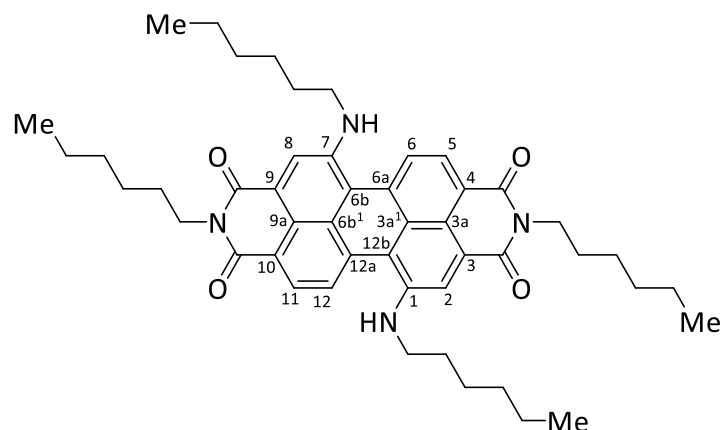
This product was isolated as side-product.

^{1}H NMR (500 MHz, CDCl$_3$): δ = 8.48 (d, ^3J = 8.1 Hz, 2H, *H*-6,12), 8.09 (d, ^3J = 8.1 Hz, 2H, *H*-5,11), 7.80 (s, 2H, *H*-2,8), 5.49 (t, ^3J = 4.8 Hz, 2H, N*H*-CH$_2$), 4.08 (t, ^3J = 7.8 Hz, 4H, (CO)$_2$N-C*H$_2$*), 3.08 (dd, ^3J = 12.1, 6.9 Hz, 4H, NH-C*H$_2$*), 1.71 (quin, ^3J = 7.5 Hz, 4H, (CO)$_2$N-CH$_2$-C*H$_2$*), 1.58 (quin, ^3J = 7.3 Hz, 4H, NH-CH$_2$-C*H$_2$*), 1.47 - 1.28 (m, 24H, NH-(CH$_2$)$_2$-(C*H$_2$*)$_3$ and (CO)$_2$N-(CH$_2$)$_2$-(C*H$_2$*)$_3$) and (CO)$_2$N-(CH$_2$)$_2$-(C*H$_2$*)$_3$), 0.96 - 0.86 (m, 12H, C*H$_3$*) ppm. **^{13}C{^{1}H} NMR** (126 MHz, CDCl$_3$): δ = 163.67 ((*C*(O)N)-3,9), 163.19 ((*C*(O)N)-4,10), 145.77 (*C*-1,7), 133.80 (*C*-6a, 12a), 129.68 (*C*-4,10), 126.60 (*C*-5,11), 122.39 (*C*-3,9), 122.08 (*C*-3a,9a), 121.31 (*C*-6,12), 120.03 (*C*-3a^1,6b^1), 117.71 (*C*-2,8), 116.56 (*C*-6b,12b), 44.67 (NH-*C*H$_2$), 40.69 ((CO)$_2$N-*C*H$_2$), 31.71 ((NH-(CH$_2$)$_4$-*C*H$_2$) or ((CO)$_2$N-(CH$_2$)$_4$-*C*H$_2$)), 31.66 ((NH-(CH$_2$)$_4$-*C*H$_2$) or ((CO)$_2$N-(CH$_2$)$_4$-*C*H$_2$)), 29.37 (NH-CH$_2$-*C*H$_2$), 28.13 ((CO)$_2$N-CH$_2$-*C*H$_2$), 27.11 (NH-(CH$_2$)$_2$-*C*H$_2$), 27.01 ((CO)$_2$N-(CH$_2$)$_2$-*C*H$_2$), 22.75 (NH-(CH$_2$)$_4$-*C*H$_2$) and ((CO)$_2$N-(CH$_2$)$_4$-*C*H$_2$), (NH-(CH$_2$)$_4$-*C*H$_2$) 14.14 (*C*H$_3$) ppm. **HRMS** (ESI): *m/z* calcd. for C$_{48}$H$_{60}$N$_4$O$_4$ 756.46091 [M+H]$^+$, found 756.46031 [M+H]$^+$. **IR** (ATR): υ = 3318 (w), 2954 (m), 2920 (m), 2852 (m), 1734 (m), 1717 (s), 1685 (m), 1653 (m), 1590 (m), 1569 (m), 1560 (m), 1507 (m), 1489 (m), 1472 (m), 1420 (m), 1338 (s), 1276 (s), 1260 (m), 1181 (m), 1122 (m), 1091 (m), 1022 (m) 866 (m), 804 (m), 720 (m),682 (m) cm^{-1}.

3.9.6 5,5'-Dibromo-2,2'-bithiopene (**51**)
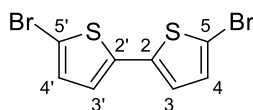
Under argon bithiophene (**88**, 2.00 g, 12.0 mmol) and *N*-bromosuccinimide (4.45 g, 25.0 mmol) were dissolved in a mixture of chloroform/acetic acid (60 mL, 1:1) and stirred at 25 °C. The reaction progress was followed by TLC and quenched after 16 h with an aq. sat. sodium bicarbonate solution (100 mL). The phases were separated, and the aqueous phase was extracted with chloroform (2 x 200 mL). The combined organic phases were washed with brine (200 mL) and dried over magnesium sulfate and the solvent was removed under reduced pressure. After filtration over a short plug of silica with *n*-heptane as eluent and removal of the solvent the resulting solid was recrystallized from hot ethanol (100 mL) to give the resulting product as white crystals (**51**, 2.02 g, 6.25 mmol, 52%). **^{1}H NMR** (601 MHz, CDCl$_3$): δ = 6.96 (d, ^3J = 3.8 Hz, 2H, *H*-3,3'), 6.85 (d, ^3J = 3.8 Hz, 2H, *H*-4,4'), ppm. **^{13}C{^{1}H} NMR** (151 MHz, CDCl$_3$): δ = 137.78 (*C*-2,2'), 130.81 (*C*-4,4'), 124.30 (*C*-3,3'), 111.67 (*C*-5,5') ppm. **HRMS** (EI, 70 eV, MAT95, direct): calculated for C$_8$H$_4$^{79}Br$_2$S$_2$$^{+\cdot}$ 321.81157 found 321.81204. **IR** (ATR): υ = 3092 (w), 3068 (w), 3039

(w), 1734 (w), 1580 (s), 1504 (w), 1415 (s), 1196 (m), 1058 (m), 967 (m), 866 (m), 785 (s), 738 (s), 681 (w) cm^{-1}. **Mp:** 140 °C. The observed data were in good accordance with the literature data.[5]

3.9.7   5,5'-*bis*(Trimethyl)silyl-2,2'-bithiopene (**90**)

Method A, similar to lit.[6]: In a Schlenk tube bithiophene (**88**, 2.60 g, 12.0 mmol) was dissolved in tetrahydrofuran (60 ml) and stirred at 0 C°. Then *n*-butyllithium (10.6 mL, 26.5 mmol) was added over 4 min. The reaction mixture was stirred at this temperature for 1 h before trimethylsilyl chloride (3.80 mL, 30.0 mL) was added and the solution was warmed to 20 °C over 14 h. Afterwards a sat. aq. ammonium chloride solution (60 mL) was added. The phases were separated, the aqueous phase was extracted with diethyl ether (2 x 80 mL). The organic phases were combined, dried over magnesium sulfate and the solvent was removed to give yellowish crystals. After the compound was purified with a small plug of silica (eluent: *n*-pentane), it was finally recrystallized from hot *n*-hexane (20 mL) to give greenish white crystals (**90**, 2.20 g, 7.08 mmol, 60%). Method B: In a Schlenk tube 5,5'-dibromo-2,2'-bithiophene (**51**, 2.00 g, 6.17 mmol) was dissolved in tetrahydrofuran (60 mL) and cooled to -80 °C. At this temperature *n*-butyllithium (5.17 mL, 13.0 mmol) was added over a course of 15 min giving a blueish reaction mixture. After 1 h at this temperature trimethylsilyl chloride (1.72 mL, 13.6 mmol) was added in one portion and the reaction mixed was allowed to warm to 25 °C over 14 h, followed by the addition of a sat. aq. ammonium chloride solution (60 mL). The phases were separated, the aq. phase was extracted with diethyl ether (80 mL, 2x). The organic phases were combined, dried over magnesium sulfate and the solvent was removed to give yellowish crystals (**90**, 1.76 g, 5.66 mmol, 92%). **^{1}H NMR** (600 MHz, CDCl$_3$): δ = 7.23 (d, ^3J = 3.1 Hz, 2H, *H*-3,3'), 7.13 (d, ^3J = 3.1 Hz, 2H, *H*-4,4'), 0.33 (d, ^3J = 7.3 Hz, 36H, C*H*$_3$) ppm. **^{13}C{^{1}H} NMR** (151 MHz, CDCl$_3$): δ = 142.56 (*C*-2,2'), 139.92 (*C*-4,4'), 134.87 (*C*-5,5'), 125.20 (*C*-3,3'), 0.05 (*C*H$_3$) ppm. **^{29}Si{^{1}H} NMR** (119 MHz, CDCl$_3$): δ = -6.55 (s) ppm. **HRMS** (EI, 70 eV, MAT95, direct): calculated for C$_{14}$H$_{22}$S$_2$Si$_2$$^{+\cdot}$ 310.06941 found 310.06964. **IR** (ATR): υ = 3092 (w), 3068 (w), 3039 (w), 2925 (w), 1422 (m), 1247 (m), 1149 (m), 1073 (m), 986 (m), 869 (m), 834 (s), 793 (s), 752 (s) cm^{-1}. **Mp**: 87 °C.

3.9.8   2,5-*bis*(Trimethyl)silylthiopene (**89**)
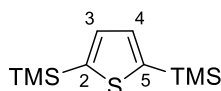
The synthesis was performed according to lit.[7]: In a Schlenk tube 2,5-dibromothiophene (**87** ,5.00 g, 20.6 mmol) was dissolved in diethyl ether (75 mL) and the mixture was cooled to -78 °C. At this temperature *n*-butyllithium (18.1 mL, 45.3 mmol, 2.5 M in hexane) was added in two portions. After 1 h at this temperature the reaction mixture was warmed to 20 °C and kept at this temperature for 30 min. After lowering the temperature (-78 °C) trimethylsilyl chloride (5.76 mL, 45.3 mmol) was added over a course of 4 min and the reaction mixture was allowed to warm in 14 h to 20 °C. The reaction mixture was poured into an sat. aq. ammonium chloride solution (150 mL). The organic phase was separated, washed two times with water (2 x 200 mL), dried over magnesium sulfate and concentrated under reduced pressure to give an yellow oil (**89**, 4.67 g, 20.4 mmol, 99%, lit.[7]: 75%). **^{1}H NMR** (600 MHz, CDCl$_3$): δ = 7.33 (s, 2H, *H*-3,4), 0.33 (s, 18H, C*H*$_3$) ppm. **^{13}C{^{1}H} NMR** (151 MHz, CDCl$_3$): δ = 145.95 (*C*-2,5), 135.21 (*C*-3,4), 0.24 (*C*H$_3$) ppm. **^{29}Si{^{1}H} NMR** (119 MHz, CDCl$_3$): δ = -6.55 (s) ppm.

HRMS (EI, 70 eV, MAT95, direct): calculated for $C_{10}H_{20}SSi_2^{+\cdot}$ 228.08188 found 228.08190. **IR** (ATR): ν = 2955 (w), 1489 (w), 1405 (w), 1267 (w), 1247 (s), 1201 (m), 1007 (w), 978 (w), 831 (s), 803 (s), 753 (s), 694 (s) cm^{-1}. The observed data were in good accordance with the literature data.[7]

3.9.9 2-Trimethylsilylfuran (**FurTMS**)
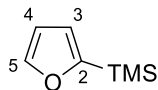
The synthesis was performed according to lit.[8]: A stirred solution of furan (**85**, 1.00 g, 14.7 mmol) in anhydrous diethyl ether (25 mL) was cooled to 0 °C. To this *n*-butyllithium (6.4 mL, 2.5 M in hexanes, 16.0 mmol) was added with a syringe pump (0.5 mL/min), the reaction was warmed to room temperature and kept for 40 min. After cooling to 0 °C, trimethylsilyl chloride (1.87 mL, 14.7 mmol) was added (fast, color change to cloudy white). After 14 h of stirring at 25 °C a sat. aq. solution of ammonium chloride (30 mL) was added followed by water (30 mL). The layers were separated, and the organic layer was washed with brine (50 mL), dried over magnesium sulfate followed carefully removing of the organic solvent. The product was obtained by Kugelrohr distillation (120 °C, 1000 mbar) as colorless oil (**FurTMS**, 453 mg, 2.87 mmol, 22%, lit.[8]: 62%). **^{1}H NMR** (600 MHz, CDCl$_3$): δ = 7.65 (d, ^3J = 1.6 Hz, 2H, *H*-5), 6.62 (m, 2H, *H*-3), 6.38 (m, 2H, *H*-4),0.27 (s, 9H, C*H*$_3$) ppm. **^{13}C{^{1}H} NMR** (151 MHz, CDCl$_3$): δ = 160.38 (*C*-2), 146.67 (*C*-5), 119.55 (*C*-3), 109.45 (*C*-4), -1.47 (*C*H$_3$) ppm. **^{29}Si{^{1}H} NMR** (119 MHz, CDCl$_3$): δ = -10.91 (s) ppm. **HRMS** (EI, 70 eV, MAT95, direct): calculated for $C_7H_{12}OSi^{+\cdot}$ 140.06519 found 140.06502. **IR** (ATR): υ = 2959 (w), 1550 (w), 1458 (w), 1249 (w), 1203 (m), 1148 (m), 1107(w), 901 (s), 885 (s), 834 (s), 754 (w), 740 (w), 696 (s) cm^{-1}. The observed data were in good accordance with the literature data.

3.9.10 1-Methyl-2-trimethylsilylpyrrole (**MePyrTMS**)
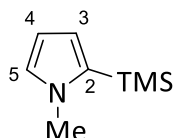
A combination of two methods[9, 10] was used: A solution of *n*-butyllithium (32.8 mL; 82.0 mmol 2.5 M in *n*-hexane) was added dropwise at 0 °C over 15 min into a solution of *N*-methylpyrrole (**86**, 6.66 g, 82.0 mmol) and tetramethylethylenediamine (12.3 g, 106 mmol) in diethyl ether (100 mL). The reaction was warmed to 25 °C and stirred for 40 min. color change to cloudy white. It was cooled back to 0 °C and trimethylsilyl chloride (9.96 mL, 82.0 mmol) were added. The mixture was stirred for 12 h at room temperature, hydrolyzed with a sat. aq. ammonium chloride solution (50 mL), extracted with diethyl ether (100 mL) and dried over magnesium sulfate. The solvents were removed and an orange oil (7.34 g) was received. The product was obtained by short path distillation (80 °C, 20 mbar) as a colorless oil (**MePyrTMS**, 6.66 g, 43.5 mmol, 53%). The product was shielded from light.

^{1}H NMR (601 MHz, CDCl$_3$): δ = 6.83 - 6.78 (m, 1H, *H*-5), 6.41 - 6.34 (s, 2H, *H*-3), 6.19 - 6.14 (s, 1H, *H*-4), 3.74 (s, 3H, N-C*H*$_3$), 0.30 (s, 9H, C*H*$_3$) ppm. **^{13}C{^{1}H} NMR** (151 MHz, CDCl$_3$): δ = 132.72 (*C*-2), 127.02 (*C*-5), 119.19 (*C*-3), 108.06 (*C*-4), 37.08 (N-*C*H$_3$), -0.20 (*C*H$_3$) ppm. **^{29}Si{^{1}H} NMR** (119 MHz, CDCl$_3$) δ = -12.59 (s) ppm. **HRMS** (EI, 70 eV, MAT95, direct): calculated for $C_8H_{15}NSi^{+\cdot}$ 153.09683 found 153.09653. **IR** (ATR): υ = 2955 (w), 1515 (w), 1445 (w), 1405 (w), 1291 (m), 1247 (m), 1204 (w), 1120 (w), 1087 (m), 1055 (w), 998 (w), 887 (w), 831 (s), 754 (s), 716 (s), 690 (m) cm^{-1}.

3.9.11 2-(Trimethylsilyl)thiophene (**TphTMS**)
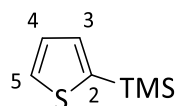
In a Schlenk tube 2-bromothiophene (**49**, 10.0 g, 61.3 mmol) was dissolved in diethylether (100 mL) and cooled to -78 °C. To this solution *n*-butyllithium (27.0 mL, 67.5 mmol, 2.5 M in *n*-hexane) was added over a period of 5 min and the reaction mixture was stirred for 1 h. Subsequently, trimethylsilyl chloride (8.10 mL, 67.4 mmol) were added in one portion and the reaction mixture was stirred for 18 h. The reaction mixture was added to a sat. aq. ammonium chloride solution (150 mL). The organic phase was separated, washed with water (2 x 150 mL), dried over magnesium sulfate, filtered, and after careful removal of the solvent (b.p.(**TphTMS**) = 70 °C(20 mbar)) the product was obtained as a colorless oil (7.52 g, 48.1 mmol, 78%). **^{1}H NMR** (600 MHz, CDCl$_3$) δ = 7.61 (dd, ^3J = 4.6 Hz, ^4J = 0.9 Hz, 1H, *H*-5), 7.28 (dd, ^3J = 3.3 Hz, ^4J = 0.9 Hz, 1H, *H*-3), 6.60 (dd, ^3J = 4.6 Hz, ^3J = 3.3 Hz, 1H, *H*-4), 0.34 (s, 9H, C*H*$_3$) ppm. **^{13}C{^{1}H} NMR** (151 MHz, CDCl$_3$) δ = 140.21 (*C*-2), 134.08 (*C*-3), 130.51 (*C*-5), 128.22 (*C*-4), 0.16 (*C*H$_3$) ppm. **^{29}Si{^{1}H} NMR** (119 MHz, CDCl$_3$) δ = -6.54 (s) ppm. **HRMS** (EI): *m/z* [M]$^{+\cdot}$ Calcd. for C$_7$H$_{12}$SiS 156.04235; Found 156.04191. **IR** (ATR): υ = 2956 (w), 1406 (m), 1325 (w), 1248 (s), 1213 (m), 1082 (m), 991 (m), 857 (m), 825 (s), 754 (s), 701 (s) cm^{-1}. Analytical data was in accordance to previously reported values.[11]

3.9.12 Dichloro-2-thienyl borane (**TphBCl₂**)
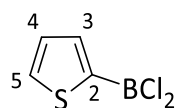
Under a argon atmosphere, 2-(trimethylsilyl)thiophene (**TphTMS**, 5.96 g, 38.1 mmol) was added to a solution of boron trichloride (60.0 mL, 60.0 mmol, 1 M in DCM) in 10 min at -50 °C. The reaction mixture was slowly warmed to 22 °C over the course of 14 h. After the solvent was removed *in vacuo*, the crude product was purified by inert Kugelrohr distillation (70 °C, 17 mbar) to give the product as a colorless oil (**TphBCl₂**, 4.66 g, 27.6 mmol, 72%). This very corrosive product was stored in the glovebox freezer. **^{1}H NMR** (500 MHz, C$_6$D$_6$) δ = 7.64 (dd, ^3J = 3.7 Hz, ^4J = 1.0 Hz, 1H, *H*-5), 7.10 (dd, ^3J = 4.6 Hz, ^4J = 1.0 Hz, 1H, *H*-3), 6.60 (dd, ^3J = 4.6 Hz, ^3J = 3.7 Hz, 1H, *H*-4) ppm. **^{13}C{^{1}H} NMR** (126 MHz, C$_6$D$_6$) δ = 143.46 (*C*-3), 140.48 (*C*-5), 139.0 (*C*-2, only HMBC), 129.75 (*C*-4) ppm. **^{11}B{^{1}H} NMR** (160 MHz, C$_6$D$_6$) δ = 48.88 (s) ppm. Due to the corrosive nature of this molecule mass spectrometry data were not obtained. The analytical data are in accordance with literature.[12]

3.9.13 4-(Trimethylsilyl)triphenylamine (**TPATMS**)
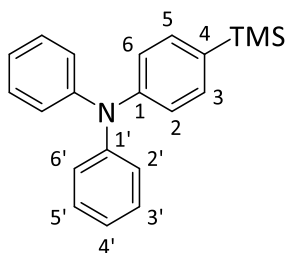
This synthetic procedure was adapted from lit.[13]: In a Schlenk flask THF (2 mL) and 1,2-dibromoethane (200 µL, 2.32 mmol) were added to magnesium turnings (4.49 g, 184.8 mmol) at 25 °C, and the resulting mixture was stirred for 5 min. To this a part (4 mL) of a 4-bromotriphenylamine (**TPABr**,

10.0 g, 30.8 mmol) solution in THF (20 mL) was added and mixture was heated to 55 °C. After 5 min stirring at this temperature the rest of the solution was added dropwise. After total addition, the reaction mixture was further stirred at 80 °C for 30 min. The warm solution was transferred into another flask and chlorotrimethylsilane (3.36 g, 30.8 mmol) was added dropwise to this solution. After complete addition, the mixture was heated to 50 °C for 2 h, and then stirred at 25 C for 2 d. To this water (100 mL) was added, and the mixture was extracted with *n*-hexane (3 x 100 mL). All organic extracts were combined, dried over magnesium sulfate, filtrated and concentrated *in vacuo* to give an yellow oil (6.95 g, 21.9 mmol, 71%, Lit.[13]: 84%). **^{1}H NMR** (600 MHz, CDCl$_3$): δ = 7.39 (d, ^3J = 7.9 Hz, 2H, *H*-3,5), 7.08 -7.03 (m, 4H, *H*-3',5'), 7.13 (d, ^3J = 7.5 Hz, 4H, *H*-2',6'), 7.08 -7.03 (m, 4H, *H*-4' and *H*-2,6), 0.27 (s, 9H, C*H*$_3$) ppm. **^{13}C{^{1}H} NMR** (151 MHz, CDCl$_3$): δ = 148.46 (*C*-1), 147.77 (*C*-1'), 134.37 (*C*-3,5), 133.43 (*C*-4), 129.36 (*C*-3',5'), 124.73 (*C*-2',6'), 123.07 (*C*-4'), 122.86 (*C*-2,6), 14.14 (*C*H$_3$) ppm. **^{29}Si{^{1}H} NMR** (119 MHz, CDCl$_3$): δ = -4.67 (s) ppm. **HRMS** (EI): *m/z* calcd. for C$_{21}$H$_{23}$NSi 317.15943 [M]$^+$, found 317.15971 [M+H]$^+$. **IR** (ATR): υ = 3019 (w), 2951 (m), 1583 (s), 1485 (s), 1325 (m), 1314 (m), 1271 (s), 1247 (m), 1109 (m), 1075 (w), 1027 (w), 833 (s), 815 (m), 749 (m), 717 (m), 692 (s) cm^{-1}. The analytical data were in agreement with reported values.[13]

3.9.14 1,7-Di(*n*-hexyl)-6,12-di(phenyl)-1,12,6,7-di([1,2]azaborinine)-*N*,*N*'-di(cyclohexyl)perylene-3,4,9,10-tetracarboxylic acid diimide (**Ph-BNCDI^{Cy}**)
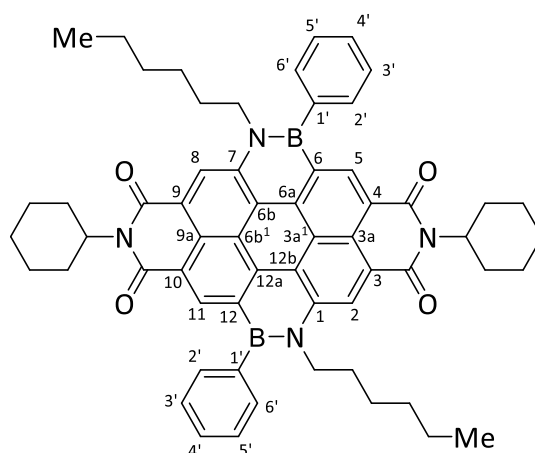
In a nitrogen filled glovebox, a Schlenk tube was charged with 1,7-di(*n*-hexylamino)-*N*,*N*'-di(cyclohexyl)perylene-3,4,9,10-tetracaboxylic acid diimide (**1,7-DHA-PDI^{Cy}**, 20.0 mg, 26.7 µmol), toluene (5.0 mL), triethylamine (0.5 mL) and dichlorophenyl borane (16.0 mg, 106 µmol). The reaction mixture was stirred for 14 h at 110 °C. After allowing the reaction to cool, all volatiles were removed and the residue was dissolved in DCM (30 mL), washed with brine (3 x 50 mL), 1 M NaOH (3 x 50 mL) and water (3 x 50 mL). After drying over magnesium sulfate, filtration and removal of the solvent, the crude product was subjected to column chromatography (silica, eluent: DCM, R$_f$ = 0.80) to give the product (**Ph-BNCDI^{Cy}**, 18 mg, 19.4 µmol, 98%) as a red-violet solid. **^{1}H NMR** (500 MHz, CDCl$_3$): δ = 9.53 (s, 2H, *H*-2,8), 9.34 (s, 2H, *H*-5,11), 7.73 (dd, ^3J = 7.7 Hz, ^4J = 1.4 Hz, 4H, Ph-*H*-2',6'), 7.69 - 7.55 (m, 6H, Ph-*H*-3',4',5'), 5.22 (tt, ^3J = 12.1 Hz , ^4J = 3.7 Hz, 2H, C*H*), 4.70 (t, ^3J = 12.1 Hz, 4H, N-C*H*$_2$), 2.69 (qd, ^3J = 12.5 Hz , ^4J = 3.3 Hz, 4H, CH-C*H*$_{ax}$), 2.09 - 1.93 (m, 8H, N-(CH$_2$)-C*H*$_2$ and CH-(CH$_2$)C*H*$_{ax}$) , 1.90 (d, ^3J = 10.9 Hz, 4H, CH-C*H*$_{eq}$), 1.75 (d, ^3J = 14.2 Hz, 2H, CH-(CH$_2$)$_2$-C*H*$_{ax}$), 1.59 - 1.45 (m, 4H, N-(CH$_2$)-C*H*$_2$), 1.46 - 1.33 (m, 6H, N-(CH$_2$)-C*H*$_2$ and CH-(CH$_2$)$_2$-C*H*$_{eq}$), 1.32 - 1.18 (m, 8H, (C*H*$_2$)$_2$-CH$_3$ and CH-(CH$_2$)C*H*$_{eq}$), 0.86 (t, ^3J = 7.0 Hz, 6H, C*H*$_3$) ppm. **^{13}C{^{1}H} NMR** (126 MHz, CDCl$_3$): δ = 165.12/165.09 ((*C*(O)N)-3,9/4,10), 138.88 (Ph-*C*-1', only HMBC), 138.69 (*C*-1,7), 137.34 (*C*-5,11), 134.01 (*C*-6a,12a), 132.68 (Ph-*C*-2',6'), 132.21 (*C*-6,12), 128.50 (Ph-*C*-4'), 128.37 (Ph-*C*-2',5'), 123.54/123.39 (*C*-3,9 or *C*-4,10), 123.26 (*C*-

3a,9a), 120.77 (C-3a$_1$,6b$_1$), 120.71 (C-2,8), 120.39 (C-6b,12b), 54.48 (CH), 50.37 (N-CH$_2$), 31.33 (N-(CH$_2$)$_3$-CH$_2$), 31.24 (CH-CH$_2$-CH$_2$), 29.52 (CH-CH$_2$), 26.83 (N-CH$_2$-(CH$_2$)$_2$-CH$_2$), 25.68 (CH-(CH$_2$)$_2$-CH$_2$), 22.63 (N-(CH$_2$)$_4$-CH$_2$), 14.08 (CH$_3$) ppm. **^{11}B{^{1}H} NMR** (160 MHz, CDCl$_3$): δ = 39.63 (br) ppm. **HRMS** (EI): m/z [M]$^+$ Calcd. C$_{84}$H$_{80}$^{11}B$_2$N$_4$O$_4$ 924.49517; Found 924.49473; [M]$^+$ Calcd. C$_{84}$H$_{80}$^{10}B$_2$N$_4$O$_4$ 922.50243; Found 922.48756. **IR** (ATR): υ = 2922 (m), 2851 (m), 1697 (s), 1654 (s), 1596 (s), 1565 (m), 1449 (m), 1437 (s), 1413 (m), 1338 (m), 1299 (s), 1244 (s), 1197 (m), 1102 (m), 1058 (m), 958 (m), 895 (m), 812 (m), 758 (m), 738 (m), 703 (s), 656 (s) cm^{-1}.

3.9.15 1,7-Di(n-hexyl)-6,12-di(phenyl)-1,12,6,7-di([1,2]azaborinine)-N,N'-bis(2,6-di(isoproypyl)phenyl)perylene-3,4,9,10-tetracarboxylic acid diimide (**Ph-BNCDI^{Dip}**)
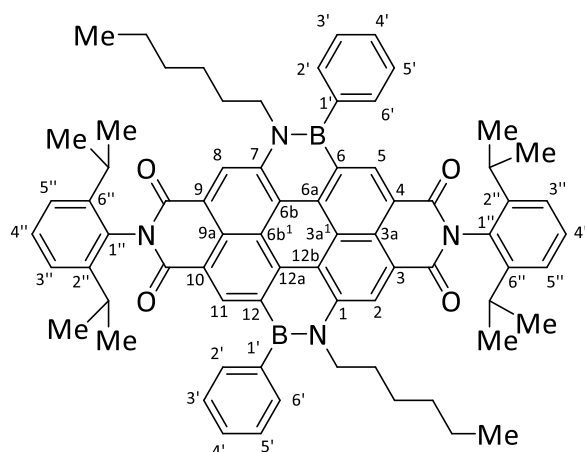
In a nitrogen filled glovebox, a Schlenk tube was charged with 1,7-di(n-hexylamino)-N,N'-bis(2,6-di(isopropyl)phenyl)perylene-3,4,9,10-tetracaboxylic acid diimide (**1,7-DHA-PDI^{Dip}**, 18.0 mg, 19.8 µmol), toluene (5.0 mL), triethylamine (0.5 mL) and dichlorophenyl borane (**PhBCl$_2$**, 16 mg, 106 µmol). The sealed tube was stirred for 14 h at 110 °C. After allowing the reaction mixture to cool, all volatiles were removed *in vacuo,* the residue was dissolved in DCM (30 mL), washed with brine (3 x 50 mL), 1 M NaOH (3 x 50 mL) and water (3 x 50 mL). After drying over magnesium sulfate, filtration and removal of the solvent, the crude product was subjected to column chromatography (silica, eluent: DCM, R$_f$ = 0.81) to give the product (**Ph-BNCDI^{Dip}**, 18 mg, 16.7 µmol, 84%) as a red-violet solid. **^{1}H NMR** (500 MHz, CDCl$_3$): δ = 9.73 (s, 2H, H-2,8), 9.52 (s, 2H, H-5,11), 7.84 - 7.77 (dd, ^3J = 7.3 Hz, ^4J = 1.2 Hz 4H, Ph-H-2',6'), 7.64 (t, ^3J = 7.3 Hz, 4H, Ph-H-3',5'), 7.60 - 7.54 (m, 2H, Ph-H-4'), 7.51 (t, ^3J = 7.3 Hz, 2H, N-(Ph-H-4'')), 7.38 (d, ^3J = 7.9 Hz, 4H, N-(Ph-H-3,5'')), 4.79 (t, ^3J = 7.7 Hz, 4H, N-CH_2), 2.89 (sept. ^3J = 6.8 Hz, 4H, Ph-(CH)-(CH$_3$)$_2$), 2.13 - 2.04 (m, 4H, N-CH$_2$-CH_2), 1.47 - 1.38 (m, 4H, N-(CH$_2$)$_2$-CH_2), 1.30 - 1.15 (m, 32 H, N-(CH$_2$)$_2$-(CH_2)$_2$ and Ph-(CH)-(CH_3)$_2$), 0.82 (t, ^3J = 7.0 Hz, 6H, CH_3) ppm. **^{13}C{^{1}H} NMR** (126 MHz, CDCl$_3$): δ = 164.78 ((C(O)N)-4,10), 164.50 ((C(O)N)-3,9), 145.87 (N-(Ph-C-2'',6'')), 139.11 (C-1,7),138.94 (Ph-C-1', only HMBC) 138.04 (C-5,11), 134.77 (C-6a,12a), 132.69 (Ph-C-2',6'), 131.15 (N-(Ph-C-1'')), 129.68 (N-(Ph-C-4'')), 128.63 (Ph-C-3',5'), 128.43 (Ph-C-4'), 124.45 (C-3a,9a), 124.18 (C-3,9 or C-4,10), 124.07 (N-(Ph-C-3'',5'')), 123.19 (C-3,9 or C-4,10), 121.53 (C-2,8), 121.12 (C-6b,12b), 120.55 (C-3a$_1$,6b$_1$), 50.60 (N-CH$_2$), 31.35 (N-CH$_2$-CH$_2$), 31.30 (N-(CH$_2$)$_4$-CH$_2$), 29.41 (Ph-(CH)-(CH$_3$)$_2$), 26.74 (NH-(CH$_2$)$_3$-CH$_2$), 24.27 and 24.22 (Ph-(CH)-(CH$_3$)$_2$), 22.50 (NH-(CH$_2$)$_4$-CH$_2$), 14.02 (CH$_3$) ppm. **^{11}B{^{1}H} NMR** (160 MHz, CDCl$_3$): δ = 41.01 (br) ppm. **HRMS** (APCI, positive mode): m/z [M+H]$^+$ Calcd. for C$_{72}$H$_{75}$^{11}B$_2$N$_4$O$_4$ 1081.59903; Found 1081. 59890. **IR** (ATR): υ = 2958 (w), 2924 (w), 2866 (w), 1708 (m), 1670 (s), 1599 (m), 1563 (m), 1446 (m), 1436 (m), 1312 (s), 1280 (m), 1247 (s), 1208 (m), 1109 (m), 1063 (m), 846 (m), 814 (m), 791 (m), 774 (m), 760 (m), 736 (s), 703 (m), 681 (m) cm^{-1}.

3.9.16 1,7-Di(*n*-hexyl)-6,12-di(phenyl)-1,12,6,7-di([1,2]azaborinine)-*N*,*N*'-di(*n*-hexyl)perylene3,4,9,10-tetracarboxylic acid diimide (**Ph-BNCDI^{nhex}**)
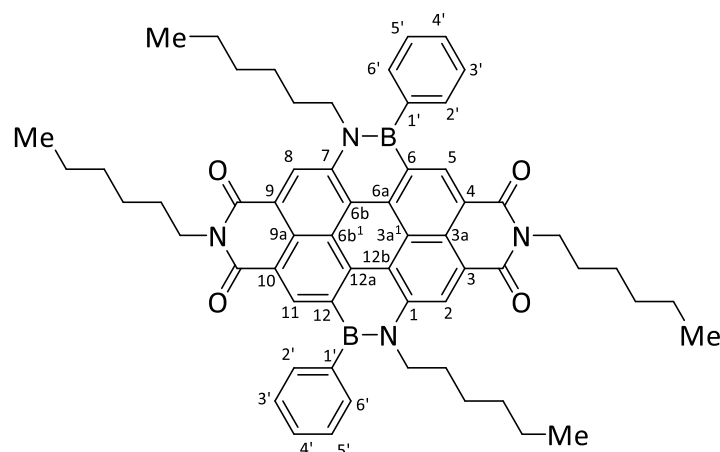

In a nitrogen filled glovebox, a Schlenk tube was charged with 1,7-di(*n*-hexylamino)-*N*,*N*'-di(*n*-hexyl)perylene-3,4,9,10-tetracaboxylic acid diimide (**1,7-DHA-PDI^{nhex}**, 50.0 mg, 66.0 µmol), toluene (10.0 mL), triethylamine (0.5 mL) and dichlorophenyl borane (40.2 mg, 264 µmol). The reaction mixture was stirred for 12 h at 110 °C. After allowing the reaction mixture to cool, the solvent was evaporated and the residue was dissolved in DCM (30 mL), washed with brine (1 x 50 mL), .1 M NaOH (1 x 50 mL) and water (1 x 50 mL). After drying over magnesium sulfate, filtration, and removal of the solvent, the crude product was purified by column (silica, eluent: DCM, R$_f$ = 0.83) to give the product as a red-violet solid (**Ph-BNCDI^{nhex}**, 29.0 mg, 31.1 µmol, 47%). **^{1}H NMR** (500 MHz, CDCl$_3$): δ = 9.55 (s, 2H, *H*-2,8), 9.38 (s, 2H, *H*-5,11*)*, 7.76 (dd, ^3J = 7.7 Hz, ^4J = 1.4 Hz, 4H, Ph-*H*-2',6'), 7.62 (m, 6H, Ph-*H*-3',4',5'), 4.71 (t, ^3J = 7.8 Hz, 4H, BN-C*H*$_2$), 4.31 (t, ^3J = 7.6 Hz, 4H, (CO)$_2$N-C*H*$_2$), 2.04 (quin., ^3J = 7.5 Hz, 4H, BN-CH$_2$-C*H*$_2$), 1.85 (quin., ^3J = 7.5 Hz, 4H, (CO)$_2$N-CH$_2$-C*H*$_2$), 1.50 (quin., ^3J = 7.5 Hz, BN-(CH$_2$)$_2$-C*H*$_2$), 1.38 (m, 14H, BN-(CH$_2$)$_4$-C*H*$_2$, (CO)$_2$N-(CH$_2$)$_2$-C*H*$_2$ and BN-CH$_2$-C*H*$_2$), 1.23 (m, 20H, (CO)$_2$N-(CH$_2$)$_4$-C*H*$_2$ and (CO)$_2$N-(CH$_2$)$_4$-C*H*$_2$ and residual grease), 0.91 (t, ^3J = 7.1 Hz, 6H, C*H*$_3$),0.86 (t, ^3J = 6.9 Hz, 6H, C*H*$_3$) ppm. **^{13}C{^{1}H} NMR** (126 MHz, CDCl$_3$): δ = 164.55 ((*C*(O)N)-4,10), 164.53 ((*C*(O)N)-3,9), 139.20 (Ph-*C*-1', only HMBC), 138.72 (*C*-1,7), 137.48 (*C*-5,11), 134.22 (*C*-6a,12a), 132.66 (Ph-*C*-2',6'), 132.41 (br, *C*-6,12), 128.56 (Ph-*C*-4'), 128.39 (Ph-*C*-3',5'), 123.52 (*C*-3,9), 123.43 (*C*-4,10), 122.92 (*C*-3a,9a), 120.78 (*C*-3a^1,6b^1), 120.57 (*C*-6b,12b), 120.18 (*C*-2,8), 50.43 (N-*C*H$_2$), 41.13 ((CO)$_2$N-*C*H$_2$), 31.75 ((BN-(CH$_2$)$_4$-*C*H$_2$), 31.34 (CO)$_2$N-(CH$_2$)$_4$-*C*H$_2$), 31.28 (BN-CH$_2$-*C*H$_2$), 29.85 ((CO)$_2$N-CH$_2$-*C*H$_2$), 28.38 (BN-(CH$_2$)$_3$-*C*H$_2$) and(CO)$_2$N-(CH$_2$)$_3$-*C*H$_2$), 27.09 (BN-(CH$_2$)$_2$-*C*H$_2$), 26.82 ((CO)$_2$N-(CH$_2$)$_2$-*C*H$_2$), 22.76 (BN-(CH$_2$)$_4$-*C*H$_2$), 22.63 ((CO)$_2$N N-(CH$_2$)$_4$-*C*H$_2$), 14.24 (BN-(CH$_2$)$_5$-*C*H$_3$), 14.08 ((CO)$_2$N-(CH$_2$)$_5$-*C*H$_3$) ppm. **^{11}B{^{1}H} NMR** (160 MHz, CDCl$_3$): δ = 40.42 ppm. **HRMS** (APCI): *m/z* [M+H]$^+$ Calcd. for C$_{60}$H$_{67}$^{11}B$_2$N$_4$O$_4$ 929.53602; Found 929.53628. **IR** (ATR): υ = 2955 (w), 2923 (w), 2865 (w), 1706 (m), 1667 (m), 1600 (m), 1562 (m), 1448 (m), 1436 (m), 1327 (m), 1281 (m), 1247 (s), 1208 (m), 1105 (m), 1029 (m), 1062 (m), 958 (m), 844 (m), 775 (s), 760 (m), 736 (m), 700 (m) cm^{-1}.

3.9.17 1,7-Di(*n*-hexyl)-6,12-di(thiophen-2-yl)-1,12,6,7-di([1,2]azaborinine)-*N*,*N*'-di(cyclohexyl)perylene-3,4,9,10-tetracarboxylic acid diimide (**Tph-BNCDI^Cy**)

In a nitrogen filled glovebox, a vial was charged with 1,7-di(*n*-hexylamino)-*N*,*N*'-di(cyclohexyl)perylene-3,4,9,10-tetracaboxylic acid diimide (**1,7-DHA-PDI^Cy**, 19.0 mg, 25.2 µmol), toluene (5.0 mL), triethylamine (0.5 mL) and dichloro-2-thienyl borane (**TphBCl₂**, 175 mg, 403 µmol). The sealed vial was heated 24 h at 110 °C. After cooling to 25 °C, all volatiles were removed *in vacuo* and the red product was dried (9.7 x 10^{-2} mbar, 70 °C, 2 h). The residue was dissolved in DCM (30 mL), washed with brine (3 x 50 mL), 1 M NaOH (3 x 50 mL) and water (3 x 50 mL). After drying over magnesium sulfate, filtration, removal of the solvent, the product was subjected to column chromatography (silica, eluent: gradient petrol ether to DCM, R*$_f$*(DCM) = 0.65) to give the product (**Tph-BNCDI^Cy**, 23 mg, 24.5 µmol, 97%) as a red-violet solid. **¹H NMR** (500 MHz, CDCl₃): δ = 9.56 (s, 2H, *H*-2,8), 9.54 (s, 2H, *H*-5,11*)*, 7.87 (dd, ^3J = 4.8 Hz, ^4J = 0.8 Hz, 22H, Tph-*H*-3'), 7.61 (dd, ^3J = 3.2 Hz, ^4J = 0.8 Hz, 2H, Tph-*H*-5'), 6.60 (dd, ^3J = 4.8 Hz, ^3J = 3.2 Hz, 2H, Tph-*H*-4'), 5.23 (tt, ^3J = 12.0, 3.8 Hz, 2H, C*H*), 4.79 (t, ^3J = 7.8 Hz, 4H, N-C*H₂*), 2.70 (qd, ^3J = 12.0, 3.0 Hz, 4H, CH-C*H*$_{ax}$), 2.12 (quin., ^3J = 7.8 Hz, 4H, N-(CH₂)-C*H₂*), 1.98 (d, ^3J = 13.5 Hz, 4H, CH-CH₂-C*H*$_{ax}$), 1.91 (d, ^3J = 12.0 Hz, 4H, CH-C*H*$_{eq}$), 1.79 (d, ^3J = 13.0 Hz, 2H, CH-(CH₂)₂-C*H*$_{ax}$), 1.59 - 1.26 (m, 18H, CH-CH₂-C*H*$_{eq}$, CH-(CH₂)₂-C*H*$_{eq}$ and N-(CH₂)₂-(C*H₂*)₃), 0.90 (t, ^3J = 7.0 Hz, 6H, C*H₃*) ppm. **¹³C{¹H} NMR** (126 MHz, CDCl₃): δ = 165.06 ((*C*(O)N)-4,10), 165.04 ((*C*(O)N)-3,9), 138.79 (*C*-1,7), 137.33 (*C*-5,11), 136.68 (Tph-*C*-2', only HMBC), 134.22 (Tph-*C*-5'), 133.85 (*C*-6a,12a), 132.51 (*C*-6,12, only HMBC), 130.03 (Tph-*C*-3'), 128.55 (Tph-*C*-4'), 123.70 (*C*-3,9 or *C*-4,10), 123.54 (*C*-3,9 or *C*-4,10), 123.15 (*C*-3a¹,6b¹), 122.67 (*C*-3a,9a), 12089 (*C*-2,8), 120.46 (*C*-6b,12b), 54.56 (*C*H), 50.70 (N-*C*H₂), 31.81 (N-CH₂-*C*H₂), 31.48 (CH-*C*H₂), 29.53 (N-(CH₂)₂-*C*H₂), 26.85 (N-(CH₂)₃-*C*H₂), 26.85 (CH-CH₂-*C*H₂), 25.70 (CH-(CH₂)₂-*C*H₂), 22.74 (N-(CH₂)₄-*C*H₂), 14.13 (*C*H₃) ppm. **¹¹B{¹H} NMR** (160 MHz, CDCl₃): δ = 38.70 (br) ppm. **HRMS** (EI): *m/z* [M]⁺ Calcd. for C₅₆H₅₈N₄O₄¹¹B₂S₂ 936.41460; Found 936.41893. **IR** (ATR): υ = 2921 (m), 2852 (m), 1698 (s), 1654 (s), 1599 (s), 1566 (m), 1450 (s), 1416 (m), 1404 (m), 1343 (w), 1302(s), 1280 (m), 1245 (s), 1202 (m), 1087 (w), 1020 (w), 897 (w), 847 (w), 812 (m), 706 (m), 651 (m), 599 (w) cm⁻¹.

3.9.18 1,7-Di(*n*-hexyl)-6,12-di(thiophen-2-yl)-1,12,6,7-di([1,2]azaborinine)-*N*,*N'*-bis(2,6-di(*iso*proypyl)phenyl)perylene-3,4,9,10-tetracarboxylic acid diimide (**Tph-BNCDI^{Dip}**)
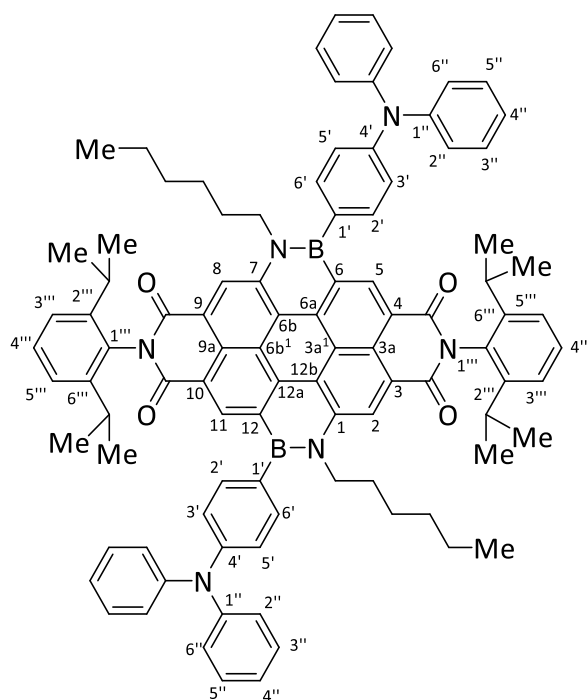

In a nitrogen filled glovebox a pressure tube (50 mL) was charged with 1,7-di(*n*-hexylamino)-*N*,*N'*-bis(di*iso*propylphenyl)perylene-3,4,9,10-tetracaboxylic acid diimide (**1,7-DHA-PDI^{Dip}**, 120 mg, 132 µmol), toluene (4.8 mL), triethylamine (200 µL) and dichloro-2-thienyl borane (100 mg, 607 µmol). The sealed was heated for 10 h at 110 °C. After cooling to 25 °C, the reaction mixture was dissolved with DCM (30 mL), washed with brine (3 x 50 mL), 1 M NaOH (3 x 50 mL) and water (3 x 50 mL). After drying over magnesium sulfate, filtration, and removal of the solvent *in vacuo*, the crude product was purified by column chromatography (silica, eluent: DCM, R$_f$(DCM) = 0.81) to give the red/violet product (**Tph-BNCDI^{Dip}**, 120 mg, 110 µmol, 83%). **^{1}H NMR** (500 MHz, CDCl$_3$): δ = 9.75 (s, 2H, *H*-5,11), 9.74 (s, 2H, *H*-2,8), 7.86 (dd, ^3J = 4.8 Hz, ^4J = 0.8 Hz, 2H, Tph-*H*-3'), 7.67 (dd, ^3J = 3.3 Hz, ^4J = 0.8 Hz, 2H, Tph-*H*-5'), 7.53 (t, ^3J = 7.9 Hz, 2H, Ph-*H*-4''), 7.50 (dd, ^3J = 4.8 Hz, ^3J = 3.3 Hz, 2H, Tph-*H*-4'), 7.40 (d, ^3J = 7.9 Hz, 4H, Ph-*H*-3'',5''), 4.79 (m$_c$, 4H, N-C*H*$_2$), 2.91 (m$_c$, 4H, Ph-(C*H*)-(CH$_3$)$_2$), 2.20 (m$_c$, 4H, NH-C*H*$_2$), 1.54 (m$_c$, 4H, N-(CH$_2$)-C*H*$_2$), 1.51 - 1.21 (m, 8H, NH-(CH$_2$)$_2$-(C*H*$_2$)$_3$), 1.22 (t, ^3J = 6.8 Hz, 24H, Ph-(CH)-(C*H*$_3$)$_2$), 0.87 (t, ^3J = 7.0 Hz, 6H, C*H*$_3$) ppm. **^{13}C{^{1}H} NMR** (126 MHz, CDCl$_3$): δ = 164.69 ((*C*(O)N)-4,10), 164.49 ((*C*(O)N)-3,9), 145.84 (Ph-*C*-2'',6''), 139.16 (*C*-1,7), 138.02 (*C*-2,8), 136.60 (Tph-*C*-2'), 134.59 (*C*-6a,12a), 134.42 (Tph-*C*-5'), 132.71 (*C*-6,12, only HMBC), 131.06 (Ph-*C*-1''), 130.13 (Tph-*C*-3'), 129.71 (Ph-*C*-4''), 128.62 (Tph-*C*-4'), 124.20 (Ph-*C*-3'',5''), 123.92 (*C*-3a$_1$,6b$_1$), 123.24 (*C*-3,4/9,10), 121.63 (*C*-3a,9a), 121.14 (*C*-5,11), 120.61 (*C*-6b,12b), 50.92 (NH-C*H*$_2$), 31.90 (NH-CH$_2$-*C*H$_2$), 31.42 (NH-(CH$_2$)$_2$-*C*H$_2$), 29.42 (Ph-(*C*H)-(CH$_3$)$_2$), 26.75 (NH-(CH$_2$)$_3$-*C*H$_2$), 24.25 and 24.23 (Ph-(CH)-(*C*H$_3$)$_2$), 22.58 (NH-(CH$_2$)$_4$-*C*H$_2$), 14.08 (*C*H$_3$) ppm. **^{11}B{^{1}H} NMR** (160 MHz, CDCl$_3$): δ = 38.21 (br) ppm. **HRMS** (APCI, MeOH/toluene, positive mode): *m/z* [M+H]$^+$ Calcd. For C$_{68}$H$_{71}$^{11}B$_2$N$_4$O$_4$S$_2$ 1093.51179; Found 1093.51256. **HRMS** (APCI, MeOH/toluene, negative mode): *m/z* [M]$^{··}$ Calcd. for C$_{68}$H$_{70}$^{11}B$_2$N$_4$O$_4$S$_2$ 1092.50507; Found 1092.50602. **IR** (ATR): υ = 2956 (w), 2921 (w), 2851 (w), 1707 (m), 1669 (m), 1600 (m), 1562 (m), 1436 (m), 1311 (s), 1280 (m), 1245 (s) 1207 (m), 1192 (m), 1053 (m), 847 (m), 813 (m), 792 (m), 759 (m), 753 (m), 720 (m), 700 (s) cm^{-1}.

3.9.19 1,7-Di(*n*-hexyl)-6,12-*bis*(4-(diphenylamino)phenyl)-1,12,6,7-*di*([1,2]azaborinine)-*N*,*N*'-di(cyclohexyl)perylene-3,4,9,10-tetracarboxylic acid diimide (**TPA-BNCDI^{Cy}**)
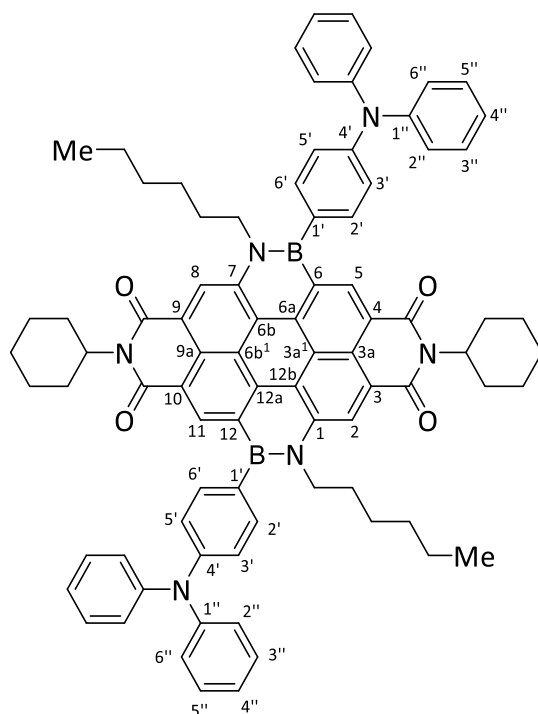
The precursor 4-(dichloroboranyl)-*N*,*N*-diphenylaniline was generated *in situ* from (4-(trimethylsilyl)phenyl)-diphenylamine (1.00 g, 3.15 mmol) using boron trichloride (3.50 mL, 3.50 mmol, 1 M in DCM) in DCM (10 mL). After stirring at 25 °C for 14 h, all volatiles were removed, and the resulting yellow oil was directly used.[13] In a nitrogen filled glovebox, a Schlenk tube was charged with 1,7-di(*n*-hexylamino)-*N*,*N*'-di(cyclohexyl)perylene-3,4,9,10-tetracaboxylic acid diimide (**1,7-DHA-PDI^{Cy}**, 111 mg, 150 μmol), toluene (10.0 mL), triethylamine (1.0 mL) and 4-(dichloroboranyl)-*N*,*N*-diphenylaniline (**TPABCl₂**, 1.02 g, 3.15 mmol). The sealed tube was stirred for 4 h at 110 °C. Afterwards all volatiles were removed *in vacuo* and the residue was dissolved in DCM (50 mL), washed with brine (3 x 50 mL), 1 M NaOH (3 x 50 mL) and water (3 x 50 mL). After drying over magnesium sulfate, filtration and removal of all volatiles *in vacuo*, the material was mixed with *n*-pentane (200 mL, 2x) and heated to 50 °C and the solution was discarded. The residual blue/violet solid was subjected to column chromatography. (silica, eluent: gradient *n*-pentane to DCM, R$_f$(DCM) = 0.75) to give the product (**TPA-BNCDI^{Cy}**, 134 mg, 0.11 mmol, 71%) as a red-violet solid. **¹H NMR** (500 MHz, CDCl₃): δ = 9.59 (s, 2H, *H*-2,8), 9.54 (s, 2H, *H*-5,11), 7.62 (d, ^3J = 8.4 Hz, 4H, B-Ph-*H*-2',6'), 7.39 - 7.30 (m, 20H, B-Ph-*H*-3',5' and TPA-Ph-*H*-2'',3'',5'',6''), 7.10 (t, ^3J = 8.4 Hz, 4H, TPA-Ph-*H*-4''), 5.24 (tt, ^3J = 12.1 Hz , ^4J = 3.6 Hz, 2H, C*H*), 4.77 (t, ^3J = 8.0 Hz, 4H, N-C*H*₂), 2.71 (qd, ^3J = 12.6 Hz , ^4J = 3.3 Hz, 4H, CH-C*H*ₐₓ), 2.07 (m$_c$, 4H, N-(CH₂)-C*H*₂), 1.98 (d, ^3J = 10.9 Hz, 4H, CH-(CH₂)C*H*ₐₓ), 1.90 (d, ^3J = 10.2 Hz, 4H, CH-C*H*ₑq), 1.79 (d, ^3J = 12.8 Hz, 2H, CH-(CH₂)₂-C*H*ₐₓ), 1.62 - 1.40 (m, 20H, N-(CH₂)-C*H*₂, N-(CH₂)-C*H*₂ and CH-(CH₂)₂-C*H*ₑq), 1.37-1.15 (m, 30H, (C*H*₂)₂-CH₃ and CH-(CH₂)C*H*ₑq), 0.90 (t, ^3J = 7.0 Hz, 6H, C*H*₃) ppm. **¹³C{¹H} NMR** (126 MHz, CDCl₃): δ = 164.83 ((*C*(O)N)-4,10), 164.66 ((*C*(O)N)-3,9), 148.08 (B-Ph-*C*-4'), 147.87 (TPA-Ph-*C*-1''), 138.97 (*C*-1,7), 137.49 (*C*-5,11), 134.26 (*C*-6a,12a), 134.01 (B-Ph-*C*-2',6'), 132.61 (*C*-6,12 only HMBC), 131.94 (B-Ph-*C*-1' only HMBC), 129.55 (TPA-Ph-*C*-3'',5''), 125.18 (TPA-Ph-*C*-2'',6''), 123.65/123.48 (*C*-3,9/4,10), 123.38 (*C*-3a,9a) 123.36 (TPA-Ph-*C*-4''), 122.63 (B-Ph-*C*-3',5'), 120.86 (*C*-6b,12b), 120.70 (*C*-3a¹,6b¹), 120.54 (*C*-2,8), 54.47 (*C*H), 50.37 (N-*C*H₂), 31.35 (N-(CH₂)-*C*H₂ and N-(CH₂)₃-*C*H₂), 29.55 (CH-*C*H₂), 26.83 (CH-(CH₂)*C*H₂), 25.68 (CH-(CH₂)₂-*C*H₂), 22.73 (N-(CH₂)₄-*C*H₂), 14.14 (*C*H₃).

^{11}**B{^{1}H} NMR** (160 MHz, CDCl$_3$): δ = 40.57 (br) ppm. **HRMS** (ESI): m/z [M-B$_2$]$^{2+}$ Calcd. C$_{84}$H$_{80}$N$_6$O$_4$ 618.3115; Found 618.31106. **IR** (ATR): υ = 2924 (w), 2856 (w), 1693 (m), 1654 (m), 1593 (s), 1566 (m), 1508 (m), 1486 (m), 1449 (m), 1436 (m), 1412 (m), 1362 (m), 1324 (m), 1299 (m), 1268 (s), 1256 (m), 1245 (m), 1194 (m), 1181 (m), 1102 (m), 813 (s), 755(s), 696 (s) cm^{-1}.

3.9.20 1,7-Di(*n*-hexyl)-6,12-*bis*(4-(diphenylamino)phenyl)-1,12,6,7-di([1,2]azaborinine)-*N*,*N*'-*bis*(2,6-di(*iso*proypyl)phenyl)perylene-3,4,9,10-tetracarboxylic acid diimide (**TPA-BNCDI^{Dip}**)

The precursor 4-(dichloroboranyl)-*N*,*N*-diphenylaniline was generated *in situ* from (4-(trimethylsilyl)phenyl)-diphenylamine (317 mg, 1.00 mmol) using boron trichloride (1.11 mL, 1.11 mmol, 1 M in DCM) in DCM (10 mL). After stirring at 25 °C for 14 h, all volatiles were removed, and the resulting yellow oil was directly used.[13] In a nitrogen filled glovebox, a multireactor vial was charged with 1,7-di(*n*-hexylamino)-*N*,*N*'-*bis*(2,6-di(*iso*propyl)phenyl)perylene-3,4,9,10-tetracaboxylic acid diimide (**1,7-DHA-PDI^{Dip}**, 98 mg, 0.10 mmol), toluene (5.0 mL), triethylamine (0.5 mL) and 4-(dichloroboranyl)-*N*,*N*-diphenylaniline (**TPA-BCl$_2$**, 326 mg, 1.00 mmol). The reaction mixture was stirred for 12 h at 110 °C. After the reaction mixture was cooled to 25 °C, it was mixed with DCM (30 mL), washed with brine (3 x 50 mL), 1 M NaOH (3 x 50 mL) and water (3 x 50 mL). After drying of the organic phase over magnesium sulfate, filtration and evaporation of all volatiles, the residue was mixed with *n*-pentane (200 mL, 2x) and heated to 50 °C were the solution was discarded. The product was subjected to column chromatography (silica, eluent: gradient *n*-pentane to DCM, R$_f$ = 0.72) to give the product (71 mg, 0.05 mmol, 50%) as a red-violet solid. ^{1}**H NMR** (500 MHz, CDCl$_3$): δ = 9.72 (s, 2H, *H*-2,8), 9.66 (s, 2H, *H*-5,11), 7.66 (d, ^3J = 8.2 Hz, 4H, B-Ph-*H*-2',6'), 7.53 (t, ^3J = 7.9 Hz, 2H, (CO)$_2$N-Ph-*H*-4'''), 7.39 (d, ^3J = 8.3 Hz, 4H, (CO)$_2$N-Ph-*H*-3''',5'''), 7.37 - 7.24 (m, 12H, B-Ph-*H*-3',5' and TPA-Ph-*H*-3'',5''), 7.29 - 7.27 (m, 8H, and TPA-Ph-*H*-2'',6''), 7.08 (tt, ^3J = 7.2 Hz, ^4J = 1.0 Hz, 4H, TPA-Ph-*H*-4''), 4.84 (t, ^3J = 8.0 Hz, 4H, N-C*H$_2$*), 2.92 (sept., ^3J = 6.8 Hz, 4H, Ph-(C*H*)-(CH$_3$)$_2$), 2.23-2.17 (m, 4H, N-CH$_2$-C*H$_2$*), 1.52 - 1.44 (m, 4H, NH-(CH$_2$)$_2$-C*H$_2$*), 1.33- 1.27 (m, 8H, N-(CH$_2$)$_3$-(C*H$_2$*)$_2$), 1.26 - 1.18 (t, ^3J = 6.8 Hz, 24H, Ph-(CH)-(C*H$_3$*)$_2$), 0.87 (t, ^3J = 6.8 Hz, 6H, C*H$_3$*) ppm. ^{13}**C{^{1}H} NMR** (126 MHz, CDCl$_3$): δ = 164.83 ((*C*(O)N)-3,9), 164.66 ((*C*(O)N)-4,10), 148.24 (B-Ph-*C*-4'), 147.82 (TPA-Ph-*C*-1''), 145.88 ((CO)$_2$N-Ph-*C*-2''',6'''),

139.23 (C-1,7), 138.13 (C-5,11), 134.80 (C-6a,12a), 133.90 (B-Ph-C-2',6'), 132.77 (C-6,12, only HMBC), 131.78 (B-Ph-C-1', only HMBC), 131.19 ((CO)$_2$N-Ph-C-1'''), 129.75 ((CO)$_2$N-Ph-C-4'''), 129.55 (TPA-Ph-C-3'',5''), 125.21 (TPA-Ph-C-2'',6''), 124.39 (C-3a,9a), 124.26/124.10 ((CO)$_2$N-Ph-C-3''',5'''), 123.40 (TPA-Ph-C-4''), 123.10/123.00 (C-3,9/4,10), 122.54 (B-Ph-C-3',5'), 121.51 (C-2,8), 121.10 (C-6b,12b), 120.45 (C-3a^1,6b^1), 50.50 (N-CH_2), 31.36 (N-CH$_2$-CH$_2$), 31.29 (N-(CH$_2$)$_2$-CH$_2$), 29.42 (Ph-(CH)-(CH$_3$)$_2$), 26.81 (N-(CH$_2$)$_3$-CH$_2$), 24.30 and 24.24 (Ph-(CH)-(CH$_3$)$_2$), 22.60 (N-(CH$_2$)$_4$-CH$_2$), 14.07 (CH$_3$) ppm. **^{11}B{^{1}H} NMR** (160 MHz, CDCl$_3$): δ = 39.10 (br) ppm. **HRMS** (ESI, IMPACT II): m/z [M+Na]$^+$ Calcd. C$_{96}$H$_{92}$^{11}B$_2$N$_6$O$_4$Na 1437.72849; Found 1437.72860. **IR** (ATR): υ = 2960 (w), 2927 (w), 2868 (w), 1706 (m), 1670 (m), 1601 (m), 1589 (m), 1566 (m), 1508 (m), 1488 (m), 1448 (m), 1438 (m), 1314 (m), 1249 (s), 1211 (m), 1195 (m), 1107 (w), 1056 (w), 988 (w), 847 (m), 815 (m), 793 (m), 739 (m), 697 (s) cm^{-1}.

3.9.21 Low-Temperature Luminescence Studies

The low-emperature measurements were performed with a cryostat (Oxford Instruments) set-up using *iso*pentane as a solvent and the same luminescence machine as mentioned above. Solutions of the respective compound were prepared in *iso*pentane (Acros Organics, reagent grade), filled in a one-piece Quartz cuvette (1 cm) and capped with a septum. The sample was cooled to 77 K and warmed by a controlled heating system.
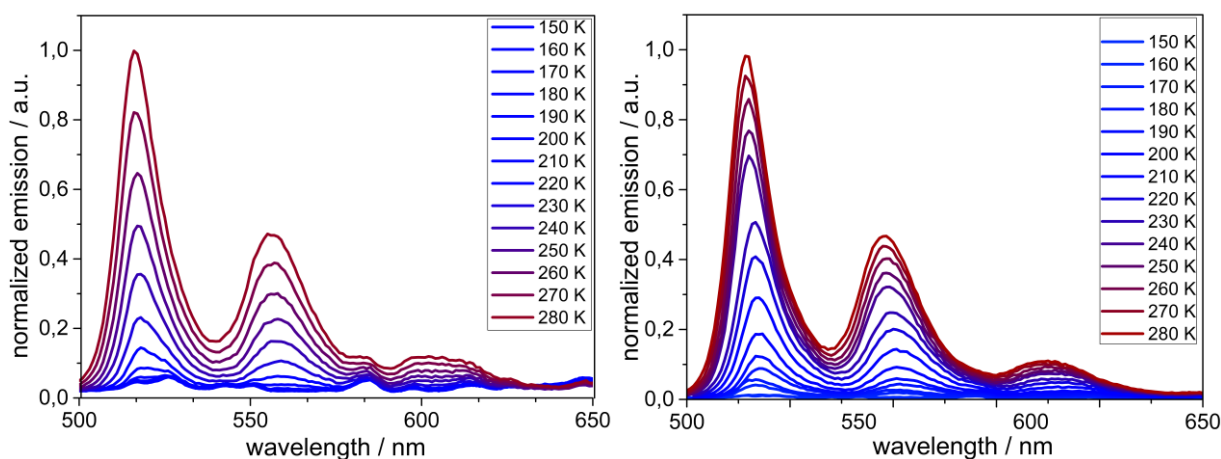
Fig. 82: Normalized emission spectra of **PDI^{Cy}** and **PDI^{Dip}** in *iso*pentane (5.3 10^{-6} M) upon heating from 150 K to 280 K.
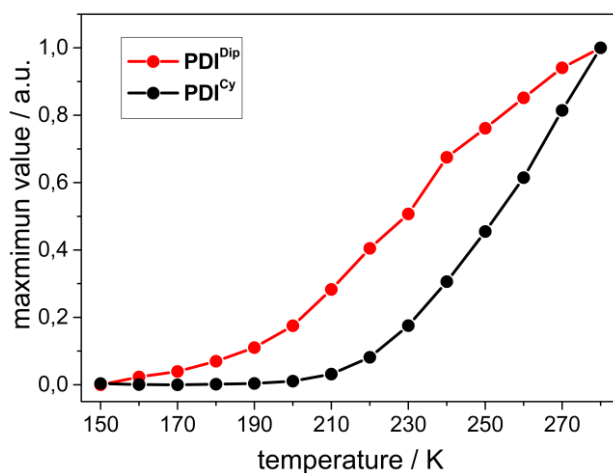
Fig. 83: Compared emission maxima of **PDI**s in *iso*pentane from 150 K to 280 K.

3.9.22 Microscopy

Microscopic images von PMMA/**BNCDI** blends were obtained with a Zeiss Axio Imager 2 with LD/ED Epiplan-NEOFLUAR 50 x and LD Epiolan 20x. Both **BNCDI**s were dissolved with PMMA in dichloromethane and drop casted on a glass substrate.
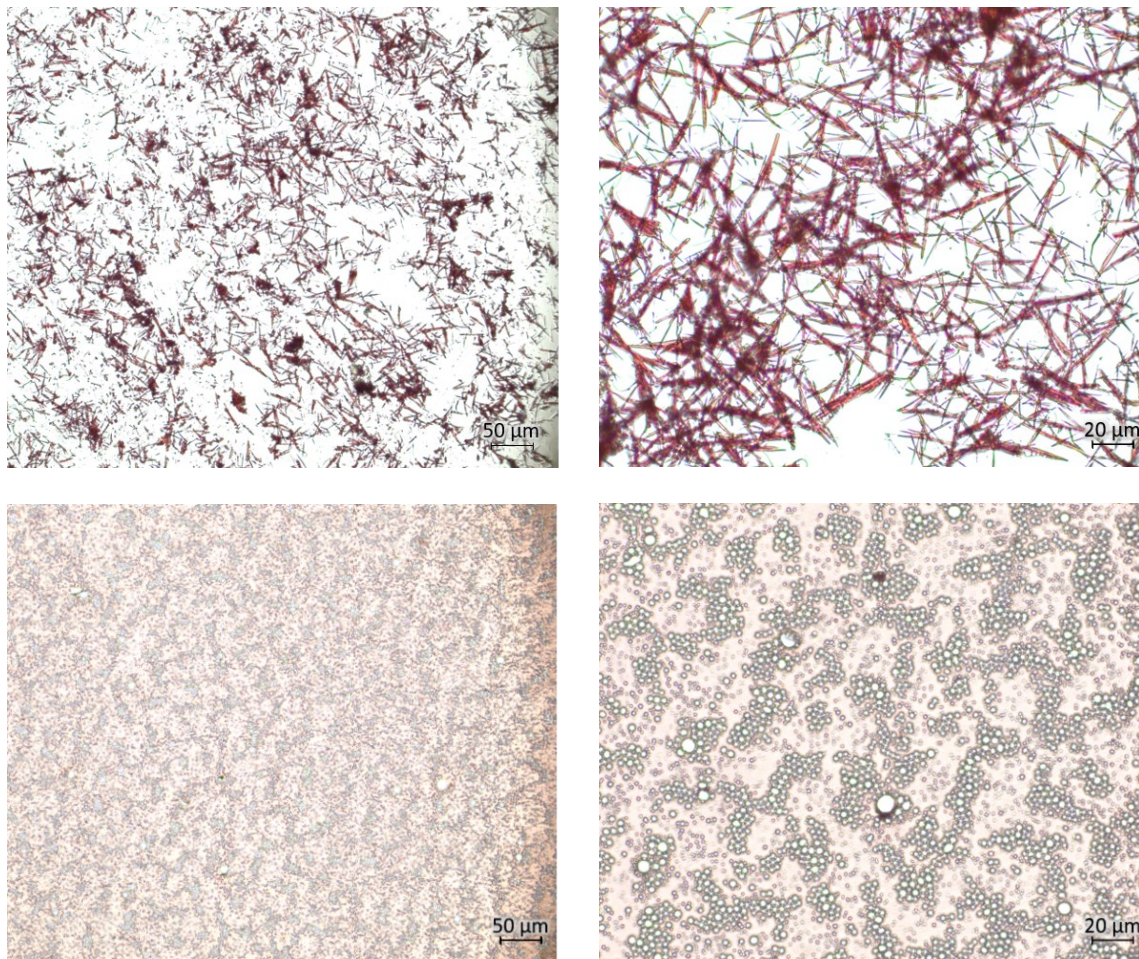
Fig. 84: Microscopic images of **Tph-BNCDI^Cy** (upper row) and **Tph-BNCDI^Dip** (bottom row) in a PMMA blend (50%) with different magnifications (20x and 50x). The bubbles may arise from the evaporation of DCM as they were clearly visible by the high profile of the measured samples. They could not be removed by drying in a vacuum chamber.

3.9.23 Electrochemistry

The electrochemical studies were carried out under argon using an Eco Chemie Autolab PGSTAT 30 potentiostat for cyclic voltammetry. A three-electrode configuration were used: the working electrode was a platinum disk, the reference electrode was a saturated calomel electrode and the counter-electrode a platinum wire. All potentials were internally referenced to the ferrocene/ferrocenium couple. For the measurements, concentrations of 10^{-3} M of the electroactive species were used in a 0.2 M solution of tetrabutylammonium hexafluorophosphate in degassed DCM. The scanning rate was 200 mV/s. Not reversible waves were corrected against Fc/Fc+ potential, whereas reversible reduction waves were corrected against $E_{1/2}p$ from ferrocene. Absolute HOMO/LUMO levels were calculated according to $E_{LUMO} = -4.8$ eV$- E_{red}$ and $E_{HOMO} = -4.8$ eV$- E_{ox}$.

3.9.24 Thermal analysis

For thermal analysis, a Mettler Toledo TGA/DSC3+ or DSC 3+ with 40 μL aluminum crucibles was used. Measurements were performed with a gas flow of 20 mL/min nitrogen and a heating rate of 10 °C/min.
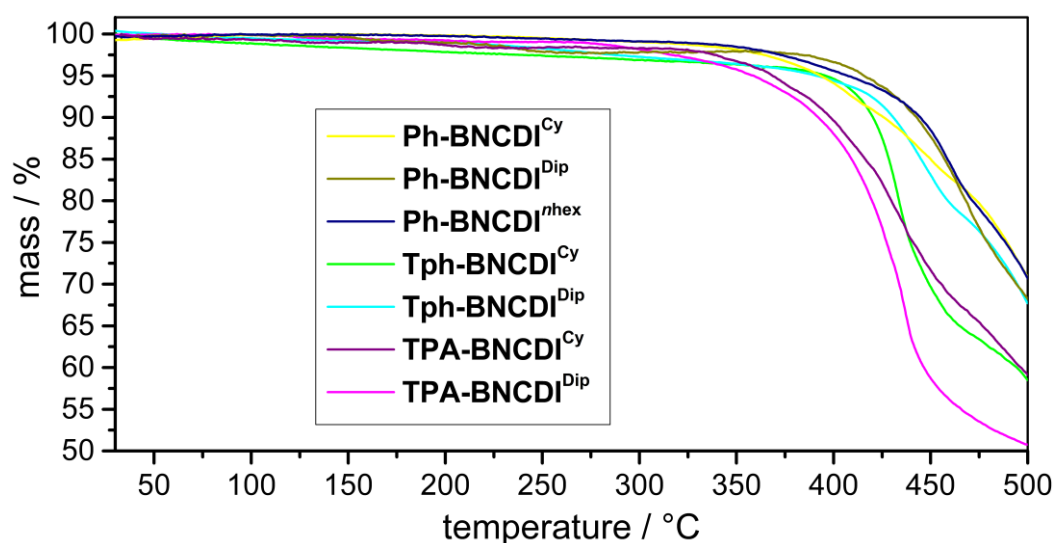
Fig. 85: Thermogravimetric analysis of all **BNCDI**s at 10 K/min with 20 mL/min nitrogen gas flow.
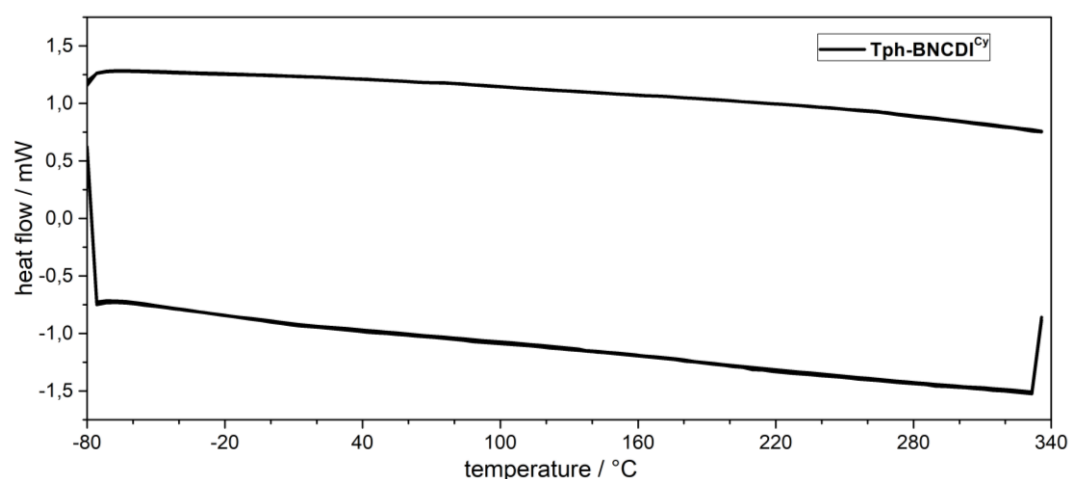
Fig. 86: Dynamic scanning analysis of **Tph-BNCDI^{Cy}** at 10 K/min with 20 mL/min nitrogen gas flow.
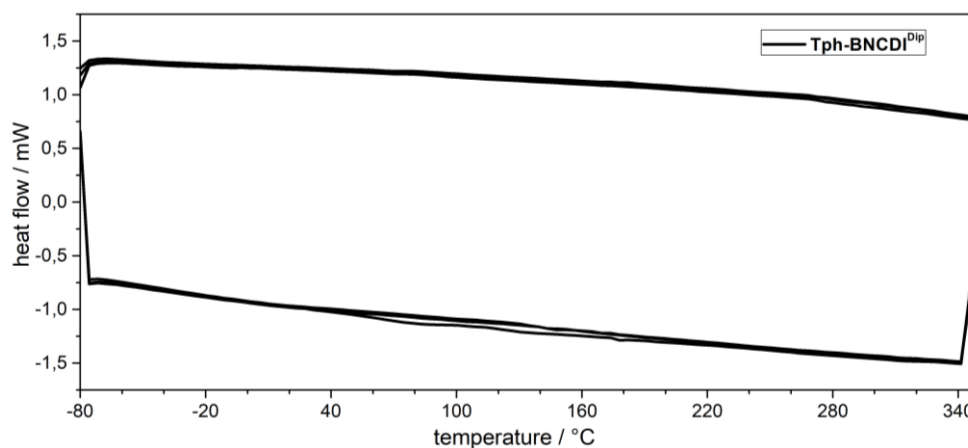
Fig. 87: Dynamic scanning analysis of **Tph-BNCDI^{Dip}** at 10 K/min with 20 mL/min nitrogen gas flow.

3.9.25 Quantum Chemical Calculations

The equilibrium geometries were optimized with Gaussian 09[14] using B3LYP/6-31-G*-level of theory with empirical dispersion correction (GD3), followed by a frequency calculation to ensure that the optimized structures were the true minima. The orbital energies of HOMO and LUMO and their energy differences were calculated for these optimized molecules.

3.9.26 **Nuclear Independent Chemical Shift Calculations**

To compare the aromaticity of the **Tph-BNCDI^{Cy}** with its all carbon congener **Tph-CDI^{Cy}** were estimated by NICS[15-17] calculations (CSGT-B3LYP/6-31-G*). The NICS values were determined 1 Å above the center of the respective ring and in plane (0 Å).
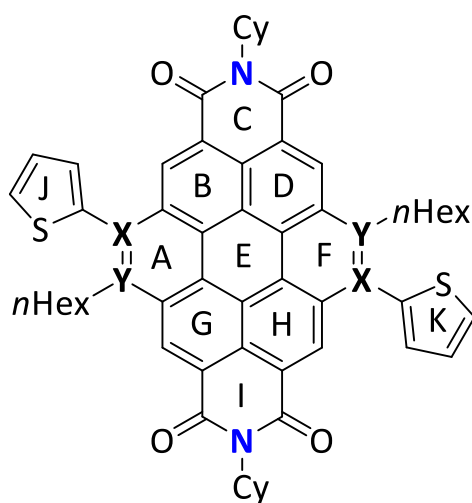
Tab. 11: NICS(0) and NICS(1) values of **Tph-BNCDI^{Cy}** and **Tph-CDI^{Cy}**.

ring	X,Y = C		X = B, Y = N	
	NICS(0)	NICS(1)	NICS(0)	NICS(1)
A	-8.68	-11.09	-3.25	-6.01
B	-9.89	-12.09	-9.53	-11.53
C	5.77	1.46	5.07	0.82
D	-9.89	-12.16	-8.24	-11.26
E	-1.18	-5.39	0.96	-3.34
F	-8.47	-10.95	-3.52	-6.26
G	-9.89	-12.09	-8.24	-13.23
H	-9.89	-12.09	-9.53	-11.53
I	5.77	1.46	5.07	0.82
J	-10.81	-8.21	-11.46	-9.08
K	-10.76	-8.94	-11.46	-9.16

3.9.27 Spectroelectrochemical Experiments

Spectroelectrochemical experiments were performed in DCM with TBAPF$_6$ as electrolyte (0.2 M). The UV/NIR spectrometer was a Jasco V-770 instrument. As cell, an Omni Cell Spec with a platinum grid as the working electrode, a platinum wire as the counter electrode and SCE reference electrode was used. In addition, a Princeton applied Research Model 362 Scanning Potentiostat was used.

Due to the fact that phenyl and thienyl substituted **BNCDI**s showed reliable optoelectronical properties, we subjected **Tph-BNCDI^{Dip}** as model substrate to the experiments. Since these system exhibited reversible reduction, we were interested in the formation of the **Tph-BNCDI$^{Dip•-}$** and **Tph-BNCDI^{Dip2-}** species upon reduction (Scheme 48).
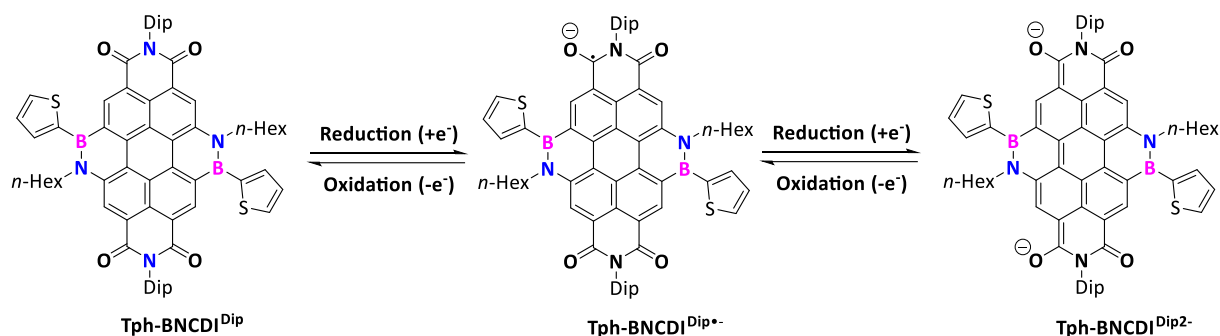
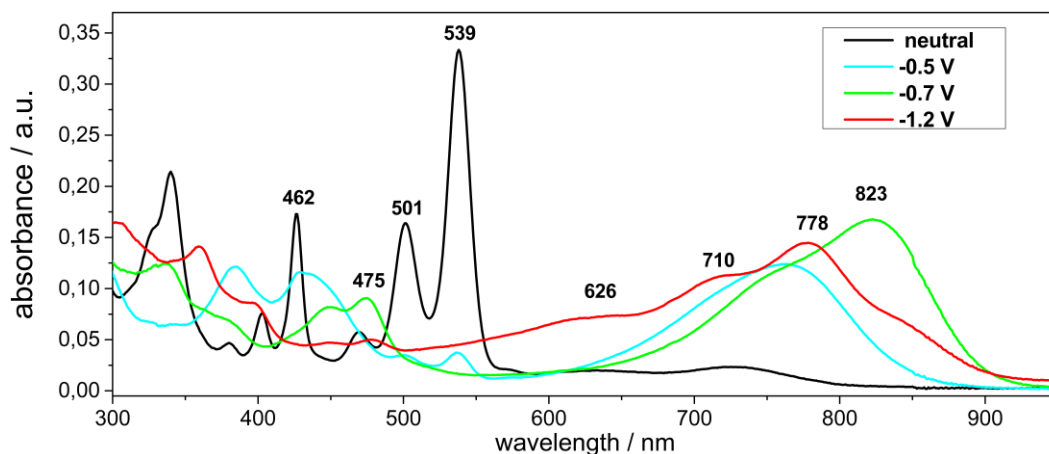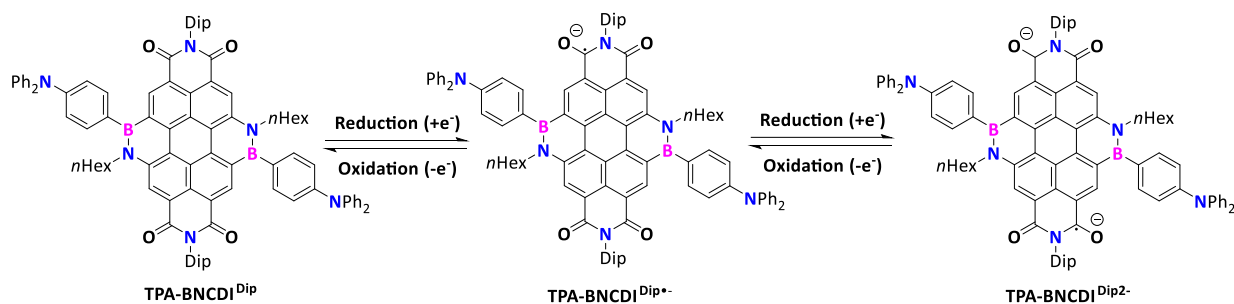**Scheme 48**: Proposed formation of **Tph-BNCDI$^{Dip•-}$** and **Tph-BNCDI^{Dip2-}** upon reduction.

Fig. 88: UV/Vis spectral change during spectroelectrochemical characterization of **Tph-BNCDI^{Dip}** in DCM with 0.2 M TBAPF$_6$ at different potentials: neutral conditions (black), -0.5 V (turquoise). -0.7 V (green) and -1.2 V (red).

The here displayed process was not reversible. After investigation of the proposed **Tph-BNCDI^{Dip}** radical anion and dianion, the spectroelectrochemical behavior of the **TPA-BNCDI^{Dip}** was investigated. Therefore, the reduction of **TPA-BNCDI^{Dip}** was conducted (Scheme 48).

Scheme 49: Formation of **TPA-BNCDI$^{Dip•-}$** and **TPA-BNCDI^{Dip2-}** upon reduction.
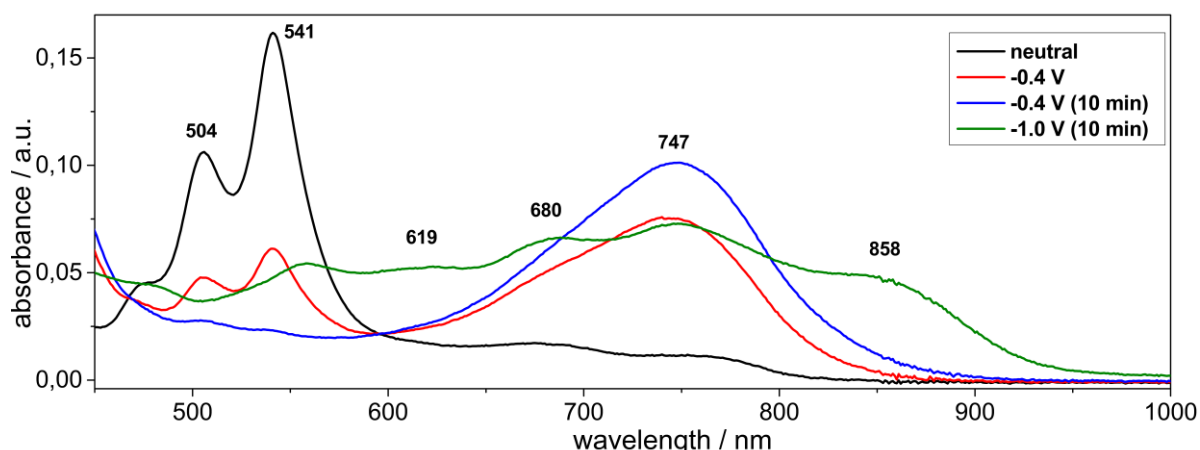
Fig. 89: Spectroelectrochemical characterization of **TPA-BNCDI$^{Dip\bullet-}$** in DCM with 0.2 M TBAPF$_6$ at different potentials.

The observed species differed slightly from the reduced **Tph-BNCDI^{Dip}**. This process was also not reversible in the spectroelectrochemical setup.

3.9.28 References for the Experimental Part

1.   J. Hoffmann, *Master Thesis: Synthesis and Characterization of Novel Perylene Diimides and Their Derivatives*, University Kiel, **2016**.
2.   H. Langhals, O. Krotz, K. Polborn, P. Mayer, *Angew. Chem. Int. Ed. Engl.*, **2005**, *44*, 2427-2428.
3.   I. Ghosh, T. Ghosh, J. I. Bardagi, B. Konig, *Science*, **2014**, *346*, 725-728.
4.   S. Sengupta, R. K. Dubey, R. W. Hoek, S. P. van Eeden, D. D. Gunbas, F. C. Grozema, E. J. Sudholter, W. F. Jager, *J. Org. Chem.*, **2014**, *79*, 6655-6662.
5.   I. Nishizawa, H. Ajito, Y. Gonmori, R. Katoh, T. Ichikawa, N. Nemoto, *Polymer*, **2019**, *167*, 93-101.
6.   X. Y. Wang, F. D. Zhuang, J. Y. Wang, J. Pei, *Chem. Commun.*, **2015**, *51*, 17532-17535.
7.   B. A. Coombs, S. R. Rutter, A. E. Goeta, H. A. Sparkes, A. S. Batsanov, A. Beeby, *RSC Advances*, **2012**, *2*, 1870.
8.   B. Huang, L. Guo, Y. Jia, *Angew. Chem. Int. Ed.*, **2015**, *54*, 13599-13603.
9.   R. Fritzsche, F. Seidel, T. Rüffer, R. Buschbeck, A. Jakob, H. Freitag, D. R. T. Zahn, H. Lang, M. Mehring, *J. Organomet. Chem.*, **2014**, *755*, 86-92.
10.   F. Denat, H. Gaspard-Iloughmane, J. Dubac, *J. Organomet. Chem.*, **1992**, *423*, 173-182.
11.   A. Lik, L. Fritze, L. Muller, H. Helten, *J. Am. Chem. Soc.*, **2017**, *139*, 5692-5695.
12.   B. Wrackmeyer, *Z. Naturforsch., B: Chem. Sci.*, **2015**, *70*, 421-424.
13.   Z. Zhang, R. M. Edkins, J. Nitsch, K. Fucke, A. Steffen, L. E. Longobardi, D. W. Stephan, C. Lambert, T. B. Marder, *Chem. Sci.*, **2015**, *6*, 308-321.
14.   M. J. Frisch, G. W. Trucks, H. B. Schlegel, G. E. Scuseria, M. A. Robb, J. R. Cheeseman, G. Scalmani, V. Barone, G. A. Petersson, H. Nakatsuji, X. Li, M. Caricato, A. V. Marenich, J. Bloino, B. G. Janesko, R. Gomperts, B. Mennucci, H. P. Hratchian, J. V. Ortiz, A. F. Izmaylov, J. L. Sonnenberg, Williams, F. Ding, F. Lipparini, F. Egidi, J. Goings, B. Peng, A. Petrone, T. Henderson, D. Ranasinghe, V. G. Zakrzewski, J. Gao, N. Rega, G. Zheng, W. Liang, M. Hada, M. Ehara, K. Toyota, R. Fukuda, J. Hasegawa, M. Ishida, T. Nakajima, Y. Honda, O. Kitao, H. Nakai, T. Vreven, K. Throssell, J. A. Montgomery Jr., J. E. Peralta, F. Ogliaro, M. J. Bearpark, J. J. Heyd, E. N. Brothers, K. N. Kudin, V. N. Staroverov, T. A. Keith, R. Kobayashi, J. Normand, K. Raghavachari, A. P. Rendell, J. C. Burant, S. S. Iyengar, J. Tomasi, M. Cossi, J. M. Millam, M. Klene, C. Adamo, R. Cammi, J. W. Ochterski, R. L. Martin, K. Morokuma, O. Farkas, J. B. Foresman, D. J. Fox, Gaussian 16 Rev. C.01, **2016**.
15.   P. V. R. Schleyer, C. Maerker, A. Dransfeld, H. Jiao, N. J. R. van Eikema Hommes, *J. Am. Chem. Soc.*, **1996**, *118*, 6317-6318.
16.   B. Goldfuss, P. v. R. Schleyer, *Organometallics*, **1997**, *16*, 1543-1552.

17. P. V. R. Schleyer, M. Manoharan, Z. X. Wang, B. Kiran, H. Jiao, R. Puchta, N. J. R. van Eikema Hommes, *Org. Lett.*, **2001**, *3*, 2465-2468.

Chapter 4: BP-Substituted Polycyclic Aromatic Hydrocarbons

4.1   Introduction

There have been numerous reported examples of BN-substituted PAHs but barely any representatives of BP-substituted PAHs. In fact, examples with both tricoordinated boron and phosphorus in a 1,2-substitution pattern have remained rare until today.

To compare the geometrical and optoelectronic effect of substituting nitrogen with phosphorus in a heterocyclic and boron-containing system the substituted dibenzo-1,4-azaborine and dibenzo-1,4-phosphaborine as a comparative example are discussed (Scheme 50).
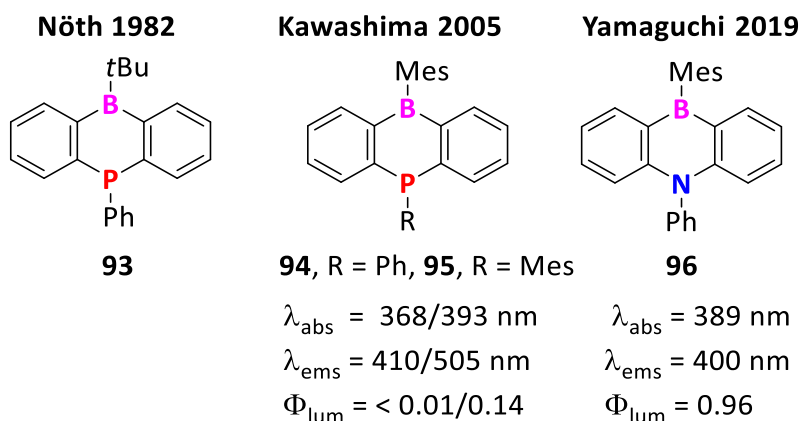
Scheme 50: Examples of dibenzo-1,4-phosphinoboranes **93**,[1] **94/95**[2] and dibenzo-1,4-azaborine **96**[3] from literature.

The aryl-substituted 1,4-phosphaborine (**93**), representing the first example of a PAH containing boron and phosphorus, was synthesized by Nöth in utilizing a hydrophosphination reaction.[1] The optical properties of this novel class of hetero-π-conjugated compounds was not investigated until 2005 when Kawashima and coworkers synthesized 1,4-phosphinoborane **94/95** *via* the reaction of a dilithiated *bis*(2-bromophenyl)(aryl)phosphine and an electrophilic boron species (MesB(OMe)$_2$).[2] In comparison to the all planar dibenzo-1,4-azaborine (**96**), which was only recently published by Yamaguchi and coworkers,[3] its heavier congener dibenzo-1,4-phosphaborane **94** exhibited an out-of-plane orientation of the phosphorus atom due to P-pyramidalization. The sum of angles at the phosphorus atom in **94** and **95** was determined (Σ_P = 307°/314°) indicating a pyramidalized (sp^3-hybridized) phosphorus atom. As a result, the overlap of the phosphorus lone pair with the π-system was weak. The optical properties were investigated: The dibenzo-1,4-phospaboranes **94/95** showed absorption maxima of λ_{abs} = 368 nm/393 nm and emission maxima of λ_{ems} = 410 nm/505 nm with low fluorescence quantum yields (Φ_{lum} < 0.01 (**94**) and Φ_{lum} = 0.14 (**95**)). In phenyl-substituted **94**, the Stokes shift ($\Delta\nu_{Stokes}$ = 2664 cm^{-1}) was smaller than in mesityl-substituted **95** ($\Delta\nu_{Stokes}$ = 5643 cm^{-1}) which was contrary to the increasing quantum yield. It was proposed that the emission properties were based on intramolecular charge transfer (ICT) processes similarly to the dibenzo-1,4-azaborine (**96**) involving low quantum yields. The influence of the aryl group at the phosphorus atom was evident as the bulkiness of mesitylene in **95** increased the quantum yield due to the decreased planarity of the 1,4-phosphaborine ring resulting in an elevation of the HOMO.[4] An stabilizing electronic effect of the σ-orbital of the exocyclic P-Ar bond with the π-scaffold, as it occurs in phospholes,[5-7] was not found in these examples. Furthermore, the existence of excimers of 1,4-phosphaborines, which was not observed in 1,4-azaborines, was assigned to the higher availability of the phosphorus lone pair in the

BP unit compared to the nitrogen's lone pair in the BN unit.[2] Such a behavior should be taken into account for designing BP-substituted π-conjugated structures.

As the synthesis of dibenzo-1,4-azaborine **96** was recently published by Yamaguchi and coworkers,[3] the photophysical investigations could be directly compared to the BP-congener **94**. In comparison to BP-compound **94,** the absorption and the emission maxima of **96** (λ_{abs} = 389 nm, λ_{ems} = 400 nm) were similar to those of compound **94** but the quantum yield was far higher (Φ_{lum} = 0.96) than in **94** (Φ_{lum} < 0.01[8]).

A major advantage of utilizing phosphorus in a π-conjugated system is the possibility to tune to optoelectronic properties by postmodification of the phosphorus atom. This concept was used on the dibenzo-1,4-phosphaborine (**94**) by chalcogenation to give **97/98** or by the formation of the phosphonium salt **99** (Scheme 51).[8]
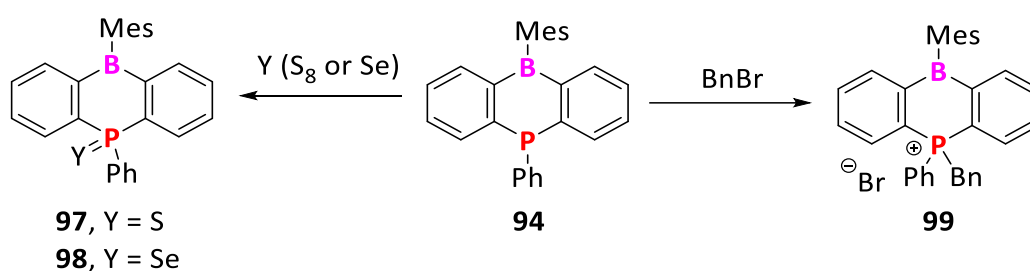
Scheme 51: Oxidation of the dibenzo-1,4-phosphinoborine **94** by chalcogens or with benzyl bromide.[8]

The post-functionalization of phosphorus by oxidation with chalcogens or benzyl bromide had a differing influence upon the electronic properties. The HOMO level could slightly increase or lowered for the sulfurized/selenized motif while both HOMO and LUMO were both strongly stabilized for the benzyl phosphonium salt. Although, no considerable change of the absorption or emission properties was observed in all cases.[8]

To conclude, the non-isostructural substitution of nitrogen with phosphorus in a 1,4-heteroborine resulted in substantial changes in the photophysical properties. The reason for this is that the nitrogen lone pair interacts strongly with the carbon's non-bonding p^z-orbital. This interaction was not present with phosphorus due to its pyramidal orientation. By variation of the aryl substituents at the phosphorus, geometries are modifiable which directly affected the photophysical properties of the 1,4-phosphaborine derivatives.

Due to their spatial separation, combinations of group 13 and group 15 elements in 1,4-orientation largely display each element's electronic and geometric properties in a separated fashion. A combination of both main group elements *via* direct linkage, as in 1,2-azaborines and 1,2-phosphaborines, enables the direct interaction of the group 15 lone pair with the group 13 empty p-orbital and represents the most thermodynamic stable isomer, as determined for azaborines.[9, 10] Due to the direct orbital overlap, the 1,2-substitution pattern mimics an adjacent pair of carbon atoms the best. Even though there have been numerous reports of 1,2-azaborines embedded in PAH structures,[11] similar examples of directly linked BP units in PAHs have been barely described. For such a substitution pattern, the pyramidalization of phosphorus and the orientation of its lone pair could lead to dimerization or oligomerization events. Therefore, these compounds require kinetic and thermodynamic stabilization with bulky groups at the boron and phosphorus atoms. Using such bulky groups, the first example of a directly linked 1,2-BP unit embedded in a π–heterocyclic system was

presented by Tokitoh and coworkers in 2011.[12] A 1,8-substituted diaryldicholorophosphinenaphthalene **100** was subjected to reduction and underwent an aryl migration to give the first example of a BP-acenaphthene **101** involving both tricoordinated boron and phosphorus atoms (Scheme 52).
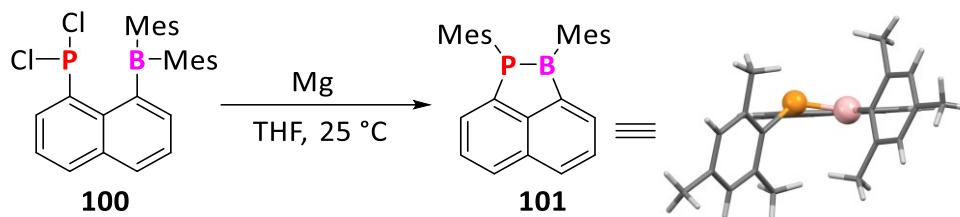
Scheme 52: Reduction of **100** with magnesium and 1,2 mesitylene shift formed the BP-acenaphthene **101**. X-Ray analysis revealed the out-of-plane orientation of phosphorus.[12]

The resulting BP-compound **101** showed a low field ^{11}B NMR resonance (δ = 77.9 ppm) and a ^{31}P NMR resonance at δ = -28.2 ppm, suggesting a tri-coordination sphere for both nuclei. This was further substantiated by X-ray analysis. The sum of the bond angles of boron (Σ = 359°) and phosphorus (Σ = 328°) and the C_{Mes}-B-P-C_{Mes} dihedral angle (φ = -52°) indicated a trigonal planar (boron) and a pyramidal-distorted (phosphorus) molecular geometry. The length of the central B-P bond was determined as 1.889(3) Å, which is longer compared to dimesitylphosphino dimesitylborane (1.839(8) Å),[13] diphenylphosphino dimesitylborane (1.859(3) Å)[14] and dimesitylphosphine di(hexafluorophenyl)borane (1.783(2) Å).[15] To investigate the effect of the BP unit on the optoelectronic properties, molecule **101** was subjected to electrochemical and photophysical measurements. It was found that the reduction of **101** (E_{red} = -2.22 V vs. Fc/Fc$^+$) occurred at a slightly higher potential than for the dimesityl(1-naphthyl)borane (E_{red} = -2.51 V vs. Fc/Fc$^+$) indicating that the LUMO is more stabilized upon substitution with the dimesitylphosphorus motif. It was claimed that this effect might be due to the higher rigidity of **101** and therefore a more intense π-π* conjugation of the vacant boron p-orbital with the carbon scaffold. The oxidation of this molecule occurred at E_{ox} = 0.65 V (vs. Fc/Fc$^+$). Therefore, the phosphorus atom does not appear to be a strong donor, based on the energetic level of its HOMO. Molecule **101** showed a weak absorption (λ_{max} = 452 nm, ε = 230 L mol^{-1} cm^{-1}) and a related low-intense but broad emission (λ_{ems} = 510-750 nm, Φ_{lum} = 0.032). As indicated by its solvent-dependency and proven by time-dependent density functional (TD-DFT) calculations, the origins of absorption and emission maxima were ICT processes, in which the energy is transferred from the phosphorus atom to the boron atom and *vice versa*.

Most recently, the embedding of a non-classical BP unit in a PAH was reported by Gilliard and coworkers:[16] After the reaction of a cyclic alkyl amino carbene (CAAC)-stabilized borafluorene **102** with sodium phosphaethynolate (NaOCP), followed by photolysis and 1,1-insertion of the phosphinidene, a BP-substituted phenanthryne **104** was obtained (Scheme 53).
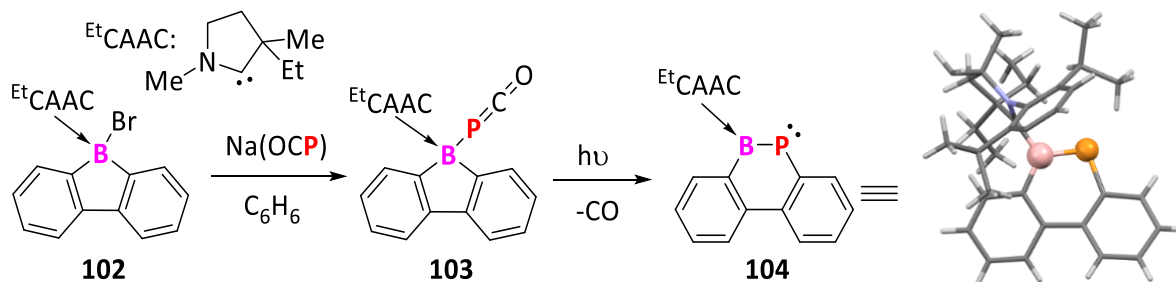
Scheme 53: Using boraphosphaketene **103** to generate BP-phenanthryne **104** starting from the CAAC-stabilized 9-bromo-borafluorene **102**.[16]

The analysis of the ^{11}B NMR (δ = 51.1 ppm) and ^{31}P NMR (δ = 142.7 ppm) chemical shifts revealed that the B-P bonding situation in this molecule is barely comparable to the hexa-aryl-substituted 1,2-phosphaborines *vide supra* (Scheme 30). This assumption was supported by X-ray diffraction experiments, which indicated a B-P bond length of 1.812(3) Å. Moreover, the sum of angles for boron was 359° and for the low-valent phosphorus 100°. The lone pair was calculated to be placed orthogonal to the B-P/C-P bonding plane. However, this molecule follows a very uncommon bonding situation as the CAAC stabilizes the boron moiety and the phosphorus atom is only bonded to two other atoms. Natural bond orbital (NBO) analysis showed that the Wiberg Bond Index (WBI)[17-19] for the B-P bond was 1.50 which represents a double bond character. For this BP-compound, a UV/Vis absorption spectrum with broad absorption (λ_{abs} = 425-650 nm, λ_{max} = 510 nm) was reported. It originated from the transition of an electron from the HOMO, located along with the B-P π-bond, to the LUMO, situated at the CAAC ligand. Nonetheless, this exotic example of a BP-substituted PAH represents the potential of a BP unit in common organic structures and its influence on the luminescence properties.[16]

4.2 BP-substituted Dibenzo[*g,p*]chrysene and Tetrathienonaphthalene

Compared to previously discussed BN units in PAHs, the uniqueness of BP units is based on the fact that they may show either pyramidal or trigonal planar configuration in PAHs. Due to the strongly favored pyramidalization of phosphorus atoms, any carbon scaffold including a BP unit might prefer a phosphinoborane or borylphosphine-like structure (see Fig. 38) depending on the stereoelectronic stabilization. This also affects the optoelectronic properties of the BP-substituted PAHs since a milder or stronger π-interaction of the BP unit with the carbon scaffold results. In direct comparison to BN units, it is further estimated that a planar BP unit holds a stronger double bond character, which should increase the rigidity of the carbon scaffold in BP-PAHs. This fact, combined with the more stabilized LUMO, the decreased aromaticity and the expected greater dipole moment in a BP-system should lead to beneficial absorption and emission properties, e.g. bathochromically shifted absorption, emission and higher quantum yields.

To examine the substitutional effects of a boron/phosphorus unit on polycyclic aromatic hydrocarbons, it was decided to investigate the BP-derivatives of dibenzo[*g,p*]chrysene (**BP-DBC**) and tetrathienonaphthalene (**BP-TTN**) (Fig. 90).

BP-DBC   **BP-TTN**
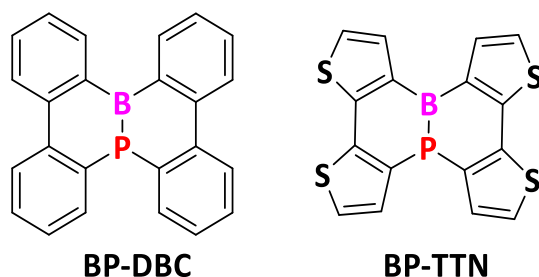
Fig. 90: BP-substituted dibenzo[g,p]chrysene (**BP-DBC**) and tetrathienonaphthalene (BP-**TTN**).

From a synthetic point of view, hetero-substituted **DBC** and **TTN** systems are readily accessible by tandem annulation reactions. For instance, **BN-DBC** and **BN-TTN** were synthesized by this method. For the BN-substituted congeners, several examples were published and it was demonstrated that these structures are suitable for applications in OFETs.[20-23] In addition, the all-carbon **DBC** derivatives were already successfully implemented in OLED devices.[24, 25] Further studies showed that due to their nearly flat molecular geometries, and since no orthogonal substituents hinder any intermolecular interaction, these systems tend to self-assemble into supramolecular structures. Especially close π-stacking behavior and resulting beneficial intermolecular charge transfer in supramolecular stacks gave rise to superior hole mobility in organic devices.[20]

Comparing the photophysical properties of **CC**-, **BN**- and **BP-DBC/TTN** derivatives could easily reveal the advantages and disadvantages of substitution with a boron/phosphorus unit. Due to the expected decreased aromaticity, stabilized LUMO and larger dipole moment in BP-compounds than in BN-systems, a further bathochromic shift and higher extinction coefficient for BP-substituted dibenzo[*g,p*]chrysene (**BP-DBC**) and tetrathienonapthalene derivatives (**BP-TTN**), compared to the CC and BN congeners is expected (Fig. 91).
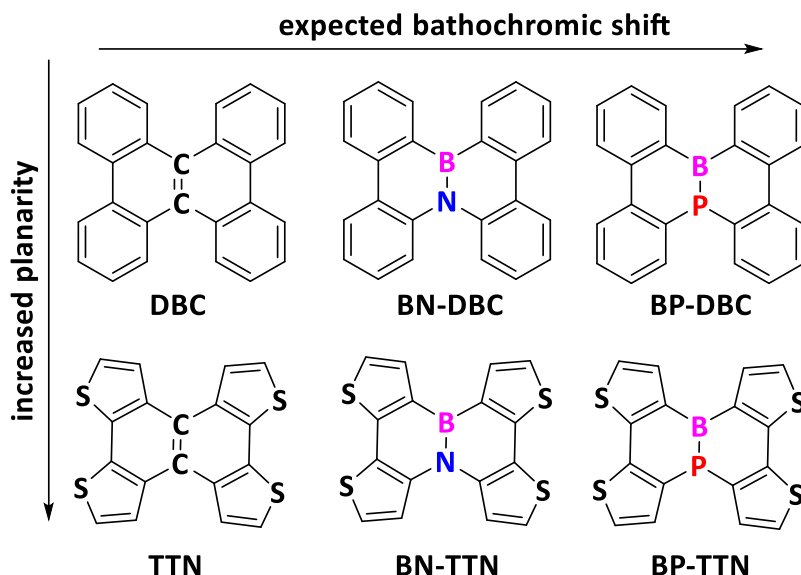
Fig. 91: Model structures bearing a C=C/B-N/B-P unit which are under investigation.

As it was found that aryl-substituted aminoborane derivatives are exclusively planar whereas phosphinoboranes are found in both planar and pyramidal geometries (see the preface for this chapter), this needs to be taken into account for designing such molecules. It is estimated that the **BP-TTN** derivative should exhibit a more planar backbone since the **BP-DBC** is likely to be slightly twisted due to the intrinsic repulsion of the biphenyls *ortho*-protons. This could lead to sterically-driven decreased BP-interaction in **BP-DBC** but exposes the lone pair for possible supramolecular BP-interaction or further post-functionalization, e.g. oxidation, sulfurization, methylsulfurization or complexation with transition metals.[26] Also, the planarization of the BP unit by adapting the scaffold, e.g. electronic or steric stabilization, could lead to an increased π-π* conjugation of the phosphorus lone pair into the vacant boron p-orbital and therefore a lower HOMO-LUMO gap. As planar PAH structures are well-known for aggregation-caused quenching (ACQ) in the solid-state, see also the **BNCDI**s (see chapter 3.5), a less rigid **BP-DBC** derivative might be more luminescent in the solid-state or electroluminescent devices. The more planar **BP-TTN** could be useful for OFET devices, where close intermolecular π-π-interactions are beneficial.

4.3 Theoretical Calculations

4.3.1 Geometry

To determine the effect of the hetero-substitution, the properties of these structures were calculated using quantum chemical density functional theory (DFT) methods with B3LYP[27-30] and 6-31G* basis set and empirical dispersion correction (GD3[31]). This level of the theory has provided satisfactory results for BP-systems.[32] A comparison of the calculated geometries including CC- and BN/BP-substituted motifs clearly stated the influence of the heteroatoms *vide infra* (Fig. 92).

DBC	BN-DBC	BP-DBC
TTN	BN-TTN	BP-TTN
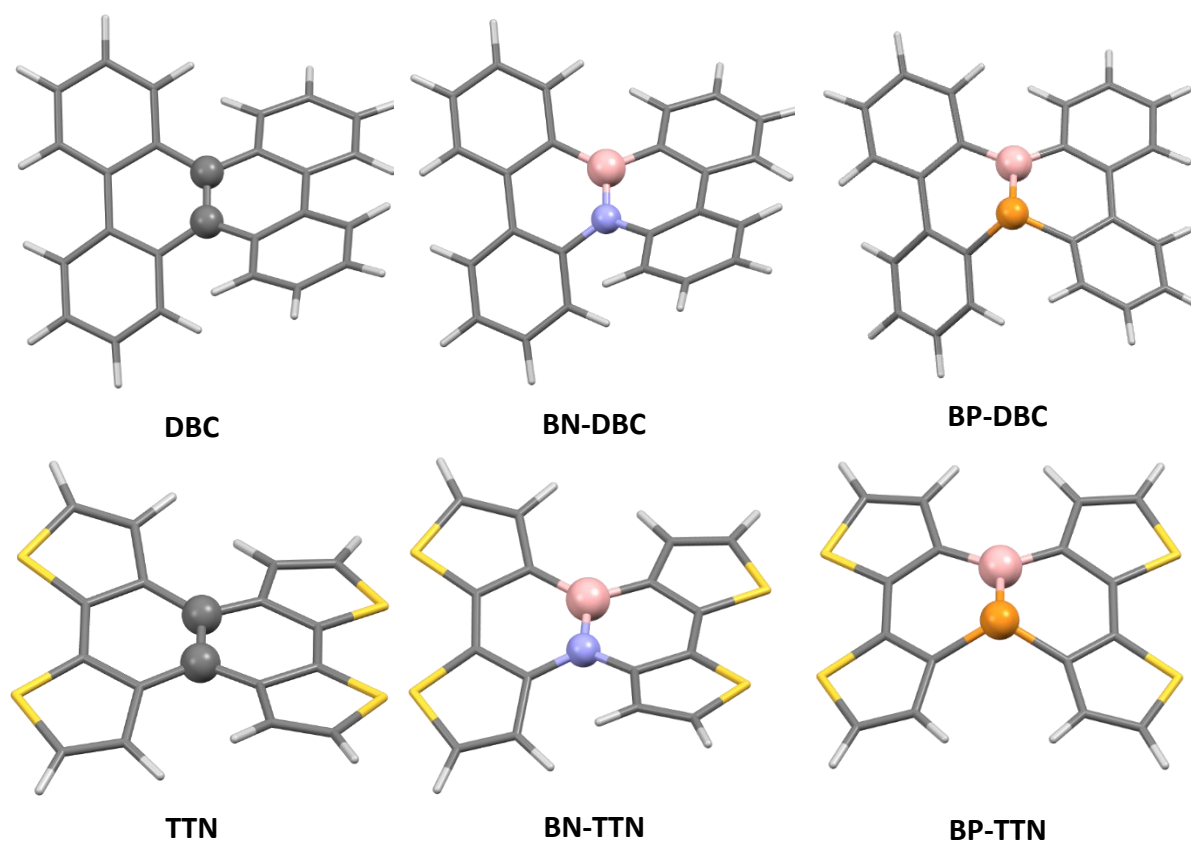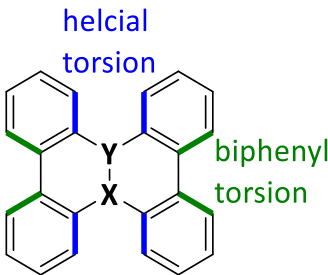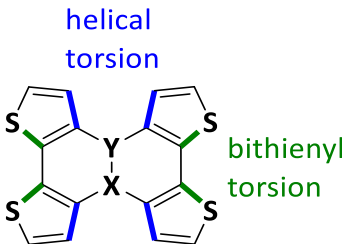
Fig. 92: Visualization of optimized geometries of all calculated molecules.

Firstly, it was found that all **DBC** or **TTN** structures have an internally twisted geometry due to proton-proton repulsion of the *ortho*-protons (Tab. 12). This is effect opposes the energetic stabilization due to planarization and π-conjugation. Due to this twisting, the unsubstituted **DBC** and **TTN** can be related to two phenanthrene-like systems that are fused. The resulting helicity of the *bay*-positioned four rings is best described by the dihedral angle of the *bay*-positioned opposing C=C bonds and is discussed below (Tab. 12).

The all-carbon **DCB** and **TTN** scaffold underwent minor changes upon substitution of the central naphthalene unit with an isoelectronic boron/nitrogen unit as in **BN-DBC** and **BN-TTN**. Geometries of BN-substituted molecules **BN-DBC/BN-TTN** insignificantly differ from their CC-analogs concerning all given structural parameters (Tab. 12). The bond length of the central BN unit was calculated with DFT methods to be 1.45 Å for **BN-DBC** and 1.48 Å in **BN-TTN** and was in good agreement with the reported crystal structures (1.426(2) Å for **BN-DBC**[20], 1.482(3) Å for **BN-TTN** [23]). In general, the B-N bond length in **BN-TTC** and **BN-DBC** was marginally longer than estimated by X-ray diffraction for common 1,2-azaborines structures (1.434(3) Å[33] and 1.4481(18) Å[34]). Therefore, both **DBC/TTN** scaffolds are expected to decrease the boron nitrogen/phosphorus interaction.

Tab. 12: Geometric parameters determined by DFT-calculations (B3LYP/6-31G* level of theory) and by single-crystal structures.

	DBC	BN-DBC	BP-DBC	TTN	BN-TTN	BP-TTN
bond	C=C	B-N	B-P	C=C	B-N	B-P
bond length	1.40 Å (1.38 Å)	1.45 Å (1.43 Å)	1.87 Å	1.43 Å (1.44 Å)	1.48 Å (1.48 Å) [b]	1.87 Å
Σ X	360.00° (360.00°)	360.00° (360.00°)	309.88°	360.00° (360.00°/ 360.00°)	360.00° (360.00°)[b]	332.63°
Σ Y			359.87°			359.99°
∠CXC	123.34° (123.38°, 122.32°)	121.87° (120.97°)	109.34°	122.47° (121.69°)	120.71° (120.60°)[b]	117.61°
∠CYC		128.57° (127.17°)	129.79°		127.11° (125.64)[b]	131.41°
φ biaryl	16.00° (-15.82°/-18.00°)	18.93 (-16.24°/-21.88°)	-13.64°/ 30.14°	-20.93°/ -20.91° (-9.23° / 5.50°)[a]	-14.70°/ -31.05°(-3.25° /-24.50°)[b]	3.81°[d]
φ helical	37.69° (40.60° / 43.10°)	-50.82°/ -38.71° (48.42° /35.73°)	-27.68°/ -33.61°	-17.16° (9.23°/ 5.50°)[a]	-17.70°/-1.05° (-3.25°/ -24.72)[b]	0.00°[d]

[a] The system showed C_2 symmetry, but two structures were included in the unit cell therefore both values are displayed here. [b] The structure had methyl groups on the 2-position of the thiophene [d] The phosphorus boron unit was out of the plane while the **TTN** moiety remained planar.

Upon substituting the boron of **BN-DBC** or **BN-TTN** by a more spatially demanding phosphorus atom, significant changes of the geometries were observed, which was due to the pyramidalization effect of the phosphorus atom. The **BP-DBC** structure revealed a more tilted orientation of both biphenyl planes and a less twisted BP-phenanthrene scaffold while the biphenyl groups (biphenyl torsion 13.64°/ 30.14°) were more distorted. The sum of angles at the phosphorus atom (Σ_P = 309.88°) indicated its pyramidalization and therefore less interaction of the phosphorus with the neighboring boron or carbon atoms was to be expected. Following the definition of Bailey and Pringle[35] this B-P bonding situation would be more defined as borylphosphine (Fig. 38) due to the low sum of angles and long B-P bond (1.87 Å). The bond length of the BP unit was in good accordance with the substituted 1,2-phosphaborine[32] (see the preface) and **101**[12] (see chapter 3.1) but being a little longer than classical a BP double bond (1.859 Å[14], 1.783(2) Å[15]).

Surprisingly, the **BP-TTN** exhibited an almost planar carbon scaffold (helical torsion 0.00°, biaryl torsion 3.81°) whilst the BP unit was oriented out-of-plane (Fig. 92). Also, here, the phosphorus atom possessed a sum of angles (Σ_P = 332.63°) which was smaller than expected for a planar phosphorus atom. By the definition of Bailey and Pringle[35] this BP-derivative would be classified more as
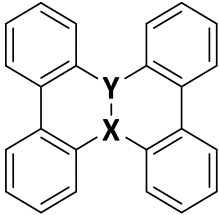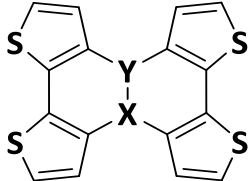
phosphinoborane since the sum of angles at the phosphorus exceeds 330°. The same applies to the B-P bond which length (1.87 Å) is in accordance with a phosphinoborane B-P bond length (<1.87 Å). Hence, it appeared that the **BP-TTN** is slightly closer to a fully planar BP unit than calculated for **BP-DBC** scaffold due to the larger sum of angles but on the other hand the BP unit is located out-of-plane and the effect of the BP unit to the π-system might be reduced by this.

As expected, the bond length of the central unit elongated, following the trend C=C (1.40 Å **DBC**, 1.43 Å **TTN**)< B-N (1.45 Å **BN-DBC**, 1.48 Å **BN-TTN**) < B-P (1.87 Å **BP-DBC**, 1.87 Å **BP-TTN**). As a result, the hetero-substituted PAHs exhibited smaller geometrical changes in the case of BN-substitution and more drastic changes in case of BP-substitution. This is well represented in **BP-TTN** since the BP unit is oriented out-of-plane. Crystal structures for **DBC**[20], **BN-DBC**,[20] **TTN**[36] and **BN-TTN**[23] were reported and are compared with the performed quantum chemical calculations (Tab. 12). In all cases, the H-H-repulsion of the protons had a slightly overestimated contribution to the geometry than expected since the calculated torsion angles are slightly increased compared to the experimentally determined values. This should only marginally interfere with the interpretation of the following theoretical studies.

4.3.2 Frontier Orbitals and Absorption Behavior

Since the substitution with BN- or BP units led to changes in the geometry, a direct influence on the optoelectronic properties was expected. The LUMO and HOMO levels and the absorption properties were calculated by DFT and TD-DFT methods. As for some structures experimental values were reported, the calculated results could be compared and were found in good agreement (Tab. 13).

Tab. 13: Results of the DFT-calculations using B3LYP-6/31-G* with empirical dispersion correction. Absorption properties were determined *via* TD-DFT using B3LYP-6/31-G* with TD = 40 states.

compound	DBC	BN-DBC	BP-DBC	TTN	BN-TTN	BP-TTN
bond type	C=C	B-N	B-P	C=C	B-N	B-P
dipole (μ)	0.00 D	0.37 D	1.59 D	0.00 D	1.18 D	0.89 D
E_{LUMO}	-1.44 eV	-1.24 eV	-1.92 eV	-1.42 eV	-1.37 eV (-2.01 eV)[c]	-1.83 eV
E_{HOMO}	-5.30 eV	-5.50 eV	-5.50 eV	-5.43 eV	-5.47 eV (-5.32 eV)[c]	-5.51 eV
$\Delta E_{HOMO/LUMO}$	3.86 eV	4.26 eV	3.58 eV	4.01 eV	4.10 eV (3.31 eV)[c]	3.68 eV
λ_{max}	355 nm (351 nm)[a]	334 nm (340 nm)[a]	418 nm	347 nm (364 nm)	350 nm (324 nm)[c]	392 nm
E_{gap}[d]	3.49 eV (3.53 eV)[a]	3.71 eV (3.65 eV)[a]	2.97 eV	3.58 eV (3.41 eV)	3.54 eV (3.31 eV)[c]	3.16 eV

[a] These data were reported and the optical gap was derived from the literature.[22] [b] These data were reported and the optical gap was derived from the literature.[36] [c]These data were only available for the methyl-substituted **BN-TTN**.[23] [d] The calculated optical gap are based on the lowest energy transition.

Upon substitution of the all-carbon scaffold with an isoelectronic and isostructural BN unit, the LUMO and HOMO levels were directly affected. Contrary to the comparison of benzene and 1,2-azaborine (Fig. 40), the HOMO and LUMO levels in **BN-DBC/TTN** were found to be stabilized (HOMO) or

energetically increased (LUMO). Therefore, the HOMO-LUMO gap was actually larger than in their CC-congeners **DBC/TTN**. This effect was confirmed by experiments and was assigned to the deficient BN double bond character[22] and inefficient p-orbital overlap due to the geometrical distortion (*vide supra*). An inevitable shift of the calculated values compared to experimental values was found in the example of **BN-TTN**: The calculated LUMO level was in fact more destabilized (E_{LUMO} = -1.37 eV) as determined by cyclic voltammetry (E_{LUMO} = -2.01 eV). However, the reported hypsochromic shift of the absorption of all-carbon **DBC/TTN** compared to their BN-congeners was well represented in the calculations *vide supra*. A yet neglected advantage of the BN-substitution is the electronic stabilization of triplet states as in **BN-DBC** that resulted in beneficial performance in OLED devices.[22] This should be considered in this subject as well, but could not be calculated due to the complexity of such calculations.

Upon substitution with a BP unit, the LUMO in **BP-DBC/BP-TTN** was found to be significantly more stabilized and therefore the resulting energy gap had reduced values too. A strong bathochromic shift in the absorption spectra for **BP-DBC** (λ_{max} = 418 nm) and **BP-TTN** (λ_{max} = 392 nm) followed this trend. The transitions were found to occur between the BP π-bond and the vacant π^*-orbital of the boron.

As it was seen for 1,2-azaborines, the dipole moment also holds a major role in the absorption properties of hetero-substituted molecules. Whereas the dipole moment in all carbon **DBC** and **CC-TTN** is clearly absent, the **BN-DBC** (μ = 0.37 D), **BN-TTN** (μ = 1.14 D), **BP-DBC** (μ = 1.59 D) and **BP-TTN** (μ = 0.89 D) have varying dipole moments depending their electronic environment. Although it was expected that the BP-congeners in general have a higher dipole moment, (see the example of diphenylphoshino diphenylborane) it appeared that the dipole moment of the **BP-TTN** was lower compared to the **BN-TTN**. An explanation would be the total planarity of the thienyl-rings in **BP-TTN** whereas the **BN-TTN** is more twisted and therefore displays less symmetry and thus a higher dipole moment.

To understand the effect of a heteroelement substitution on the **DBC** or **TTN** motif, the frontier orbitals (HOMO/LUMO) are displayed and discussed below. (Fig. 93).
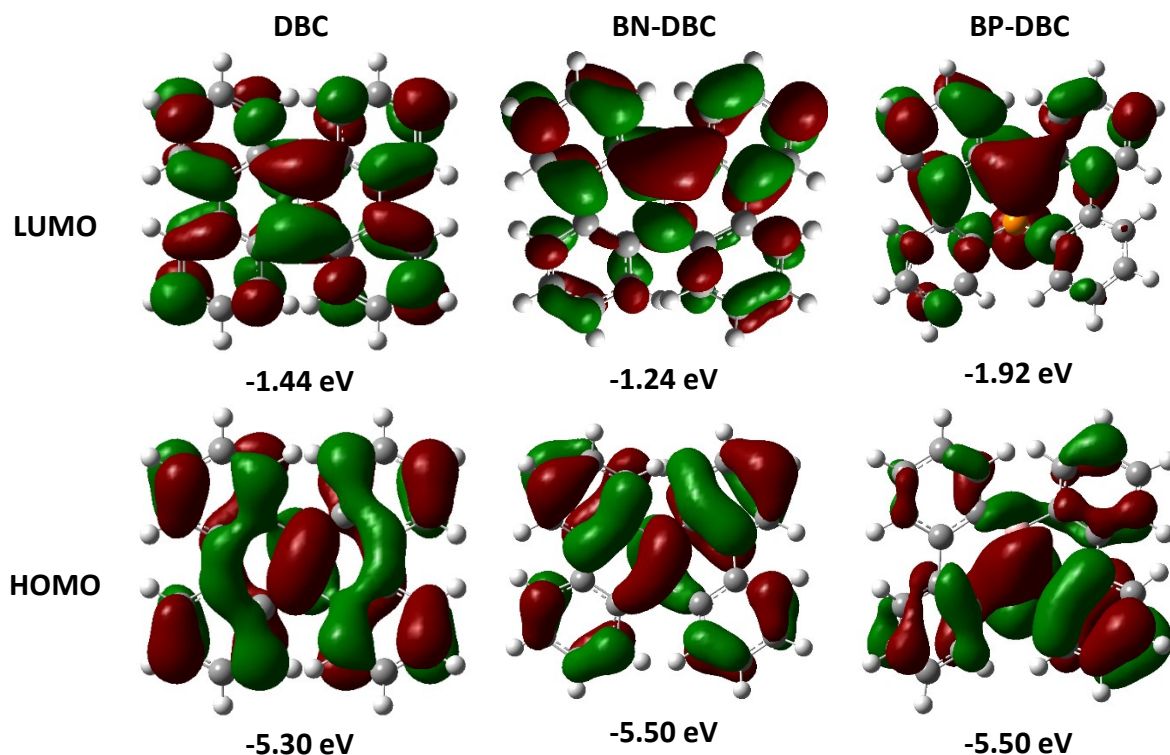

Fig. 93: Display of the HOMOs and LUMOs of **CC/BN/BP-DBC**s at an isovalue of 0.02.

Depending on the planarity of all **DBC** congeners, the HOMOs and LUMOs were more widely (**BN-DBC**), or less widely (**BP-DBC**) extended over the molecule. In **DBC**, the HOMO and LUMO were oriented in an orthogonal fashion, which is unfavorable for a photoinduced transition from the HOMO into the LUMO and *vice versa*.[37] While the HOMO in **BN-DBC** was more present in the periphery of the boron atom, the LUMO was more located on the B-N bond.[20] The extension of the HOMO/LUMO was the lowest in BP-substituted **BP-DBC** due to the tiled orientation of both biphenyl planes. While the LUMO was more located at the boron atom, the HOMO was situated at the phosphorus atom. This strong localization of the frontier orbitals might result in interesting optical properties as charge-transfer processes.

The frontier orbitals which were obtained for the more planar bithienyl **TTN** derivatives followed the same trends observed for the **DBC** derivatives (Fig. 94).
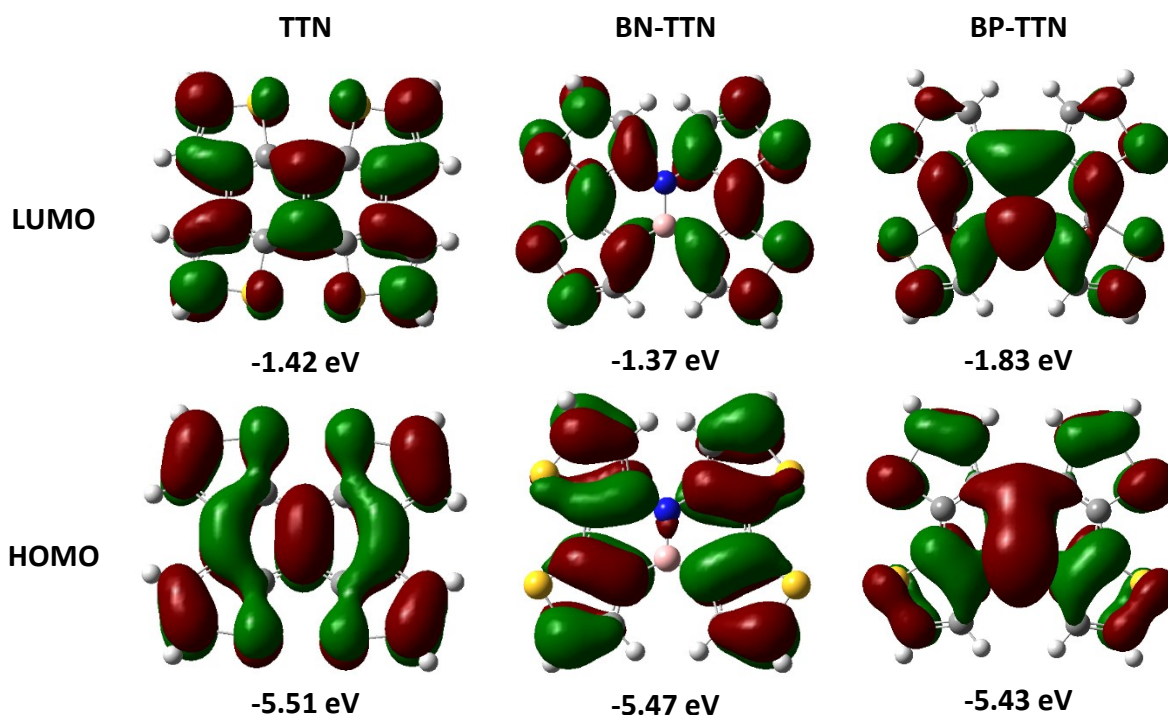
Fig. 94: Display of the HOMOs and LUMOs of all **TTN** derivatives at an isovalue of 0.02.

For the planar **TTN**, the molecular frontier orbitals had an orthogonal relation which is unfavorable for the transition of one electron from the HOMO to the LUMO. Such an orientation could result in inferior optical properties, e.g. the low reported luminescence quantum yield for TTN ($\Phi_{lum} < 0.01$).[36] In comparison to the **DBC** systems, the higher planarity of the BN/BP-congeners led to the full delocalization of the HOMOs and LUMOs. This might indicate superior absorption and luminescence properties due to small spatial changes of the ground and excited state upon photoexcitation. It appeared that the BN unit in **BN-TTN** is the center of a node in both frontier orbitals impugning the effect of the B-N bond on the frontier orbitals. Furthermore, the HOMO of **BP-TTN** is located along with the B-P bond. It has a high contribution from the phosphorus lone pair, and in the LUMO the vacant boron p-orbital describes the central point of the LUMO.

4.3.3 Aromaticity

Since the incorporation of main group elements in π-systems has direct effects on the aromaticity, the respective nucleus-independent chemical shifts (NICS),[38-40] an approximation for aromaticity, were calculated for all model structures. For instance, are 6 π-electrons shared in 1,2-azaborine but due to the highly polar B-N bond, the aromaticity is strongly decreased.[41] Furthermore, a correlation between aromaticity and the HOMO-LUMO gap was found, which indicated that a decreased aromaticity was associated with a smaller HOMO-LUMO gap.[42] Negative NICS values imply a diatropic ring current (aromaticity), while positive values indicate a paramagnetic ring current (antiaromaticity). For NICS(0) and NICS(1) shielding, calculated in the center of the ring (NICS(0)) and 1 Å perpendicular to the center of the ring (NICS(1). The NICS(0) values correspond mostly to the σ-π contribution to aromaticity and NICS(1) corresponds to the π-π contribution to aromaticity of the respective system.[40] To compare NICS(0) and NICS(1) values for the effect of BP-substitution all model structures were subjected to these calculations (Fig. 95).
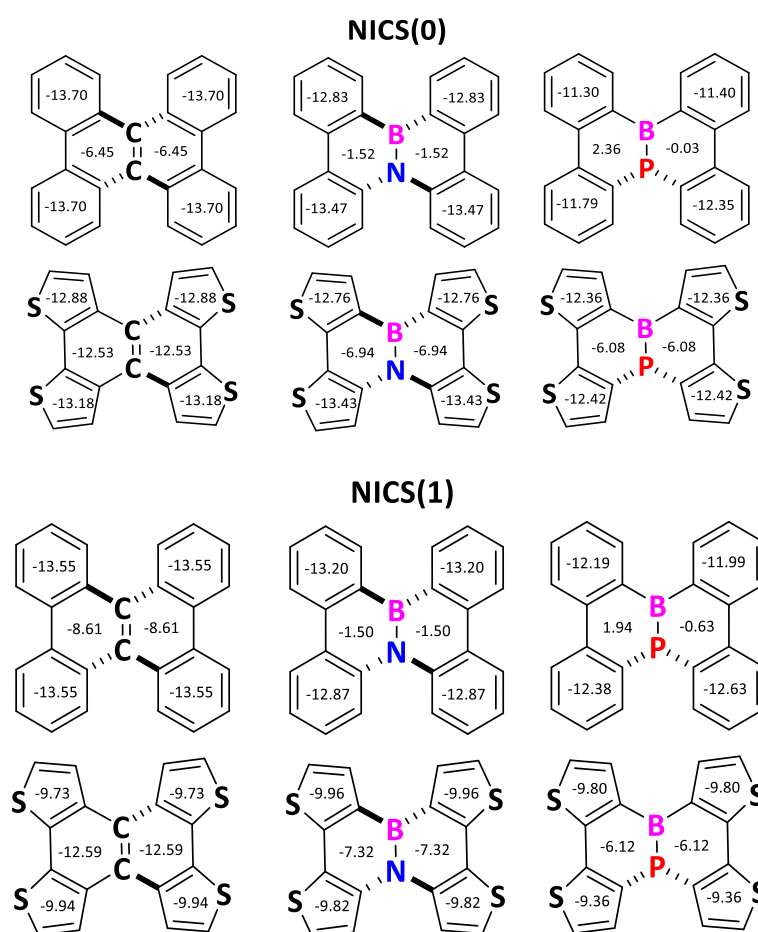
Fig. 95: NICS(0)/NICS(1) values for structures bearing a CC/BN/BP unit calculated with B3LYP-6-31G*. The orientations of the molecules are indicated by the respective bond highlighting. For simplification and due to the geometry of most compounds the NICS(1) was determined from the average both NICS(1) values above and beneath the ring.

The aromaticity of the central rings of **BN-DBC** and **BP-DBC** decreased as the NICS values were more positive compared to all-carbon **DBC**. In BN-structures, the aromaticity was decreased due to the large electronegativity difference between boron and nitrogen. Thus, fewer π-electrons are delocalized to the carbon moiety.[10] The lower aromaticity in BP-substituted structures was largely unaffected by polarization effects since the out-of-plane orientation of the phosphorus atom and the decreased overlap of the p-orbitals resulted in lower aromaticity. The differences between NICS(0) and NICS(1)

values were in these examples marginally and indicated that the aromaticity is uniformly based on both σ-π and π-π interaction. In general, the **TTN** derivatives exhibited more negative NICS(0)/NICS(1) values since the electron-rich condensed thienyl rings add more electron density compared to the biphenyl derivatives. However, the NICS(0) values for the BN- and BP-naphthalene motifs **BN/BP-TTN** were found in the more negative region due to the increased planarity, more efficient π-conjugation and strong aromatic character of the resulting system. There was no observed significance between the results of NICS(0) and NICS(1) values in the BN- and BP-substituted **TTN**s, which indicates that equal σ-π and π-π-interaction contribute to the aromaticity.

4.3.4 Electronic Structure and Bonding Situation

Due to the fact that the calculated bond distances of the BP-substituted derivatives indicated a weaker double bond situation, the σ- and π-interactions and electronic structure of the BP-containing structures were investigated by natural bond orbital (NBO) analysis.[43] This analysis focuses on the bonding situation between two heteroelements and gives insights into the nature of the bonding type. Based on the application of this method, an element-element bond might be classified as single or multiple covalent or dative bond. However, the method is merely the first estimation and more parameters such as bond length and bond environment must be considered as well.

The main NBOs of **BP-TTN** and **BP-DBC** and their electron distribution are displayed below (Fig. 96).
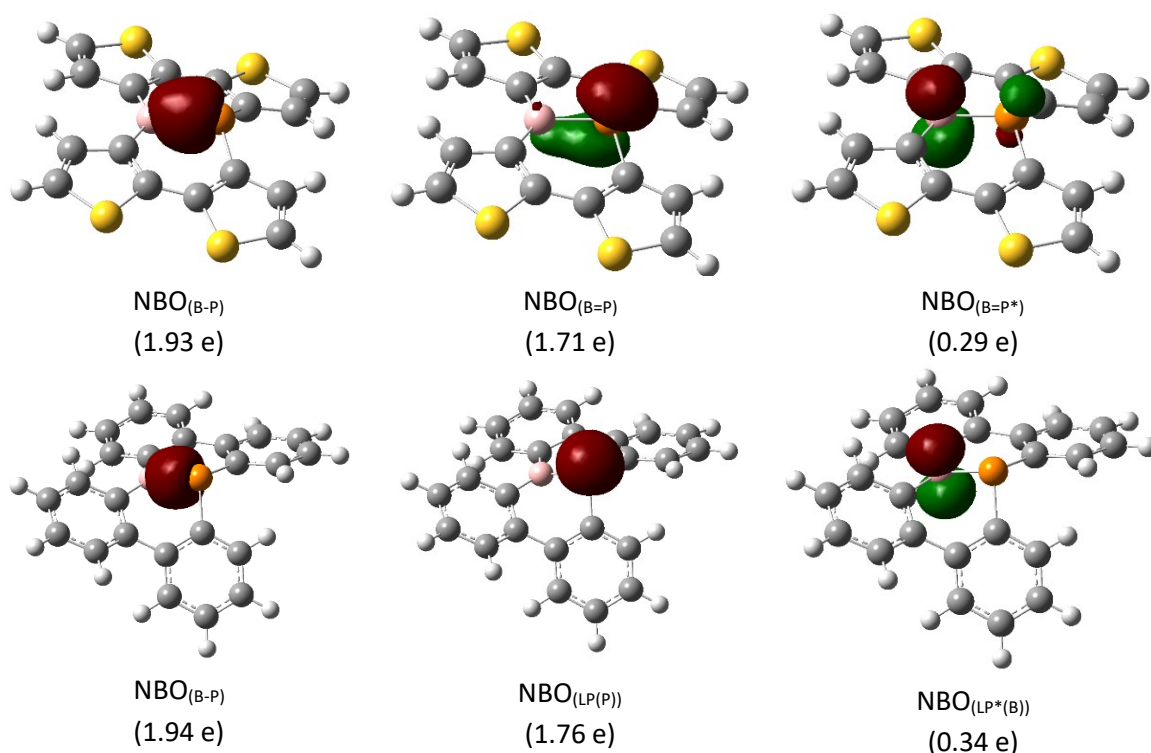

NBO$_{(B-P)}$
(1.93 e)

NBO$_{(B=P)}$
(1.71 e)

NBO$_{(B=P*)}$
(0.29 e)

NBO$_{(B-P)}$
(1.94 e)

NBO$_{(LP(P))}$
(1.76 e)

NBO$_{(LP*(B))}$
(0.34 e)

Fig. 96: Display of selected NBOs of **BP-TTN** (top) and **BP-DBC** (bottom) at an isovalue of 0.08. The occupation of the NBOs is given in electrons (e).

For the **BP-TTN**, the NBO analysis indicated two NBOs along with the B-P bond. One of them represented a σ-bond, and the other one the lone pair contribution of the phosphorus into the boron vacant orbital giving a BP-double bond. The σ-bond electrons were equally shared and the NBO originates from the phosphorus $s^{0.35}p^{0.62}$ and the boron $s^{0.27}p^{0.73}$ orbitals. The BP-double bond electrons were mainly contributed from the phosphorus (83%) p-orbital and less from the boron (17%). A significant amount of bond electrons (0.29 electrons) was found in the π*-antibonding NBO of the BP-

double bond as well and indicates a small contribution from π-back bonding. The shape of the π-bond was in perfect agreement with what Power[13] predicted for the bond in phosphinoboranes.

NBO analysis furthermore disclosed that in **BP-DBC**, the BP unit exhibited a single bond and an internal BP Lewis pair. This is in contrast to the calculated bond lengths which were in agreement with common B=P bond situations. The BP's σ-bond electrons were equally shared between boron and phosphorus using similar orbital geometry (P = $s^{0.23}p^{0.76}$, B = $s^{0.30}p^{0.70}$). Furthermore, a lone pair at the phosphorus atom formed a Lewis pair (1.76 electrons) with antibonding π^*-orbital (0.35 electrons) located at the boron atom. The stabilization of this interaction was calculated by second-order perturbation theory to be 13.6 kcal/mol. Therefore, this phosphorus atom could be accessible for late-stage functionalization as oxidation, sulfurization or methylsulfurization as described in the example of dibenzo-1,4-phosphaborine[8] (Scheme 50).

Moreover, the Wiberg Bond Indices (WBI)[17-19] and the NBO charges were calculated and combined to estimate a description of the bonding situations in the BP-substituted PAHs (Fig. 97).

WBI and NBO charge analysis

BP-TTN   **BP-DBC**
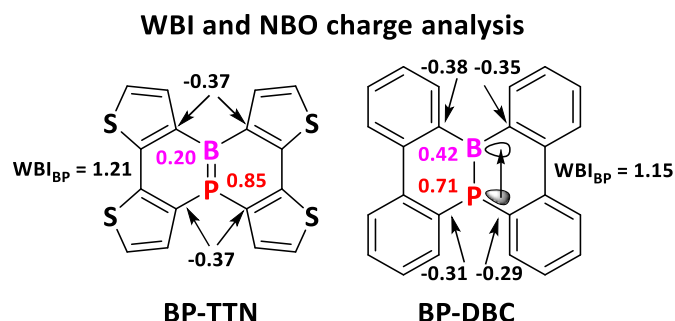
Fig. 97: Calculated NBO charges and Wiberg bond indices with DFT methods. The use of formal charges in this case is neglected to maintain the expression of NBO charges.

The WBI for the BP-structures was found to be 1.21 for **BP-TTN** and 1.15 for **BP-DBC**, which revealed that in both cases a slight double bond character was found. As expected, the charges of the BP units were inverted to a classical BN unit: The boron atom exhibited a less positive charge (0.20/0.42) and the phosphorus was charged positively (0.85/0.71) as well. This was in accordance with the observation made by Coates and Livingstone (see Fig. 36/37).[44]

To conclude, as it was predicted by the geometry optimization, the **BP-TTN** motif supports the formation of a phosphino borane bonding situation whereas the **BP-DBC** is best represented by the borylphosphino situation as NBO analysis indicated. Overall, the bond indices of both BP units were relatively low due to resonance stabilization by the carbon scaffold. This was in agreement with experimental observation for the long B-N bond lengths in **BN-DBC** and **BN-TTN** *vide supra*. In case of **BP-DBC** the BP-interactions were based on the σ-bond and unilateral donation of the phosphines lone pair towards the borane. The stabilization energy for the Lewis adduct was found to be 13.6 kcal/mol, therefore this structure should be readily accessible for late-stage oxidation.

4.4 Synthetic Strategy

Synthetic strategies to form intramolecular aryl-substituted phosphinoborane units in carbon scaffold are rare and the implementation of BP units into large PAHs has not been reported. Therefore, synthetic concepts for embedding a BP unit into a cyclic π-system are a milestone to access BP-substituted PAHs. This would be a vital step to investigate the optoelectronic properties of BP-PAHs in detail and further to allow analyzing the comparability of BN vs. BP-compounds.

Since the most common method of embedding BN units in PAHs is represented by the formation of the BN unit by electrophilic borylation of a *bay*-positioned amine, it needs to be investigated whether this concept can be transferred to forming BP-substituted PAHs. In fact, BN-substituted dibenzochrysene (**BN-DBC**, Scheme 32)[20] and BN-substituted tetrathienylnapthalene (**BN-TTN**, Scheme 33)[45] derivatives were prepared using intramolecular dual ring annulation reactions. The BP-congeners **BP-DBC** and **BP-TTN** might be accessible by similar methods (Scheme 54).
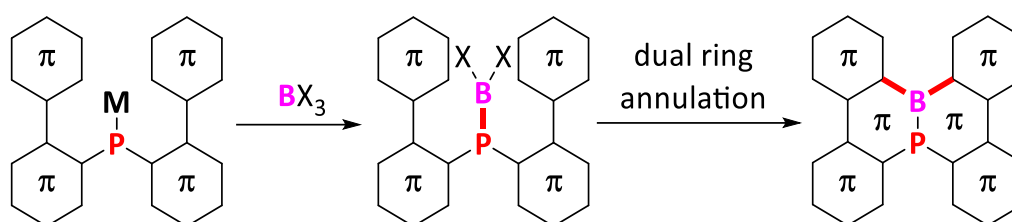
Scheme 54: Conceptual synthesis towards BP-annulated π-systems *via* borylation of *bis*(biaryl)phosphide and followed by tandem ring annulation reactions. The newly formed bonds are highlighted in red. The aryl substituents might be phenyl or thienyl derivatives.

The intermediary diarylphosphino dihaloborane might be accessible by the reaction of a diarylphosphide with a boron species equipped with three leaving groups. In contrast to the synthesis of the BN-congeners, in which diarylamines are commonly used, the reaction of a diarylphosphine with an electrophilic boron species would presumeably result in the formation of the Lewis adduct. Since the P-H bond is less polarized than the N-H bond, a loss of a HX species is less likely. Consequently, the more nucleophilic metal diarylphosphide species are likely to be required to form the diarylphosphino dihaloborane directly. Such a methodology was reported already in the synthesis of some BN-PAHs, e.g. **BN-DBC**[20, 21] and **BN-TTN**,[46] in which deprotonation of the diarylamine with an organolithium base was required prior to the reaction with the boron electrophile. The final cyclization should include a tandem bora-Friedel-Crafts reaction.[47, 48] This reaction already proved to be a versatile tool for the synthesis of BN-substituted PAHs. Furthermore, it has been shown that for electron-rich arenes, the reaction occurred even without any catalyst,[45] whereas the use of phenyl-substituents required the aid of a nitrogen-base, e.g. TEA, and a Lewis acid, e.g. aluminum trichloride.[20]

As a conceivable alternative, the ring annulation could be performed using an electrophilic phosphorus species. A protocol for the tandem phospha-Friedel−Crafts reaction of a dichloro(*m*-teraryl)phosphine to the corresponding phosphorus PAH species was reported.[49] However, as boron-carbon bonds are less stable than carbon-phosphorus bonds,[50] it needs to be considered that during the electrophilic phosphorylation might cleave boron-carbon bonds as a side reaction.

To access the diarylphosphide, it is assumed that the reaction of protected dichlorophosphine with two equivalents of an *ortho*-metallated biaryl followed by subsequent deprotection and reduction can be conducted (Scheme 55).
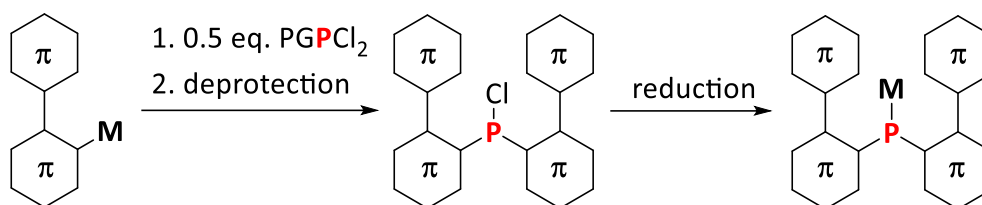

Scheme 55: Synthetic concept to access *bis*(biaryl)phosphides.

To prevent triple substitution on the phosphorus atom, a protection group strategy was envisaged, in which one site on P was blocked by an appropriate group. This concept to generate the phosphide has been previously reported for the *bis*(biphenyl)phosphide derivative.[51] An alternative route would be to form the triarylphosphine followed by selective cleavage of an aryl group with an alkali metal to give the diarylphosphide.[52, 53] However, this alternative process is considered unfavorable as it includes the loss of one-third of the aryl species during the reduction.

In general, the suggested synthetic route should be applicable for both biphenyl and bithienyl moieties giving **BP-DBC** and **BP-TTN** in similar ways. Due to the electron-rich properties of the thienyl scaffold, it is expected that the ring annulation should be more facile than for the phenyl derivatives. As most recently the combination of thienyl and phenyl groups was reported also for the BN-substituted dibenzodithienoacenapthylene (**BN-DBDTA**, Scheme 34),[54] such a BP-system could be also accessible.

4.5 Synthesis Towards BP-Substituted Dibenzochrysene (BP-DBC)

To investigate the general synthesis of BP-substituted PAHs *via* ring-annulation reaction, the synthesis of the BP-substituted dibenzochrysene **BP-DBC** will be detailed in the following. In contrary to its thienyl-analog **BP-TTN**, the biphenyl substituents at the phosphorus atom should be more resistant towards metalation and electrophilic aromatic substitution. The synthesis of the **BP-DBC** should be based on the reaction of an *ortho*-metaled biphenyl with a protected phosphorus species, followed by a reduction and a reaction with an electrophilic boron species (Scheme 56).
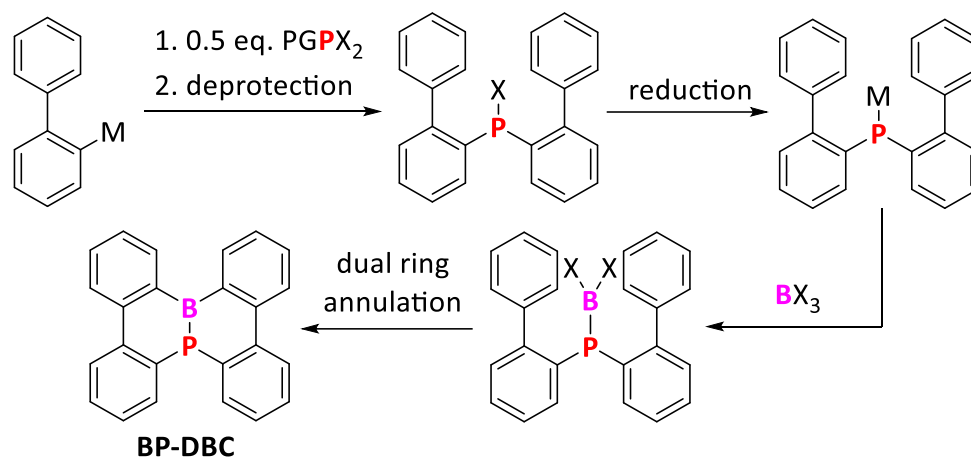
Scheme 56: Proposed reaction procedure to access **BP-DBC**.

4.5.1 Synthesis of the Phosphorus Precursor

To selectively form the diarylphosphine species, an amino-protected dichlorophosphine **106** was synthesized by the reaction of phosphorus trichloride (**105**) and two equivalents of di*iso*propylamine according to a literature protocol (Scheme 57).[55]
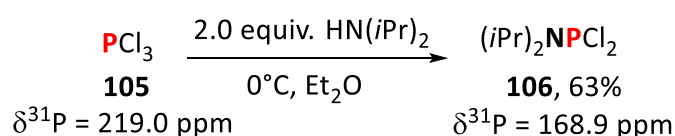
Scheme 57: Reaction of phosphorus trichloride (**105**) with two equivalents of di*iso*propylamine to access the protected the (di*iso*propylamino)(dichloro)phosphine (**106**).

The reaction was reproduced on a multigram scale and after filtration of the ammonium salts, the pure product could be obtained by short path inert distillation in good yield (63%). The ^{31}P NMR chemical shift (δ = 168.9 ppm) of **106** was in accordance with reported values.[55]

4.5.2   Syntheses towards **BP-DBC**

The synthesis towards a metaled *bis*(biphenyl)phosphide **107** was already reported as a consecutive reaction.[51] The procedure included a bromide-lithium exchange of 2-bromobiphenyl (**108**) with two equivalents *t*BuLi, followed by the reaction with half an equivalent diethylphosphoramidous dichloride to form the protected diarylphosphine **109**. Subsequently, **109** was deprotected with hydrogen chloride to form the diarylchlorophosphine followed by reduction with lithium wire to give **107** (Scheme 58).[51]
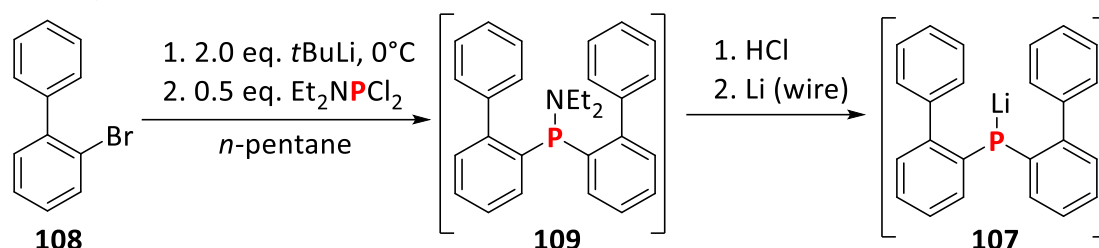
Scheme 58: The synthetic procedure towards lithium diarylphosphide **107** according to Le Drian and coworkers.[51]

Since the total synthesis towards **107** was performed *in situ*, the complete reaction procedure was investigated in detail. Starting with the initial bromide/metal exchange reaction and quenching with the di(*iso*propyl)phosphoramidous dichloride (**106**) should obtain molecule **110** (Tab. 14).

Tab. 14: Optimization of the reaction towards **110** using different metalation species, solvents and temperatures.
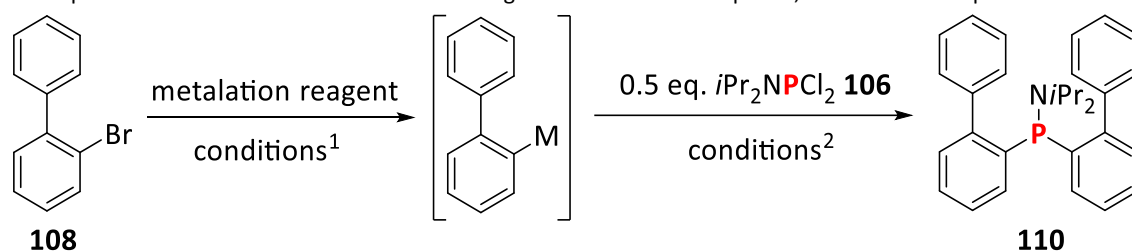
entry	metalation	conditions¹	conditions²	result
1	2.0 eq. *t*BuLi[a]	cyclohexane, 0 °C to 25 °C, 15 h	0 °C, neat	mixture of unidentified products was formed
2	2.0 eq. *t*BuLi[b]	THF, -78 °C, 1 h, 25 °C 1 h	-78 °C, neat	20% of **110** were isolated after purification
3	1.3 eq. *n*BuLi[c]	Et₂O, -78 °C, 1 h, 25 °C 1 h	0 °C, dissolved in THF	mixture of unidentified products
4	1.05 eq. *i*PrMgCl LiCl in THF[d]	THF, 25 °C, 24 h	-78 °C, neat	no reaction was observed
5	2.0 eq. Mg and DBE[e]	Et₂O, 50 °C, 2 h	-78 °C, neat	product was majorly formed as observed by ³¹P NMR but could not be isolated
6	BiPhMgBr 0.5 M Et₂O[f]	THF, 0 °C, neat		
7	BiPhMgBr 0.5 M Et₂O[f]	THF, 0 °C, dissolved in THF		
8	BiPhMgBr 0.5 M Et₂O[f]	*n*-pentane, 25 °C, neat		97% of **110** after purification

Metalation procedures were adapted from: [a] Le Drian and coworkers [51] [b]Feringa and coworkers[56] [c]Baudoin and coworkers[57] [d]Krasovskiy and Knochel [58] or [e]Klumpp and coworkers [59]. [f] This reagent was purchased from Sigma Aldrich.

Since the reported procedure was not reproducible (entry 1), the metalation reagent, the solvent and the reaction temperature were varied to access molecule **110**. Using reported bromo/lithium exchange procedures (entries 2-4) followed by quenching with **106**, showed that the metalation reactions were incomplete in most cases as numerous by-products were observed by ^{31}P NMR experiments. Although Le Drian and coworkers[51] clearly stated that aryl magnesium bromides were not providing the respective protected phosphine **110**, initial reactions with the *in situ* formed biphenyl Grignard (BiPhMgBr) were promising (entry 5). Due to the formation of by-products, it appeared that the Grignard reaction itself was not complete. The reaction was repeated with the commercially available Grignard reagent and in *n*-pentane as a solvent. Although the reaction mixture was very inhomogeneous, ^{31}P NMR experiments indicated that the product **110** was formed selectively. It could be isolated by crystallization in excellent yields and purity (entry 8).

Product **110** showed stability against moisture and air which was not observed for its phenyl derivative. Therefore, it was concluded that the biphenyl ligands sterically shield the phosphorus atom which was confirmed by single-crystal X-ray analysis (see Chapter 4.5.9).

After the exploration of a suitable method to obtain and purify molecule **110**, it was converted to the respective phosphine chloride **111** by using an excess of hydrogen chloride in an etheric solution (Scheme 59).
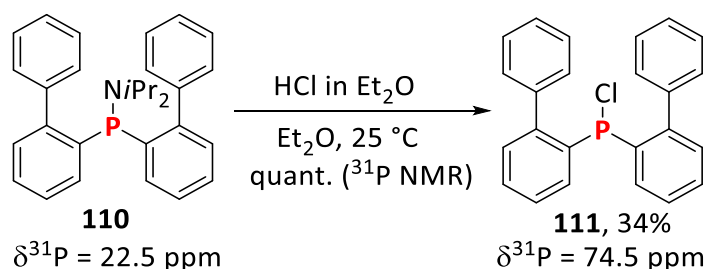
Scheme 59: Synthesis of the *bis*(biphenyl)chlorophosphine (**111**).

Initial investigations indicated quantitative conversion towards **111**, which was obtained in reasonable purity after separation from the ammonium salts. The isolation of this molecule was maintained using high temperature, high vacuum Kugelrohr (180 °C, 3.2 x 10^{-2} mbar) technique and resulted in pure compound **111** but in a low yield of 34%. Over the course of this distillation, side products, which are likely to be phosphinic chlorides (δ = 34.0 ppm) and phosphine oxides (δ = 15.9 ($^1J_{PH}$ = 503.3 Hz) ppm), occurred. However, the isolation of this product was not pursued further as *in situ* performed ^{31}P{^{1}H} NMR analysis showed quantitative conversion. In the following, the chlorophosphine **111** was subjected directly to reduction towards the lithium phosphide **107** using elemental lithium wire as previously reported (Scheme 60).[51]
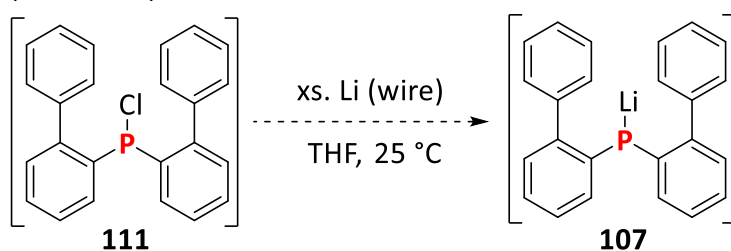
Scheme 60: Reduction of *bis*(biphenyl)chlorophosphine **111** towards the respective phosphide **107** using lithium.

Using an excess of lithium wire resulted in a dark green solution without any resonance in ^{31}P{^{1}H} NMR experiments. Although phosphides generally exhibit broad ^{31}P NMR signals, which makes them sometimes difficult to observe, a total absence of any signal may indicate a reductive cleavage of all C-

P bonds due to over-reduction processes. This would further explain the occurrence of a deep green colored solution as lithium biphenyl absorbs light in this region.[60] Decreasing the amount of lithium wire to 3.0 equivalents led to the formation of several $^{31}P\{^1H\}$ NMR active species (Fig. 98).

111
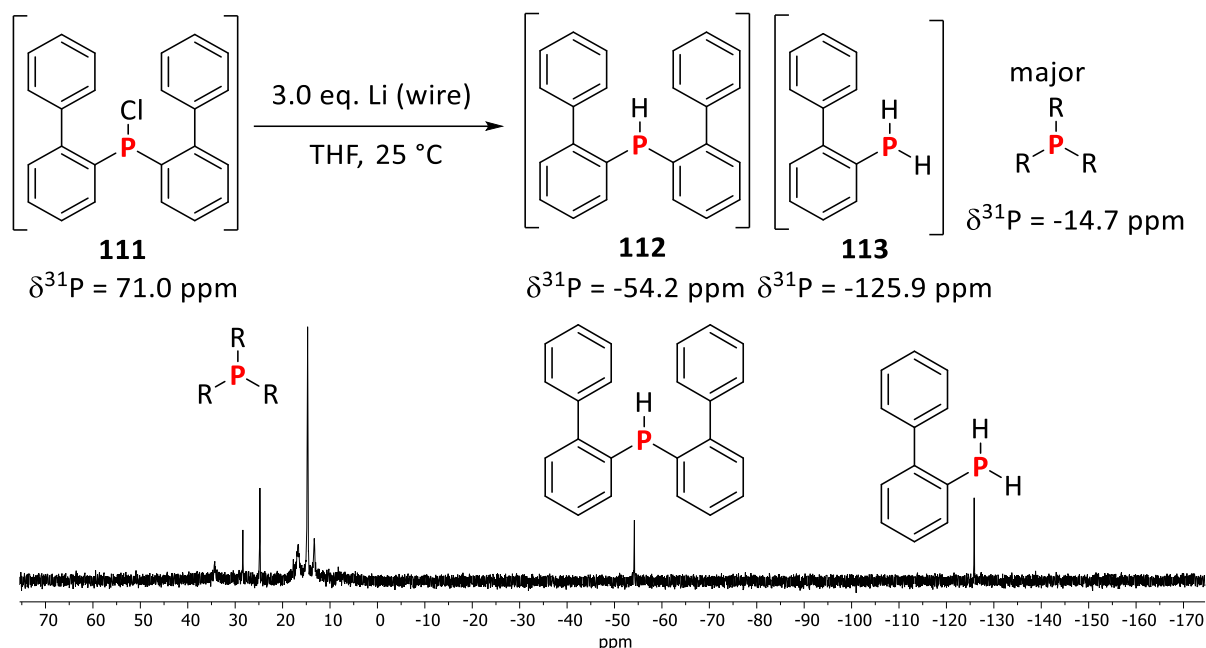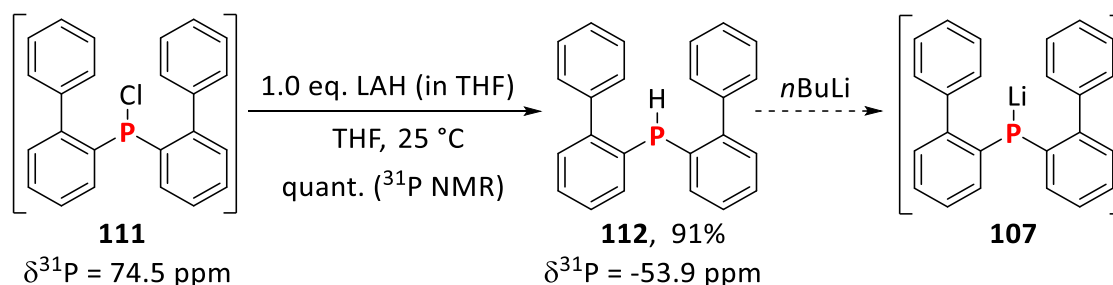$\delta^{31}P = 71.0$ ppm

3.0 eq. Li (wire)
THF, 25 °C

112
$\delta^{31}P = -54.2$ ppm

113
$\delta^{31}P = -125.9$ ppm

major
$\delta^{31}P = -14.7$ ppm

Fig. 98: No-lock $^{31}P\{^1H\}$ NMR (162 MHz) spectrum of an aliquot sampled from the reaction mixture of lithium wire (3.0 eq.) with **111** after filtration of residual lithium and protonation with methanol.

In addition to signals in the low-field range of the spectrum (the most intense signal was at $\delta = 14.7$ ppm, without splitting in the ^1H-coupled experiment), two signals in the high-field ($\delta = -54.2$ and -125.9 ppm) were observable. These latter signals could be assigned to the *bis*(biphenyl)phosphine (**112**), *vide infra*, and biphenylphosphine[61] (**113**). The occurrence of a primary arylphosphine **113** in this process could indicate an unselective reduction of diarylchlorophosphine **111** *via* cleavage of one aryl group. This was not surprising, since a common synthetic pathway to access diarylphosphides origins from triarylphosphines by removal of one aryl group with elemental alkalimetals.[52, 53]

Since the reduction with lithium was apparently unselective, the respective phosphine **112** was to be obtained applying the milder reductant lithium aluminum hydride (LAH). Next, deprotonation with an organolithium base like *n*BuLi could, then, lead to the lithium *bis*(biphenyl) phosphide (**107**). Following this route, the phosphine **112** was obtained after the reduction of the chlorophosphine **111** with a THF solution of lithium aluminum hydride (Scheme 61).

111
$\delta^{31}P = 74.5$ ppm

1.0 eq. LAH (in THF)
THF, 25 °C
quant. (^{31}P NMR)

112, 91%
$\delta^{31}P = -53.9$ ppm

*n*BuLi

107

Scheme 61: Successful reduction of the chlorophosphine **111** with lithium aluminum hydride solution gave the phosphine **112** as the pure product after distillation. This phosphine might be metalated by *n*BuLi in a further step to access the phosphide **107**.

The reduction resulted in the full conversion as determined by $^{31}P\{^1H\}$ NMR analysis. Initial attempts to purify the product by column chromatography failed as the phosphine **112** oxidized readily.

However, the isolation of the compound **112** succeeded using high temperature (160 °C), high vacuum (10^{-2} mbar) inert Kugelrohr distillation in excellent yields. After cooling the product, it readily crystallized readily (the crystal structure is discussed in chapter 4.5.9).

Since the phosphine **112** was not stable against oxidation, it was stabilized by transforming it to the respective phosphine-borane **114**. To access **114**, three synthetic routes were conducted: 1) simultaneous reduction/protection of chlorophosphine **111** with lithium aluminum hydride and the borane THF adduct: 2) successive reduction with lithium aluminum hydride to access the phosphine **112** (*vide supra*) and further protection with the borane THF adduct 3) direct reduction of the chlorophosphine **110** with lithium borohydride (Scheme 62).
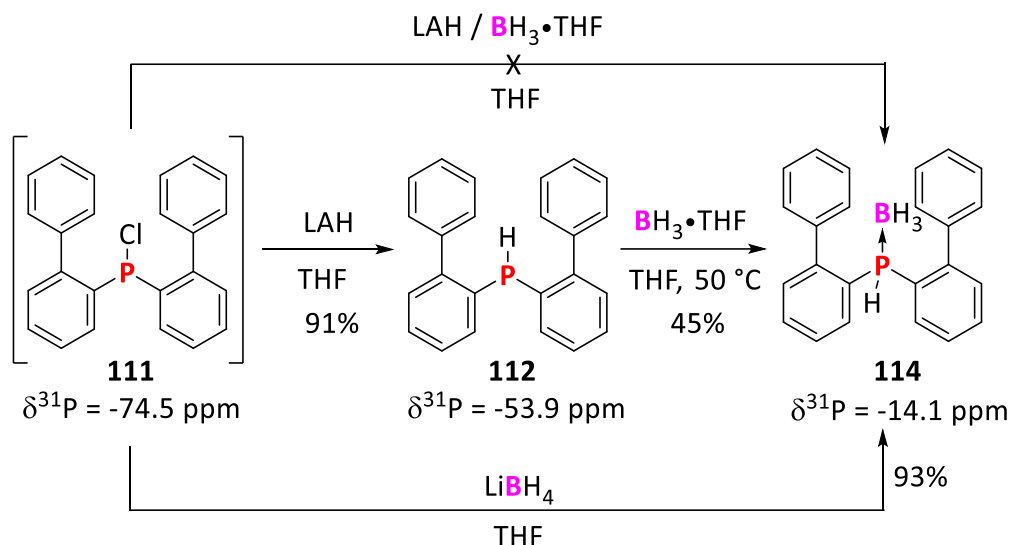
Scheme 62: Synthesis towards the *bis*(biphenyl)phosphine borane (**114**) starting from chlorophosphine 111.

Initial attempts to obtain phosphine borane **114** in a one-pot synthesis starting with the reduction of diarylchlorophosphine **111** with lithium aluminum hydride followed by the reaction with borane THF adduct were unsuccessful. Therefore, the sequential reduction/protection sequence was studied: The reduction of diarylchlorophosphine **111** with lithium aluminum hydride to give the respective phosphine **112** had already been successfully conducted (see above). The subsequent protection of the phosphine **112** with the borane THF adduct at 25 °C initially showed no conversion. Upon heating to 50 °C it was possible to obtain nearly quantitative conversion towards the phosphino borane **114** as determined by ^{31}P NMR (δ = -14.09 ppm). The borane adduct **114** could be isolated by crystallization in a 45% yield. Finally, a reduction/borylation procedure using lithium borohydride in THF gave the product **114** in an excellent yield of 93% after crystallization. The resulting crystals of **114** were suitable for X-ray analysis (See chapter 4.5.9).

Unfortunately, the phosphine borane **114** was moisture-, air- and temperature-sensitive, forming the respective phosphine **112** upon decomposition. Therefore, this synthetic procedure had no direct synthetic advantage compared to the isolation of the phosphine **112** by distillation in high yields.

After obtaining the pure phosphine **112**, the respective phosphide was to be generated *in situ* with *n*BuLi and directly reacted with a trihaloborane. To conduct such an experiment, varied metalation and quenching conditions were investigated and ^{31}P NMR spectra of the reaction mixtures were performed (Fig. 99).
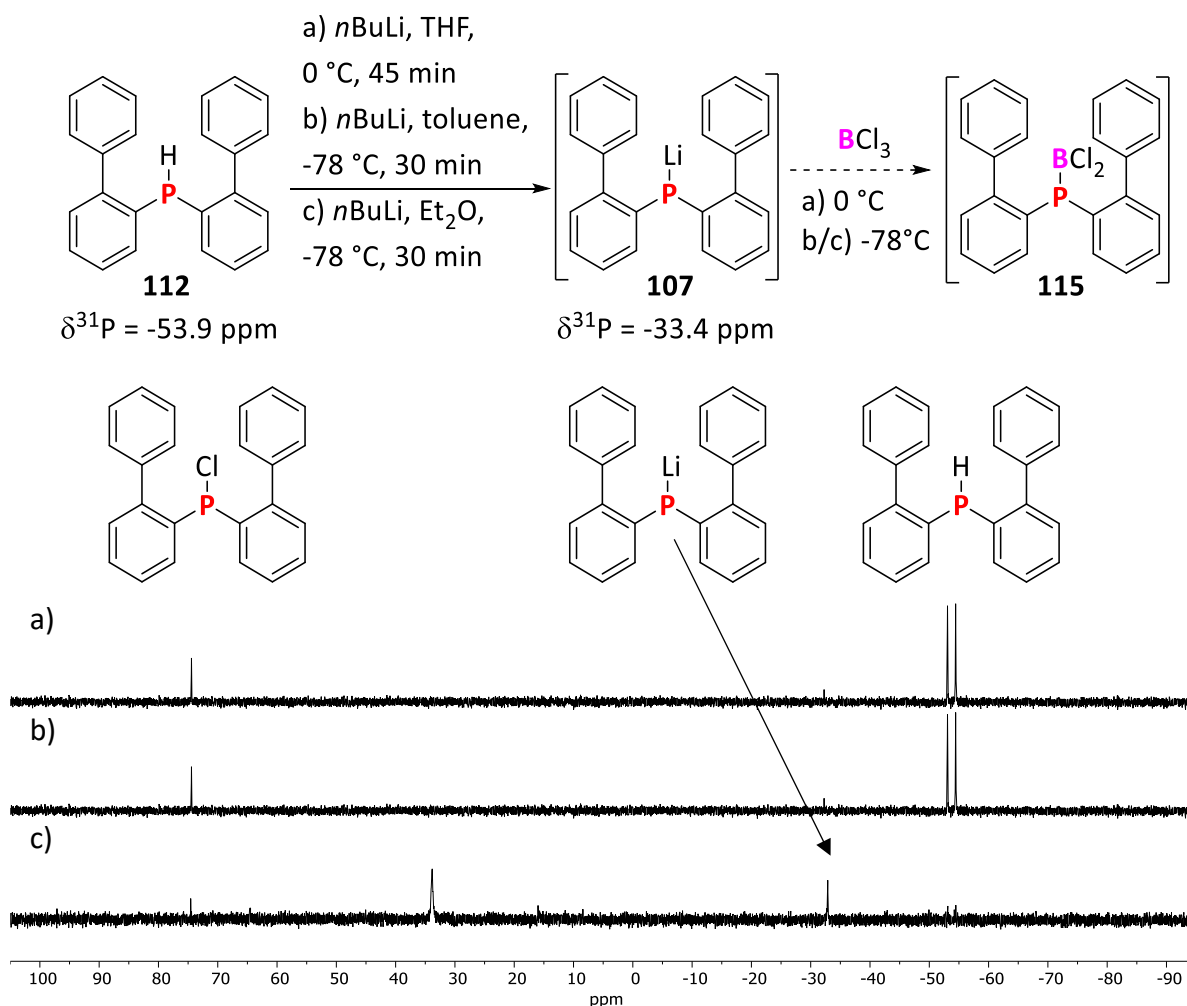

Fig. 99: ^{31}P (162 MHz) spectra of the reaction of phosphine **112** with *n*BuLi and followed by the addition of BCl$_3$ in *n*-hexane under varying conditions were varied. In all experiments the solvents were removed *in vacuo* and the residues were dissolved in C$_6$D$_6$.

The lithiation was performed in THF, toluene and diethyl ether respectively to evaluate the effect of the solvent on the formation of phosphide **107** and on the borylation reaction. After the given lithiation time, the color of the reaction mixture changed to yellow or red in all cases indicating the formation of lithium phosphide **107**. Upon the addition of boron trichloride, the color instantly vanished and the formation of a white precipitate was observed. The evaluation of the NMR samples, which were obtained after removal of all volatiles under inert condition, revealed the presence of starting material **112** (^{31}P{^{1}H} NMR: δ = -53.9 ppm) and *bis*(biphenyl)chlorophosphine (**110**) (^{31}P{^{1}H} NMR: δ = 74.5 ppm) irrespective of the solvent (THF or toluene) or the reaction temperature. The formation of the chlorophosphine **111** was unpredicted and indicated an oxidation process of the phosphide **107**. The respective ^{11}B{^{1}H} NMR experiments showed no NMR active species at all. The reaction performed in diethyl ether showed two novel singlets (^{31}P{^{1}H} NMR: δ = 34.0, -32.9 ppm). Later it was found that the high-field signal represents the coordinated phosphide species **107** *vide infra*. As a side notice, a trace of the diarylchlorophosphine **111** (δ = 74.5 ppm) was observable. Therefore, both the phosphide **107** and the chlorophosphine **111** were in the reaction mixture and did not react further. The respective

^{11}B{^{1}H} NMR experiments showed the formation of a tetracoordinate boron species (^{11}B{^{1}H} NMR: $\delta = 18.4$ (br) ppm) which remained unidentified.

4.5.3 Synthesis of Phenyl-Substituted Tricoordinated BP-Compounds

Since the initial experimental results were inconclusive, further fundamental studies of this reaction type were conducted with diphenylphosphine (**116**) as a test substrate. To further prevent using any coordinating solvent, the lithium species (Ph$_2$PLi) was generated *in situ* by lithiation of diphenylphosphine (**116**) with *n*BuLi in either *n*-pentane or toluene at low temperature.[62] This was followed by addition with boron trichloride to furnish the diphenylphosphino dichloroborane (**117**) or its dimer **118** (Scheme 63).
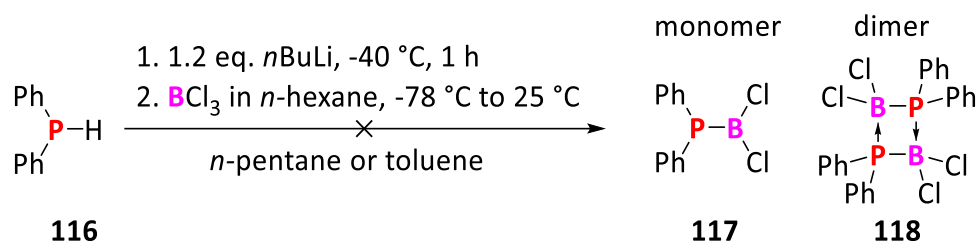
Scheme 63: Lithiation of diphenylphosphine (**116**) with *n*BuLi and further reaction with boron trichloride to access the desired product **117**. As this product highly unstable, its dimer **118** might be formed too.

Upon the addition of *n*BuLi to **116**, a color changed was observed, which indicated the formation of the lithium diphenylphosphide (**119**). After the addition of boron trichloride at low temperature, the reaction mixture returned to colorless. After removal of the solvents in both attempts, no signals in either ^{31}P{^{1}H} or ^{11}B{^{1}H} NMR experiments were observed. This indicated either decomposition or the generation of NMR silent species. Further analysis of the reaction mixture gave no result.

As this simple synthetic approach did not form any product and another synthetic pathway to access tricoordinated BP-species was investigated. Early studies of Coates and Livingstone performed the B-P bond formation without using a phosphide but a phosphine species.[44] They established a synthetic route utilizing diphenylphosphine (**116**), chlorodiphenylborane (**PhBCl$_2$**) and triethylamine to access a phosphinoborane (**71**) (Scheme 64).
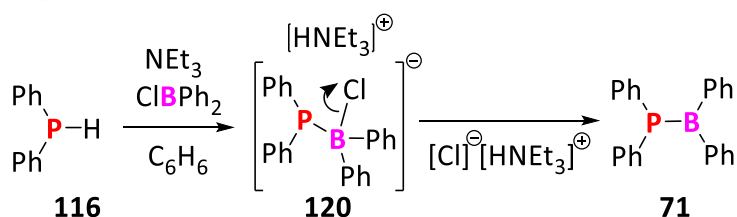
Scheme 64: Formation of (diphenylphosphine)diphenylborane (**71**) by methods presented from Coates and Livingstone.[44]

They reported that upon addition of the phosphine to a premixed solution of diphenylchloroborane (**PhBCl$_2$**) and triethylamine, the [Ph$_2$PB(Cl)Ph$_2$]$^-$[Et$_3$NH]$^+$ (**120**) salt was formed. After elimination of the chloride as triethylammonium salt, product **71** was formed as monomeric species. The fact that **71** is stable as a monomer is due to the stabilization by the aryl groups at both heteroatoms. Additionally, it was found that omitting a base in this process led to the formation of the respective Lewis base / Lewis acid adduct [Ph$_2$PH·ClBPh$_2$] (**121**) withstanding the elimination of HCl.[44]

Transferring this concept to the present problem led to the investigation of the synthesis towards the diphenylphosphine dihaloborane (**124**) from a diphenylphosphine (**116**), an electrophilic boron species, and a strong organic base to deprotonate the phosphine (Scheme 65).
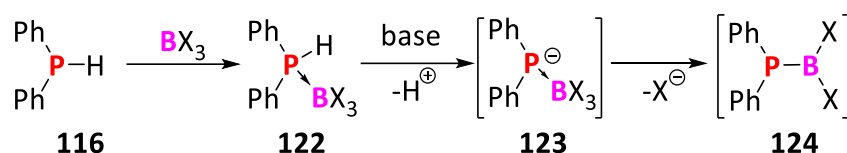
Scheme 65: Reaction sequence of diphenylphosphine (**116**) its reaction with an electrophilic boron to form the Lewis adduct **122**, followed by a base-induced elimination of HX to access phosphino borane **124**.

Thus, diphenylphosphine (**116**), boron trichloride and 1,8-diazabicyclo[5.4.0]undec-7-en (DBU) were used to facilitate the formation of tricoordinated BP-compound **117** or its dimer **118** (Scheme 66).
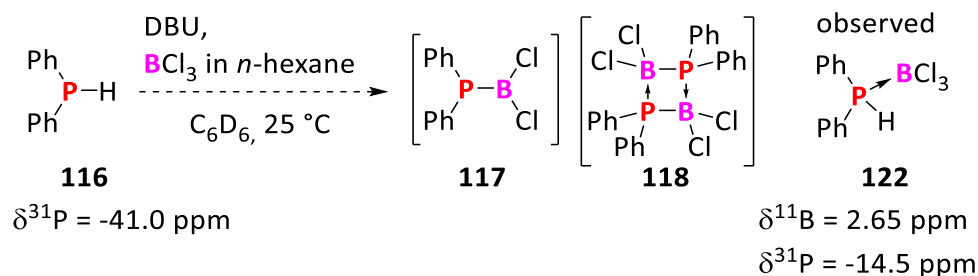
Scheme 66: Reaction of diphenylphosphine (**116**) with DBU and boron trichloride.

Primarily, the formation of the phosphine borane adduct **122** was observed which could be characterized by ^{31}P NMR experiments (Fig. 100).
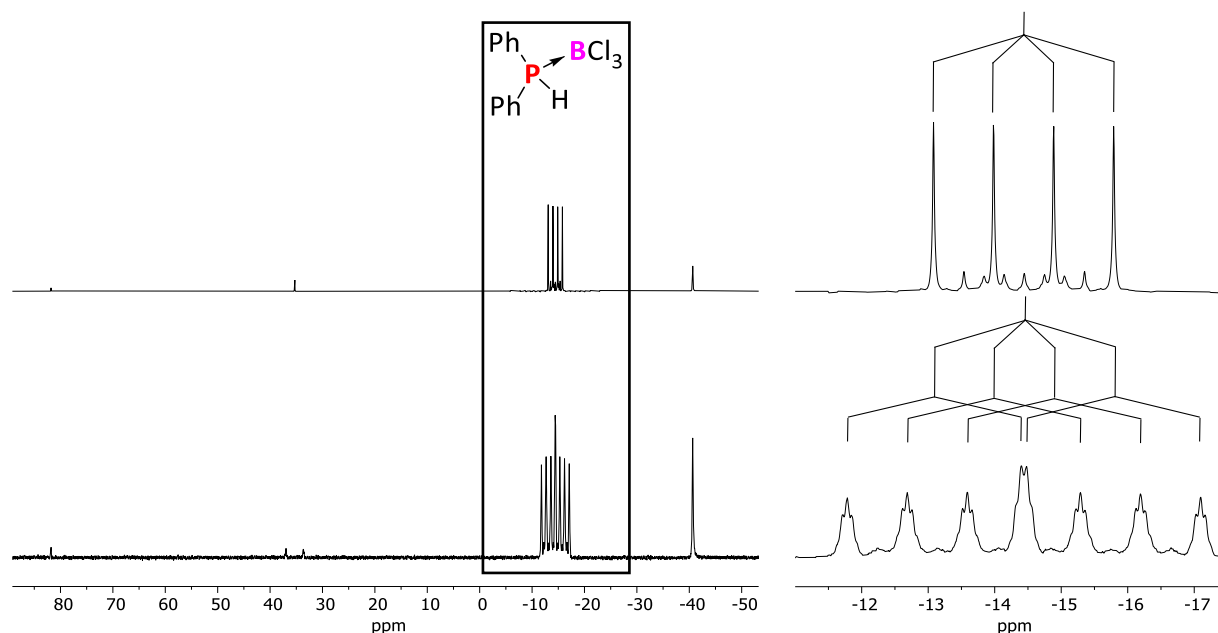

Fig. 100: ^{31}P{^{1}H}(top)/^{31}P NMR (162 MHz)(bottom) spectra of the reaction mixture consisting of DBU, diphenylphoshine (**116**) and boron trichloride in C_6D_6. A magnified version of the signal at 14.5 ppm is found on the right.

Due to the spin of ^{31}P ($I = 1/2$) and ^{11}B ($I = 3/2$) the expected multiplicity ($M = 2I * n+1$ (with $n = 1$), $M = 4$)) for a B-P bond should be a quartet with four signals of equal intensity as shown above. The ^{31}P-^{11}B coupling constant was determined as $^{1}J_{P_{11}B} = 146.2$ Hz. The respective signal for the ^{10}B-species ($I = 3$, natural abundance 20%) is expected to be a septet with peaks of equal intensity and is visible in the decoupled ^{31}P NMR spectra. It had a coupling constant of $^{1}J_{P_{10}B} = 49.2$ Hz. The phosphorus-proton coupling constant of the diphenylphosphine borane **122** was found to be $^{1}J_{PH} = 421.9$ Hz and was in perfect agreement with literature reports.[63]

184

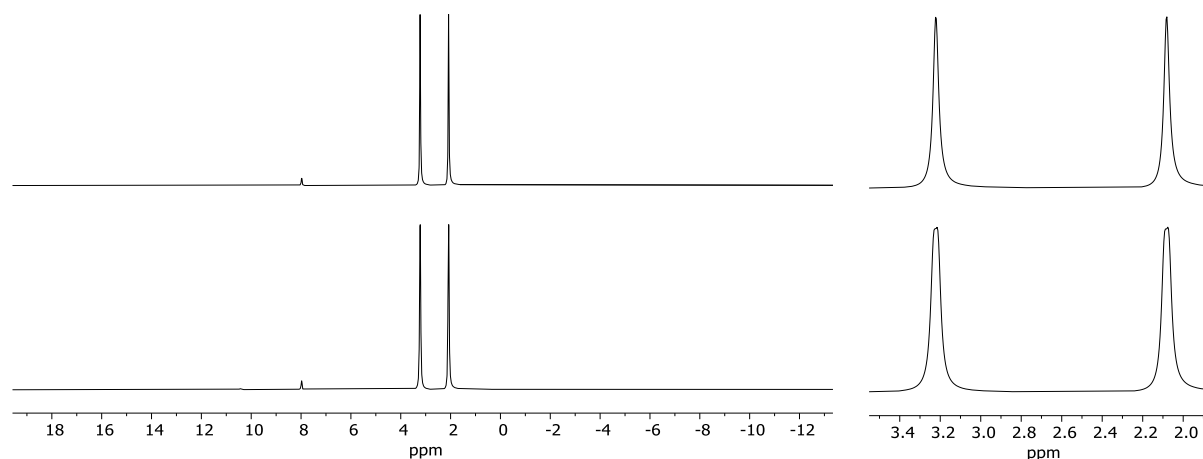The ^{11}B NMR experiments of the reaction mixture revealed a distinctive doublet signal (Fig. 101).

Fig. 101: *In situ* [11]B{^{1}H}(top) /[11]B(bottom) NMR (128 MHz) spectra of the reaction mixture consisting of DBU, diphenylphoshine (**116**) and BCl$_3$ (*n*-hexane solution) in C$_6$D$_6$.

Due to the [31]P (I = 1/2) and [11]B (I = 3/2) nuclei, the expected multiplicity (M = 2S∗n+1; with n = 1, M = 2), the respective signal was found with a coupling constant of $^1J_{11BP}$ = 146.2 Hz and a further coupling to the phosphine proton with a coupling constant of $^2J_{11BH}$ = 3.0 Hz in the coupled ^{11}B NMR spectrum. All the mentioned proton couplings were found vice-versa in the ^{1}H NMR experiments as well.

Attempts to eliminate hydrogen chloride from Lewis adduct **122** to generate the respective diphenylphosphino dichloroborane (**117**) remained unsuccessful though the reaction was performed at elevated temperature (Scheme 67).

δ^{11}B = 2.65 ppm

δ^{31}P = -14.5 ppm
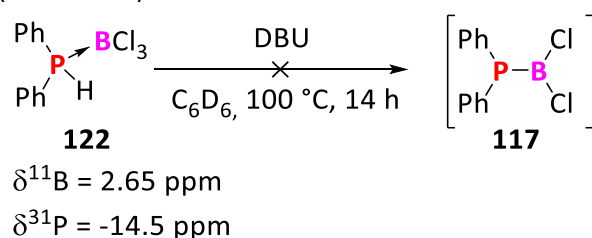
Scheme 67: Attempted synthesis of diphenylphosphino dichoroborane **117** *via* elimination of hydrogen chloride from **122**.

Apparently, the protocol which was successfully deployed to obtain the diphenylphosphino diphenylborane (**71**),[44] was not transferable to access tricoordinated BP-species with two halides on the boron atom.

Another way to pursue the formation of a phosphorus-boron bond is a boron/tetrel transmetalation approach. Initial work was performed by Nöth[64] in the 1960s where he transferred the concept of forming B-N bonds *via* reaction of alkylsilylamines with alkylchloroboranes[65] to form B-P bonds from (alkyl)silylphosphines and alkylchloroboranes (Scheme 68).
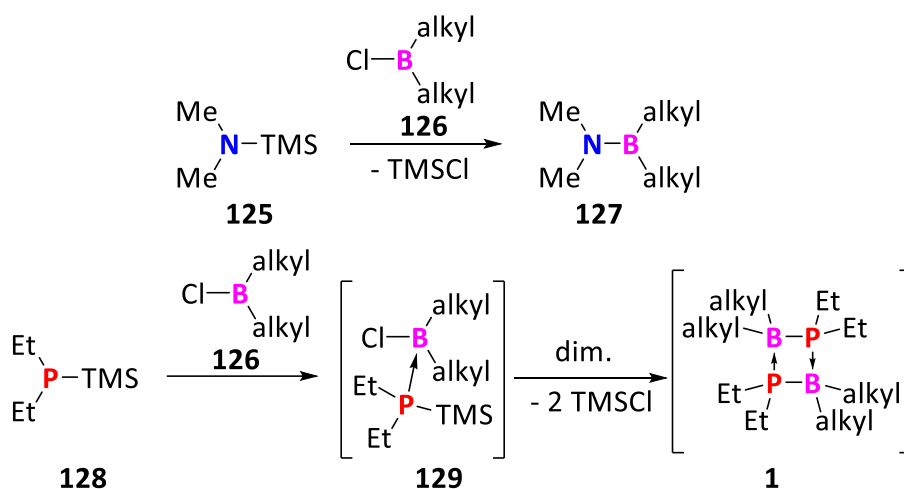
Scheme 68: BN vs. BP-chemistry: Comparing the reaction of trimethylsilyl-substituted dialkylamine **125** and dialkylphosphine **128** with a halo(dialkyl)borane **126**.[64]

In contrast to alkylaminoboranes, their BP-congeners alkylphosphinoboranes are commonly found as dimer where all BP-species were tetracoordinated. It was suspected that the formation of the dimeric species occurred after the initial formation of the Et$_2$PTMS·Cl-B(alkyl)$_2$ (**129**) intermediate. In general, monomeric alkylphosphinoboranes were only found in the case of using sterically demanding groups (cyclohexyl, aryl) at the boron atom.

Moreover, boron-tetrel exchange reactions with trihaloboranes as boron source were also conducted by Nöth[66] and resulted in the formation of dimers **131** (Scheme 69).
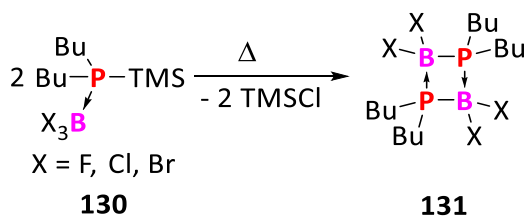
Scheme 69: Thermolysis of trimethylsilyl-substituted phosphine borane adduct **130** to generate the phosphino borane dimer **131**.[66]

At elevated temperature, the elimination of trimethylsilylhalide occurred and the respective dimer **131** was formed. This methodology could be also transferred to aryl-substituted phosphines and boranes to access diphenylphosphino diphenylborane (**71**) using diphenyl(trimethylsilyl)phosphine (**132**) and chloro(diphenyl)borane[67] or the synthesis of the elusive diphenylphosphino(pinacol)borane.[68] Therefore, the boron-silyl exchange is a versatile tool to form a B-P bond.

For this purpose, the usage of trimethyltetrel groups as leaving group on the diarylphosphine were chosen as they are easily accessible. The commercially available diphenyl(trimethylsilyl)phosphine (**132**) was used as a starting material for a silicon-boron exchange reaction (Scheme 70).
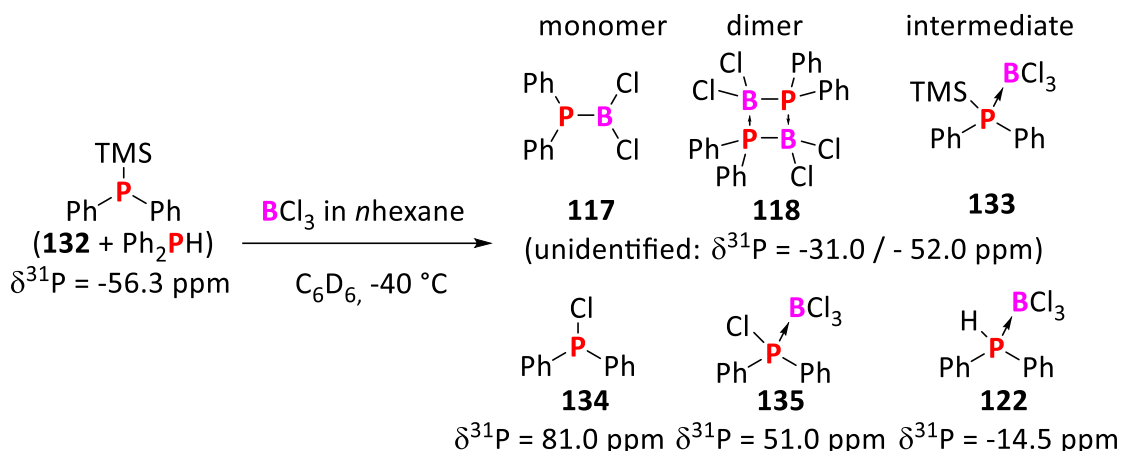
Scheme 70: Reaction of phosphine **132** with boron trichloride to obtain diphenylphosphino dichloroborane **117**. Due to the instability of the silylphosphines, it was observed that the commercially available product was already partly decomposed to the diphenylphoshine **116**.

Most species could be identified based on their characteristic BP-coupling or PH-coupling in the ^{31}P proton-coupled and decoupled NMR experiments. During the reaction and after evaporation of all volatiles different signal sets were observed in the ^{31}P NMR experiments (Fig. 102).
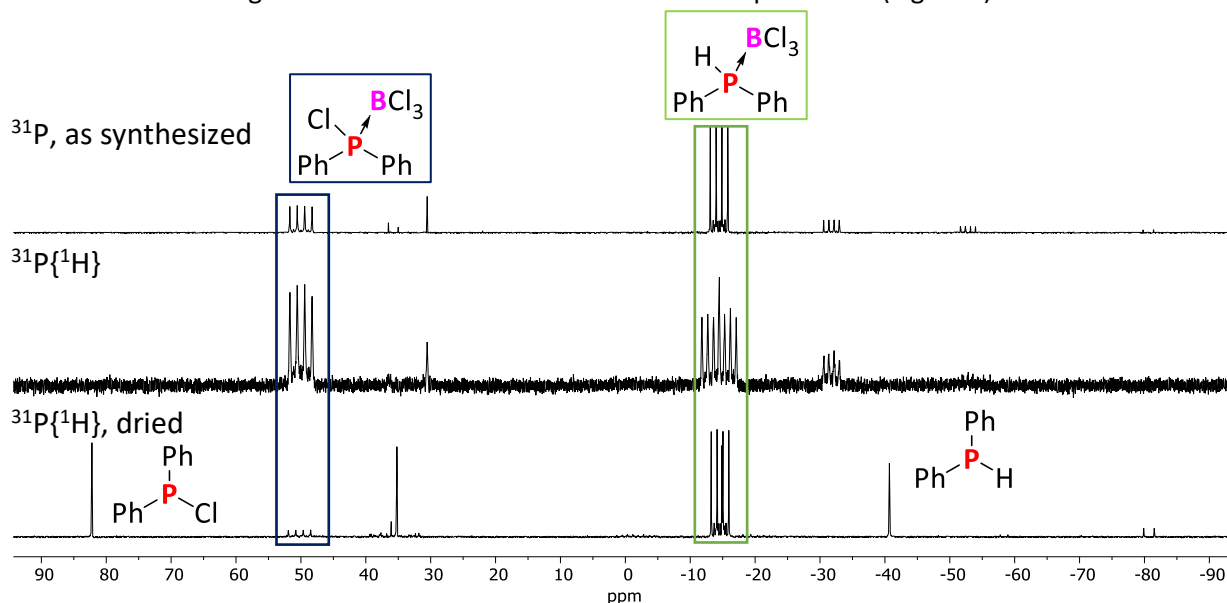

Fig. 102: ^{31}P{^{1}H} (162 MHz) spectrum of the reaction mixture consisting of diphenyl(trimethylsilyl)phosphine (**132**), residual diphenylphosphine (**116**) and with boron trichloride: as prepared in C$_6$D$_6$ (top) coupled ^{31}P NMR experiment (middle) dried in vacuum for 2 h and dissolved in C$_6$D$_6$ (bottom).

Initially, the absence of silylphosphine **132** in the ^{31}P{^{1}H} NMR spectrum (δ = -56.3 ppm) was noticed, which indicated that a silicon-boron exchange had occurred. Besides this observation six novel species, four of them with BP coupling, were detectable in the ^{31}P NMR spectra: δ = 48.9 (q, $^1J_{BP}$ = 185.0 Hz, diphenylchlorophosphine trichloroborane (**135**))[69], 30.54 (s), -13.5 (dq, $^1J_{BP}$ = 145.6 Hz, diphenylphosphine trichloroborane **122**), -31.0 (q, $^1J_{BP}$ = 130.0 Hz), -52.0 (q, $^1J_{BP}$ = 126.2 Hz), -80.6 (d, J = 262.6 Hz) ppm. Both signals in the high field region (δ = -31.0, -52.0 ppm) were the most likely to arise from the diphenylphosphino dichloroborane species (**117**). The formation of the dimer **118** was

excluded since no A_2B_2 spin system was observed in the spectrum. It would form a complex splitting behavior in ^{31}P NMR spectrum and a triplet in the ^{11}B NMR spectrum which was not observed in either experiment. In general, the ^{11}B NMR spectrum revealed numerous signals with a similar chemical shift ($\delta = 9.0\text{ -}2.0$ ppm) holding overlapping coupling behavior and therefore only two species were assignable: diphenylchlorophosphine trichloroborane (**135**) ($\delta = 2.79$ (d, $^1J_{BP} = 185.1$ Hz) ppm) and diphenylphosphine trichloroborane (**122**) ($\delta = 2.48$ (d, $^1J_{BP} = 145.6$ Hz) ppm).

After removal of all volatiles, the spectra were measured again and revealed that diphenylchlorophosphine (**134**) ($\delta = 81.0$ ppm) and diphenylphosphine **116** ($\delta = -41.0$ ppm) were formed as a product of BCl_3 cleavage. In general, the occurrence of the chlorophosphine products was unexpected. In fact, reactions of diphenylphosphine (**116**) towards the diphenylchlorophosphine (**134**) are only reported for the diphenylphosphine oxide (**136**) and a chlorination agent, e.g. phosphorus trichloride or acetyl chloride.[70, 71]

Apparently, the reaction of the trimethylsilyl phosphine **132** with boron trichloride was unselective. To reduce the reactivity of the tetrelphosphine, the tin derivative was generated by the reaction of potassium diphenylphosphide (**137**) with trimethyltin chloride. This led to the formation of the desired product **138** (^{31}P NMR: $\delta = -56.6$ ppm ($^1J_{PSn} = 580$ Hz)) and the formation of diphenylphosphine (**116**, ^{31}P NMR: $\delta = -41.0$ ppm) in small quantities. Due to the instability of stannylphosphines and the inseparability of this reaction mixture, it was directly subjected to a tin-boron exchange by using boron trichloride (Scheme 71).
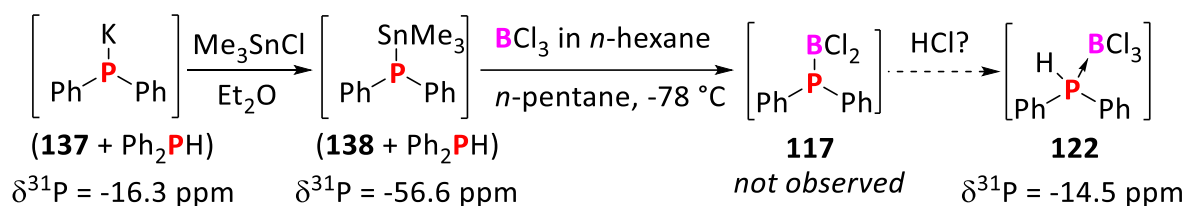
Scheme 71: The trimethylphosphine **138** was generated *in situ* of phosphide **137**, which was contaminated with diphenylphosphine **116**, with trimethyltin chloride. Next, the phosphine **138** was reacted with boron trichloride resulting in the formation of phosphine borane adduct **122**.

By ^{31}P NMR experiments, two novel signals were observed (^{31}P NMR $\delta = 36.0$ (s), -14.5 (q) ppm)(Fig. 103).
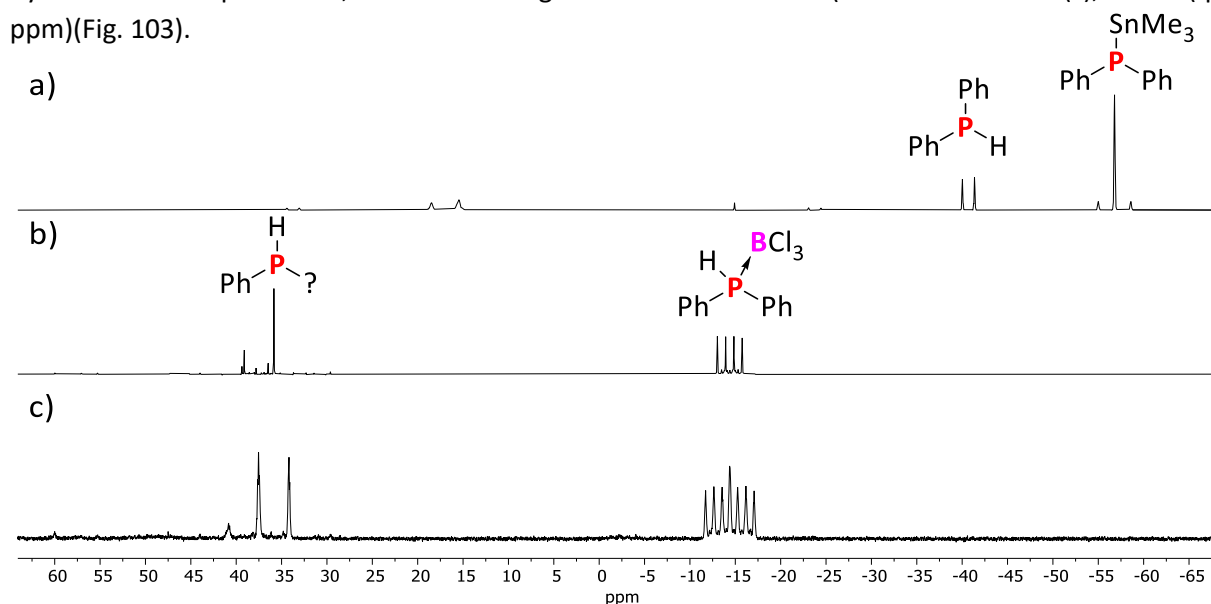

Fig. 103: a) ^{31}P NMR (162 MHz) spectra diphenylphoshine (**116**)/diphenyl(trimethylstannly)phosphine (**138**) in C_6D_6. b)/c) $^{31}P\{^1H\}/^{31}P$ NMR addition of boron trichloride measured in C_6D_6.

The high field signal (δ = -14.5 ppm) was assigned to the diphenylphosphine boron trichloride adduct (**122**) while the second signal set indicated that a secondary phosphine was still present. Therefore, the tin-boron exchange was achieved but unfortunately, the generated species was the phosphine borane adduct (**122**). A reason for this observation could be the acidolysis of the tricoordinated phosphino(dichloro)borane **117** by residual hydrogen chloride in the reagent (Scheme 71).

Since the tin/silicon-boron exchange was possible and promising tricoordinated species in the high field region of the ^{31}P NMR spectra were detectable, the reaction of stannyl/silylphosphines with trihaloboranes might a possible method to access aryl-substituted phosphino(dihalo)borane species. On the other hand, such a reaction might suffer the instability of a tricoordinated BP-species.

.

4.5.4 Synthesis of (Trimethyltetrel)phosphines for further tetrel-boron exchange

Due to the fundamental experiments with diphenylphoshines, it was concluded that a sufficient method to obtain a phosphorus-boron bond could be a tetrel-boron exchange although the formed species were in most cases the diarylphosphine trihaloborane adducts. Adapting this concept to the *bis*(biphenyl)phosphines could be valuable for obtaining a tricoordinated BP species for further ring annulation reactions (Scheme 72).
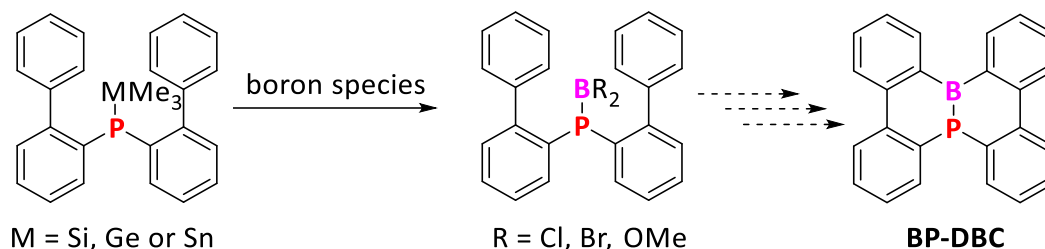
Scheme 72: Synthetic strategy to obtain a tricoordinated BP-species *via* boron-tetrel exchange reaction.

The trimethylsilyl moiety is representing the most accessible trimethyltetrel derivative as there are numerous protocols for synthesizing silylphosphines.[72] In general, three major pathways were considered the most promising to obtain silylphosphines: 1) reaction of an electrophilic chlorophosphine with a lithiated silane 2) formation of the P-Si bond utilizing strong silylation agents and organic bases 3) reaction of phosphides with organosilyl halides (Scheme 73).
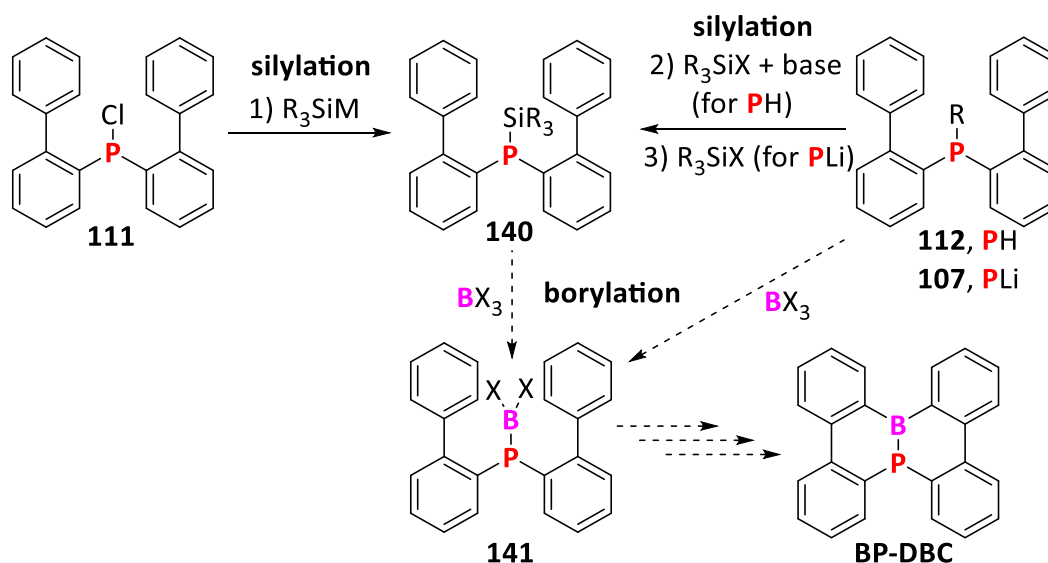
Scheme 73: Concepts to access diarylsilylphosphine **140** via 1) reaction of nucleophilic silane with the chlorophosphine **111** 2) deprotonation of the phosphine **112** and reaction with a silane transfer agent 3) reaction of phosphide **107** with electrophilic organosilane.

4.5.4.1 Reaction of nucleophilic silane with the chlorophosphine

The most facile synthetic approach to obtain silylphosphines uses the reaction of the lithiated dimethylphenylsilane (**142**) and a diarylchlorophosphine **111** (Scheme 74).
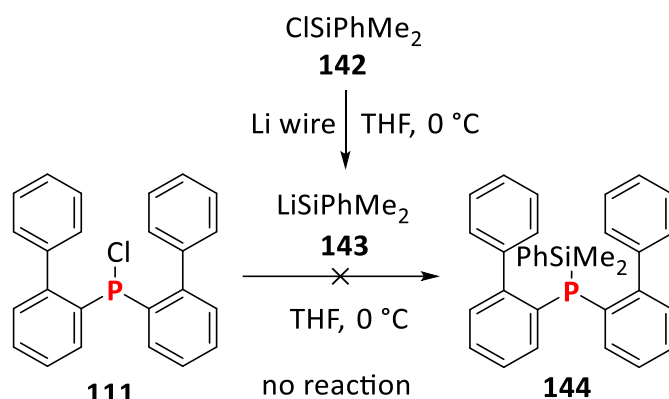

Scheme 74: *In situ* generation of the lithiated dimethylphenylsilane **143** and reaction with diarylchlorophosphine **111** did not give the desired silylphosphine **144.** The initial lithiation procedure was adapted from literature.[73]

The lithiated silane derivative **143** was generated *in situ* from the chloro(dimethyl)phenylsilane (**142**) and was added to the chlorophosphine **111**. Although both reactants are highly reactive species, the ^{31}P$\{^1$H$\}$ NMR experiments showed that no conversion took place. In fact, both the nucleophile and the electrophile were coexistent in solution. This may be due to sterically shielding of the phosphorus atom by the biphenyl ligands and the size of the nucleophile **143**.

4.5.4.2 Deprotonation of the phosphine **112** and reaction with a silane transfer agent

Another promising pathway to obtain trimethyltetrel phosphines is to use trimethyltetrel electrophiles and an organic nitrogen-containing base. Synthetic procedures for trimethylsilylphosphines were already reported[74, 75] and were transferred to the *bis*(biphenyl)phosphine **112** scaffold. To obtain the silylphosphine **145,** two different reported protocols, using triethylamine/trimethylsilyliodide[75] or TMP/trimethylsilyltriflate,[74] were investigated (Scheme 75).
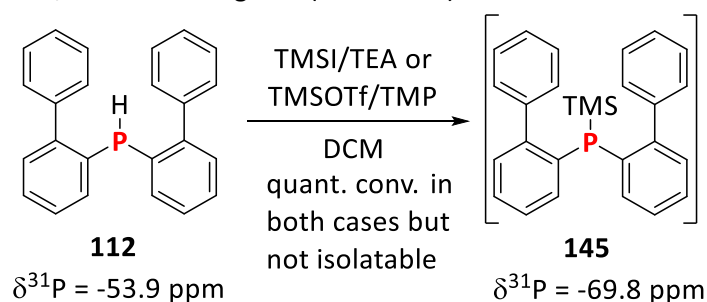
Scheme 75: Synthesis of trimethylsilylphosphines **145**.

Initially, in both reactions, quantitative conversion to the silylphosphine **145** was found by ^{31}P$\{^1$H$\}$ NMR experiments. Unfortunately, in both cases, the product could not be separated from the reagents and therefore an isolation was impossible. Attempts to distill silylphosphine **145** resulted in the cleavage of the P-Si bond giving the respective phosphine **112**.

Since the silylation of phosphine with TMP/trimethylsilyltriflate[74] was initially reported for phosphine boranes, the postmodification of the phosphine borane **114** *via* this protocol was also conducted. The product presents a precursor for a thermolysis reaction[66] to access a tricoordinated BP-compound **147** (Scheme 76).

$\delta^{31}P$ = -14.1 ppm
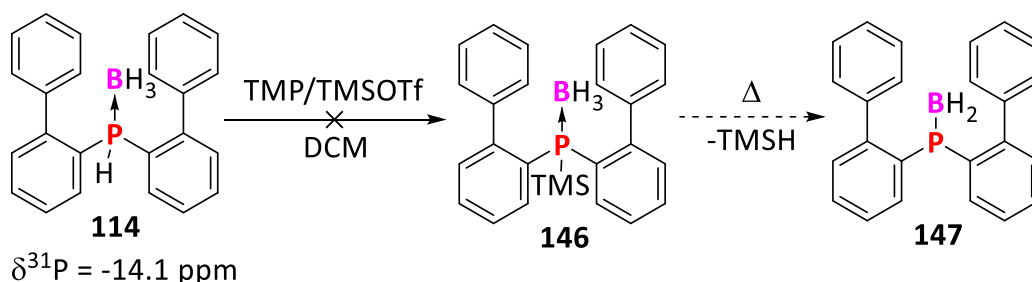
**Scheme 76**: Attempted silylation of the phosphine borane **114**.

The reaction was unsuccessful and highlighted the sensitivity of the phosphine borane **114** against these reactive reagents. The prospective diarylsilylphoshine borane **146** would be a versatile precursor the accessing tricoordinated BP-species by removal of trimethylsilane upon heating as reported by Nöth *vide supra*.[66] If such a reaction proves successful, the phosphine might be protected with a dichloroborane (BHCl$_2$) and the resulting product would be the diarylphosphino(dihalo)borane **115**. This species could enable the ring annulation reactions to access the **BP-DBC**.

However, because it appeared that a combination of a base and an electrophile would lead to the phosphorus-tetrel bond, a similar reaction using trimethyltin chloride and triethylamine was conducted (Scheme 77).
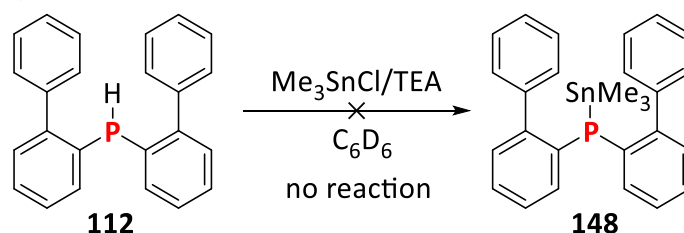
Scheme 77: Attempted stannylation of phosphine **112** with triethylamine and trimethyltin chloride.

The reaction did not occur although the reaction mixture was treated at elevated temperature (80 °C). Instead, trimethylstannyl phosphine **148** could be obtained in high yield using (dimethylamino)trimethyltin as a trimethylstannyl transfer reagent (Scheme 78).[76]

148, 99%

$\delta^{31}P$ = -62.0 ppm
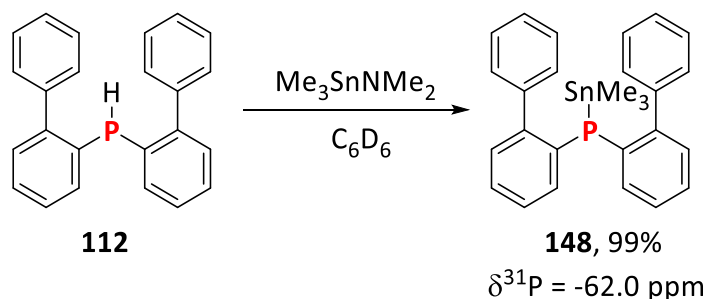
Scheme 78: Stannylation of phosphine **112** with (dimethylamino)trimethyltin.

In contrast to the synthesis of the silyl phosphines *vide supra*, the occurrence of the residual reagents species in the reaction mixture was unproblematic since dimethylamine could be easily removed by applying vacuum.

4.5.4.3 Generation of phosphide **107** and its reaction with electrophilic organosilanes

Since the synthesis of silylphosphine **145** was successful *in situ*, but the substance could not be separated from the other reagents, a metalation-silylation procedure was followed. This required an investigation of the metalation of *bis*(biphenyl)phosphine (**112**) in greater detail. However, the metalation conditions and silyl electrophiles were varied to access silylphosphines **140** (Tab. 15).

Tab. 15: Metalation of phosphine **112** under different conditions, followed by the reaction with silyl electrophiles.
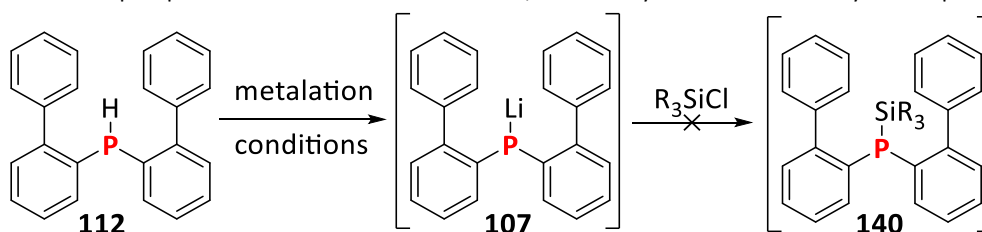
entry	metalation reagent	conditions	silicon reagent
1	1.1 eq. *n*BuLi	THF, -40 °C, 1 h	TMSCl
2	1.1 eq. *n*BuLi	THF, -60 °C, 1 h	TMSCl
3	1.1 eq. *n*BuLi	THF, -80 °C, 1 h	TMSCl
4	1.1 eq. *n*BuLi	THF, -100 °C, 1 h	TMSCl
5	1.1 eq. *n*BuLi	THF, -80 °C, 1 h	TIPSCl
6	1.1 eq. *n*BuLi	toluene, -80 °C, 1 h	TMSCl
7	1.1 eq. NaHMDS	Et$_2$O, -80 °C, 1 h	TIPSCl

A standard procedure for the silylation of aromatic secondary phosphines was reported by Ramírez-López et al.[77] using *n*BuLi in THF at -80 °C and a silylation temperature of -60 °C. Transferring this methodology to the present system and varying the temperature from -40 °C to -100 °C (entries 1-4) resulted in all cases to initial formation of a deep red colored solution. It appeared that the colorful species was only persistent at lower temperatures (< -60 °C). However, the colour vanished after the addition of trimethylsilyl chloride. After the removal of all volatiles, the desired silylphosphine did not occur, but only the starting material **112** was re-isolated. As it was not certain what caused this observation, the metalation/silicon reagent and the solvents were varied but this did not lead to the formation of the product (entries 5-7). For entries 6 and 7 only slight color changes were observed which might indicate an incomplete metalation. Also here only the starting material was re-isolated.

However, attempts were made to observe the phosphide species **107** by ^{31}P NMR experiments (Scheme 79).

112
δ^{31}P = -53.9 ppm

107, 99%
δ^{31}P (THF/C$_6$D$_6$) = -36.0/-52.4 ppm
δ^{7}Li (THF) = -0.1 ppm
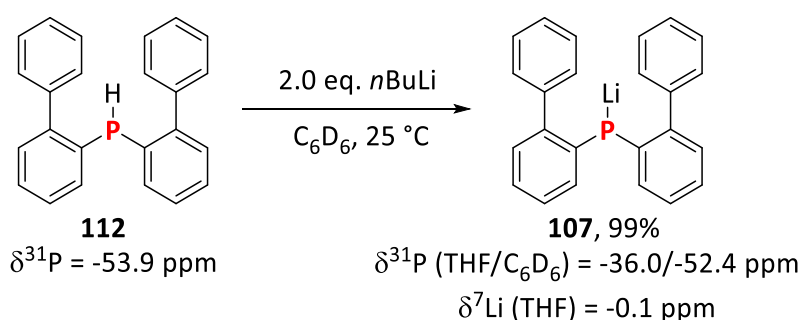
Scheme 79: Metalation of phosphine **112** with *n*BuLi giving the phosphide **107**. The phosphide was only slightly soluble in C$_6$D$_6$, therefore no ^{7}Li NMR signal was found. In THF, the ^{7}Li and ^{31}P NMR species were clearly observable.

When the reaction was performed in deuterated benzene an instantly formed precipitate upon addition of *n*BuLi and an intense orange color was observed. The full conversion towards the bad

soluble phosphide **107** was achieved by using two equivalents of *n*BuLi at 25 °C and was proven by ^{31}P{^{1}H} NMR experiments. The phosphide was stable at 25°C in the glove box but decomposed rapidly upon mixing with ethers or other solvents besides benzene and toluene. This behavior might explain the failure of optimization procedures described in Tab. 15 since in most cases coordinating solvents were used.

The ^{31}P{^{1}H} NMR shift of **107** was strongly dependent on the solvent and was observed as a broad signal in C_6D_6 (δ = -52.4 ppm). In a mixture with THF, the signal was shifted downfield (δ = -36.0 ppm) due to the coordination of the solvent. Crystals of phosphide **107** without coordinating solvent could be grown and revealed that **107** is found as a dimer with each phosphorus atom interacting with two lithium atoms forming a P_2Li_2 planar ring (Chapter 4.5.9).

Next, reactions with trimethyltetrel chlorides were conducted (Scheme 80).
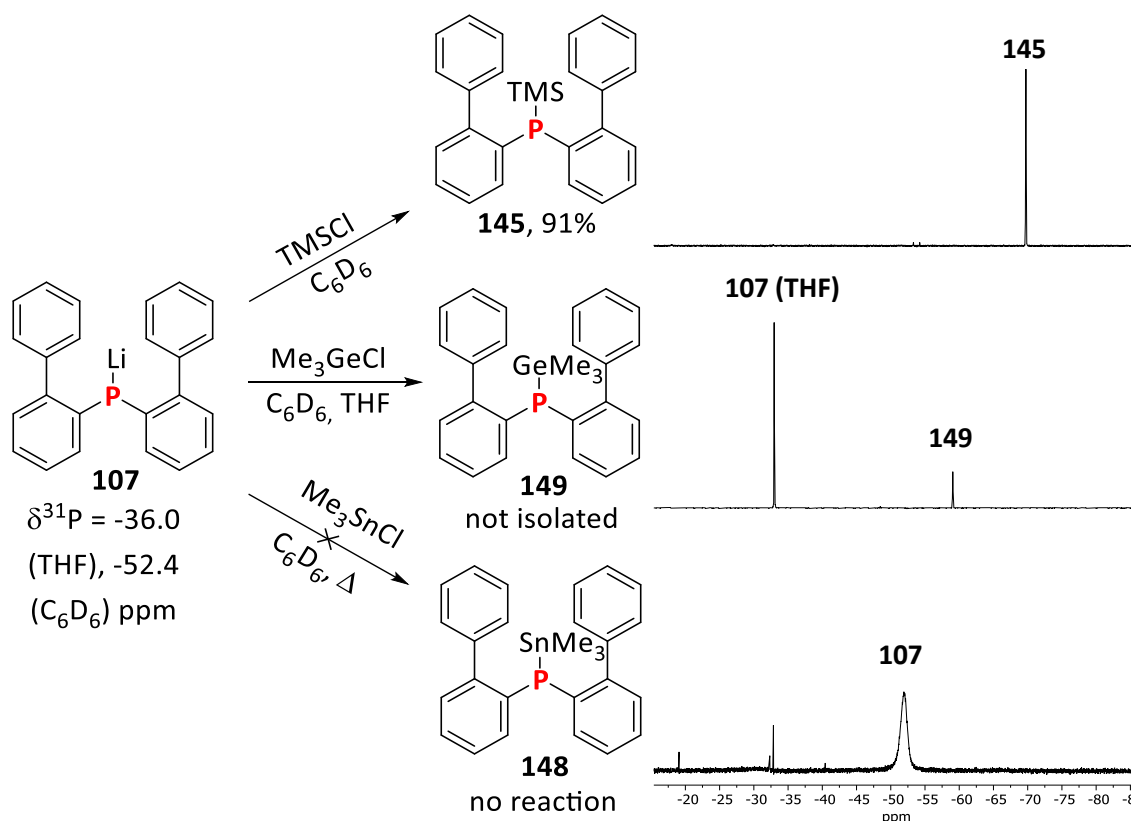
Scheme 80: Reaction of phosphide **107** with several trimethyl tetrel chlorides. On the right the^{31}P NMR (162 MHz) spectra of the experiments is displayed. The silylphosphine decomposed readily therefore a small signal of the phosphine **112** is present.

The reaction towards the silyl-substituted phosphine **145** occurred immediately and the product could be isolated in a yield of 91%. The silylphosphine **145** decomposed over time in solution and under high-temperature distillation conditions to its respective phosphine **112**.

The reaction of the phosphide **107** with trimethylgermanium chloride did not occur initially. To further facilitate the solubility of the trimethylgermanium chloride, THF was added. The ^{31}P{^{1}H} NMR (δ = -59.1 ppm) experiment showed that the reaction was not completed directly (see spectrum above). Full conversion could be obtained by using an excess of the trimethylgermanium chloride. Unfortunately, product **149** was not pure as determined by ^{1}H NMR spectroscopy and could not be purified further due to its reactivity.

Interestingly, no reaction was observed using trimethyltin chloride as an electrophile. Even when the reaction mixture was treated at elevated temperature (70 °C, 3 h) and mixed with THF to increase the solubility, no reaction occurred.

4.5.5 Tetrel-Boron Exchange Reactions

After successfully isolating the trimethylsilylphosphine **145**, *via* a metalation-silylation reaction, and trimethyltinphosphine **148**, *via* a group-transfer strategy, both derivatives were subjected to tetrel-boron transmetalation reactions, which were analyzed *in situ* by ^{31}P{^{1}H} NMR (Fig. 104).
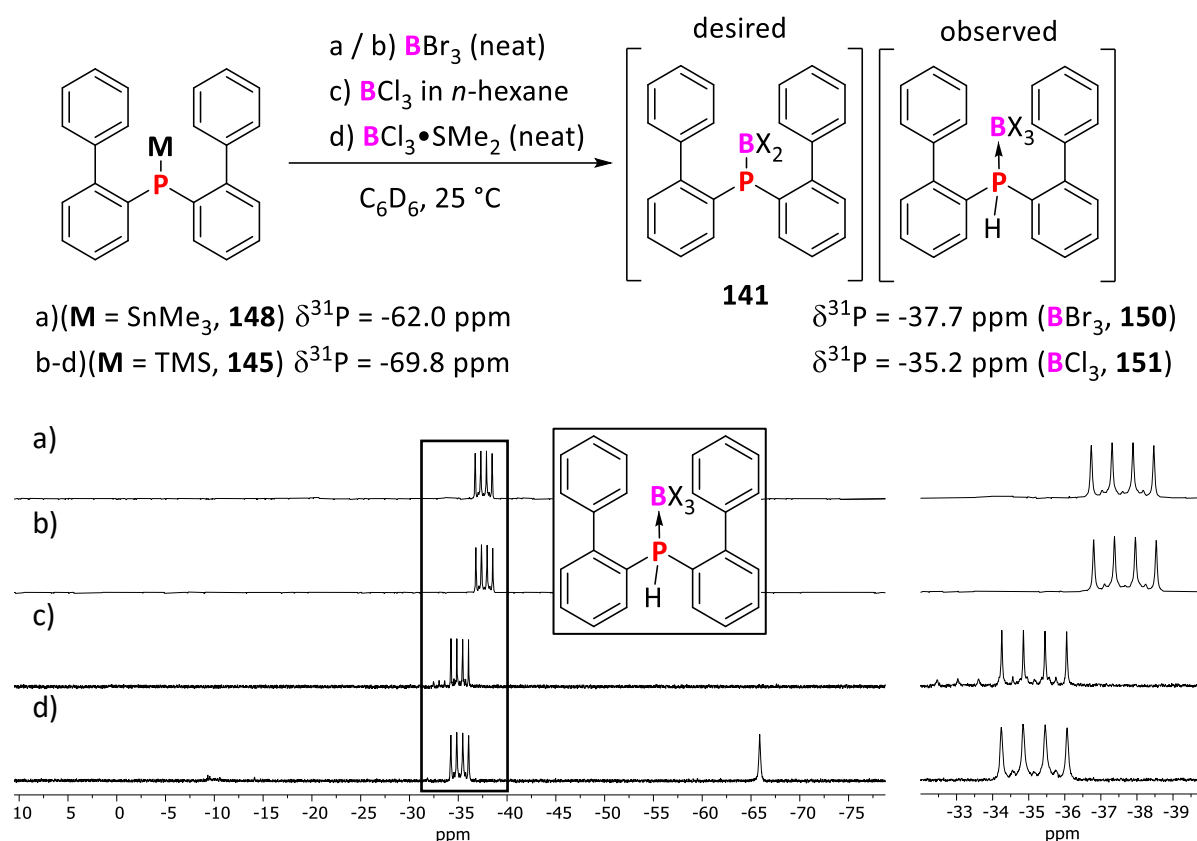

a)(**M** = SnMe$_3$, **148**) δ^{31}P = -62.0 ppm

b-d)(**M** = TMS, **145**) δ^{31}P = -69.8 ppm

δ^{31}P = -37.7 ppm (**B**Br$_3$, **150**)

δ^{31}P = -35.2 ppm (**B**Cl$_3$, **151**)

Fig. 104: ^{31}P{^{1}H} NMR (243 MHz) spectra of the reaction of trimethylstannylphosphine **148** with a) BBr$_3$ (neat) and of trimethylsilyl-phosphine **145** with b) BBr$_3$ (neat) c) BCl$_3$ (*n*-hexane solution) d) BCl$_3$•SMe$_2$ after dissolving in C$_6$D$_6$. A magnification of the signals at -35.0 ppm is displayed at the right side.

As the NMR experiments disclosed, the tetrel-boron exchange was successful in all cases, but the product that was formed, was the phosphine boron trihalide adducts **150** and **151**. Those occurred independent of whether trimethyltin or trimethylsilane was used as the leaving group. The *bis*(biphenyl)phosphino tribromoborane (**150**) was characterized with multinuclear NMR studies (^{31}P{^{1}H}: δ = -37.67 (q, $^1J_{BP}$ = 140.5 Hz) ppm and ^{11}B{^{1}H}: δ = -16.1 (d, $^1J_{BP}$ = 140.5 Hz) ppm). A respective boron trichloride adduct **151** was found with similar NMR properties (^{31}P{^{1}H}: δ = -35.1 (q, $^1J_{BP}$ = 145.8 Hz) ppm and ^{11}B{^{1}H}: δ = 3.53 (d, $^1J_{BP}$ = 145.8 Hz). In all cases, the ^{11}B{^{1}H} NMR experiments indicated that only the borane adducts were formed.

Because the formation of BP-compounds *via* silicon-boron exchanges presumably follows an addition-elimination mechanism (See Chapter 4.5.3), it might be concluded that the Lewis acidity of electrophilic boron species plays a major role in this process. Therefore, and to exclude that residual traces of hydrogen chloride were the reason for the acidolysis, the solid boron trichloride dimethylsulfide was used as a reactant. Due to the Lewis acid/base interaction with the protection group, the reactivity of

the trichloroborane should differ substantially. Surprisingly, the reaction with the phosphine **145** also led to the formation of the phosphine boron trichloride adduct **151**. As indicated in the ^{31}P{^{1}H} NMR (Fig. 104), the reaction did not proceed to full conversion, although an excess of the borane complex was added.

To conclude: In all reactions, a tetrel-silicon exchange was observed. However, the products were not the phosphino borane **141** but the phosphine boranes **150** and **151**. It was unclear where the additional proton for the formation of the phosphine borane originated. Still, the reaction of **145** with trichloroborane dimethylsulfide did not fully convert to the phosphine borane **151**. As the reaction with the other electrophilic boron species resulted fully in the conversion towards phosphine boranes **150** and **151**, a relation to the Lewis acidity of the boron species is suspected.

4.5.6   Reactions of the *bis*(Biphenyl)phosphide with Boron Electrophiles

Although the initial metalation-borylation experiments were already conducted (see chapter 4.5.2), with the isolated phosphide **107** in hand, reactions with various electrophilic boron species, e.g. boron trichloride in *n*-hexane, boron tribromide (neat), trimethylborate in toluene, boron trichloride dimethyl sulfide complex (neat), were investigated (Fig. 105).
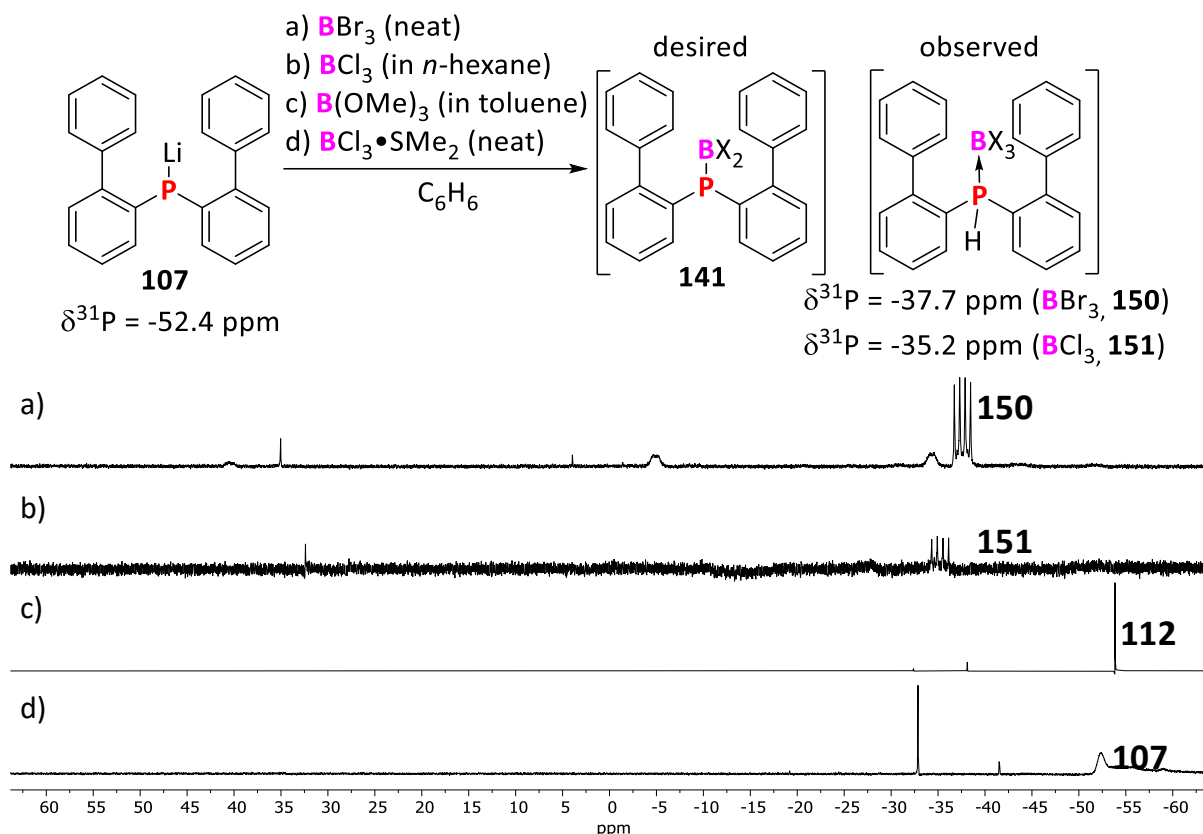

Fig. 105: ^{31}P{^{1}H} NMR (243 MHz) spectra of the reaction of phosphide **107** with a) BCl$_3$ (solution) b) BBr$_3$ (neat) c) B(OMe)$_3$ (solution) d) BCl$_3$•SMe$_2$ (neat) after dissolving in C$_6$D$_6$.

The reaction of the phosphide **107** with the Lewis acid boron tribromide resulted in the formation of the respective Lewis adduct **150** (^{31}P{^{1}H}: δ = -33.0 ppm) and three broad signals (δ = -34.3, -4.87, 40.9 ppm). Due to the broad doublet shape of these signals and the coupling constant (J = 145 Hz) all of these signals were possibly representing a B-P species. Unfortunately, none of them had a signal in the respective ^{11}B NMR spectrum. Upon reacting the phosphide **107** with a solution of boron trichloride, the Lewis adduct of the phosphine and boron trichloride was found (^{31}P{^{1}H}: δ = -35.1 (q, $^1J_{BP}$ = 145.8 Hz) ppm) albeit in low quantity, which was confirmed by the existence of the B-P coupling

in the ^{11}B NMR experiment (δ = 3.53 (d, $^1J_{BP}$ = 145.8 Hz) ppm). Using trimethyl borate as a boron precursor led to the exclusive formation of the phosphine and a product with a resonance at δ = -38.1 ppm that could not be isolated. Since trimethyl borate is a weaker Lewis-acid, the formation of the phosphine-borate adduct was not observed in the ^{31}P NMR. The outcome of this reaction was surprising since it is very unlikely that the proton resulted from the methyl groups. To use a boron trihalide species, which was should be not contaminated with traces of acids, the dimethylsulfide complex of boron trichloride was used as an electrophile. This electrophile is less reactive than the neat boron trichloride due to the coordination by the Lewis base leading to higher electron negativity on the boron. Upon addition of the complex to the phosphide under glove box conditions, a new signal (^{31}P{^{1}H}: δ = -32 ppm) was observed, while the signal for the phosphide was still present. Due to its shift, it was suspected that a coordinated phosphide species was present. In the ^{11}B NMR spectrum, only the signal for starting material was still present, which led to the conclusion that a reaction did not occur. Therefore, the reaction mixture was treated at elevated temperature to facilitate the reaction or to remove the dimethylsulfide as a gas but no change of neither ^{11}B nor ^{31}P NMR spectra was observed. This coexistence of the starting material and novel species was surprising as was not observed for the other boron species but in the tetrel-boron exchange reactions *vide supra*.

As the results of the experiments were inconclusive, the reaction of the phosphide **107** with trihaloboranes was conducted by titration experiments in high dilution (Fig. 106).

Fig. 106: ^{31}P{^{1}H} NMR (243 MHz) spectra of the reaction of phosphide **107** with left) BCl$_3$ (heptane solution) right) BBr$_3$ (heptane solution) after dissolving in deuterated benzene and mixing with increasing amount of trihaloborane solution. From top to bottom: 0.2 eq., 0.4 eq., 0.6 eq., 0.8 eq., 1.0 eq. and 1.2 eq. of a diluted solutions trihaloborane was added.

In both cases the decrease of the signal for the phosphide (^{31}P{^{1}H}: δ = -52.4 ppm) was noted but no intense novel signal could be observed. A minor signal set (δ = -31.0 (d, J = 130 Hz ppm) was observed at the addition with boron trichloride solution which origin remained unknown.

Simultaneously to the ^{31}P NMR experiments, ^{11}B NMR experiments revealed a novel signal occurring in the high field (δ = -11.8 ppm) (Fig. 107), while the ^{31}P NMR did not show any novel signal.
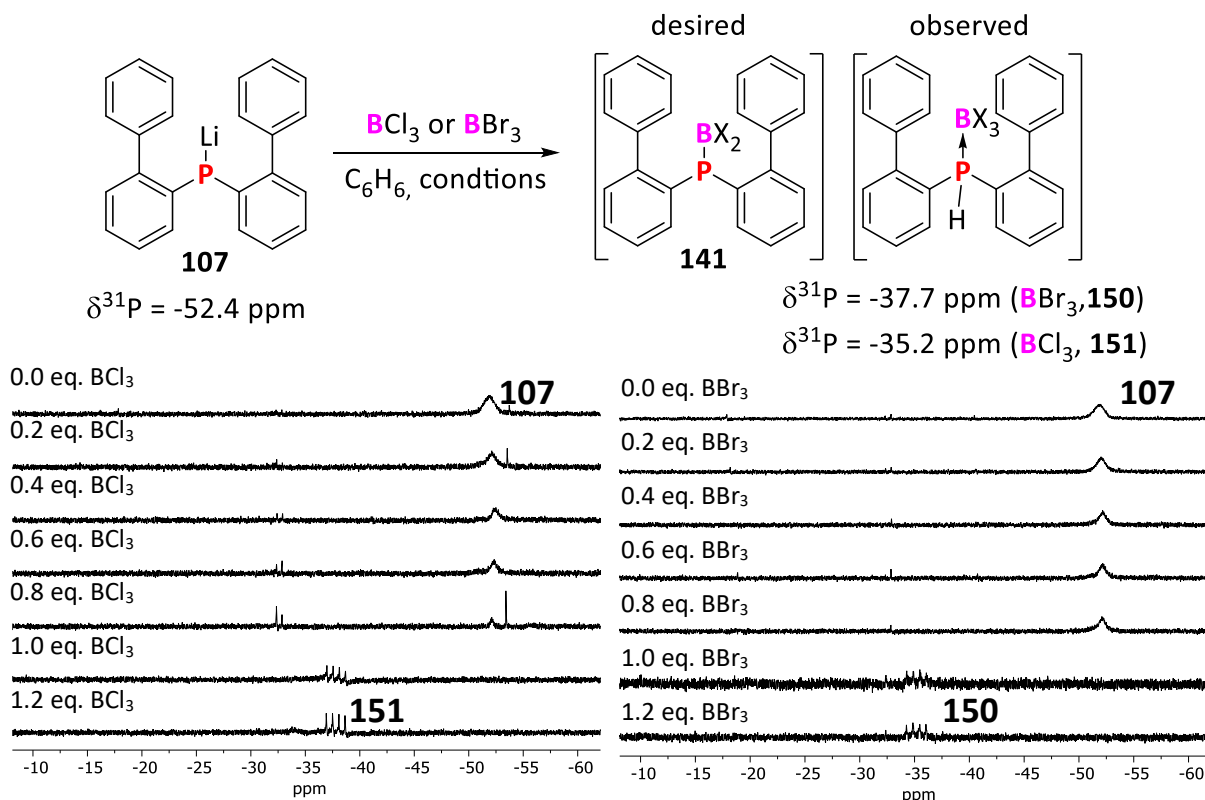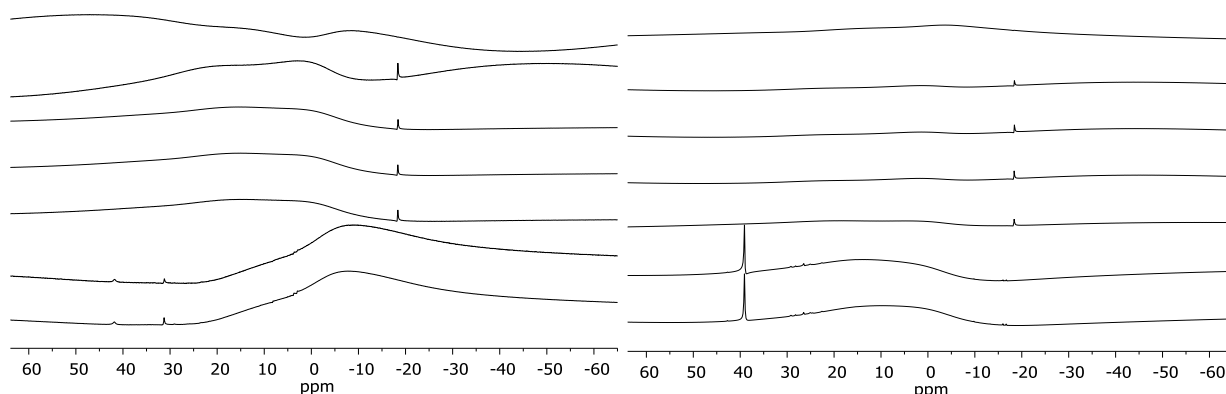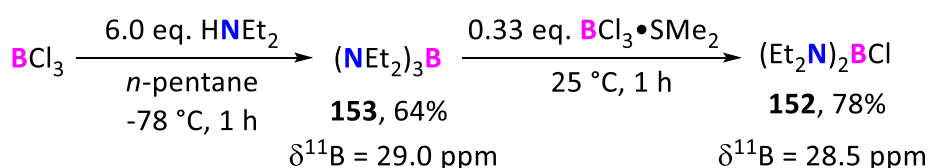

Fig. 107: ^{11}B{^{1}H} NMR (193 MHz) spectra of the reaction of phosphide **107** with left) BCl$_3$ (heptane solution) right) BBr$_3$ (heptane solution) after dissolving in deuterated benzene and mixing with increasing amount of trihaloborane solution. From top to bottom: 0.2 eq., 0.4 eq., 0.6 eq., 0.8 eq., 1.0 eq. and 1.2 eq. of a diluted solutions trihaloborane was added. Due to the disadvantageous signal/noise ration the phase was optimized for each spectrum.

Surprisingly, the signal's shift (δ = -18.3 ppm) was unaffected by either the bromo- or chloro-substituent at the boron, which discards the presence of a tricoordinated X$_2$BPAr$_2$-species. After addition of more than one equivalent trihaloborane species, the signal (δ = -18.3 ppm) disappeared in both cases and signals for the Lewis acid/ Lewis base adduct (δ = 3.42 (d, *J* = 145.2 Hz, (**151** with BCl$_3$) / -16.2 (d, *J* = 139.8 Hz) (**150** with BBr$_3$) ppm (barely visible) and for the free BX$_3$ (δ = 41.7 (BCl$_3$) / 38.9 (BBr$_3$) ppm) were detected. Moreover, an unidentified species at δ = 31.3 ppm in the case of adding the boron trichloride was found, which was unaffected by the addition of more BX$_3$ species. In general, in both ^{11}B and ^{31}P NMR experiments, the resonance of the observed species was low. This could indicate that NMR silent species or broad resonances were present.

Since borane and borate species seemed to be too reactive or contaminated with residual acid, we investigated the use of the diprotected *bis*(diethyl)amino chloroborane (**152**) as an electrophile. It was synthesized from boron trichloride and diethylamine to give **153**,[78] followed by a subsequent mixture with trichloroborane dimethylsulfide to give the product **152** in high yields.[79, 80]

$$\textbf{B}Cl_3 \xrightarrow[\substack{n\text{-pentane} \\ -78\,°C,\,1\,h}]{6.0\ eq.\ H\textbf{N}Et_2} (\textbf{N}Et_2)_3\textbf{B} \xrightarrow[25\,°C,\,1\,h]{0.33\ eq.\ \textbf{B}Cl_3\bullet SMe_2} (Et_2\textbf{N})_2\textbf{B}Cl$$

153, 64% $\qquad\qquad\qquad$ **152**, 78%

δ^{11}B = 29.0 ppm $\qquad\qquad$ δ^{11}B = 28.5 ppm

Scheme 81: Synthesis towards the double protected electrophilic boron species **152** via aminolysis of boron trichloride and reaction to **153** with borontrichloride dimethylsulfide complex.

The latter was reacted with phosphide **107** to form the respective phosphino borane **154** in quantitative fashion. This could be isolated in an excellent yield of 90% (Scheme 82).
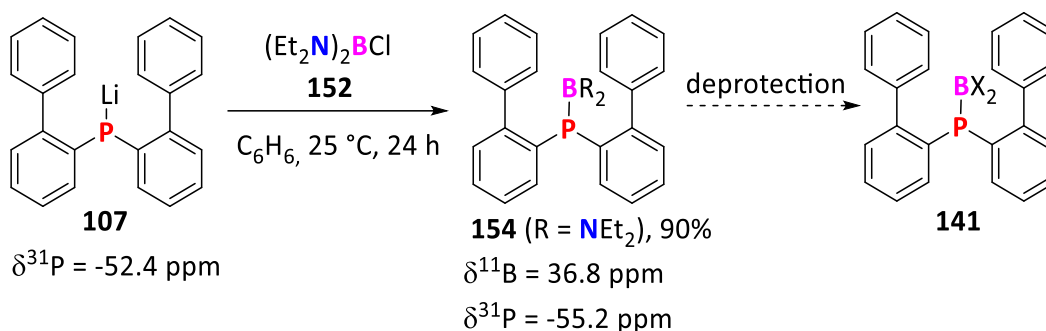
Scheme 82: Reaction of phosphide **107** with *bis*(diethylamino)chloroborane (**152**) giving the phosphino borane **154** in a high yield.

The product **154** showed a singlet in the ^{11}B NMR experiment in the low field region (δ = 36.8 ppm) and a singlet in the ^{31}P NMR spectrum (δ = -55.2 ppm) (Fig. 108).
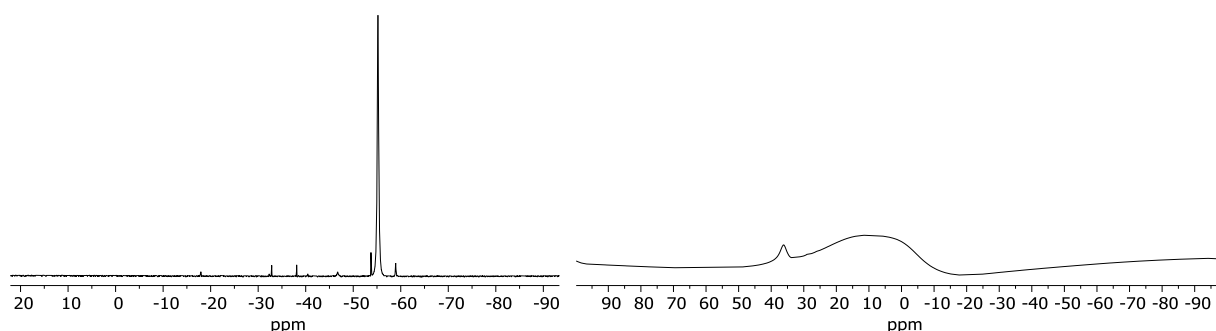

Fig. 108: ^{31}P{^{1}H} (243 MHz) and ^{11}B{^{1}H} (193 MHz) NMR spectra of **154** in C$_6$D$_6$.

The NMR shifts were in the same region compared to a similar structure, the diphenylphosphino(*bis*(diethylamino))borane (^{31}P{^{1}H}: δ = -47.6 ppm, ^{11}B{^{1}H}: δ = 41.3 ppm). [81]

Unfortunately, the product was obtained as an oil and did not crystallize even at low temperatures. Moreover, phosphino borane **154**, was not stable in solution and decomposed to the phosphine **112**.

Although a variety of electrophilic boranes (BBr$_3$, BCl$_3$, B(OMe$_3$) and BCl$_3$•SMe$_2$) were reacted with the phosphide **107**, only the reaction with borane **152** resulted in the formation of a phosphino borane. On the one hand, this could be related to the fact that species **152** presents an electrophile with only one substitution site. On the other hand, the amino groups at the boron in **152** increases the boron's electron density due to the BN-π-bond which decreases the Lewis acidity drastically, see the comparison of BX$_3$ and B(NMe$_2$)$_3$ presented by Beckett and coworkers.[82] This resonance stabilization supports the BP unit in structure **154**. In fact, the phosphorus lone pair in such a system is available since Nöth and Sze, [81] observed that the similar diphenylphosphino(*bis*(diethylamino))borane coordinated transition metals with phosphorus lone pair to give stable complexes. Therefore, the description of the B-P bond in such constellation is best described as borylphosphine according to the definition of Bailey and Pringle (see Fig. 38).[35]

Apparently, the stability or formation of diarylphosphino boranes is highly dependent on the Lewis acidity of the boron species. This contradicts the purpose of the borane for further ring annulation reactions where a high Lewis acidity of the BP-compound is required. Therefore, attempts were made to generate the diarylphosphino(dihalo)borane *in situ* from phosphino borane **154**. For the deprotection of the phosphinoborane **154**, to access the BP-compound **115**, two different concepts were investigated: a) reaction with two-thirds of boron trichloride b) removal of the amino protecting groups with hydrochloric acid to access phosphino(dihalo)borane **115** (Scheme 83).
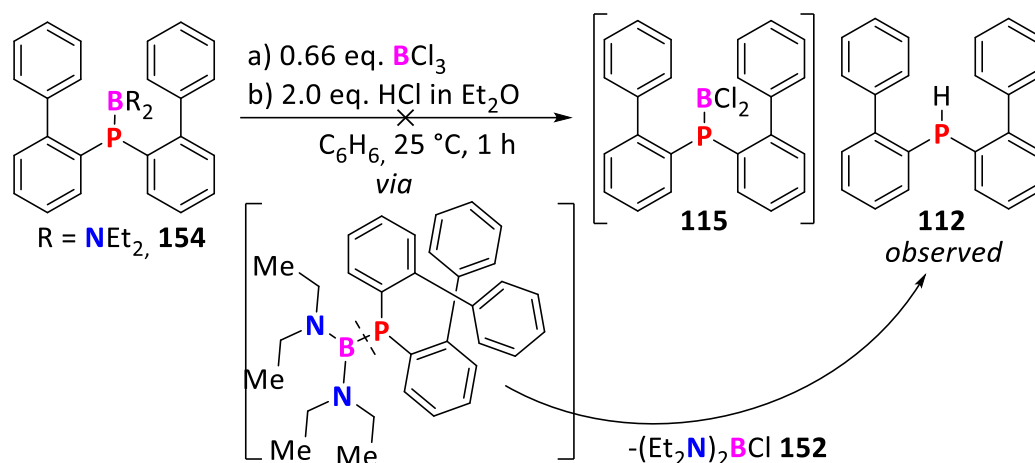
Scheme 83: Deprotection of phosphino borane **154** by metathesis or acidolysis to access key intermediate **115** led to the formation of the phosphine **112**.

Unfortunately, in both reactions exclusively the formation of the respective phosphine **112** was observed. This indicated that the B-P bond was rather easily cleaved than the B-N bond under these conditions.

4.5.7 Cyclization Reactions

Since the isolation of the phosphino(dihalo)borane **141** remained elusive, the phosphine borane adducts **150** and **151**, which were observed in most reactions, were determined as a possible precursor for a dual ring annulation reaction to provide the targeted **BP-DBC**. This further requires an initial elimination of a HX species to obtain the intermediate phosphino(dihalo)borane **141**. Similar reactions were performed by Wagner and coworkers[83] with tBu$_2$PH•BX$_3$ using two equivalents LiHMDS as base forming the dimer (tBu$_2$PH•BX$_3$)$_2$. This protocol was adapted to the parent system and phosphine tribromoborane/trichloroborane **150** and **151** were reacted with two equivalents of LiHMDS to give the phospino borane **141** (Fig. 109).
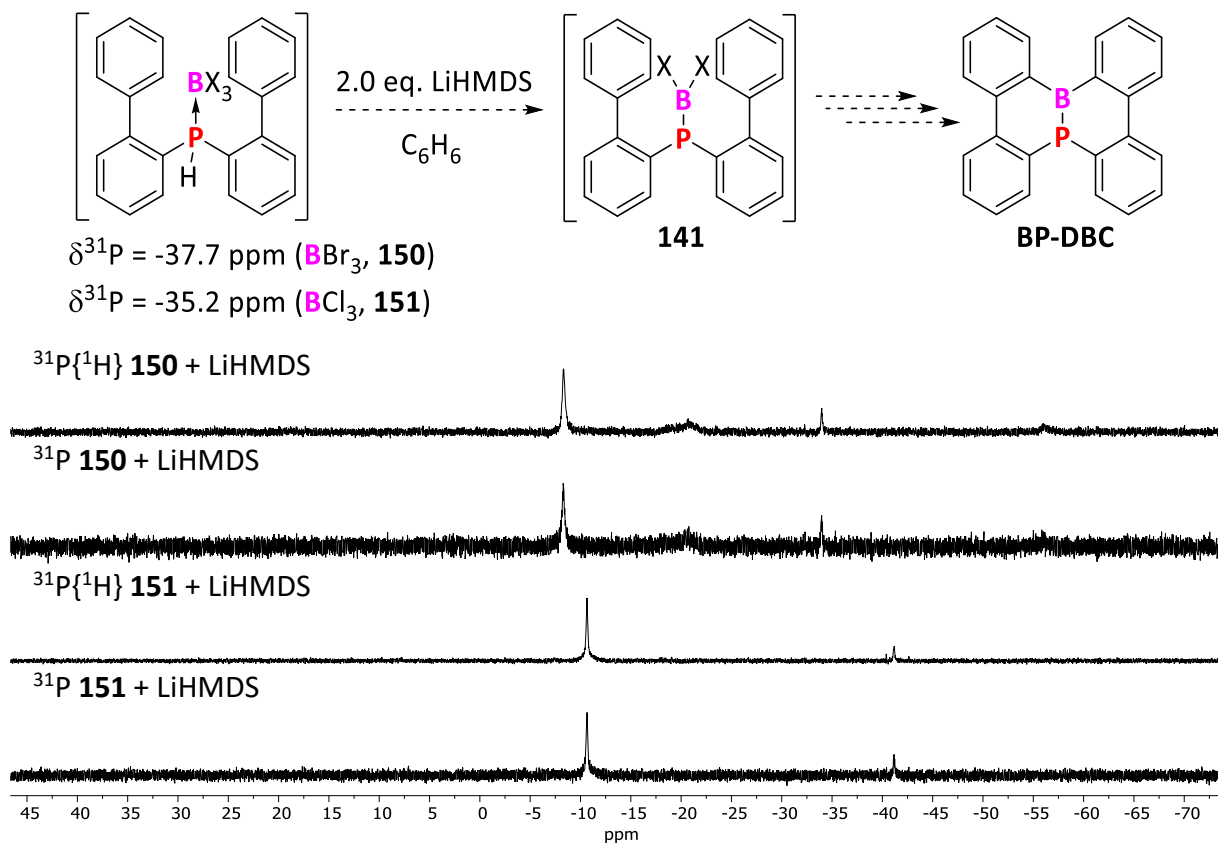

δ^{31}P = -37.7 ppm (**B**Br$_3$, **150**)

δ^{31}P = -35.2 ppm (**B**Cl$_3$, **151**)

Fig. 109: ^{31}P{^{1}H}/^{31}P (243 MHz) spectra of the reaction Lewis adducts **150** (the top two)/ **151** (the bottom two) with LiHMDS to access the phosphino borane **141**.

As the LiHMDS was added to the phosphine trihaloborane species an intense yellow color occurred, indicating chemical changes at the phosphorus center, which was shown by ^{31}P NMR experiments. The formation of the tricoordinated phosphino(dihalo)borane species should result in a high-field shift of the signal compared to the starting material. In both reactions, broad signals at δ = -10.6/-8.3 ppm were found in the ^{31}P{^{1}H} NMR spectra. These signals remain unchanged in the coupled experiment and therefore the loss of the phosphine proton is highly probable. The ^{11}B NMR experiments revealed no signal at all. Further analysis of these species after methanolysis failed.

Overall, the formation of the phosphino(dihalo)borane **141** is very unlikely due to the low intensity of the signals in the ^{31}P NMR and the absence of a signal in the ^{11}B NMR.

However, also elimination of a HX species followed by direct ring annulation with a Lewis acid was investigated. To pursue this, the phosphine trihaloboranes **150** and **151**, respectively, were mixed with an organic base (TEA/TMP) and a Lewis acid (AlCl$_3$). The progress of these reactions were observed with ^{31}P$\{^1$H$\}$ NMR experiments (Fig. 110).
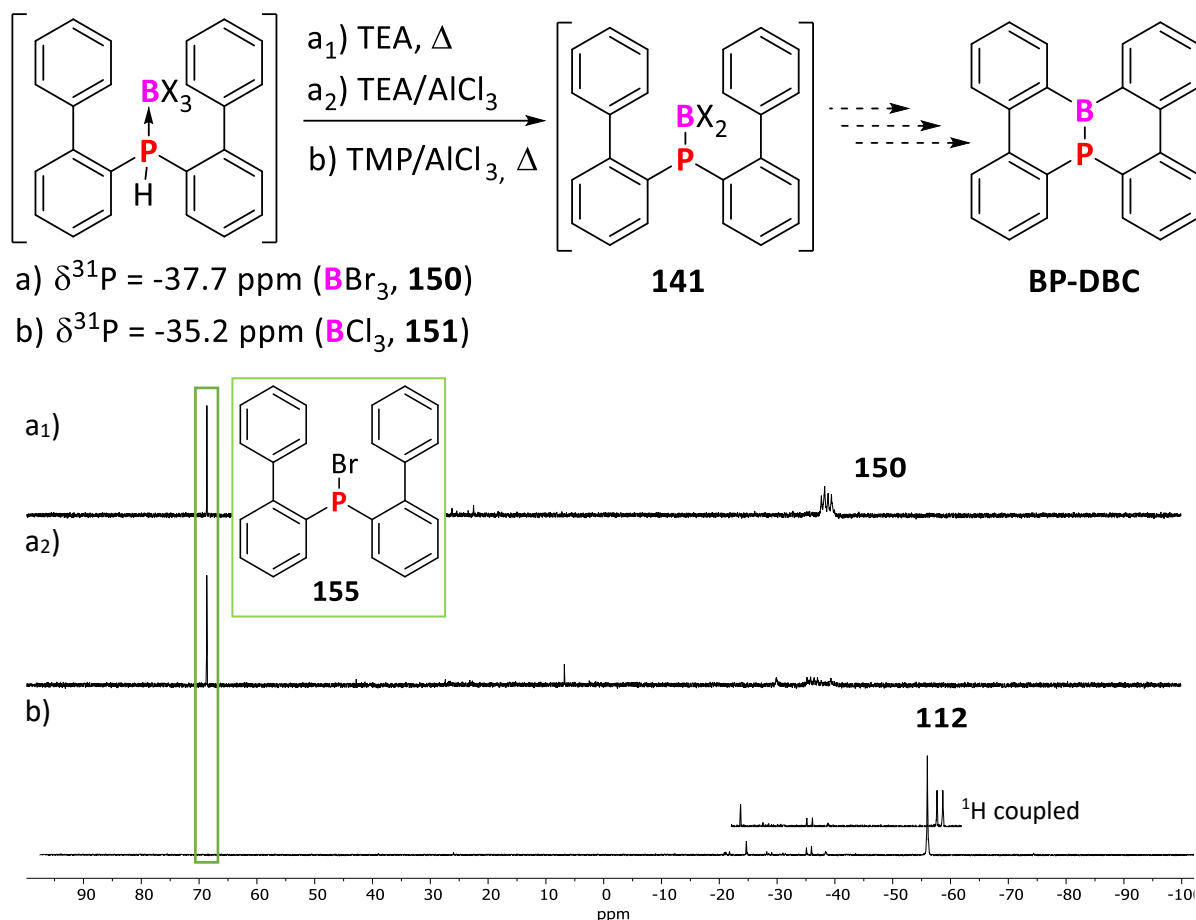

a) δ^{31}P = -37.7 ppm (**B**Br$_3$, **150**)

b) δ^{31}P = -35.2 ppm (**B**Cl$_3$, **151**)

Fig. 110: ^{31}P$\{^1$H$\}$ (243 MHz) spectra of the reaction of phosphine tribromoborane 150 with a$_1$) TEA in dichlorobenzene, 180 °C, 5 h a$_2$) TEA and AlCl$_3$ in dichlorobenzene, as prepared and b$_1$) phosphine trichloroborane 151 with TMP and AlCl$_3$ in dichlorobenzene, 180 °C, 14 h.

Heating the phosphine tribromoborane **150** with triethylamine at high temperatures (180 °C, 5 h), led to the formation of a novel signal at δ = 68.7 ppm, which was assigned to the diarylbromophosphine **155** and indicated the decomposition of the phosphine borane. After the addition of the Lewis acid (AlCl$_3$), the phosphorus species were mostly converted to its respective diarylbromophosphino **155**.

A similar reaction performed with the diarylphosphino trichloroborane adduct **151**, TMP and AlCl$_3$ did not give the desired product but the regeneration of the diarylphosphine **112** after handled at high temperatures.

Overall, in these reactions, it appeared that the phosphorus once decomposed into its diarylbromophosphine **155** and once into its phosphine **112** species.

4.5.8 Investigation on BP-phenanthrene as Model BP-Compound for Ring Annulation Reactions

Since almost all attempts to synthesize a stable *bis*(biphenyl)phosphine joint with an electrophilic boron were unsuccessful, it was concentrated on the smaller **BP-phenanthrene** system. This represents the smallest carbocyclic system where an electrophilic BP-annulation reaction can be investigated in detail. Its retrosynthetic analysis shows that already present methods and reagents could be used to access the **BP-phenanthrene** (Scheme 84).
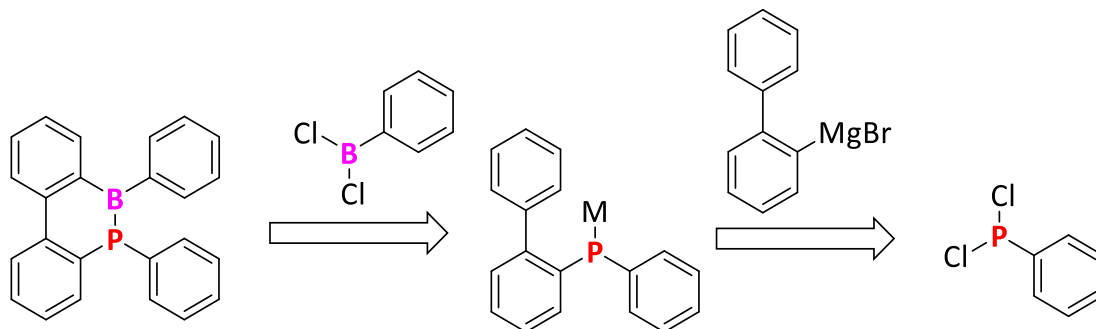
Scheme 84: Retrosynthetic analysis of the smaller **BP-phenanthrene** to investigate the ring annulation reaction.

The forward synthesis of **BP-phenanthrene** was readily conducted with similar starting molecules as utilized beforehand (Scheme 85).
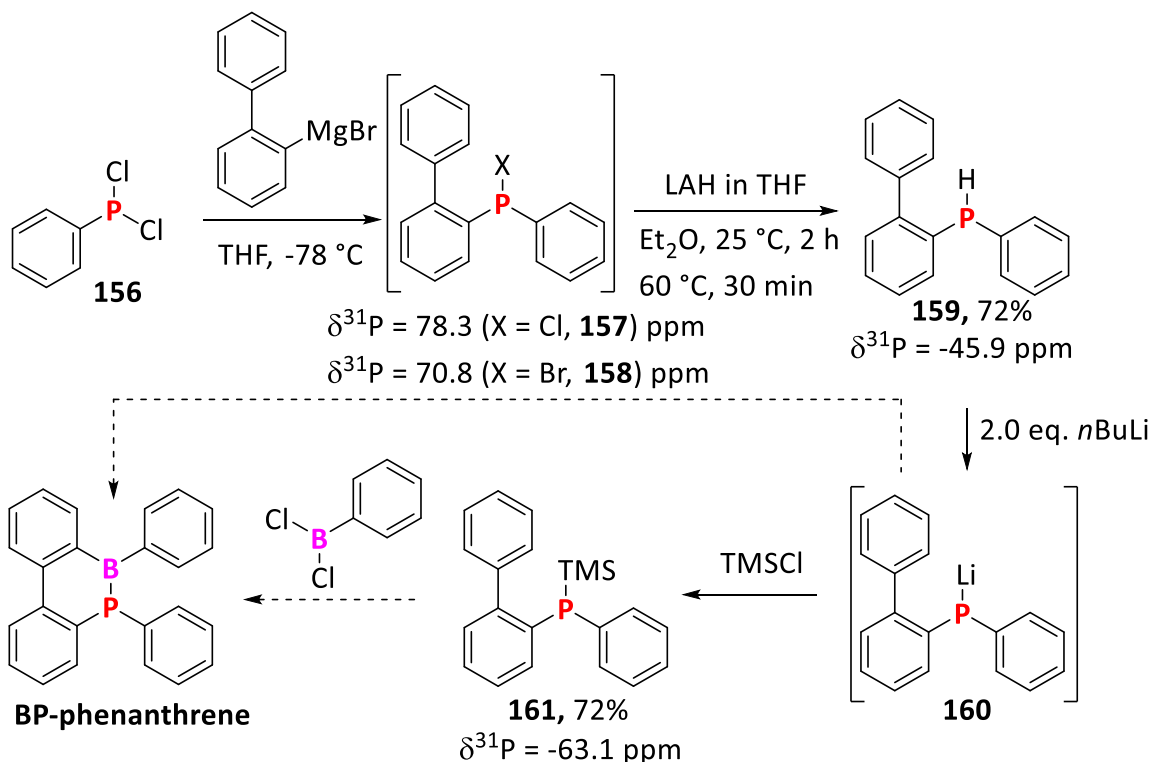
Scheme 85: Syntheses towards **BP-phenanthrene**.

Dichlorophenylphosphine (**156**) and an equimolar amount **BiPhMgBr** were reacted to result in a quantitative formation of the diarylchlorophosphine (**157**). This was found as a mixture of chloro and bromophosphine (**157/158**) due to halogen scrambling (observed by $^{31}P\{^1H\}$ NMR spectroscopy). Without isolation, the reduction with lithium aluminum hydride was performed and the phosphine **159** was isolated in a yield of 72% by inert Kugelrohr distillation. From this precursor, the synthetic route was followed as mentioned for the *bis*(biphenyl)phosphine (see Chapter 4.6.2). The lithiation of

phosphine **159** led to the observation of a strong precipitate and therefore, no NMR experiments on the phenyl(biphenyl)phosphide **160** could be performed. This observation contrasted with the formation of the *bis*(biphenyl)phosphide (**107**) which exhibit a high solubility. However, the *in situ* formation of phosphide **160** is highly probable as the reaction with trimethylsilyl chloride formed the silyl phosphine **161** in high yields.

Since methods to synthesize the silylphosphine **161** and phosphide **160** were developed, we further conducted lithium/boron and silicon/boron transmetalation experiments with dichlorophenyl borane (**PhBCl₂**) and followed the reaction *in situ* by ^{31}P NMR experiments (Fig. 111).
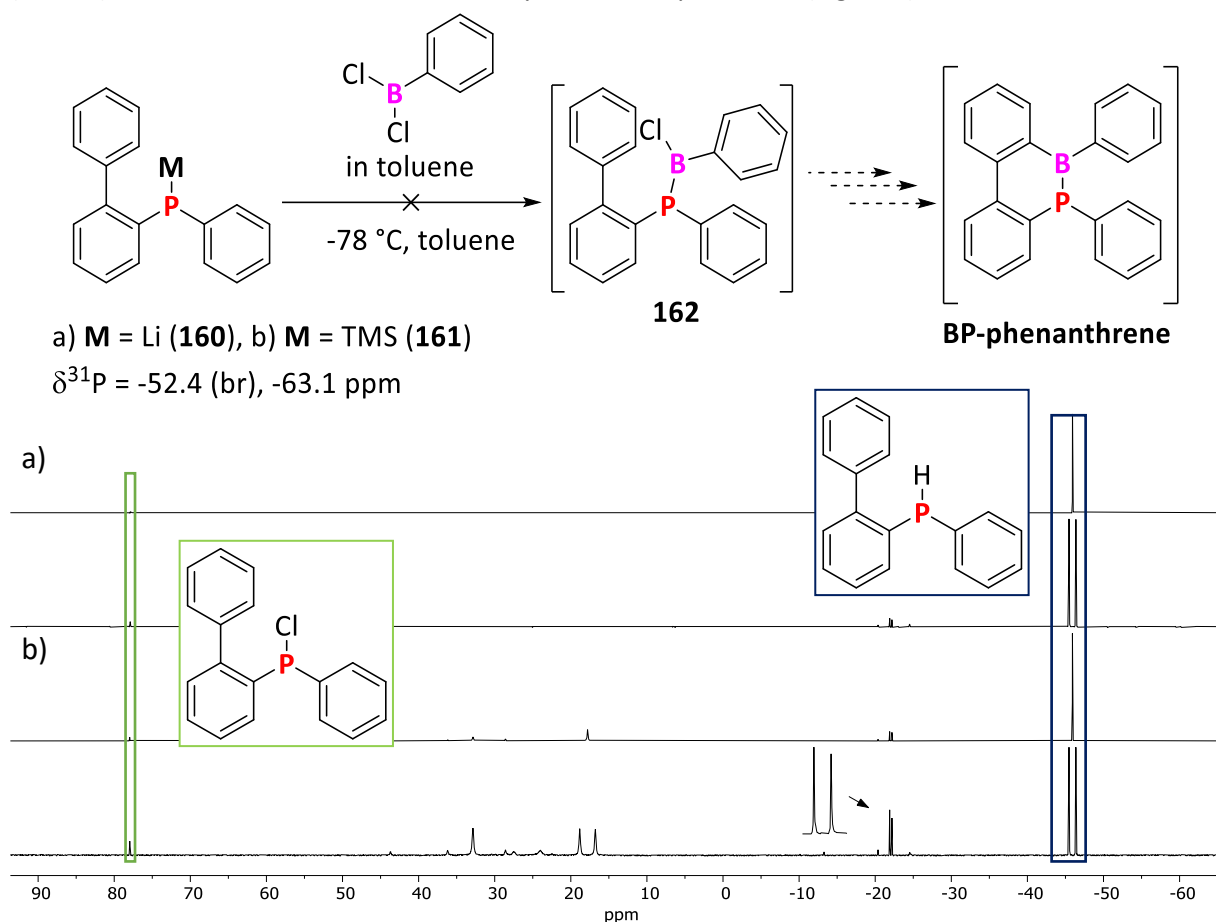

a) **M** = Li (**160**), b) **M** = TMS (**161**)

δ^{31}P = -52.4 (br), -63.1 ppm

Fig. 111: ^{31}P{^{1}H} (243 MHz) spectra of the reaction mixtures with a toluene solution of PhBCl₂ in toluene was added to a) **160** or b) **161** at -80 °C and warmed to 25 °C. The ^{31}P NMR trace of the region with P-P coupling at -22 ppm is shown as inset.

The addition of a solution of dichlorophenyl borane into a solution of the phosphide **160** led to the formation of the phenyl(biphenyl)phosphine (**159**) (δ = -45.9 ($^1J_{PH}$ = 414 Hz) ppm). However, the reaction of silylphosphine **161** with **PhBCl₂** resulted mainly in the acidolysis of the silylphosphine to retain the phenyl(biphenyl)phosphine (**159**) but also various side-products. Some of these signals could be assigned to a dimerization product with a P-P bond ((δ = 22.0 (d, $^1J_{PP}$ = 65.8 Hz) ppm) and the phenyl(biphenyl)chlorophosphine (**157**, δ = 78.0 (s) ppm). For both reactions, the ^{11}B NMR revealed the formation of various species with none of them holding a P-B coupling. Overall, also in these proof-of-concept reactions mostly the regeneration of the phosphine and in some cases oxidation products were observed. Additionally, the investigation on this reaction should be followed in the future.

4.5.9 Structural Features

During this research project crystal structures of *bis*(biphenyl)di*iso*proylamido phosphine (**110**), *bis*(biphenyl)phosphine (**112**), *bis*(biphenyl)phosphine borane adduct (**114**) and lithium *bis*(biphenyl)phosphide (**107**) were characterized by single-crystal X-ray analysis. In the following, the structures will be discussed and a conclusion towards their reactivity will be outlined. Initially, all structures are depicted, and their key crystal parameters are listed below (Fig. 112, Tab. 16).

110

112

107 (dimer)

114
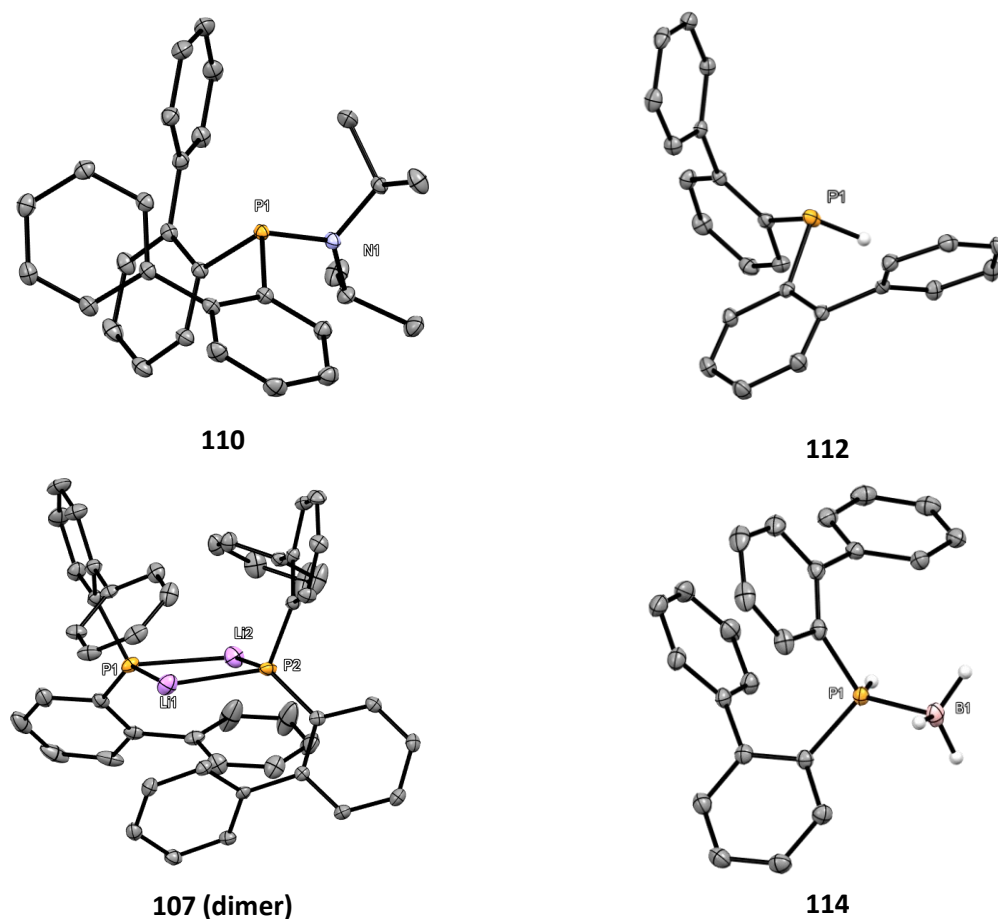
Fig. 112: Overview of isolated crystal structures. For **114** residual solvent molecules and hydrogen atoms were removed for clarity.

Tab. 16: Overview key crystal structure details for **110**, **112**, **107** and **114**.

	110	112	107	114
crystal system	triclinic	monoclinic	monoclinic	monoclinic
space group	P-1	P2$_1$/c	P2$_1$/c	P2$_1$/n
P-X bond length	1.6917(7) Å	1.32(2) Å	1.30(1)/1.926(1) Å	2.503(2)/2.490(3) Å 2.507(3)/2.567(2) Å
P-C bond length	1.8491(6) Å	1.837(1) Å	1.817(1) Å	1.820(1)/1.822(1) Å
P-C bond length	1.8546(9) Å	1.847(1) Å	1.812(1) Å	1.821(1)/ 1.824(1) Å
∠$_{C-P-C}$	99.39°	102.30°	104.93°	104.33°/103.58°
Σ P	307.71°	297.23°	316.13°	326.29°
φ biaryl$_1$	-56.2(1)°	-65.2(2)°	-49.7(1)°	66.2(2)°/69.3(2)°
φ biaryl$_2$	-55.6(1)°	-65.6(2)°	-113.3(1)°	76.3(2)°/58.6(2)°

While structure **110** crystalized in a triclinic crystal system, the other structures were found in a monoclinic crystal system. Structure **110** has a P-N bond length of 1.6917(7) Å which is a typical value for P(III)-N bond systems similar to the 1,2-*bis*(diphenylphosphino)(benzyl)aminoethane (1.68(1) Å)[84]. Interestingly, this structure did not oxidize whereas its phenyl-derivative was prone to oxidization. Although the sum of angles at the phosphorus (Σ = 307.71°) indicated sufficient space for oxidation events, the similar biphenyl of dialkylbiphenyl phosphines, also referred to as Buchwald ligands,[85] is known to prevent the ligand's oxidation effectively.[86] The C-P-C angle (99.39°), of structure **110** was the lowest value in the here reported quartet. The biphenyl groups of **110** showed internal twisting as indicated by the respective large torsion angles (56.2° and 55.6°).

The crystal structure of phosphine **112** had the space group P2$_1$/c. The sum of angles at the phosphorus atom (Σ = 297.23°) was the lowest from the here presented structures. As visualized, the geometry of the biphenyl ligand was so spacious that still chemical modification at the phosphorus atom was possible and the structure underwent oxidation rapidly. Therefore, it was protected with borane to form structure **114** which was found in space group P2$_1$/c. The key interest in this system was the P-B bond length, which was determined as 1.926(1) Å. This was similar to a common P-B bond length of 1.915(3) Å in *bis*(*ortho-N,N*-dimethylaniline)phosphine borane.[87]

The lithium *bis*(biphenyl)phosphide (**107**) crystalized as a phosphide-bridged dimer in the space group P2$_1$/n. The central unit of the crystal structure was a quasi-planar four-membered rhombic P$_2$Li$_2$ ring with a small dihedral angle (φ(P-Li-P-Li) = 4.73°) and nearly orthogonal Li-P-Li angles ($\angle$(Li1-P1-Li2) = 80.60°, $\angle$(Li1-P2-Li2) = 82.18). The biphenyl ligands filled the edges in this ring structure in an orthogonal fashion. The P-Li bond distances (2.503(2)/2.490(3) Å, 2.507(3)/2.567(2) Å) were similar compared to other reported organo arylphosphides.[88] For the carbon atoms of the second biphenyl ring and the lithium atoms Li•••π interaction was present (Fig. 113).

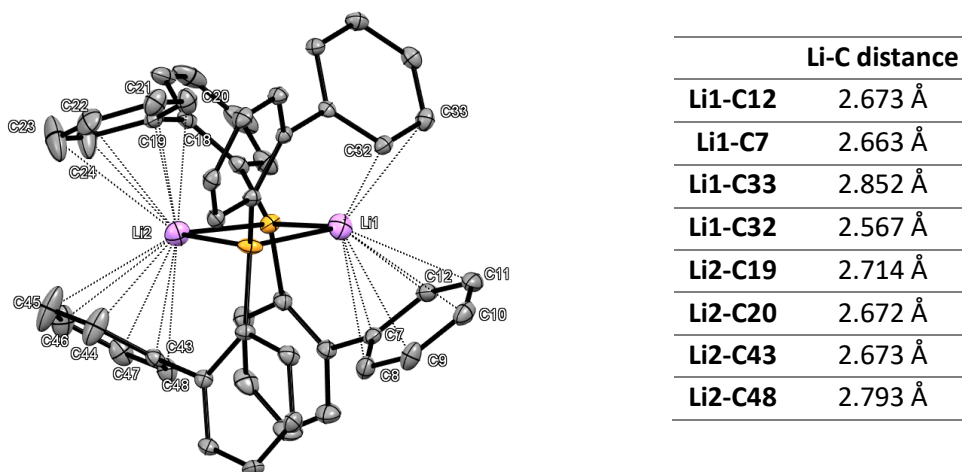|	Li-C distance
Li1-C12	2.673 Å
Li1-C7	2.663 Å
Li1-C33	2.852 Å
Li1-C32	2.567 Å
Li2-C19	2.714 Å
Li2-C20	2.672 Å
Li2-C43	2.673 Å
Li2-C48	2.793 Å

Fig. 113: Overview of isolated crystal structures of the phosphide **107** and close contacts of the lithium atom with various carbon atoms. The hydrogen atoms were omitted for clarity.

Due to the sterically demand of the biphenyl ligands, the central Li$_2$P$_2$ ring appeared to be peripherical shielded and hinders the formation of amorph polymeric structures. Hence, this allowed the isolation of the **107** dimer. The dimeric motif is common for organolithium structures, e.g. see *ortho*-tolyllithium and *para*-tolyllithium[89]. Furthermore, it should be highlighted that this crystal structure is one of the rare examples of a phosphide where the metal is not coordinated by any nitrogen or oxygen. For such an example including a planar P$_2$Li$_2$ ring, the diphenyl lithium phosphide TMEDA adduct is reported.[90] Overall, the close interaction of the biphenyl ligands with the lithium atoms might explain the high

stability of the phosphides in solid and solution. This was in good agreement with the observation that the phosphide decomposed as it was mixed with coordinating solvents (THF, diethyl ether).

4.5.10 Conclusion and Perspective

In comparison with BN-chemistry, the underdevelopment of chemical methods to implement BP unit in organic structures have hampered the screening of BP-based optical materials. Therefore, initially synthetic methods need to be developed. To investigate the effect of a BP-substitution and to implement such a motif, a carbon scaffold that has been previously reported for BN-PAHs motifs was chosen: dibenzo[g,p]chrysene (**BP-DBC**) and tetrathienonaphthalene (**BP-TTN**) (Fig. 114).
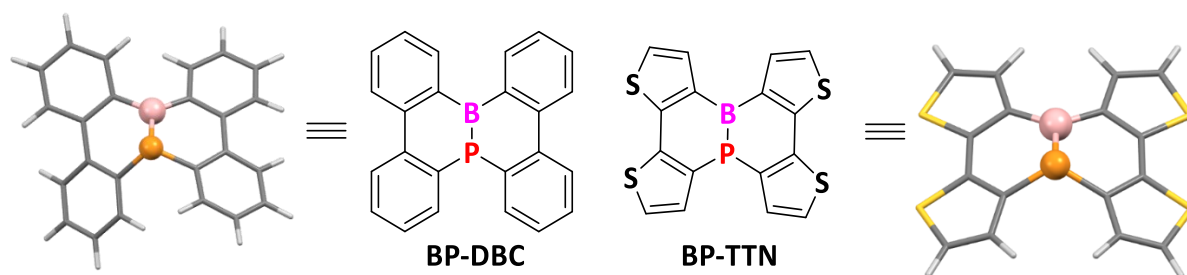

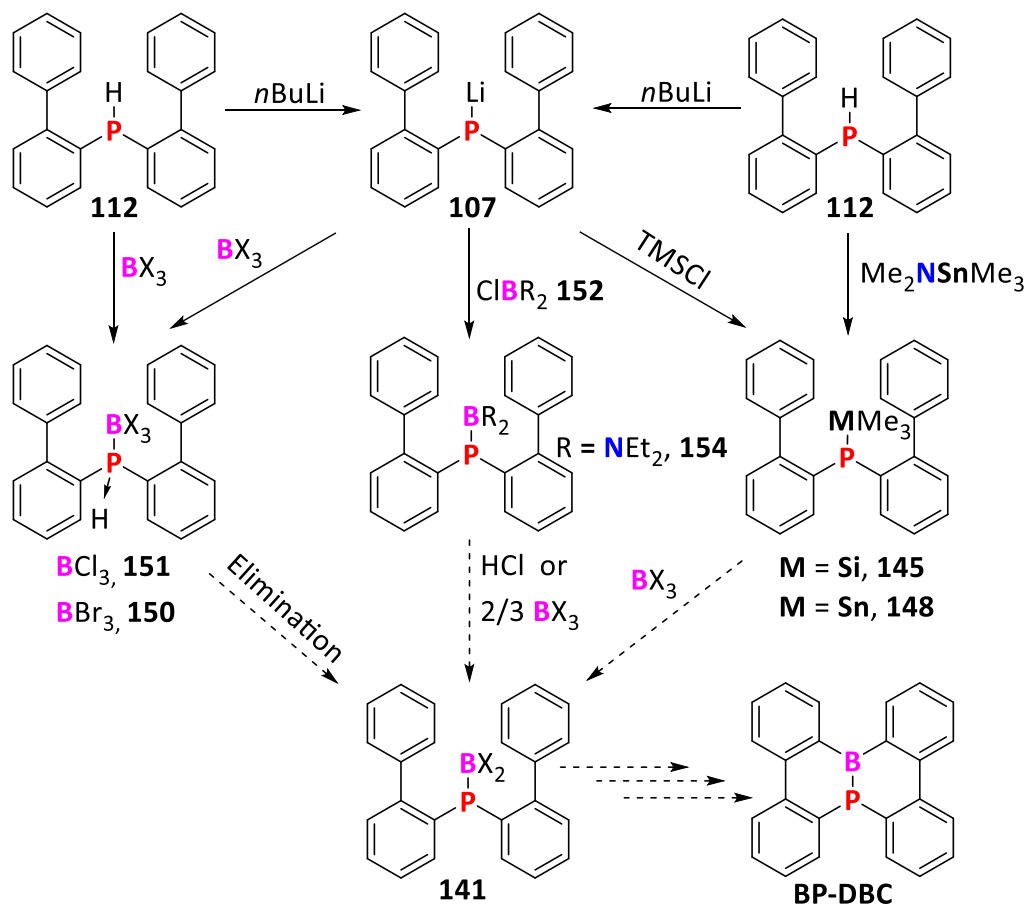**Fig. 114**: BP-substituted dibenzo[g,p]chrysene (**BP-DBC**) and tetrathienonaphthalene (**BP-TTN**).

For the BP-systems **BP-DBC** and **BP-TTN**, the geometries, frontier orbitals (HOMO/LUMO), bonding situation (NBO analysis), aromaticity and absorption properties were calculated by density functional theory and compared to the BN-structures and their all-carbon congeners. It was found that the BP units did not feature a completely planar conformation as it was found for the BN unit. The sum of angles at the phosphorus atom was determined **BP-DBC** (Σ = 309.88°) and **BP-TTN** (Σ = 332.63°) respectively which indicated pyramidalization of the phosphorus atom in the π-system. Due to the implementation of the more spacious phosphorus atom and its preferred pyramidal geometry, **BP-DBC** held a more distorted orientation of the two-biphenyl ring system. In the case of **BP-TTN** this effect led to the planarization of the **TTN** scaffold with an out-of-plane orientation of the BP unit. Fundamentally, the BP-derivatives held a stronger double bond character than their BN-analogs as well as an inverted polarization of the boron-phosphorus bond. Here the boron holds more electron negativity than the phosphorus atom due to the electron donation from the phosphorus lone pair. The BP-motifs exhibited a narrower HOMO-LUMO gap and a bathochromically shifted absorption due to a strongly stabilized LUMO level. Determination of the NICS values of the BP-derivatives exhibited a decrease in the aromaticity of the internal phosphaborine rings compared to the azaborine or benzene derivatives. Due to these findings, both model systems were found to be suitable candidates for a synthetic examination.

Initially, a phosphorus precursor was synthesized and preliminary experiments were conducted towards the **BP-DBC** model system. After numerous optimizations of the synthesis towards the diaryl(amino)phosphine **110**, the diarylchlorophosphine **111** and the key motif *bis*(biaryl)phosphine **112** could be isolated (Scheme 86).
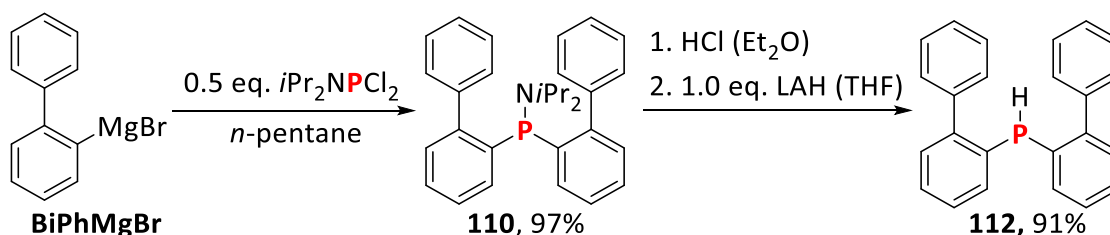
Scheme 86: The phosphine **112** was obtained in high yields.

This phosphine **112** was the precursor for several synthetic approaches to obtain the BP-substituted dibenzochrysene (Scheme 87).
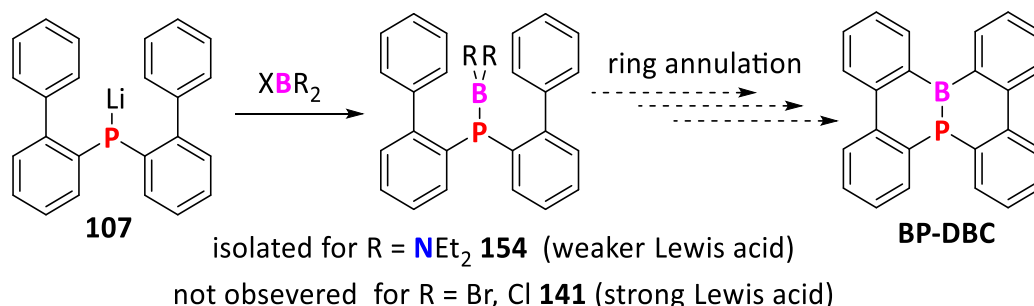

Scheme 87: Synthesis toward BP-substituted dibenzochrysene (**BP-DBC**).

Initially, the phosphide was generated *in situ* and various electrophilic (aryl)borane species were reacted with it leading mostly to the formation of the phosphine **112** or the phosphine borane adduct **114**. The latter could be selectively accessed by reaction of the phosphine **114** with trihaloboranes as Lewis acid-base adduct. Unfortunately, no novel BP-species were obtained when this adduct was treated with strong bases, Lewis acids and heat. In fact, side-products of reactions with the Lewis acid leading to the oxidation of the phosphorus were observed throughout this process. This could limit further attempts for the ring annulation to access BP-substituted PAHs by these methods.

However, to install a better leaving group at the phosphorus atom, which should allow the subsequent conduct of a metal-boron exchange, the synthesis of trimethyltetrelphosphines and lithium phosphide was successfully investigated. However, in all cases, a metal-boron exchange reaction did not form the desired phosphino(dihalo)borane **141** but acidolyzed by-products. The reaction of the phosphide with boron trichloride and tribromide was investigated in depth by titration. In fact, no clear evidence for the formation of **154** was found. Upon addition of one equivalent trihaloborane, the ^{31}P NMR spectra remained silent and as the next step, the phosphine borane adducts were formed.

Finally, the reaction of lithium diarylphosphide with a deprotected electrophilic boron precursor led to the formation of a tricoordinated phosphino borane **154**. It became evident that the reaction of phosphide **107** with several boron species was only successful for the reaction with the amine-substituted chloroborane **152**. Therefore, it was concluded that Lewis acidity of the borane had a major

contribution to the stability of the phosphinoborane. Hence, if only mild Lewis acidic borane species form stable products after reaction with phosphide **107**, the following ring annulation reaction towards the **BP-DBC** with the less acidic borane might be unfavorable (Scheme 88).


isolated for R = **N**Et$_2$ **154** (weaker Lewis acid)

not obseverd for R = Br, Cl **141** (strong Lewis acid)

Scheme 88: The influence of the Lewis acidity on the stability of the BP-species **141** contradicts with the required Lewis acidity for the ring annulation reaction towards **BP-DBC**.

Attempts to interconvert species **154** to the more Lewis acidic **141** *in situ* could be a possible way to circumvent this problem. Though, neither deprotection of **154** with hydrochloric acid nor its reaction with a two/third excess of trihaloborane were successful. For further reactions, modification on the phosphorus or boron atom might endure the formation of a phosphino borane species.

In total, phosphide **107**, two trimethyltetrel-substituted phosphines **145/148** and phosphino borane **114** were synthesized to access the tricoordinated BP-compound **141**, which represents a valuable precursor for further ring annulation reactions. For most key intermediates, the crystal structure could be determined. Here, the crystal structure of the phosphide **107** indicated interaction of the biphenyl ligands with the lithium atoms.

In summary, the presented synthetic procedures did not form the desired BP-substituted dibenzochrysene but gave good insights into the chemistry of *bis*(biphenyl)phosphines. To concentrate more on the ring annulation reaction, the smaller **BP-phenanthrene** was chosen as a synthetic model system to investigate the ring-closing reaction in detail and to reduce the ring annulation to one electrophilic substitution rather than a tandem reaction as in **BP-DBC**. Accordingly, the synthesized trimethylsilylphosphine **161** and the lithium phosphide **160** were reacted with **PhBCl$_2$** (Scheme 89).
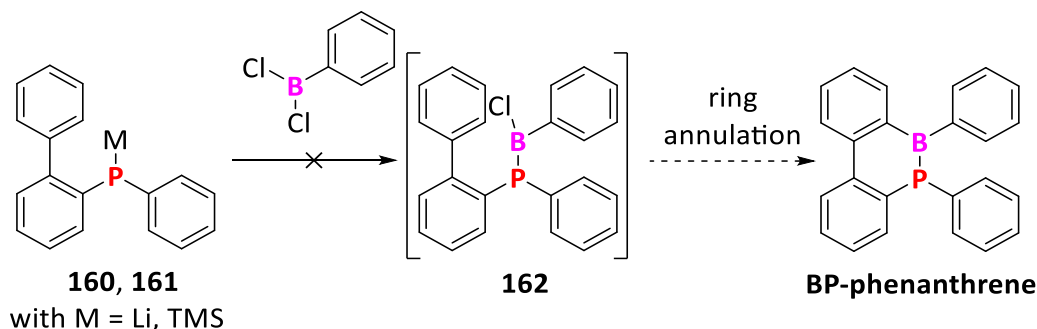
Scheme 89: Utilizing phenyl(biphenyl)phosphide **160** and phenyl(biphenyl)phosphine **161** to access **BP-phenanthrene** *via* ring annulation reaction with dichlorophenylborane (**PhBCl$_2$**).

Unfortunately, the formation of **BP-phenanthrene** was not found but acidolysis was observed. During this work, it appeared that the tricoordinated BP-bond is highly sensitive, leading to the cleavage of the BP-bond in most cases. Therefore, the synthetic equivalence of BP and BN-substituted PAHs and the transferability of the annulation reactions were not found.

As such different insights were obtained for a successful and robust synthesis of a BN unit and the complex synthesis of BP units in PAHs, maybe other concepts to synthesis BP-PAHs must be devolved.

The idea to reduce the complexity of the model systems, in general, could be useful to initially generate synthetic methods to generate BP-PAHs by ring annulation reaction or other methods. So far BP-phenanthrene remained elusive but Wagner and coworkers[91] obtain a BP-phenanthrene with tetracoordinated boron and phosphorus (Scheme 90).
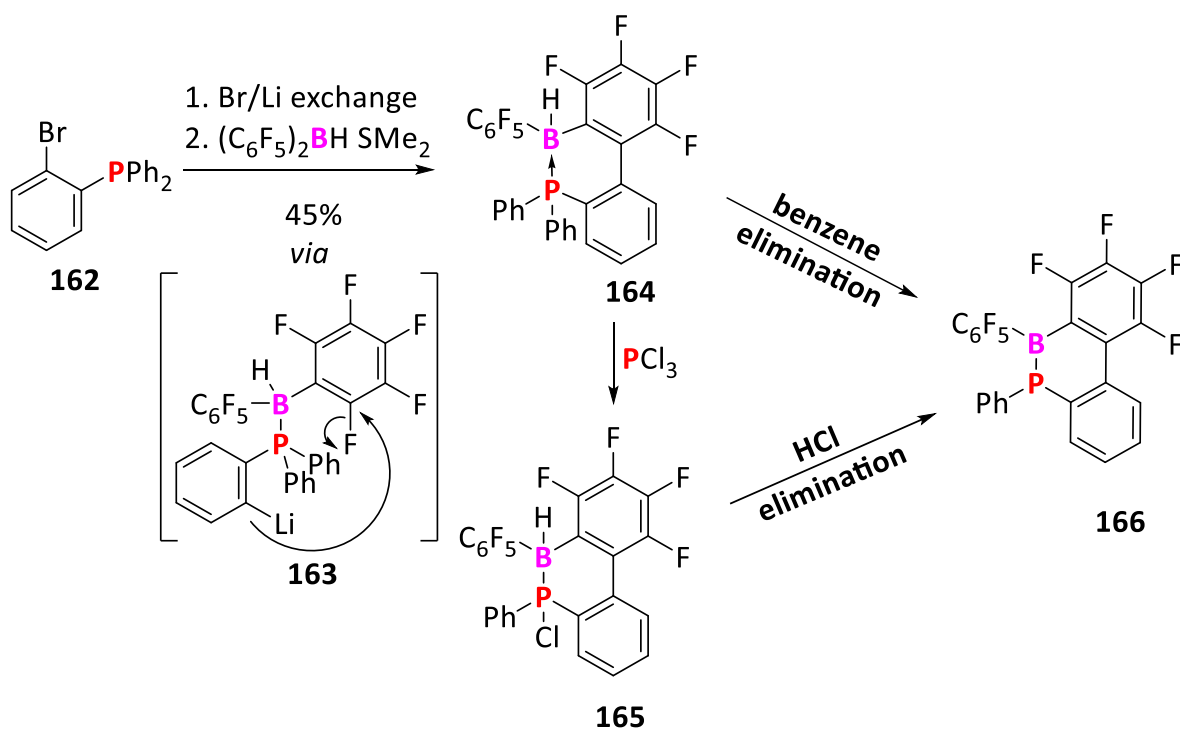
Scheme 90: Suggested synthesis towards BP-phenanthrene **165**.

Due to the fact that the dative P-B bond in **163** is formed initially, the attack of the *ortho*-lithiated carbon atom occurs at an electrophilic carbon atom at the pentafluorophenyl substituent. The resulting BP-phenanthrene derivative **164** holding both tetracoordinated boron and phosphorus atoms were isolated but further reactions were not performed. However, direct elimination of either benzene or HCl, after substitution of one phenyl group by chloride using phosphorus trichloride, could access the BP-phenanthrene derivative **166**. As the BP-bond orbital overlap is maximized when boron bears electron-withdrawing groups, in such a system the formation of a phosphinoborane bonding situation should be stabilized and the optoelectronic properties compared to BN-phenanthrenes should be comparable.

Another synthetic way to generate BP-phenanthrene derivatives could be the reduction of a 2,2'-disubstituted biphenyl holding a diarylborane and dichlorophosphine group, followed by 1,2-aryl shift (Scheme 91).
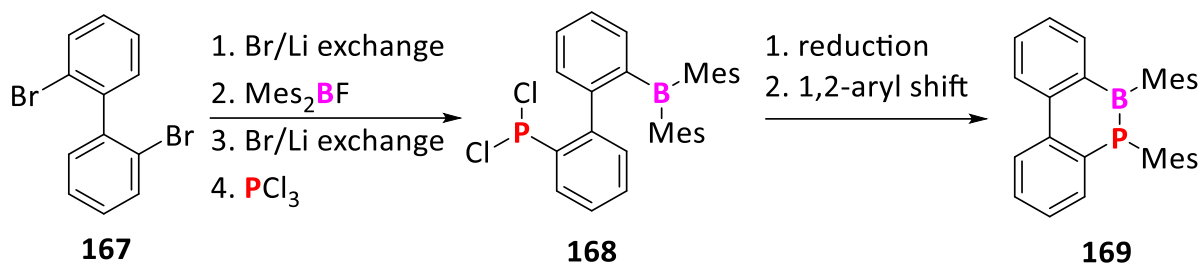
Scheme 91: Proposed synthesis towards BP-phenanthrene **169** *via* reduction of **168** and 1,2-aryl shift.

A similar method has been previously utilized to obtain BP-acenaphthene.[12] Here again the resulting BP-phenanthrene could be useful for fundamental comparative studies with BN-phenanthrenes. The mesityl substituent could be advantageous as it should stabilize the BP unit due to its bulky nature. This synthetic method is limited to smaller exocyclic situated BP units and might not be compatible with other functional groups due to the strongly alkaline synthetic conditions.

Besides the development of novel synthetic methods for forming BP-substituted PAHs, the most exciting benefit of boron/phosphorus systems is the possibility of post functionalization. It is suggested that the optoelectronic properties of BP-PAHs might be tunable by oxidation of the phosphorus atom: Besides oxygenation, also sulfurization, methyl sulfurization, methylation or coordination to transition metals should be possible (Fig. 115).

potential post-modifications
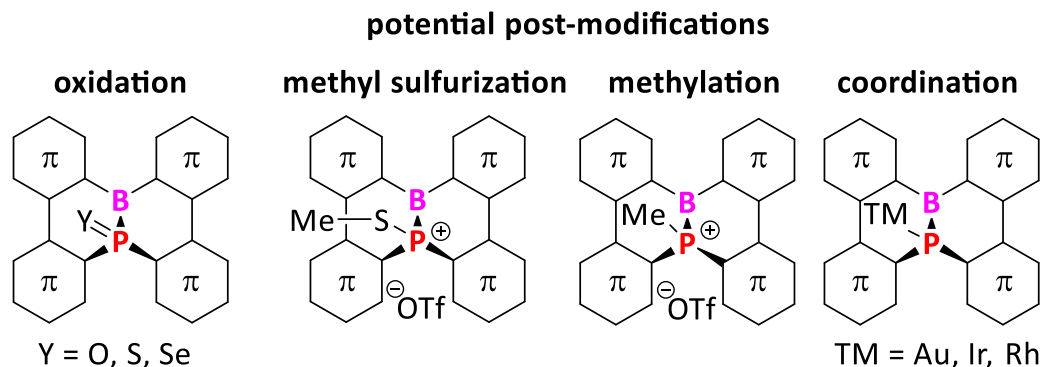
Fig. 115: Potential modifications of BP-substituted PAHs to modify the optical properties.

As the overlap of the resulting tetragonal phosphorus atom with the orbitals of both neighboring carbon atoms and the boron atom might be reduced, the influence of such derivatization is of fundamental interest.

Overall investigations concerning the analogy of BN- and BP-substituted PAHs gained great interest in main group chemistry. In contrast to the well-established BN-chemistry, synthetic methods to obtain aromatic BP-systems are still scarce and require harsh conditions. In this work, pathways to synthesize BP-substituted PAHs were investigated and promising progress has been achieved. Especially methods that are common in BN-chemistry, e.g. intramolecular ring annulation reactions, did not result in the formation of BP units. It is still a long way to obtain a variety of BP-systems, but interesting photophysical properties and possible post functionalization should be worth it.

4.6   References

1. H.-O. Berger, H. Nöth, *J. Organomet. Chem.*, **1983**, *250*, 33-48.
2. T. Agou, J. Kobayashi, T. Kawashima, *Org. Lett.*, **2005**, *7*, 4373-4376.
3. M. Ando, M. Sakai, N. Ando, M. Hirai, S. Yamaguchi, *Org. Biomol. Chem.*, **2019**, *17*, 5500-5504.
4. S. Sasaki, K. Sutoh, F. Murakami, M. Yoshifuji, *J. Am. Chem. Soc.*, **2002**, *124*, 14830-14831.
5. W. Schaefer, A. Schweig, F. Mathey, *J. Am. Chem. Soc.*, **1976**, *98*, 407-414.
6. M. P. Duffy, W. Delaunay, P. A. Bouit, M. Hissler, *Chem. Soc. Rev.*, **2016**, *45*, 5296-5310.
7. F. Mathey, *Phosphorus, Sulfur, and Silicon and the Related Elements*, **1994**, *87*, 139-148.
8. T. Agou, J. Kobayashi, T. Kawashima, *Inorg. Chem.*, **2006**, *45*, 9137-9144.
9. M. H. Matus, S. Y. Liu, D. A. Dixon, *J. Phys. Chem. A*, **2010**, *114*, 2644-2654.
10. M. Baranac-Stojanovic, *Chemistry*, **2014**, *20*, 16558-16565.
11. J.-Y. Wang, J. Pei, *Chin. Chem. Lett.*, **2016**, *27*, 1139-1146.
12. A. Tsurusaki, T. Sasamori, A. Wakamiya, S. Yamaguchi, K. Nagura, S. Irle, N. Tokitoh, *Angew. Chem. Int. Ed.*, **2011**, *50*, 10940-10943.
13. D. C. Pestana, P. P. Power, *J. Am. Chem. Soc.*, **1991**, *113*, 8426-8437.
14. X. Feng, M. M. Olmstead, P. P. Power, *Inorg. Chem.*, **1986**, *25*, 4615-4616.
15. J. H. W. LaFortune, Z. W. Qu, K. L. Bamford, A. Trofimova, S. A. Westcott, D. W. Stephan, *Chemistry*, **2019**, *25*, 12063-12067.
16. W. Yang, K. E. Krantz, D. A. Dickie, A. Molino, D. J. D. Wilson, R. J. Gilliard, Jr., *Angew. Chem. Int. Ed.*, **2020**, *59*, 3971-3975.
17. K. B. Wiberg, *Tetrahedron*, **1968**, *24*, 1083-1096.
18. L. K. Harper, A. L. Shoaf, C. A. Bayse, *ChemPhysChem*, **2015**, *16*, 3886-3892.
19. I. Mayer, *J. Comput. Chem.*, **2007**, *28*, 204-221.
20. T. Hatakeyama, S. Hashimoto, S. Seki, M. Nakamura, *J. Am. Chem. Soc.*, **2011**, *133*, 18614-18617.
21. T. Hatakeyama, S. Hashimoto, T. Oba, M. Nakamura, *J. Am. Chem. Soc.*, **2012**, *134*, 19600-19603.
22. S. Hashimoto, T. Ikuta, K. Shiren, S. Nakatsuka, J. Ni, M. Nakamura, T. Hatakeyama, *Chem. Mater.*, **2014**, *26*, 6265-6271.
23. X.-Y. Wang, F.-D. Zhuang, X. Zhou, D.-C. Yang, J.-Y. Wang, J. Pei, *J. Mater. Chem. C*, **2014**, *2*, 8152-8161.
24. S. Tokito, K. Noda, H. Fujikawa, Y. Taga, M. Kimura, K. Shimada, Y. Sawaki, *Appl. Phys. Lett.*, **2000**, *77*, 160-162.
25. X.-Y. Liu, X. Tang, Y. Zhao, D. Zhao, J. Fan, L.-S. Liao, *Dyes Pigment.*, **2017**, *146*, 234-239.
26. F. Riobé, R. Szűcs, C. Lescop, R. Réau, L. Nyulászi, P.-A. Bouit, M. Hissler, *Organometallics*, **2017**, *36*, 2502-2511.
27. A. D. Becke, *J. Chem. Phys.*, **1993**, *98*, 5648-5652.
28. C. Lee, W. Yang, R. G. Parr, *Phys. Rev. B: Condens. Matter*, **1988**, *37*, 785-789.
29. S. H. Vosko, L. Wilk, M. Nusair, *Can. J. Phys.*, **1980**, *58*, 1200-1211.
30. P. J. Stephens, F. J. Devlin, C. F. Chabalowski, M. J. Frisch, *J. Phys. Chem.*, **1994**, *98*, 11623-11627.
31. S. Grimme, J. Antony, S. Ehrlich, H. Krieg, *J. Chem. Phys.*, **2010**, *132*, 154104.
32. J. H. Barnard, P. A. Brown, K. L. Shuford, C. D. Martin, *Angew. Chem. Int. Ed.*, **2015**, *54*, 12083-12086.
33. H. Braunschweig, C. Horl, L. Mailander, K. Radacki, J. Wahler, *Chemistry*, **2014**, *20*, 9858-9861.
34. J. Pan, J. W. Kampf, A. J. Ashe Iii, *Organometallics*, **2008**, *27*, 1345-1347.
35. J. A. Bailey, P. G. Pringle, *Coord. Chem. Rev.*, **2015**, *297-298*, 77-90.
36. A. Yamamoto, E. Ohta, N. Kishigami, N. Tsukahara, Y. Tomiyori, H. Sato, Y. Matsui, Y. Kano, K. Mizuno, H. Ikeda, *Tetrahedron Lett.*, **2013**, *54*, 4049-4053.
37. C. L. Eversloh, C. Li, K. Mullen, *Org. Lett.*, **2011**, *13*, 4148-4150.
38. P. V. R. Schleyer, C. Maerker, A. Dransfeld, H. Jiao, N. J. R. van Eikema Hommes, *J. Am. Chem. Soc.*, **1996**, *118*, 6317-6318.

39. B. Goldfuss, P. v. R. Schleyer, *Organometallics*, **1997**, *16*, 1543-1552.
40. P. V. R. Schleyer, M. Manoharan, Z. X. Wang, B. Kiran, H. Jiao, R. Puchta, N. J. R. van Eikema Hommes, *Org. Lett.*, **2001**, *3*, 2465-2468.
41. R. Carion, V. Liégeois, B. Champagne, D. Bonifazi, S. Pelloni, P. Lazzeretti, *J. Phys. Chem. Lett.*, **2010**, *1*, 1563-1568.
42. R. Gershoni-Poranne, A. P. Rahalkar, A. Stanger, *Phys. Chem. Chem. Phys.*, **2018**, *20*, 14808-14817.
43. F. Weinhold, C. R. Landis, E. D. Glendening, *Int. Rev. Phys. Chem.*, **2016**, *35*, 399-440.
44. G. E. Coates, J. G. Livingstone, *J. Chem. Soc.*, **1961**, 1000.
45. X. Y. Wang, H. R. Lin, T. Lei, D. C. Yang, F. D. Zhuang, J. Y. Wang, S. C. Yuan, J. Pei, *Angew. Chem. Int. Ed.*, **2013**, *52*, 3117-3120.
46. X. Y. Wang, D. C. Yang, F. D. Zhuang, J. J. Liu, J. Y. Wang, J. Pei, *Chemistry*, **2015**, *21*, 8867-8873.
47. F. Miyamoto, S. Nakatsuka, K. Yamada, K. Nakayama, T. Hatakeyama, *Org. Lett.*, **2015**, *17*, 6158-6161.
48. S. Oda, T. Hatakeyama, *Bull. Chem. Soc. Jpn.*, **2020**.
49. T. Hatakeyama, S. Hashimoto, M. Nakamura, *Org. Lett.*, **2011**, *13*, 2130-2133.
50. T. L. Cottrell, *The strengths of chemical bonds*, Butterworths, London, **1958**.
51. S. Schweizer, J.-M. Becht, C. Le Drian, *Adv. Synth. Catal.*, **2007**, *349*, 1150-1158.
52. G. W. Luther, G. Beyerle, *Lithium Diphenylphosphide and Diphenyl(Trimethylsilyl)Phosphine*, in *Inorg. Synth.*, eds. D. Cox and K. Cohn, McGraw-Hill, Inc., **1977**, vol. XVII, ch. 49, 186-188.
53. A. M. Aguiar, J. Beisler, A. Mills, *J. Org. Chem.*, **1962**, *27*, 1001-1005.
54. Y. Chen, W. Chen, Y. Qiao, X. Lu, G. Zhou, *Angew. Chem.*, **2020**, *132*, 7188-7196.
55. S. Han, C. M. Harris, T. M. Harris, H.-Y. H. Kim, S. J. Kim, *J. Org. Chem.*, **1996**, *61*, 174-178.
56. M. Giannerini, V. Hornillos, C. Vila, M. Fananas-Mastral, B. L. Feringa, *Angew. Chem. Int. Ed.*, **2013**, *52*, 13329-13333.
57. P. M. Holstein, M. Vogler, P. Larini, G. Pilet, E. Clot, O. Baudoin, *ACS Catalysis*, **2015**, *5*, 4300-4308.
58. A. Krasovskiy, P. Knochel, *Angew. Chem. Int. Ed. Engl.*, **2004**, *43*, 3333-3336.
59. A. Sumita, M. Gasonoo, K. J. Boblak, T. Ohwada, D. A. Klumpp, *Chemistry*, **2017**, *23*, 2566-2570.
60. S. V. Bondarchuk, M. Carrera, M. de la Viuda, A. Guijarro, *New J. Chem.*, **2018**, *42*, 5168-5177.
61. I. Bonnaventure, A. B. Charette, *J. Org. Chem.*, **2008**, *73*, 6330-6340.
62. E. C. Ashby, R. Gurumurthy, R. W. Ridlehuber, *J. Org. Chem.*, **1993**, *58*, 5832-5837.
63. B. Rapp, J. E. Drake, *Inorg. Chem.*, **1973**, *12*, 2868-2873.
64. H. Nöth, W. Schrägle, *Chem. Ber.*, **1965**, *98*, 352-362.
65. H. Nöth, *Z. Naturforsch., B: Chem. Sci.*, **1961**, *16*, 618-620.
66. H. Nöth, W. Schrägle, *Z. Naturforsch., B: Chem. Sci.*, **1961**, *16*, 473-474.
67. E. W. Abel, R. A. N. McLean, I. H. Sabherwal, *J. Chem. Soc. A*, **1968**, *0*, 2371-2373.
68. S. J. Geier, C. M. Vogels, N. R. Mellonie, E. N. Daley, A. Decken, S. Doherty, S. A. Westcott, *Chemistry*, **2017**, *23*, 14485-14499.
69. E. Muylle, G. P. van der Kelen, *Spectrochim. Acta, Part A*, **1976**, *32*, 599-603.
70. R. E. Montgomery, L. D. Quin, *J. Org. Chem.*, **1965**, *30*, 2393-2395.
71. J.-Q. Zhang, S. Yang, L.-B. Han, *Tetrahedron Lett.*, **2020**, *61*, 151556.
72. J. Pietruszka, *Product Subclass 22: Silyl Phosphines*, in *Category 1, Organometallics*, eds. I. Fleming and S. V. Ley, Georg Thieme Verlag, Stuttgart, 1st Edition edn., **2002**, vol. 4.
73. V. T. Trepohl, M. Oestreich, *Chem. Commun.*, **2007**, 3300-3302.
74. G. R. Whittell, E. I. Balmond, A. P. M. Robertson, S. K. Patra, M. F. Haddow, I. Manners, *Eur. J. Inorg. Chem.*, **2010**, *2010*, 3967-3975.
75. D. M. Schubert, A. D. Norman, *Inorg. Chem.*, **1985**, *24*, 1107-1109.
76. Y. Li, S. Chakrabarty, C. Muck-Lichtenfeld, A. Studer, *Angew. Chem. Int. Ed.*, **2016**, *55*, 802-806.
77. P. Ramírez-López, A. Ros, B. Estepa, R. Fernández, B. Fiser, E. Gómez-Bengoa, J. M. Lassaletta, *ACS Catalysis*, **2016**, *6*, 3955-3964.
78. F. Duboudin, M. Birot, O. Babot, J. Dunoguès, R. Calas, *J. Organomet. Chem.*, **1988**, *341*, 125-132.

79. B. Carboni, F. Carreaux, *Product Subclass 15: Aminoboranes and Borane–Amine Complexes*, in *Science of Synthesis, 6: Category 1, Organometallics (Boron Compounds)*, eds. Kaufmann, Matteson, Schaumann and Regitz, Houben-Weyl, **2005**.

80. C. Sole, E. Fernandez, *Angew. Chem. Int. Ed.*, **2013**, *52*, 11351-11355.

81. H. Nöth, S. N. Sze, *Z. Naturforsch., B: Chem. Sci.*, **1978**, *33*, 1313-1317.

82. M. A. Beckett, G. C. Strickland, J. R. Holland, K. Sukumar Varma, *Polymer*, **1996**, *37*, 4629-4631.

83. F. Dornhaus, S. Scholz, I. Sänger, M. Bolte, M. Wagner, H.-W. Lerner, *Z. Anorg. Allg. Chem.*, **2009**, *635*, 2263-2272.

84. M. S. Balakrishna, R. M. Abhyankar, J. T. Mague, *J. Chem. Soc., Dalton Trans.*, **1999**, 1407.

85. D. S. Surry, S. L. Buchwald, *Chem. Sci.*, **2011**, *2*, 27-50.

86. T. E. Barder, S. L. Buchwald, *J. Am. Chem. Soc.*, **2007**, *129*, 5096-5101.

87. M. C. MacInnis, R. McDonald, L. Turculet, *Organometallics*, **2011**, *30*, 6408-6415.

88. K. Izod, P. Evans, P. G. Waddell, *Dalton Trans.*, **2017**, *46*, 13824-13834.

89. A. Bodach, R. Hebestreit, M. Bolte, L. Fink, *Inorg. Chem.*, **2018**, *57*, 9079-9085.

90. R. E. Mulvey, K. Wade, D. R. Armstrong, G. T. Walker, R. Snaith, W. Clegg, D. Reed, *Polyhedron*, **1987**, *6*, 987-993.

91. J. M. Breunig, F. Lehmann, M. Bolte, H.-W. Lerner, M. Wagner, *Organometallics*, **2014**, *33*, 3163-3172.

4.7 Experimental

In general, NMR-tubes and glassware were dried in an oven at 200 °C overnight before use. If not stated otherwise, all reaction vessels were heated to minimum of 200 °C under vacuum (1.3×10^{-2} mbar to 6.2×10^{-2} mbar) and purged with nitrogen or argon at least three times before adding reagents. Syringes were purged with nitrogen or argon three times prior use. In general, a nitrogen filled glovebox from Inert, Innovative Technology, Inc. Company (< 0.1 ppm O_2 and < 0.1 ppm H_2O) was used unless noted otherwise. All dry solvents were taken from the solvent purification system (SPS, Inert Technology or MB-SPS-800), degassed by three freeze-pump-thaw cycles and stored under a nitrogen atmosphere unless noted otherwise. Kugelrohr distillation was performed with a Büchi B-585 Kugelrohr oven.

All NMR -spectra were carried out at 23 C. ^{1}H NMR (600 MHz) and ^{13}C{^{1}H} NMR (150 MHz) spectra were recorded on a Bruker Avance Neo spectrometer equipped with a TXI probe head. ^{1}H NMR (600 MHz), ^{13}C{^{1}H} NMR (150 MHz), ^{11}B{^{1}H} NMR (XX MHz), ^{29}Si{^{1}H} NMR (119 MHz), ^{31}P{^{1}H} NMR (243 MHz), ^{119}Sn{^{1}H} NMR (223 MHz) spectra were recorded on a Bruker Avance Neo spectrometer equipped with a BBO probe head. The ^{11}B{^{1}H} NMR (162 MHz) and ^{31}P{^{1}H} NMR (162 MHz) spectra were recorded on a Bruker AV III with a ^{1}H frequency of 400 MHz equipped with a BBFO probe head. The reference of the ^{11}B NMR spectra was boron trifluoride etherate in CDCl$_3$. The ^{29}Si{^{1}H} NMR spectra were referenced against tetramethylsilane. All ^{31}P NMR spectra were referenced against phosphoric acid (85%) in water. The ^{119}Sn NMR spectra were referenced against tetramethyltin in CDCl$_3$. Where possible, NMR signals were assigned using ^{1}H COSY, ^{1}H/^{1}H NOESY, ^{1}H/^{13}C HSQC and ^{1}H/^{13}C HMBC experiments. IR spectra were recorded on a Nicolet Thermo iS10 scientific spectrometer with a diamond ATR unit. Electron impact (EI) mass experiments were measured using the direct inlet or indirect inlet methods on a MAT95 XL double-focusing mass spectrometer from Finnigan MAT (Thermo Fisher SCIENTIFIC). Melting points were obtained. The ionization energy of the electron impact ionization was 70 eV. Atmospheric pressure chemical ionization (APCI) and electron spray ionization (ESI) experiments were performed on a Bruker Impact II from Bruker Daltonics. Melting points of solids were measured on a Büchi M-5600 Melting Point apparatus and are uncorrected.

4.7.1 Dichloro-*N*,*N*-di*iso*propylphosphanamine (**106**)
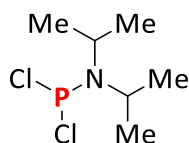
The synthetic procedure was adapted from lit.[1]: Under argon atmosphere phosphorus trichloride (18.7 mL, 213 mmol) was dissolved in diethyl ether and cooled to 0 °C. To this di*iso*propylamine (60.0 mL, 427 mmol) was added over 2 h *via* a dropping funnel. The reaction mixture was warmed to 25 °C and stirred for additional 14 h. The white suspension was transferred to a Schlenk frit, was filtrated and washed with diethyl ether (100 mL). The volatiles of the filtrate were distilled of at 50 °C and the residual oil was distilled (80 °C, 5 mbar) to give a clear liquid (**106**, 27.7 g, 137 mmol, 64%, lit.[1]: 76%) which crystallized upon cooling. **^{1}H NMR** (600 MHz, C$_6$D$_6$): δ = 3.56 (s (br), 2H, C*H*), 0.92 (d, ^3J = 6.7 Hz, 12H, C*H*$_3$) ppm. **^{13}C{^{1}H} NMR** (151 MHz, C$_6$D$_6$): δ = 48.23 (d, $^3J_{C-P}$ = 14.2 Hz, *C*H), 23.20 (s, *C*H$_3$) ppm. **^{31}P{^{1}H} NMR** (243 MHz, C$_6$D$_6$): δ = 168.88 (s) ppm. **HRMS** (EI, 70 eV, MAT95, direct): *m/z* [M]$^{+\cdot}$ Calcd. for C$_6$H$_{14}$NPCl$_2$ 201.02354; Found 201.02350.

### 4.7.2 *bis*(Biphenyl-2-yl)-*N,N*-di*iso*propylphosphanamine (**110**)
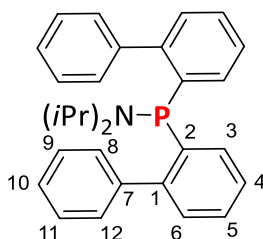
Under constant stirring at 0 °C 2-biphenylmagensium bromide (30.0 mL, 15.0 mmol, 0.5 M in diethyl ether) was added to *n*-pentane (100 mL). To this **104** (1.30 mL, 7.07 mmol) were added dropwise and the solution formed a white precipitate. The reaction progress was followed by ^{31}P NMR spectroscopy. After 14 h of stirring at 25 °C the solids were filtrated of and washed with *n*-pentane (100 mL). All volatiles were removed at reduced pressure and recrystallization of the solid was performed by dissolving the residue in a minimal amount of DCM and adding acetonitrile (100 mL) in an open flask. Using fractional crystallization, the product was obtained in high purity as colorless crystals (**110**, 3.02 g, 6.91 mmol, 97%) which were also suitable for X-ray analysis. **^{1}H NMR** (601 MHz, DCM-d_2): δ = 7.42 (dd, ^3J = 7.4 Hz, ^4J = 1.5 Hz, 2H, *H*-3), 7.31 (td, ^3J = 7.4, ^4J = 1.5 Hz, 2H, *H*-5), 7.27 (td, ^3J = 7.4 Hz, ^4J = 1.5 Hz, 2H, *H*-4), 7.25 - 7.18 (m, 6H, *H*-9,10,11), 7.06 (ddd, ^3J = 7.4, ^3J = 4.7, ^4J = 1.5 Hz, 2H, *H*-6), 7.04 (d, ^3J = 7.5 Hz, 4H, *H*-8,12), 3.24 - 3.13 (two hept., ^3J = 6.7 Hz, 2H, C*H*), 0.68 (d, ^3J = 6.7 Hz, 12H, C*H*$_3$) ppm. **^{13}C {^{1}H} NMR** (151 MHz, DCM-d_2): δ = 146.79 (d, $^2J_{\text{C-P}}$ = 27.8 Hz, *C*-1), 142.78 (d, $^3J_{\text{C-P}}$ = 4.2 Hz, *C*-7), 139.98 (d, $^1J_{\text{C-P}}$ = 20.0 Hz, *C*-2), 133.81 (s (br), *C*-3), 130.73 (d, $^4J_{\text{C-P}}$ = 4.3 Hz, *C*-8,12), 130.61 (d, $^3J_{\text{C-P}}$ = 3.4 Hz, *C*-6), 128.43 (s, *C*-5), 127.89 (s, *C*-9,10,11), 127.66 (d, $^3J_{\text{C-P}}$ = 5.0 Hz, *C*-4), 47.74 (s (br), *C*H), 23.50 (s, *C*H$_3$) ppm. **^{31}P {^{1}H} NMR** (243 MHz, DCM-d_2): δ = 22.52 (s) ppm. **IR (ATR)**: ν = 3053 (w), 2964 (w), 2925 (w), 1456 (w), 1443 (w), 1424 (w), 1386 (w), 1360 (w), 1191 (w), 1174 (w), 1118 (m), 1071 (s), 1008 (w), 962 (m), 912 (w), 775 (w), 744 (s), 698 (s) cm^{-1}. **HRMS** (EI, 70 eV, MAT95, direct): *m/z* [M-H]$^+$ Calcd. for C$_{30}$H$_{31}$NP 436.21886; Found 436.21914; [M]$^{+\cdot}$ Calcd. for C$_{30}$H$_{32}$NP 437.22669; Found 437.22676: **MS** (EI): *m/z* 437.3 (35%) [M]$^{+\cdot}$, 337.2 (49%) [M-N(*i*Pr)$_2$]$^{+\cdot}$, 183.0 (100%) [M-H,(N(*i*Pr)$_2$),(C$_{12}$H$_9$)]$^+$. **Mp:** 125 °C.

4.7.3 *bis*(Biphenyl-2-yl)chlorophosphine (**111**)
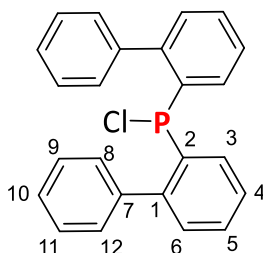
In a schlenk flask **110** (1.00 g, 2.28 mmol) was dissolved in diethyl ether (60 mL). To this a hydrogen chloride solution (8.00 mL, 16.0 mmol, 2.0 M in diethyl ether) were added. The reaction mixture turned cloudy directly and was stirred for 2 h while the reaction progress was observed with ^{31}P NMR. The reaction mixture was allowed to settle and afterwards it was transferred into another Schlenk flask using syringe filters. A yellow oil was received after drying (25 °C, 2.2 x 10^{-2} mbar) and used for further steps. For analytical purposes, a part of the reaction mixture (247 mg, 0.67 mmol) was distilled by inert fractional Kugelrohr distillation (180 °C, 3.2 x 10^{-2} mbar) to give the crystalline product (**111**, 86 mg, 0.23 mmol, 34%). Crystals which were suitable for X-ray analysis could be directly taken from the solidified distillate. Due to the high temperature in this process also oxidation products (phosphinic

chloride (^{31}P NMR δ = 34.0 ppm), phosphine oxides (^{31}P NMR δ = 15.9 ($^1J_{PH}$ = 503.3 Hz) ppm)) were detectable after distillation. **^{1}H NMR** (601 MHz, CDCl$_3$): δ = 7.72 (m, 2H, *H*-3), 7.48 - 7.40 (m, 4H, *H*-5 and *H*-4), 7.35 - 7.30 (m, 2H, *H*-10), 7.26 (t, ^3J = 7.6 Hz, 4H, *H*-9,11), 7.22 - 7.19 (m, 2H, *H*-6), 6.99 (d, ^3J = 7.6 Hz, 4H, *H*-8,12) ppm. **^{13}C {^{1}H} NMR** (151 MHz, CDCl$_3$): δ = 146.79 (d, $^2J_{C-P}$ = 32.4 Hz, *C*-1), 140.31 (d, $^3J_{C-P}$ = 6.6 Hz, *C*-7), 137.03 (d, $^1J_{C-P}$ = 38.9 Hz, *C*-2), 132.52 (d, $^2J_{C-P}$ = 2.1 Hz, *C*-3), 130.06 (s, *C*-5), 130.01 (d, $^3J_{C-P}$ = 3.4 Hz, *C*-6), 129.74 (d, $^4J_{C-P}$ = 4.9 Hz, *C*-8,12), 127.96 (s, *C*-9,11), 127.78 (s, *C*-4), 127.55 (s, *C*-10) ppm. **^{31}P {^{1}H} NMR** (243 MHz, CDCl$_3$): δ = 74.53 (s) ppm. **HRMS** (EI, 70 eV, MAT95, direct): *m/z* [M-H]$^+$ Calcd. for C$_{24}$H$_{17}$PCl 371.07509; Found 371.07512; [M-H,HCl]$^{+\cdot}$ Calcd. for C$_{24}$H$_{16}$P 335.09841; Found 355.09838. **MS** (EI): *m/z* 371.2 (100%) [M-H]$^+$, 335.2 (27%) [M-H,HCl]$^{+\cdot}$, 183.0 (60%) [M-H,HCl),(C$_{12}$H$_9$)]$^+$.

4.7.4   *bis*(Biphenyl-2-yl)phosphine (**112**)
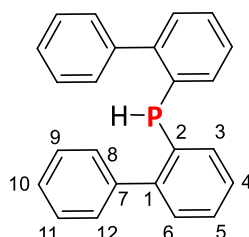
To a solution of freshly prepared **111** (0.32 mmol) in THF (40 mL) lithium aluminum hydride solution (0.32 mL, 0.32 mmol, 1.0 M in THF) were added at 25 °C. The reaction mixture was stirred for 15 h and the reaction progress was observed *via* ^{31}P NMR. After completion of the reaction the solvent was removed *in vacuo* and the residue was dissolved in toluene (2.0 mL) and was filtered over Celite. The product was obtained using inert Kugelrohr distillation (130-160 °C, 2.0 x 10^{-3} mbar) and the product was isolated as white solid (**112**, 99 mg, 0.29 mmol, 91%). Crystals which were suitable for X-ray analysis were obtained after solidification of the distillate. **^{1}H NMR** (601 MHz, C$_6$D$_6$): δ = 7.32 (ddd, ^3J = 7.4, 5.7 Hz, ^4J = 0.9 Hz, 2H, *H*-3), 7.18 (m, 4H, *H*-8,12), 7.16 - 7.12 (m, 2H, *H*-6), 7.09 - 7.03 (m, 4H, *H*-5, *H*-9,11 and *H*-10), 7.06 (tt, ^3J = 7.5 Hz, ^4J = 1.1 Hz, 2H, *H*-4), 4.97 (d, $^1J_{P-H}$ = 223.0 Hz, 1H, P*H*) ppm. **^{13}C {^{1}H} NMR** (151 MHz, C$_6$D$_6$): δ = 147.18 (d, $^2J_{C-P}$ = 16.4 Hz, *C*-1), 142.10 (d, $^3J_{C-P}$ = 3.3 Hz, *C*-7), 135.55 (d, $^1J_{C-P}$ = 10.1 Hz, *C*-3), 134.24 (d, $^2J_{C-P}$ = 15.9 Hz, *C*-2), 129.91 (d, $^3J_{C-P}$ = 2.7 Hz, *C*-6), 129.91 (d, $^3J_{C-P}$ = 3.1 Hz, *C*-8,12), 128.27 (s, *C*-5), 127.85 (overlapping with C$_6$D$_6$ signal, *C*-9,11), 129.74 (d, $^4J_{C-P}$ = 3.4 Hz, *C*-4), 127.05 (s, *C*-10) ppm. **^{31}P {^{1}H} NMR** (243 MHz, CDCl$_3$): δ = -53.87 (s) ppm. **^{31}P NMR** (243 MHz, CDCl$_3$): δ = -53.87 (d, $^1J_{P-H}$ = 223.0 Hz) ppm. **HRMS** (EI, 70 eV, MAT95, direct): *m/z* [M-H]$^+$ Calcd. for C$_{24}$H$_{18}$P 337.11406; Found 337.11412. **MS** (EI, 120 °C): *m/z* 337.1 (80%) [M-H]$^+$, 335.2 (27%) [M]$^{\cdot}$, 183.0 (100%) [M-H),(C$_{12}$H$_9$)]$^+$.

### 4.7.5   Lithium *bis*(biphenyl-2-yl)phosphide (**107**)
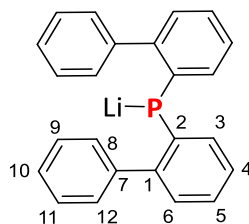
In the glove box JH136 (20.0 mg, 59.7 µmol) was dissolved in benzene (10 mL) and *n*-butyllithium (0.50 mL, 125 µmol, 2.5 M in hexanes) was added a 25 °C. The reaction mixture was stirred for 2 h and the supernatant was filtered through syringe filters. The solution was crystalized by over layering the

solution with *n*-hexane to give the product as orange solids (**107**, 19.7 mg, 58.9 µmol, 99%). **^{1}H NMR** (601 MHz, C$_6$D$_6$:THF-d_8 80:20): δ = 7.32 (dd, ^3J = 7.4, 5.7 Hz, ^4J = 1.4 Hz, 2H, *H*-3), 7.18 (^3J = 7.6 Hz, 4H, *H*-8,12), 7.09 - 7.03 (m, 4H, *H*-6 and *H*-9,11), 6.98 (t, ^3J = 7.0 Hz, 2H, *H*-4), 6.94 (t, ^3J = 7.7 Hz, 2H, *H*-10), 6.85 (t, ^3J = 7.8 Hz, 2H, *H*-5) ppm. **^{13}C {^{1}H} NMR** (151 MHz, C$_6$D$_6$:THF-d_8 80:20): δ = 153.92 (d, $^1J_{C\text{-}P}$ = 49.6 Hz, *C*-2), 146.45 (d, $^3J_{C\text{-}P}$ = 3.1 Hz, *C*-7), 142.10 (d, $^3J_{C\text{-}P}$ = 20.6 Hz, *C*-1), 135.55 (s, *C*-3), 129.67 (d, $^3J_{C\text{-}P}$ = 5.8 Hz, *C*-8,12), 129.67 (d, $^3J_{C\text{-}P}$ = 2.1 Hz, *C*-6), 126.96 (s, *C*-9,11), 125.65 (s, *C*-10), 125.06 (s, *C*-4), 120.45 (s, *C*-5) ppm. **^{9}Li NMR** (233 MHz, C$_6$D$_6$:THF-d_8 80:20): δ = -0.06 (s) ppm. **^{31}P NMR** (243 MHz, C$_6$D$_6$:THF-d_8 80:20): δ = -33.39 (s) ppm. **^{31}P NMR** (243 MHz, C$_6$D$_6$): δ = -52.41 (s) ppm.

4.7.6   *bis*(Biphenyl-2-yl)phosphine borane (**114**)
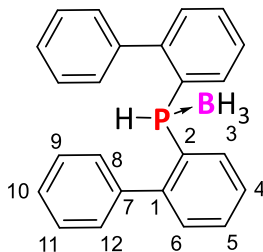
Method A: In a Schlenk flask **112** (169 mg, 0.50 mmol) was dissolved in THF (20 mL). To this the borane solution (0.50 mL, 0.50 mmol, 1.0 M in THF) were slowly added. The reaction was stirred at 50 °C for 2 h. After removal of the solvent the residue was mixed with *n*-hexane (20 mL) and stirred for 30 min. Afterwards the white cloudy solution was allowed so settle for 14 h. The supernatant was transferred through syringe filters into a another Schlenk flask. The flask was stored at -8 °C giving a cloudy color to the glass surface. After 6 days the solution was decanted, and the white solids were collected. The recrystallization from *n*-hexane (50 mL) gave colorless crystals (**114**, 85 mg, 0.24 mmol, 48%). These crystals were suitable for X-Ray analysis. Method B: To a solution of LiBH$_4$ (6.5 mg, 0.30 mmol) in diethyl ether (5.0 mL) a solution of **111** (49.4 mg, 0.131 mmol) in THF (5.0 mL) was added dropwise at 0 °C. Reaction progress was monitored with ^{31}P NMR and visible signals for the product were recognized. After 1h stirring at 25 °C the solvent was removed, and the reaction mixture was dissolved in *n*-hexane (10 mL) at 60 °C. This solution was transferred through syringe filters into another Schlenk flask and stored in a freezer (-30 °C) in the glove box to obtain colorless crystals (**114**, 44 mg, 0.125 mmol, 94%). **^{1}H NMR** (601 MHz, C$_6$D$_6$): δ = 7.89 (dd, ^3J = 12.8, 7.6 Hz, 2H, *H*-3), 7.12 -6.98 (m, 10H, *H*-4,5 and *H*-9,10,11), 6.95 (dd, ^3J = 7.6, ^4J = 3.3 Hz, 2H, *H*-6), 6.84 (s (br), 4H, *H*-8,12), 6.30 (dq, $^1J_{P\text{-}H}$ = 396.4 Hz, $^2J_{PH\text{-}BH3}$ = 6.7 Hz , 1H, P*H*), 2.13 (d, $^1J_{BH}$ = 126.9 Hz, 3H, B*H*$_3$) ppm. **^{13}C {^{1}H} NMR** (151 MHz, C$_6$D$_6$): δ = 146.79 (d, $^2J_{C\text{-}P}$ = 2.8 Hz, *C*-1), 140.21 (d, $^3J_{C\text{-}P}$ = 3.6 Hz, *C*-7), 134.51 (d, $^3J_{C\text{-}P}$ = 15.2 Hz, *C*-3), 130.87 (d, $^4J_{C\text{-}P}$ = 2.4 Hz, *C*-5), 130.53 (d, $^3J_{C\text{-}P}$ = 6.2 Hz, *C*-6), 129.35 (s, *C*-8,12), 128.21 (overlap with benzene, *C*-9,11), 127.72 (s, *C*-10), 127.66 (within $^3J_{C\text{-}P}$ = 11.8 Hz, *C*-4), 126.96 (d, $^1J_{C\text{-}P}$ = 54.5 Hz, *C*-2) ppm. **^{11}B {^{1}H} NMR** (193 MHz, C$_6$D$_6$): δ = -36.69 (s, br) ppm. **^{11}B NMR** (193 MHz, C$_6$D$_6$): δ = -36.69 (d, $^1J_{B\text{-}H}$ = 52.7 Hz) ppm. **^{31}P {^{1}H} NMR** (243 MHz, C$_6$D$_6$): δ = -14.09 (s) ppm. **^{31}P NMR** (243 MHz, C$_6$D$_6$): δ = -14.09 (d, $^1J_{P\text{-}H}$ = 397.9 Hz) ppm. **HRMS** (ESI, Impact II, DCM/acetonitrile) : *m/z* [M+K]$^+$ Calcd. for C$_{24}$H$_{22}$PBK 391.11838; Found 391.11864, [(M-BH$_3$)+K]$^+$ Calcd. for C$_{24}$H$_{18}$PK 377.08560; Found 377.08567, [M+Na]$^+$ Calcd. for C$_{24}$H$_{22}$PBNa 375.14444; Found 375.14472, [(M-BH$_3$)+Na]$^+$ Calcd. for C$_{24}$H$_{19}$PNa 361.11166; Found 361.11159.

### 4.7.7 *bis*(Biphenyl-2-yl)(trimethylsilyl)phosphine (**145**)
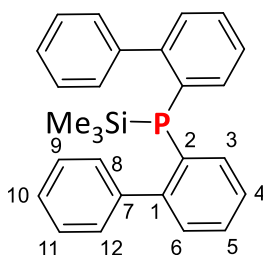
To a solution of **107** (63 mg, 59.0 µmol) in benzene (2.0 mL) *n*-butyllithium (47 µL, 118 µmol, 2.5 M in hexanes) were added and the reaction mixture was stirred at 25 °C for 2 h giving an intense orange color. To this solution trimethylsilyl chloride (100 µL, 786 µmol) was added in one portion. The reaction mixture was allowed to settle and the supernatant was transferred to another flask. After removal of all volatiles and drying (25 °C, 2 h, 1 x 10^{-3} mbar) a white waxy solid was obtained (**145**, 22 mg, 53.8 µmol, 91%). **^{1}H NMR** (601 MHz, C_6D_6): δ = 7.60 - 7.57 (m, 2H, *H*-3), 7.23 - 7.20 (m, 4H, *H*-8,12), 7.19 - 7.16 (m, overlapping with residual benzene signals, 2H, *H*-6), 7.16 - 7.12 (m, 4H, *H*-9,11), 7.11 - 7.07 (m, 4H, *H*-5 and *H*-10), 7.05 (td, ^3J = 7.4 Hz, ^4J = 1.1 Hz, 2H, *H*-4), -0.03 (d, $^3J_{P\text{-}Si(CH3)3}$ = 4.50 Hz, 9H, C*H*$_3$) ppm. **^{13}C {^{1}H} NMR** (151 MHz, C_6D_6): δ = 148.49 (d, $^2J_{C\text{-}P}$ = 26.0 Hz, *C*-1), 143.28 (d, $^3J_{C\text{-}P}$ = 4.9 Hz, *C*-7), 136.32 (d, $^1J_{C\text{-}P}$ = 10.1 Hz, *C*-3), 135.82 (d, $^2J_{C\text{-}P}$ = 21.0 Hz, *C*-2), 131.31 (d, $^3J_{C\text{-}P}$ = 4.9 Hz, *C*-6), 130.59 (d, $^3J_{C\text{-}P}$ = 3.9 Hz, *C*-8,12), 128.35 (s, *C*-10), 127.99 (s, overlapping with C_6D_6 signal, *C*-9,11 and *C*-5), 127.10 (d, $^4J_{C\text{-}P}$ = 5.3 Hz, *C*-4), -0.48 (d, $^2J_{C\text{-}P}$ = 12.7 Hz, P-Si(*C*H$_3$)$_3$ ppm. **^{29}Si {^{1}H} NMR** (243 MHz, C_6D_6): δ = 1.90 (d, $^2J_{P\text{-}Si}$ = 25.4 Hz) ppm. **^{31}P {^{1}H} NMR** (243 MHz, C_6D_6): δ = -69.77 (s) ppm. **^{31}P NMR** (243 MHz, C_6D_6): δ = -69.77 (dec., $^3J_{P\text{-}Si(CH3)3}$= 4.5 Hz) ppm. **HRMS** (EI, 70 eV, MAT95, indirect in *n*-hexane): *m/z* [M-H]$^+$ Calcd. for $C_{27}H_{27}NPSi$ 409.15359; Found 409.15359. **MS** (EI): *m/z* 409.3 (10%) [M]$^{+\cdot}$, 337.2 (14%) [M-TMS]$^+$, 183.0 (45%) [M-H,(TMS),($C_{12}H_9$)]$^+$, 73.1 (100%) [TMS]$^+$.

4.7.8 *bis*(Biphenyl-2-yl)(trimethyltin)phosphine (**148**)
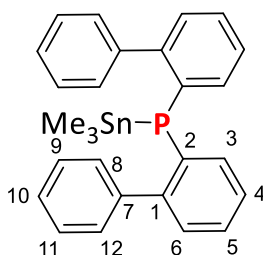
The synthesis was conducted similar to lit.[2]: In a glovebox, a an inert NMR tube was charged with **112** (10.0 mg, 29.6 µmol) and dimethylamino(trimethyl)tin (15.0 mg, 72.0 µmol). To this C_6D_6 (0.5 mL) was added and the tube was shaken intensively. The reaction progress was followed by ^{31}P NMR spectroscopy. Since the wanted species was not totally formed the tube was rotated for 2 h at a rotary evaporator. Afterwards the reaction mixture was dried *in vacuo* (25 °C,24 h, 10^{-3} mbar) and the resulting wax (**148**, 14.8 mg, 29.5 µmol, 99%) was isolated. **^{1}H NMR** (601 MHz, C_6D_6): δ = 7.59 - 7.53 (m, 2H, *H*-3), 7.44- 7.39 (m, 4H, *H*-8,12), 7.19 - 7.16 (m, 2H, *H*-6), 7.13 - 7.09 (m, 4H, *H*-9,11), 7.09 - 7.02 (m, 4H, *H*-4, *H*-5 and *H*-10), -0.03 (d, $^3J_{P\text{-}SnCH33}$ = 1.70 Hz, 9H, C*H*$_3$) ppm. **^{13}C {^{1}H} NMR** (151 MHz, C_6D_6): δ = 147.75 (d, $^2J_{C\text{-}P}$ = 25.6 Hz, *C*-1), 143.00 (d, $^3J_{C\text{-}P}$ = 4.7 Hz, *C*-7), 137.62 (d, $^1J_{C\text{-}P}$ = 10.1 Hz, *C*-2), 136.68 (s, *C*-3), 131.17 (d, $^3J_{C\text{-}P}$ = 3.9 Hz, *C*-6), 130.12 (d, $^3J_{C\text{-}P}$ = 5.0 Hz, *C*-8,12), 128.32 (d, $^3J_{C\text{-}P}$ = 7.7 Hz, *C*-10), 127.78 (s, overlapping with C_6D_6 signal, *C*-9,11 and *C*-5), 127.45 (d, $^4J_{C\text{-}P}$ = 42.4 Hz, *C*-4), -7.78 (d, $^2J_{C\text{-}P}$ = 6.0 Hz, P-Sn(CH$_3$)$_3$) ppm. **^{31}P {^{1}H} NMR** (243 MHz, C_6D_6): δ = -61.98 (s, $^1J_{P\text{-}Sn}$ satellites : 661 Hz) ppm. **^{119}Sn{^{1}H} NMR** (224 MHz, C_6D_6): δ = 0.67 (d, $^1J_{P\text{-}Sn}$ = 661.8 Hz) ppm. **HRMS** (EI, 70 eV, MAT95, indirect

in n-hexane): m/z [M-H]$^+$ Calcd. for $C_{27}H_{26}P^{116}Sn$ 497.07846; Found 497.07859, [M-CH$_3$]$^+$ Calcd. for $C_{26}H_{24}P^{116}Sn$ 483.06280; Found 483.06283. **MS** (EI, giving for ^{120}Sn): m/z 502.2 (35%) [M]$^{+\cdot}$, 487.2 (22%) [M-Me]$^+$, 457.1 (3%) [M-Me$_3$]$^{+\cdot}$, 337.2 (30%) [M-H,(SnMe$_3$)]$^+$, 183.0 (100%) [M-H,(SnMe$_3$),(C$_{12}$H$_9$)]$^{+\cdot}$.

### 4.7.9 *tris*(Diethylamino)borane (**153**)
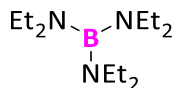
The synthesis was adapted from lit.[3]: In a Schlenk flask, boron trichloride (1 M in n-heptane, 22.0 mL, 22.0 mmol) was added to diethylamine (14.1 mL, 136 mmol) in n-pentane (15 mL) at -80 °C. The stirring was maintained at this temperature for 30 min and the reaction mixture was warmed to 25 °C. The precipitate was filtered of with a Schlenk frit with a small Celite plug (2 cm). The product was isolated by inert Kugelrohr distillation (1.3 x 10^{-1} mbar, 60 °C) as colorless oil (**153**, 3.20 g, 14.1 mmol, 64%, lit.[3]: 67%) **^{1}H NMR** (600 MHz, C$_6$D$_6$): δ = 2.89 (q, ^3J = 7.0 Hz, 12H, C*H*$_2$), 1.00 (t, ^3J = 7.0 Hz, 18H, C*H*$_3$) ppm. **^{13}C {^{1}H} NMR** (151 MHz, C$_6$D$_6$): δ = 40.58 (*C*H$_2$), 15.17 (s, *C*H$_3$) ppm. **^{11}B NMR** (193 MHz, C$_6$D$_6$): δ = 28.96 (s) ppm. **HRMS** (EI, 70 eV, MAT95, direct): m/z [M]$^+$ Calcd. for $C_{12}H_{30}N_3{}^{10}B$ 226.25636; Found 226.25629, [M]$^+$ Calcd. for $C_{12}H_{30}N_3{}^{11}B$ 227.25273; Found 227.25293.

4.7.10 Chloro-*bis*(diethylamino)borane (**152**)
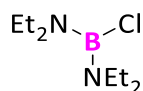
A procedure according to lit.[4] was used: In the glovebox, the boron trichloride dimethylsulfide complex (0.591 g, 3.30 mmol) were dissolved in **153** (1.50 g, 6.60 mmol) and stirred for 2 h at 25 °C. The oil that was purified by Kugelrohr distillation (105 °C, 20 mbar) to yield the product as colorless oil (**152**, 1.47 g, 7.71 mmol, 78%, lit.[4]: 85%). The product was stored in the glove box freezer (-30 °C). **^{1}H NMR** (600 MHz, C$_6$D$_6$): δ = 2.97 (q, ^3J = 7.0 Hz, 8H, C*H*$_2$), 0.97 (t, ^3J = 7.0 Hz, 12H, C*H*$_3$) ppm. **^{13}C {^{1}H} NMR** (151 MHz, C$_6$D$_6$): δ = 42.75 (*C*H$_2$), 15.28 (*C*H$_3$) ppm. **^{11}B NMR** (193 MHz, C$_6$D$_6$): δ = 28.56 (s) ppm. **HRMS** (EI, 70 eV, MAT95, direct): m/z [M]$^+$ Calcd. for $C_8H_{20}N_2{}^{11}B^{35}Cl$ 190.14038; Found 190.14026.

4.7.11 *bis*(biphenyl-2-yl)phosphino(*bis*(Diethylamino))borane (**154**)
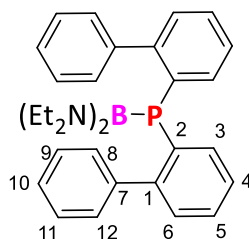

To a freshly prepared phosphide solution (0.354 mmol in 6.0 mL benzene), **152** (170 mg, 0.90 mmol) in benzene (1 mL) was added at 25 °C. After 24 h stirring all volatiles were removed (50 °C, 10^{-2} mbar, 4 h) and the reaction was extracted with n-hexane (20 mL). The solvent was removed again, and the product was isolated as white wax (**154**, 156 mg, 0.316 mmol, 90%). **^{1}H NMR** (601 MHz, C$_6$D$_6$): δ = 7.59 - 7.53 (m, 2H, *H*-3), 7.46 (d, ^3J = 7.0 Hz, 4H, *H*-8,12), 7.20 - 7.18 (m, 2H, *H*-6), 7.14 (t, ^3J = 7.6 Hz, 4H, *H*-9,11), 7.09 - 7.02 (m, 6H, *H*-4, *H*-5 and *H*-10), 2.90 (q, ^3J = 7.1 Hz, 8H, C*H*$_2$), 0.97 (t, ^3J = 7.1 Hz, 12H, C*H*$_3$) ppm. **^{13}C {^{1}H} NMR** (151 MHz, C$_6$D$_6$): δ = 147.63 (d, $^2J_{\text{C-P}}$ = 25.3 Hz, *C*-1), 143.00 (d, $^3J_{\text{C-P}}$ = 5.4 Hz, *C*-7), 137.40 (d, $^1J_{\text{C-P}}$ = 12.6 Hz, *C*-2), 135.59 (s, *C*-3), 129.99 (d, $^3J_{\text{C-P}}$ = 4.9 Hz, *C*-6), 129.72 (d, $^3J_{\text{C-P}}$ = 4.2 Hz, *C*-

8,12), 127.18 (d, $^3J_{\text{C-P}}$ = 7.7 Hz for *C*-5 and *C*-10), 126.66 (d, $^4J_{\text{C-P}}$ = 42.4 Hz, *C*-4), 42.10 ($^3J_{\text{C-P}}$ = 5.4 Hz, *C*H$_2$), 14.31 (s, *C*H$_3$) ppm. ^{11}**B {^{1}H} NMR** (193 MHz, C$_6$D$_6$): δ = 36.80 (s) ppm. ^{31}**P {^{1}H} NMR** (243 MHz, C$_6$D$_6$): δ = -55.20 (s) ppm. **HRMS** (EI, 70 eV, MAT95, indirect in *n*-hexane): *m/z* [M]$^{+\cdot}$ Calcd. for C$_{32}$H$_{38}$NP^{11}B 492.28602; Found 492.28606. **MS** (EI): *m/z* 492.4 (6%) [M]$^{+\cdot}$, 337.2 (5%) [M-H,(B(NEt$_2$)$_2$)]$^{+\cdot}$, 183.1 (100%) [M-H,(B(NEt$_2$)$_2$), (C$_{12}$H$_9$)]$^+$,155.2 [(B(NEt$_2$)$_2$)] (100%).

4.7.12 (Biphen-2-yl)(phenyl)phosphine (**159**)
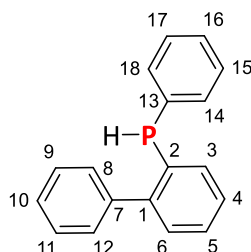
The reaction was performed like lit.[5] :A Schlenk flask was charged with dichlorophenylphosphine (**156** 0.89 g, 5.00 mmol) in THF (7.5 mL). At -78 °C a solution of 2-biphenylmagnesium bromide (**BiPhMgBr**, 10.0 mL, 5.00 mmol, 0.5 M in diethyl ether) was slowly added and reaction was stirred for 1 h at -78 °C. After the reaction temperature slowly raised to 25 °C, the reaction was continued to stir for 16 h. The reaction procedure was observed by ^{31}P{^{1}H} NMR (δ = 78.25 (**157**), 70.77 (**158**) ppm). The supernatant was transferred into a solution of lithium aluminum hydride (5.00 mL, 5.00 mmol, 1.0 M in THF) in diethyl ether (10 mL) using syringe filters. After stirring 4 h at 25 °C and 30 min at 60 °C the reaction mixture was diluted with diethyl ether (20 mL) and transferred to the glove box where it was transferred into another flask using syringe filters. The residue was washed with THF (5 mL), and combined fractions were dried *in vacuo* (3 mbar, 25 °C, 3 h). The product was obtained using inert Kugelrohr distillation (140-160 °C, 1.0 x 10^{-1} mbar) as colorless oil (**159**, 953 mg, 3.63 mmol, 72%, lit.[5]:71%). ^{1}**H NMR** (601 MHz, C$_6$D$_6$): δ = 7.39 (ddd, ^3J = 7.4, 5.7 Hz, ^4J = 1.4 Hz, 1H, *H*-3), 7.31 - 7.29 (m, 2H, *H*-8,12), 7.28 (dd, ^3J = 7.3 Hz, ^4J = 2.4 Hz, 1H, *H*-6), 7.18 (ddd, ^3J = 7.4, 5.7 Hz, ^4J = 1.4 Hz, 1H, *H*-5), 7.15 - 7.06 (m, 4H, *H*-9,11 and *H*-14,18), 7.03 -6.95 (m, 4H, *H*-4, *H*-15,17 and *H*-16), 5.17 (d, $^1J_{\text{P-H}}$ = 223.0 Hz, 1H, P*H*) ppm.) ^{13}**C {^{1}H} NMR** (151 MHz, C$_6$D$_6$): δ = 147.24 (d, $^2J_{\text{C-P}}$ = 16.5 Hz, *C*-1), 142.53 (d, $^3J_{\text{C-P}}$ = 3.3 Hz, *C*-7), 135.32 (d, overlap with next signal, *C*-2), 135.27 (d, $^2J_{\text{C-P}}$ = 10.1 Hz, *C*-3), 134.98 (d, $^2J_{\text{C-P}}$ = 15.9 Hz, *C*-14,18), 134.74 (d, $^1J_{\text{C-P}}$ = 14.1 Hz, *C*-13), 130.35 (d, $^3J_{\text{C-P}}$ = 2.8 Hz, *C*-6), 129.65 (d, $^4J_{\text{C-P}}$ = 3.2 Hz, *C*-8,12), 128.68 (s, *C*-9,11 or *C*-14,18), 128.63 (s, *C*-9,11 or *C*-14,18), 127.98 (overlap with solvent signal, *C*-5 and *C*-16), 127.49 (s, *C*-10), 127.47 (d, $^3J_{\text{C-P}}$ = 2.7 Hz, *C*-4), ppm. ^{31}**P NMR** (243 MHz, C$_6$D$_6$): δ = -45.92 (d, $^1J_{\text{P-H}}$ = 223.0 Hz) ppm. ^{1}**H NMR** (601 MHz, CDCl$_3$): δ = 7.46 (ddd, ^3J = 7.4, 5.7 Hz, ^4J = 1.4 Hz, 1H, *H*-3),7.43 -7.23 (m, 14H, all aromatic protons), 5.12 (d, $^1J_{\text{P-H}}$ = 223.1 Hz, 1H, P*H*) ppm.) ^{13}**C {^{1}H} NMR** (151 MHz, CDCl$_3$): δ = 146.80 (d, $^2J_{\text{C-P}}$ = 16.6 Hz, *C*-1), 142.06 (d, $^3J_{\text{C-P}}$ = 3.6 Hz, *C*-7), 134.90 (d, $^2J_{\text{C-P}}$ = 7.3 Hz, *C*-3), 134.76 (d, $^2J_{\text{C-P}}$ = 17.6 Hz, *C*-14,18), 134.63 (d, $^1J_{\text{C-P}}$ = 11.0 Hz, *C*-2), 134.17 (d, $^1J_{\text{C-P}}$ = 17.6 Hz, *C*-13), 130.05 (d, $^3J_{\text{C-P}}$ = 2.8 Hz, *C*-6), 129.38 (d, $^4J_{\text{C-P}}$ = 3.2 Hz, *C*-8,12), 128.59 (s, *C*-5 or *C*-16), 128.53 (d, $^3J_{\text{C-P}}$ = 2.7 Hz, *C*-15,17), 128.48 (s, *C*-5 or *C*-16), 128.16 (s, *C*-9,11), 127.49 (s, *C*-10), 127.47 (d, $^3J_{\text{C-P}}$ = 2.7 Hz, *C*-4) ppm. ^{31}**P NMR** (243 MHz, CDCl$_3$): δ = -46.05 (d, $^1J_{\text{P-H}}$ = 223.0 Hz) ppm. **HRMS** (EI, 70 eV, MAT95, indirect in *n*-hexane): *m/z* [M-H]$^+$ Calcd. for C$_{18}$H$_{14}$P 261.08276; Found 261.08331. The NMR analytics were not in comparison with the data published,[5] where it needs to be mentioned that either the solvent was given, nor the atoms were assigned.

4.7.13 (Biphenyl-2-yl)(phenyl)(trimethylsilyl)phosphine (161)
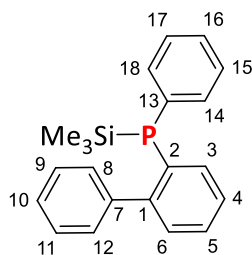
A Schlenk flask was charged with phosphine (**159**, 115 mg, 0.44 mmol) and toluene (5 mL). At 0 °C *n*-butyllithium (0.22 mL, 0.88 mmol, 2.5 M in hexanes) was added and the reaction was stirred at this temperature for 1 h and at 25 °C for 2 h. Afterwards trimethylsilyl chloride (108 mg, 1.00 mmol) was added and the reaction mixture was stirred for 14 h at 25 °C. All volatiles were removed, and the residue was extracted with *n*-hexane (10 mL). After removal of the solvent of a colorless/turbid oil was received. (**161**, 103 mg, 0.31 mmol, 72%). **¹H NMR** (601 MHz, C$_6$D$_6$): δ = 7.68 (ddd, ^3J = 7.6, 3.4 Hz, ^4J = 1.4 Hz, 1H, *H*-3), 7.44 - 7.41 (m, 2H, *H*-8,12), 7.37 - 7.33 (m, 2H, *H*-14,18), 7.27 (ddd, ^3J = 7.6, 4.3 Hz, ^4J = 1.5 Hz, 1H, *H*-6), 7.16 - 7.10 (m, overlap with solvent signal, 3H, *H*-9,11 and *H*-5), 7.15 - 7.06 (m, 2H, *H*-4 and *H*-10), 7.03 -7.00 (m, 2H, *H*-15,17), 6.99 - 6.95 (m, 1H, *H*-16), 0.06 (d, $^3J$$_{P-Si(CH3)3}$ = 4.8 Hz, 9H, C*H*$_3$) ppm. **¹³C {¹H} NMR** (151 MHz, C$_6$D$_6$): δ = 149.71 (d, $^2J$$_{C-P}$ = 26.1 Hz, *C*-1), 143.15 (d, $^3J$$_{C-P}$ = 5.5 Hz, *C*-7), 138.51 (d, $^1J$$_{C-P}$ = 18.5 Hz, *C*-13), 136.34 (d, $^2J$$_{C-P}$ = 2.6 Hz, *C*-3), 134.27 (d, $^1J$$_{C-P}$ = 17.5 Hz, *C*-2), 133.24 (d, $^2J$$_{C-P}$ = 17.0 Hz, *C*-14,18), 131.29 (d, $^3J$$_{C-P}$ = 5.1 Hz, *C*-6), 130.36 (d, $^3J$$_{C-P}$ = 4.0 Hz, *C*-8,12), 128.58 (s, *C*-5), 128.50 (d, $^3J$$_{C-P}$ = 6.2 Hz, *C*-15,17), 127.99 (s, *C*-9,11), 127.24 (s, *C*-4 or *C*-10), 127.21 (s, *C*-4 or *C*-10), 126.96 (s, *C*-16), -0.78 (d, $^2J$$_{C-P}$ = 13.1 Hz, C*H*$_3$) ppm. **²⁹Si{¹H} NMR** (119 MHz, C$_6$D$_6$): δ = 2.00 (d, $^1J$$_{P-Si}$ = 23.8 Hz) ppm. **³¹P NMR** (243 MHz, C$_6$D$_6$): δ = -63.07 (br) ppm. **HRMS** (EI, 70 eV, MAT95, indirect in *n*-hexane): *m/z* [M-H]⁺ Calcd. for C$_{18}$H$_{14}$P 333.12229; Found 333.12261.

4.7.14 Quantum chemical calculations

The equilibrium geometries were optimized with Gaussian 09[6] using B3LYP/6-31-G*-level of theory with empirical dispersion correction (GD3), followed by a frequency calculation to ensure that the optimized structures were the true minima. The orbital energies of HOMO and LUMO and their energy differences were calculated for these optimized molecules. NBO analysis were performed with the optimized structures using the NBO analysis which is implemented in Gaussian 09. Absorption calculations were performed with the B3LYP/6-31-G*-level of theory and TD = 40 states. NICS calculations (CSGT-B3LYP/6-31-G*) were determined 1 Å above/below the center of the respective ring and in plane (0 Å).[7, 8]

4.7.15 Single-crystal analysis

Air and moisture sensitive compounds were transferred in the glovebox into a wax and then mounted on the diffractometer. In general X-ray measurements were performed at 100 K on a Bruker Venture D8 diffractometer with graphite-monochromated Mo-Kα (0.7107 Å) radiation. All structures were solved by intrinsic phasing and refined based on F2 by use of the SHELX program package, as implemented in Olex2.[9] All non-hydrogen atoms were refined using anisotropic displacement parameters. The refinement was performed by E. Lork (Univ. Bremen). Hydrogen atoms attached to carbon atoms were included in geometrically calculated positions using a riding model. Figures were created using Mercury.[10]

Tab. 17: Overview of essential crystal structure details for **110**, **112**, **107** and **114**.

	110	112	107	114
Empirical formula	$C_{30}H_{32}NP$	$C_{24}H_{19}P$	$C_{24}H_{18}LiP$	$C_{27}H_{25}BP$
Formula weight	437.53	338.36	344.29	391.25
Temperature/K	100.0	100.0	100.0	100.0
Crystal system	triclinic	monoclinic	monoclinic	monoclinic
Space group	P-1	$P2_1/c$	$P2_1/n$	$P2_1/c$
a/Å	9.4189(3)	7.5529(2)	12.6051(9)	11.8705(5)
b/Å	11.1819(4)	20.0280(6)	16.0123(12)	10.2205(4)
c/Å	12.7140(4)	11.7785(3)	18.4340(12)	17.8670(7)
α/°	89.0990(10)	90	90	90
β/°	76.1210(10)	94.2750(10)	104.712(2)	93.7090(10)
γ/°	70.6150(10)	90	90	90
Volume/Å^3	1223.28(7)	1776.77(8)	3598.7(4)	2163.13(15)
Z	2	4	8	4
ρ_{calc} g/cm^3	1.188	1.265	1.271	1.201
μ / mm^{-1}	0.130	0.157	0.156	0.137
F(000)	468.0	712.0	1440.0	828.0
Crystal size/mm^3	0.23 × 0.21 × 0.18	0.28 × 0.19 × 0.16	0.24 × 0.23 × 0.21	0.26 × 0.2 × 0.19
Radiation	MoKα (λ = 0.71073)	MoKα (λ = 0.71073)	MoKα (λ = 0.71073)	MoKα (λ = 0.71073)

2Θ range for data collection/°	5.472 to 66.998	5.346 to 57	4.2 to 61.016	4.594 to 59.996
Index ranges	$-14 \leq h \leq 14$, $-17 \leq k \leq 17$, $-19 \leq l \leq 19$	$-10 \leq h \leq 9$, $-26 \leq k \leq 26$, $-15 \leq l \leq 15$	$-18 \leq h \leq 18$, $-22 \leq k \leq 22$, $-26 \leq l \leq 26$	$-16 \leq h \leq 16$, $-14 \leq k \leq 14$, $-25 \leq l \leq 25$
Reflections collected	102866	36505	108594	78277
Independent reflections	9585 [R_{int} = 0.0282, R_{sigma} = 0.0149]	4485 [R_{int} = 0.0402, R_{sigma} = 0.0225]	10966 [R_{int} = 0.0504, R_{sigma} = 0.0288]	6303 [R_{int} = 0.0291, R_{sigma} = 0.0146]
Data/restraints/ parameters	9585/0/293	4485/0/231	10966/0/469	6303/3/277
Goodness-of-fit on F^2	1.050	1.040	1.035	1.056
Final R indexes [I>=2σ (I)]	R_1 = 0.0333, wR_2 = 0.0922	R_1 = 0.0389, wR_2 = 0.0874	R_1 = 0.0447, wR_2 = 0.1085	R_1 = 0.0352, wR_2 = 0.0927
Final R indexes [all data]	R_1 = 0.0381, wR_2 = 0.0960	R_1 = 0.0466, wR_2 = 0.0912	R_1 = 0.0603, wR_2 = 0.1170	R_1 = 0.0403, wR_2 = 0.0974
Largest diff. peak/hole / e Å^{-3}	0.48/-0.29	0.38/-0.32	0.50/-0.36	0.38/-0.31

4.7.16 References for the Experimental Part

1. S. Han, C. M. Harris, T. M. Harris, H.-Y. H. Kim, S. J. Kim, *J. Org. Chem.*, **1996**, *61*, 174-178.
2. Y. Li, S. Chakrabarty, C. Muck-Lichtenfeld, A. Studer, *Angew. Chem. Int. Ed.*, **2016**, *55*, 802-806.
3. F. Duboudin, M. Birot, O. Babot, J. Dunoguès, R. Calas, *J. Organomet. Chem.*, **1988**, *341*, 125-132.
4. P. Y. Chavant, M. Vaultier, *J. Organomet. Chem.*, **1993**, *455*, 37-46.
5. M. Peer, J. C. de Jong, M. Kiefer, T. Langer, H. Rieck, H. Schell, P. Sennhenn, J. Sprinz, H. Steinhagen, B. Wiese, G. Helmchen, *Tetrahedron*, **1996**, *52*, 7547-7583.
6. M. J. Frisch, G. W. Trucks, H. B. Schlegel, G. E. Scuseria, M. A. Robb, J. R. Cheeseman, G. Scalmani, V. Barone, G. A. Petersson, H. Nakatsuji, X. Li, M. Caricato, A. V. Marenich, J. Bloino, B. G. Janesko, R. Gomperts, B. Mennucci, H. P. Hratchian, J. V. Ortiz, A. F. Izmaylov, J. L. Sonnenberg, Williams, F. Ding, F. Lipparini, F. Egidi, J. Goings, B. Peng, A. Petrone, T. Henderson, D. Ranasinghe, V. G. Zakrzewski, J. Gao, N. Rega, G. Zheng, W. Liang, M. Hada, M. Ehara, K. Toyota, R. Fukuda, J. Hasegawa, M. Ishida, T. Nakajima, Y. Honda, O. Kitao, H. Nakai, T. Vreven, K. Throssell, J. A. Montgomery Jr., J. E. Peralta, F. Ogliaro, M. J. Bearpark, J. J. Heyd, E. N. Brothers, K. N. Kudin, V. N. Staroverov, T. A. Keith, R. Kobayashi, J. Normand, K. Raghavachari, A. P. Rendell, J. C. Burant, S. S. Iyengar, J. Tomasi, M. Cossi, J. M. Millam, M. Klene, C. Adamo, R. Cammi, J. W. Ochterski, R. L. Martin, K. Morokuma, O. Farkas, J. B. Foresman, D. J. Fox, Gaussian 16 Rev. C.01, **2016**.
7. P. V. R. Schleyer, M. Manoharan, Z. X. Wang, B. Kiran, H. Jiao, R. Puchta, N. J. R. van Eikema Hommes, *Org. Lett.*, **2001**, *3*, 2465-2468.
8. J. Kapp, C. Schade, A. M. El-Nahasa, P. von Ragué Schleyer, *Angew. Chem. Int. Ed.*, **1996**, *35*, 2236-2238.
9. O. V. Dolomanov, L. J. Bourhis, R. J. Gildea, J. A. K. Howard, H. Puschmann, *J. Appl. Crystallogr.*, **2009**, *42*, 339-341.
10. C. F. Macrae, I. Sovago, S. J. Cottrell, P. T. A. Galek, P. McCabe, E. Pidcock, M. Platings, G. P. Shields, J. S. Stevens, M. Towler, P. A. Wood, *J. Appl. Crystallogr.*, **2020**, *53*, 226-235.

Résumé

Cette thèse traite de la synthèse, la caractérisation et les propriétés photo physiques de nouveaux systèmes π-conjugués intégrant des éléments du bloc p: bore, azote, phosphore, silicium, germanium et étain.

Préface A: Influence des éléments lourds du groupe 14 sur les systèmes π-conjugués et les matériaux fonctionnels

Il a été souligné que les organotétrels présentent une double fonctionnalité lorsqu'ils sont présents dans des hétérocycles ou des matériaux fonctionnels organiques. S'ils sont incorporés dans des systèmes π-conjugués, ils permettent la stabilisation du niveau de l'orbitale Basse Vacante (BV) et conduisent à un décalage vers le rouge de l'absorption et de l'émission. Les organotétrels liés de manière exocyclique servent de groupes partants dans les réactions de couplage croisé et dans les réactions d'échange tétrel/métal.

Chapitre I: Etude des propriétés optiques et redoxs d'hétérocycles contenant de l'étain

L'insertion de l'étain dans un hétérocycle à cinq chaînons, appelé stannole, a une influence drastique sur les propriétés électroniques. Le niveau BV est stabilisé en raison de la conjugaison σ*-π* des orbitales exocycliques σ*-bond avec l'orbitale π* du butadiène. Par conséquent, les stannoles présentent en général un écart HO/BV plus faible que leurs analogues de thiophène et présentent une absorption/émission décalée vers le rouge. Cela a été prouvé pour le monomère et le dimère de stannole substitué par des *bis*-thiényle qui sont l'équivalent du terthiophène et du sexithiophène (fig. 1).
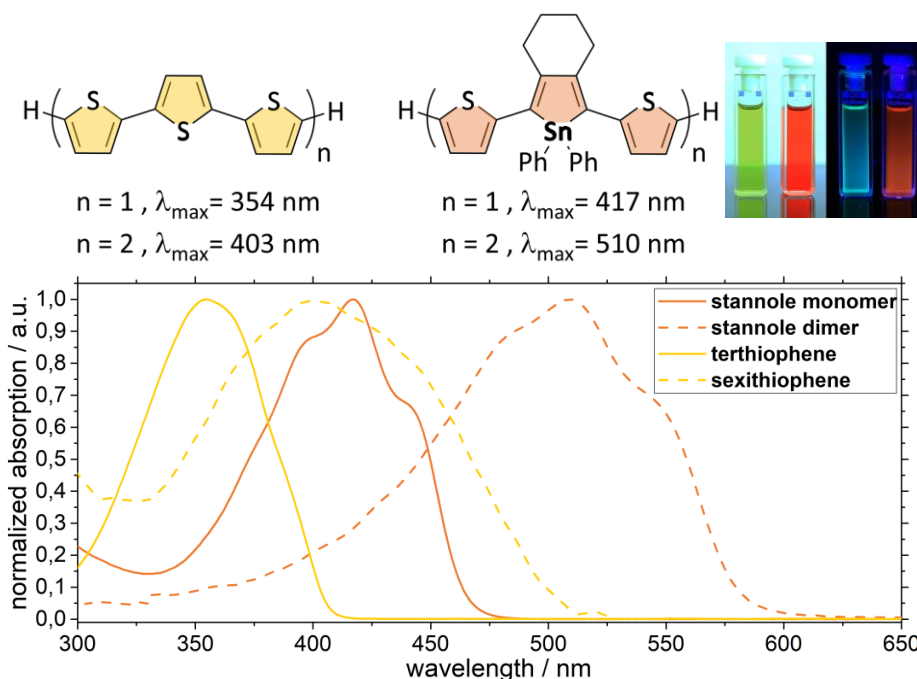

Fig. 1: Vue d'ensemble des stannoles flanqués de *bis*-thiényle, de leurs analogs d'oligothiophène et des spectres d'absorption respectifs dans le DCM. De plus, une image du monomère et du dimère de stannole sous la lumière ambiante et sous irradiation UV sont représentées.

Les dérivés de stannole ont entraîné un décalage bathochrome de 63/74 nm par rapport aux dérivés de thiényle et un faible écart de bande calculé par des méthodes optiques de 2.66/2.13 eV. En plus de présenter une BV stabilisée, le comportement électrochimique du monomère et du dimère de stannole était similaire à celui de leurs analogues de thiophène, par ex. le dimère de stannole présente une oxydation totalement réversible qui n'a pas été observée pour le monomère de stannole. En raison

de l'analogie thiophène/stannole, une électropolymérisation du stannole monomère substitué de thiényle (n = 1) et du dimère (n = 2) a été testée et une formation de films électrodéposés a été observée. Au cours de l'étude, la stabilité électrochimique du monomère et du dimère a été estimée par des méthodes spectroélectrochimiques et une décomposition partielle dans des conditions oxydantes a été trouvée. Contrairement au monomère stannole (n = 1) a présenté une photoinstabilité. Outre l'énorme décalage bathochrome lié à la présence d'un atome d'étain dans des motifs thiényle, la stabilité du stannole doit être optimisée pour une application ultérieure dans l'électronique organique.

Chapitre II: Influence des tétrels (C, Si, Ge, Sn) sur les propriétés structurales, thermiques et optiques des dérivés d'azobenzènes

Le remplacement des molécules fonctionnelles par des (organo)tétrels plus lourds est très prometteur car ils pourraient servir de précurseurs synthétiques pour les réactions d'échange métal-lithium ou de couplage croisé catalysées par un métal de transition. Ce concept a été étudié pour les azobenzènes *ortho*-stannylés (schéma 1).
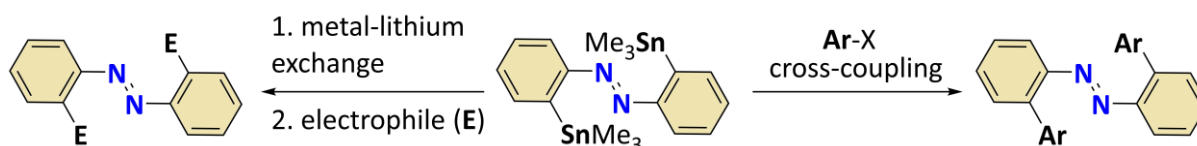

Schéma 1: 2,2'-*bis*(triméthylstannyl) azobenzène comme matière de départ pour les réactions de couplage croisé ou d'échange métal-lithium.

Le groupe triméthylétain a été introduit par une voie de couplage croisé de l'hexaméthylditine et d'un azobenzène *ortho*-halogéné. Une étude des séquences de réaction d'échange étain-lithium (cuivre) et un piégeage par divers électrophiles a été réalisée. En utilisant le cuprate «mou» comme précurseur, des rendements plus élevés ont pu être obtenus pour les nucléophiles «doux», par exemple, l'iodure de méthyle ou l'iodure de triméthylsilyle. Le *bis*(*ortho*-méthythio) azobenzène a également pu être obtenu et sa structure cristalline a été étudiée par analyse de surface d'Hirshfeld. En résumé, quatre azobenzènes substitués par des *ortho*-triméthyltétrels (C, Si, Ge, Sn) ont pu être synthétisés et l'influence du groupe tétrel sur les propriétés structurales, thermiques et photophysiques de l'azobenzène a été étudiée (fig. 2).
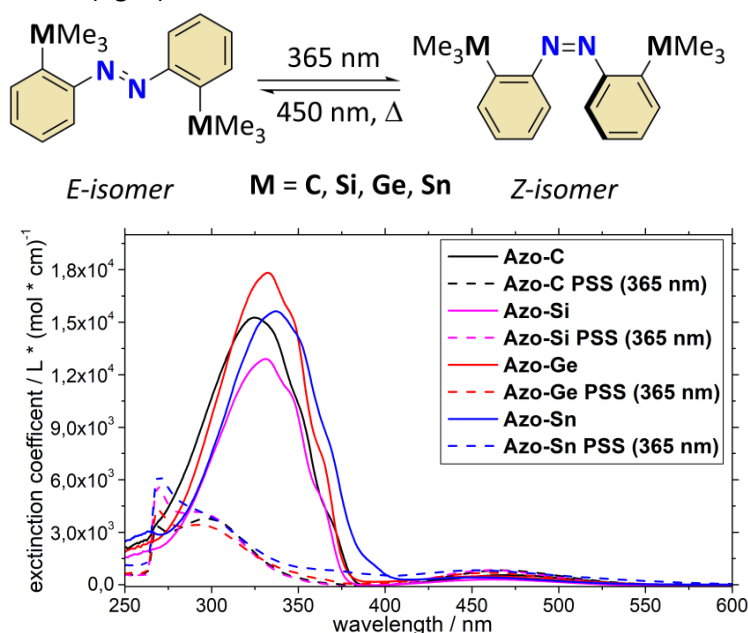

Fig. 2: Spectres d'absorption des azobenzènes tétrel-substitués avant et après irradiation (365 nm).

En plus de cela, ces nouveaux azobenzènes ont pu être utilisés dans des réactions de couplage croisé spécifiques impliquant des atomes de Si, Ge ou Sn avec divers halogénures d'aryle, donnant lieu à une méthodologie pour la construction de commutateurs moléculaires à base d'arène. Les premières réactions dans les conditions de couplage croisé de Stille ont montré des résultats positifs pour cette tentative de transformation. Pour d'autres projets, l'azobenzène *ortho*-dinucléophile représente un précurseur approprié pour la synthèse d'azobenzènes *ortho*-pontés (par exemple les diazocines).

Préface B: Incorporation d'unités triel/pnictogène dans des structures organiques pour des propriétés optoélectroniques supérieures: principes fondamentaux, synthèse, photophysique et analyse des matériaux

La substitution isoélectronique d'une unité C=C dans un système π cyclique par une unité BN ou BP influence effectivement la géométrie, la polarisation, l'aromaticité et surtout l'écart HO/ BV du système cyclique. Le décalage bathochrome qui en résulte peut-être mis à profit dans les matériaux ayant une application en électronique (OSC, OFET, OLED). Les principales différences des unités BN et BP par rapport à leurs analogues carbonés sont des facteurs géométriques et électroniques. Alors que l'atome d'azote dans les systèmes BN est plan trigonal, le phosphore préfère généralement une géométrie pyramidale dans les unités BP. Cette P-pyramidalisation est contrôlable par des substituants stéréoélectroniques au niveau du phosphore.

Chapitre III: Synthèse, propriétés optoélectroniques et application dans les dispositifs opto-electronic organiques (OLED/OFET) de nouveaux diimides de coronène contenant du bore/azote

Jusqu'à présent, la variété des BN-HAP décrits se concentrait sur les HAP riches en électrons et neutres en électrons. La combinaison d'unités BN avec des HAP accepteurs d' électrons n'a pas été réalisée. Les accepteurs d'électrons non-fullerèniques les plus étudié sont les rylène-diimides, par ex. le diimide de naphtalène (**NDI**), le diimide de pérylène (**PDI**) et le diimide de coronène (**CDI**). L'extension π longitudinale des rylènes, par ex. de NDI à **PDI**, conduit à un décalage bathochrome de l'absorption/émission tandis que l'extension π latérale, par ex. du **PDI** au **CDI**, amène à des propriétés optiques déplacés vers le bleu. Dans ce projet, il a été étudié si l'introduction de deux unités BN dans les **CDI**, donnant des **BNCDI**, pouvait influencer ces propriétés optoélectroniques. Par conséquent, l'extension latérale du noyau des diimides de pérylène substitués par un amino vers les **BNCDI** *via* la borylation électrophile a été développée (schéma 2).
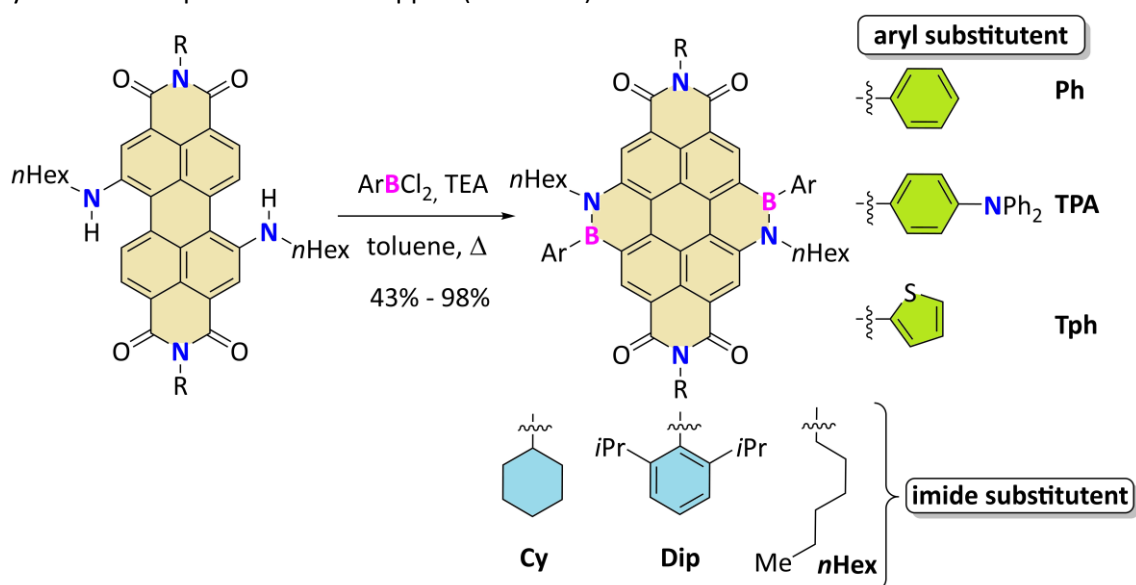

Schéma 2: La borylation électrophile en tandem avec divers aryldichloroboranes et **PDI** substitués par 1,7-di(*n*-hexylamino) tenant divers substituants à la position imide a conduit à la formation de sept nouveaux **BNCDI**.

Au total, sept **BNCDI** ont été synthétisés avec des rendements bons à excellents. Un choix judicieux de l'imide et des substituants aryle devrait influencer la relation structure-propriété de ces nouveaux BN-PAH à l'état solide et en solution. En général, les **BNCDI** ont présenté des propriétés optoélectroniques bénéfiques par rapport aux **CDI** tout carbone d'origine: de forts déplacements bathochromes et des coefficients d'extinction molaire plus élevés ont été obtenus, soutenus par des propriétés de fluorescence favorables, par ex. de petits décalages de Stokes et des rendements quantiques élevés jusqu'à l'unité (Fig. 3).
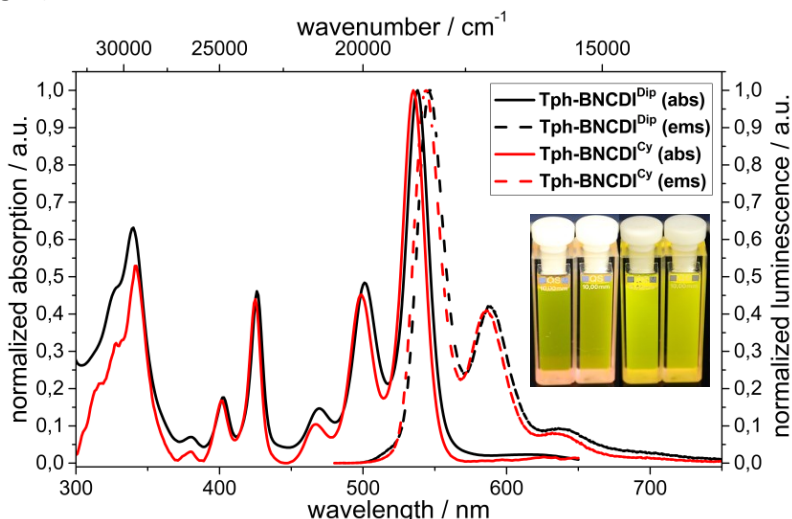

Fig. 3: Spectres d'absorption et d'émission des composés **Tph-BNCDI^{Cy}** et **Tph-BNCDI^{Dip}**. En outre, une photographie des deux substances avec la lumière ambiante (à gauche) et à une irradiation de 365 nm (à droite) est affichée.

Les spectres d'absorption étaient assez similaires à l'absorption des **CDI** et des **PDI**. Cela s'explique par l'orientation négative verticale (de type **CDI**) et longitudinale (de type **PDI**) des orbitales frontières. L'effet des substituants imide était marginal sur les propriétés optoélectroniques en solution mais différait sensiblement à l'état solide. Pour les études des **BNCDI**, deux **BNCDI** à substituant thiényles ont été choisis qui ne diffèrent que par la position imide (2,6-di*iso*propylphényle vs. cyclohexyle) (fig. 4).
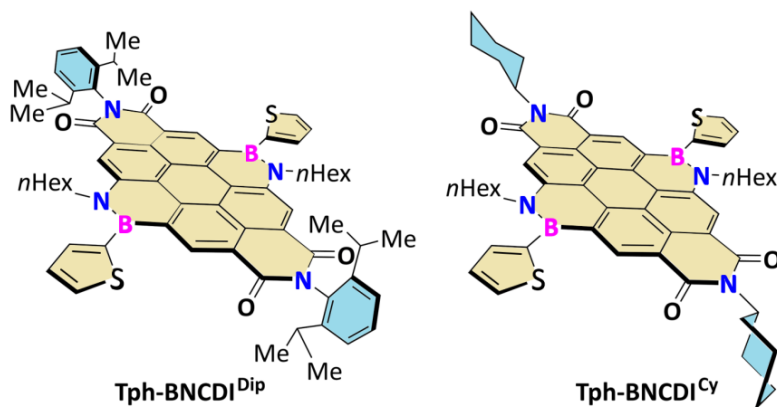

Fig. 4: Structures moléculaires de **Tph-BNCDI^{Cy}** et **Tph-BNCDI^{Dip}**

L'effet des substituants imide était marginal sur les propriétés optoélectroniques en solution mais différait sensiblement à l'état solide. Les **BNCDI** substituées par cyclohexyl et 2,6-di*iso*propylphényle ont montré des effets d'agrégation divergents tels que déterminés par spectroscopie de luminescence à basse température. L'incorporation des deux **BNCDI** dans une matrice PMMA montre des processus d'extinction de luminsecence provoqués par l'agrégation (ACQ) lors de l'augmentation de la concentration. Il a été montré que le motif cyclohexyle était moins efficace pour empêcher l'agrégation

que le substituant 2,6-di*iso*propylphénylimide. En raison de leurs propriétés optoélectroniques optimales et de leur stabilité thermique, les deux dérivés **Tph-BNCDI** ont été testés dans des dispositifs OLED. Comme les **BNCDI** purs souffraient d'effets ACQ, ils ont été utilisés comme dopants dans des matrices (DPVBi et CBP). Les spectres d'électroluminescence résultants variaient en fonction de la matrice utilisée et en fonction du substituant imide au niveau du **BNCDI** (fig. 5).
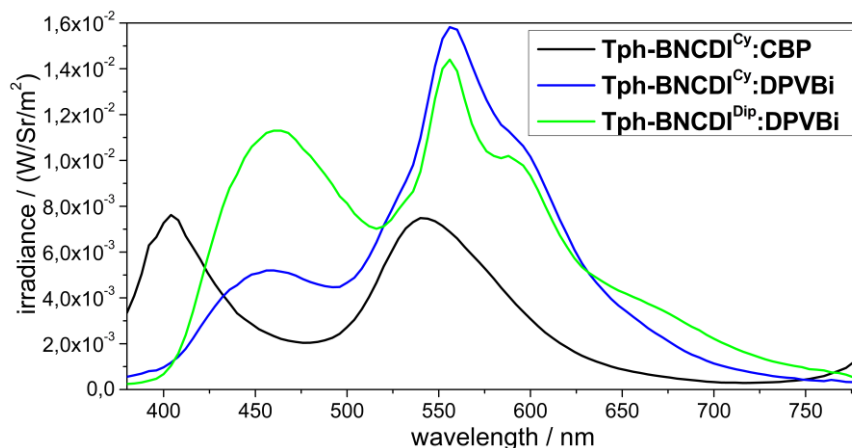

Fig. 5: Spectres d'électroluminescence des dispositifs OLED des meilleures pratiques avec des **Tph-BNCDI** avec différents substituants imide ou des hôtes différents.

En combinaison avec des matrices émettant dans le bleu, des dispositifs OLED (WOLED) à émission de couleur blanche avec une efficacité quantique externe (EQE) jusqu'à 1,5% ont été obtenus. En outre, des tensions seuil de mise en marche (3.7 V) étonnamment faibles et une luminance jusqu'à 1001 cd/m^2 ont été obtenues. Au cours de cette étude, il a été constaté qu'en cas d'augmentation des taux de dopage **BNCDI**, les performances des dispositifs OLED diminuaient considérablement. Ceci a été attribué aux processus ACQ qui ont été observés au préalable dans le mélange PMMA et les expériences de luminescence à basse température. De plus, le **Tph-BNCDI^{Cy}** à agrégation plus forte a été implémenté dans un dispositif OFET produisant de faibles performances (rapport de courant marche/arrêt I$_{on}$/I$_{off}$ = 36, mobilités à effet de champ d'environ (μ_{FE}) 10^{-8} cm^2 V^{-1} s^{-1}, seuil tension V$_{th}$ ≈ 20 V).

L'effet des groupes aryle au niveau de l'atome de bore a ensuite été étudié: pour la première fois en chimie BN, l'atome de bore d'un BN-PAH accepteur d'électrons a été connecté à un substituant donneur d'électrons fort, ici la triphénylamine, conduisant à la formation d'une triade DAD (fig. 6).
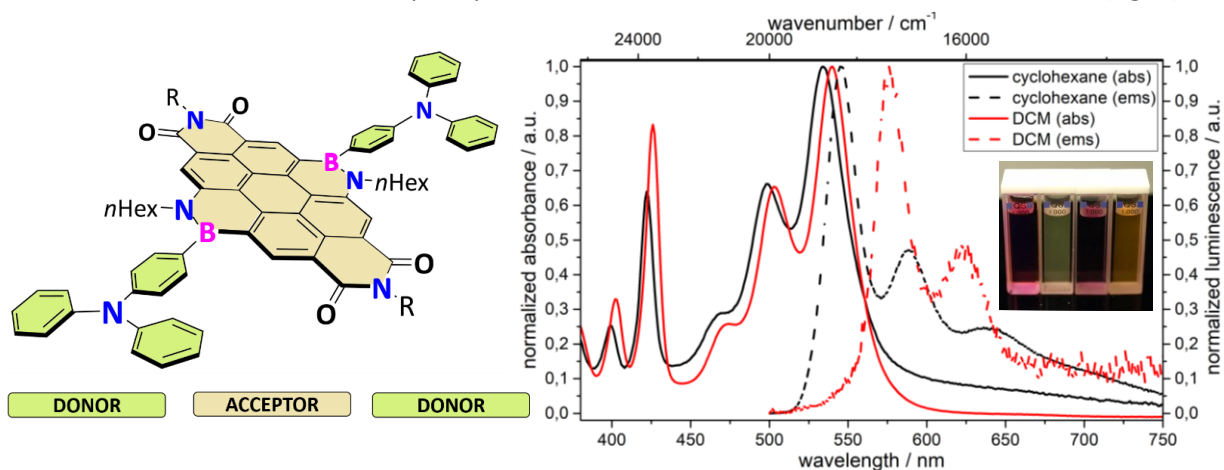

Fig. 6: Spectres d'absorption et d'émission du **TPA-BNCDI^{Cy}** dans le DCM et le cyclohexane. La photographie montre **TPA-BNCDI^{Cy}** dans DCM (à gauche)/ cyclohexane (à droite) et **TPA-BNCDI^{Dip}** dans DCM (à gauche)/cyclohexane (à droite) sous irradiation avec une lampe UV à 365 nm.

La combinaison de la triphénylamine donneuse d'électrons forte avec le **BNCDI** attracteur d'électrons a conduit à des solutions faiblement luminescentes dans des solutions DCM avec un grand déplacement de Stokes. Il a été constaté que les solutions de **TPA-BNCDI** dans les solvants non-polaires présentaient des rendements quantiques de fluorescence élevés ainsi que de petits décalages de Stokes. Etant donné qu'un tel comportement n'était pas présent pour les **BNCDI** à substitution phényle/thiényle, l'effet était clairement attribuable aux effets stéréoélectroniques du substituant triphénylamine au niveau de l'atome de bore. Un transfert d'électrons photoinduit a été proposé.

Pour comprendre les propriétés électroniques uniques des **TPA-BNCDI**, ces derniers ont été étudiés par voltampérométrie cyclique et comparés à un **BNCDI** thiényle substitué (fig. 7).
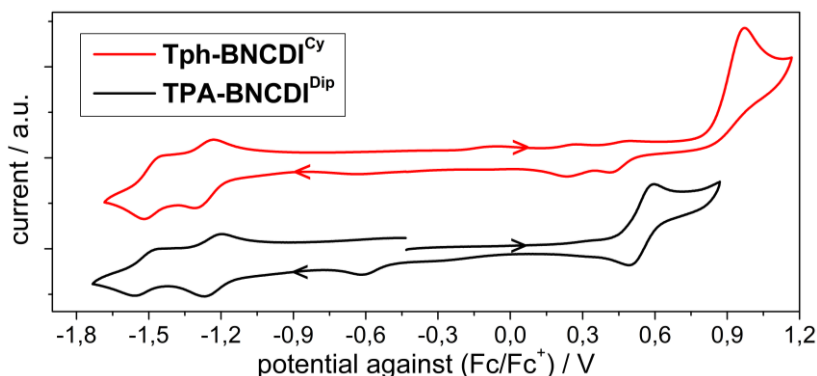

Fig. 7: Voltammogramme cyclique de **TPA-BNCDI**[Dip] et **Tph-BNCDI**[Cy] (10^{-3} M) dans DCM avec nBu$_4$NPF$_6$ (0.2 M) comme sel conducteur.

Les **BNCDI** substitués par la triphénylamine présentaient un potentiel d'oxydation plus faible et un écart HO/BV diminué. Cela pourrait expliquer la luminescence dépendant du solvant des **TPA-BNCDI**, qui n'avait pas été observée pour les **Ph/Tph-BNCDI**. D'autres **BNCDI** substitués par la triphénylamine ont montré des propriétés redox entièrement réversibles observées par des expériences spectroélectrochimiques et prouvant la stabilité de la nouvelle triade D-A-D à base de BN. De plus, ces nouveaux systèmes ont également été étudiés pour leur réponse vis à vis de l'ajout de bases de Lewis et d'acides de Lewis, donnant naissance à des espèces qui montrent une absorption dans la région NIR (fig. 8).
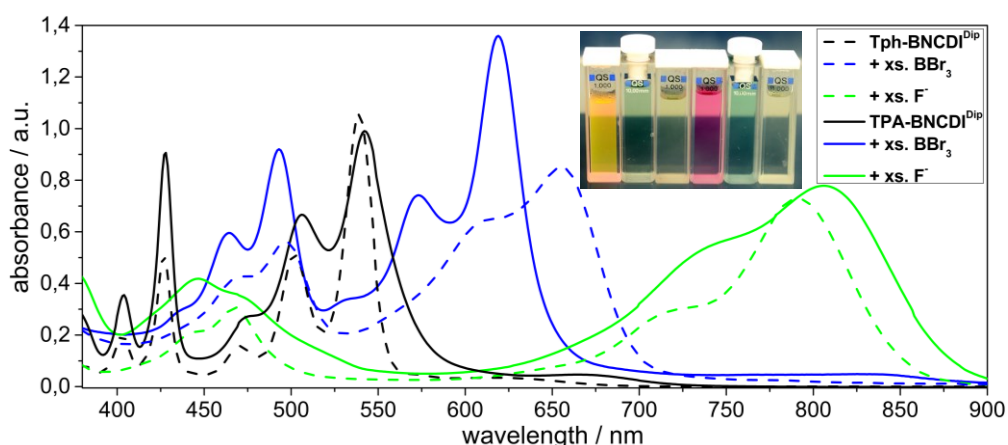

Fig. 8: Spectres d'absorption de **TPA-BNCDI**[Dip]/**Tph-BNCDI**[Dip] et leur interaction avec BBr$_3$ et TBAF. L'image photographique montre des solutions de **Tph-BNCDI**[Dip] dans DCM, avec BBr$_3$ et avec TBAF (de gauche à droite) ainsi que **TPA-BNCDI**[Dip] dans DCM, avec BBr$_3$ et avec TBAF.

Le titrage des **BNCDI** avec une source de fluorure ou du tribromure de bore a révélé que la formation des adduits de Lewis est un processus en deux étapes. Par conséquent, les deux unités BN interagissaient individuellement en tant que base/acide de Lewis. De manière remarquable, l'adduit de fluorure **BNCDI** était toujours émissif et a montré un signal d'émission large dans la région NIR (700-

1000 nm) qui pourrait être utile à des fins de détection. De plus, tous les **BNCDI** présentaient une interaction avec des solvants à faible coordination, par ex. THF, acétonitrile ou triéthylamine, comme indiqué par les maximas d'absorption décalés vers le rouge. Un effet auxiliaire du substituant triphénylamine vis-à-vis de l'acidité/basicité de Lewis ou de la coordination par des solvants n'a pas été trouvé. Il a été conclu que les changements conformationnels de l'unité BN lors de la coordination avaient des effets drastiques sur la planéité du noyau de diimide de coronène et résultaient donc en un décalage bathochrome de l'absorption/émission.

Chapitre IV: Nouveaux concepts pour synthétiser des HAP uniques incorporés au bore/phosphore

Même si de nombreux systèmes cycliques ou polycycliques à substitution BN ont été décrits au cours de la dernière décennie, très peu d'études sur les systèmes π à substitution BP ont été reportées. Les hydrocarbures aromatiques polycycliques conjugués à substitution BP présentent un grand potentiel en électronique organique, car une stabilisation du niveau de la BV devrait conduire à un écart HO/BV plus petit par rapport aux CC/BN-PAH. En outre, les BP-PAHS substitués au niveau de l'atome de phosphore (oxydation, complexation), peuvent être utilisés pour affiner les propriétés optoélectroniques.

Pour étudier l'effet d'une substitution BP, dans ce projet, le motif dibenzochrysène (**DBC**) et tétrathiénonaphtalène (**TTN**) a été choisi comme structure carbonée. Puisque les DBC/TTN normaux et BN-substitués ont déjà été synthétisés avec succès, une comparaison directe avec les structures BP-substituées devrait être possible. Initialement, les **DBC/TTN** substitués par BP ont été comparés à leurs congénères CC/BN par des méthodes de calcul théoriques, mettant en évidence les effets géométriques et électroniques du phosphore dans les unités BP. En raison de l'atome de phosphore pyramidal, le **BP-DBC/TTN** correspondant présentait une géométrie distordue avec une orientation hors du plan de l'unité BP par rapport aux structures CC/BN correspondantes (fig. 9).
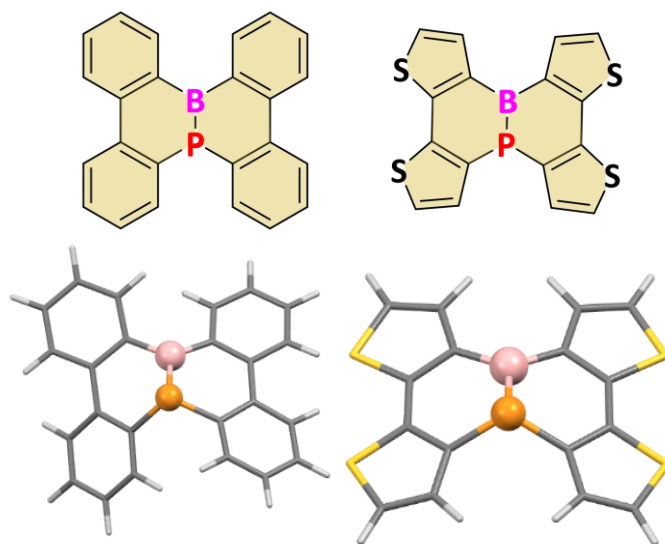

Fig. 9: BP-substitué dibenzo[g,p]chrysène (**BP-DBC**) et tétrathiénonaphtalène (**BP-TTN**) et leurs géométries optimisées (B3LYP-6-31G*).

La somme des angles au niveau des atomes de phosphore (Σ = 309.88°/332.63°) indiquait sa pyramidalisation et donc une moindre interaction du phosphore avec les atomes de bore ou de carbone voisins était suspectée. De plus, la nature des liaisons au sein des nouvelles structures BP a été étudiée par analyse d'occupation des liaisons naturelles (NBO). Dans le dérivé **BP-TTN**, une liaison classique B=P était présente tandis que le dérivé **BP-DBC** contenait un caractère de liaison simple combiné avec une description de paires de Lewis. Étant donné que l'atome de phosphore interagissait

à peine avec l'atome de bore, il pourrait être accessible pour une post-fonctionnalisation ultérieure du **BP-DBC** pour modifier les niveaux HO/BV. Outre les effets géométriques, les structures BP ont modifié les structures électroniques des motifs **DBC** et **TTN**: un niveau BV stabilisé et une absorption décalée vers le rouge par rapport aux congénères CC/BN respectifs ont été trouvés. D'autres calculs d'aromaticité (NICS) ont révélé que l'anneau central avait une aromaticité diminuée par rapport à leurs congénères CC/BN. Tous ces résultats préliminaires théoriques étaient très prometteurs pour une application en électronique organique.

En général, les méthodes d'accès aux HAP substitués par BP sont à peine décrites et souffrent encore d'une applicabilité synthétique. Par analogie avec la chimie BN, de nouvelles méthodes de synthèse pour préparer des HAP substitués par BP par des réactions d'annulation d'une phosphine positionnée en baie ont été étudiées (schéma 3).
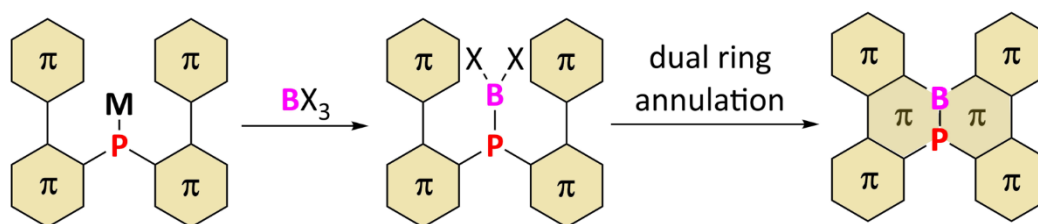

Schéma 3: Synthèse vers des systèmes π annulés BP par borylation de *bis*(diaryle)phosphure et suivie de réactions d'annulation de cycle en tandem.

Il était prévu que la réaction de double annulation pourrait être la partie la plus difficile dans cette procédure puisque la liaison P-B n'est pas stable. Pour réaliser ces réactions, le précurseur du motif **BP-DBC**, la bis (biphényl) phosphine a été synthétisée. Le diarylphosphine amide et la structure clé bis (biaryl) phosphine pourraient être isolés avec des rendements élevés après optimisation préalable (schéma 4).
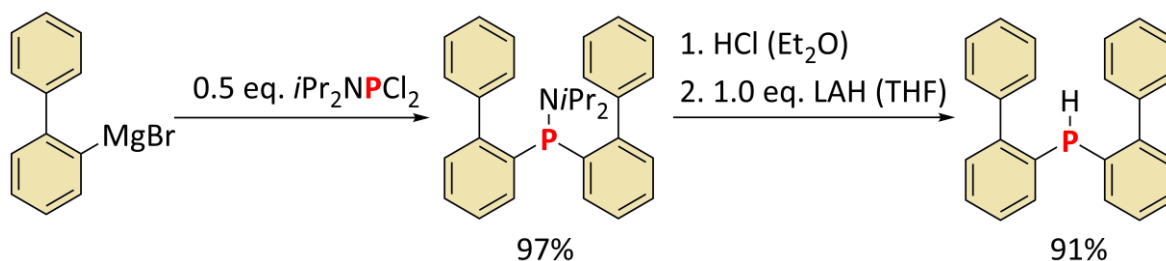

Schéma 4: Synthèse de la phosphine.

Pour ces précurseurs et la phosphine protégée par le borane, des structures cristallines ont été obtenues et ont montré un encombrement stérique de l'atome de phosphore par les deux ligands biphényles qui diminue les possibles réactions d'oxydation (fig. 10).
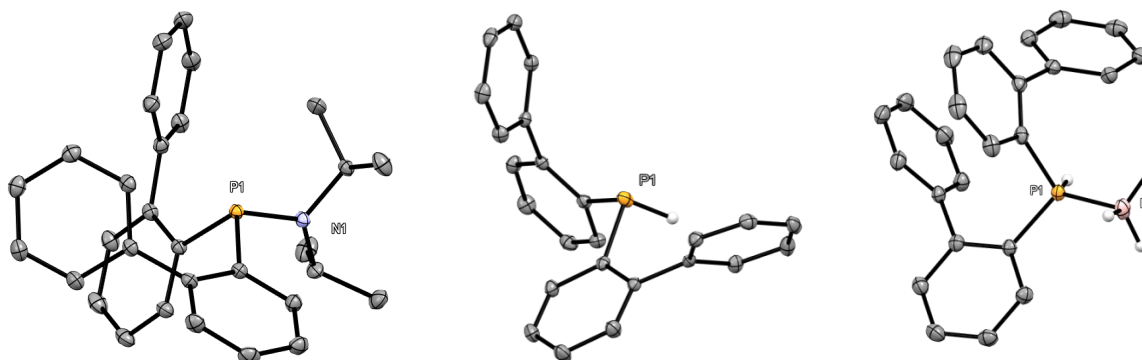

Fig. 10: Structures cristallines de la phosphine amide, de la phosphine et la phosphine protégée par le borane.

Pour accéder à la structure **BP-DBC**, des réactions de *bis*(biphényl)phosphures/phosphines avec des espèces de bore ont été réalisées (schéma 5).
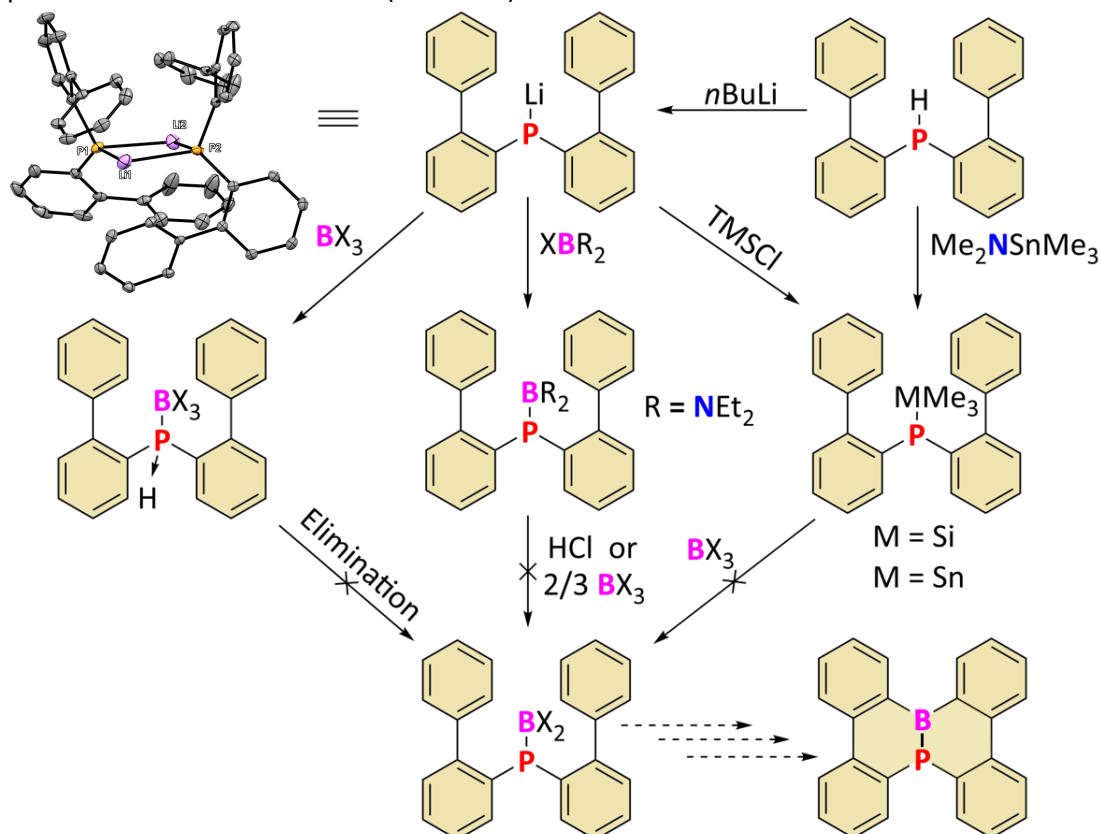

Schéma 5: La séquence de réaction pour obtenir des HAP substitués par BP a conduit dans la plupart des cas à l'adduit de phosphine borane.

Dans la plupart des cas, l'approche pour produire les HAP substitués BP souhaités n'a pas été couronnée de succès et la formation d'adduits de phosphine borane a été observée. Des résultats similaires ont été obtenus par des réactions d'échange tétrel(Si/Sn)-bore. La réaction des dérivés nucléophiles de phosphine avec divers boranes électrophiles a révélé que l'acidité de Lewis des boranes avait un effet majeur sur la réaction elle-même. Seul l'acide de Lewis doux (Et$_2$N)$_2$BCl a réagir avec un phosphure donnant le seul composé BP à faible valence dans ce projet.

Il a été conclu que des boranes avec un caractère moins acide au sens de Lewis stabilisent les phosphino boranes correspondants. Malheureusement, c'est contradiction avec l'acidité de Lewis requise pour accéder au **BP-DBC** via une réaction d'annulation de cycle (schéma 6).

isolated for R = **N**Et$_2$ (weaker Lewis acid)
not obsevered for R = Br, Cl (strong Lewis acid)

BP-DBC

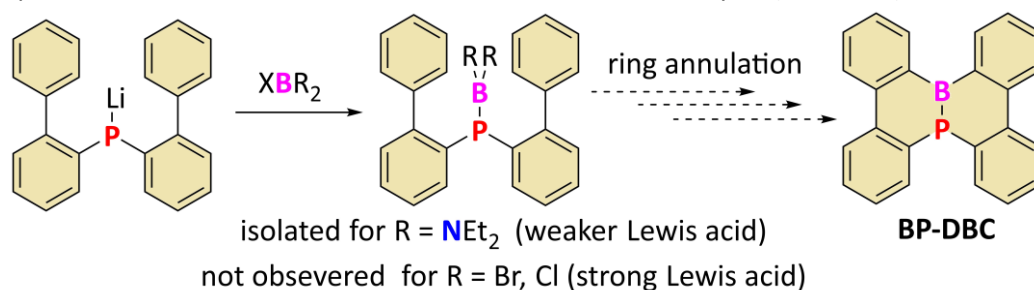**Schemá 6**: The influence of the Lewis acidity on the stability of the BP-species **141** opposes the required Lewis acidity for the ring annulation reaction towards **BP-DBC**.

Bien que les tentatives initiales pour échanger les substituants au niveau de l'atome de bore aient échoué, cela pourrait être un moyen possible d'accéder à un précurseur approprié pour la réaction d'annulation du cycle.

Zusammenfassung

Diese Arbeit behandelt die Synthese, Charakterisierung und photophysikalische Eigenschaften von neuartigen π-konjugierten organischen Strukturen, welche die Elemente des p-Blocks Bor, Stickstoff, Phosphor, Silikon, Germanium oder Zinn enthalten.

Vorwort A: Einfluss von schweren Gruppe-14-Elementen auf organische π-konjugierte Systeme

Eingänglich wurde gezeigt, dass Organotetrele eine duale Funktionalität aufweisen, da sie eingebunden in Heterozyklen (endozyklisch) oder als funktionelle Gruppe (exozyklisch) in organischen Funktionsmaterialien verwendet werden können. Durch die endozyklische Integration von Organotetrelen in π-konjugierte Strukturen wird das LUMO Niveau stark abgesenkt. Dies führt im Allgemeinen zu einer Rotverschiebung der Absorptions- und Emissionsmaxima. Hingegen finden exozyklisch gebundene Organotetrele häufig als Abgangsgruppe in Kreuzkupplungs und in Tetrel/Metallaustauschreaktionen Verwendung.

Kapitel I: Untersuchungen der optischen Eigenschaften von zinnhaltigen Heterozyklen und Studien zu deren elektrochemischen Stabilität

Die Integration von Zinn in einen konjugierten fünfgliedrigem Heterozyklus, ein sogenanntes Stannole, führt zu einer außerordentlichen Veränderung der elektronischen Eigenschaften des Zyklus: Das LUMO Niveau wird durch den σ*-π* Konjugationseffekt der exozyklischen σ*-Bindungsorbitalen mit dem π*-Orbital des Butadiens stabilisiert. Im Vergleich zu anderen Heterozyklen, z.B. Thiophen, besitzen Stannole daher eine geringere HOMO/LUMO Lücke und eine signifikante Rotverschiebung von Absorption und Emission. Dieser Effekt konnte für Thienyl-flankierte Stannole im Vergleich zu seinen Thiophenanaloga Ter- und Sexithiophen beschrieben werden (Fig. 1).
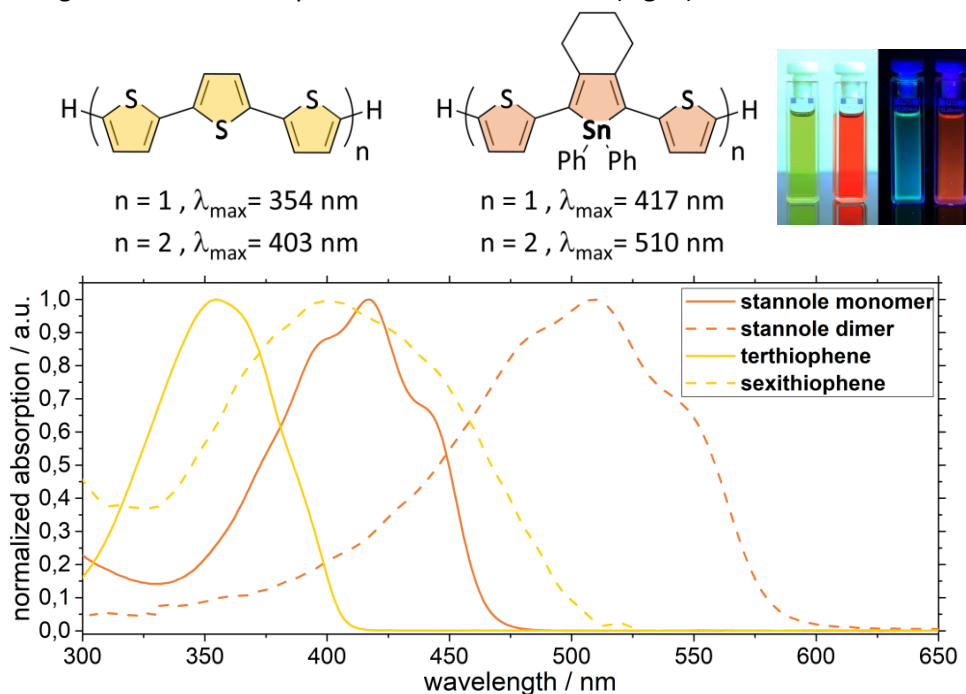

n = 1 , λ_{max}= 354 nm
n = 2 , λ_{max}= 403 nm

n = 1 , λ_{max}= 417 nm
n = 2 , λ_{max}= 510 nm

Fig. 1: Übersicht der Thiophen-flankierten Stannole, die entspechende Thienylanaloga und die Absorptionsspektren in DCM. Weiterhin ist eine Abbildung der beiden Stannolderivate unter Tageslicht und mit Bestrahlung durch UV-Licht zu sehen.

Die Stannolderivate zeigten eine bathochrome Verschiebung von 63/74 nm im Vergleich zu den entsprechenden Thienylderivaten und eine geringe optische Bandlücke von 2.66/2.13 eV. Trotz des formellen Zinn/Schwefel-Austausches war das elektrochemische Verhalten des Stannolmonomers und des Dimers ähnlich zu ihren Thiophenanaloga: Das Stannoldimer zeigte eine vollständig reversible

zweistufige Oxidation, welche nicht für das Stannolmonomer beobachtet wurde. Aufgrund der Thiophen/Stannol-Analogie wurde die Elektropolymerisation von Thienyl-flankiertem Stannol untersucht und die Bildung von Filmen auf Elektrodenoberflächen beobachtet. Im Verlauf der Studie wurde zudem die elektrochemische Stabilität des Monomers und Dimers durch spektroelektrochemische Verfahren geprüft. Es konnte eine teilweise Zersetzung unter oxidativen Bedingungen festgestellt werden. Weiterhin wurde beobachtet, dass das Stannoldimer (n = 2) eine Photoinstabilität aufwies, welche nicht für das Stannolmonomer (n = 1) beobachtet werden konnte. Die photo- und elektrochemische Instabilität stehen somit dem Vorteil des stabilisiertem LUMO Niveaus gegenüber. Für eine weitere Anwendung in der organischen Elektronik sollten die Parameter zunächst optimiert werden.

Kapitel II: Einfluss von Tetrelen (C, Si, Ge, Sn) auf die strukturellen, thermischen und optischen Eigenschaften von Azobenzolderivaten

Die Substitution funktioneller Moleküle mit schweren (Organo-)Tetrelen ist vielversprechend, da sie als synthetische Vorstufen für Metall-Lithium-Austausch oder Übergangsmetall-katalysierte Kreuzkupplungsreaktionen dienen können. Dieses Konzept konnte für *ortho*-stannylierte Azobenzole realisiert werden (Schema 1).
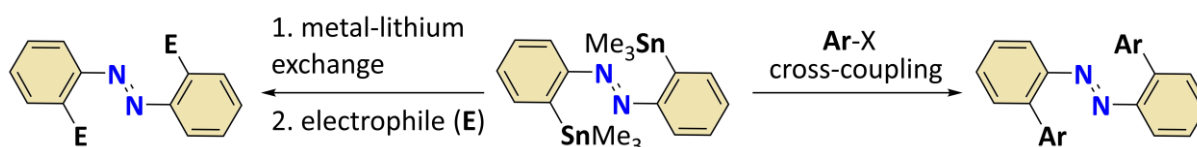
Schema 1: 2,2'-*bis*(Trimethylstannyl)azobenzol als Edukt für Kreuzkupplung und Metall-Lithium-Austauschreaktionen.

Die Trimethylzinngruppen könnten über eine Kreuzkupplung von Hexamethylditin und einem orthohalogenierten Azobenzol eingeführt werden. Daraufhin folgte eine Untersuchung des Zinn-Lithium-(Kupfer)-Austausches und die anschließende Reaktion mit verschiedenen Elektrophilen. Unter Verwendung des "weichen" Cuprats als Vorstufe konnten höhere Ausbeuten für "weiche" Nucleophile erhalten werden, z.B. Methyliodid oder Trimethylsilyliodid. Durch den Zinn-Lithium-Austausch konnte auch das *bis*(*ortho*-Methythio)azobenzol erhalten werden. Dessen Kristallstruktur wurde weiterhin durch Hirshfeld-Oberflächenanalyse untersucht. Insgesamt konnten vier *ortho*-Trimethyltetrel-substituierte Azobenzole (C, Si, Ge, Sn) synthetisiert und der Einfluss der Tetrelgruppe auf die strukturellen, thermischen und photophysikalischen Eigenschaften des Azobenzols untersucht werden (Fig. 2).
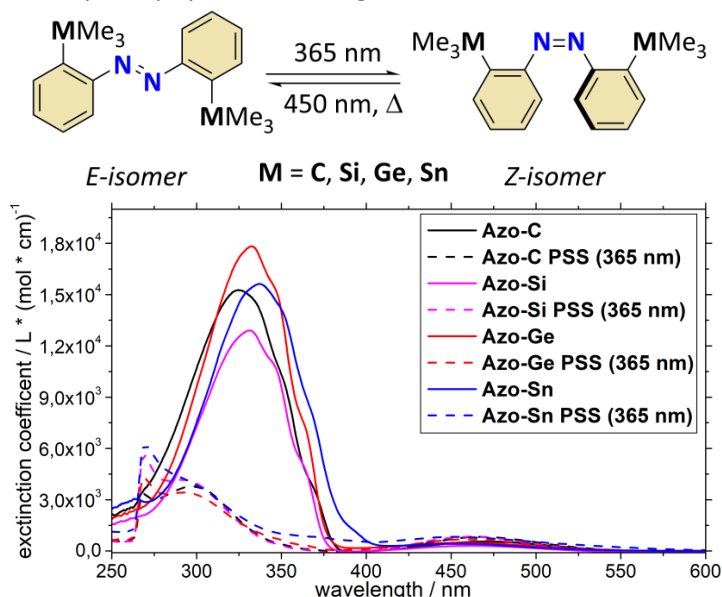

Fig. 2: Absorptionsspektren der substituieren Azobenzole vor und nach Bestrahlung mit UV-Licht (365 nm).

Alle Azobenzole konnten durch UV-Licht in ihre *Cis*-Form überführt werden. Hierbei wurde festgestellt, dass zinnhaltige Azobenzole sich durch Bestrahlung zersetzten. Diese neuen Azobenzole könnten zukünftig für Si, Ge und Sn-spezifische Kreuzkupplungsreaktionen mit verschiedenen Arylhalogeniden verwendet werden. Erste Reaktionen unter Stille-Kreuzkupplungsbedingungen zeigten positive Ergebnisse für diesen Reaktionstyp. Für weitere Projekte stellt das dinukleophile Azobenzol einen geeigneten Vorläufer für *ortho*-verbrückte Azobenzole (z. B. Diazocine) dar.

Vorwort B: Integration von Triel/Pnictogen-Gruppen in organischen Strukturen, um verbesserte optoelektronische Eigenschaften zu erhalten

Die isoelektrische Substitution einer C=C-Einheit in einem cyclischen π-konjugierten System durch eine BN-Einheit oder BP-Einheit beeinflusst effektiv die Geometrie, Polarisation, Aromatizität und vor allem die HOMO/LUMO-Lücke des Ringsystems. Der Fokus hierbei lag im Besonderen auf die resultierende bathochrome Verschiebung, welche für Materialien mit Anwendung in der organischen Elektronik (OSC, OFET, OLED) sehr vorteilhaft ist. Die Hauptunterschiede zwischen BN- und BP-Einheiten in Kohlenstoffgerüsten basieren hauptsächlich auf geometrischen und elektronischen Faktoren: Während das Stickstoffatom in BN-Systemen trigonal planar ist, bevorzugt Phosphor üblicherweise eine pyramidale Geometrie in BP-Einheiten. Diese P-Pyramidalisierung ist durch stereoelektronische Substituenten am Phosphor kontrollierbar und kann auch in eine planare Konfiguration überführt werden.

Kaptiel III: Synthese, optoelektronische Eigenschaften und Anwendung von Bor/Stickstoff-modifizierter Coronene Diimde in organischer Elektronik (OLED/OFET)

Bisher konzentrierte sich die Vielzahl der bekannten BN-substituierten PAKs auf elektronenreiche und elektronenneutrale Strukturen. Hingegen wurde die Kombination von BN-Einheiten mit elektronenakzeptierenden PAKs kaum erforscht. Eine der am meisten untersuchten elektronenakzeptierenden Molekülengruppen sind Rylendiimide, z.B. Naphthalindiimide (**NDI**), Perylendiimide (**PDI**) und Coronendiimide (**CDI**). Die longitudinale π-Extension der Rylenediimide, z.B. von **NDI** zu **PDI**, führt generell zu einer bathochrome verschobenen Absorption/Emission. Im Gegensatz dazu führt die laterale π-Extension, z.B. von **PDI** zu **CDI**, zu nachteilhaften optischen Eigenschaften, z.B. hypsochrome Verschiebung der Absorption und geringere Fluoreszenzquantenausbeute. In diesem Projekt wurde untersucht, ob die Einführung von zwei BN-Einheiten in **CDI**s, daher **BNCDI**s, deren optoelektronischen Eigenschaften beeinflussen können. Daher wurde die laterale Extension von aminosubstituierten Perylendiimiden zu **BNCDI**s mittels einer elektrophilen Borylierung entwickelt (Schema 2).
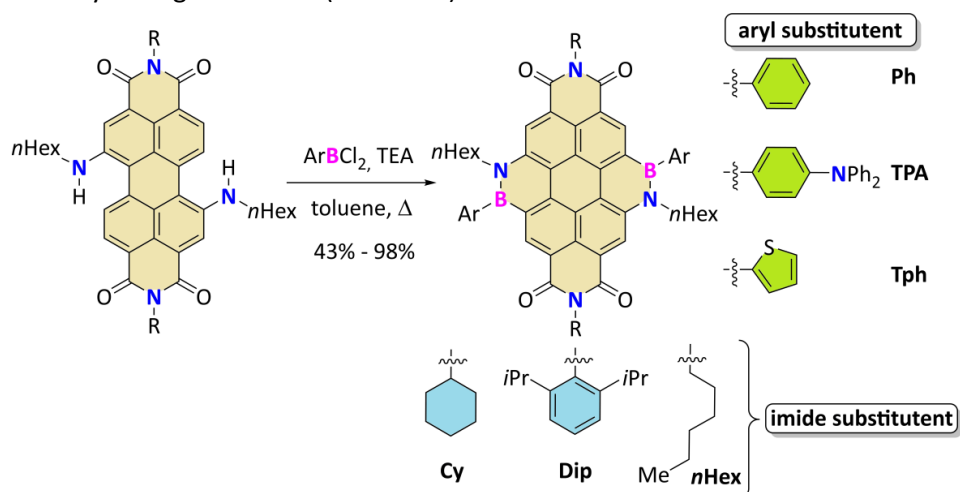
Schema 2: Durch duale elektrophile Borylierung von variablen Dichloroarylboranen mit 1,7-Di(*n*-hexyl)-substituierten PDIs, welche unterschiedliche Imidsubstituenten hatten, konnten gesamt sieben **BNCDI**s dargestellt werden.

Die Struktur-Eigenschafts-Beziehung dieser neuen BN-PAKs wurden durch Variationen der Imid- und Arylsubstituenten untersucht: Die Imidsubstituenten sollten das Aggregationsverhalten der **BNCDI**s beeinflussen, während die Arylsubstituenten einen direkten Einfluss auf die optoelektronischen Eigenschaften haben sollten. Insgesamt konnten sieben **BNCDI**s in guten bis ausgezeichneten Ausbeuten dargestellt werden.

Die **BNCDI**s zeigten verbesserte optoelektronische Eigenschaften im Vergleich zu den C=C-analogen Coronen Diimiden: Es wurde eine starke bathochrome Verschiebung und ein höherer molarer Extinktionskoeffizient im Vergleich zu den **CDI**s erhalten. Des Weiteren wurden kleine Stokes-Verschiebungen und hohe Quantenausbeuten (> 94%) beobachtet (Fig. 3).
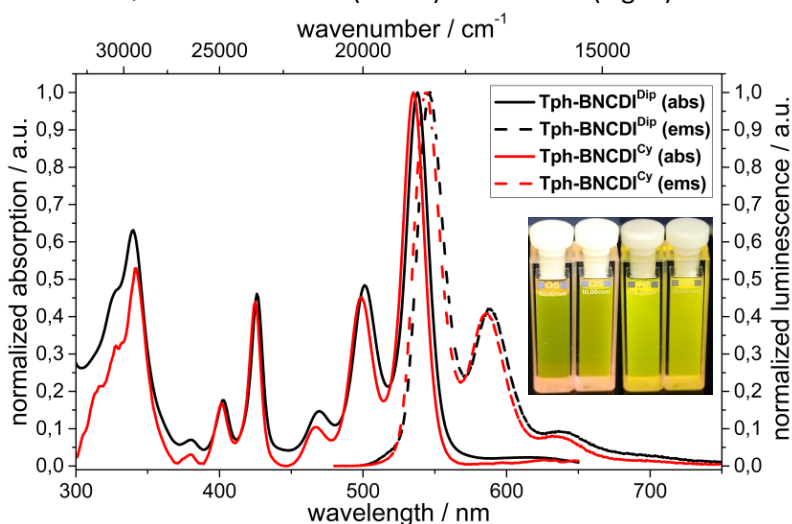

Fig. 3: Absorption- und Emissionsspektren von **Tph-BNCDI^{Cy}** und **Tph-BNCDI^{Dip}**. Weiterhin ist ein Foto der beiden Substanzen in DCM Lösungen bei Tageslicht und unter Bestrahlung (365 nm) abgebildet.

Die Absorptionsspektren waren der Absorption von **CDI**s eher ähnlich als von **PDI**s. Dies wurde durch die nachteilige vertikale (**CDI**-ähnliche) und longitudinale (**PDI**-ähnliche) Ausrichtung der Grenzorbitale erklärt. Die Wirkung der Imidsubstituenten auf die optoelektronischen Eigenschaften war in Lösung gering, unterschied sich jedoch im Feststoff erheblich. Für die Festkörperuntersuchungen der **BNCDI**s wurden zwei Thienyl-substituierte **BNCDI**s ausgewählt, die sich nur in der Imidposition unterscheiden (2,6-Di*iso*propylphenyl vs. Cyclohexyl) (Fig. 4).
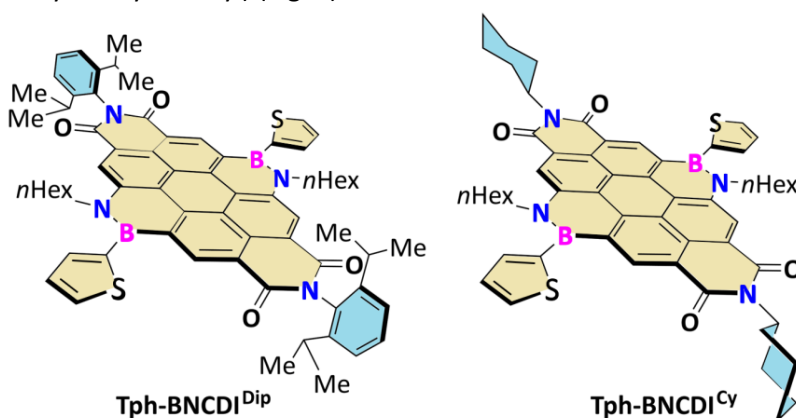
Fig. 4: Strukturen von **Tph-BNCDI^{Cy}** und **Tph-BNCDI^{Dip}**.

Die Cyclohexyl- und 2,6-Di*iso*propylphenyl-substituierten **BNCDI**s zeigten divergierende Aggregationseffekte, die initial durch Tieftemperatur-Lumineszenzspektroskopie bestimmt werden konnte. Verdünnungsexperimente mit einer transparenten festen Matrix (PMMA) zeigten, dass beide **BNCDI**s bei steigender Konzentration aggregationsbedingte Lumineszenzquenchprozesse (ACQ) vorlagen. Insgesamt wurde gezeigt, dass das Cyclohexylmotiv die Aggregation weniger wirksam

verhinderte als der 2,6-Di*iso*propylphenyl-imidsubstituent. Aufgrund ihrer optimalen optoelektronischen Eigenschaften und thermischen Stabilität wurden beide **Tph-BNCDI**s in Mehrschicht-OLEDs eingesetzt. Da vorher gezeigt wurde, dass reine **BNCDI**s nicht lumineszierten, weil sie ACQ-Effekten unterlagen, wurden sie zusammen mit blauen Emittermatrizen (**DPVBi** und **CBP**) verdampft. Hierdurch konnten Aggregationsprozess unterdrückt werden. Die resultierenden Elektrolumineszenzspektren variierten in Abhängigkeit der Matrix und in Bezug auf die entsprechenden Imidsubstituenten der **Tph-BNCDI**s (Fig. 5).
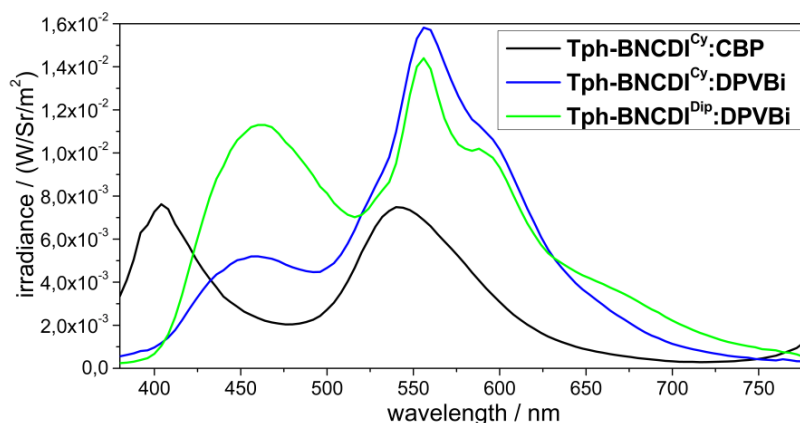

Fig. 5: Elektrolumineszenspektren der hellsten OLEDs basierend auf zwei **Tph-BNCDI**s, welche sich nur an der Imidposition unterschieden. Für die OLEDs wurden zwei Matrizen verwendet (**CBP** und **DPVBi**).

In Kombination mit den blau emittierenden Matrizen wurden in einigen Fällen weiß leuchtende OLEDs (WOLEDs) mit einer externen Quanteneffizienz (EQE) von bis zu 1.5% hergestellt. Darüber hinaus wurden überraschend niedrige Einschaltspannungen (3.7 V) und eine Leuchtdichte von bis zu 1001 cd/m^2 erhalten. Während dieser Studie wurde festgestellt, dass bei erhöhten **BNCDI**-Dotierungsraten die Leistung der OLEDs signifikant abnahm. Dies wurde den ACQ-Prozessen zugeordnet, die zuvor in den Experimenten mit PMMA-Mischung und Tieftemperatur-Lumineszenz beobachtet wurden. Darüber hinaus konnte mit dem stärker aggregierenden **Tph-BNCDI^{Cy}** eine OFET erstellt werden, welche nur eine schwache Funktionsweise aufwies (I$_{on}$/I$_{off}$ = 36, Feldeffektmobilitäten (μ$_{FE}$) im Bereich von 10^{-8} cm^2 V^{-1} s^{-1}, Schwellenspannung V$_{th}$ ≈ 20 V).

Da somit der Einfluss des Imidsubstituenten auf die Festkörperlumineszenz und Leistung in OLEDs untersucht wurde, wurde anschließend der Einfluss der Arylgruppen am Boratom betrachtet. Zum ersten Mal in der BN-Chemie wurde das Boratom eines elektronenarmen BN-PAKs mit einem elektronenreichen Substituenten, hier Triphenylamin verbunden, was zur Bildung einer formellen D-A-D-Triade mit besonderen Absorptions-/Emissionsspektren führte (Fig. 6).

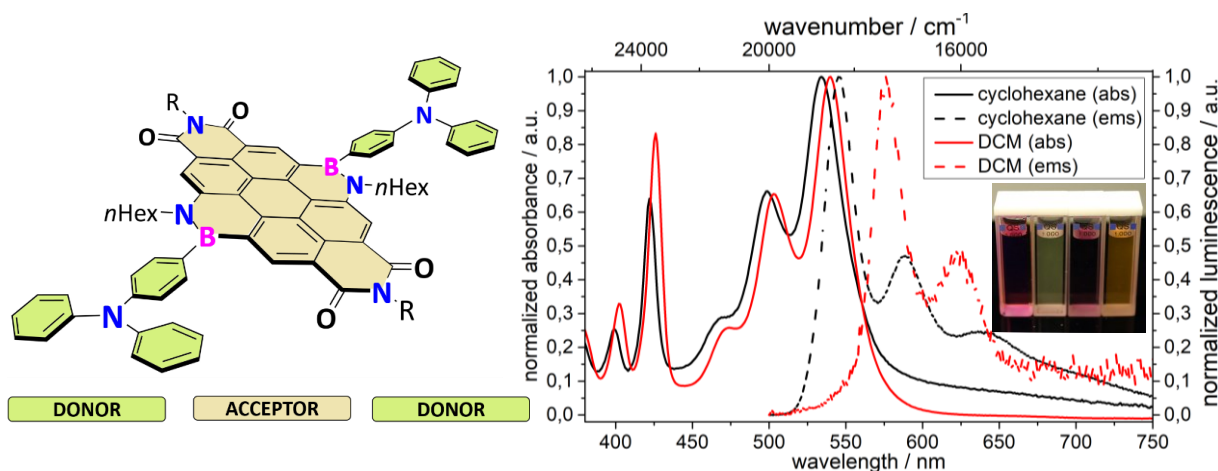**Fig. 6**: Absorption- and Emissionspektren von **TPA-BNCDI^{Cy}** in DCM und Cyclohexan. Das Bild zeigt das entsprechende **TPA-BNCDI^{Cy}** in DCM (links)/Cyclohexan (rechts) und das **TPA-BNCDI^{Dip}** in DCM (links)/Cyclohexan (rechts) unter UV-Licht.

Überraschenderweise führte diese Kombination von stark elektronenreichen Triphenylamin mit elektronenziehendem **BNCDI** zu schwach lumineszierenden Lösungen in DCM mit größerer Stokes-Verschiebung. Im Gegensatz dazu wurden in unpolaren Lösungsmitteln hohe Fluoreszenzquantenausbeuten und kleiner Stokes-Verschiebungen beobachten. Da ein solches Verhalten für Phenyl/Thienyl-substituierte **BNCDI**s nicht vorhanden war, war der Effekt eindeutig auf stereoelektronische Effekte des Triphenylamins am Boratom zurückzuführen. Um diesen Effekt besser zu verstehen, wurden die **TPA-BNCDI**s durch Cyclovoltammetrie untersucht und mit den **Tph-BNCDI**s verglichen (Fig. 7).
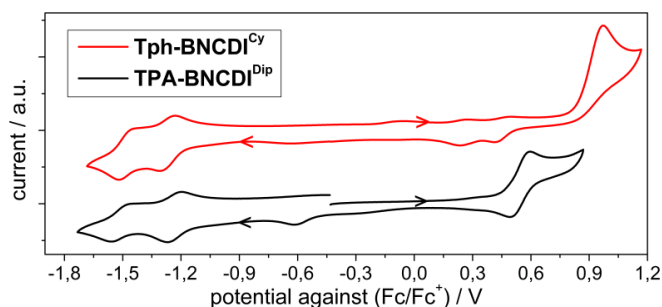

Fig. 7: Cyclovoltammogram von **TPA-BNCDI^{Dip}** und **Tph-BNCDI^{Cy}** (10^{-3} M) in DCM mit nBu$_4$NPF$_6$ (0.2 M) als Leitsalz.

Die Triphenylamin-substituierten **BNCDI**s zeigten ein signifikant niedrigeres Oxidationspotential und damit eine verringerte HOMO/LUMO-Lücke. Dies konnte die lösungsmittelabhängige Lumineszenz der **TPA-BNCDI**s erklären, welche einem photoinduziertem Elektronentransfer zugeordnet werden konnte. Zusätzlich zeigten Triphenylamin-substituierte **BNCDI**s vollständig reversible Redoxeigenschaften, die durch spektroelektrochemische Experimente beobachtet wurden und die Stabilität der neuen BN-basierten D-A-D-Triade belegen. Darüber hinaus wurden diese neuen Systeme auch auf ihre Reaktion mit Lewis-Basen und Lewis-Säuren untersucht, was zu Spezies führte, die eine Absorption in der NIR-Region des Lichts aufwiesen (Fig. 8).
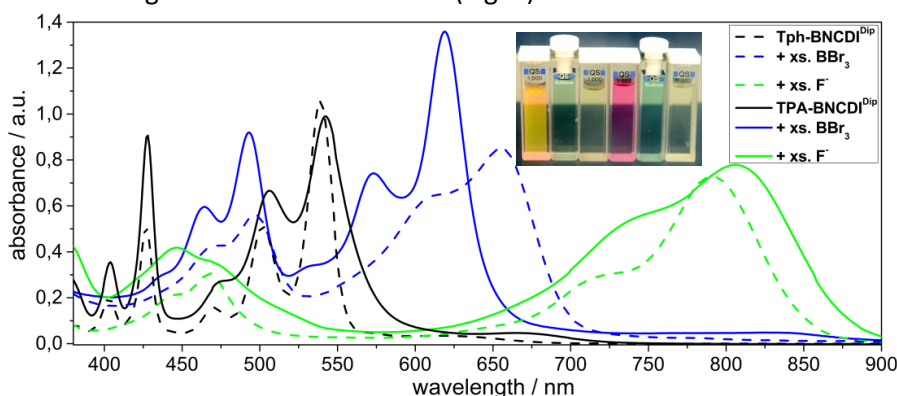

Fig. 8: Absorptionsspektren von **TPA-BNCDI^{Dip}/Tph-BNCDI^{Dip}** und die resultierenden Spezies nach Interaktion BBr$_3$ und TBAF. Das Foto zeigt **Tph-BNCDI^{Dip}** in DCM, mit BBr$_3$ und TBAF (von links nach rechts) und **TPA-BNCDI^{Dip}** in DCM, mit BBr$_3$ und TBAF (von links nach rechts).

Die Titration von **BNCDI**s mit einer Fluoridquelle oder Bortribromid ergab, dass die Bildung der Lewis-Addukte in einem zweistufigen Prozess stattfindet. Dies bedeutet, dass jede BN-Einheit einzeln mit der Lewis Säure oder Base interagiert. Daher wechselwirkten beide BN-Einheiten unabhängig als Lewis-Base/Säure. Trotz seines polaren Charakters war das Fluorid-**BNCDI**-Addukt immer noch emittierend und zeigte ein breites Emissionssignal im NIR-Bereich (700-1000 nm). Dies könnte für hochsensitive analytische Nachweiszwecke nützlich sein. Darüber hinaus zeigten alle **BNCDI**s eine Wechselwirkung mit schwach koordinierenden Lösungsmitteln, z.B. THF, Acetonitril oder Triethylamin, wie sich durch bathochrome verschobene Absorptionsmaxima darstellte. Ein zusätzlicher Effekt des Triphenylamins auf die Lewis-Acidität/Basizität oder Koordination durch Lösungsmittel wurde nicht beobachtet. Es

wurde konkludiert, dass Konformationsänderungen der BN-Einheit durch Koordination drastische Auswirkungen auf die Planarität des Coronendiimidkerns hatten und daher zu einer bathochrom verschobenen Absorption/Emission führten.

Kapitel IV: BP-substituierte polyzyklische Kohlenwasserstoff

Obwohl im letzten Jahrzehnt über zahlreiche BN-substituierte cyclische oder polycyclische Systeme berichtet wurde, ist Forschung von BP-substituierten π-konjugierten Systeme und eine detaillierte Untersuchung ihrer optoelektronischen Eigenschaften kaum beschrieben. BP-substituierte polycyclische aromatische Kohlenwasserstoffe haben ein großes Potenzial in der organischen Elektronik, da eine Stabilisierung des LUMO-Niveaus im Vergleich zu CC/BN-PAKs zu einer geringeren HOMO/LUMO-Lücke führen sollte. Darüber hinaus ist das Potential von BP-substituierten Verbindungen für zusätzliche chemische Postmodifikationen (Oxidation, Komplexierung) am Phosphoratom, die zur Modifikation der optoelektronischen Eigenschaften genutzt werden können, aufgrund ihrer Unzugänglichkeit bislang nicht bekannt.

Um den Effekt einer BP-Substitution zu untersuchen, wurden in diesem Projekt Dibenzochrysen (**DBC**) und Tetrathienonapthalen (**TTN**) als Kohlenstoffgerüst ausgewählt. Da bereits BN-substituierten **DBC/TTN**s erfolgreich synthetisiert wurden, sollte ein direkter Vergleich mit den BP-substituierten Strukturen möglich sein. Zunächst wurden die BP-substituierten Strukturen mit ihren CC/BN-Kongeneren durch quantenchemische Rechnungen verglichen. Hierbei wurde im Speziellen die geometrischen und elektronischen Effekte des Phosphors in den BP-Einheiten hervorgehoben. Aufgrund des geräumigen und pyramidenförmigen Phosphoratoms zeigten die entsprechenden **BP-DBC /BP-TTN** im Vergleich zu den CC/BN-Strukturen eine stärker verdrehte Geometrie oder eine Lokalisierung außerhalb der BP-Bindungsebene (Fig. 9).
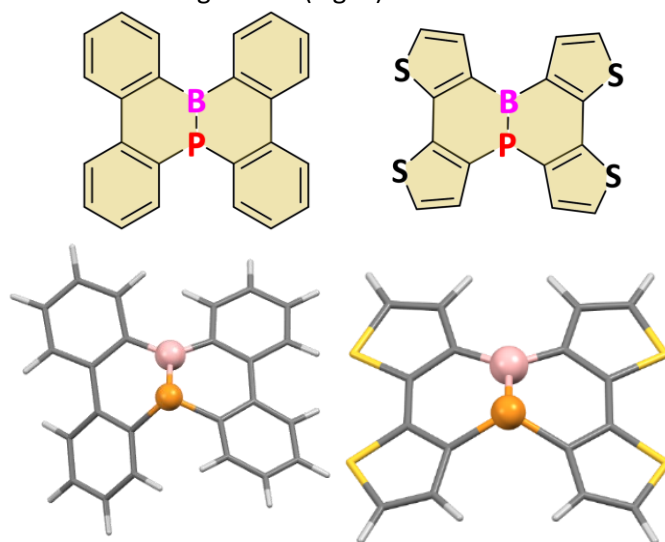
Fig. 9: Die optimierten Geometrien (B3LYP-6-31G*) von BP-substituierten Dibenzo[g,p]chrysen (**BP-DBC**) und Tetrathienonaphthalen (**BP-TTN**).

Die Summe der Winkel an den Phosphoratomen ($\Sigma = 309.88°/332.63°$) indizierte eine Pyramidalisierung des Phosphors. Daher wurde eine geringere Wechselwirkung des Phosphors mit den benachbarten Bor- oder Kohlenstoffatomen vermutet. Darüber hinaus wurde die Bindung der BP-Strukturen durch NBO-Analyse (Natural Bond Occupation) analysiert. Im **BP-TTN**-Derivat war eine klassische B=P-Bindung vorhanden, während das **BP-DBC**-Derivat eine Einfachbindung in Kombination mit einer Lewis-Paar-Beschreibung aufwies. Da das freie Elektronpaar am Phosphoratom kaum mit dem Boratom wechselwirkte, könnte es für eine weitere Postfunktionalisierung des **BP-DBC** zugänglich sein, um weiterhin das HOMO/LUMO-Niveau zu modifizieren. Abgesehen von geometrischen Effekten

beeinflussten die BP-Einheiten die elektronischen Strukturen der **DBC**- und **TTN**-Motive: Es wurde ein stabilisiertes LUMO-Niveau und eine bathochrom verschobene Absorption im Vergleich zu den jeweiligen CC/BN-Kongeneren berechnet. Die Bestimmung der nucleus independent chemcial shifts (NICS) ergaben, dass der Zentralring im Vergleich zu seinen CC/BN-Kongeneren eine verringerte Aromatizität aufwies. All diese theoretischen Erkenntnisse waren für eine Anwendung in der organischen Elektronik vielversprechend.

Im Allgemeinen sind Methoden zur Synthese von BP-PAKs kaum beschrieben. In Analogie zur BN-Chemie sollten neuartige Synthesemethoden zur Herstellung von BP-substituierten PAK durch Annellierungsreaktionen eines Phosphins in *bay*-Position untersucht werden (Schema 3).
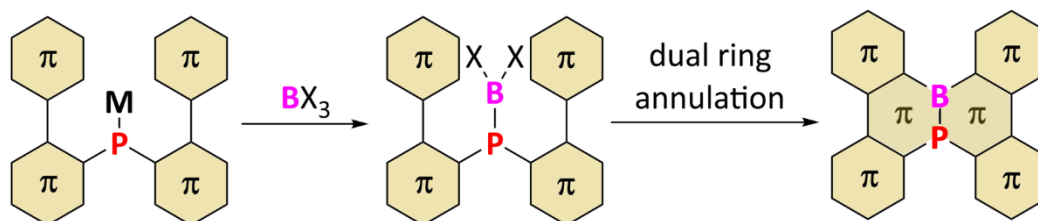
Schema 3: Synthese von BP-annullierte konjugierte Systeme durch Borylierung von *bis*(Diaryl)phosphiden.

Die finale doppelte Annelierungsreaktion stelle hierbei die größte Herausforderung dar, da die BP-Bindung in diesem Falle relativ instabil ist.

Um diese Reaktionen durchzuführen, wurde die Synthese von **BP-DBC** forciert. Hierfür wurde das *bis*(Biphenyl)phosphin dargestellt. Dies gelang durch Reaktion von einer Arylmagnesiumbromid Spezies, welche mit einem halben Äquivalent eines geschützten elektrophilen Phosphors umgesetzt wurde. Das erhaltene Aminophosphine wurde dann mit etherischer Salzsäure entschützt und mit Lithiumaluminiumhydrid zum Phosphin reduziert (Schema 4).
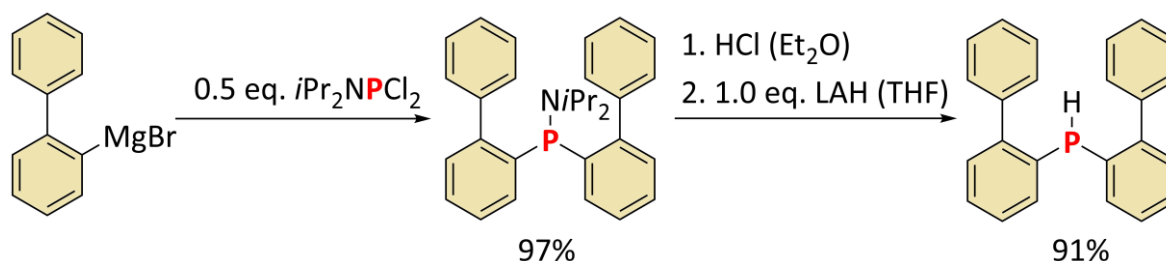
Schema 4: Die Synthese des Phosphoramids und des Phosphans

Beide Synthesen wurden optimiert, sodass hohe Ausbeuten erzielt wurden. Weiterhin konnten Kristallstrukturen dieser Verbindungen und des geschützten Phosphans erhalten werden (Fig. 10)
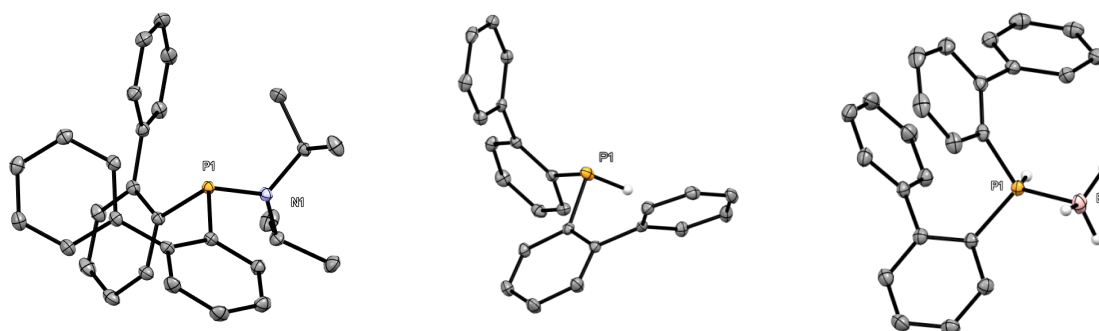

Fig. 10: Kristallstrukturen des Phosphans, des Phosphinaminds und des mit Boran-geschütztem Phosphans.

Das Phosphin konnte anschließend in das entsprechende Phosphid und zwei Trimethyltetrelphosphine überführt werden um danach Reaktionen mit elektrophil Borverbindungen durchzuführen (Schema 5).

Schema 5: Reaktionsübersicht, um das Zielmolekül **BP-DBC** zu synthetisieren.

Zumeist scheiterten die Versuche die BP-substituierten PAKs zu erhalten und die Bildung von Phosphin-Boran-Addukten wurde beobachtet. Die versuchte Eliminierung von HX war nicht erfolgreich. Ähnliche Ergebnisse wurden durch Tetrel (Si/Sn)-Bor-Austauschreaktionen erhalten. Die Reaktion der nukleophilen Phosphinderivate mit verschiedenen elektrophilen Boranen zeigte, dass die Lewis-Azidität der Borane einen großen Einfluss auf die Reaktion selbst hatte.

Im Gesamten konnte gezeigt werden, dass die Lewis Acidität der Borspezies entscheidenden Einfluss auf die Stabilität der BP-Verbindung hatte. Nur die milde Lewis-Säure (Et$_2$N)$_2$BCl konnte in diesem Projekt mit einem Phosphid umgesetzt werden, so dass eine niedrigvalente BP-Struktur erhalten wurde.

Die Stabilität der BP-Verbindung war nur für schwache Lewis-Säuren gegeben was im Gegensatz zu der starken Lewis Acidität für die Ringschlussreaktionen steht (Schema 6).

isolated for R = **N**Et$_2$ (weaker Lewis acid)
not obseved for R = Br, Cl (strong Lewis acid)

Schema 6: Einfluss der Lewis Acidität auf die Stabilität der BP-Verbindung.

Eine mögliche Lösung für dieses Problem ist die Aktivierung der schwachen Lewis Säuren durch Entschützung, welches erstmalig in dieser Arbeit probiert wurde.